

UNIVERSITÉ DE STRASBOURG

École doctorale des Sciences de la Terre et de l'environnement (ED 413)

Institut Terre et Environnement de Strasbourg, UMR 7063

THÈSE présentée par :

Flora HOCHSCHEID

soutenue le : **8 décembre 2022**

pour obtenir le grade de : **Docteur de l'Université de Strasbourg**

Discipline/ Spécialité : Géologie - Géochimie

Traceurs géochimiques des interactions fluide-roche dans les domaines de manteau exhumé : une étude des processus de serpentisation, du terrain au laboratoire

THÈSE dirigée par :

M. ULRICH Marc

Maître de conférences, Université de Strasbourg - ITES

M. MUÑOZ Manuel

Professeur des Universités, Université de Montpellier - Géosciences Montpellier

RAPPORTEURS :

Mme. CANNAT Mathilde

Directeur de recherche CNRS, Sorbonne Université - IPGP

M. BRUNET Fabrice

Directeur de recherche CNRS, Université Grenoble Alpes - ISTerre

EXAMINATEURS :

Mme. DELACOUR Adélie

Maître de conférences, Université Jean Monnet Saint-Etienne - LGL

M. MILLOT Romain

Directeur de recherche, BRGM Orléans

M. MANATSCHAL Gianreto

Professeur des Universités, Université de Strasbourg - ITES

INVITÉ :

M. LEMARCHAND Damien (encadrant)

Maître de conférences, Université de Strasbourg - ITES

Remerciements

Tout d'abord, je tiens à remercier les membres du jury, Mmes Mathilde Cannat et Adélie Delacour, ainsi que M Fabrice Brunet et Romain Millot d'avoir accepté de juger mon travail de thèse.

Mes remerciements vont ensuite à mes directeurs et encadrant de thèse, Marc Ulrich, Manuel Muñoz et Damien Lemarchand. Marc, merci de m'avoir fait confiance depuis ma première année de master en me proposant un stage de recherche sur les processus magmatiques en Nouvelle Calédonie. Merci de m'avoir proposé de continuer dans la recherche et de découvrir la serpentinitisation. Merci pour m'avoir transmis ton savoir depuis toutes ces années. Manu, merci d'avoir co-encadré cette thèse avec Marc. Merci pour ta pédagogie tout au long de cette thèse, malgré la distance. Damien, merci pour ton aide sur la géochimie du bore. Merci pour ta patience et le temps accordé pendant cette thèse. Gianreto Manatschal, merci d'avoir été présent dès que j'avais une question sur les marges. C'est toujours un plaisir d'échanger avec toi sur ce sujet.

Je tiens également à remercier les ingénieurs de recherche de l'ITES Mathieu Granet, Eric Pelt, René Boutin, Amélie Aubert sans qui tout le travail accompli durant cette thèse n'aurait sans doute pas été possible. Mathieu, un grand merci pour ton aide et ton soutien pendant les longs mois de galère avec le Neptune. Cette période compliquée aura été au final très enrichissante pour moi, me permettant de comprendre en détail le mécanisme du Neptune. Eric, tout d'abord merci pour ton encadrement durant mon stage de Master 2. Merci de m'avoir initiée à l'isotopie (Sr, Nd, Hf), et formée aux mesures isotopiques au Neptune et au Triton. Merci pour le temps passé à m'aider à comprendre les problèmes rencontrés lors des séparations sur colonnes. René, merci pour toutes les analyses que tu as effectuées pour moi, depuis 6 ans maintenant. Amélie, merci pour toutes les analyses DRX, merci pour le temps que tu m'as accordé pour mes séparations minérales. Thierry Perrone, merci pour tous les coups de mains accordés depuis toutes ces années, que ce soit en salle blanche ou expérimentale, tu ne m'as jamais laissé sans solution. Merci également à Sophie Gangloff, Colin Fourtet pour avoir effectué les analyses anioniques, John Moine pour avoir fait toutes mes lames minces.

Florian Osselin, merci de m'avoir ouvert les portes de l'ISTO avec Michel Pichavant pour que je puisse faire mes expériences de serpentinitisation. Sans vous une partie de

cette thèse n'aurait pas vu le jour. Merci pour ton accueil et le temps accordé durant chacun de mes déplacements. Merci également au personnel technique de l'ISTO, Rémi Champallier et Frédéric Savoy qui m'ont aidé pour l'ouverture des autoclaves. Merci à Ida Di Carlo pour son aide pour les analyses MEB.

Une pensée pour mes collègues doctorants et post-doctorants passés par l'ITES : Pierre Olivier Couette, Coralie Ranchoux, Beshad Koohbor, Matthias Oursin, Manon Lincker, Nicolas Dall'Asta... on aura quand même passés de bons moments à Strasbourg et en conférences !

Merci à ma famille, qui m'a laissé le choix dans mes études. Merci pour votre soutient.

Merci également à mes amis qui sont toujours présent : Jennifer, Florianne, Laura, Anthony, Anaïs. Merci à mes copines de l'écurie, mes camarades de course de l'ASL la Robertsau, mes coachs... qui m'ont permis de penser à autre chose que la thèse autour d'une balade à cheval ou sur la piste d'athlé.

Et pour finir, un grand Merci à Xavier qui a toujours été présent et me soutient quotidiennement depuis toutes ces années. Merci de croire en moi, de m'encourager (et de me supporter!).

Table des matières

1	Introduction	8
1.1	General background	9
1.1.1	Serpentinization	9
1.1.2	The serpentine minerals	10
1.1.3	Stability of serpentine species	11
1.1.4	The (micro)-textures of serpentine	13
1.1.5	Methods for identify the serpentine polymorphs	15
1.1.6	Serpentinization in natural environments	18
1.2	Major issues	22
1.3	Geological study	23
1.3.1	Evolution of the Alpine Tethys magma-poor rifted margins through time	23
1.3.2	Geological setting	25
1.4	Experimental study	33
1.4.1	Previous serpentinization experiments	33
1.5	Geochemical tools	45
1.5.1	Geochemical tracers	45
1.5.2	Geothermometer	48
1.6	Approach of the thesis	49
2	Materials and methods	65
2.1	Geological study	66
2.1.1	Sampling strategy	66
2.1.2	Sample preparation and analytical investigations	67
2.2	Experimental study	79
2.2.1	Experimental approach	79
2.2.2	Sample preparation and analytical investigations	83

3 The Sr isotope geochemistry of oceanic ultramafic-hosted mineralizations	87
3.1 Introduction	89
3.2 Geological setting	90
3.2.1 The Platta nappe	90
3.2.2 The Marmorera-Cotschen Hydrothermal System	92
3.3 Methods	94
3.3.1 Field sampling	94
3.3.2 Analytical methods	95
3.4 Sr isotope compositions of altered rocks from the Platta nappe	98
3.4.1 Fe-Ca silicates in veins and pervasively replacing serpentinites	98
3.4.2 Carbonates veins and shear bands in serpentinites and basalts	98
3.4.3 Serpentinites	98
3.4.4 Mafic rocks	99
3.4.5 Rodingites and blackwalls	99
3.5 Discussion	101
3.5.1 Multiple Sr reservoirs involved during seafloor hydrothermalism in Ocean Continent Transition	101
3.5.2 Mineral textures as a proxy of fluid/rock ratios during hydrothermal alteration	102
3.5.3 Hydrothermal alteration during the final rifting and breakup of the Platta nappe	104
3.5.4 Timing of the hydrothermal alteration at the Marmorera-Cotschen Hydrothermal System	107
3.5.5 Consequences for the formation of ultramafic-hosted metal deposits	108
3.6 Conclusions	110
3.7 Supplementary materials	112
4 The Alpine Tethys passive margins : Serpentinization as a tape-recorder of mantle exhumation	120
4.1 Introduction	123
4.2 Geological setting	125
4.2.1 The Platta nappe	125
4.2.2 The Totalp nappe	126
4.2.3 The Tasna nappe	127
4.3 Materials and methods	129
4.3.1 Sampling and analytical strategies	129
4.3.2 X-Ray Diffraction	129

4.3.3 Raman spectroscopy	129
4.3.4 Mineral chemistry	130
4.4 Results	133
4.4.1 Petrography and micro-textures of serpentinites	133
4.4.2 Serpentine chemistry	137
4.5 Discussion	147
4.5.1 Serpentinization as a marker of multi-stages mantle exhumation	147
4.5.2 Serpentinization along the Ocean-Continent Transition zone	153
4.5.3 Is serpentinization in present-day MOR comparable to serpentinization in OCT ?	156
4.6 Conclusions	160
4.7 Supplementary materials	162
5 Fluid and mineral geochemistry during experimental seawater-based ser-	
pentinization	180
5.1 Introduction	182
5.2 Methods	184
5.2.1 Starting materials	184
5.2.2 Experimental setup	185
5.2.3 Solid samples analyses	186
5.2.4 Aqueous solution samples analyses	188
5.3 Results	188
5.3.1 Characterization of solid phase reactants and products	188
5.3.2 Bulk rock geochemistry	194
5.3.3 Fluid chemistry	197
5.3.4 Mass balance calculations	208
5.4 Discussion	213
5.4.1 Mineralogical evolution	213
5.4.2 Serpentinization, mass-fluxes and (U-)VMS, what can we learn ?	221
5.5 Conclusions	225
5.6 Supplementary materials	227
6 Experimental study of boron isotope fractionation during peridotite ser-	
pentinization by seawater from 225 to 325°C and 450 bars	238
6.1 Introduction	240
6.1.1 The distribution of boron and boron isotopes between the earth envelopes	242
6.1.2 B isotope speciation and isotopic fractionation	242

6.1.3	The boron behavior during serpentinization	246
6.2	Methods	246
6.2.1	Starting materials	247
6.2.2	Experimental setup	247
6.2.3	Mineral separation	248
6.2.4	Analyses of solids products	249
6.2.5	Mannitol procedure	249
6.2.6	Boron isotopes geochemistry	249
6.3	Results	250
6.3.1	Boron isotope geochemistry of fluid phases	250
6.3.2	Boron isotope geochemistry of solid phases	255
6.4	Discussion	260
6.4.1	How to explain the different boron isotopes fractionation recorded by fluids ?	260
6.4.2	B geochemistry of separated minerals : what do we really read ?	267
6.4.3	Effect of the temperature on B geochemistry	273
6.5	Conclusions and perspectives	276
6.6	Supplementary materials	278
7	Conclusions and perspectives	293
7.1	General conclusions	294
7.1.1	Geological study	294
7.1.2	Experimental study	295
7.2	Perspectives	297
7.2.1	Publication strategies	297
7.2.2	Perspectives	298
8	Introduction	318
8.1	Contexte général	319
8.1.1	La serpentinisation	319
8.1.2	Les minéraux de serpentine	320
8.1.3	Stabilité des espèces serpentineuse	321
8.1.4	Les (micro)-textures de serpentine	324
8.1.5	Méthodes pour identifier les polymorphes de serpentine	326
8.1.6	Serpentinisation dans les environnements naturels	329
8.2	Principaux enjeux	333
8.3	Etude géologique	334

8.3.1	Évolution temporelle des marges riftées pauvres en magma de la Téthys Alpine	334
8.3.2	Contexte Géologique	336
8.4	Etude expérimentale	344
8.4.1	Etudes expérimentales de serpentinitisation antérieures	344
8.5	Les outils géochimiques	359
8.5.1	Les traceurs géochimiques	359
8.5.2	Géothermomètres	363
8.6	Approche de la thèse	364

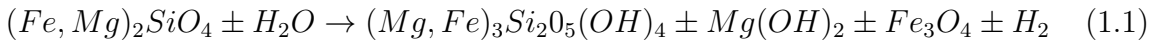
Chapitre 1

Introduction

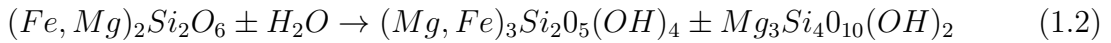
1.1 General background

1.1.1 Serpentinization

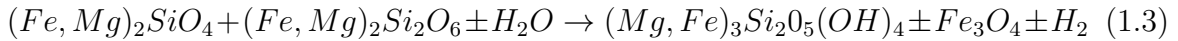
Serpentinization consists in the hydration of ultramafic rocks (i.e., peridotites) that constitute a part of the upper mantle. These peridotites are composed of primary ferro-magnesian minerals, typically olivine, orthopyroxene and clinopyroxene. During the serpentinization, in contact with fluids these ferro-magnesian minerals are replaced by secondary hydrous minerals and (hydr)-oxides as serpentine \pm talc \pm brucite \pm magnetite. Di-hydrogen can also be released if conditions are favorable (e.g., Mével 2003), reactions can be summarized as follow :



olivine \pm water \rightarrow serpentine \pm brucite \pm magnetite \pm hydrogen



orthopyroxene \pm water \rightarrow serpentine \pm talc



olivine \pm orthopyroxene \pm water \rightarrow serpentine \pm magnetite \pm hydrogen

The serpentine minerals can integrate significant amount of water in their structure, up to 13 wt.%, depending on the serpentine species. The serpentinization process occurred in most geodynamic settings, from divergent settings including the mid-oceanic ridges or passive margins, to convergent like the subduction zones. Consequently, the serpentinization take place to once water can interact with ultramafic rocks and thus, under a variety of conditions, from low temperature $<50^{\circ}\text{C}$ and pressure near the sea-floor to high temperature $\pm 450^{\circ}\text{C}$ and pressure in subduction zones (e.g., Mével 2003).

1.1.2 The serpentine minerals

The serpentine minerals are hydrous phyllosilicates which have the idealized formula $Mg_3Si_2O_5(OH)_4$. The serpentine minerals, consist of alternation of tetrahedral layers (4-coordinated Si) and octahedral layers (6-coordinated Mg; Wicks and Whittaker 1975 ; Figure 8.1). As mentioned previously, serpentization process is ubiquitous to the Earth's surface, consequently serpentine minerals formed under a wide range of temperatures, pressure and fluid chemistry, and a variety of serpentine (i.e., polymorphs) can be generated (e.g., Mével 2003). The most common serpentine polymorphs are lizardite, chrysotile, polygonal and antigorite. The lizardite, chrysotile and polygonal serpentine are mainly observed in divergent domains. However, the presence of antigorite in oceanic domains is less common, although some study have reported their presence (e.g., Roumejon et al. 2015 ; Ribeiro Da Costa et al. 2008). Antigorite is rather observe in serpentinites from convergent domains like the subduction zones (e.g., Trommsdorff and Evans 1977).

These polymorphs of serpentine result from different structural configurations (e.g., Wicks and O'Hanley 2018). The lizardite is characterized by a planar structure (Figure 8.1A), the chrysotile have a cylindrical structure (Figure 8.1B), and the polygonal serpentine display a tubular structure (Figure 8.1D). The antigorite is characterized by a wavy structure (Figure 8.1C), with a loss of an octahedral coordinates sites due to a periodic reverses of the inter layer Mellini et al. 1987. The tetrahedral sheet inverts its polarity through six and eight tetrahedral rings (6 and 8 reversals) Capitani and Mellini 2004. This periodic reversion of the inter layer allows to strengthened the covalent Si-O bounds Capitani and Mellini 2004. The antigorite has a distinct formula than the other serpentine species, characterized by : $Mg_{3m-3}Si_{2m}O_{5m}(OH)_{4m-6}$ with m being the number of tetrahedrons along an entire wavelength Mellini et al. 1987.

The chrysotile, lizardite and antigorite are characterized by different Fe^{3+}/Fe_{tot} and Si/Mg ratios, with Fe^{3+}/Fe_{tot} ratios decreasing and Si/Mg ratios increasing from lizardite to chrysotile to antigorite O'Hanley and Dyar 1993. Antigorite is systematically enriched in silica because of the loss of Mg and $(OH)_4$ with respect to Si Wicks and Zussman 1975. Furthermore, in most serpentine minerals, substitutions of Si by Al and Fe^{3+} may occur in the tetrahedral sites, and Fe^{2+} , Fe^{3+} , Cr, Al^{3+} , Ni and Mn can substitutes Mg in the octahedral sites (e.g., Page 1968 ; Mével 2003).

Caruso and Chernosky 1979 argue that the Al^{3+} and Fe^{3+} substitutions for Mg and Si allow to stabilizes lizardite. The cylindrical structure of chrysotile strongly affect its

stability (Evans 2004). It would seem that both crystals structures and substitutions can affect the stability of serpentine minerals.

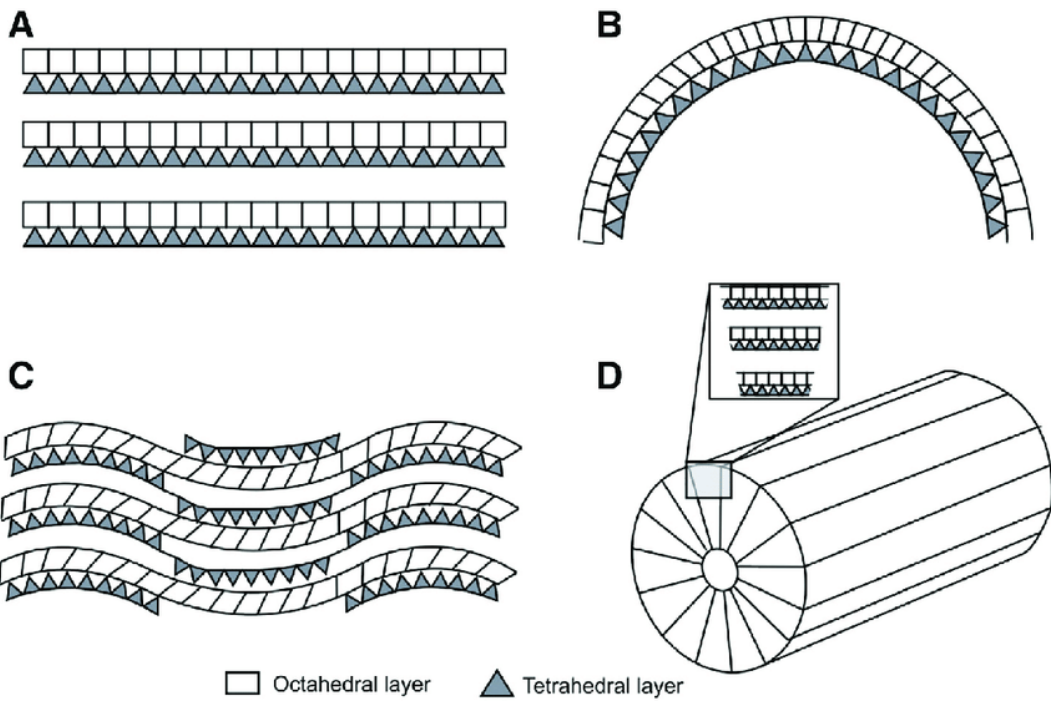


FIGURE 1.1 – Schematic representation of serpentine minerals crystal structure. A) planar lizardite, B) cylindrical chrysotile, C) modulated antigorite, D) tubular polygonal serpentine. Triangles represent 4-coordinated Si and more or less deformed squares represent 6-coordinated Mg (Figure from Mével 2003).

1.1.3 Stability of serpentine species

Based on experimental study coupled to thermodynamic data and isotopic evidence, it is generally recognized that in the $\text{MgO}-\text{SiO}_2-\text{H}_2\text{O}$ (MSH) system lizardite and chrysotile are stable at lower temperatures than antigorite Figure 8.2 (e.g., Moody 1976 ; Mével 2003 ; Evans 2004). From isotopic analyses of natural serpentinites, Wenner and Taylor 1971 estimates the temperature of lizardite formation at 125°C, chrysotile at 180°C and antigorite at 235°C (Figure 8.2). Evans et al. 1976 proposes that the chrysotile to antigorite transition occurs at temperatures between 270 and 300°C and at pressure below 0.7 GPa. More recently, the experimental results of Grauby et al. 1998, suggest that lizardite is more stable than chrysotile at 200°C and 300°C. Viti and Mellini 1998 proposes that chrysotile evolves spontaneously to polygonal serpentine and

then to lizardite serpentine by arrival of new fluids and additional time. Chrysotile is a metastable phase ?

The field observations combined to isotopic and experimental study suggested that the formation of antigorite is mostly attributed to an increase of temperature from $\sim 250^{\circ}\text{C}$ to $>500^{\circ}\text{C}$ and/or pressure (e.g., Coleman 1971 ; Wenner and Taylor 1971 ; Moody 1976 ; Wunder et al. 2001). Capitani and Mellini 2004 proposes that the periodic reverses of the inter layer in antigorite, allows to stabilize antigorite at higher temperature and pressure than the lizardite. This is in accordance with the phase diagram proposed by Evans 2004 (Figure 8.2), attesting that antigorite is stable at temperature above 350°C . However, some study have reported the presence of antigorite in oceanic domains, (e.g., Roumejon et al. 2015 ; Ribeiro Da Costa et al. 2008), raising questions about their stability fields and its conditions of formation. Especially, can we still attribute the formation of antigorite exclusively to subduction zones or their presence in divergent domains was underestimated ?

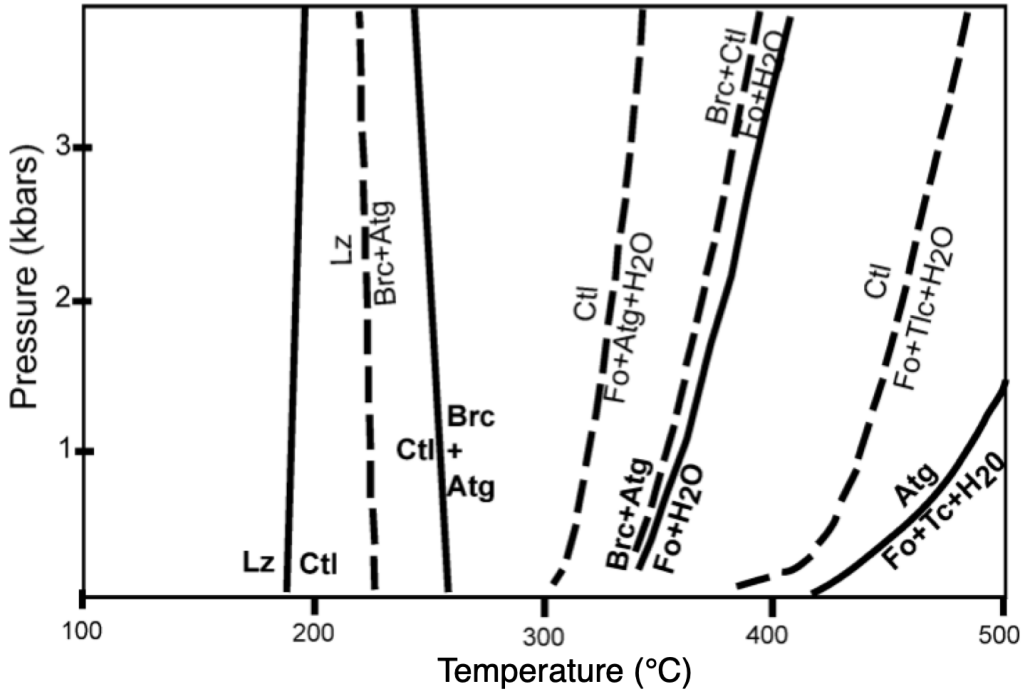


FIGURE 1.2 – A possible phase diagram for the MgO–SiO₂–H₂O (MSH) system, in function of pressure (kbar) and temperature (°C). Continuous lines represent stable reaction curves, dashed lines, metastable reaction curves. Atg : antigorite, Bct : brucite, Ctl : chrysotile, Fo : forsterite, Lz : lizardite, Tc : talc (Figure from Mével 2003).

1.1.4 The (micro)-textures of serpentine

Because serpentinization occurred in a variety of conditions (at low temperature near the seafloor to high temperature/pressure at deeper depths), a variety of serpentine (micro)-textures were observed.

The early stage of serpentinization occurred generally in static conditions, leading to the pseudomorphic replacement of olivine by serpentine lizardite in mesh or hourglass, and pyroxenes are replaced by serpentine lizardite bastite (Wicks et al. 1977; Figure 8.3A, B respectively). These textures are typically developed in abyssal serpentinites of oceanic domains (e.g., Mével 2003).

However, serpentinites contain generally several generations of serpentine veins which crosscut previous mesh and bastites textures, as observed in oceanic domains (e.g., Früh-Green et al. 1996, 1990; Dilek et al. 1997).

Typically, chrysotile occurs mostly in veins in serpentinites which already have a considerable degree of serpentinization. Chrysotile forms banded veins made of finely spaced bands perpendicular to the crack wall with low birefringence that alternates between white and black color under the cross-polarized light (Figure 8.3C), or crack-seal characterized by lens-shape and higher birefringence (Figure 8.3D). This kind of veins forms typically by extension or extensional shearing where the formation of narrow fracture is followed by filling of the open space by crystalline material (e.g., Ramsay 1980; Andreani et al. 2004). However, under the microscope it is not easy to distinguish the polygonal serpentine from the chrysotile because they can have the same appearance.

The polyhedral serpentine is characterized by a typical extinction cross under the polarized light Figure 8.3E. Polyhedral serpentine mostly forms as an alteration products of pyroxenes or in late veins Andreani et al. 2008.

Antigorite occurs in veins or patches replacing the previous serpentine textures like serpentine lizardite meshes or veins. Under the cross polarized light, antigorite are characterized by a typical interlocking texture (Figure 8.3F).

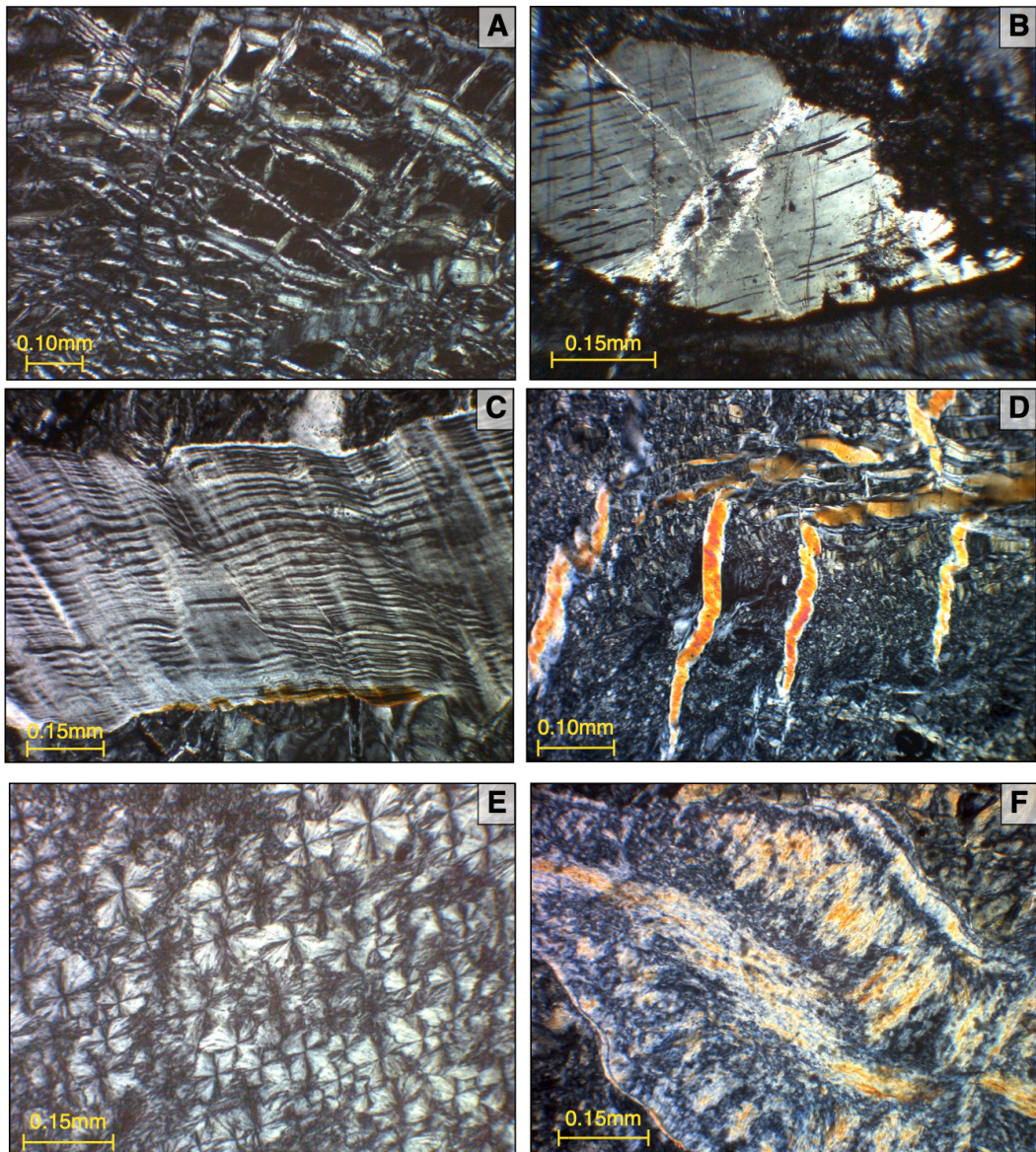


FIGURE 1.3 – Representative texture of serpentine observed under cross-polarized light. A) lizardite in pseudomorphing olivine, B) lizardite pseudomorphing bastite, C) chrysotile in banded veins, D) chrysotile in crack-seals, E) polyhedral serpentine, F) interlocking texture of antigorite (personal micro-photographs).

1.1.5 Methods for identify the serpentine polymorphs

As mentioned above, it is not always easy to identify the serpentine polymorphs solely on the basis of serpentine micro-textures. Especially it is complicated to distinguish the polygonal and polyhedral serpentine from the chrysotile. Consequently, several methods were developed to determine the polymorphs of serpentine.

The first method uses to distinguished the different serpentine species, was the X-ray diffraction (XRD) Whittaker and Zussman 1956, Wicks and Zussman 1975. However, this method requires to grind the sample, which destroys the structural relation between the coexisting phases. Although antigorite is easily distinguishable from lizardite and chrysotile, the lizardite, chrysotile, polygonal and polyhedral serpentine are poorly distinguishable by their XRD patterns.

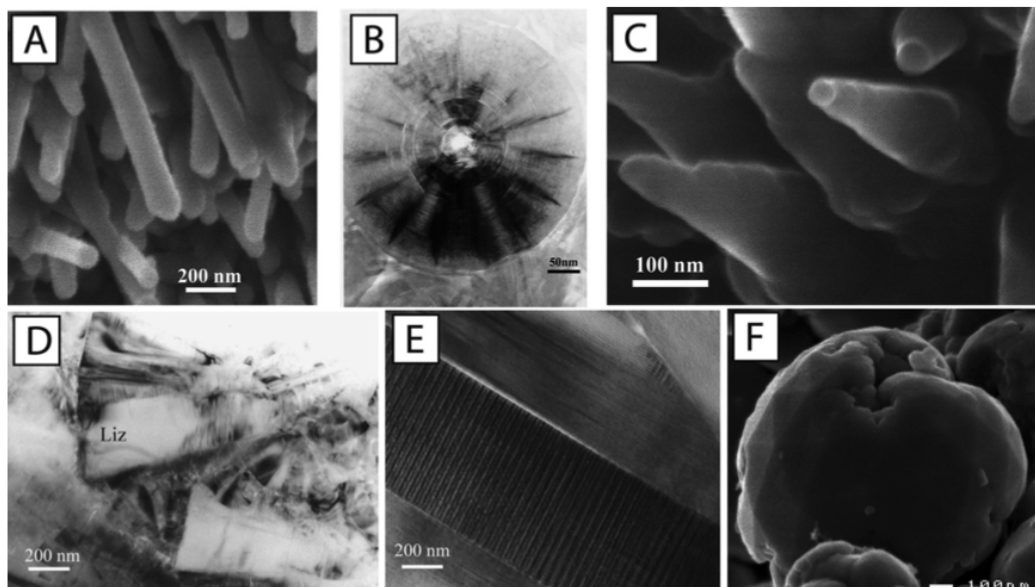


FIGURE 1.4 – Photography from scanning electron microscopy (SEM) and transmission electron microscopy (TEM) of the various type of serpentine. A) cylindrical chrysotile (SEM Figure), B) polygonal serpentine (TEM image), C) conical chrysotile (SEM image), D) planar lizardite (TEM image), E) modulated structure of antigorite (TEM), F) spherical polyhedral serpentine (Figure from Andreani et al. 2008).

The various serpentine species are better distinguishable by scanning electron microscopy (SEM) and transmission electron microscopy (TEM; e.g., Andreani et al. 2004, 2008 ; Figure 8.4). The TEM method allows to observe the crystal structure of serpentine. In particular, with this method it is possible to distinguish the polygonal serpentine from the chrysotile, the first one which is characterized by larger fibers diameter Baronnet and Devouard 1996. Today, TEM is probably the best tool for determine the serpentine polymorphs. Nevertheless, the interpretation of the electron diffraction patterns is not always easy and the sample preparation is complex.

The spectroscopy Raman is also a powerful method for distinguish the different serpentine species and have several advantages. Indeed, the Raman spectrometry is a fast and not destructive method and relatively low cost. This method allow to distinguish rapidly the most common serpentine minerals, including lizardite, chrysotile and antigorite. Today, this method is probably the most used to differentiate chrysotile, lizardite and antigorite. Indeed, lizardite, chrysotile and antigorite are characterized by different raman spectra in the 100-1200 and also in the high wave number region (between 3600 and 3750 wavenumber/cm) (e.g., Auzende et al. 2004 ; Groppo et al. 2006 ; Figure 8.5). However, some recent studies (Tarling et al. 2018 ; Compagnoni et al. 2021) have shown that polygonal serpentine and lizardite are roughly distinguishable.

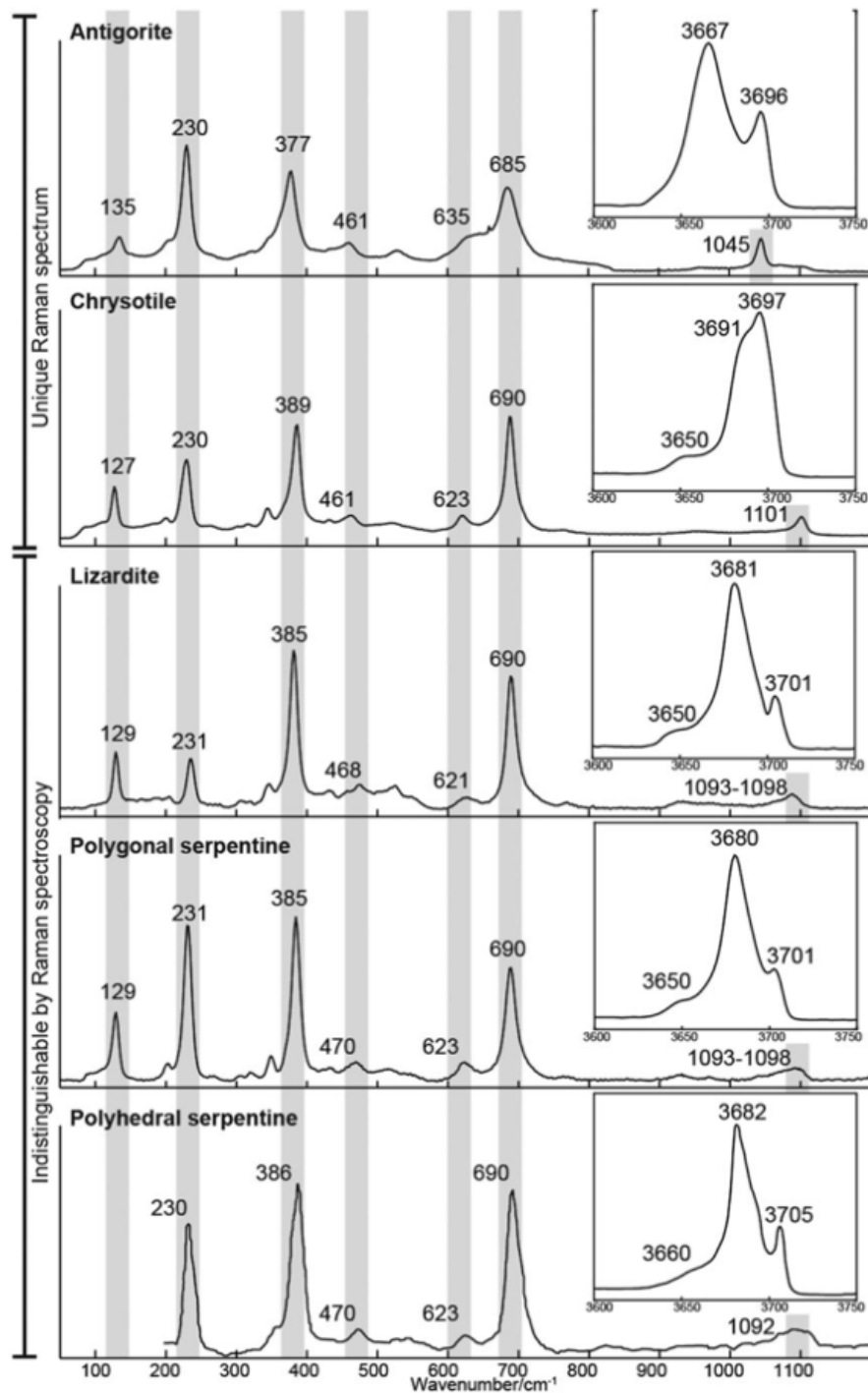


FIGURE 1.5 – Representative Raman spectra of the different species of serpentine, including antigorite, chrysotile, lizardite, polygonal and polyhedral serpentine (Figure from Tarling et al. 2018).

1.1.6 Serpentinization in natural environments

Because the serpentinization process is ubiquitous on the Earth's surface, serpentinitization occurs in most tectonics settings from convergent domains like subduction zones to divergent domains like mid-ocean ridges and passive margins (Figure 8.6). Serpentinitization plays a key role in many processes including geodynamic, the recycling of elements and the origin of life.

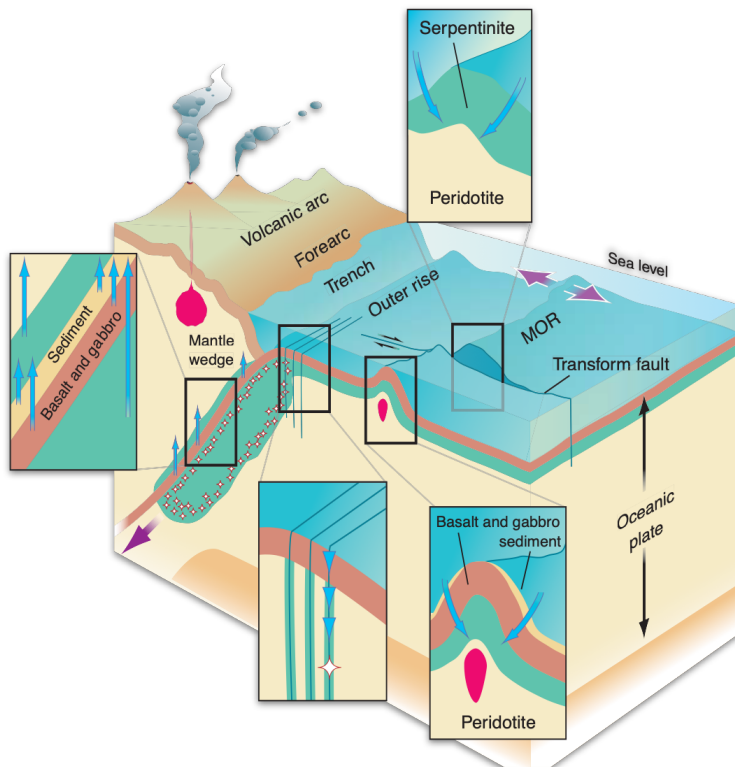


FIGURE 1.6 – Schematic representations of the major location of the serpentinization process on the Earth's surface (Figure from Kerrick 2002).

The integration of water by serpentine minerals causes an increase of the volume of the altered rock of about 30%, resulting in a weaker rock with a significantly lower density $\sim 2.60 \text{ g/cm}^3$ (e.g., O'Hanley 1992; Klein and Roux 2020). These effects induced by the serpentinization process, impacted extensively the strength of the oceanic lithosphere (e.g., Escartin et al. 1997, 2001). Particularly in mid oceanic ridge (MOR) domains, serpentinization allows to localize the deformation (e.g., Pérez-Gussinyé and Reston 2001) and facilitate the exhumation of the mantle (e.g., Bayrakci et al. 2016). During the final rifting and breakup, extensional tectonics leads to the formation of

high-angle normal and exhumation faults, which create preferential pathways for fluid circulations Jackson 1987. Some studies have shown that the final phase of rifting and lithospheric rupture in passive margins is controlled by serpentinization (e.g., Manatschal 2004; Manatschal et al. 2007). The serpentinization process is thus clearly related to the mantle exhumation. However, today the conditions in which the mantle exhumation occurred in passive margins, including temperature, pressure, fluid/rock ratios are still poorly constrained. In subduction zones, serpentinites act as a lubricant for the exhumation of high pressure to ultra high pressure rocks (Guillot et al. 2000).

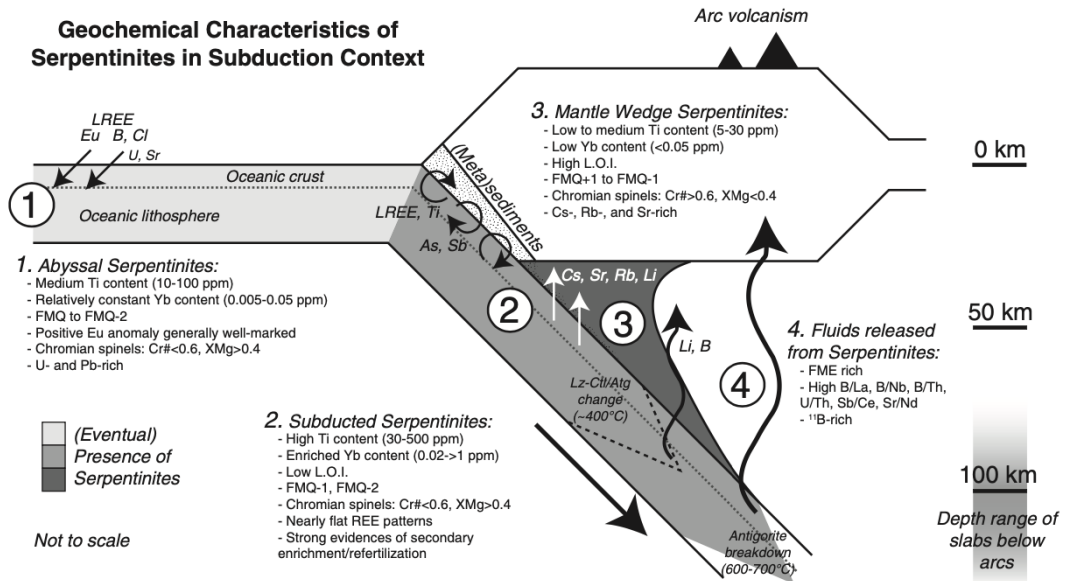


FIGURE 1.7 – Schematic representations of the geochemical transfer associate to serpentinization from oceanic domains to subduction zone. (Figure from Deschamps et al. 2013).

The serpentinization reaction strongly affects the geochemical budgets of the lithosphere and oceans by the uptake and/or release of many major and minor components (e.g., Thompson and Melson 1970 ; Snow and Dick 1995 ; Bach et al. 2001 ; Früh-Green et al. 2004). For example, Snow and Dick 1995 have estimated that serpentinization release about 10^{12} moles of magnesium per year in the ocean, the main component of mantle minerals. Some studies, have demonstrated that during serpentinization, the upper part of the lithosphere was strongly enriched in some fluid-mobile elements (e.g., Vils et al. 2008 ; Alt et al. 2013). Boron, which is concentrated in seawater and depleted in the mantle, is significantly enriched in serpentinites (e.g., Thompson and Melson 1970 ; Moody 1976 ; Spivack and Edmond 1987 ; Vils et al. 2008 ; Boschi et al. 2008 ;

Marschall 2018 ; McCaig et al. 2018), highlighting the chemical exchanges between the mantle and the hydrosphere. In their study Deschamps et al. 2011 propose that serpentinites can integrate large amounts of fluid mobile elements (FME : B, Li, As, Sb, Pb, U, Cs, Sr, Ba) from near the seafloor and transport these elements to shallow depth (between 100 and 170 km) in subduction zones. The incorporation and release of traces elements from oceanic domains to subduction zones are represented in the Figure 8.7.

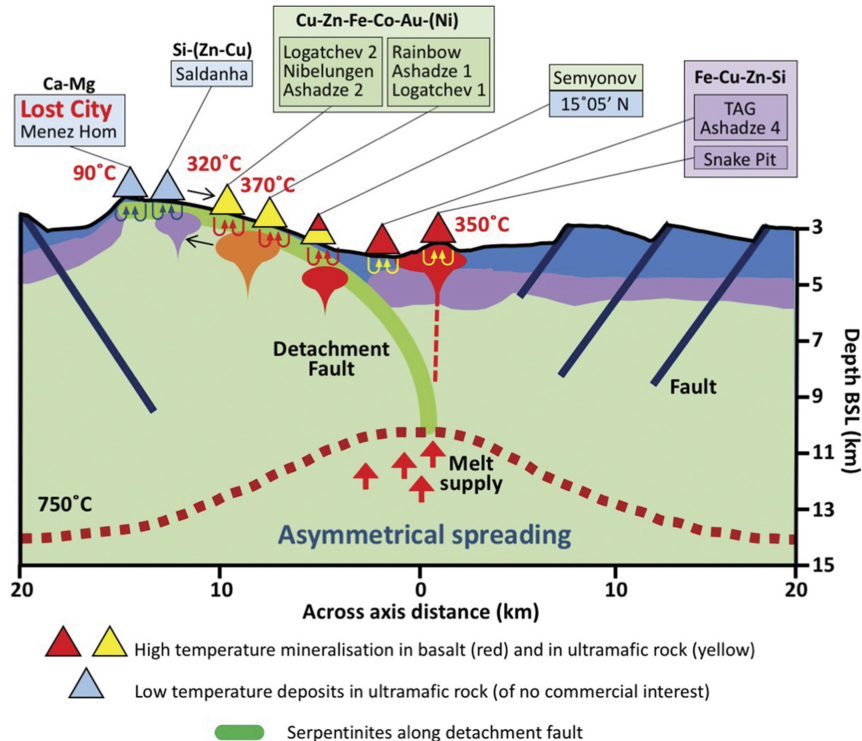


FIGURE 1.8 – Schematic model of the composition of major hydrothermal deposits along the Mid Atlantic Ridge. Vent locations related to detachment faults (heavy green line) Figure from Johnson 2019.

Seafloor explorations revealed the presence of deep-sea hydrothermal vents and a variety of metal deposits such as polymetallic nodules, cobalt rich crusts and polymetallic massive sulfides at or near the seafloor (e.g., Hannington et al. 2005). These deposits are composed by elements of economic interest such as Cu, Zn, Pb, Au and Ag (Figure 8.8 ; e.g., Fouquet et al. 2013 ; Jamieson and Gartman 2020). Almost 65% of the hydrothermal sites occur at mid ocean ridges Hannington et al. 2005. These hydrothermal systems and associated metal deposits result of fluids circulations occurring along normal faults (e.g., Rona 1984 ; Rona et al. 1993 ; Hannington et al. 2001). The numerous studies on natural samples, hydrothermal experiments or numerical model-

ling, suggested that the ultramafic rocks potentially play a key role in the formation of minerals deposits on the seafloor (e.g., Allen and Seyfried Jr 2003; Klein et al. 2015; Klein and McCollom 2013). However, at the present time impacts of serpentinization on the transfer of trace elements, including transition metals in the formation of minerals deposits are poorly constrained.

Serpentinization reaction can generate molecular hydrogen H₂ due to ferrous iron oxidation (e.g., Marcaillou et al. 2011; Klein and McCollom 2013; McCollom et al. 2020a, 2016), leading the formation of fluids with various pH values, depending on the temperature. At low temperatures <200°C, serpentinization leads to the formation of highly reducing conditions and alkaline fluids at pH ~9-10 (e.g., Barnes and O'NEIL 1969; Kelley et al. 2001; Seyfried Jr et al. 2007; Hansen et al. 2017; McCollom et al. 2020b). At high temperatures >300°C, serpentinization generates more acidic fluids with pH values comprising between 2.8 and 5.4, as suggested by serpentinization experiments (e.g., Seyfried Jr and Dibble Jr 1980; Allen and Seyfried Jr 2003, 2005). In oceanic domains, releases of H₂ may be used as an energy source by lithotrophic bacteria Holm and Charlou 2001. Moreover, the continuous release of hydrogen allows the formation of abiotic methane (CH₄) by the reduction of carbon (HCO₃⁻, CO, CO₂) via a Fischer-Tropsch type and Sabatier type reactions (e.g., Proskurowski et al. 2006; Proskurowski et al. 2008; Holm et al. 2015; Etiope 2017). This supports microbial activities at/or near the seafloor (e.g., Holm and Charlou 2001; Kelley et al. 2001; Früh-Green et al. 2004; McCollom and Seewald 2007; Delacour et al. 2008a; Russell et al. 2010; Miller et al. 2016).



1.2 Major issues

As mentioned earlier, serpentinization occurs in most geodynamic settings and under a variety of conditions, from relatively low temperature and pressure near the seafloor at mid-ocean ridges (MOR ; e.g., Alt and Shanks III 2003 ; Mével 2003 ; Ranero et al. 2003 ; Andreani et al. 2007 ; Rouméjon and Cannat 2014) to high temperature and pressure in subduction zones (e.g., Deschamps et al. 2013, 2011, 2010). During the last two decades serpentinization process was largely documented in these two major geological settings (e.g., Guillot et al. 2015), in contrast to that of magma-poor rifted margins. However, at rifted margins serpentinization largely involved in the transfer of elements between the mantle and the seawater (e.g., Pinto et al. 2017) and tectonic processes leading to the mantle exhumation Manatschal 2004. Additionally, at MOR and magma-poor rifted margins serpentinization reactions may also be involved in the formation of (ultramafic-)volcanic massive sulfide (U-VMS) deposits in which numerous transition metals concentrate Patten et al. 2021. Albers et al. 2021 suggest that at passive margins serpentinization may produce particularly high amounts of H₂. At present time, there are still major issues about serpentinization at passive margins :

- what is the impact of fluid-rock interactions on mantle exhumation ?
- what is the source of serpentinizing fluids at passive margins ?
- in which conditions, in particular at which temperature fluid-rock interactions occurred ?
- how chemical elements are mobilized during serpentinization and is there any link between serpentinization and formation of metal deposits ?

In particular, the determination of temperature at which serpentinization occurred is fundamental for the understanding of the rheology, the spreading rate and also the thermal regime associated to magma-poor rifted margins. The temperature also influences the chemical mobility and the formation of second minerals.

1.3 Geological study

1.3.1 Evolution of the Alpine Tethys magma-poor rifted margins through time

The Alpine Tethys basin which separates the Eurasian/Iberian plates from the Adriatic/African plates was opening in Late Triassic at ~ 200 Ma (Figure 8.9E). Before the onset of rifting at Triassic time, the crust was ~ 30 km wide.

During the stretching phase between 200 ± 5 to 185 ± 5 Ma (Figure 8.9D), numerous normal faults were developed in the upper crust allowing to distribute the extension over a wide area Manatschal et al. 2022.

Then, during the necking phase was initiated at 185 ± 5 Ma (Figure 8.9C) deformation is started focusing in the future distal margin and post-tectonic sediments start to fill-in in the half graben basins. At this time, extensional detachment faults allowed to exhume the mid-crustal levels to the seafloor Mohn et al. 2012.

The onset of the hyper extension phase (Figure 8.9B) is marked by the formation of new faults (i.e., successive in and out sequence extensional detachment faults) which are able to penetrate into the underlying sub continental mantle (Mohn et al. 2012; Gillard et al. 2016a). During the hyper extensions phase, the deformation is clearly asymmetrical Gillard et al. 2016b. Hydrothermal fluid circulations were evidenced by the occurrence of mantle-derived elements (Ni, Cr and V) in secondary minerals along extensional detachment faults in the continental crust (e.g., Pinto et al. 2015). The extensional detachment faults allow to exhumed on the seafloor the subcontinental lithospheric mantle at ~ 170 Ma.

Mantle exhumation is accompanied by the inception of the magmatic activity at distal domains characterize the proto-oceanic phase (Figure 8.9A). The magmatic activity is evidenced by the occurrence of pillow lava and gabbroic intrusions dated at 161 ± 1 Ma (Desmurs et al. 2001; Desmurs et al. 2002; Schaltegger et al. 2002; Epin et al. 2019; Amann et al. 2020a).

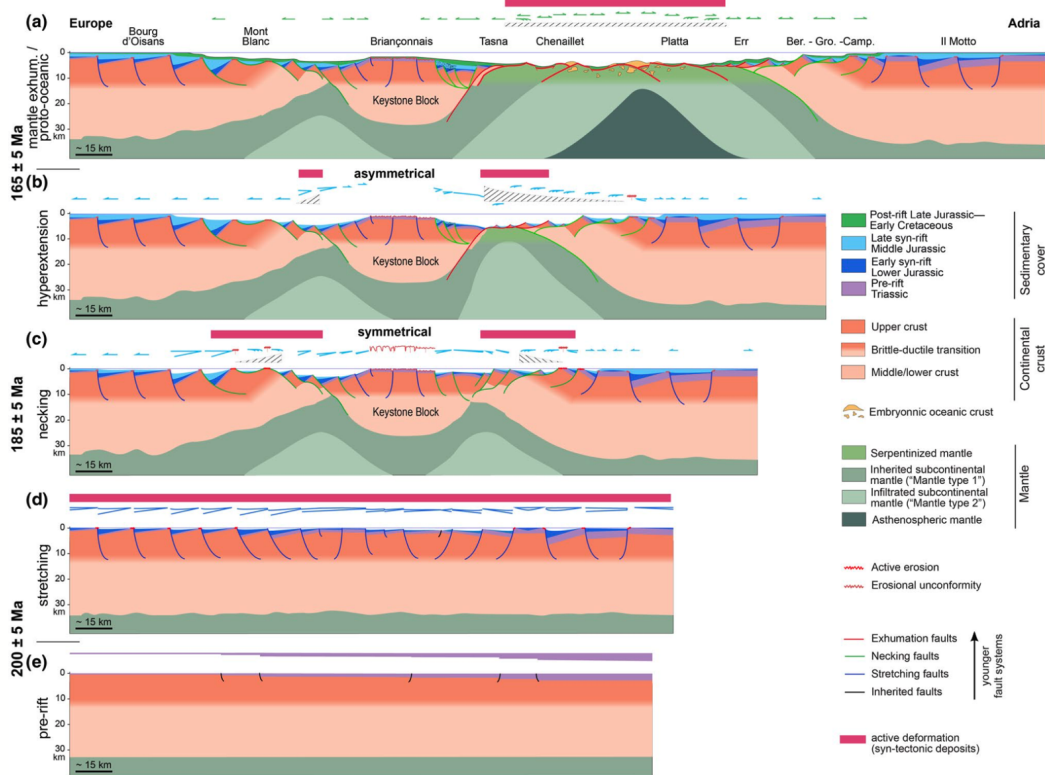


FIGURE 1.9 – Main phases of the Alpine Tethys rift evolution, from Manatschal et al. 2022 A) mantle exhumation phase (formation of proto-oceanic crust) during the Middle Jurassic ; B) hyperextension phase at late Early Jurassic (Pliensbachian–Toarcian) ; C) necking phase at Early Jurassic (Sinemurian–Pliensbachian) ; D) stretching phase from latest Triassic to Early Jurassic and E) pre-rift situation in Late Triassic.

1.3.2 Geological setting

The OCT Alpine Tethys is particularly well preserved in the South-Eastern part of the Swiss Alps. In particular, in the Platta, Tasna and Totalp nappes which were sampled in this study. In these nappes, the pre-Alpine rift-related contacts between the subcontinental mantle and syn-rift sediments particularly well preserved Manatschal 2004. Hence, the petrological and mineralogical results of serpentinites from these units are not (or only poorly) affected by the Alpine subduction. The serpentinization associated to the mantle exhumation in these units is therefore comparable to those of present day OCT zones, including the Iberian-Newfoundland passive margin (e.g., Manatschal et al. 2007).

These remnants are now exposed as ophiolitic nappes in the Central Alps, in the southeastern part of Switzerland (Figure 8.10 ; Manatschal and Nievergelt 1997 ; Müntener et al. 2004 ; Müntener and Piccardo 2004). As mentioned above, these ophiolites represent OCTs of the ancient Adriatic-European-Briançonnais conjugate margins (Figure 8.10B ; Florineth and Froitzheim 1994). These ophiolitic nappes are located at the north of the Engadine line, which corresponds to a North East - South West (NE-SW) trending antiform in southeastern Switzerland (Figure 8.10C).

The three localities sampled in this thesis (Platta, Totalp and Tasna nappes), derived from the South East margins of the Alpine Tethys. The platta and Totalp nappes devired from the Adriatic margin (Figure 8.10B, C), and the Tasna nappe was a part of the conjugate European-Briançonnais margin (Figure 8.10B ; Manatschal and Müntener 2009).

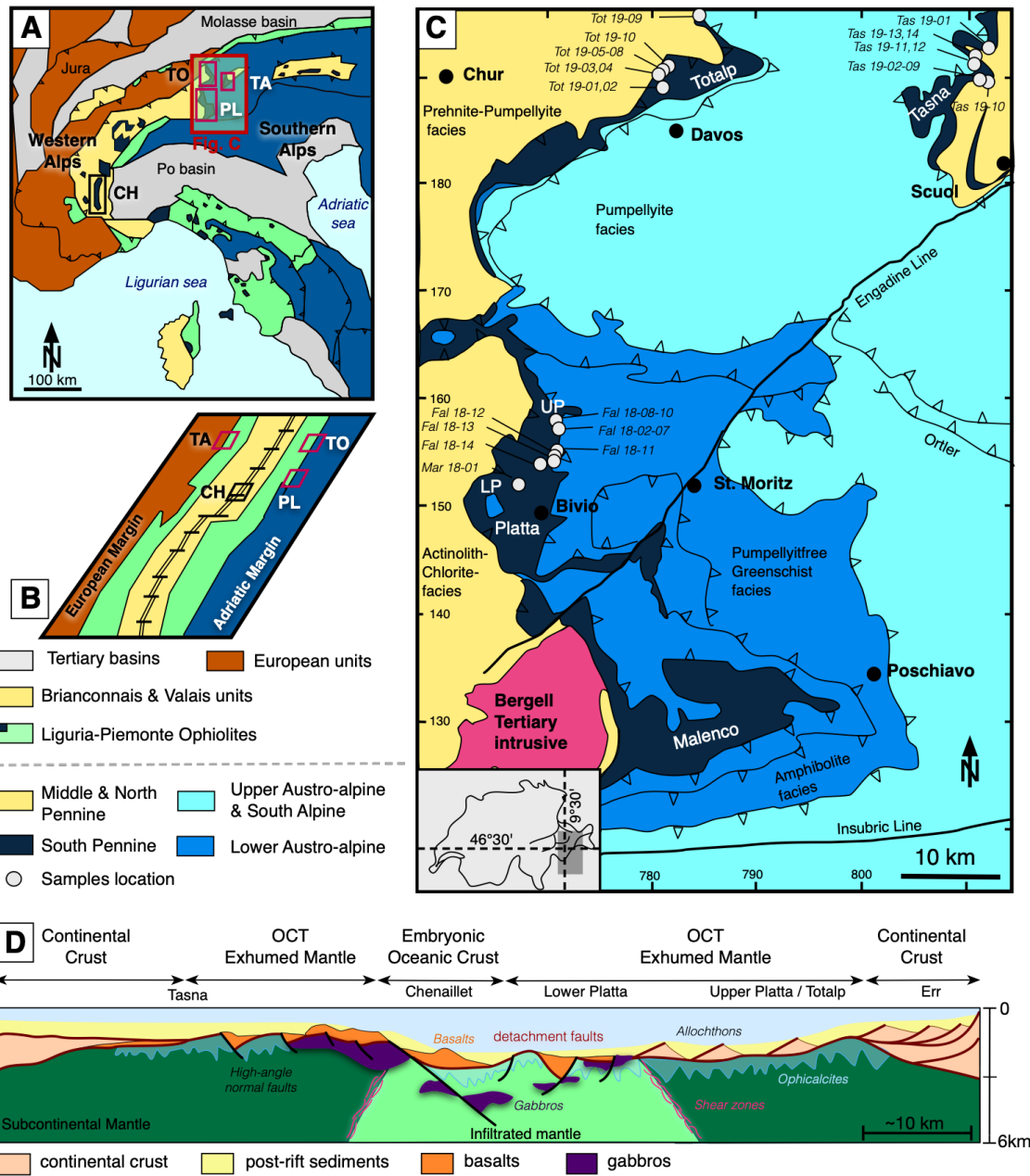


FIGURE 1.10 – A) Present-day location of the ophiolites massifs in the Central-Western-Ligurian Alps (modified after Manatschal and Müntener 2009). B) Schematic paleo-reconstruction of the Piemonte-Ligurian oceanic basin at Late Jurassic time, with location of the major ophiolite sequences (modified after Manatschal and Müntener 2009). C) Simplified geological map of the Penninic and Austro Alpine Nappes (modified after Florineth and Froitzheim 1994), including samples location. D) Distribution of subcontinental and infiltrated mantle along an ocean-continent-transition of the Alpine Tethys (modified after Müntener and Piccardo 2004).

The Platta nappe



FIGURE 1.11 – Panoramic view of the Platta nappe (personal photography).

The Platta nappe is derived from the SE margin of the Alpine Tethys and forms a part of the Austro-alpine and Pennine nappes (Figure 8.10C). The Platta nappe is subdivided into two units separated by shear zones (Figure 1D) : i) the Upper Platta unit, which mainly consists of mantle rocks that originally formed the inherited sub-continental mantle of the Adriatic margin (i.e., the Err domain Schaltegger et al. 2002; Müntener et al. 2010, 2004; Picazo et al. 2016; Epin and Manatschal 2018); and ii) the Lower Platta unit, which was originally located oceanwards and consists of a large mantle domain locally intruded and covered by melt-derived rocks (gabbros and lavas) of a Jurassic age (Desmurs et al. 2002; Amann et al. 2020b). Contrarily to mantle rocks from the Upper Platta which are free from any syn-rift melt imprint and equilibrated at low temperature $\sim 850^{\circ}\text{C}$, those from the Lower Platta were largely refertilized by melt percolation during final rifting and recorded higher temperature ($\sim 1000^{\circ}\text{C}$; Müntener et al. 2010, 2004). Slivers of continental origin also occur in the Platta nappe and have been interpreted as extensional allochthons (Froitzheim and Manatschal 1996). Some outcrops in the Platta nappe are overlaid by ophicalcites (Dietrich 1970).

The Platta nappe was relatively preserved from Alpine metamorphism (low-temperature prehnite-pumpellyite metamorphism, $<350^{\circ}\text{C}$; Froitzheim and Rubatto 1998; Chalot-Prat et al. 2003; Epin et al. 2019). However, an increase in Alpine metamorphism from north to south is characterized by the transition lizardite/chrysotile serpentine type in the Platta nappe to the antigorite type in Malenco, representing the southern continuation of the Upper Platta unit (Dietrich 1969; Trommsdorff 1983; Trommsdorff and Evans 1977; Burkhard and O’Neil 1988).

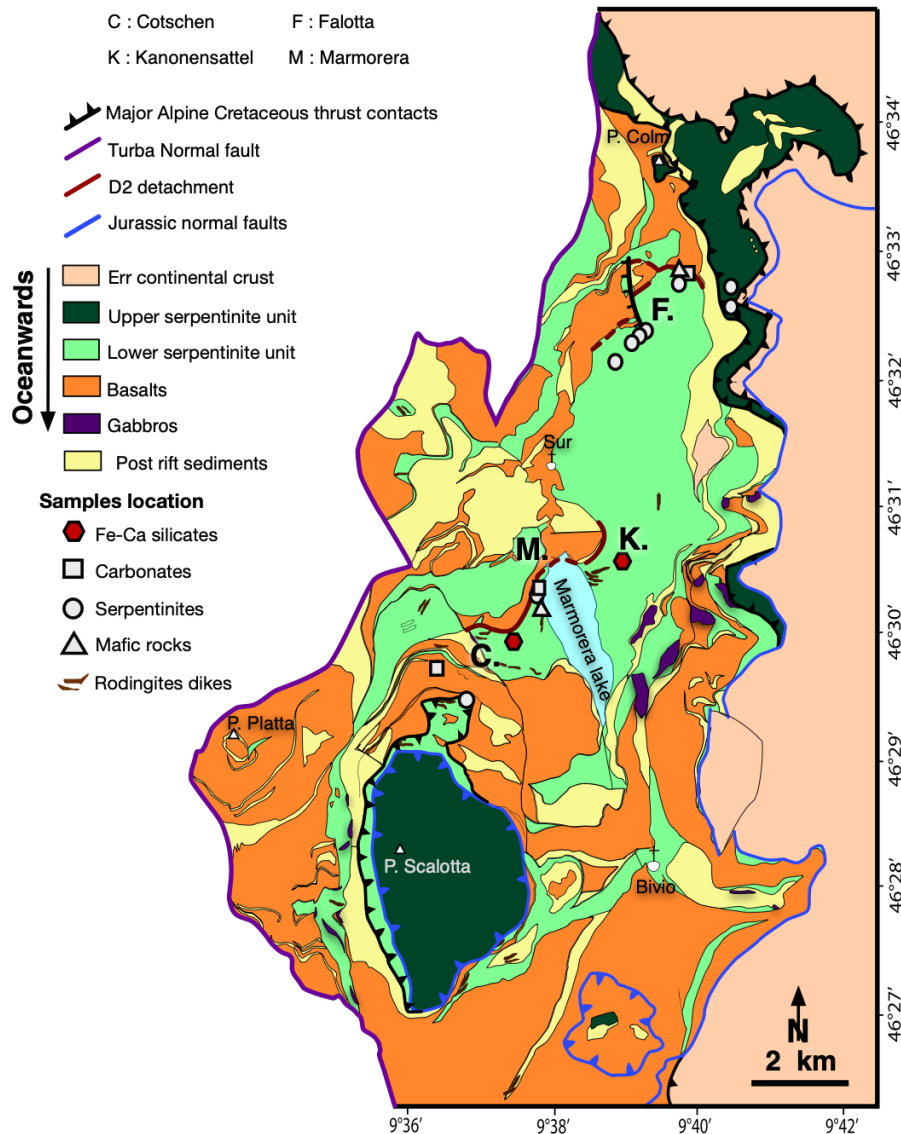


FIGURE 1.12 – Geological map of the Platta nappe with samples location, Figure from Hochscheid et al. (2022)

The Totalp nappe



FIGURE 1.13 – Serpentinites outcrop from the Totalp nappe (personal photography).

The Totalp nappe nowadays located to the north of Platta nappe (Figure 8.10B), is also a part of the South Pennine and Austro Alpine nappes, derived from the SE margin of the Alpine Tethys and thrust over the middle and north Penninic units during the late Eocene (Froitzheim and Manatschal 1996; Figure 8.10C). The Totalp nappe is made of foliated serpentinitized spinel lherzolites, occasionally crosscut by pyroxenites and covered by ophicalcites and pelagic sediments. Magmatic rocks are rare and mainly consist of flaser gabbros and doleritic dykes Peters and Mathews 1963.

Comparatively to the Platta nappe, the Totalp nappe underwent a slightly greater Alpine metamorphism peak of a prehnite-bearing assemblage near the contact zone with the surrounding gneisses Peters and Mathews 1963, allowing a better paleogeographic reconstruction than the northern Platta nappe (Manatschal, 2004; Manatschal and Müntener, 2009). Serpentinitized mantle is often crosscut by calcite veins because its location near the seafloor (Weissert and Bernoulli 1985; Bernoulli and Weissert 1985; Picazo et al. 2013). Similarly to the Platta nappe, relics of the pre-Alpine contacts between exhumed mantle rocks, ophicalcites and sediments are locally well-preserved Picazo et al. 2013, thus making a very good place to study fluid-rock interaction related to mantle exhumation at the seafloor. $^{40}\text{Ar}/^{39}\text{Ar}$ on phlogopite from pyroxenite suggest a Jurassic ages 160 ± 8 Ma of cooling/exhumation (Peters and Stettler 1987a; Peters and Stettler 1987b; Manatschal et al. 2006).

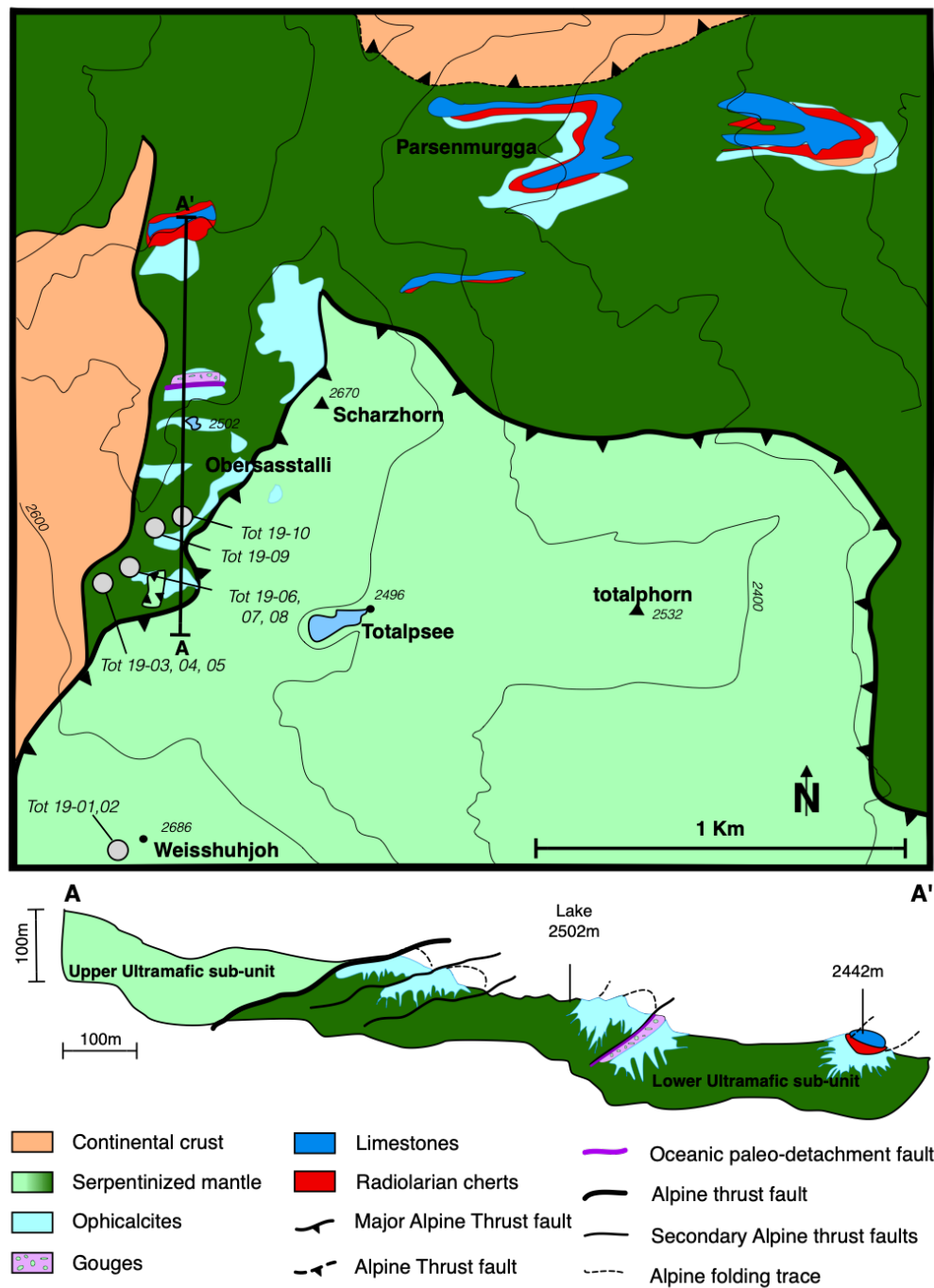


FIGURE 1.14 – Geological map of the Totalp nappe with samples location, modified after Picazo et al. 2013.

The Tasna nappe



FIGURE 1.15 – Panoramic view of the Tasna nappe (personal photography).

The Tasna nappe was initially located along the Briançonnais/European margin (Figure 1B ; Florineth and Froitzheim 1994 ; Manatschal et al. 2006). This nappe consists to a stack of Austro Alpine nappes and Pennine nappes established during Eocene to Oligocene period (Figure 8.10C ; Manatschal et al. 2006). Similarly to the Platta nappe, the Tasna nappe was only weakly affected by Alpine metamorphism at low grade <350° corresponding to the greenschist facies (Florineth and Froitzheim 1994 ; Froitzheim and Manatschal 1996 ; Bousquet et al. 2008 ; Manatschal et al. 2006 ; Ribes et al. 2020). Consequently, the pre-Alpine contacts the Tasna nappe are not affected by the Alpine metamorphism.

The Tasna nappe is made of a wedge of continental crust that is separated from the underlying mantle by two detachment faults, the Lower Tasna Detachment (LTD), which separates continental rocks from mantle rocks, and the Upper Tasna Detachment (UTD) that truncates the LTD and represent an exhumed top-basement detachment fault (Figure 8.16 ; Froitzheim and Rubatto 1998 ; Manatschal et al. 2006 ; Ribes et al. 2020). The mantle and continental rocks were covered by undeformed Late Barremian post-rift sediments, that is characteristic of the Briançonnais/European domain Froitzheim and Rubatto 1998. Mantle rocks consist of strongly serpentinized spinel lherzolites with abundant spinel websterite layers and high temperature spinel foliation Manatschal et al. 2006. The $^{40}\text{Ar}/^{39}\text{Ar}$ ages measured on phlogopites, together with clinopyroxene composition and equilibrium temperature calculated on coexisting pyroxenes from spinel-lherzolites and pyroxenites (Manatschal et al., 2006) are similar to those from the Totalp unit at $\sim 900^\circ\text{C} \pm 50^\circ\text{C}$ (Peters and Stettler, 1987a).

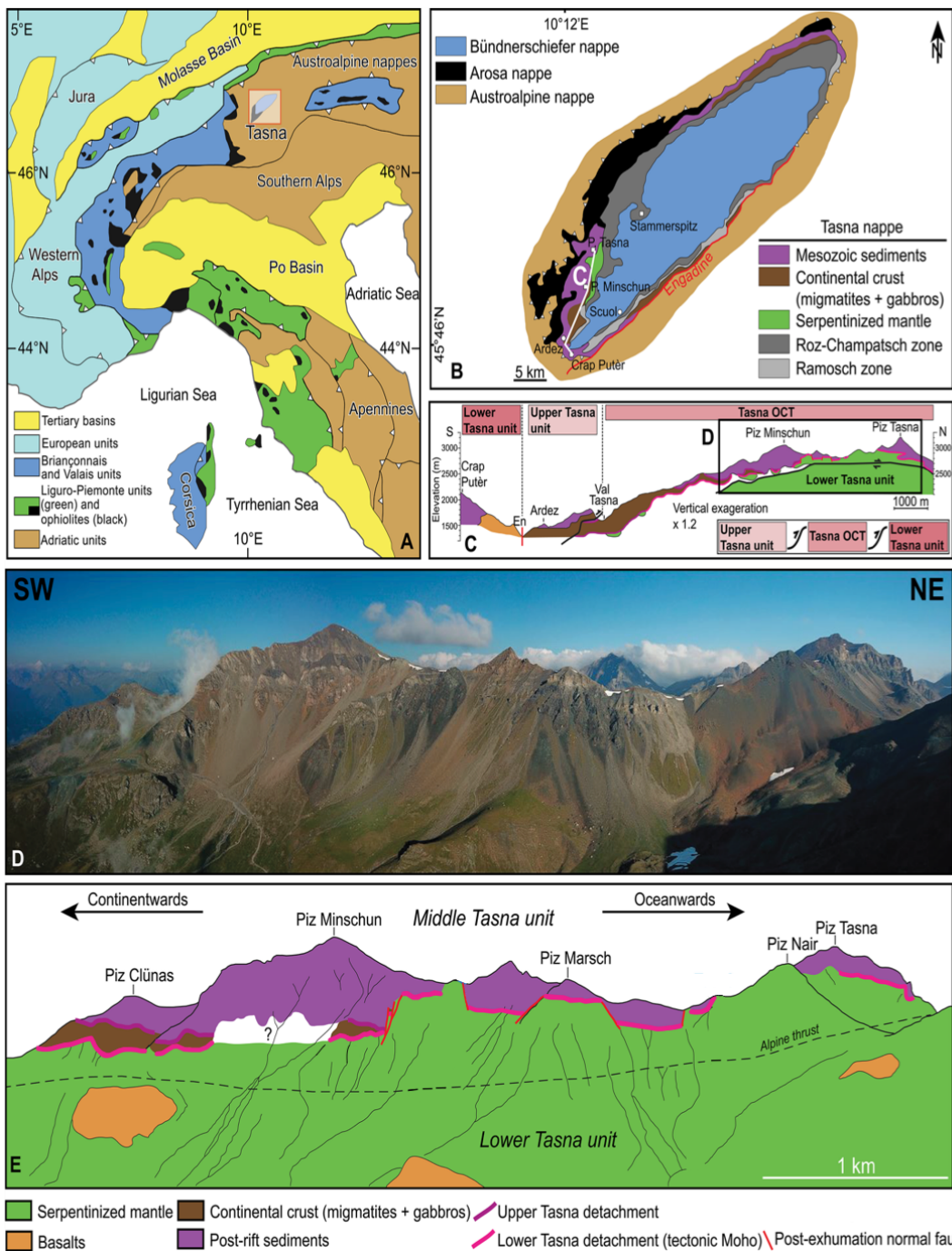


FIGURE 1.16 – A) Simplified geological map of the Alpine system in Western Europe, from Schaltegger et al. 2002. B) Geological map of the Engadine window in the southeastern Alps, Switzerland. C) North-south-striking cross section along the Tasna nappe and schematic representation of the nappe stacking architecture from Coltat et al. 2022 modified after Ribes et al. 2020 ; OCT : ocean continent transition ; P : Piz. D,E) Southwest-northeast-oriented field view of the Tasna section from Ribes et al. 2020.

1.4 Experimental study

1.4.1 Previous serpentinization experiments

Over the last four decades, in order to understand the hydrothermal systems observed at the seafloor, serpentinization reaction has been extensively studied under laboratory conditions, with the first experiments of (Martin and Fyfe 1970 ; Seyfried Jr and Dibble Jr 1980 ; Seyfried Jr 1987 ; Janecky and Seyfried 1986), then (e.g., Marcaillou et al. 2011 ; Malvoisin et al. 2012a,b ; Klein et al. 2015 ; McCollom et al. 2016) ; and more recently (e.g., McCollom et al. 2020a,b ; Tichadou 2021). During serpentinization experiments, many parameters were tested : temperature, pressure, fluid composition and pH, protolith composition and initial grain size... These experiments showed that these different parameters affect the kinetics of reaction and the production of hydrogen. Martin and Fyfe 1970 and Wegner et al. 1983 were the first to show experimentally that temperature, pressure and initial grain size affected the conversion of olivine to serpentine in contact of water. Since, numerous experiences have been performed. Below, we summarized the impacts of the different parameters on serpentinization.

Different closed experimental setups exist, however the commonly used are flexible gold-titanium reaction cells designed by Seyfried Jr 1987 Figure8.17 and gold capsules Figure8.18, each with advantages and disadvantages.

The first one allows large volume experiments with an accurate control on pressure. This apparatus allows using large volume of fluid and/or rock and thus testing different water/rock ratios. In addition this apparatus allowing to sample fluids during the experiments and characterize fluid change during hydrothermal experiments like serpentinization. The main disadvantage is the long duration of experiments, the heating and the cooling of several hours and the no negligible risk of leakage during experiments.

The second type of settings allow faster experiments at higher pressure but with restricted volume of reagents (only few grams), nor fluid sampling during experiments. However, with this apparatus it is possible to measure magnetic susceptibility without opening the experiment cell (Malvoisin et al. 2012b), which can be useful for monitoring serpentinization kinetics and hydrogen production, related to production of magnetite during serpentinization.



FIGURE 1.17 – Photography of the large volume autoclave, personal photography.

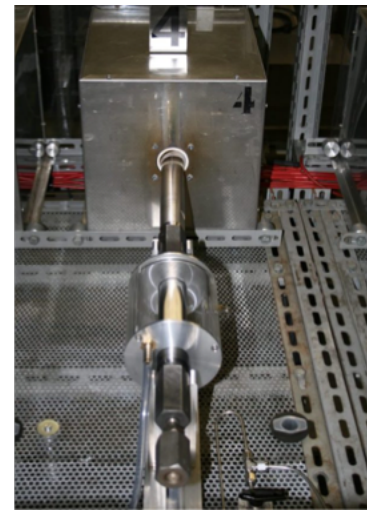


FIGURE 1.18 – Photography of the gold capsule from the ISTO laboratory.

These last years, new apparatus were developed in order to conducted experiments in open system (i.e., reactive transport), most representative of the natural systems. These apparatus aim to quantify elements transport during fluid-rock interactions or the evolution of the petrophysical characteristics of the sample (e.g., Escario et al. 2018 ; Tutolo et al. 2018 ; Osselin et al. 2022).

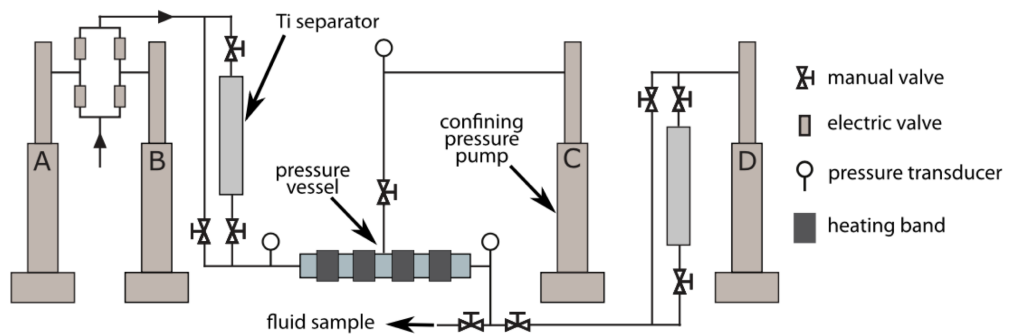


FIGURE 1.19 – Schematic representation of one type of experimental apparatus utilized for reactive transport experiments, illustrating the injection, collection, and confining pumps, hydrothermal pressure vessel, pressure transducers used for permeability measurements, and valve for monitoring fluid chemistry Figure from Tutolo et al. 2018

Temperature

Martin and Fyfe 1970 were the first to demonstrate that the serpentinization reaction rate is related to the temperature by conducting serpentinization experiments in gold capsules. By reacting synthetic forsterite with water, they determined that the serpentinization reaction rate forms a bell-shaped curve depending of the temperature with a peak (i.e., maximum conversion of olivine into serpentine) between 250°C and 300°C, for initial grain size of 58 to 79 μ m. Wegner et al. 1983 realized the same experiments in gold capsules and determined a maximum percentage of conversion at about 305°C in accordance with the previous results of Martin and Fyfe 1970. However, the dependency of serpentinization rates with temperature formed an asymmetric bell curve. The results of Wegner et al. 1983 were confirmed by the study of Malvoisin et al. 2012a, which differ strongly from those of Martin and Fyfe 1970, with serpentinization reaction rate approximately 60 times slower. Malvoisin et al. 2012a propose that these differences of serpentinization reaction rates may be a consequence of the nature of the forsterite that differ between the three studies (synthetic in Martin and Fyfe 1970 and natural san Carlos olivine in the two others). Results from study of McCollom et al. 2016 were also consistent with those from Malvoisin et al. 2012a, suggesting that the serpentinization reaction rate of olivine in natural systems may be significantly slower than the earlier studies of Martin and Fyfe 1970 and Wegner et al. 1983.

In contrast to these previous experiments, Lamadrid et al. 2021 showed that serpentinization of olivine is faster at 250°C, and that serpentinization rates display an almost symmetrical concave downward shape curve. Nevertheless, in contrast to the previous experiments, Lamadrid et al. 2021 used a different composition of fluids, which affects the serpentinization rates by increasing serpentinization rate in the presence of seawater aqueous solution. The authors compared their results with serpentinization rates from the literature (Figure 8.20). It is now clearly established that the serpentinization reaction rates depends on temperature.

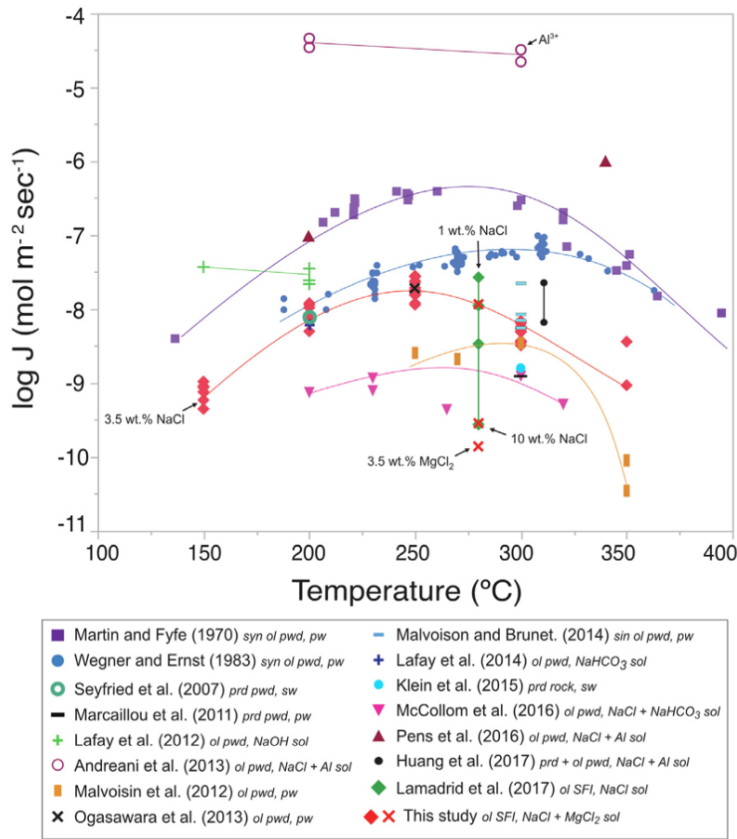


FIGURE 1.20 – Figure summarizing the serpentinization rates from the literature in $\log J$ (quantity of energy) versus the temperature ($^{\circ}\text{C}$), figure from Lamadrid et al. 2021.

Pressure

In contrast to other parameters, how pressure influences the serpentinization process was less studied so far and remains poorly constrained. However, past studies suggest that pressure is a non-negligible feature controlling the serpentinization.

Wegner et al. 1983 investigated the effects of pressure on serpentinization rates through experiments at 270°C during 20 days. Their main results showed an increase of serpentinization degree from 21% at 1 kbar, to 30% at 2 kbar and 36% at 3 kbar.

Nakatani and Nakamura 2016 performed a series of hydration experiments at temperatures of 400–580 °C and pressures of 13 and 18 kbar with three different bulk compositions : olivine, orthopyroxene-clinopyroxene mixture and olivine-orthopyroxene mixture, to determine serpentinization rate in fore-arc conditions. In all experiments lizardite and albuminous lizardite was formed, except those at 18 kbar and 580°C in the olivine-orthopyroxene system, in which antigorite was formed because the reactions

generally obeyed an interface-controlled rate law. At 400°C where lizardite is developed, the reactions were transport controlled.

Recently Huang et al. 2017 highlighted that the decrease in chlorine content in serpentine minerals with increasing pressures may be linked with an increase in SiO₂ contents and a decrease in FeO contents. Thereafter, Huang et al. 2020 showed that serpentinization rates strongly increase with pressure, with 19% of reaction extent achieved within 20 days for experiments at 500°C and 3.0 kbar for olivine grain sizes less than 30 μm, which increased to 96% at 20 kbar over the same period and the same temperature (Figure 1.21). Through thermodynamic calculations, they also show that Gibbs energy during olivine serpentinization decreases with increasing pressure.

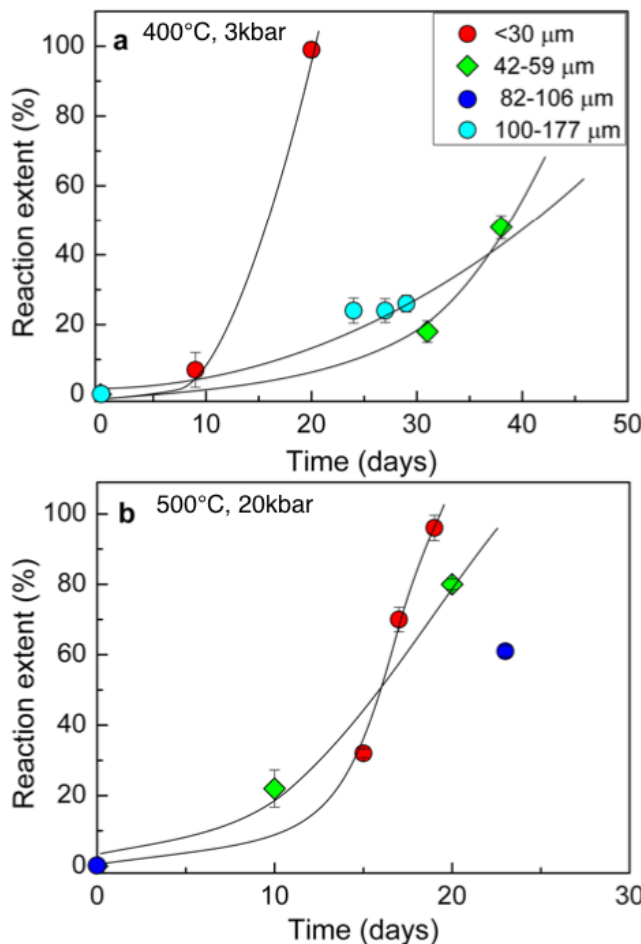


FIGURE 1.21 – Serpentinization reaction rate (%) as function of initial grain size versus time of reaction in days, for pressure of 3kbar (a) and 20 kbar (b) figure from Huang et al. 2020.

Water/rock ratios

How water/rock ratios influences serpentinization was poorly studied experimentally and numerically, while it is a key parameter during hydrothermal circulations impacting the formation of mineral deposits (e.g., Nast and Williams-Jones 1991).

Janecky and Seyfried 1986 conducted serpentinization experiments by interacting natural peridotite with IAPSO standard seawater in flexible Au/Ti reaction cell at 200°C and 300 °C and water-rock ratios of 10 and 30. In these experiments, they observe similar assemblages at water/rock ratios of 10 and 30 but in different proportions. In particular, in experiment at w/r of 10 the solution approach saturation with enstatite and olivine while lower amounts of enstatite is observe in experiment at w/r of 30.

In the numerical study of Klein et al. 2013, serpentinization reaction were modelled in function of three water-rock ratios : 0.5, 1 and 10 (Figure8.22). Their results suggested no variation in mineral assemblages for olivine serpentinization but slightly variations in the proportions of secondary minerals consistently with the experimental results of Janecky and Seyfried 1986. Their results suggested also that hydrogen production is strongly influenced by the amount of water. At low w/r ratios the amount of hydrogen is concentrated in a small volume of interacting fluid. In contrast, at high w/r ratios the hydrogen is diluted in a larger volume of fluid and thus the conditions are less reducing, and less hydrogen is generated.

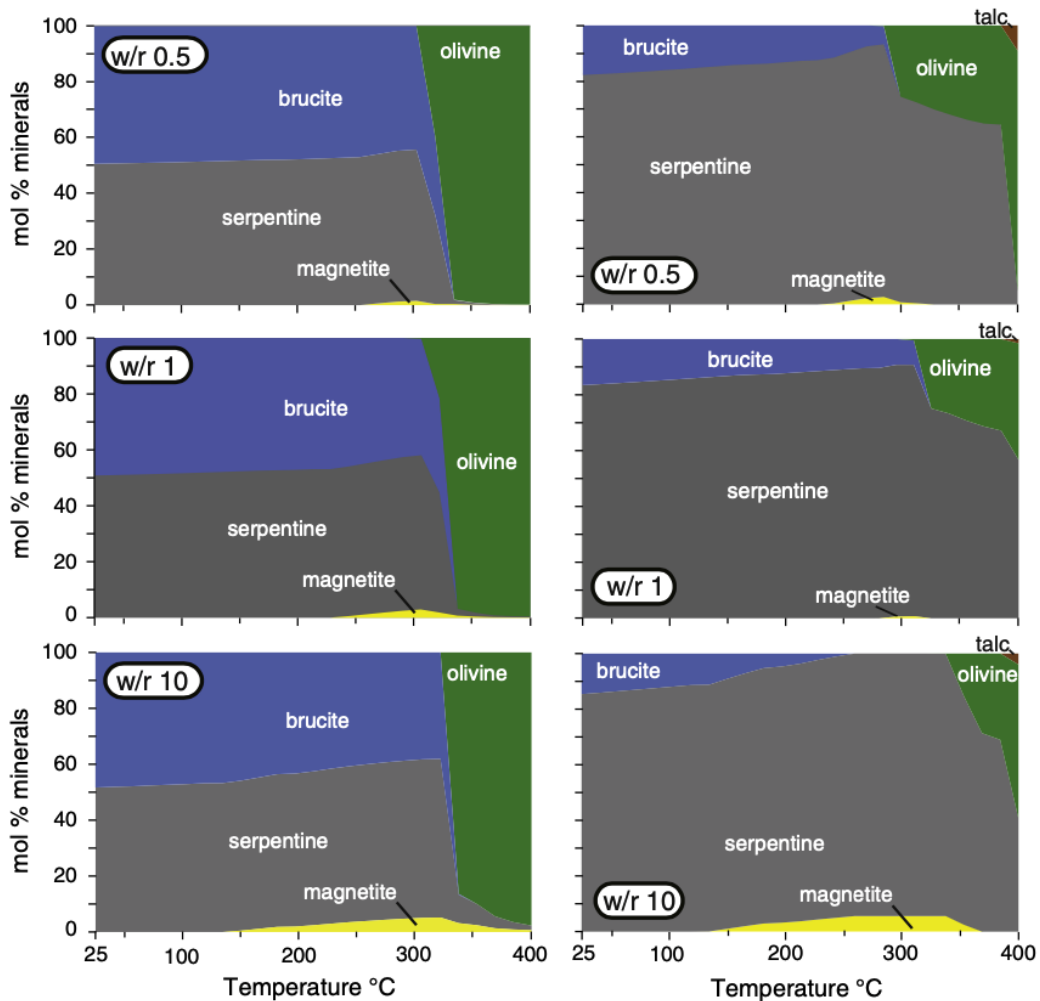


FIGURE 1.22 – Mineral assemblages predicted for serpentinization of olivine and clinopyroxene-free harzburgite as function of temperature and water-rock ratios from Klein et al. 2013.

Initial grain size

Several studies have focused on effects of initial grain size on serpentinization rates. From the first serpentinization experiments performed by Martin and Fyfe 1970, in which the authors showed that for serpentinization experiments at 250°C during 3 weeks, the amount of serpentine produced for an increase of initial grain size from 50 μm to 150 μm decreases from 25% down to 0%. More recently, Lafay et al. 2012 made the same observation, and determined serpentinization rates at 200°C varying from $3.6 \times 10^{-6} \text{ s}^{-1}$ for olivine grains lower than 30 μm to $1.4 \times 10^{-7} \text{ s}^{-1}$ for olivine grains of 56–150 μm . Malvoisin et al. 2012a showed that 80% of serpentinization was achieved after 60 day for olivine grain sizes of 5–15 μm and after 500 days for grain sizes of 50–63 μm , (Figure 8.23). Additionally they demonstrated that the initial olivine grain size influences the nature of serpentine minerals, with a preferential formation of lizardite for olivine grains of 50–63 μm and chrysotile for olivine grains lower than 5 μm .

These studies allowed to highlight the importance of porosity and reactive surface on serpentinization kinetics and development of secondary serpentine species and textures. These results were useful to better estimate the timing of serpentinization reaction and life-duration of natural hydrothermal systems.

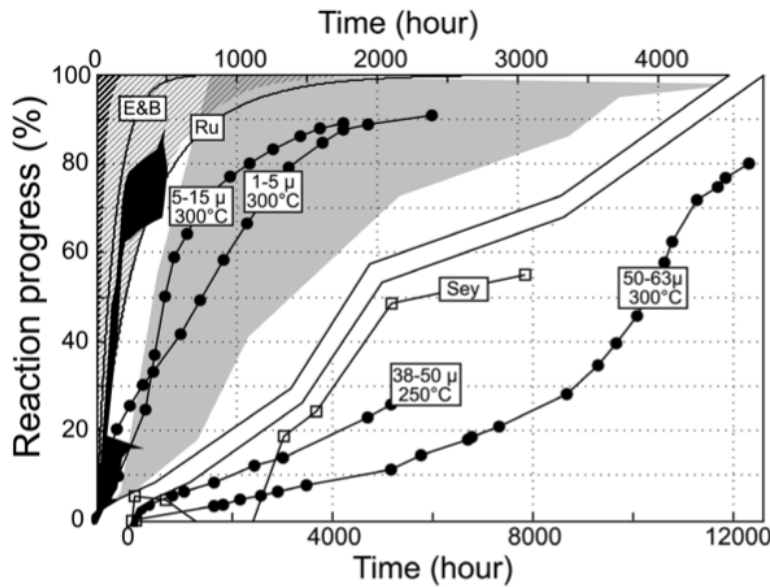


FIGURE 1.23 – Summary of serpentinization rates from literature and the study of Malvoisin et al. 2012a depending to initial grain size and temperature. Figure from Malvoisin et al. 2012a.

Protolith composition

Allen and Seyfried Jr 2003 investigated experimentally different protolith in order to better assess alteration and mass transfer in ultramafic hosted hydrothermal systems at mid-ocean ridges. Four experiments were conducted, by interacting olivine, orthopyroxene and clinopyroxene individually and in combinations (including orthopyroxene/clinopyroxene 60%/40% and olivine/orthopyroxene/clinopyroxene 76%/17%/7%) with NaCl/MgCl₂ fluid at 400°C and 500 bars in flexible Au/Ti reaction cell. In these conditions, pyroxenes are more reactive than olivine and produced high dissolved concentration of SiO₂, Ca and H₂ resulting in the production of low-pH fluids (~4.90-5.30). Fluid resulting from olivine/pyroxenes mixture are similar to those produced by pyroxenes reaction alone.

The experimental study of Huang et al. 2017 was focused on the production of iron oxide during peridotite serpentinization and particularly the influence of pyroxene. They conducted serpentinization experiments at 311 °C and 3 kbar in gold capsules on natural orthopyroxene, olivine and peridotite. They observed that iron oxide preferentially formed after olivine serpentinization and that pyroxene in peridotite gained some Fe from olivine during the serpentinization process, which may decrease the production of iron oxide like magnetite.

Klein et al. 2009 shown that serpentinization of harzburgite generates more serpentine due to the higher amount of SiO₂ in the system, serpentine being Fe-enriched and that the predicted concentration of hydrogen is higher than in pure olivine experiments. These numerical models highlighted also that secondary minerals products change depending to the protolith used, in accordance with the experimental results of Allen and Seyfried Jr 2003. Serpentinization of pure olivine protolith mostly produces serpentine with minor amount of brucite and magnetite, consistently with that is observed for dunite serpentinization. In contrast, the serpentinization of protolith that integrates significant amount of pyroxene (typically harzburgite), releases silica that may lead to the production of additional mineral phases can developed like talc, tremolite depending of the temperature.

Thereafter Klein et al. 2013 have performed thermodynamic modelling to examine mineral assemblages, mineral composition of secondary products and composition of resulting fluid of 21 different ultramafic rock compositions and 10 distinct compositions of olivine between 25 °C and 400 °C at 50 MPa. Their thermodynamic modelling show

systematic differences between serpentinization of peridotite and pyroxenite, such as that serpentinization of peridotite produces Fe-poor serpentine, Fe-rich brucite at temperature below 320 °C and magnetite at temperatures higher than 200 °C. While no magnetite was generated and Fe-rich serpentine and talc formed in serpentinization of pyroxenite (Figure 8.24). The lack of magnetite results mostly of all partitioning of iron into serpentine. Proportion of hydrogen released is systematically higher in serpentinization of peridotite and olivine-rich protolith because more ferric iron in secondary minerals is produced.

Today it is clear that the nature of the protolith used in serpentinization experiments strongly affects the composition of solid products and resulting fluids. Further work is needed to better understand fluid composition observed in hydrothermal systems on the seafloor and composition of secondary mineral products.

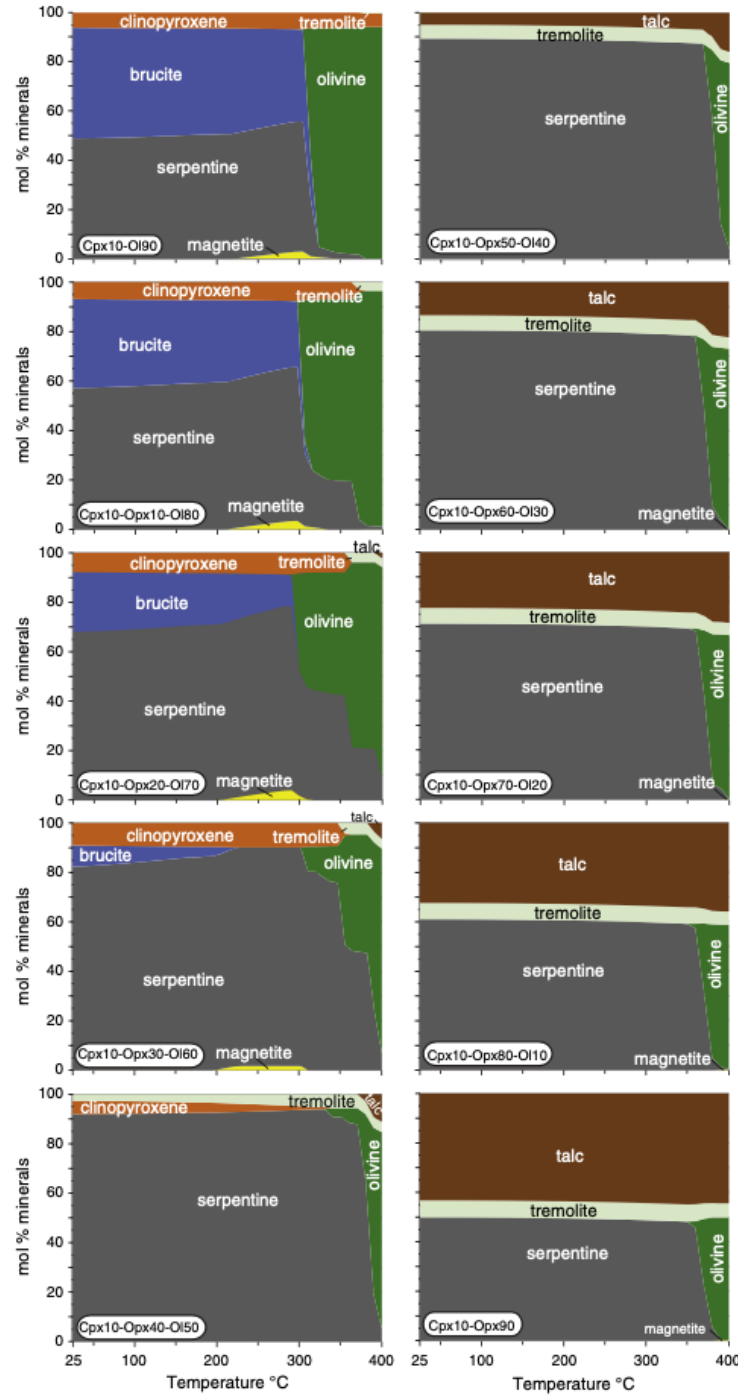


FIGURE 1.24 – Mineral assemblage for serpentinization of peridotite and pyroxenite, from Klein et al. 2013.

Initial fluid composition

Based on serpentinization experiments, Lafay et al. 2012 proposed that alkaline solutions increase the serpentinization rates. Afterward Pens et al. 2016 suggested that the presence of aluminium in fluid affects the serpentinization rate of olivine and orthopyroxene, with faster serpentinization rates of olivine in presence of aluminium.

Recently, a particular importance has been taken in influence of fluid salinity during serpentinization. Lamadrid et al. 2017 showed that serpentinization rates of olivine are strongly controlled by fluid salinity, which decreases by 1 to 2 orders of magnitude with increasing fluid salinity from 1 wt% to 10 wt% NaCl. Huang et al. 2018, 2017 suggested that chlorine is hosted in a structurally-bound site of serpentine. The proportion of chlorine integrated in serpentine minerals is strongly dependent on the mobility of iron, aluminum and silica. They proposed that chlorine is needed for the redistribution of cations during serpentinization. Lamadrid et al. 2021 demonstrated that increasing fluid salinity and the associated decrease in water activity slows down the serpentinization reaction (Figure 1.25). They demonstrated also that the presence of Mg^{2+} cations in fluid can favor the in congruent dissolution of olivine. These authors proposed that differences in serpentinization rates determined experimentally resulted from the use of different composition of starting fluids.

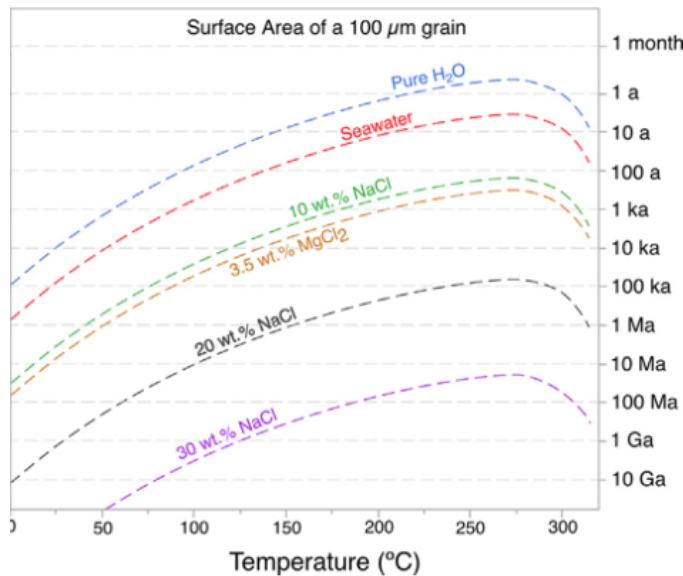


FIGURE 1.25 – Dependence of serpentinization rates on fluid chemistry, figure from Lamadrid et al. 2021.

1.5 Geochemical tools

Since the discovery of hydrothermal systems on the seafloor (e.g., Rona 1984), many investigations were performed with the aim to i) characterize the source of fluids leading to the formation of these hydrothermal systems and the associated metal deposits, and ii) determine at which temperatures fluid-rock interactions occurred. The radiogenic (e.g., Sr, Nd, Hf) and stable isotope (e.g., C, O, S, B, Li) are power full tracers of fluid-rock interactions in oceanic domains (e.g., Mcculloch et al. 1980 ; Albarede et al. 1981 ; Shanks et al. 1995 ; Vils et al. 2008). The stable isotopes allowed also to determine the temperature of fluid-rock interactions (e.g., Wenner and Taylor 1971).

1.5.1 Geochemical tracers

Radiogenic isotopes

The main hydrothermal reservoirs including seawater, the mantle, the oceanic crust and the continental crust have different Sr content and isotopic signatures. For example, the seawater contains 8 ppm of with $^{87}\text{Sr}/^{86}\text{Sr} = 0.70917$ while the mantle (DMM) contains 6 ppm of Sr and have $^{87}\text{Sr}/^{86}\text{Sr} = 0.7022$ (Veizer and Compston 1974 ; Salters and Stracke 2004). Consequently, the Sr isotopes were extensively applied to hydrothermal systems and ophiolitic systems to determine the sources of fluids, quantify the fluid-rock interactions or estimated the depth of fluid penetration in ophiolites (e.g., Spooner et al. 1977 ; Albarede et al. 1981 ; Staudigel et al. 1995 ; Bach et al. 2004 ; Delacour et al. 2008b ; Schwarzenbach et al. 2021).

Some study have shown the potential use of Nd as a tracer of fluid-rock interactions for very high fluid/rock ratios (>100) because Nd is mostly immobile and unaffected by low fluid/rock ratios (e.g., Snow et al. 1994 ; Delacour et al. 2008b). Although, Nd isotopes are mostly used to determined the magmatic sources of basalts or gabbros (e.g., Schaltegger et al. 2002).

Stable isotopes

The stable isotopes can be also used as tracers of fluid-rock interactions in most tectonic settings. Indeed, similar to the radiogenic Sr isotopes, stable isotopes have significant different isotopic signatures in most reservoirs of the Earth, including seawater, the continental and oceanic crusts or the mantle (Figure 8.26; Shanks et al. 1995). Consequently, stable isotopes like oxygen was particular applied in oceanic domains (e.g., Agrinier et al. 1995 ; Shanks et al. 1995 ; Früh-Green et al. 1996) and in ophiolitic settings in serpentinites (e.g., Wenner and Taylor Jr 1973 ; Früh-Green et al. 1990 ; Ulrich et al. 2020), carbonated rocks (Weissert and Bernoulli 1984) to determine the fluid/rock ratios and the source of fluids. However, the significance of oxygen isotopes in ophicalcite in the Alps is debated. Bernoulli and Weissert 2021 suggested that the oxygen isotope compositions of Jurassic oceanic ophicalcites were entirely reequilibrated during the Alpine orogeny. In contrast, Coltart et al. 2021 argued that the oxygen isotope signature from a specific exposure in the Platta nappe (Falotta) was not affected by Alpine overprint and recorded the isotopic signature acquired during oceanic hydrothermalism during Jurassic rifting.

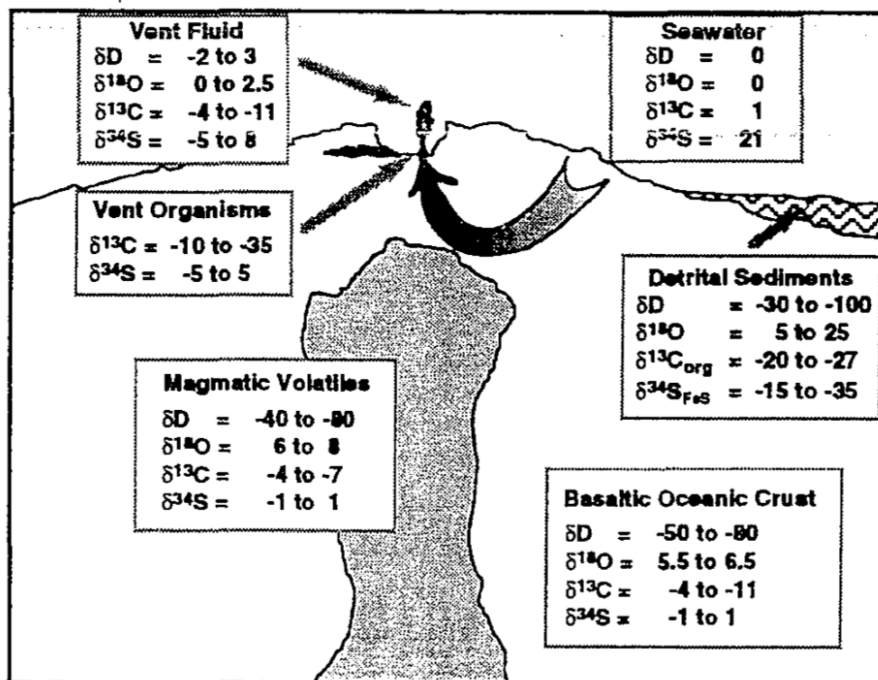


FIGURE 1.26 – Schematic representation of the isotopic signatures in D, C, O and S of the different reservoirs at the mid oceanic ridge hydrothermal system. Figure from Shanks et al. 1995.

Sulfur isotopes was used to determine the redox conditions and the variations in fluid fluxes, in oceanic domains (e.g., Delacour et al. 2008a) and ophiolites (e.g., Schwarzenbach et al. 2012). Sulfur isotopes lead also to determine the source of sulfide minerals in massive sulfide deposits (e.g., Garuti et al. 2008). High values of $\delta^{34}\text{S} \sim 8.9\text{\textperthousand}$ were measured in basalts where sulfur derived from the leaching of magmatic sulfides source and inorganic reduction of seawater. In contrast serpentinite formed near the seafloor have low $\delta^{34}\text{S}$ (2.5-5.8 ‰), suggesting more oxidizing conditions in response to a sulfate reducing bacteria process. More recently, Iron, Zn and Cu stable isotopes have shown their potential for the determination of source of metals and tracing the mobility of metal in hydrothermal systems (e.g., Rouxel et al. 2004a,b; Debret et al. 2018). Boron isotopes are also interesting tracers of fluid-rock interactions, especially between the hydrosphere and the lithosphere reservoirs. Boron have concentrations and isotopic signature sufficiently different in these reservoirs to be use as effective tracers of sources. Boron in the seawater reservoir is about ~ 4.5 ppm Spivack et al. 1987 with an isotopic ratio $\delta^{11}\text{B} = +39.6\text{\textperthousand}$ Foster et al. 2010. In the mantle reservoir, including the depleted MORB mantle (DMM) have a low concentration in boron with in average 0.06 ppm Salters and Stracke 2004 and a isotopic ratio $\delta^{11}\text{B} = -7.1\text{\textperthousand}$ Marshall et al. 2017. In the past two decades, several studies have used the Li isotopes as an effective tracers of fluid-rock interactions, because similarly to other stable isotopes Li concentrations and isotopic signature of the Earth reservoirs are different. In the DMM, Li concentrations is high (± 1.20 ppm Marschall et al. 2017), relative to seawater (± 0.18 ppm Li 1982). The seawater have a $\delta^7\text{Li} = +30.8\text{\textperthousand}$ higher than the DMM $\delta^7\text{Li} = +3.4\text{\textperthousand}$ Tomascak et al. 2008. However, recently Marschall and Tang 2020 have shown that Li isotopes failed to trace fluid-rock interactions, because strong diffusive fractionation occurred in magmatic and metamorphic systems. However, the fractionation related to the diffusivity can be used as potential geochronometer of the timescales of geological processes. Liu et al. 2020 have suggested that the elemental and isotopic variations recorded by olivine, clinopyroxene and orthopyroxene of abyssal peridotites highlighted a two stage process, with i) high-temperature mineral-melt Li diffusion during melt impregnation overprinted by ii) low-temperature mineral-fluid Li diffusion during dissolution and serpentization.

The stable isotopes can be used as tracers only if no fractionation occurred. Fractionation corresponds to the partitioning of isotopes between phases (e.g., aqueous or solid). The hydrothermal circulations depend of many factors, including the temperature, oxidation-reduction, pH which can affects the isotopes fractionation. This can

impacts the interpretation of stable isotopes as tracers of sources. In this case it can be more relevant to used the radiogenic isotopes like the Sr which are not affected by isotope fractionation. However, the isotope fractionation leads to use the stable isotope for determine the conditions including the temperature or pH of these fluid-rocks interactions. As a consequence, several geothermometer were developed based of the fractionation of these isotopes.

1.5.2 Geothermometer

Currently, the temperature serpentinization is estimated on the basis of two geothermometers which were not calibrated on serpentinite. The first one was developed by Wenner and Taylor 1971 and is based on the fractionation of oxygen isotopes ($^{18}\text{O}/^{16}\text{O}$) between coexisting Fe-Ti oxides and chlorite in low-grade pelitic schists. The results were then extrapolated on the serpentine-magnetite couple of serpentinite, although its application on such system has never been clearly demonstrated so far. The second geothermometer was proposed more recently by Saccoccia et al. 2009. This study investigated the oxygen and hydrogen isotopes fractionation between serpentine and water during the recrystallization of lizardite into chrysotile in the range of 250-450°C. However, lower temperatures of serpentinization are expected at passive margins (<200°C; Agrinier et al. 1995; Skelton and Valley 2000). The development of a new geothermometer is needed for a more precise determination of temperature of serpentinization. Although so far this geothermometer was largely used to determine temperature of fluid-rock interactions, serpentinization and carbonation in hydrothermal systems (e.g., Hess Deep Früh-Green et al. 1996 ; Iberia Abyssal plain Skelton and Valley 2000) and ophiolitic domains (e.g., Western Alps Lafay et al. 2017; Eastern Central Alps Burkhard and O’Neil 1988 ; Incerpi et al. 2020).

Recently, boron geothermometry based on isotopes fractionation between muscovite and tourmaline was experimentally calibrated by Codeço et al. 2019 with the aim to study the mineralization conditions and the evolution of the fluids associated to magmatic hydrothermal systems. Muscovite and tourmaline coexist in many hydrothermal ore deposits and in the associated granites or pegmatites. The difference in $\delta^{11}\text{B}/\delta^{10}\text{B}$ ratios between these coexisting minerals expressed as $\Delta^{11}\text{B}_{\text{mica-tourmaline}} = \delta^{11}\text{B}_{\text{mica}} - \delta^{11}\text{B}_{\text{tourmaline}}$ is thermo dependant. Millot et al. 2010 conducted seawater/basalt experiment and shown that lithium isotopic exchange is strongly dependant of the temperature and that significant fractionation occurred during the formation of

secondary minerals. Their results highlights also that lithium isotopes allowed the characterization of the origin of geothermal waters and the nature of their reservoir rocks.

1.6 Approach of the thesis

In this thesis we investigated the serpentinization process during mantle exhumation at magma-poor rifted passive margins. In particular, we aim at :

- characterizing the different steps of fluid-rock interaction during mantle exhumation
- estimating the conditions of serpentinization (temperature, depth and fluid/rock ratios)
- determining the sources of serpentinizing fluids
- understanding how these fluids interacted with mantle rocks and characterizing their evolution
- characterizing the mobilization of transition metals and formation of metal deposits in hydrothermal system

All these questions have been addressed applying two complementary approaches :

The first one consists in the study of serpentined peridotites sampled in Alpine ophiolites, which are remnants of an ancient Ocean Continent Transition (OCT) of the Alpine Tethys ocean which separated the European and Adriatic margins in the Jurassic. The three nappes of Platta, Tasna and Totalp, all located in the southeast of Switzerland, were sampled during this thesis. These nappes were mostly preserved from Alpine metamorphic overprint (e.g., Froitzheim and Rubatto 1998), thus keeping the pre-Alpine rift-related contacts between the subcontinental mantle and syn-rift sediments particularly well preserved Manatschal 2004. In this part, we combined petrological, mineralogical and geochemical investigations to serpentinites with the aim to determine the different steps of mantle exhumation and their conditions (temperature, fluid/rocks ratios, pressure) recorded by different serpentinization events. In parallel, a complementary study was conducted with the aim of identifying the sources of fluids involved in the formation of Fe-Ca silicates formed in metals deposits of a Jurassic mineralized system hosted in serpentinites described in the Platta nappe Coltat et al. 2019. Here, we combined petrological and isotopic approaches. We have measured the Sr isotope compositions of the Fe-Ca silicates and the potential contributors (i.e., the metasomatic rocks : serpentinites, altered gabbros and basalts).

The second approach of this thesis consists in reproducing experimentally the serpentinization reaction, in order to i) identify and quantify the mass fluxes during serpentinization with the aim of estimating the potential mobilization of transitions metals during hydrothermal alteration of mantle and the formation of U-VMS ; ii) determine the boron isotope fractionation between serpentine and fluid and between serpentine and magnetite, to develop a new geothermometer of serpentinization, with the aim to be applied on natural samples, and determined temperature of serpentinization. Indeed, since boron is a fluid mobile element, depleted in the mantle but enriched in the seawater, it is thus a sensitive tracer of fluid-rock interactions between these two reservoirs. Some studies have demonstrated that oceanic serpentinites are strongly enriched in boron in contrast to peridotites from the depleted mantle (e.g., Vils et al. 2009). We conducted serpentinization experiments by interacting fresh peridotites including lherzolite and harzburgite with natural seawater in a titanium bag itself placed into an autoclave. This experimental setup allows to control precisely the temperature and pressure of experiments and sample the fluid during the experiments. These experiments were conducted at 5 temperatures : 225°C, 260°C, 280°C, 300°C and 325°C, at 450 bar and at low fluid/rock ratios which are comprised between 1.6 and 2.1, promoting the formation of magnetite which was necessary for the development a new geothermometer.

Bibliographie

- Agrinier, P., Hékinian, R., Bideau, D., and Javoy, M. (1995). O and h stable isotope compositions of oceanic crust and upper mantle rocks exposed in the hess deep near the galapagos triple junction. *Earth and Planetary Science Letters*, 136(3-4):183–196.
- Albarede, F., Michard, A., Minster, J. F., and Michard, G. (1981). 87sr/86sr ratios in hydrothermal waters and deposits from the east pacific rise at 21°N. *Earth and Planetary Science Letters*, 55:229–236.
- Albers, E., Bach, W., Pérez-Gussinyé, M., McCammon, C., and Frederichs, T. (2021). Serpentization-driven h₂ production from continental break-up to mid-ocean ridge spreading : unexpected high rates at the west iberia margin. *Frontiers in Earth Science*, 9.
- Allen, D. E. and Seyfried Jr, W. (2003). Compositional controls on vent fluids from ultramafic-hosted hydrothermal systems at mid-ocean ridges : An experimental study at 400 c, 500 bars. *Geochimica et Cosmochimica Acta*, 67(8):1531–1542.
- Allen, D. E. and Seyfried Jr, W. (2005). Ree controls in ultramafic hosted mor hydrothermal systems : an experimental study at elevated temperature and pressure. *Geochimica et Cosmochimica Acta*, 69(3):675–683.
- Alt, J. C., Schwarzenbach, E. M., Früh-Green, G. L., Shanks III, W. C., Bernasconi, S. M., Garrido, C. J., Crispini, L., Gaggero, L., Padrón-Navarta, J. A., and Marchesi, C. (2013). The role of serpentinites in cycling of carbon and sulfur : Seafloor serpentinization and subduction metamorphism. *Lithos*, 178:40–54.
- Alt, J. C. and Shanks III, W. C. (2003). Serpentinization of abyssal peridotites from the mark area, mid-atlantic ridge : sulfur geochemistry and reaction modeling. *Geochimica et cosmochimica Acta*, 67(4):641–653.
- Amann, M., Ulrich, M., Manatschal, G., Pelt, E., Epin, M.-e., Autin, J., and Sauter, D. (2020a). Geochemical characteristics of basalts related to incipient oceanization : The example from the alpine-tethys ocs. *Terra Nova*, 32(1):75–88.
- Amann, M., Ulrich, M., Manatschal, G., Pelt, E., Epin, M. E., Autin, J., and Sauter, D. (2020b). Geochemical characteristics of basalts related to incipient oceanization : The example from the alpine-tethys ocs. *Terra Nova*, 32:75–88.
- Andreani, M., Baronnet, A., Boullier, A.-M., and Gratier, J.-P. (2004). A microstructural study of a “crack-seal” type serpentine vein using sem and tem techniques. *European Journal of Mineralogy*, 16(4):585–595.
- Andreani, M., Grauby, O., Baronnet, A., and Muñoz, M. (2008). Occurrence, composition and growth of polyhedral serpentine. *European Journal of Mineralogy*, 20(2):159–171.

- Andreani, M., Mevel, C., Boullier, A. M., and Escartin, J. (2007). Dynamic control on serpentine crystallization in veins : Constraints on hydration processes in oceanic peridotites. *Geochemistry, Geophysics, Geosystems*, 8.
- Auzende, A.-L., Daniel, I., Reynard, B., Lemaire, C., and Guyot, F. (2004). High-pressure behaviour of serpentine minerals : a raman spectroscopic study. *Physics and Chemistry of Minerals*, 31(5):269–277.
- Bach, W., Alt, J. C., Niu, Y., Humphris, S. E., Erzinger, J., and Dick, H. J. (2001). The geochemical consequences of late-stage low-grade alteration of lower ocean crust at the sw indian ridge : Results from odp hole 735b (leg 176). *Geochimica et Cosmochimica Acta*, 65(19):3267–3287.
- Bach, W., Garrido, C. J., Paulick, H., Harvey, J., and Rosner, M. (2004). Seawater-peridotite interactions : First insights from ODP leg 209, MAR 15°N. *Geochemistry, Geophysics, Geosystems*, 5.
- Barnes, I. and O’NEIL, J. R. (1969). The relationship between fluids in some fresh alpine-type ultramafics and possible modern serpentization, western united states. *Geological Society of America Bulletin*, 80(10):1947–1960.
- Baronnet, A. and Devouard, B. (1996). Topology and crystal growth of natural chrysotile and polygonal serpentine. *Journal of Crystal Growth*, 166(1-4):952–960.
- Bayrakci, G., Minshull, T., Sawyer, D. S., Reston, T. J., Klaeschen, D., Papenberg, C., Ranero, C., Bull, J., Davy, R., Shillington, D., et al. (2016). Fault-controlled hydration of the upper mantle during continental rifting. *Nature Geoscience*, 9(5):384–388.
- Bernoulli, D. and Weissert, H. (1985). Sedimentary fabrics in alpine ophicalcites, south pennine arosa zone, switzerland. *Geology*, 13(11):755–758.
- Bernoulli, D. and Weissert, H. (2021). Oxygen isotopes in ophicalcites : an ever-lasting controversy ? *International Journal of Earth Sciences*, 110(1):1–8.
- Boschi, C., Dini, A., Früh-Green, G. L., and Kelley, D. S. (2008). Isotopic and element exchange during serpentization and metasomatism at the atlantis massif (mar 30 n) : insights from b and sr isotope data. *Geochimica et Cosmochimica Acta*, 72(7):1801–1823.
- Bousquet, R., Oberhänsli, R., Goffé, B., Wiederkehr, M., Koller, F., Schmid, S. M., Schuster, R., Engi, M., Berger, A., and Martinotti, G. (2008). Metamorphism of metasediments at the scale of an orogen : a key to the tertiary geodynamic evolution of the alps. *Geological Society, London, Special Publications*, 298(1):393–411.
- Burkhard, D. J. and O’Neil, J. R. (1988). Contrasting serpentization processes in the eastern central alps. *Contributions to Mineralogy and Petrology*, 99(4):498–506.
- Capitani, G. and Mellini, M. (2004). The modulated crystal structure of antigorite : The m= 17 polysome. *American Mineralogist*, 89(1):147–158.
- Caruso, L. J. and Chernosky, J. (1979). The stability of lizardite. *Can. Mineral*, 17(4):757–769.
- Chalot-Prat, F., Ganne, J., and Lombard, A. (2003). No significant element transfer from the oceanic plate to the mantle wedge during subduction and exhumation of the tethys lithosphere (western alps). *Lithos*, 69(3-4):69–103.
- Codeço, M. S., Weis, P., Trumbull, R. B., Glodny, J., Wiedenbeck, M., and Romer, R. L. (2019). Boron isotope muscovite-tourmaline geothermometry indicates fluid cooling during magmatic-hydrothermal w-sn ore formation. *Economic Geology*, 114(1):153–163.

- Coleman, R. G. (1971). Petrologic and geophysical nature of serpentinites. *Geological Society of America Bulletin*, 82(4):897–918.
- Coltat, R., Boulvais, P., Branquet, Y., Collot, J., Epin, M. E., and Manatschal, G. (2019). Syntectonic carbonation during synmagmatic mantle exhumation at an ocean-continent transition. *Geology*, 47:183–186.
- Coltat, R., Boulvais, P., Branquet, Y., Poujol, M., Gautier, P., and Manatschal, G. (2021). Discussion to “oxygen isotope in ophicalcites : an ever-lasting controversy ?”. *International Journal of Earth Sciences*, 110(3):1117–1121.
- Coltat, R., Boulvais, P., Branquet, Y., Richard, A., Tarantola, A., and Manatschal, G. (2022). Moho carbonation at an ocean-continent transition. *Geology*, 50(3):278–283.
- Compagnoni, R., Cossio, R., and Mellini, M. (2021). Raman anisotropy in serpentine minerals, with a caveat on identification. *Journal of Raman Spectroscopy*, 52(7):1334–1345.
- Debret, B., Beunon, H., Mattielli, N., Andreani, M., da Costa, I. R., and Escartin, J. (2018). Ore component mobility, transport and mineralization at mid-oceanic ridges : A stable isotopes (zn, cu and fe) study of the rainbow massif (mid-atlantic ridge 36°14N). *Earth and Planetary Science Letters*, 503:170–180.
- Delacour, A., Früh-Green, G. L., Bernasconi, S. M., and Kelley, D. S. (2008a). Sulfur in peridotites and gabbros at lost city (30 n, mar) : Implications for hydrothermal alteration and microbial activity during serpentinization. *Geochimica et Cosmochimica Acta*, 72(20):5090–5110.
- Delacour, A., Früh-Green, G. L., Frank, M., Gutjahr, M., and Kelley, D. S. (2008b). Sr-and Nd-isotope geochemistry of the atlantis massif (30 n, mar) : implications for fluid fluxes and lithospheric heterogeneity. *Chemical Geology*, 254(1-2):19–35.
- Deschamps, F., Godard, M., Guillot, S., and Hattori, K. (2013). Geochemistry of subduction zone serpentinites : A review. *Lithos*, 178:96–127.
- Deschamps, F., Guillot, S., Godard, M., Andreani, M., and Hattori, K. (2011). Serpentinites act as sponges for fluid-mobile elements in abyssal and subduction zone environments. *Terra Nova*, 23(3):171–178.
- Deschamps, F., Guillot, S., Godard, M., Chauvel, C., Andreani, M., and Hattori, K. (2010). In situ characterization of serpentinites from forearc mantle wedges : timing of serpentinization and behavior of fluid-mobile elements in subduction zones. *Chemical Geology*, 269(3-4):262–277.
- Desmurs, L., Manatschal, G., and Bernoulli, D. (2001). The Steinmann Trinity revisited : mantle exhumation and magmatism along an ocean-continent transition : the Platta nappe, eastern Switzerland. *Contributions to Mineralogy and Petrology*, 144:365–382.
- Desmurs, L., Müntener, O., and Manatschal, G. (2002). Onset of magmatic accretion within a magma-poor rifted margin : a case study from the Platta ocean-continent transition, eastern Switzerland. *Contributions to Mineralogy and Petrology*, 144(3):365–382.
- Dietrich, V. (1970). *Die Stratigraphie der Platta-Decke : Fazielle Zusammenhänge zwischen Oberpenninikum und Unterostalpin*. Geologisches Institut der Eidg. Technischen Hochschule und der Universität.

- Dietrich, V. J. (1969). *Die Ophiolithe des Oberhalbsteins (Graubünden) und das Ophiolithmaterial der ostschweizerischen Molasseablagerungen : ein petrographischer Vergleich.* PhD thesis, ETH Zurich.
- Dilek, Y., Coulton, A., Hurst, S. D., et al. (1997). Serpentinization and hydrothermal veining in peridotites at site 920 in the mark area. In *Proceedings-Ocean Drilling Program Scientific Results*, pages 35–60. National Science Foundation.
- Epin, M.-E. and Manatschal, G. (2018). Three-dimensional architecture, structural evolution, and role of inheritance controlling detachment faulting at a hyperextended distal margin : The example of the err detachment system (SE Switzerland). *Tectonics*, 37(12):4494–4514.
- Epin, M. E., Manatschal, G., Amman, M., Ribes, C., Clausse, A., Guffon, T., and Lescanne, M. (2019). Polyphase tectono-magmatic evolution during mantle exhumation in an ultra-distal, magma-poor rift domain : example of the fossil platta ophiolite, se switzerland. *International Journal of Earth Sciences*, 108:2443–2467.
- Escario, S., Godard, M., Gouze, P., and Leprovost, R. (2018). Experimental study of the effects of solute transport on reaction paths during incipient serpentinization. *Lithos*, 323:191–207.
- Escartin, J., Hirth, G., and Evans, B. (1997). Effects of serpentinization on the lithospheric strength and the style of normal faulting at slow-spreading ridges. *Earth and Planetary Science Letters*, 151(3-4):181–189.
- Escartin, J., Hirth, G., and Evans, B. (2001). Strength of slightly serpentinized peridotites : Implications for the tectonics of oceanic lithosphere. *Geology*, 29(11):1023–1026.
- Etiope, G. (2017). Abiotic methane in continental serpentinization sites : an overview. *Procedia Earth and Planetary Science*, 17:9–12.
- Evans, B. W. (2004). The serpentinite multisystem revisited : chrysotile is metastable. *International Geology Review*, 46(6):479–506.
- Evans, B. W. et al. (1976). Stability of chrysotile and antigorite in the serpentinite multisystem. *Schweiz. Mineral. Petrol. Mitt.*, 56(1):79–93.
- Florineth, D. and Froitzheim, N. (1994). Transition from continental to oceanic basement in the tasna nappe : evidence for early cretaceous opening of the valais ocean. *Schweizerische Mineralogische und Petrographische Mitteilungen*, 74(3):437 ?448.
- Foster, G., Pogge von Strandmann, P. A., and Rae, J. (2010). Boron and magnesium isotopic composition of seawater. *Geochemistry, Geophysics, Geosystems*, 11(8).
- Fouquet, Y., Cambon, P., Etoubleau, J., Charlou, J. L., Ondreas, H., Barriga, F. J., Cherkašov, G., Semkova, T., Poroshina, I., Bohn, M., Donval, J. P., Henry, K., Murphy, P., and Rouxel, O. (2013). Geodiversity of hydrothermal processes along the Mid-Atlantic Ridge and ultramafic-hosted mineralization : A new type of oceanic cu-zn-co-au volcanogenic massive sulfide deposit. *Geophysical Monograph Series*, 188:321–367.
- Froitzheim, N. and Manatschal, G. (1996). Kinematics of jurassic rifting, mantle exhumation, and passive-margin formation in the austroalpine and penninic nappes (eastern switzerland). *Geological society of America bulletin*, 108(9):1120–1133.

- Froitzheim, N. and Rubatto, D. (1998). Continental breakup by detachment faulting : field evidence and geochronological constraints (tasna nappe, switzerland). *Terra Nova*, 10(4):171–176.
- Früh-Green, G. L., Connolly, J. A., Plas, A., Kelley, D. S., and Grobety, B. (2004). Serpentinization of oceanic peridotites : implications for geochemical cycles and biological activity. *The subseafloor biosphere at mid-ocean ridges*, 144:119–136.
- Früh-Green, G. L., Plas, A., and Lécuyer, C. (1996). 14. petrologic and stable isotope constraints on hydrothermal alteration and serpentinization of the epr shallow mantle at hess deep (site 895). In *Proceedings of the ocean drilling program, scientific results*, volume 147, pages 255–291.
- Früh-Green, G. L., Weissert, H., and Bernoulli, D. (1990). A multiple fluid history recorded in Alpine ophiolites. *Journal of the Geological Society*, 147(6):959–970.
- Garuti, G., Bartoli, O., Scacchetti, M., and Zaccarini, F. (2008). Volcanic massive sulfide deposits in the northern apennines, italy geological setting and structural styles of volcanic massive sulfi de deposits in the northern apennines (italy) : evidence for seafloor and sub-seafloor hydrothermal activity in unconventional ophiolites of the mesozoic tethys. *Boleten dela Sociedad Geologica Mexicana*, 60:121–145.
- Gillard, M., Autin, J., and Manatschal, G. (2016a). Fault systems at hyper-extended rifted margins and embryonic oceanic crust : Structural style, evolution and relation to magma. *Marine and Petroleum Geology*, 76:51–67.
- Gillard, M., Manatschal, G., and Autin, J. (2016b). How can asymmetric detachment faults generate symmetric ocean continent transitions ? *Terra Nova*, 28(1):27–34.
- Grauby, O., Baronnet, A., Devouard, B., Schoumacker, K., and Demirdjian, L. (1998). The chrysotile-polygonal serpentine-lizardite suite synthesized from a 3mgo-2sio₂-excess h₂o gel. In *The 7th International Symposium on Experimental Mineralogy, Petrology, and Geochemistry, Orléans, Abstracts. Terra Nova, supplement*, volume 1, page 24.
- Groppi, C., Rinaudo, C., Cairo, S., Gastaldi, D., and Compagnoni, R. (2006). Micro-raman spectroscopy for a quick and reliable identification of serpentine minerals from ultramafics. *European Journal of Mineralogy*, 18(3):319–329.
- Guillot, S., Hattori, K. H., and de Sigoyer, J. (2000). Mantle wedge serpentinization and exhumation of eclogites : insights from eastern ladakh, northwest himalaya. *Geology*, 28(3):199–202.
- Guillot, S., Schwartz, S., Reynard, B., Agard, P., and Prigent, C. (2015). Tectonic significance of serpentinites. *Tectonophysics*, 646:1–19.
- Hannington, M., Herzig, P., Stoffers, P., Scholten, J., Botz, R., Garbe-Schönberg, D., Jonasson, I., and Roest, W. (2001). First observations of high-temperature submarine hydrothermal vents and massive anhydrite deposits off the north coast of iceland. *Marine Geology*, 177(3-4):199–220.
- Hannington, M. D., De Ronde, C. E., and Petersen, S. (2005). Sea-floor tectonics and submarine hydrothermal systems. *Society of Economic Geologists*, pages 111–141.
- Hansen, C. T., Meixner, A., Kasemann, S. A., and Bach, W. (2017). New insight on li and b isotope fractionation during serpentinization derived from batch reaction investigations. *Geochimica et Cosmochimica Acta*, 217:51–79.

- Hochscheid, F., Coltat, R., Ulrich, M., Munoz, M., Manatschal, G., and Boulvais, P. (2022). The sr isotope geochemistry of oceanic ultramafic-hosted mineralizations. *Ore Geology Reviews*, page 104824.
- Holm, N. G. and Charlou, J. L. (2001). Initial indications of abiotic formation of hydrocarbons in the rainbow ultramafic hydrothermal system, mid-atlantic ridge. *Earth and Planetary Science Letters*, 191(1-2):1–8.
- Holm, N. G., Oze, C., Mousis, O., Waite, J., and Guillet-Lepoutre, A. (2015). Serpentization and the formation of h₂ and ch₄ on celestial bodies (planets, moons, comets). *Astrobiology*, 15(7):587–600.
- Huang, R., Ding, X., Lin, C.-T., Zhan, W., and Ling, M. (2018). Effect of saline fluids on chlorine incorporation in serpentine. *Solid Earth Sciences*, 3(3):61–66.
- Huang, R., Song, M., Ding, X., Zhu, S., Zhan, W., and Sun, W. (2017). Influence of pyroxene and spinel on the kinetics of peridotite serpentinization. *Journal of Geophysical Research : Solid Earth*, 122(9):7111–7126.
- Huang, R., Sun, W., Ding, X., Zhao, Y., and Song, M. (2020). Effect of pressure on the kinetics of peridotite serpentinization. *Physics and Chemistry of Minerals*, 47(7):1–14.
- Incerpi, N., Martire, L., Manatschal, G., Bernasconi, S. M., Gerdes, A., Czuppon, G., Palcsu, L., Karner, G. D., Johnson, C. A., and Figueredo, P. H. (2020). Hydrothermal fluid flow associated to the extensional evolution of the adriatic rifted margin : Insights from the pre-to post-rift sedimentary sequence (se switzerland, n italy). *Basin Research*, 32(1):91–115.
- Jackson, J. A. (1987). Active normal faulting and crustal extension. *Geological Society, London, Special Publications*, 28:3–17.
- Jamieson, J. W. and Gartman, A. (2020). Defining active, inactive, and extinct seafloor massive sulfide deposits. *Marine Policy*, 117:103926.
- Janecky, D. and Seyfried, W. (1986). Hydrothermal serpentinization of peridotite within the oceanic crust : Experimental investigations of mineralogy and major element chemistry. *Geochimica et Cosmochimica Acta*, 50(7):1357–1378.
- Johnson, D. E. (2019). Protecting the lost city hydrothermal vent system : All is not lost, or is it ? *Marine Policy*, 107:103593.
- Kelley, D. S., Karson, J. A., Blackman, D. K., Früh-Green, G. L., Butterfield, D. A., Lilley, M. D., Olson, E. J., Schrenk, M. O., Roe, K. K., Lebon, G. T., et al. (2001). An off-axis hydrothermal vent field near the mid-atlantic ridge at 30° n. *Nature*, 412(6843):145–149.
- Kerrick, D. (2002). Serpentinite seduction. *Science*, 298(5597):1344–1345.
- Klein, F., Bach, W., Jöns, N., McCollom, T., Moskowitz, B., and Berquo, T. (2009). Iron partitioning and hydrogen generation during serpentinization of abyssal peridotites from 15° n on the mid-atlantic ridge. *Geochimica et Cosmochimica Acta*, 73(22):6868–6893.
- Klein, F., Bach, W., and McCollom, T. M. (2013). Compositional controls on hydrogen generation during serpentinization of ultramafic rocks. *Lithos*, 178:55–69.
- Klein, F., Grozeva, N. G., Seewald, J. S., McCollom, T. M., Humphris, S. E., Moskowitz, B., Berquo, T. S., and Kahl, W.-A. (2015). Experimental constraints on fluid-rock reactions during incipient serpentinization of harzburgite. *American Mineralogist*, 100(4):991–1002.

- Klein, F. and McCollom, T. M. (2013). From serpentinization to carbonation : new insights from a co₂ injection experiment. *Earth and Planetary Science Letters*, 379:137–145.
- Klein, F. and Roux, V. L. (2020). Quantifying the volume increase and chemical exchange during serpentinization. *Geology*, 48:552–556.
- Lafay, R., Baumgartner, L. P., Stephane, S., Suzanne, P., German, M.-H., and Torsten, V. (2017). Petrologic and stable isotopic studies of a fossil hydrothermal system in ultramafic environment (chenaillet ophicalcites, western alps, france) : processes of carbonate cementation. *Lithos*, 294:319–338.
- Lafay, R., Montes-Hernandez, G., Janots, E., Chiriac, R., Findling, N., and Toche, F. (2012). Mineral replacement rate of olivine by chrysotile and brucite under high alkaline conditions. *Journal of Crystal Growth*, 347(1):62–72.
- Lamadrid, H., Zajacz, Z., Klein, F., and Bodnar, R. (2021). Synthetic fluid inclusions xxiii. effect of temperature and fluid composition on rates of serpentinization of olivine. *Geochimica et Cosmochimica Acta*, 292:285–308.
- Lamadrid, H. M., Rimstidt, J. D., Schwarzenbach, E. M., Klein, F., Ulrich, S., Dolocan, A., and Bodnar, R. J. (2017). Effect of water activity on rates of serpentinization of olivine. *Nature Communications*, 8(1):1–9.
- Li, Y.-H. (1982). A brief discussion on the mean oceanic residence time of elements. *Geochimica et Cosmochimica Acta*, 46(12):2671–2675.
- Liu, P.-P., Liang, J., Dick, H. J., Li, X.-H., Chen, Q., Zuo, H.-Y., and Wu, J.-C. (2020). Enormous lithium isotopic variations of abyssal peridotites reveal fast cooling and melt/fluid-rock interactions. *Journal of Geophysical Research : Solid Earth*, 125(9):e2020JB020393.
- Malvoisin, B., Brunet, F., Carlut, J., Rouméjon, S., and Cannat, M. (2012a). Serpentinization of oceanic peridotites : 2. kinetics and processes of san carlos olivine hydrothermal alteration. *Journal of Geophysical Research : Solid Earth*, 117(B4).
- Malvoisin, B., Carlut, J., and Brunet, F. (2012b). Serpentinization of oceanic peridotites : 1. a high-sensitivity method to monitor magnetite production in hydrothermal experiments. *Journal of Geophysical Research : Solid Earth*, 117(B1).
- Manatschal, G. (2004). New models for evolution of magma-poor rifted margins based on a review of data and concepts from west iberia and the alps. *International Journal of Earth Sciences*, 93:432–466.
- Manatschal, G., Chenin, P., Ghienne, J.-F., Ribes, C., and Masini, E. (2022). The syn-rift tectono-stratigraphic record of rifted margins (part i) : Insights from the alpine tethys. *Basin Research*, 34(1):457–488.
- Manatschal, G., Engström, A., Desmurs, L., Schaltegger, U., Cosca, M., Müntener, O., and Bernoulli, D. (2006). What is the tectono-metamorphic evolution of continental break-up : the example of the tasna ocean–continent transition. *Journal of Structural Geology*, 28(10):1849–1869.
- Manatschal, G. and Müntener, O. (2009). A type sequence across an ancient magma-poor ocean–continent transition : the example of the western alpine tethys ophiolites. *Tectonophysics*, 473(1-2):4–19.

- Manatschal, G., Müntener, O., Lavier, L., Minshull, T., and Péron-Pinvidic, G. (2007). Observations from the alpine tethys and iberia–newfoundland margins pertinent to the interpretation of continental breakup. *Geological Society, London, Special Publications*, 282(1):291–324.
- Manatschal, G. and Nievergelt, P. (1997). A continent-ocean transition recorded in the err and platta nappes (eastern switzerland). *Eclogae Geologicae Helvetiae*, 90(1):3–28.
- Marcaillou, C., Munoz, M., Vidal, O., Parra, T., and Harfouche, M. (2011). Mineralogical evidence for h2 degassing during serpentization at 300 c/300 bar. *Earth and Planetary Science Letters*, 303(3-4):281–290.
- Marschall, H. R. (2018). Boron isotopes in the ocean floor realm and the mantle. *Boron isotopes*, pages 189–215.
- Marschall, H. R. and Tang, M. (2020). High-temperature processes : is it time for lithium isotopes? *Elements : An International Magazine of Mineralogy, Geochemistry, and Petrology*, 16(4):247–252.
- Marschall, H. R., Wanless, V. D., Shimizu, N., Von Strandmann, P. A. P., Elliott, T., and Monteleone, B. D. (2017). The boron and lithium isotopic composition of mid-ocean ridge basalts and the mantle. *Geochimica et Cosmochimica Acta*, 207:102–138.
- Marshall, E. W., Barnes, J. D., and Lassiter, J. C. (2017). The role of serpentinite-derived fluids in metasomatism of the colorado plateau (usa) lithospheric mantle. *Geology*, 45(12):1103–1106.
- Martin, B. and Fyfe, W. (1970). Some experimental and theoretical observations on the kinetics of hydration reactions with particular reference to serpentization. *Chemical Geology*, 6:185–202.
- McCaig, A. M., Titarenko, S. S., Savov, I. P., Cliff, R. A., Banks, D., Boyce, A., and Agostini, S. (2018). No significant boron in the hydrated mantle of most subducting slabs. *Nature communications*, 9(1):1–10.
- McCollom, T. M., Klein, F., Moskowitz, B., Berquó, T. S., Bach, W., and Templeton, A. S. (2020a). Hydrogen generation and iron partitioning during experimental serpentization of an olivine–pyroxene mixture. *Geochimica et Cosmochimica Acta*, 282:55–75.
- McCollom, T. M., Klein, F., Robbins, M., Moskowitz, B., Berquó, T. S., Jöns, N., Bach, W., and Templeton, A. (2016). Temperature trends for reaction rates, hydrogen generation, and partitioning of iron during experimental serpentization of olivine. *Geochimica et Cosmochimica Acta*, 181:175–200.
- McCollom, T. M., Klein, F., Solheid, P., and Moskowitz, B. (2020b). The effect of ph on rates of reaction and hydrogen generation during serpentization. *Philosophical Transactions of the Royal Society A*, 378(2165):20180428.
- McCollom, T. M. and Seewald, J. S. (2007). Abiotic synthesis of organic compounds in deep-sea hydrothermal environments. *Chemical reviews*, 107(2):382–401.
- Mcculloch, M. T., Gregory, R. T., Wasserburg, G. J., and Taylor, H. P. (1980). A neodymium, strontium, and oxygen isotopic study of the cretaceous samail ophiolite and implications for the petrogenesis and seawater-hydrothermal alteration of oceanic crust. *Earth and Planetary Science Letters*, 46:201.

- Mellini, M., Trommsdorff, V., and Compagnoni, R. (1987). Antigorite polysomatism : behaviour during progressive metamorphism. *Contributions to Mineralogy and Petrology*, 97(2):147–155.
- Mével, C. (2003). Serpentinization of abyssal peridotites at mid-ocean ridges. *Comptes Rendus Geoscience*, 335(10-11):825–852.
- Miller, H. M., Matter, J. M., Kelemen, P., Ellison, E. T., Conrad, M. E., Fierer, N., Ruchala, T., Tominaga, M., and Templeton, A. S. (2016). Modern water/rock reactions in oman hyperalkaline peridotite aquifers and implications for microbial habitability. *Geochimica et Cosmochimica Acta*, 179:217–241.
- Millot, R., Scaillet, B., and Sanjuan, B. (2010). Lithium isotopes in island arc geothermal systems : Guadeloupe, martinique (french west indies) and experimental approach. *Geochimica et Cosmochimica Acta*, 74(6):1852–1871.
- Mohn, G., Manatschal, G., Beltrando, M., Masini, E., and Kusznir, N. (2012). Necking of continental crust in magma-poor rifted margins : Evidence from the fossil alpine tethys margins. *Tectonics*, 31(1).
- Moody, J. B. (1976). Serpentinization : a review. *Lithos*, 9(2):125–138.
- Müntener, O., Manatschal, G., Desmurs, L., and Pettke, T. (2010). Plagioclase peridotites in ocean-continent transitions : refertilized mantle domains generated by melt stagnation in the shallow mantle lithosphere. *Journal of Petrology*, 51(1-2):255–294.
- Müntener, O., Pettke, T., Desmurs, L., Meier, M., and Schaltegger, U. (2004). Refertilization of mantle peridotite in embryonic ocean basins : trace element and nd isotopic evidence and implications for crust–mantle relationships. *Earth and Planetary Science Letters*, 221(1-4):293–308.
- Müntener, O. and Piccardo, G. B. (2004). Melt migration in ophiolitic peridotites : The message from alpine-apennine peridotites and implications for embryonic ocean basins. *Geological Society Special Publication*, 218:69–89.
- Nakatani, T. and Nakamura, M. (2016). Experimental constraints on the serpentization rate of fore-arc peridotites : Implications for the upwelling condition of the slab-derived fluid. *Geochemistry, Geophysics, Geosystems*, 17(8):3393–3419.
- Nast, H. J. and Williams-Jones, A. E. (1991). The role of water-rock interaction and fluid evolution in forming the porphyry-related sisson brook w-cu-mo deposit, new brunswick. *Economic Geology*, 86(2):302–317.
- O'Hanley, D. S. (1992). Solution to the volume problem in serpentization. *Geology*, 20(8):705–708.
- O'Hanley, D. S. and Dyar, M. D. (1993). The composition of lizardite 1t and the formation of magnetite in serpentinites. *American Mineralogist*, 78(3-4):391–404.
- Osselin, F., Pichavant, M., Champallier, R., Ulrich, M., and Raimbourg, H. (2022). Reactive transport experiments of coupled carbonation and serpentization in a natural serpentinite. implication for hydrogen production and carbon geological storage. *Geochimica et Cosmochimica Acta*, 318:165–189.
- Page, N. J. (1968). Chemical differences among the serpentine “polymorphs”. *American Mineralogist : Journal of Earth and Planetary Materials*, 53(1-2):201–215.

- Patten, C. G., Coltat, R., Junge, M., Peillod, A., Ulrich, M., Manatschal, G., and Kolb, J. (2021). Ultramafic-hosted volcanogenic massive sulfide deposits : an overlooked sub-class of vms deposit forming in complex tectonic environments. *Earth-Science Reviews*, page 103891.
- Pens, M., Andreani, M., Daniel, I., Perrillat, J.-P., and Cardon, H. (2016). Contrasted effect of aluminum on the serpentinization rate of olivine and orthopyroxene under hydrothermal conditions. *Chemical Geology*, 441:256–264.
- Pérez-Gussinyé, M. and Reston, T. J. (2001). Rheological evolution during extension at nonvolcanic rifted margins : Onset of serpentinization and development of detachments leading to continental breakup. *Journal of Geophysical Research : Solid Earth*, 106(B3):3961–3975.
- Peters, P. C. and Mathews, J. (1963). Gravitational radiation from point masses in a keplerian orbit. *Physical Review*, 131(1):435.
- Peters, T. and Stettler, A. (1987a). Radiometric age, thermobarometry and mode of emplacement of the totalp peridotite in the eastern swiss alps. *Schweizerische Mineralogische und Petrographische Mitteilungen*, 67(3):285–294.
- Peters, T. and Stettler, A. (1987b). Time, physico-chemical conditions, mode of emplacement and geologic setting of the totalp peridotite in the eastern swiss alps. *Schweiz. Mineral. Petrogr. Mitt*, 67:285–294.
- Picazo, S., Manatschal, G., Cannat, M., and Andréani, M. (2013). Deformation associated to exhumation of serpentized mantle rocks in a fossil Ocean Continent Transition : The Totalp unit in SE Switzerland). *Lithos*, 175:255–271.
- Picazo, S., Müntener, O., Manatschal, G., Bauville, A., Karner, G., and Johnson, C. (2016). Mapping the nature of mantle domains in Western and OCentral Europe based on clinopyroxene and spinel chemistry : Evidence for mantle modification during an extensional cycle. *Lithos*, 266:233–263.
- Pinto, V. H. G., Manatschal, G., Karpoff, A. M., Ulrich, M., and Viana, A. R. (2017). Seawater storage and element transfer associated with mantle serpentinization in magma-poor rifted margins : A quantitative approach. *Earth and Planetary Science Letters*, 459:227–237.
- Pinto, V. H. G., Manatschal, G., Karpoff, A. M., and Viana, A. (2015). Tracing mantle-reacted fluids in magma-poor rifted margins : The example of a lpine t ethyan rifted margins. *Geochemistry, Geophysics, Geosystems*, 16(9):3271–3308.
- Proskurowski, G., Lilley, M. D., Kelley, D. S., and Olson, E. J. (2006). Low temperature volatile production at the lost city hydrothermal field, evidence from a hydrogen stable isotope geothermometer. *Chemical Geology*, 229(4):331–343.
- Proskurowski, G., Lilley, M. D., Seewald, J. S., Fruh-Green, G. L., Olson, E. J., Lupton, J. E., Sylva, S. P., and Kelley, D. S. (2008). Abiogenic hydrocarbon production at lost city hydrothermal field. *Science*, 319(5863):604–607.
- Ramsay, J. G. (1980). The crack-seal mechanism of rock deformation. *Nature*, 284(5752):135–139.
- Ranero, C. R., Phipps Morgan, J., McIntosh, K., and Reichert, C. (2003). Bending-related faulting and mantle serpentinization at the middle america trench. *Nature*, 425(6956):367–373.

- Ribeiro Da Costa, I., Barriga, F. J., Viti, C., Mellini, M., and Wicks, F. J. (2008). Antigorite in deformed serpentinites from the mid-atlantic ridge. *European Journal of Mineralogy*, 20(4):563–572.
- Ribes, C., Petri, B., Ghienne, J.-F., Manatschal, G., Galster, F., Karner, G. D., Figueiredo, P. H., Johnson, C. A., and Karpoff, A.-M. (2020). Tectono-sedimentary evolution of a fossil ocean-continent transition : Tasna nappe, central alps (se switzerland). *Bulletin*, 132(7-8):1427–1446.
- Rona, P. A. (1984). Hydrothermal activity at the trans-atlantic geotraverse hydrothermal field, mid-atlantic ridge crest at 26°N. *Journal of Geophysical Research*, 89:11365–11377.
- Rona, P. A., Hannington, M. D., Raman, C., Thompson, G., Tivey, M. K., Humphris, S. E., Lalou, C., and Petersen, S. (1993). Active and relict sea-floor hydrothermal mineralization at the TAG hydrothermal field, Mid-Atlantic Ridge. *Economic Geology*, 88(8):1989–2017.
- Rouméjon, S. and Cannat, M. (2014). Serpentinization of mantle-derived peridotites at mid-ocean ridges : Mesh texture development in the context of tectonic exhumation. *Geochemistry, Geophysics, Geosystems*, 15(6):2354–2379.
- Roumejon, S., Cannat, M., Agrinier, P., Godard, M., and Andreani, M. (2015). Serpentinization and fluid pathways in tectonically exhumed peridotites from the southwest indian ridge (62–65 e). *Journal of Petrology*, 56(4):703–734.
- Rouxel, O., Fouquet, Y., and Ludden, J. N. (2004a). Copper isotope systematics of the lucky strike, rainbow, and logatchev sea-floor hydrothermal fields on the Mid-Atlantic Ridge. *Economic Geology*, 99:585–600.
- Rouxel, O., Fouquet, Y., and Ludden, J. N. (2004b). Subsurface processes at the lucky strike hydrothermal field, Mid-Atlantic Ridge : Evidence from sulfur, selenium, and iron isotopes. *Geochimica et Cosmochimica Acta*, 68:2295–2311.
- Russell, M., Hall, A., and Martin, W. (2010). Serpentinization as a source of energy at the origin of life. *Geobiology*, 8(5):355–371.
- Saccoccia, P. J., Seewald, J. S., and Shanks III, W. C. (2009). Oxygen and hydrogen isotope fractionation in serpentine–water and talc–water systems from 250 to 450 c, 50 mpa. *Geochimica et Cosmochimica Acta*, 73(22):6789–6804.
- Salters, V. J. and Stracke, A. (2004). Composition of the depleted mantle. *Geochemistry, Geophysics, Geosystems*, 5(5).
- Schaltegger, U., Desmurs, L., Manatschal, G., Müntener, O., Meier, M., Frank, M., and Bernoulli, D. (2002). The transition from rifting to sea-floor spreading within a magma-poor rifted margin : Field and isotopic constraints. *Terra Nova*, 14(3):156–162.
- Schwarzenbach, E. M., Früh-Green, G. L., Bernasconi, S. M., Alt, J. C., Shanks III, W. C., Gaggero, L., and Crispini, L. (2012). Sulfur geochemistry of peridotite-hosted hydrothermal systems : comparing the ligurian ophiolites with oceanic serpentinites. *Geochimica et Cosmochimica Acta*, 91:283–305.
- Schwarzenbach, E. M., Vogel, M., Früh-Green, G. L., and Boschi, C. (2021). Serpentinization, Carbonation, and Metasomatism of Ultramafic Sequences in the northern Apennine Ophiolite (NW Italy). *Journal of Geophysical Research : Solid Earth*, 126.

- Seyfried Jr, W. (1987). Experimental and theoretical constraints on hydrothermal alteration processes at mid-ocean ridges. *Annual Review of Earth and Planetary Sciences*, 15(1):317–335.
- Seyfried Jr, W. and Dibble Jr, W. (1980). Seawater-peridotite interaction at 300 c and 500 bars : implications for the origin of oceanic serpentinites. *Geochimica et Cosmochimica Acta*, 44(2):309–321.
- Seyfried Jr, W., Foustaoukos, D., and Fu, Q. (2007). Redox evolution and mass transfer during serpentinization : An experimental and theoretical study at 200 c, 500 bar with implications for ultramafic-hosted hydrothermal systems at mid-ocean ridges. *Geochimica et Cosmochimica Acta*, 71(15):3872–3886.
- Shanks, W., Boehlke, J. K., Seal, R., et al. (1995). Stable isotopes in mid-ocean ridge hydrothermal systems : Interactions between fluids, minerals, and organisms. *Geophysical Monograph-American Geophysical Union*, 91:194–194.
- Skelton, A. D. and Valley, J. W. (2000). The relative timing of serpentinisation and mantle exhumation at the ocean–continent transition, iberia : constraints from oxygen isotopes. *Earth and Planetary Science Letters*, 178(3-4):327–338.
- Snow, J. E. and Dick, H. J. (1995). Pervasive magnesium loss by marine weathering of peridotite. *Geochimica et Cosmochimica Acta*, 59(20):4219–4235.
- Snow, J. E., Hart, S. R., and Dick, H. J. (1994). Nd and sr isotope evidence linking mid-ocean-ridge basalts and abyssal peridotites. *Nature*, 371(6492):57–60.
- Spivack, A. and Edmond, J. (1987). Boron isotope exchange between seawater and the oceanic crust. *Geochimica et Cosmochimica Acta*, 51(5):1033–1043.
- Spivack, A., Palmer, M., and Edmond, J. (1987). The sedimentary cycle of the boron isotopes. *Geochimica et Cosmochimica Acta*, 51(7):1939–1949.
- Spooner, E., Chapman, H., and Smewing, J. (1977). Strontium isotopic contamination and oxidation during ocean floor hydrothermal metamorphism of the ophiolitic rocks of the troodos massif, cyprus. *Geochimica et Cosmochimica Acta*, 41(7):873–890.
- Staudigel, H., Davies, G., Hart, S. R., Marchant, K., and Smith, B. M. (1995). Large scale isotopic sr, nd and o isotopic anatomy of altered oceanic crust : Dsdp/odp sites417/418. *Earth and Planetary Science Letters*, 130(1-4):169–185.
- Tarling, M. S., Rooney, J. S., Viti, C., Smith, S. A., and Gordon, K. C. (2018). Distinguishing the raman spectrum of polygonal serpentine. *Journal of Raman Spectroscopy*, 49(12):1978–1984.
- Thompson, G. and Melson, W. G. (1970). Boron contents of serpentinites and metabasalts in the oceanic crust : implications for the boron cycle in the oceans. *Earth and Planetary Science Letters*, 8(1):61–65.
- Tichadou, C. (2021). *Etude des processus de serpentinisation et de production d'hydrogène dans la zone Nord-Pyrénéenne occidentale : du terrain à la caractérisation expérimentale.* PhD thesis, Université Montpellier.
- Tomascak, P. B., Langmuir, C. H., le Roux, P. J., and Shirey, S. B. (2008). Lithium isotopes in global mid-ocean ridge basalts. *Geochimica et Cosmochimica Acta*, 72(6):1626–1637.

- Trommsdorff, V. (1983). Metamorphose magnesiumreicher gesteine : kristallischer vergleich von natur, experiment und thermodynamischer datenbasis. *Fortschritte der Mineralogie*, 61(2):283–308.
- Trommsdorff, V. and Evans, B. W. (1977). Antigorite-ophicarbonates : contact metamorphism in valmalenco, italy. *Contributions to Mineralogy and Petrology*, 62(3):301–312.
- Tutolo, B. M., Luhmann, A. J., Tosca, N. J., and Seyfried Jr, W. E. (2018). Serpentinization as a reactive transport process : The brucite silicification reaction. *Earth and Planetary Science Letters*, 484:385–395.
- Ulrich, M., Muñoz, M., Boulvais, P., Cathelineau, M., Cluzel, D., Guillot, S., and Picard, C. (2020). Serpentinization of new caledonia peridotites : from depth to (sub-) surface. *Contributions to Mineralogy and Petrology*, 175(9):1–25.
- Veizer, J. and Compston, W. (1974). $^{87}\text{Sr}/^{86}\text{Sr}$ composition of seawater during the phanerozoic. *Geochimica et Cosmochimica Acta*, 38.
- Vils, F., Pelletier, L., Kalt, A., Müntener, O., and Ludwig, T. (2008). The lithium, boron and beryllium content of serpentized peridotites from odp leg 209 (sites 1272a and 1274a) : implications for lithium and boron budgets of oceanic lithosphere. *Geochimica et Cosmochimica Acta*, 72(22):5475–5504.
- Vils, F., Tonarini, S., Kalt, A., and Seitz, H.-M. (2009). Boron, lithium and strontium isotopes as tracers of seawater–serpentinite interaction at mid-atlantic ridge, odp leg 209. *Earth and Planetary Science Letters*, 286(3-4):414–425.
- Viti, C. and Mellini, M. (1998). Mesh textures and bastites in the elba retrograde serpentinites. *Eur. J. Mineral*, 10:1341–1359.
- Wegner, W. W., Ernst, W., et al. (1983). Experimentally determined hydration and dehydratation reaction rates in the system mgo-sio₂-h₂o. *American Journal of Science*, 283:151–180.
- Weissert, B. J. H. and Bernoulli, D. (1985). A transform margin in the Mesozoic Tethys : evidence from the Swiss Alps. *Geologische Rundschau*, 74:665–679.
- Weissert, H. and Bernoulli, D. (1984). Oxygen isotope composition of calcite in alpine ophicarbonates : a hydrothermal or alpine metamorphic signal ? *Eclogae Geologicae Helvetiae*, 77(1):29–43.
- Wenner, D. B. and Taylor, H. P. (1971). Temperatures of serpentization of ultramafic rocks based on o₁₈/o₁₆ fractionation between coexisting serpentine and magnetite. *Contributions to mineralogy and petrology*, 32(3):165–185.
- Wenner, D. B. and Taylor Jr, H. P. (1973). Oxygen and hydrogen isotope studies of the serpentization of ultramafic rocks in oceanic environments and continental ophiolite complexes. *American Journal of Science*, 273(3):207–239.
- Whittaker, E. and Zussman, J. (1956). The characterization of serpentine minerals by x-ray diffraction. *Mineralogical magazine and journal of the Mineralogical Society*, 31(233):107–126.
- Wicks, F., Whittaker, E., and Zussman, J. (1977). An idealized model for serpentine textures after olivine. *The Canadian Mineralogist*, 15(4):446–458.
- Wicks, F. and Zussman, J. (1975). Microbeam x-ray diffraction patterns of the serpentine minerals. *The Canadian Mineralogist*, 13(3):244–258.

- Wicks, F. J. and O'Hanley, D. S. (2018). Serpentine minerals : structures and petrology. In *Hydrous phyllosilicates*, pages 91–168. De Gruyter.
- Wicks, F. J. and Whittaker, E. (1975). A reappraisal of the structures of the serpentine minerals. *The Canadian Mineralogist*, 13(3):227–243.
- Wunder, B., Wirth, R., and Gottschalk, M. (2001). Antigorite : Pressure and temperature dependence of polysomatism and water content. *European Journal of Mineralogy*, 13(3):485–496.

Chapitre 2

Materials and methods

2.1 Geological study

2.1.1 Sampling strategy

In this thesis, we focused on fluid-rock interactions and especially serpentinitization occurring at the fossil Ocean-continent-Transition (OCT) zone of the Alpine Tethys (Figure 8.10). The OCT zone corresponds to a zone of tens to hundred kilometers located between the continental and the oceanic crust, where the continental crust was extremely thinned and large volume of mantle was exhumed on the seafloor by successive detachment faulting (e.g., Reston 2005).

The study of these fossil OCT zones offers several advantages. Firstly, the access to samples is easier than in present day OCT zone. Secondly, the tectonic and magmatic evolution of these nappes were extensively investigated (e.g., Manatschal and Nievergelt 1997; Manatschal et al. 2006; Schaltegger et al. 2002; Picazo et al. 2013; Epin et al. 2019; Amann et al. 2020) allowing to focus exclusively on the serpentinitization process related to the mantle exhumation.

We have sampled 43 moderately to fully serpentinitized peridotites (i.e., serpentinites) from remnants of the Jurassic Ocean-Continent Transition (OCT) of the Alpine Tethys (Platta, Totalp and Tasna, described in the previous section). We have sampled 14 serpentinites in the Platta nappe, including 9 samples in the Upper Platta unit belonging to the continentwards/proximal domain of the Adriatic margin, and 5 samples in the Lower Platta Unit the oceanwards/distal domain. Another 13 serpentinites were sampled in the Totalp nappe which is located to the north of the Platta nappe in the Adriatic margin. In addition, 16 serpentinites have been sampled in the Tasna nappe (proximal domain) of the Adriatic-European-Briançonnais conjugated margins.

The sampling was done with the aim to characterize fluid-rock interactions at different positions along the OCT, i.e., from proximal domains, (Upper Platta, Tasna and Totalp) to distal (Lower Platta) domains.

All serpentinites were characterized by :

- macroscopic and microscopic observation, to identify the serpentine generations
- X-ray diffraction, to identify minerals and their respective proportions in serpentinites
- Raman spectroscopy, to identify serpentine species
- Bulk rocks major and trace element analyses
- In situ major and trace analyses of serpentine minerals, to assess chemical mo-

- bilities during serpentinization and associated mass fluxes along the margin
- Bulk rocks isotopic Sr and B analyses to determine the source of fluids leading to serpentinization

2.1.2 Sample preparation and analytical investigations

After a macroscopic description of the samples made in the field, the samples were sawed for the preparation of the thin sections. These thin sections were observed under a microscope with the aim to observe the different texture of serpentine, typically the pseudomorphic and veins. These observations allowed also to characterize the different generation of serpentine by inspecting the overlaps of serpentine veins. A fraction of these samples were crushed and then milled with a agate ball mills for mineralogical and chemical analyses.

Loss on Ignition (LOI) was obtained by weighted precisely 1g of rock powder in an alumina crucible that was dried in an furnace. The samples were heated at 1000°C during 3 hours. Successive losses of mass during each step of the procedure is indicative of the amount of water contained in the samples.

Mineralogical investigations

X-Ray Diffraction

The serpentinites finely grounded were inspected by X-Ray diffraction (a non destructive method) with the aim to detect the different minerals constituting the serpentinites. The XRD analyses were performed using a Bruker D8 advance Eco instrument (Figure 2.1) at the Institut Terre et Environnement de Strasbourg (ITES, University of Strasbourg). A large X-ray beam was emitted by a copper source with a 40 kV accelerating voltage and a 25 mA current. Intensities were recorded at 0.014 ° 2θ step intervals from 3 to 80° 2θ , with a dwell time of 0.8 s.

The XRD patterns are then retreated by Rietveld refinement using Profex-BGMIN software Doebelin and Kleeberg 2015 with the aim to quantify the mineralogical compositions. The mineral phases were identified based on JCPDS/ICDD and AMCD references.



FIGURE 2.1 – Photography of the Brucker D8 Advance Eco instrument used for the XRD analyses (photography from ITES website).



FIGURE 2.2 – Photography of the HORIBA LabRAM ARAMIS spectrometer used for the Raman analyses (photography from ICube website).

Raman spectroscopy

The Raman spectra were acquired on $30\mu\text{m}$ thick polished thin sections, using a HORIBA LabRAM ARAMIS spectrometer at the Laboratoire des sciences de l'ingénieur, de l'informatique et de l'imagerie (ICube, University of Strasbourg). We used an argon laser with a wavelength of 632 nm and an output laser power of 100 mW. Measurements were performed using an Olympus lens of 100X to focus the laser beam onto an area of $\sim 1 \mu\text{m}$ in diameter. All analyses were performed using an integrating time of 30 s to optimize the signal-to-noise ratio. Raman spectra were recorded in two wavelength intervals : 100–1120 cm^{-1} for structural bonding characterization and 3500–3750 cm^{-1} for the characterization of hydroxyl bonds. The serpentine species were identified by comparison with reference spectra taken from the literature, in particular on the stretching range of the OH groups (e.g., Auzende et al. 2004; Lemaire 2000).

Chemical investigations

Bulk rock major elements analyses

The dried powders after the LOI were re-ground and compress to 5 mm diameter pellets for analyses of the major elements compositions using a micro X-Ray fluorescence Brucker M4 Tornado at ITES (Figure 2.3. For each samples, 10 measurements were performed in order to check the reproducibility.

The instrument is equipped with a Rh anode operating at $700 \mu\text{A}$ with an accelerating voltage of 50 kV. Polycapillary lenses were used to focus the X-ray beam down to 1 mm full-width-at-half-maximum at the sample surface. Two energy-dispersive silicon drift detectors of 125 eV resolution, and with an active area of 60 mm^2 each were used to measure fluorescence spectra (300s counting time per spectrum). Measurements were performed in a vacuum chamber at 2 mbar to minimize air absorption and ensure the best signal-to-noise ratio. The μ -XRF spectra were calibrated after repeated analyses of Smithsonian mineral standards of diopside (NMNH 117733) and San Carlos olivine (NMNH 111312-44; (Jarosewich, 2002; Jarosewich et al., 1980), and in-house mineral standards of clinochlore, chrysotile and antigorite. Total Fe content was calculated on a divalent basis, as FeO.



FIGURE 2.3 – Photography of the M4 tornado used for μ XRF measurements (photography from ICube website).

Bulk rock trace elements analyses

The whole rock trace elements analysis of the serpentinites were carried out following the analytical procedure of Chauvel et al. 2011. About 100 mg of rock powder was precisely weighed and dissolved in Savillex beakers in a HF-HNO₃-HClO₄ (5:1:1) mixture, during a minimum of 7 days at 140°C on a hot plate. The solution was then evaporated and the residue dissolved in 1 mL H₃BO₃ (boric acid) and 3 mL of 3 M HCl. The boric acid lead to neutralise excess HF. This mixture is heated at 90°C during 12 hours. Then this mixture was evaporated and further dissolved in concentrated HNO₃. Finally the residue is diluted in about 40 ml of 7 M HNO₃ before the trace elements analyses. The measurement of trace elements were performed at the Institut Terre et Environnement de Strasbourg (ITES) using a Inductively Coupled Plasma Mass Spectrometry (ICP-MS) Thermo Scientific X series II instrument and ICAP RQ Thermo Scientific instrument.

Bulk rock strontium isotope analyses

The analytical procedure for the Sr isotopes analysis is similar to those described for the trace elements. However, about 150 mg (100 mg for the trace elements) of rocks were digested because the low concentrations of Sr in our samples. Furthermore, at the end of the acid procedure, the residue is dissolved in chloridric acid (nitric acid was used for trace elements) because the next chemical separation procedure is done with chloridric acid.

The first separation step consists to the elimination of major elements (most of the

cations) and part of the rare earth elements. For do that, we used a 2 mL Biorad AG 50 Wx8 200-400 mesh cationic resin. The column was cleaned four times with 4 M HNO₃. After that the columns was conditioned by 2 mL of 2 M HCl. The sample introduction is done with 2 mL of 2 M HCl. Then the elution is done by 3 mL of 2 M HCl, allowing to removes most of the cations. After this 3 mL, the Sr is releases and recovered in 14 mL of 2 M HCl. The detailed procedure is visible in Table 2.1.

TABLE 2.1 – Different steps for the major elements separation using the 2 mL Biorad AG 50Wx8 200-400 mesh cationic resin.

Step	Reactant	Volume (ml)
cleaning	4 M HNO ₃	4 full
cleaning	H ₂ O	half
conditioning	2 M HCL	2x 2 mL
introduction	2 M HCL	2 mL
cleaning	2 M HCL	2x 0.5 mL
cleaning	2 M HCL	2 mL
Sr recovery	2 M HCL	14 mL

After this first separation step, the 14 mL recovered are evaporated at 120°C. The residue is then dissolved in 1 mL of 2 M HNO₃, evaporated and dissolved in 2 mL of 2 M HNO₃ before being loaded in the second columns resin. The second columns are filled by 300µL of Eichrom Sr-spec biorad resin. The columns was washed with 5.5 ml of 7 M HNO₃ and then eluted with 2.4 ml of 0.05 M HNO₃. Chemical separation and purification were performed following an analytical procedure modified after Pin and Zaldueguil 1997 and Deniel and Pin 2001 and are summarized in Table 2.2.

TABLE 2.2 – Different steps for the Sr recovery using the Eichrom Sr-spec resin.

Step	Reactant	Volume (ml)
conditioning	2 M HNO ₃	2x 1mL
introduction	2 M HNO ₃	2 mL
cleaning	2 M HNO ₃	2x 0.25 mL
cleaning	2 M HNO ₃	1 mL
cleaning	7 M HNO ₃	2x 0.5 mL
cleaning	7 M HNO ₃	3 mL
Sr recovery	0.05 M HNO ₃	2x 0.2 mL
Sr recovery	0.05 M HNO ₃	2 mL

The 2.4 ml recovered after the second step of separation is evaporated and dissolved in 1.5 mL of 0.5 M HCl for the isotopes measurements. The Sr isotope compositions of the serpentinites were determined at ITES using a Neptune Thermo Scientific instrument Multi-Collector Inductively Coupled Plasma Mass Spectrometer (MC-ICP-MS) (Figure 2.4). The samples containing very low quantity of Sr, were measured by a Thermo Finnigan Triton instrument Thermal Ionisation Mass Spectrometer (TIMS) Figure 2.5. For isotopic measurements using a TIMS, the purified Sr solution recovered after the second step separation column is dried and deposited on double filament of rhenium.

The measured $^{87}\text{Sr}/^{86}\text{Sr}$ ratios were normalized to $^{86}\text{Sr}/^{88}\text{Sr} = 0.1194$. During the collection of isotopic data, replicate analysis of NBS 987 (SrCO_3) reference material gave a mean value of 0.710260 ± 8 (2 SE, $n = 26$). The total procedural blank for the whole chemical treatment was 207–233 pg, which is negligible for all samples.



FIGURE 2.4 – Photography of the (MC-ICP-MS) Neptune Thermo Scientific instrument (photography from ITES website).



FIGURE 2.5 – Photography of the Triton TIMS Thermo Scientific instrument (photography from ITES website).

Bulk rock boron isotopes analyses

Sample digestion, boron separation and purification in bulk-rock and mineral separates were done applying the procedure of Lemarchand et al. 2012 and Roux et al. 2015. About 50 mg of sample was mixed with 250 mg of powdered K₂CO₃ and fused in Pt-Au crucibles, in a furnace at 975°C during 45 minutes. After cooling at room temperature, the fusion residue is then dissolved in 400 µL of bi-distilled HCl mixed with 35 mL of milli-Q water (18.2 MΩ·cm H₂O), to reach an acidic pH of ±2-3, and precisely weighed. Repeated centrifugation and decantation assured quantitative extraction of boron. A B-free solid residue after centrifugation and is removed Lemarchand et al. 2012.

The procedure is followed by a two-steps ion exchange chromatography that is represented in Figure 2.6. The first column loaded with 2.8 mL of Biorade AG50W-X12 (200-400 mesh) cation resin is cleaned several times with 6 M HCl. The column is then

conditioned by adding 3x2 mL of 0.01 M HCl. The sample is then loaded and eluted by adding 2x1 mL of 0.01 M HCl. This first step aims at removing cations from the solution, and particularly the potassium contained in K_2CO_3 used as flux for the alkali fusion, but also Fe, Ni, Cr which are significantly concentrated in our samples.

TABLE 2.3 – First step column procedure using the Biorade AG50W-X12 (200-400 mesh) cationic resin.

step	reactant	volume (mL)
conditioning	0.01 M HCL	3x 2 mL
introduction pH 2-3	HCl	5 mL
recovery	0.01 M HCL	2x 1 mL
lavage	6 M HCL	1 full

A second column filled with 0.5 mL of Amberlite IRA743 B-specific (100–200 mesh) resin is used to separate boron. This column is rinsed several times with about 30 mL of 1 M HCl. The column is then conditioned with ultra-pure H_2O in three steps : 1 mL, and 2x2 mL. Then the 7 mL solution collected after the first separation step is loaded onto the Amberlite column. Before sample introduction, pH was readjusted at 8-9 by addition of clean 0.5N NaOH (i.e., B-purified NaOH with Amberlite resin). Three step of rinsing/elution followed the sample introduction, by adding 2.5 mL of ultra-pure H_2O , 2.5 mL of NaCl and 2.5 mL of ultra-pure H_2O . All steps are achieved by adding 1x0.5 mL and 2x1 mL of reactant. NaCl is used to remove anions potentially sorbed by the Amberlite resin due to the presence of tertiary amino groups in the resin. B is then eluted with 5 mL of 0.5N HCl (1x1 mL and 2x2 mL, waiting 10 minutes between the two steps to ensure the resin becomes acidic and all B is desorbed from the resin. The recovered solution collected in 1.2 mL is then diluted if necessary for analyses of boron concentration and isotopes by multi-collector inductively coupled plasma mass-spectrometer (MC-ICP-MS).

The determination of isotope ratio was performed then on the Neptune Thermo Scientific MC-ICP-MS instrument at the ITES laboratory. The bracketing standard solution was prepared with the same 0.5N HCl solution as the one used for elution. The acid used for rinsing was also the same that those used for samples and standard bracketing, to avoid potential isotopic bias induced by the use of various acid media matrices as shown by Roux et al. 2015. The MC-ICP-MS was equipped with eight movable and one fixed Faraday cups. The acquisition of ^{10}B and ^{11}B isotopes was achieved simultaneously by using the H3 and L3 Faraday cups respectively. The measured $^{10}B/^{11}B$ ratio

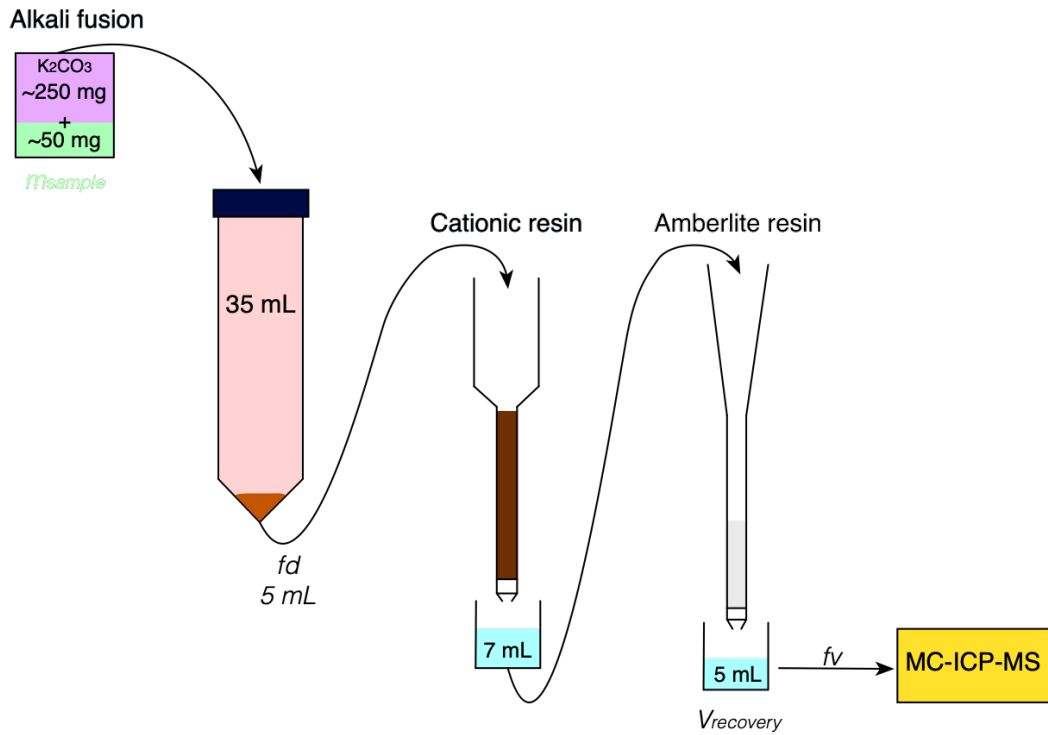


FIGURE 2.6 – Schematic representation of the procedure for boron separation and calculation of the boron concentrations.

was corrected from the instrumental mass bias using the standard-sample-standard bracketing method. Several analyses of seawater and/or rock standards were made during each analytical session to minimize the instrumental deviation. Before each samples and standard measurements, a rinsing time of 20 min. with a 0.5 M HCl solution was done to ensure an accurate baseline determination and correct the signal from any blank contribution. The uptake time for samples was set to 4 min to maximize the signal stability.

The boron isotope compositions are expressed in the conventional delta notation ($\delta^{11}\text{B}$) as per mil (‰) deviations from the NIST SRM 951 standard, certified $^{11}\text{B}/^{10}\text{B}$ value =4.04362 Catanzaro 1970.

$$\delta^{11}\text{B} = \left(\frac{(^{11}\text{B}/^{10}\text{B})_{sample}}{(^{11}\text{B}/^{10}\text{B})_{standard}} - 1 \right) * 1000 \quad (2.1)$$

The measured $^{10}\text{B}/^{11}\text{B}$ ratio was corrected from the instrumental mass bias using the calibrator-sample-bracketing method. In this method, the measured $^{10}\text{B}/^{11}\text{B}$ ratio of the samples is calculated including the measurement of the NIST SRM 951 before and after the sample. The procedure accuracy was estimated by replicate analyses of solution and rock standard (Seawater : [B] = 4.4 ppm 11, $\delta^{11}\text{B}$ = 39.5 ‰ ±1.1 (2SD, N=29); UB-N : [B] = 128 ± 25, $\delta^{11}\text{B}$ = 10.8 ‰ ±0.9 (2SD, N=9)). The repeatability of the measurements, including the analytical procedure with alkaline fusion chemistry approximates ±0.5‰ (2SD).

Boron concentration can be recalculated by using the signal of the ^{11}B and ^{10}B isotopes measured by the MC-ICP-MS. The intensity of the ion beam is linearly proportional to the B concentrations of the standard solutions.

$$[B]_{sample} = [std] * \left(\frac{^{11}\text{B}_{sample}}{^{11}\text{B}_{standard}} \right) * fv * \frac{m_{recovery}}{fd} * \frac{35}{m_{sample}} \quad (2.2)$$

With [std] the concentration of the standard NIST SRM 951 (ppm), $^{11}\text{B}_{sample}$ and $^{11}\text{B}_{standard}$ the measured signal in mV of the sample and the standard, fv the dilution factor to measure 50 ng of B by the MC-ICP-MS, $V_{recovery}$ volume recovered after the amberlite resin, fd the dilution factor before sample introduction in the cationic resin, 35 the weighed volume after the alkali fusion and m_{sample} the mass of sample in mg (Figure 2.6).

In situ major and trace elements analyses

The in situ major element concentrations were measured on 30 µm thick polished thin sections by micro X-ray fluorescence (μ -XRF) measurements a Brucker M4 Tornado instrument at ITES. The spot size was 20 µm using a collimated Rh source, under a 50 kV acceleration voltage and intensity of 400 µA, for 180s counting time. Similar to bulk rock, measurements were performed in a vacuum of 2 mbar to ensure the best signal/noise ratio.

The in situ trace elements analyses were acquired on a High-Resolution Laser

Ablation Inductively Coupled Plasma Mass spectrometer (HR-LA-ICP-MS) Thermo-Finnigan Element 2 instrument coupled with a 193 nm Geolas laser at the Géosciences laboratory of Montpellier (France).

TABLE 2.4 – Second step columns procedure using the Amberlite specific resin.

	reactant	volume
conditioning	H ₂ O	1 mL + 2x 2 mL
introduction pH 8-9	-	1 mL + 6 mL
cleaning	H ₂ O	1x 0.5 mL + 2x 1 mL
cleaning	0.5 M NaCl	1x 0.5 mL + 2x 1 mL
cleaning	H ₂ O	1x 0.5 mL + 2x 1 mL
B recovery	0.5 M HCl	1x 1 mL (+10 min) + 2x 2 mL

2.2 Experimental study

2.2.1 Experimental approach

Today, effect of fluid composition was largely focus on impact on serpentinization rates. However, resulting fluid and solid products were almost not observed. Furthermore, no serpentinization experiments were conducted with natural seawater and focused on the impact of natural seawater on secondary minerals products and resulting fluids. While hydrothermal systems and serpentinization on the seafloor involves seawater, and it seems fundamental to understand the impact of seawater.

In this thesis, we have tried to realize serpentinization experiments in open systems with the aim to characterize and quantify the element mobility. For do that, we have used the classical mixed-flow reactor experiments such as described by (e.g., Pokrovsky and Schott 2000 ; Bouissonnié et al. 2018). In this apparatus, 50 mL titanium reactor containing the peridotite powder and the seawater was connected to a Gilson Minipuls 3 peristaltic pump that allows flow rates ranging from 0.01 to 10 mL/min. The reactor is also connected to a temperature monitor, allowing to conducted experiments until about 285°C. The reactor was continuously stirred with a floating Teflon supported magnetic stirrer. See the schematic representation of the open flow apparatus Figure 2.7.

However, this apparatus (Figure 2.8) was slightly damaged by previous experiments using HCl solution. Consequently we had many leaks during our tests of serpentinization experiments. Furthermore, these leaks were amplified at temperature higher 100°C. We have never been able to maintain high temperatures ($>100^{\circ}\text{C}$) without leaks. This was very problematic due to the very low serpentinization reaction rates at low temperatures. Consequently, we have abandoned the idea to realize serpentinization experiments in open system with this apparatus. The cost of repairs was also very expensive.

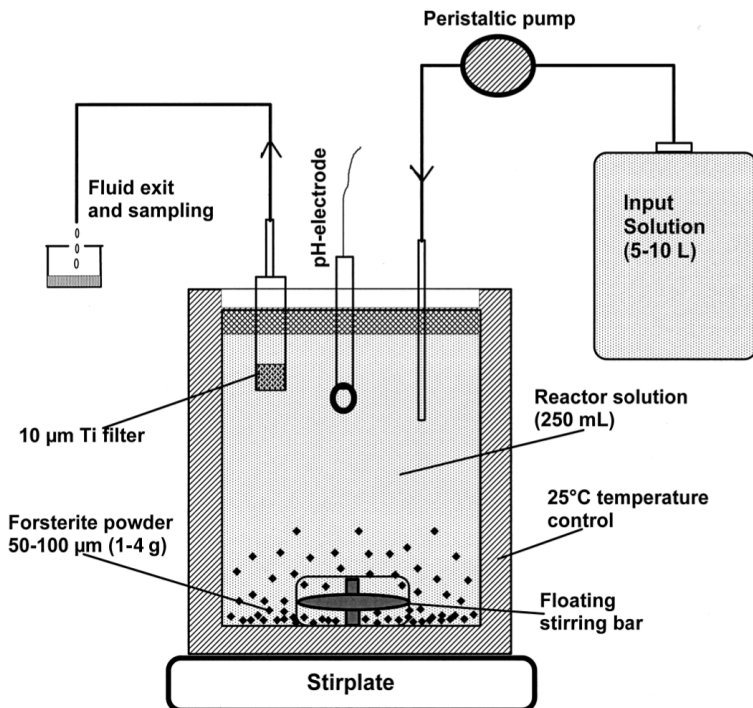


FIGURE 2.7 – Schematic representation of the principle of the experimental apparatus for mixed flow reactor experiments described by Pokrovsky and Schott 2000



FIGURE 2.8 – Photography of the open flow experimental setup used at the beginning of this thesis. (personal photography)

After this first tentative, we conducted serpentinization experiments in closed systems Figure 2.9. This apparatus is composed of a 50 mL titanium reactor connected to a temperature monitor, allowing to conduct experiments until about 285°C. With this apparatus, no control of the pressure is available nor fluid sampling during the course of experiment.

A total of 6 serpentinization experiments of about 90 days were conducted by testing several parameters (fluid/rock ratios, injection of argon to remove the oxygen in seawater, nature of fluid), but hematite was systematically formed. This was very problematic concerning our motivation to calibrate experimentally a new geothermometer based on the serpentine-magnetite pairs.



FIGURE 2.9 – Photography of the close experimental setup used at the beginning of this thesis. (personal photography)

Then we have conducted serpentinization experiment in the apparatus developed by Seyfried Jr 1987 at the Institut des Sciences de la Terre d'Orléans (ISTO). This apparatus allow to conduct high volume serpentinization experiments (~ 150 mL). In addition this apparatus allow the periodic sampling of fluids during the experiments. The experimental setup is schematically represented in the Figure 2.11. The peridotite powder and the fluid are placed in a titanium bag. This titanium bag is placed in a autoclave (a steel container) filled by approximately 1L of water allowing to regulate the pressure of experiment (Figure 2.11). A thermocouple allow to measure continuously the temperature of the experiments. The periodic sampling of fluids is done by a gas tight syringe which is connected to the titanium sampling tube fixed to the head of the titanium bag.



FIGURE 2.10 – Photography of the experimental setup used in this thesis. In this picture is represented the temperature and pressure command (in the left) and the two autoclaves used (i.e., Robert and Raymonde) are in the center (personal photography).

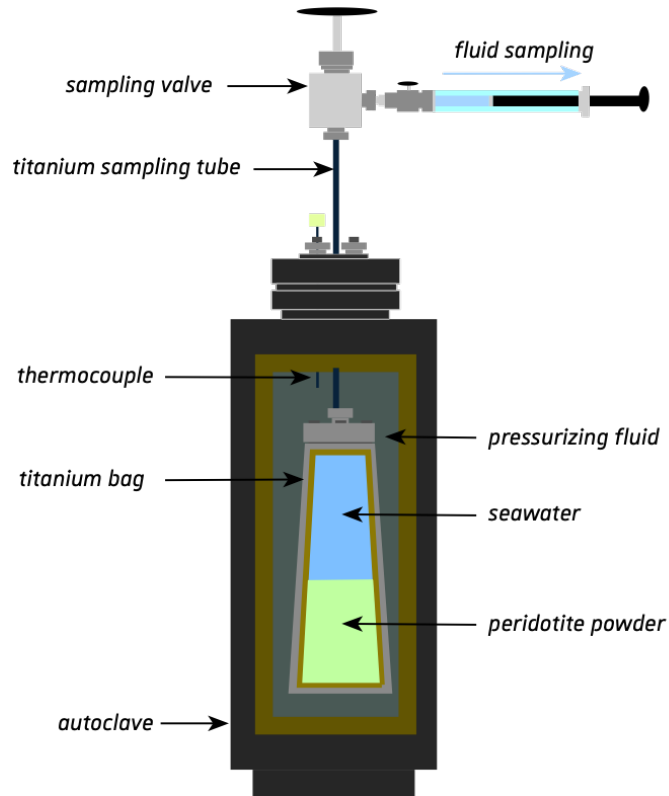


FIGURE 2.11 – Schematic illustration of the experimental setup used in this thesis, figure modified from Fauguerolles 2016

2.2.2 Sample preparation and analytical investigations

Solid samples analyses

Before mineralogical characterization, the solid products were rinsed three times with ultra-pure water ($18.2 \text{ M}\Omega \text{ cm}$) provided by a Milli-Q Gradient water purification system, and then dried in an oven at 40°C for a minimum of 72 hours. A small fraction of each experiment was taken for X-Ray Diffraction (XRD) and Scanning Electron Microscope (SEM) analyses. The XRD analyses is described previously in section 2.1.2.

SEM analyses were performed on powders by a Merlin compact Zeiss instrument at the Institut des Sciences de la Terre d'Orléans laboratory (ISTO), using both secondary (SE) and back scattered electron (BSE) detectors (resolution 15 kV, 0.8 nm).

Similar to the natural serpentinite, before major and trace elements analyses, solid products were finely ground with an agate ball mill. These powders were weighed precisely, placed in crucibles and heated in a furnace at 1100°C for the Loss on Ignition (LOI) calculations. Then, these dried powders were ground again and pressed to 5 mm diameter pellets for micro X-ray fluorescence (μ -XRF) measurements of major elements (bulk rock). The in situ chemical composition of peridotite-bearing minerals before hydrothermal experiments were measured on $30 \mu\text{m}$ thick polished thin sections, also using a (μ -XRF) fluorescence Brucker M4 Tornado instrument at ITES laboratory (University of Strasbourg), see the previous section for more details.

The trace elements compositions were measured by Inductively Coupled Plasma Mass Spectrometry (ICP-MS) using a Thermo Scientific iCAP RQ instrument at ITES laboratory (University of Strasbourg). The same analytical procedure than for natural serpentinites was applied (the analytical procedure described by Chauvel et al. 2011, see previous section for more details).

Aqueous solution samples analyses

Dissolved hydrogen was determined with a Perkin-Elmer Clarus 580 gas chromatograph (GC), using a 30 m, 0.53 mm (ID) fused silica capillary column (Carboxen 1010 PLOT) (Superclo) and a thermal conductivity captor (TCD), at ISTO. Hydrogen quantification was made following the procedure described by Fauguerolles 2016. For each sampling, three analyses were performed to check the reproducibility. Before each chemical fluids analyses, fluids sampling during experiments were filtered with $0.45 \mu\text{m}$ cellulose filters.

For major element analyses, fluids were diluted 100 times in 2M HNO₃ and then analyzed by inductively coupled plasma atomic emission spectroscopy (ICP-AES) using a Thermo Scientific ICAP 6500 instrument (cations) and ion chromatography (IC) using a ICS-5000+ Thermo Fischer instrument for anions.

Trace element concentrations were analyzed by diluting sampled fluids 100 times in 0.5 M HNO₃, before measurements with inductively coupled plasma mass spectrometry (ICP-MS ; Thermo Scientific iCAP-RQ instrument). Both analyses were performed at ITES laboratory (University of Strasbourg).

Bibliographie

- Amann, M., Ulrich, M., Manatschal, G., Pelt, E., Epin, M.-e., Autin, J., and Sauter, D. (2020). Geochemical characteristics of basalts related to incipient oceanization : The example from the alpine-tethys ocs. *Terra Nova*, 32(1):75–88.
- Auzende, A.-L., Daniel, I., Reynard, B., Lemaire, C., and Guyot, F. (2004). High-pressure behaviour of serpentine minerals : a raman spectroscopic study. *Physics and Chemistry of Minerals*, 31(5):269–277.
- Bouissonnié, A., Daval, D., Marinoni, M., and Ackerer, P. (2018). From mixed flow reactor to column experiments and modeling : Upscaling of calcite dissolution rate. *Chemical Geology*, 487:63–75.
- Catanzaro, E. J. (1970). *Boric acid : isotopic and assay standard reference materials*, volume 260. National Bureau of Standards, Institute for Materials Research.
- Chauvel, C., Bureau, S., and Poggi, C. (2011). Comprehensive chemical and isotopic analyses of basalt and sediment reference materials. *Geostandards and Geoanalytical Research*, 35(1):125–143.
- Deniel, C. and Pin, C. (2001). Single-stage method for the simultaneous isolation of lead and strontium from silicate samples for isotopic measurements. *Analytica Chimica Acta*, 426:95–103.
- Doebelin, N. and Kleeberg, R. (2015). Profex : a graphical user interface for the rietveld refinement program bgmn. *Journal of applied crystallography*, 48(5):1573–1580.
- Epin, M. E., Manatschal, G., Amman, M., Ribes, C., Clausse, A., Guffon, T., and Lescanne, M. (2019). Polyphase tectono-magmatic evolution during mantle exhumation in an ultra-distal, magma-poor rift domain : example of the fossil platta ophiolite, se switzerland. *International Journal of Earth Sciences*, 108:2443–2467.
- Fauguerolles, C. (2016). *Experimental study of H₂ generation associated with peridotite serpentinization at slow spreading ridges*. PhD thesis, Université d’Orléans.
- Jarosewich, E. (2002). Smithsonian microbeam standards. *Journal of research of the National Institute of Standards and Technology*, 107(6):681.
- Jarosewich, E., Nelen, J., and Norberg, J. A. (1980). Reference samples for electron microprobe analysis. *Geostandards Newsletter*, 4(1):43–47.
- Lemaire, C. (2000). *Application des spectroscopies vibrationnelles à la détection d’amiante dans les matériaux et à l’étude des serpentines*. PhD thesis, Paris 7.
- Lemarchand, D., Cividini, D., Turpault, M.-P., and Chabaux, F. (2012). Boron isotopes in different grain size fractions : Exploring past and present water–rock interactions from

- two soil profiles (strengbach, vosges mountains). *Geochimica et Cosmochimica Acta*, 98:78–93.
- Manatschal, G., Engström, A., Desmurs, L., Schaltegger, U., Cosca, M., Müntener, O., and Bernoulli, D. (2006). What is the tectono-metamorphic evolution of continental break-up : the example of the tasna ocean–continent transition. *Journal of Structural Geology*, 28(10):1849–1869.
- Manatschal, G. and Nievergelt, P. (1997). A continent-ocean transition recorded in the err and platta nappes (eastern switzerland). *Eclogae Geologicae Helvetiae*, 90(1):3–28.
- Picazo, S., Manatschal, G., Cannat, M., and Andréani, M. (2013). Deformation associated to exhumation of serpentinized mantle rocks in a fossil Ocean Continent Transition : The Totalp unit in SE Switzerland). *Lithos*, 175:255–271.
- Pin, C. and Zaldueguil, J. F. S. (1997). Sequential separation of light rare-earth elements, thorium and uranium by miniaturized extraction chromatography : Application to isotopic analyses of silicate rocks. *Analytica Chimica Acta*, 339:79–89.
- Pokrovsky, O. S. and Schott, J. (2000). Kinetics and mechanism of forsterite dissolution at 25 °C and pH from 1 to 12. *Geochimica et Cosmochimica Acta*, 64(19):3313–3325.
- Reston, T. J. (2005). Polyphase faulting during the development of the west galicia rifted margin. *Earth and Planetary Science Letters*, 237(3-4):561–576.
- Roux, P., Lemarchand, D., Hughes, H. J., and Turpault, M.-P. (2015). A rapid method for determining boron concentration (id-icp-ms) and $\delta^{11}\text{B}$ (mc-icp-ms) in vegetation samples after microwave digestion and cation exchange chemical purification. *Geostandards and Geoanalytical Research*, 39(4):453–466.
- Schaltegger, U., Desmurs, L., Manatschal, G., Müntener, O., Meier, M., Frank, M., and Bernoulli, D. (2002). The transition from rifting to sea-floor spreading within a magma-poor rifted margin : Field and isotopic constraints. *Terra Nova*, 14(3):156–162.
- Seyfried Jr, W. (1987). Experimental and theoretical constraints on hydrothermal alteration processes at mid-ocean ridges. *Annual Review of Earth and Planetary Sciences*, 15(1):317–335.

Chapitre 3

The Sr isotope geochemistry of oceanic ultramafic-hosted mineralizations

Article published in Ore Geology Review, March 2022 <https://doi.org/10.1016/j.oregeorev.2022.104824>

Abstract

The source of metals involved in the formation of oceanic ultramafic-hosted hydrothermal Cu-Fe-Co-Zn-Ni mineralization remains poorly constrained. Here, we focus on a fossil ultramafic-hosted hydrothermal mineralized system preserved in the Platta nappe (SE Switzerland), where mantle rocks were exhumed along detachment faults to the seafloor during Jurassic rifting. The Cu-Fe-Co-Zn-Ni mineralization, associated with Fe-Ca-metasomatism (ilvaite-hydroandradite-diopside), represents an analogue of the root zone of present-day hydrothermal systems formed at mid-ocean ridges (e.g., Rainbow hydrothermal field at the Mid-Atlantic Ridge). We apply the Sr isotope geochemistry to Fe-Ca silicates and secondary, alteration products that include serpentinites, altered mafic and carbonated rocks to constrain the source(s) of metals and to characterize the plumbing system. The Fe-Ca silicates and carbonates have Sr isotope ratios close to that of Jurassic seawater, suggesting a near seafloor, seawater-dominated hydrothermal system with high fluid/rock ratios. The altered mafic rocks have $^{87}\text{Sr}/^{86}\text{Sr}$ ratios lower than those of Jurassic seawater. In contrast, serpentinites display a large range of Sr isotope ratios, including values higher than those of Jurassic seawater, indicating long lived fluid/rock interactions and multi-stage fluid infiltrations. These results suggest that hydrothermal activity started during final crustal thinning, when seawater percolated along normal faults through the hyper-thinned crust, acquiring high Sr isotope ratios before penetrating and initiating serpentinization of the subcontinental mantle rocks. At this early stage, the system was rock-dominated (i.e., low fluid/rock ratios), leading to high $^{87}\text{Sr}/^{86}\text{Sr}$ ratios in serpentinites. On their way-back to seafloor, the uprising, serpentinization-derived fluids mixed with seawater resulting in the precipitation of metal sulfides and Fe-Ca silicates, with subsequent carbonation in a fluid-dominated system. Our study shows that the Sr isotope geochemistry can be used to identify reservoirs involved in the formation of mineral deposits and for the characterization of the plumbing system of oceanic ultramafic-hosted mineralizations.

Keywords : Ultramafic-hosted metal deposits, Sr isotope geochemistry, Hydrothermal alteration, Ocean-Continent Transition, Alps

3.1 Introduction

Seawater circulation through the oceanic lithosphere plays a key role in heat and element transfers between the main Earth reservoirs, such as the mantle and seawater (Wolery and Sleep 1976; Bonatti et al. 1984; Alt 1995; Allen and Seyfried Jr 2004; Seyfried Jr et al. 2015; Humphris and Klein 2018; Le Gal et al. 2018). During final rifting and breakup, extensional tectonics leads to the formation of high-angle normal and exhumation faults, which create preferential pathways for fluid circulation (Jackson 1987). While hydrothermal fluids flow along these faults, they interact with the surrounding rocks, forming a variety of secondary rocks such as serpentinites, altered mafic rocks (among which rodingites) and ophicalcites (Spooner et al., 1974). These alteration processes occur under a wide range of temperature, pH and redox conditions, leading to the formation of hydrothermal fluids with various chemical compositions (e.g., Früh-Green et al. 1990; Von Damm 1995; Seyfried Jr et al. 2004; Bach et al. 2004). Among them, moderate to high-temperature, acidic and reduced fluids are responsible for the formation of mineralized systems at or near the seafloor (Rona 1984; Rona et al. 1993; Hannington et al. 2001; Douville et al. 2002). The discovery of ultramafic-hosted hydrothermal systems along slow- to ultra-slow-spreading ridges (Krasnov 1995; Fouquet et al. 1998; Cherkashov et al. 2008; Melchert et al. 2008; Tao et al. 2014, 2020) or fossil systems in ophiolites preserved in the Alps (Garuti et al. 2008; Toffolo et al. 2017; Coltat et al. 2019b) highlighted that hydrated ultramafic rocks may be suitable sinks for metals. In these geological settings, mineralization is commonly enriched in base (Cu, Zn, Ni), critical (Co), and precious metals (Au and Ag, Fouquet et al. 2013).

Although our understanding of the formation of ultramafic-hosted hydrothermal systems has improved these last years, the source of metals in the mineralization is not fully constrained yet. Iron, Zn and Cu stable isotope systematics may bring constraints to decipher the source of metals and offer an interesting way of tracing metal mobility in hydrothermal cells (Rouxel et al. 2004a,b; Debret et al. 2018). However, multiple factors control isotopic fractionation in these systems, including temperature, oxidation-reduction, multi-step processes, preventing to obtain a straightforward interpretation from isotopic compositions solely (Zhu et al. 2002). On the opposite, the strontium isotopes are not subject to significant mass-dependent isotopic fractionation. The Sr isotope systematics are thus likely easier to interpret especially as the main terrestrial reservoirs (mantle reservoirs, continental crust, seawater) have distinct and well-defined Sr isotope compositions. Whereas exchanges between these reservoirs using Sr isotopes

have been widely investigated (e.g., Veizer and Compston 1974; Chapman and Spooner 1977; Mcculloch et al. 1980; Albarede et al. 1981; Burke et al. 1982; Bach and Humphris 1999; Boschi et al. 2008; Delacour et al. 2008; Augustin et al. 2012; Schwarzenbach et al. 2021), their application to mineralized systems has not been considered so far.

In the Platta nappe, in the SE Swiss Alps, Coltat et al. 2019b identified a Jurassic mineralized system hosted in serpentinites considered to represent an analogue of the root zone of active hydrothermal systems at slow-spreading ridges. The precipitation of metal-bearing phases (sulfides and oxides) was contemporaneous with a Fe-Ca-metasomatism responsible for the precipitation of Fe-Ca silicates (i.e., ilvaite, hydroandradite, diopside, Coltat et al. 2019b). Since Ca and Sr share close chemical properties, these Fe-Ca metasomatic assemblages represent suitable targets for a Sr isotope-based tracing. These assemblages may have recorded isotopic information related to the metal source(s) involved in the formation of seafloor metal ore deposits and its related plumbing system.

Following this idea, we have measured the Sr isotope compositions of the Fe-Ca silicates that act as Sr sink. We also analyzed the potential contributors (i.e., the metasomatic rocks) and we compiled data from the literature. We discuss the implications of our results for the overall understanding of the formation of mineralized systems and more generally of fluid/rock interactions that occur during detachment-related mantle exhumation in oceanic domains.

3.2 Geological setting

3.2.1 The Platta nappe

The Platta nappe is located in the Central Alps in Grisons, SE Switzerland (Figure 3.1A). It corresponds to a remnant of the Alpine Tethys Ocean-Continent Transition (OCT), which formed during late Middle Jurassic when Europe and Adria separated. The Platta nappe is composed by serpentized peridotites, mafic rocks (including basalts and gabbros) and post-rift sediments (Dietrich 1969, Manatschal and Nievergelt 1997; Desmurs et al. 2002; Schaltegger et al. 2002; Epin et al. 2019). The Platta nappe is subdivided into two Alpine units (Figure 3.1B, C). The Upper Platta Unit mainly consists of serpentized peridotites that originally formed the inherited subcontinental mantle of the Adriatic distal margin (i.e., the Err domain Schaltegger

et al. 2002; Müntener et al. 2010, 2004; Picazo et al. 2016; Epin and Manatschal 2018). The Lower Platta Unit, originally located further oceanward, consists of a large serpentinized mantle domain locally intruded by Jurassic gabbros and covered by pillow lavas, pillow breccias and locally also lava flows (Desmurs et al. 2002; Amann et al. 2020). Contrarily to the mantle rocks from the Upper Platta Unit that do not exhibit any syn-rift melt imprint, those from the Lower Platta Unit have been largely refertilized by melt percolation during final rifting and breakup (Müntener et al., 2010, 2004).

The Platta nappe is separated, along an Alpine thrust, from the nappe stack preserving remnants of the former distal Adriatic continental margin (e.g. Err and more proximal domains of the former Adriatic margin). Slivers of continental origin also occur in the Platta nappe and have been interpreted as extensional allochthons (Froitzheim and Manatschal 1996). Based on this observation and the subcontinental nature of the mantle, the Platta nappe has been considered as a magma-poor OCT of late Middle Jurassic age (Froitzheim and Manatschal 1996; Manatschal and Nievergelt 1997; Figure 3.1). Mantle exhumation in the OCT was accommodated along multiple detachment faults (Epin et al. 2019) accompanied with the inception of mafic magmatism. More detailed mapping enabled to propose the existence of a well preserved mantle core complex, capped by a main extensional detachment and overprinted by later high-angle faults Epin et al. 2019. U-Pb dating on zircons from syn-tectonic mafic intrusions provided a Jurassic age of 161 ± 1 Ma for the timing of mantle exhumation (Schaltegger et al. 2002). This exhumation phase was accompanied by intense fluid circulations, leading to (i) serpentization of ultramafic rocks, (ii) rodingitization of mafic intrusive and epidotization-chloritization of mafic extrusive rocks (Desmurs et al. 2002; Amann et al. 2020), (iii) formation of mineralized systems (Dietrich et al. 1972; Perseil and Latouche 1989; Coltat et al. 2019b) and (iv) carbonation of serpentinites and basalts near and at the seafloor along the exhumed detachment surface (Coltat et al., 2019a, 2020).

Reactivation of the Alpine Tethys margin during Alpine convergence can be subdivided into three stages. During a first Late Cretaceous phase (D1 of Froitzheim 1994, the whole Adriatic margin was telescoped along major, west-verging thrusts during which the Platta nappe became part of the main Alpine nappe stack (Figure 3.1B, C). The second phase (D2) corresponds to a late Cretaceous extensional event forming top-to-the-east to top-to-the-southeast normal faults. This phase is followed by a third phase (D3) that produced east-west trending folds with steeply dipping axial planes and a few north-vergent folds and thrusts with minor displacement (some few meters at a maxi-

mum). It is worthy to note that the whole Platta Nappe has been relatively preserved from Alpine deformation (only D1 results in a main overprint) and the metamorphic overprint was weak with maximum conditions corresponding to prehnite-pumpellyite metamorphism (less than 350°C; see Coltat et al. 2021). It is also important to note that the Platta nappe remained in the hanging wall of the Late Cretaceous to Cenozoic subduction, which differs from most Alpine ophiolites exposed in the Western Alps. Therefore, the pre-Alpine seafloor-related structures and hydrothermal alterations remained largely preserved (Froitzheim and Manatschal 1996; Chalot-Prat et al. 2003; Epin et al. 2019).

3.2.2 The Marmorera-Cotschen Hydrothermal System

A well-preserved fossil ultramafic-hosted hydrothermal system, namely the Marmorera-Cotschen hydrothermal system, has been recently identified in the Platta Nappe (Coltat et al., 2021, 2019b). This hydrothermal system is preserved in the serpentized footwall of a detachment fault juxtaposing basalts onto serpentinites (Figure 3.1B, Coltat et al. 2019b). The serpentinite-hosted mineralization is geometrically associated with mafic intrusions indicating that the latter acted as preferential pathways for the fluid. The Cu-Fe-Co-Zn-Ni mineralization consists of sulfides (mainly chalcopyrite, pyrrhotite, (Co-)pentlandite and sphalerite) and oxides (magnetite). Geochemical analyses performed on massive sulfides show enrichments up to 27.7 wt. % Cu, 0.28 wt. % Zn, 0.16 wt. % Co and Ni content of about ~1500 ppm, similar to those of unaltered mantle rocks (Coltat et al., 2021). Gold was never concentrated enough to be detected in Cu-rich massive sulfides but Ag concentration reach up to ~120 ppm in the most mineralized samples (Coltat et al., 2021). A Fe-Ca-metasomatism responsible for the formation of Fe-Ca silicates such as ilvaite, hydroandradite and Fe-rich diopside as stockwork zones and pervasive replacement zones in serpentinites was coeval with the mineralization (Coltat et al., 2019b). Based on petrographic and structural features, the Marmorera-Cotschen hydrothermal system is assumed to represent the root of an ultramafic-hosted black smoker system (Coltat et al., 2019b).

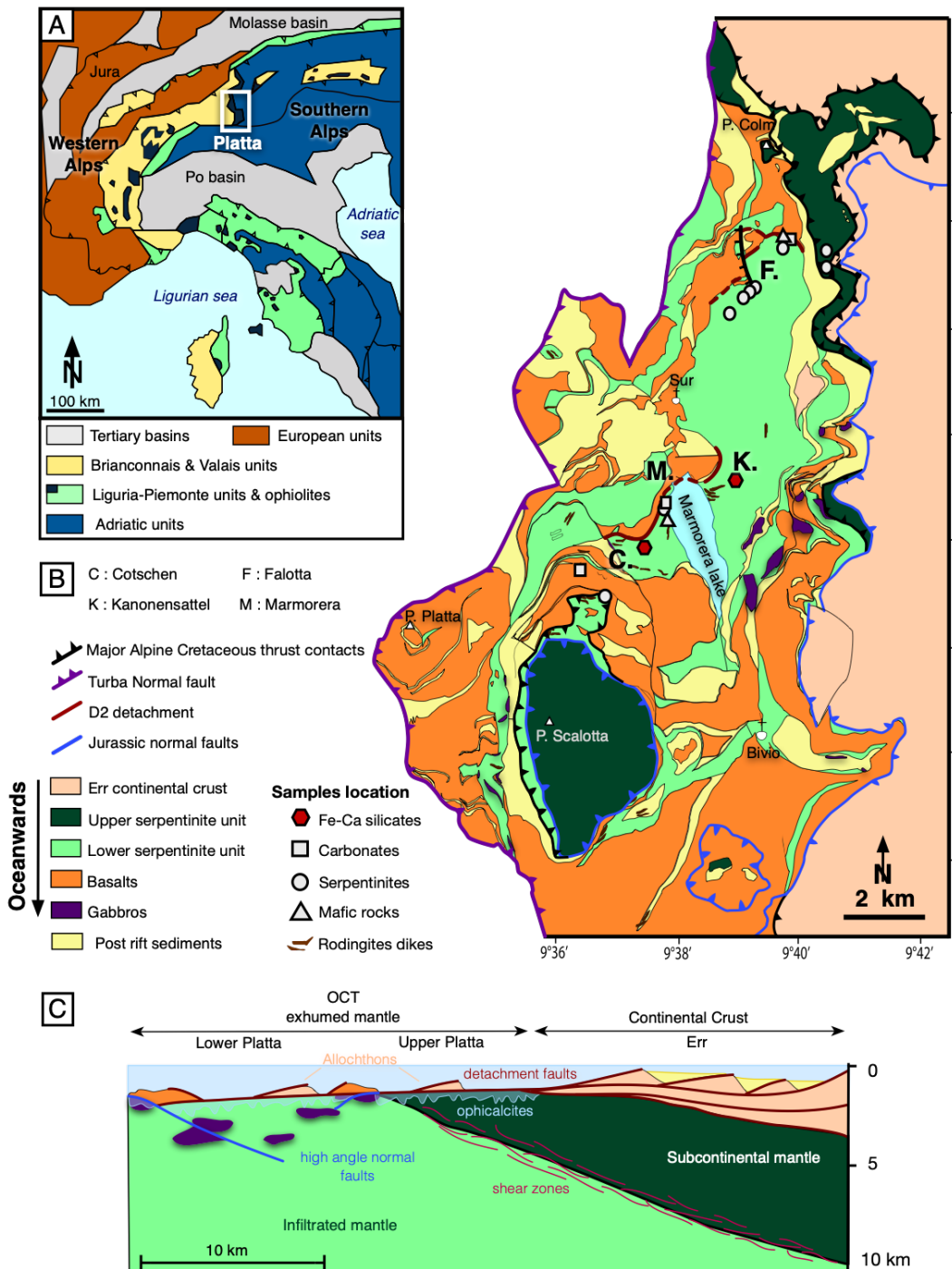


FIGURE 3.1 – A) Simplified map of the major paleogeographic units of the Western and Central Alps and the Apennines, with location of the study area (white frame) modified after Manatschal and Müntener 2009. B) Geological map of the Platta nappe with samples location (modified after Schallegger et al. 2002). C) Distribution of subcontinental and infiltrated mantle domains along an ocean-continent-transition of the former Alpine Tethys (modified after Müntener and Piccardo 2004).

3.3 Methods

3.3.1 Field sampling

In this study, we present the Sr isotope compositions of 64 samples from the Platta nappe including Fe-Ca silicate minerals (12 samples), carbonated rocks (15 samples), serpentinites (24 samples) and mafic rocks (8 samples). In order to unravel the hydrothermal alterations during the tectonic evolution of the margin, we collected samples at different structural positions along the margin, from the continentward (Upper Platta) to the oceanward (Marmorera-Cotschen, Lower Platta) domains (Table 3.1 ; Figure 3.1B, C). Several Sr sources are supposed to be involved for the considered hydrothermal alterations, such as the Jurassic seawater , the subcontinental lithospheric mantle and the continental crust.

The Fe-Ca silicate minerals were sampled at two different sites : Cotschen and Kanonensattel (i.e., the eastern prolongation of the Marmorera-Cotschen hydrothermal system, for location see Figure 3.1B). The site of Cotschen corresponds to the deepest structural position of the hydrothermal system and is located about 150 m below the detachment/seafloor. Based on mineralogical assemblages reported in the mineralization at Kanonensattel, this site also likely corresponds to a deep part of the hydrothermal system, although the contact between serpentinites and mafic rocks (i.e., the detachment surface) has not been observed. The potential variations of the fluid/rock interactions during Fe-Ca-metasomatism were tested by sampling both Fe-Ca silicate minerals in the stockwork zone (Figure 3.2A) and those that pervasively replaced the serpentinites (Figure 3.2B).

Carbonated rocks, especially marine carbonates are often used to determine the Sr isotope composition of seawater through geological times since they presumably precipitated at isotopic equilibrium with seawater (Burke et al. 1982). In the Jurassic, the $^{87}\text{Sr}/^{86}\text{Sr}$ ratio of seawater is between 0.7068 and 0.7078 (DePaolo and Ingram 1985, Hess et al. 1986, McArthur et al. 1993, Jones et al. 1994, Veizer et al. 1999. In the Platta nappe, ophicalcites and carbonated mafic rocks from different sites (i.e. Cotschen, Marmorera, Falotta, Figure 3.1B ; Table 3.1) were analyzed in order to better constrain the Sr isotope value of seawater when carbonation occurred. The sampled rocks include discrete calcite veins crosscutting the serpentinites (i.e. fracture infilling ophicalcites in Coltat et al. 2019a) and mafic rocks (Figure 3.2C) as well as thick carbonated shear bands in serpentinites (i.e., foliated ophicalcites in Coltat et al. 2019a ; Figure 3.2D).

The latter are assumed to form under higher fluid/rock ratios than the former, making them suitable candidates to record the original $^{87}\text{Sr}/^{86}\text{Sr}$ value of seawater.

The Sr reservoirs implied in the serpentinization of mantle rocks can be deduced from the isotope compositions of serpentinites through the Platta nappe. The serpentinites display several generations of serpentine minerals, with a predominant one presenting a typical mesh texture (the groundmass), and a series of green veins crosscutting the mesh (Figure 3.2E ; referred to as veins in Table 3.1). These two types of serpentinite are supposed to record different conditions of formation during mantle exhumation Picazo et al. 2013.

In addition to serpentinites and carbonates, eight mafic rocks, including epidotized and chloritized basalts (Figure 3.2F) and chlorite/actinolite-bearing mafic intrusions have been analyzed. Our geochemical dataset (Table 3.1) is completed by data from the literature for mafic rocks, rodingites and associated blackwalls of the Platta nappe (See supplementary material Table 3.2 ; Stille et al. 1989 ; Schaltegger et al. 2002 and Amann 2017).

3.3.2 Analytical methods

The whole-rock analysis of serpentinites and mafic rocks was carried out to determine the Sr and Rb contents of the rocks. Trace elements were measured by Inductively Coupled Plasma Mass Spectrometry (ICP-MS ; Thermo Scientific X series II instrument) at the Institut Terre et Environnement de Strasbourg (ITES). Following the analytical procedure of Chauvel et al. 2011, about 100 mg of rock powder was precisely weighed and dissolved in Savillex beakers in a HF-HNO₃-HClO₄ (5:1:1) mixture, during a minimum of 7 days at 140°C on a hot plate. The solution was then evaporated and the residue dissolved in concentrated HNO₃ and evaporated before dilution in about 40 ml of 7 M HNO₃.

The Sr isotope compositions of whole rock samples (serpentinites, mafic rocks, rodingites and blackwall) were determined at the Institut Terre et Environnement de Strasbourg (ITES) using a Neptune Thermo Scientific instrument Multi-Collector Inductively Coupled Plasma Mass Spectrometer (MC-ICP-MS) and a Thermo Finnigan Triton instrument Thermal Ionisation Mass Spectrometer (TIMS). About 100 mg of rock powder was dissolved and digested in a HF:HNO₃:HClO₄ (5:1:1) mixture for 7 days. The samples were then evaporated and the residues taken up in concentrated HNO₃ to ensure complete dissolution. After another evaporation, the samples were fi-

nally dissolved in 2ml of 2 M HNO₃ before being loaded in resin columns (Eichrom Sr-spec resin), washed with 5.5 ml of HNO₃ 7 M and then eluted with 2.4 ml of HNO₃ 0.05 M. Chemical separation and purification were performed following an analytical procedure modified after Pin and Zaldueguil 1997 and Deniel and Pin 2001. Measured ⁸⁷Sr/⁸⁶Sr ratios were normalized to ⁸⁶Sr/⁸⁸Sr = 0.1194. During the collection of isotopic data, replicate analysis of NBS 987 (SrCO₃) reference material gave a mean value of 0.710260 ± 8 (2 SE, n = 26). The total procedural blank for the whole chemical treatment was 207-233 pg, negligible for all samples.

The Sr isotope composition of carbonates were determined at Geosciences Rennes, Université de Rennes 1, using a Mat Finnigan 262 instrument (TIMS). Approximately 10 mg of rock powder were sampled by micro drilling and then dissolved in 2.5 M HCl before chemical separation.

The ⁸⁷Sr/⁸⁶Sr ratios for serpentinites, mafic rocks, rodingites and blackwalls were recalculated at 160 Ma, based on the age of magmatic intrusions and gabbros of the Platta nappe. For Fe-Ca silicates, Rb concentrations were systematically below the detection limit, and for carbonated rocks, it was presumed that the Rb content is extremely low, giving a Rb/Sr ratio close to zero; therefore it was assumed that the ⁸⁷Sr/⁸⁶Sr ratio of these samples did not significantly evolve during the last 160 Ma (Table 3.1).

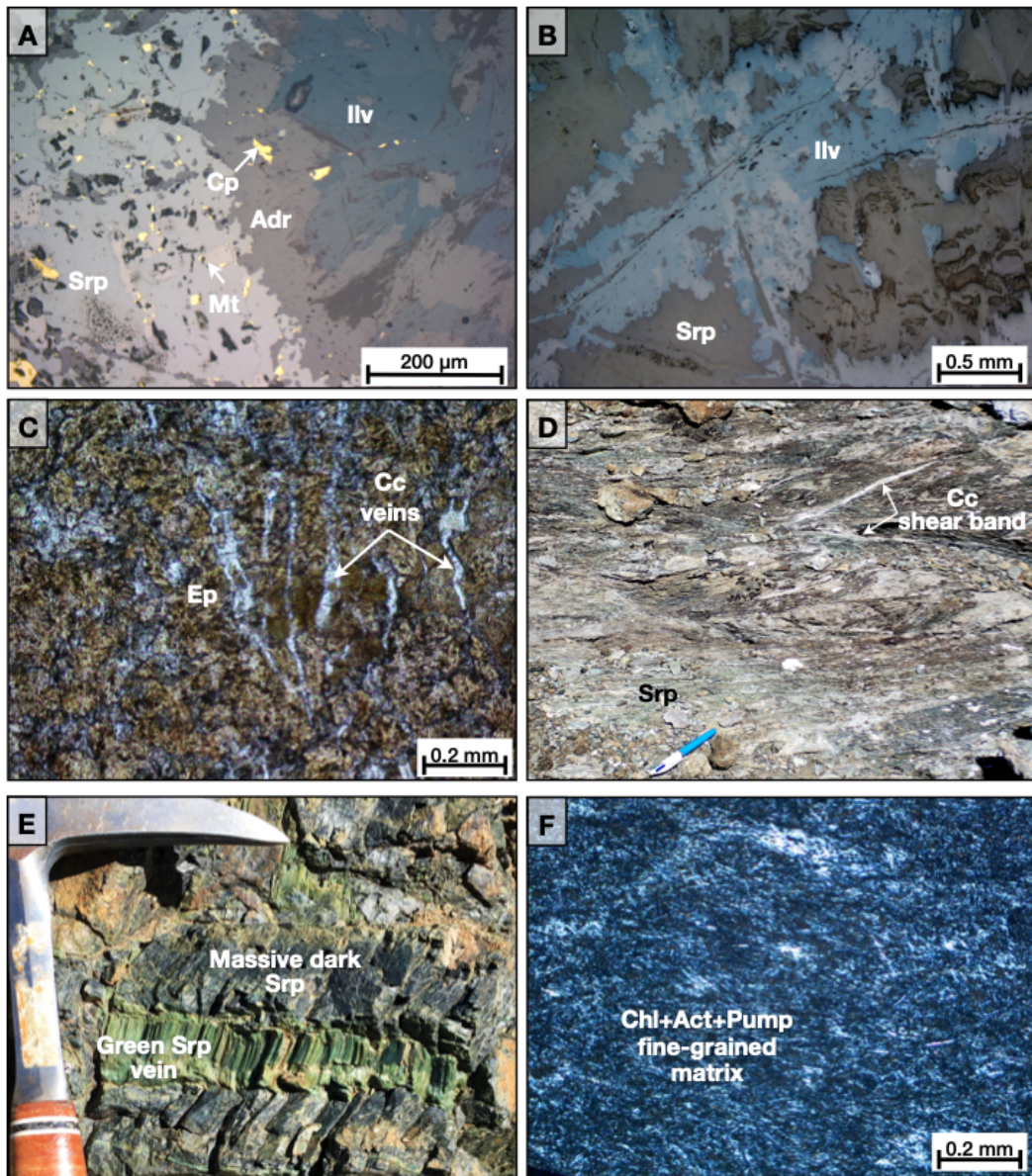


FIGURE 3.2 – Representative macroscopic and microscopic pictures illustrating the different lithologies reported in the Platta nappe (Cotschen and Falotta sites). A) Fe-Ca silicates (ilvaite and andradite) associated with sulfides (sphalerite, chalcopyrite) and oxides (magnetite (Mt) pervasively replacing serpentinite. B) Fe-Ca silicate (ilvaite) in veins (stockwork structure) cutting through serpentinite. C) Discrete calcite veins crosscutting an epidotized basalt. D) Calcite shear band cutting through serpentinite. E) Green serpentine vein crosscutting a massive dark serpentine. F) Basalt altered to an assemblage made of chlorite, actinolite and pumpellyite. Chl=chlorite ; Act=actinolite ; Pump=pumpellyite ; Ilv=ilvaite ; Adr=(hydro)andradite ; Srp=serpentine ; Mt=magnetite ; Sph=sphalerite ; Cp=chalcopyrite ; Cc=calcite

3.4 Sr isotope compositions of altered rocks from the Platta nappe

3.4.1 Fe-Ca silicates in veins and pervasively replacing serpentinites

The Sr isotope ratios of Fe-Ca silicates range from 0.70592 to 0.70785 with an average composition close to the value of Jurassic seawater (~ 0.7068 , $n = 12$, Figure 3.3). At Kanonensattel, Fe-Ca silicates that pervasively replaced serpentine are more radiogenic than those from Cotschen (mean values of 0.70708 and 0.70648, respectively, Table 3.1). At Cotschen, Fe-Ca silicates occurring as pervasive replacement are slightly more radiogenic than those in veins crosscutting serpentinites (0.70676 and 0.70621, respectively Table 3.1).

3.4.2 Carbonates veins and shear bands in serpentinites and basalts

The $^{87}\text{Sr}/^{86}\text{Sr}$ ratios of carbonates are centered around 0.70668 ($n = 15$; Table 3.1), close to the value of Jurassic seawater (Figure 3.3). The carbonated rocks from Falotta display Sr isotope ratios comprised between 0.70624 and 0.70729, with a mean value of 0.70684, while carbonates from Cotschen are less radiogenic (0.70645 in average). Carbonates from Marmorera exhibit low Sr isotope ratios, with maximum at 0.70548. Carbonate veins in serpentinites show the highest variability of Sr isotope compositions, ranging from 0.70419 to 0.70729, with a mean value slightly below the Jurassic seawater (0.70640, Table 3.1). At Falotta, discrete carbonate veins in serpentinites display Sr isotope ratios higher than their equivalents in mafic rocks (0.70706 vs. 0.70665, respectively) or than carbonated shear bands in serpentinites (0.70686; Table 3.1). At Marmorera, carbonates in pervasive replacement of serpentinites display lower Sr isotope ratios than calcite veins in serpentinites (0.70468 and 0.70484, respectively; Table 3.1).

3.4.3 Serpentinites

Serpentinites are characterized by $^{87}\text{Sr}/^{86}\text{Sr}$ ratios of 0.70394 to 0.7939, values that range between those of the sub-continental lithospheric mantle and the mean value

of the continental crust (Figure 3.3). Numerous samples display Sr isotope ratios higher than the Jurassic seawater. As for carbonate veins, part of the isotope heterogeneity seems to be related to the structural position along the margin : serpentinites from the Upper Platta (proximal part of the paleo-margin) have higher $^{87}\text{Sr}/^{86}\text{Sr}$ ratios (0.70783 in average, $n = 10$) than those from the Lower Platta (0.70741, $n = 14$). In the latter, the less radiogenic sample is from Marmorera (0.70394), while serpentinites from Kanonensattel and Cotschen have similar and relatively high Sr isotope ratios (0.70717 in average ; Table 3.1), close to the value of Jurassic seawater. In Falotta (Lower Platta), the Sr isotope ratios of serpentinites are more heterogeneous, with a mean value of 0.70741 ($n = 10$; Table 3.1), higher than the Jurassic seawater. In addition, green serpentine veins (0.70832 in average) are characterized by higher Sr isotope compositions than serpentinites forming the groundmass (0.70717 in average).

3.4.4 Mafic rocks

The Sr isotope ratios of mafic rocks are consistent with those available in the literature (Stille et al. 1989 ; Schaltegger et al. 2002 ; Amann 2017 ; supplementary material Table 3.2). They range between the Jurassic seawater and the sub-continental lithospheric mantle (0.70181 to 0.70641 ; Figure 3.3). The mafic rocks from Marmorera ($^{87}\text{Sr}/^{86}\text{Sr}=0.70400$) have Sr isotope ratios lower than other samples from the Lower Platta (0.70603 in average), consistent with what is described for carbonates and serpentinites. Intrusive rocks display $^{87}\text{Sr}/^{86}\text{Sr}$ ratios lower than those for basalts (0.70351 and 0.70551 in average, respectively, Table 3.1). Extrusive rocks display quite homogenous Sr isotope compositions regardless of their alteration (i.e., epidotization or chloritization), with a slightly less radiogenic composition for epidotized basalts when compared to chloritized basalts (0.70524 and 0.70606, respectively ; Table 3.1).

3.4.5 Rodingites and blackwalls

Rodingites and blackwalls display $^{87}\text{Sr}/^{86}\text{Sr}$ ratios between 0.70345 and 0.70641 (see supplementary material online), overlapping those of mafic rocks (Figure 3.3). Rodingites display more radiogenic Sr compositions than blackwalls (0.70589, $n = 6$ and 0.70440, $n = 4$, respectively).

3.4. SR ISOTOPE COMPOSITIONS OF ALTERED ROCKS FROM THE PLATTA NAPPE
 CHAPITRE 3.

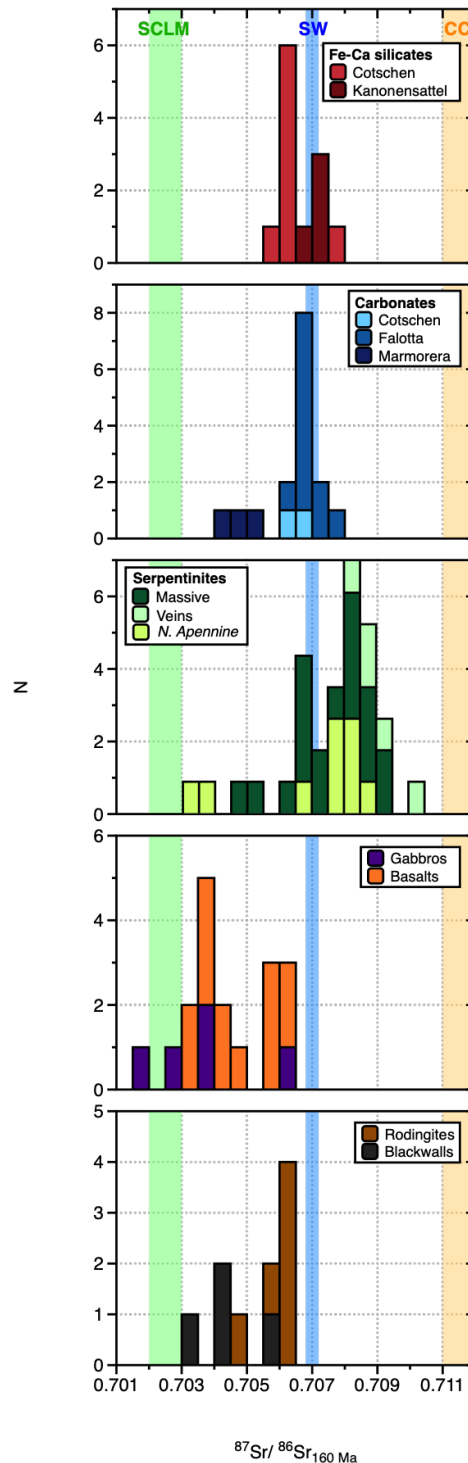


FIGURE 3.3 – Histograms of $^{87}\text{Sr}/^{86}\text{Sr}$ recalculated at 160 Ma for the different lithologies. SCLM : Sub Continental Lithospheric Mantle from McDonough et al. 1985, SW : Seawater from Jones et al. 1994 and CC : Continental Crust values from Willbold and Andreas 2010. N. Apennine serpentinites from Schwarzenbach et al. 2021.

3.5 Discussion

3.5.1 Multiple Sr reservoirs involved during seafloor hydrothermalism in Ocean Continent Transition

Regardless the timing of the different hydrothermal alterations reported in the Platta nappe, the Sr isotope compositions of the altered rocks highlight that different Sr contributors were involved during hydrothermalism. The Sr isotope compositions of Fe-Ca silicates and carbonates are centered around the Jurassic seawater value (Figure 3.3). This suggests that seawater was the main contributor of strontium for these two lithologies, assuming that isotopic equilibrium was achieved. This is consistent with the development of ophicalcites within serpentinites close to the seafloor Weissert and Bernoulli 1984, and/or thanks to the infiltration of seawater during the syntectonic carbonation along the detachment fault and the serpentinite-basalt contact as evidenced by homogeneous stable $\delta^{18}\text{O}$ and $\delta^{13}\text{C}$ signatures of carbonates in the Falotta area (Coltat et al. 2019b).

By contrast with other hydrothermal alteration products, many serpentinites display Sr isotope compositions significantly higher than the Jurassic seawater. This implies that the fluids responsible for serpentinization previously interacted with the continental crust, the latter reservoir being significantly more radiogenic than Jurassic seawater (Figure 3.3). Hence, serpentinization of the sub-continental mantle occurred before its exhumation at the seafloor. A similar interpretation was proposed recently for serpentinization of mantle rocks in the Apennines Schwarzenbach et al. 2021.

The Sr isotope compositions of altered mafic rocks (i.e., epidotized and chloritized basalts) are slightly higher than those of fresh gabbros (Table 3.1). This observation can hardly be attributed to different magmatic parental sources since structural and geochemical relationships between intrusive and extrusive mafic rocks in the Platta nappe indicate they share a common genetic origin (Epin et al. 2019; Amann et al. 2020). Consequently, we consider that the higher $^{87}\text{Sr}/^{86}\text{Sr}$ compositions of extrusive mafic rocks result from the interaction with seawater at higher fluid/rock ratios than for gabbros, which is similar to previous work (e.g., Burke et al. 1982; Rampone et al. 1998). This inference is confirmed by the calculated percentage of Sr isotopic exchanged and fluid/rock ratios (Table 3.1). As the Jurassic seawater has a higher Sr isotope ratio than the sub-continental lithospheric mantle, intense alteration implying seawater circulation interacting with mafic rocks would ultimately lead to an increase of the Sr

isotope compositions of the altered rocks.

As for mafic rocks, the Sr isotope compositions of rodingites and blackwalls range between the sub-continental lithospheric mantle value and that of Jurassic seawater (Figure 3.3), suggesting here again that the source of Sr predominantly derives from these two reservoirs during the hydrothermal alteration of mafic rocks. Rodingites and blackwalls have higher $^{87}\text{Sr}/^{86}\text{Sr}$ ratios than mafic rocks, which might also be explained by a more intense alteration highlighted by high Sr isotope exchange (supplementary materials Table 3.2). The involvement of modified seawater or different magmatic sources is an unlikely scenario that is discarded here. Indeed, in the rodingites from Falotta, which display the highest Sr isotope compositions (up to 0.7068), primary minerals are completely replaced by secondary minerals (chlorite, grossular, diopside Amann 2017). Besides, it is widely accepted that rodingites are formed by successive interactions between mafic rocks and fluids released after serpentinization reactions (e.g., Coleman 1967 ; Frost 1975 ; Evans 1977 ; Palandri and Reed 2004 ; Panseri et al. 2008, Bach and Klein 2009 ; Salvioli-Mariani et al. 2020). As shown earlier, some serpentinites have more radiogenic Sr isotope compositions than Jurassic seawater, especially at Falotta. Consequently, serpentinization-derived fluids reacting with mafic rocks would likely confer to rodingites and associated blackwalls higher Sr isotope compositions than those of the parental magmatic protolith.

3.5.2 Mineral textures as a proxy of fluid/rock ratios during hydrothermal alteration

The fluid/rock ratios prevailing during alteration can be calculated using the Sr isotope compositions of the altered rocks following the procedure described in Delacour et al. 2008. Besides the isotopic variability explained by sourcing distinct reservoirs in variable amounts, some of the variability observed for a given lithology (dispersion of histograms ; Figure 3.3) seems to be directly related to mineral textures, especially for Fe-Ca silicate minerals from Cotschen. The minerals in veins are less radiogenic than those in pervasive replacement of serpentinites (Table 3.1). This may relate to variable fluid/rock ratios and/or variable modes of secondary mineral formation during hydrothermal alteration (replacement vs. open-space infilling). This suggests close relationships between the replacement process and the resulting Sr isotope compositions. During hydrothermal alteration, the Sr isotope composition of secondary minerals is related to the amount of fluid available and its capacity to percolate into the rock.

When large amounts of fluid are available (i.e., high fluid/rock ratio), the Sr isotope composition of the fluid remains unchanged during interaction with the country rocks and consequently, secondary minerals will record the isotopic signature of this fluid. On the contrary, if the amount of fluid available is low (i.e., low fluid/rock ratio), the initial Sr isotope composition of the fluid is modified during fluid/rock interactions and thus secondary minerals will record these fluid/rock interactions.

In cases where a large quantity of seawater was available, pervasive replacement of primary minerals occurred, and the resulting Sr isotope compositions of altered rocks are close to the value of seawater (Figure 3.3). The initial Sr isotope compositions of protoliths, i.e., serpentinites both for Fe-Ca silicate minerals and carbonates, were erased during intense interaction with Jurassic seawater.

Conversely, if small amounts of seawater were involved, discrete veins preferentially formed, yielding Sr isotope compositions which were not buffered by seawater but rather preserved the ones of the primary host rocks. For instance, at Cotschen, the Fe-Ca silicate minerals produced during pervasive replacement of serpentinites display Sr isotope compositions close to that of Jurassic seawater (~ 0.70676) and very large Sr isotope exchange (from 84 to 100 %), whereas isolated Fe-Ca silicate veins in serpentinites have slightly lower Sr isotope compositions (~ 0.70621) and lower Sr isotope exchange (from 75 to 87 %). This supports the hypothesis of Coltat et al. 2019b, who proposed that the fluid/rock ratio increased from the outer zone (i.e., host serpentinites) where discrete veining occurred in the stockwork to the inner zone (i.e., Cu-rich massive sulfides) where Fe-Ca silicate minerals pervasively replaced the serpentinites.

As for Fe-Ca silicates, the textural variability of the carbonates at Falotta seems to control the Sr isotope compositions of altered rocks. Coltat et al. 2019a inferred that an infinite isotopic reservoir was available during the formation of thick foliated ophicalcites (~ 10 m). Fracture-filling carbonates, which formed under lower fluid/rock ratios than those prevailing for foliated ophicalcites, have higher Sr isotope compositions than the latter (0.70706 and 0.70686, respectively; Table 3.1). The percentage of Sr exchange calculated is about 96 % for foliated ophicalcites. This supports the idea that the textural variability of altered rocks is controlled by variations of the fluid/rock ratio during hydrothermal alteration, leading to distinct Sr isotope compositions of the secondary minerals. Where the fluid/rock ratio was high, secondary minerals recorded the Sr isotope composition of the fluid solely (i.e., seawater), whereas at low fluid/rock ratio, they recorded interactions between the hydrothermal fluid and the surrounding rocks (i.e., acquiring intermediate Sr isotope compositions between those of the fluid

and the surrounding rocks). Similarly, Schwarzenbach et al. 2021 have measured Sr and stable isotopes in calcite veins in ophicalcites from Apennine ophiolites, and proposed that carbonation resulted from extensive seawater circulation.

A different trend is recorded by serpentinites. At Falotta, the serpentine veins are more radiogenic than the groundmass of serpentines with mesh texture (0.70898 and 0.70756, respectively ; Table 3.1). Mesh formation requires very low fluid/rock ratios and supports a diffusion process in a roughly closed system (where the amount of fluid is limited ; Viti and Mellini 1998 ; Evans 2004 ; Andreani et al. 2007). In contrast, vein formation corresponds to higher fluid/rock ratios, especially during the latest vein formation in an open system near the seafloor Andreani et al. 2007. The serpentine veins were formed after interaction with seawater that previously percolated through the continental crust. The oxygen isotope compositions measured in late serpentine veins from the Platta nappe by Früh-Green et al. 1990, are consistent with interaction with metamorphic fluids channelized along discrete brittle fractures and at grain boundaries in a rock-dominated system. More recently, Schwarzenbach et al. 2021 proposed that hydrogen isotopes compositions measured in serpentinites from the Apennine ophiolites resulted of a seafloor process and interaction with an evolved seawater-derived fluid. In the absence of evidence of metamorphic overprint in the area and in line with our results, we argue that this latter explanation is the most plausible.

3.5.3 Hydrothermal alteration during the final rifting and breakup of the Platta nappe

Part of the isotopic variability in serpentinites cannot be explained by variations of the fluid/rock ratios nor by mineral textures, e.g., the wide disparities in the groundmass serpentinites between sites (Table 3.1). Serpentinites in a more continentward position (Upper Platta) have $^{87}\text{Sr}/^{86}\text{Sr}$ ratios higher than serpentinites from a more oceanward position (Lower Platta ; Table 3.1). For mafic rocks, epidotized basalts from Marmorera (distal domain) are less radiogenic than those from Falotta (distal domain ; Table 3.1). Moreover, at Falotta, epidotized basalts recorded a higher Sr isotope exchange and fluid/rock ratio than those at Marmorera (Table 3.1). Therefore, the contribution of the Sr reservoirs likely evolved with the position along the margin and thus a change in the nature and the proportion of the Sr contributors during the margin formation may be inferred.

Serpentinization of mantle rocks resulted from the interaction of the sub-continental

lithospheric mantle with hydrothermal fluids (Table 3.1 ; Figure 3.3) that previously interacted with the continental crust. During rifting, the continental crust was progressively thinned due to the interplay between brittle detachment faulting in upper crustal level and ductile shearing in middle and lower crustal levels (Mohn et al. 2012). Hence, before reacting with mantle rocks, seawater likely percolated through the permeable faults and interacted with crustal rocks (Incerpi et al. 2020). In a later stage of rifting, shear zone allowed to thin the crust less than 10 km and completely brittle, enabling faults and fluids to penetrate across the residual thinned crust into the mantle initiating serpentization. At a following stage, mantle was exhumed to the seafloor by in and out of sequence detachment systems, whereby domains near the crust experienced contamination by continent-derived Sr, while this contamination decreased oceanward. This led to the Sr isotope gradient observed in serpentinites with lower Sr isotope compositions oceanward. Hence, a significant part of the isotopic heterogeneity of serpentinites is likely due to long-term serpentization reactions during extensional tectonics, from the hyperextension phase to the exhumation phase (i.e., creation of the distal domain).

To a lesser extent, the position along the margin may also have influenced the Sr isotope compositions of carbonated rocks. Indeed, samples from Falotta (Figure 1B) display higher Sr isotope compositions than carbonated rocks from the more oceanward Cotschen and Marmorera domains. This could be explained by higher Sr isotope compositions of the host rocks at Falotta than at Marmorera-Cotschen (i.e., serpentinites Table 3.1 ; Figure 3.3). Hence, during carbonation, at a given fluid/rock ratio, the seawater that would have interacted with serpentinites having higher Sr isotope ratios at Falotta than at Marmorera-Cotschen likely formed carbonates with higher Sr isotope compositions at Falotta.

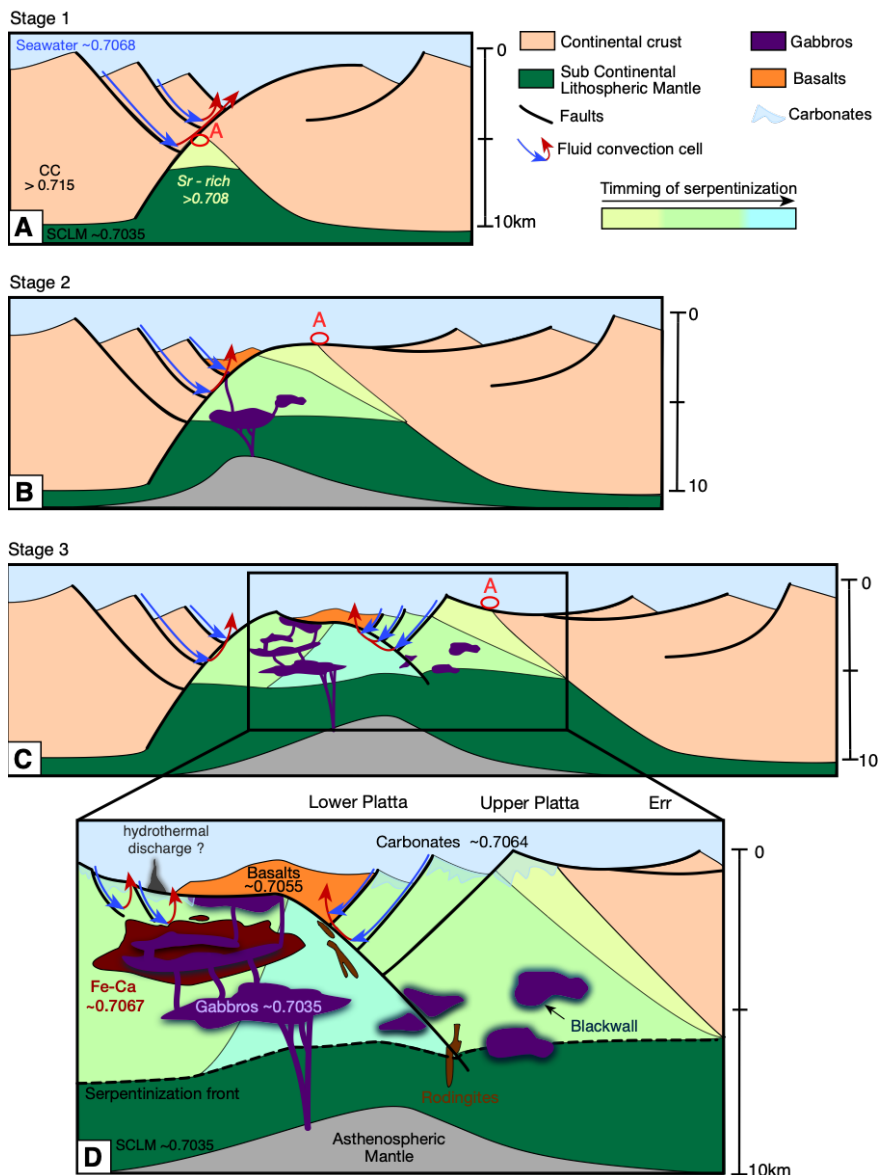


FIGURE 3.4 – Schematic model showing the evolution of the OCT and associated fluid circulations leading to the formation of Fe-Ca silicates, modified from Epin et al. 2019. A) Stage 1 : serpentinization initiated from fluids with radiogenic Sr (CC-derived fluids) leading to formation of serpentinites with Sr isotope compositions higher than SW. B) Stage 2 : first exhumation of subcontinental lithospheric mantle previously serpentinized and onset of magmatism, serpentinization continues to occur by seawater with a lesser continental influence. C) Stage 3 : increase of magmatic rocks and alteration (rodingitization, epidotization-chloritization of mafic extrusives) by serpentinization derived fluids mixing with seawater infiltrated along faults. Serpentinization continues to occur with pristine seawater. D) Schematic model showing fluids pathways, the different alteration products and their associated Sr isotope compositions. Fluids resulting from the alteration of mafic rocks and serpentinization migrated upwards and mixed with seawater to form Fe-Ca silicates. Carbonation was the last hydrothermal event recording in ultramafic and mafic rocks.

3.5.4 Timing of the hydrothermal alteration at the Marmorera-Cotschen Hydrothermal System

All the points discussed above allow to propose a timing for the hydrothermal alteration and formation of the Marmorera-Cotschen hydrothermal plumbing system (Figure 3.4). In the Platta nappe hydrothermal alteration story, the serpentinization of mantle rocks was the first event (Figure 3.4, stage1). It started during the hyper-extension phase of the rifting, when the sub-continental lithospheric mantle was still capped by a thinned continental crust (less than 10 km thick), forming the highly radiogenic serpentinites (Figure 3.3 ; Table 3.1). Serpentinization continued after mantle rocks exhumation at the seafloor (i.e., formation of the Ocean Continent Transition after continental breakup), leading to the interaction between mantle rocks and isotopically pristine seawater that circulated along the detachment faults (Figure 3.4, stage 2).

Mantle exhumation was accompanied by the emplacement of mafic magmatism (Desmurs et al. 2002; Epin et al. 2019; Amann et al. 2020). Extrusive rocks were emplaced onto an active exhumation fault and were further altered during hydrothermal circulations, leading to epidotization, chloritization and late carbonation at the serpentinite-basalt interface (Coltat et al., 2019a, 2020). Rodingitization and associated blackwalls formed synchronously to the serpentinization of mantle rocks, through a diffusional metasomatism process between serpentinized-derived fluids and mafic rocks, such as described in Bach and Klein 2009 (Figure 3.4, stage 2). Here again, the heterogeneous Sr isotope compositions of rodingites and blackwalls are consistent with long-term fluid/rock interactions and multi-stage infiltration of fluids Salvioli-Mariani et al. 2020. The fluids released during the rodingitization of mafic rocks migrated upwards and likely interacted with serpentinization-derived fluids and isotopically unmodified seawater to form Fe-Ca silicate minerals and late carbonates (Figure 3.4, stage 3 and 4, respectively).

The Sr isotope compositions of Fe-Ca silicate minerals and carbonated rocks are centered around the value of seawater, especially those at Cotschen (Figure 3.3). The homogeneity of Sr isotope ratios and the large Sr exchange suggest short-lived fluid circulations under high fluid/rock ratios. Based on oxygen isotope compositions of ophiocalcites, a similar interpretation was proposed by Coltat et al. 2019a at the Falotta site (Lower Platta Unit) and in the Apennine ophiolites Schwarzenbach et al. 2021. Consistently, in our model, carbonation of mafic rocks and serpentinites was the latest

hydrothermal event in the story. It is assumed to have occurred in high-permeability zones like the basalt-serpentinites interface during the mixing between seawater and uprising hydrothermal fluids. Towards the seafloor, the seawater component became more predominant (Figure 3.4, stage 4).

3.5.5 Consequences for the formation of ultramafic-hosted metal deposits

The Sr isotope compositions of Fe-Ca silicates accompanying mineralization in the Platta nappe are consistent with a contribution from the surrounding magmatic rocks (altered mafic and ultramafic rocks) but also from seawater (Figure 3.4D). The latter was also involved in metal precipitation (e.g. Co, Cu, Ni, Zn), during mixing with the hydrothermal fluid, as proposed for the Rainbow hydrothermal field (Debret et al., 2018) and the fossil Marmorera-Cotschen hydrothermal system (Coltat et al., 2021). However, it is unlikely that metals derived from seawater itself, even considering large fluid/rock ratios, since seawater contains infinitesimal proportions of metals compared to the surrounding rocks (e.g., Fouquet et al. 2013 and references therein). Rather, we propose that the main part of the metal stock involved for the Marmorera-Cotschen hydrothermal system mineralization derived from the surrounding rocks (serpentinites and mafic rocks) with minor involvement of seawater.

Based on S and Pb isotope geochemistry of ultramafic-hosted mineralizations, a similar scenario was proposed to explain metal enrichments at oceanic hydrothermal systems (Zeng et al. 2017). These authors indicate that the contribution of seawater-derived sulfur taking part to mineralized systems was less than 36 %, whereas on the basis of Pb isotope compositions it was argued that lead solely derived from the surrounding magmatic rocks. In addition, Debret et al. 2018 recently investigated the Fe, Cu and Zn systematics of barren and mineralized rocks from the ultramafic-hosted Rainbow hydrothermal system (MAR). They showed that serpentization of mantle rocks was responsible for metal leaching from the parental peridotite (e.g., decreasing of metal concentrations from peridotite to serpentinite). Mantle rocks may thus represent a major contributor for metals involved in the formation of ultramafic-hosted mineralized systems.

Finally, the results from the present study highlight that the formation of ultramafic-hosted mineralized systems depends on the availability of both mafic and ultramafic reservoirs to extract metals that form economic mineralization enriched in base (Cu, Ni,

Zn), critical (Co) and precious (Au) metals, similar to what is observed in present-day systems (Fouquet et al. 2013). Recently, a review of fossil ultramafic-hosted mineralized systems preserved on-land has been proposed (Patten et al. 2021). The main results are that : i) these systems are not scarce but rather represent a self-standing sub-group of the so-called volcanogenic massive sulfides (VMS) deposits, ii) they form in complex tectonic environments preserved in the geological record (e.g., ocean-continent transition, mid-oceanic ridge, supra-subduction zone), iii) they present specific alteration and deformation features (i.e. associated with serpentinites, carbonated mantle rocks and talc-chlorite-tremolite schists along extensional structures generally at the contact between mantle rocks and overlying mafic and/or sedimentary rocks), and iv) according to the Zipf's law, many deposits are still undiscovered. Although a genetic model is still missing for ultramafic-hosted VMS deposits, in which the Marmorera-Cotschen hydrothermal system belongs, our study, focused on the Sr isotope systematics, demonstrates that mafic and ultramafic reservoirs are important components that control the formation of polymetallic deposits. Similar mineralized systems have been reported at the contact between mantle and sedimentary rocks (e.g., Bouvier et al. 1990 ; Peltonen et al. 2008), implying that mafic rocks are not a prerequisite to produce ultramafic-hosted metal deposits. Further studies are needed to produce a proper genetic model for ultramafic-hosted VMS, especially concerning their relationships with the different hydrothermal alterations and the seafloor-related extensional tectonics, but this model will likely be implemented by Sr isotope investigations.

3.6 Conclusions

In the Platta nappe, the Fe-Ca silicates ($^{87}\text{Sr}/^{86}\text{Sr} = 0.70668$) and associated mineral deposits (the Marmorera-Cotschen hydrothermal system, of late Middle Jurassic age) formed through intense leaching of surrounding mafic and ultramafic rocks during interactions with seawater ($^{87}\text{Sr}/^{86}\text{Sr} = 0.70628$, this value being estimated using the most carbonated serpentines, i.e., the foliated ophicalcites). The Sr isotope compositions and textural features of altered rocks allowed to reconstruct the timing of the hydrothermal alteration and formation of the Marmorera-Cotschen hydrothermal plumbing system. The Sr isotope compositions of serpentinites recorded multiple and long-time fluid/rock interactions. In particular, the involvement of seawater is demonstrated, both during early stage (hyperextension phase) for which it interacted with continental crust and during late exhumation stage (mantle exhumation at the seafloor) during which it mixed with serpentinization-derived fluids. Obviously, the involvement of seawater became dominant during serpentinization and carbonation near the paleoseafloor. Mafic rocks also recorded multiple fluid histories, involving variable amounts of hydrothermal fluids, leading to a diversity of Sr isotope compositions (from 0.70334 to 0.70624). In contrast, the Fe-Ca silicates and the ophicalcites mostly recorded latest stages of fluid/rock interactions dominated by seawater under high fluid/rock ratios. Rather than giving a straightforward information on the source of the metals present in ultramafic-hosted oceanic deposits, the Sr systematics thus helps identify the reservoirs involved in the mineralization and constrain the plumbing system through which mineralization occurred.

Acknowledgments

Yannick Branquet (University of Rennes 1) helped a lot during field work. David Vilbert (Géosciences Rennes) and Clément Bujisho (Master 1 internship at the University of Rennes 1) performed the analyses on carbonates and some Fe-Ca silicates. Eric Pelt (ITES - University of Strasbourg) helped for isotopic measurements and René Boutin performed ICP-MS analyses. This work was supported by the French National program INSU-SYSTER and by the AAP interne of ITES.

TABLE 3.1 – Sr isotope compositions of Fe-Ca silicates and carbonates, serpentinites, carbonates and mafic rocks sampled in the Platta nappe, $^{87}\text{Sr}/^{86}\text{Sr}$ in italic refers as $^{87}\text{Sr}/^{86}\text{Sr}$ without Rb correction. ep : epidotized, ch : chloritized, PR : pervasive replacement, MI : mafic intrusion.

Site	Sample	Latitude N	Longitude E	$^{87}\text{Sr}/^{86}\text{Sr}$ mes	2 SE $\times 10^5$	$^{87}\text{Sr}/^{86}\text{Sr}$ 160 Ma	Sr (ppm)	Rb (ppm)	Sr ex (%)	W/R close	W/R open	Comment
<i>Fe-Ca-silicates</i>												
Cotschen	Cot18_40	46°29'56	9°37'16	0.706462	10	0.70646			87	nd	nd	PR
	Cot18_46	46°29'57	9°37'16	0.707848	12	0.70785			nd	nd	nd	PR
	Cot18_50	46°29'58	9°37'16	0.706456	13	0.70646			87	nd	nd	veins in serp.
	Cot18_57	46°29'55	9°36'55	0.70592	22	0.70592			75	nd	nd	veins in serp.
	Cot18_66	46°29'54	9°36'58	0.706325	10	0.70633			84	nd	nd	PR
	Cot18_67	46°29'54	9°36'58	0.706419	11	0.70642			86	nd	nd	veins in serp.
	Cot18_70	46°29'54	9°36'58	0.706422	15	0.70642			86	nd	nd	PR
	Cot18_72	46°29'54	9°36'58	0.706027	13	0.70603			77	nd	nd	veins in serp.
Kanonensatellit	Kan19_3	46°30'48	9°38'35	0.707114	29	0.70711			nd	nd	nd	PR
	Kan19_5	46°30'48	9°38'35	0.707456	10	0.70746			nd	nd	nd	PR
	Kan19_7	46°30'48	9°38'35	0.707045	13	0.70705			100	nd	nd	PR
	Kan19_9	46°30'48	9°38'35	0.706708	13	0.70671			93	nd	nd	PR
<i>Carbonates</i>												
Cotschen	Cot16_49a	46°30'02	9°36'42	0.706588	10	0.70659			90	nd	nd	veins in serp.
	Cot16_52	46°30'02	9°36'42	0.706311	10	0.70631			84	nd	nd	veins in serp.
Marmorera	Mar16_37	46°30'18	9°37'40	0.704193	10	0.70419			36	nd	nd	veins in serp.
	Mar16_40e	46°30'18	9°37'40	0.705481	10	0.70548			65	nd	nd	veins in serp.
	Mar16_40e	46°30'18	9°37'40	0.704675	10	0.70468			46	nd	nd	PR in serp.
Falotta	Fal16_16	46°32'42	9°39'36	0.707294	10	0.70729			nd	nd	nd	discret veins in serp.
	Fal16_17	46°32'42	9°39'36	0.706677	10	0.70668			92	nd	nd	discret veins in serp.
	Fal17_28	46°32'42	9°39'36	0.707220	10	0.70722			nd	nd	nd	discret veins in serp.
	Fal17_63	46°32'42	9°39'36	0.706866	10	0.70687			96	nd	nd	PR in serp.
	Fal17_64	46°32'42	9°39'36	0.706835	10	0.70684			95	nd	nd	PR in serp.
	Fal17_65	46°32'42	9°39'36	0.706868	10	0.70687			96	nd	nd	PR in serp.
	Fal17_35	46°32'42	9°39'36	0.706813	10	0.70681			95	nd	nd	veins in ep. basalt
	Fal17_42	46°32'42	9°39'36	0.706731	10	0.70673			93	'nd	nd	veins in ep. basalt
	Fal17_49b	46°32'42	9°39'36	0.706418	10	0.70642			86	nd	nd	veins in ep. basalt
	Fal17_51	46°32'42	9°39'36	0.706657	10	0.70666			91	nd	nd	veins in ep. basalt
<i>Serpentinites</i>												
Cotschen	Tal18-01	46°29'43	9°37'21	0.707668	18	0.706826	0.55	0.07	95	16.0	2.4	
	Tal18-06a		9°37'19	0.709049	25	0.707798	0.42	0.08	nd	nd	nd	
	Mar18-01	46°30'20	9°37'41	0.704621	40	0.703939	4.40	0.59	30	0.5	0.4	
Kanonensatellit	KAN-19-10	46°30'48	9°38'35	0.707677	13	0.706885	12.8	1.54	97	35	4.2	
Falotta LP	Fal17_18	46°32'51	9°39'9	0.708068	15	0.708068	1.12	0.00	nd	nd	nd	
	Fal17_20	46°32'51	9°39'9	0.708075	10	0.708075	1.14	0.00	nd	nd	nd	
	Fal17_22	46°32'51	9°39'9	0.709308	10	0.708580	5.55	0.62	nd	nd	nd	veins
	Fal17_23	46°32'51	9°39'9	0.709408	10	0.708134	1.13	0.22	nd	nd	nd	veins
	Fal18-11	46°32'44	9°39'39	0.706826	10	0.706303	1.50	0.12	83	6.3	2.3	
	Fal18-12	46°32'43	9°39'34	0.706754	6	0.706481	13.5	0.58	87	8.7	2.6	
	Fal18-13	46°32'42	9°39'35	0.707383	4	0.705745	5.00	1.24	71	3.0	1.5	
	Fal18-14	46°32'30	9°39'40	0.708211	6	0.706755	2.00	0.44	94	18.3	3.4	
	TG-P-1a	46°32'51	9°39'9	0.707431	10	0.707431			nd	nd	nd	
	TG-P-1b	46°32'51	9°39'9	0.708495	10	0.708495			nd	nd	nd	
Falotta UP	Fal18-02a	46°32'51	9°40'10	0.709274	9	0.708432	0.70	0.09	nd	nd	nd	veins
	Fal18-02b	46°32'51	9°40'10	0.709006	9	0.708579	2.40	0.17	nd	nd	nd	
	Fal18-03	46°32'51	9°40'10	0.708520	3	0.708122	6.10	0.39	nd	nd	nd	
	Fal18-04	46°32'51	9°40'10	0.710033	6	0.708752	0.90	0.18	nd	nd	nd	veins
	Fal18-05	46°32'51	9°40'10	0.708889	11	0.707704	0.50	0.09	nd	nd	nd	veins
	Fal18-06	46°32'51	9°40'10	0.708954	10	0.708226	4.10	0.45	nd	nd	nd	
	Fal18-07	46°32'51	9°40'10	0.705323	10	0.704852	13.4	0.96	51	1.3	0.9	
	Fal18-08	46°32'57	9°40'7	0.708644	15	0.708144	1.60	0.12	nd	nd	nd	
	Fal18-09	46°32'57	9°40'7	0.709482	3	0.709391	3.50	0.55	nd	nd	nd	
	Fal18-10	46°32'57	9°40'7	0.706453	4	0.706135	1.40	0.07	80	nd	nd	
<i>Mafic rocks</i>												
Marmorera	A	46°30'22	9°37'39	0.704651	9	0.704628	393	0.76	45	1.0	0.8	ep. basalt
	D	46°30'22	9°37'39	0.704638	10	0.704342	1240	56.6	39	0.8	0.6	ep. basalt
	Mar18_17	46°30'18	9°37'40	0.703860	10	0.703337	37.4	0.60	16	0.2	0.2	MI
	Mar18_28	46°30'18	9°37'40	0.703781	10	0.70369	80.6	1.20	24	0.4	0.3	MI (mineralized)
Falotta LP	Fal17_38	46°32'42	9°39'36	0.706243	10	0.706243	3.94	0.00	82	5.7	2.2	ch. basalt
	Fal17_39	46°32'42	9°39'36	0.705879	10	0.705879	3.68	0.00	74	3.5	1.7	nodule of ch. basalt
	Fal17_44	46°32'42	9°39'36	0.706071	10	1 P ¹ 06026	1840	13.1	77	4.2	1.8	ep. basalt
	Fal17_49a	46°32'42	9°39'36	0.705990	9	0.705967	4790	16.1	76	3.9	1.8	ep. basalt

3.7 Supplementary materials

TABLE 3.2 – Sr isotope compositions of mafic rocks, rodingite and blackwall collected in the Platta nappe from previous studies. Metabasalt from Stille et al. 1989, basalt and gabbros from Schaltegger et al. 2002 and rodingite and blackwall from Amann et al. 2020.

Sample	Type	$^{87}\text{Sr}/^{86}\text{Sr}$ mes	$^{87}\text{Sr}/^{86}\text{Sr}$ 160 Ma	Sr (ppm)	Rb (ppm)	Sr ex (%)	W/R close	W/R open
MO 6	Metabasalt	0.70452	0.704295	-	-	38	0.8	0.6
MO 8	Metabasalt	0.70609	0.704962	-	-	53	1.4	0.9
MO 9	Metabasalt	0.7048	0.703654	-	-	23	0.4	0.3
P5	Basalt	0.70348	0.703448	-	-	19	0.3	0.3
P8	Basalt	0.704973	0.703522	82.0	18.0	21	0.3	0.3
P3	Gabbros	0.706398	0.706231	-	-	82	5.6	2.1
P4	Gabbros	0.705560	0.701811	82.0	45.2	nd	nd	nd
P6	Gabbros	0.702991	0.702862	92.8	2.27	5	0.1	0.1
P9	Gabbros	0.704014	0.703976	116	0.00	31	0.6	0.50
30-13	Gabbros	0.703771	0.703771	1490	0.79	26	0.4	0.4
03-03	Rodingite	0.706318	0.706159	14.0	0.33	80	5.1	2.0
03-05	Rodingite	0.706451	0.706406	26.4	0.19	86	7.5	2.4
03-06	Rodingite	0.706158	0.706113	80.4	0.43	79	4.7	2.0
03-07	Rodingite	0.705862	0.705817	10.8	0.6	72	3.3	1.6
03-08-BA	Rodingite	0.706336	0.706291	13.3	0.11	83	6.2	2.2
04-05-BA	Rodingite	0.704562	0.704562	29.2	0.02	44	1.0	0.4
30-14	Blackwall	0.704181	0.704067	2.46	0.04	33	0.6	0.5
30-15	Blackwall	0.703815	0.703451	2.32	0.13	19	0.3	0.3
03-08-BW	Blackwall	0.705944	0.705762	5.77	0.15	71	3.1	1.6
04-05-BW	Blackwall	0.704529	0.704302	42.4	1.45	38	0.8	0.6

Bibliographie

- Albarede, F., Michard, A., Minster, J. F., and Michard, G. (1981). $^{87}\text{Sr}/^{86}\text{Sr}$ ratios in hydrothermal waters and deposits from the east pacific rise at 21°N. *Earth and Planetary Science Letters*, 55:229–236.
- Allen, D. E. and Seyfried Jr, W. (2004). Serpentization and heat generation : constraints from Lost City and Rainbow hydrothermal systems. *Geochimica et Cosmochimica Acta*, 68(6):1347–1354.
- Alt, J. C. (1995). Subseafloor processes in mid-ocean ridge hydrothermal systems. *Geophysical Monograph-American Geophysical Union*, 91:85–85.
- Amann, M. (2017). Evolution du magmatisme et du metasomatisme dans une marge passive pauvre en magma durant l'initiation de l'accrétion océanique : Exemple de la marge fossile de la platta (alpes suisses) et comparaison avec le système actuel iberie-terre neuve.
- Amann, M., Ulrich, M., Manatschal, G., Pelt, E., Epin, M. E., Autin, J., and Sauter, D. (2020). Geochemical characteristics of basalts related to incipient oceanization : The example from the Alpine-Tethys OCTs. *Terra Nova*, 32:75–88.
- Andreani, M., Mevel, C., Boullier, A. M., and Escartin, J. (2007). Dynamic control on serpentine crystallization in veins : Constraints on hydration processes in oceanic peridotites. *Geochemistry, Geophysics, Geosystems*, 8.
- Augustin, N., Paulick, H., Lackschewitz, K., Eisenhauer, A., Garbe-Schönberg, D., Kuhn, T., Botz, R., and Schmidt, M. (2012). Alteration at the ultramafic-hosted logatchev hydrothermal field : Constraints from trace element and sr-o isotope data. *Geochemistry, Geophysics, Geosystems*, 13(3).
- Bach, W., Garrido, C. J., Paulick, H., Harvey, J., and Rosner, M. (2004). Seawater-peridotite interactions : First insights from ODP leg 209, MAR 15°N. *Geochemistry, Geophysics, Geosystems*, 5.
- Bach, W. and Humphris, S. E. (1999). Relationship between the sr and o isotope compositions of hydrothermal fluids and the spreading and magma-supply rates at oceanic spreading centers. *Geology*, 27(12):1067–1070.
- Bach, W. and Klein, F. (2009). The petrology of seafloor rodingites : insights from geochemical reaction path modeling. *Lithos*, 112(1-2):103–117.
- Bonatti, E., Lawrence, J. R., and Morandi, N. (1984). Serpentization of oceanic peridotites : temperature dependence of mineralogy and boron content. *Earth and Planetary Science Letters*, 70(1):88–94.

- Boschi, C., Dini, A., Früh-Green, G. L., and Kelley, D. S. (2008). Isotopic and element exchange during serpentinization and metasomatism at the atlantis massif (mar 30 n) : insights from b and sr isotope data. *Geochimica et Cosmochimica Acta*, 72(7):1801–1823.
- Bouvier, J.-D., Dabrowski, H., Jaffe, F. C., and Vuagnat, M. (1990). Le gisement cuprifère de saint-véran. *Archives Des Sciences*, 43:273–294.
- Burke, W. H., Denison, R. E., Hetherington, E. A., Koepnick, R. B., Nelson, H. F., and Otto, J. B. (1982). Geology variation of seawater $^{87}\text{Sr}/^{86}\text{Sr}$ throughout phanerozoic time variation of seawater $^{87}\text{Sr}/^{86}\text{Sr}$ throughout phanerozoic time. *The geology society of America*, 10:516–519.
- Chalot-Prat, F., Ganne, J., and Lombard, A. (2003). No significant element transfer from the oceanic plate to the mantle wedge during subduction and exhumation of the Tethys lithosphere (Western Alps). *Lithos*, 69(3-4):69–103.
- Chapman, H. J. and Spooner, E. T. C. (1977). ^{87}Sr enrichment of ophiolitic sulphide deposits in cyprus confirms ore formation by circulating seawater. *Earth and Planetary Science Letters*, 35:71–78.
- Chauvel, C., Bureau, S., and Poggi, C. (2011). Comprehensive chemical and isotopic analyses of basalt and sediment reference materials. *Geostandards and Geoanalytical Research*, 35(1):125–143.
- Cherkashov, G., Bel'tenev, V., Ivanov, V., Lazareva, L., Samovarov, M., Shilov, V., Stepanova, T., Glasby, G., and Kuznetsov, V. (2008). Two new hydrothermal fields at the Mid-Atlantic Ridge. *Marine Georesources and Geotechnology*, 26(4):308–316.
- Coleman, R. G. (1967). Low-temperature reaction zones and Alpine ultramafic rocks of California, Oregon and Washington. *Geological Survey Bulletin* 1247, page 46.
- Coltat, R., Boulvais, P., Branquet, Y., Collot, J., Epin, M. E., and Manatschal, G. (2019a). Syntectonic carbonation during synmagmatic mantle exhumation at an ocean-continent transition. *Geology*, 47:183–186.
- Coltat, R., Boulvais, P., Riegler, T., Pelleter, E., and Branquet, Y. (2021). Element distribution in the root zone of ultramafic-hosted black smoker-like systems : Constraints from an Alpine analog. *Chemical Geology*, 559.
- Coltat, R., Branquet, Y., Gautier, P., Boulvais, P., and Manatschal, G. (2020). The nature of the interface between basalts and serpentized mantle in oceanic domains : Insights from a geological section in the Alps. *Tectonophysics*, 797.
- Coltat, R., Branquet, Y., Gautier, P., Rodriguez, H. C., Poujol, M., Pelleter, E., McCleaghan, S., Manatschal, G., and Boulvais, P. (2019b). Unravelling the root zone of ultramafic-hosted black smokers-like hydrothermalism from an Alpine analog. *Terra Nova*, 31:549–561.
- Debret, B., Beunon, H., Mattielli, N., Andreani, M., da Costa, I. R., and Escartin, J. (2018). Ore component mobility, transport and mineralization at mid-oceanic ridges : A stable isotopes (zn, cu and fe) study of the rainbow massif (mid-atlantic ridge 36°14N). *Earth and Planetary Science Letters*, 503:170–180.
- Delacour, A., Früh-Green, G. L., Frank, M., Gutjahr, M., and Kelley, D. S. (2008). Sr-and nd-isotope geochemistry of the atlantis massif (30 n, mar) : implications for fluid fluxes and lithospheric heterogeneity. *Chemical Geology*, 254(1-2):19–35.

- Deniel, C. and Pin, C. (2001). Single-stage method for the simultaneous isolation of lead and strontium from silicate samples for isotopic measurements. *Analytica Chimica Acta*, 426:95–103.
- DePaolo, D. J. and Ingram, B. L. (1985). High-resolution stratigraphy with strontium isotopes. *Science*, 227(4689):938–941.
- Desmurs, L., Müntener, O., and Manatschal, G. (2002). Onset of magmatic accretion within a magma-poor rifted margin : a case study from the Platta ocean-continent transition, eastern Switzerland. *Contributions to Mineralogy and Petrology*, 144(3):365–382.
- Dietrich, V. et al. (1972). Die sulfidischen vererzungen in den oberhalbsteiner serpentiniten.
- Dietrich, V. J. (1969). Die ophiolithe des oberhalbsteins (graubünden) und das ophiolithmaterial der ostschweizerischen molasseablagerungen : ein petrographischer vergleich.
- Douville, E., Charlou, J. L., Oelkers, E. H., Bienvenu, P., Colon, C. F. J., Donval, J. P., Fouquet, Y., Prieur, D., and Appriou, P. (2002). The rainbow vent fluids (36°14N, MAR) : the influence of ultramafic rocks and phase separation on trace metal content in Mid-Atlantic Ridge hydrothermal fluids. *Chemical Geology*, 184:37–48.
- Epin, M.-E. and Manatschal, G. (2018). Three-dimensional architecture, structural evolution, and role of inheritance controlling detachment faulting at a hyperextended distal margin : The example of the Err detachment system (SE Switzerland). *Tectonics*, 37(12):4494–4514.
- Epin, M. E., Manatschal, G., Amman, M., Ribes, C., Clausse, A., Guffon, T., and Lescanne, M. (2019). Polyphase tectono-magmatic evolution during mantle exhumation in an ultra-distal, magma-poor rift domain : example of the fossil Platta ophiolite, SE Switzerland. *International Journal of Earth Sciences*, 108:2443–2467.
- Evans, B. W. (1977). Metamorphism of Alpine peridotite and serpentinite. *Annual Review of Earth and Planetary Sciences*, 5:397–447.
- Evans, B. W. (2004). The serpentinite multisystem revisited : chrysotile is metastable. *International Geology Review*, 46(6):479–506.
- Fouquet, Y., Barriga, F., Charlou, J.-L., Elderfield, H., German, C., Ondreas, H., Parson, L., Radford-Knoery, J., Relvas, J., Ribeiro, A., et al. (1998). Flores diving cruise with nautile near the azores-first dives on the rainbow field : hydrothermal seawater/mantle interaction. *InterRidge News*, 7(1):24–28.
- Fouquet, Y., Cambon, P., Etoubleau, J., Charlou, J. L., Ondreas, H., Barriga, F. J., Cherkašov, G., Semkova, T., Poroshina, I., Bohn, M., Donval, J. P., Henry, K., Murphy, P., and Rouxel, O. (2013). Geodiversity of hydrothermal processes along the Mid-Atlantic Ridge and ultramafic-hosted mineralization : A new type of oceanic cu-zn-co-au volcanogenic massive sulfide deposit. *Geophysical Monograph Series*, 188:321–367.
- Froitzheim, N. (1994). Repeated change from crustal shortening to orogenparallel extension in the austroalpine units of graubünden. *Eclogae Geol.*, 87:559–612.
- Froitzheim, N. and Manatschal, G. (1996). Kinematics of jurassic rifting, mantle exhumation, and passive-margin formation in the Alpineustroalpine and penninic nappes (eastern switzerland). *Geological society of America bulletin*, 108(9):1120–1133.

- Frost, R. (1975). Contact metamorphism of serpentinite, chloritic blackwall and rodignite at Paddy-Go-Easy Pass, Central Cascades, Washington. *Journal of Petrology*, 16(2):272–313.
- Früh-Green, G. L., Weissert, H., and Bernoulli, D. (1990). A multiple fluid history recorded in Alpine ophiolites. *Journal of the Geological Society*, 147(6):959–970.
- Garuti, G., Bartoli, O., Scacchetti, M., and Zaccarini, F. (2008). Volcanic massive sulfide deposits in the northern Apennines, Italy geological setting and structural styles of volcanic massive sulfide deposits in the northern Apennines (Italy) : evidence for seafloor and sub-seafloor hydrothermal activity in unconventional ophiolites of the mesozoic Tethys. *Boleten de la Sociedad Geologica Mexicana*, 60:121–145.
- Hannington, M., Herzig, P., Stoffers, P., Scholten, J., Botz, R., Garbe-Schönberg, D., Jonasson, I., and Roest, W. (2001). First observations of high-temperature submarine hydrothermal vents and massive anhydrite deposits off the north coast of Iceland. *Marine Geology*, 177(3-4):199–220.
- Hess, J., Bender, M. L., and Schilling, J.-G. (1986). Evolution of the ratio of strontium-87 to strontium-86 in seawater from cretaceous to present. *Science*, 231(4741):979–984.
- Humphris, S. E. and Klein, F. (2018). Progress in deciphering the controls on the geochemistry of fluids in seafloor hydrothermal systems. *Annual review of marine science*, 10:315–343.
- Incerpi, N., Martire, L., Manatschal, G., Bernasconi, S. M., Gerdes, A., Czuppon, G., Palcsu, L., Karner, G. D., Johnson, C. A., and Figueredo, P. H. (2020). Hydrothermal fluid flow associated to the extensional evolution of the adriatic rifted margin : Insights from the pre-to post-rift sedimentary sequence (se switzerland, n italy). *Basin Research*, 32(1):91–115.
- Jackson, J. A. (1987). Active normal faulting and crustal extension. *Geological Society, London, Special Publications*, 28:3–17.
- Jones, C. E., Jenkyns, H. C., Coe, A. L., and Hesselbo, S. P. (1994). Quantification and restoration of extensional deformation along the Western Iberia and Newfoundland rifted margins. *Geochimica et Cosmochimica Acta*, 58(14):3061–3074.
- Krasnov, S. G. (1995). Detailed geological studies of hydrothermal fields in the north atlantic. *Geological Society, London, Special Publications*, 87:43–64.
- Le Gal, V., Lucaleau, F., Cannat, M., Poort, J., Monnin, C., Battani, A., Fontaine, F., Goutorbe, B., Rolandone, F., Poitou, C., et al. (2018). Heat flow, morphology, pore fluids and hydrothermal circulation in a typical Mid-Atlantic Ridge flank near oceanographer fracture zone. *Earth and Planetary Science Letters*, 482:423–433.
- Manatschal, G. and Müntener, O. (2009). A type sequence across an ancient magma-poor ocean-continent transition : the example of the Western Alpine Tethys ophiolites. *Tectonophysics*, 473(1-2):4–19.
- Manatschal, G. and Nievergelt, P. (1997). A continent-ocean transition recorded in the Err and Platta nappes (Eastern Switzerland). *Eclogae Geologicae Helvetiae*, 90(1):3–28.
- McArthur, J., Thirlwall, M., Chen, M., Gale, A., and Kennedy, W. (1993). Strontium isotope stratigraphy in the late cretaceous : numerical calibration of the sr isotope curve and intercontinental correlation for the campanian. *Paleoceanography*, 8(6):859–873.

- Mcculloch, M. T., Gregory, R. T., Wasserburg, G. J., and Taylor, H. P. (1980). A neodymium, strontium, and oxygen isotopic study of the cretaceous samail ophiolite and implications for the petrogenesis and seawater-hydrothermal alteration of oceanic crust. *Earth and Planetary Science Letters*, 46:201.
- McDonough, W., McCulloch, M., and Sun, S. (1985). Isotopic and geochemical systematics in tertiary-recent basalts from southeastern australia and implications for the evolution of the sub-continental lithosphere. *Geochimica et Cosmochimica Acta*, 49(10):2051–2067.
- Melchert, B., Devey, C. W., German, C., Lackschewitz, K., Seifert, R., Walter, M., Mertens, C., Yoerger, D., Baker, E., Paulick, H., et al. (2008). First evidence for high-temperature off-axis venting of deep crustal/mantle heat : The nibelungen hydrothermal field, southern mid-atlantic ridge. *Earth and Planetary Science Letters*, 275(1-2):61–69.
- Mohn, G., Manatschal, G., Beltrando, M., Masini, E., and Kusznir, N. (2012). Necking of continental crust in magma-poor rifted margins : Evidence from the fossil alpine tethys margins. *Tectonics*, 31(1).
- Müntener, O., Manatschal, G., Desmurs, L., and Pettke, T. (2010). Plagioclase peridotites in ocean–continent transitions : refertilized mantle domains generated by melt stagnation in the shallow mantle lithosphere. *Journal of Petrology*, 51(1-2):255–294.
- Müntener, O., Pettke, T., Desmurs, L., Meier, M., and Schaltegger, U. (2004). Refertilization of mantle peridotite in embryonic ocean basins : trace element and nd isotopic evidence and implications for crust–mantle relationships. *Earth and Planetary Science Letters*, 221(1-4):293–308.
- Müntener, O. and Piccardo, G. B. (2004). Melt migration in ophiolitic peridotites : The message from Alpine-Apennine peridotites and implications for embryonic ocean basins. *Geological Society Special Publication*, 218:69–89.
- Palandri, J. L. and Reed, M. H. (2004). Geochemical models of metasomatism in ultramafic systems : serpentization, rodingitization, and sea floor carbonate chimney precipitation. *Geochimica et Cosmochimica Acta*, 68(5):1115–1133.
- Panseri, M., Fontana, E., and Tartarotti, P. (2008). Evolution of rodingitic dykes : Metasomatism and metamorphism in the Mount Avic serpentinites (Alpine Ophiolites, southern Aosta Valley). *Lithos*, 33:165–185.
- Patten, C. G., Coltat, R., Junge, M., Peillod, A., Ulrich, M., Manatschal, G., and Kolb, J. (2021). Ultramafic-hosted volcanogenic massive sulfide deposits : an overlooked sub-class of vms deposit forming in complex tectonic environments. *Earth-Science Reviews*, page 103891.
- Peltonen, P., Kontinen, A., Huhma, H., and Kuronen, U. (2008). Outokumpu revisited : new mineral deposit model for the mantle peridotite-associated cu–co–zn–ni–ag–au sulphide deposits. *Ore Geology Reviews*, 33(3-4):559–617.
- Perseil, E. A. and Latouche, L. (1989). Decouverte de microstructures de nodules polymétalliques dans les mineralisations manganésifères métamorphiques de falotta et de parsettens (grisons-suisse). *Mineral. Deposita*, 24:111–116.
- Picazo, S., Manatschal, G., Cannat, M., and Andréani, M. (2013). Deformation associated to exhumation of serpentized mantle rocks in a fossil ocean continent transition : The totalp unit in se switzerland. *Lithos*, 175:255–271.

- Picazo, S., Müntener, O., Manatschal, G., Bauville, A., Karner, G., and Johnson, C. (2016). Mapping the nature of mantle domains in western and central europe based on clinopyroxene and spinel chemistry : Evidence for mantle modification during an extensional cycle. *Lithos*, 266:233–263.
- Pin, C. and Zaldueguil, J. F. S. (1997). Sequential separation of light rare-earth elements, thorium and uranium by miniaturized extraction chromatography : Application to isotopic analyses of silicate rocks. *Analytica Chimica Acta*, 339:79–89.
- Ramponi, E., Hofmann, A. W., and Raczek, I. (1998). Isotopic contrasts within the internal liguride ophiolite (n. italy) : the lack of a genetic mantle-crust link. *Earth and Planetary Science Letters*, 163:175–189.
- Rona, P. A. (1984). Hydrothermal activity at the trans-atlantic geotraverse hydrothermal field, Mid-Atlantic Ridge crest at 26°N. *Journal of Geophysical Research*, 89:11365–11377.
- Rona, P. A., Hannington, M. D., Raman, C., Thompson, G., Tivey, M. K., Humphris, S. E., Lalou, C., and Petersen, S. (1993). Active and relict sea-floor hydrothermal mineralization at the TAG hydrothermal field, Mid-Atlantic Ridge. *Economic Geology*, 88(8):1989–2017.
- Rouxel, O., Fouquet, Y., and Ludden, J. N. (2004a). Copper isotope systematics of the lucky strike, rainbow, and logatchev sea-floor hydrothermal fields on the Mid-Atlantic Ridge. *Economic Geology*, 99:585–600.
- Rouxel, O., Fouquet, Y., and Ludden, J. N. (2004b). Subsurface processes at the lucky strike hydrothermal field, Mid-Atlantic Ridge : Evidence from sulfur, selenium, and iron isotopes. *Geochimica et Cosmochimica Acta*, 68:2295–2311.
- Salvioli-Mariani, E., Boschetti, T., Toscani, L., Montanini, A., Petriglieri, J. R., and Bersani, D. (2020). Multi-stage rodingitization of ophiolitic bodies from northern apennines (italy) : Constraints from petrography, geochemistry and thermodynamic modeling. *Geoscience Frontiers*, 11(6):2103–2125.
- Schaltegger, U., Desmurs, L., Manatschal, G., Müntener, O., Meier, M., Frank, M., and Bernoulli, D. (2002). The transition from rifting to sea-floor spreading within a magma-poor rifted margin : Field and isotopic constraints. *Terra Nova*, 14(3):156–162.
- Schwarzenbach, E. M., Vogel, M., Früh-Green, G. L., and Boschi, C. (2021). Serpentinization, carbonation, and metasomatism of ultramafic sequences in the Northern Apennine Ophiolite (nw italy). *Journal of Geophysical Research : Solid Earth*, 126.
- Seyfried Jr, W., Foustoukos, D., and Allen, D. (2004). Ultramafic-hosted hydrothermal systems at mid-ocean ridges : Chemical and physical controls on ph, redox and carbon reduction reactions. *Mid-Ocean Ridges : Hydrothermal Interactions Between the Lithosphere and Oceans*, 148:267–284.
- Seyfried Jr, W., Pester, N. J., Tutolo, B. M., and Ding, K. (2015). The Lost City hydrothermal system : Constraints imposed by vent fluid chemistry and reaction path models on subseafloor heat and mass transfer processes. *Geochimica et Cosmochimica Acta*, 163:59–79.
- Spooner, E., Beckinsale, R., Fyfe, W., and Smewing, J. (1974). O18 enriched ophiolitic metabasic rocks from e. liguria (italy), pindos (greece), and troodos (cyprus). *Contributions to Mineralogy and Petrology*, 47(1):41–62.

- Stille, P., Clauer, N., and Abrech, J. (1989). Nd isotopic composition of jurassic Tethys seawater and the genesis of Alpine mn-deposits : Evidence from sr-nd isotope data. *Geochemica et Cosmochimica*, 53:1095–1099.
- Tao, C., Li, H., Jin, X., Zhou, J., Wu, T., He, Y., Deng, X., Gu, C., Zhang, G., and Liu, W. (2014). Seafloor hydrothermal activity and polymetallic sulfide exploration on the southwest indian ridge. *Chinese Science Bulletin*, 59(19):2266–2276.
- Tao, C., Seyfried, W., Lowell, R., Liu, Y., Liang, J., Guo, Z., Ding, K., Zhang, H., Liu, J., Qiu, L., et al. (2020). Deep high-temperature hydrothermal circulation in a detachment faulting system on the ultra-slow spreading ridge. *Nature communications*, 11(1):1–9.
- Toffolo, L., Nimis, P., Martin, S., Tumiati, S., and Bach, W. (2017). The Cogne magnetite deposit (Western Alps, italy) : A late jurassic seafloor ultramafic-hosted hydrothermal system ? *Ore Geology Reviews*, 83:103–126.
- Veizer, J., Ala, D., Azmy, K., Bruckschen, P., Buhl, D., Bruhn, F., Carden, G. A., Diener, A., Ebneth, S., Godderis, Y., et al. (1999). $87\text{sr}/86\text{sr}$, $\delta^{13}\text{C}$ and $\delta^{18}\text{O}$ evolution of phanerozoic seawater. *Chemical geology*, 161(1-3):59–88.
- Veizer, J. and Compston, W. (1974). $87\text{sr}/86\text{sr}$ composition of seawater during the phanerozoic. *Geochimica et Cosmochimica Acta*, 38.
- Viti, C. and Mellini, M. (1998). Mesh textures and bastites in the elba retrograde serpentinites. *Eur. J. Mineral*, 10:1341–1359.
- Von Damm, K. L. (1995). Controls on the chemistry and temporal variability of seafloor hydrothermal fluids. *Seafloor hydrothermal systems : Physical, chemical, biological, and geological interactions*, 91:222–247.
- Weissert, H. and Bernoulli, D. (1984). Oxygen isotope composition of calcite in Alpine ophicarbonates : a hydrothermal or Alpine metamorphic signal ? *Eclogae Geologicae Helvetiae*, 77(1):29–43.
- Willbold, M. and Andreas, S. (2010). Formation of enriched mantle components by recycling of upper and lower continental crust. *Chemical Geology*, 276(3-4):188–197.
- Wolery, T. J. and Sleep, N. H. (1976). Hydrothermal circulation and geochemical flux at mid-ocean ridges. *The Journal of Geology*, 84(3):249–275.
- Zeng, Z., Ma, Y., Chen, S., Selby, D., Wang, X., and Yin, X. (2017). Sulfur and lead isotopic compositions of massive sulfides from deep-sea hydrothermal systems : Implications for ore genesis and fluid circulation. *Ore Geology Reviews*, 87:155–171.
- Zhu, X., Guo, Y., Williams, R., Onions, R., Matthews, A., Belshaw, N., Canters, G., De Waal, E., Weser, U., Burgess, B., et al. (2002). Mass fractionation processes of transition metal isotopes. *Earth and Planetary Science Letters*, 200(1-2):47–62.

Chapitre 4

**The Alpine Tethys passive
margins : Serpentinization as a
tape-recorder of mantle exhumation**

Abstract

Fluid-rock interactions in mantle rocks that turns peridotite into serpentinite have been widely documented during the past two decades, for geological settings such as mid-ocean ridges (MOR) and subduction zones. In contrast, serpentinitization at rifted margins has received much less attention, while serpentinites at these settings are largely involved in geochemical and tectonic processes that occur from continental break-up to the establishment of a steady-state MOR. This study presents new petro-geochemical and mineralogical investigations on peridotites that were part of the subcontinental mantle exhumed along a former Ocean-Continent Transition (OCT) of the Jurassic Alpine Tethys, nowadays exposed as ophiolitic nappes (Platta, Tasna and Totalp) in the southeastern part of the Swiss Alps. These peridotites experienced various degrees of serpentinitization, from moderate to complete. At Totalp, the proximal side of the OCT (i.e., continent wards), serpentinitization appears as a typical lizardite bastite and mesh textures that surrounds relics of primary minerals. Locally, the hydrothermal alteration of clinopyroxene leads to the formation of an assemblage of andradite and polyhedral serpentine, reflecting serpentinitization at low temperature, under almost near-isochemical conditions. At Lower Platta derived from the distal OCT (i.e., ocean wards), serpentinitization is extensive and, similarly to Totalp, predominantly formed by mesh and bastite lizardite. The serpentine mesh texture observed at both sides suggests a fluid-rock interaction with a low water-to-rock ratio. At Upper Platta and Tasna, which both derive from more proximal domains of the OCT, serpentinites are characterized by several superimposed serpentinitization events marked by successive generations of serpentine-filling veins with distinct morphologies and textures, that include : mesh and bastite texture (S1) → polyhedral serpentine (S2) banded veins (S3) → lamellar veins (S4) → crack seals (S5). Banded veins (S2) are made of several serpentine species including chrysotile, polygonal serpentine, polyhedral serpentine and lizardite. They formed as a result of gradual opening during mantle exhumation from a supersaturated solution. The gradual evolution from chrysotile → polygonal → lizardite in banded veins is attributed to the progressive increases of fluid/rock ratio with arrival of new fluids. The transition in lizardite is kinetically favored by the decrease of the fluid supersaturation and increasing reaction times. A decrease of temperatures occurs possibly with this transition. Locally antigorite (S4) replaces the lizardite mesh S1 or some chrysotile banded veins S3 in response to a local increase of pressure induced by the shortening. This event took place at shallower levels the previous serpentinitization events. Cracks

seals consist of chrysotile veins formed at shallow depth after strain release and under high fluid/rock ratios. This study highlights that serpentinization at passive margins is comparable to MOR. Finally, this study shows that antigorite is not only restricted to convergent prograde orogenic domains, and can, surprisingly, also occur during mantle exhumation in both OCT and (ultra)-slow spreading systems.

Keywords : fluid-rock interaction, serpentine geochemistry, magma-poor rifted margins, Ocean-Continent Transition, Alps

4.1 Introduction

Along Ocean-Continent Transition (OCT) zones of magma-poor rifted margins, mantle peridotites are exhumed at the seafloor by large long offset normal faults, also called detachment faults (Karson and Rona 1990 ; Cannat 1993 ; Cann et al. 1997 ; Lavier et al. 1999 ; Smith et al. 2006). Mantle exhumation is closely linked to hydrothermal circulations responsible for intense fluid-rock interactions, and resulting in pronounced chemical and mineralogical transformations such as serpentinization (Früh-Green et al. 1996, 1990 ; Paulick et al. 2006 ; Bach et al. 2006 ; Schwarzenbach et al. 2021). These fluid-rock interactions affect the geochemical budgets of the oceans (Thompson and Melson 1970 ; Snow and Dick 1995) and are associated with microbial processes near the seafloor (Janecky and Seyfried 1986 ; Alt and Shanks III 1998 ; Kelley et al. 2001 ; Früh-Green et al. 2004). Furthermore, serpentinization results in an increase in volume of the altered rock Klein and Roux 2020, resulting in a significant decrease in density and seismic velocities of the oceanic lithosphere (Christensen 1972 ; Escartin et al. 1997, 2001 ; Carlson and Miller 1997).

The serpentinization process has been extensively studied using petrological and geochemical investigations on serpentinized peridotites (e.g., Alt 1995 ; Mével 2003 ; Bach et al. 2004 ; Foustaoukos et al. 2008 ; Dessimoulie et al. 2020 ; Tao et al. 2020), and experimental approach (e.g., Seyfried Jr and Dibble Jr 1980 ; Janecky and Seyfried 1986 ; Allen and Seyfried Jr 2004, 2005 ; Malvoisin et al. 2012 ; Klein et al. 2015). These studies have shown that serpentinization can occur in various tectonic settings and under broad (temperature, pressure, pH, silica activity and redox conditions and different fluid-rock ratios). During serpentinization, primary olivine and pyroxenes are respectively, replaced by serpentine mesh and bastite textures Wicks and Whittaker 1977. These pseudomorphic textures dominated by lizardite and chrysotile, are typical of serpentinization under static conditions and low fluid-rock ratios, near stoichiometry (Viti and Mellini 1998 ; Evans 2004 ; Andreani et al. 2007). These primary textures are often overprinted by later serpentine veins and recrystallization, especially at oceanic domains (Früh-Green et al. 2004, 1996 ; Andreani et al. 2007 ; Boschi et al. 2013 ; Rouméjon et al. 2019, 2015, 2018). These studies mainly attribute the development of these serpentinization sequences to the progressive exhumation of peridotites towards the seafloor, accompanied by changes in the conditions of serpentinization, in particular an increase in the fluid-rock ratios. On the other hand, the formation of antigorite is mostly related to prograde metamorphism characterized by an increase in temperature

and pressure (Coleman 1971; Evans 1977; Wicks and Whittaker 1977; Mellini et al. 1987; Wunder and Schreyer 1997; Evans 2004; Auzende et al. 2006; Schwartz et al. 2013). However some studies have shown the presence of antigorite in oceanic domains such as at the Mid Atlantic Ridge (MAR) and the South West Indian Ridge (SWIR), and attributed its formation to intense shear stress (Ribeiro Da Costa et al. 2008) and/or moderate Si-metasomatism (Rouméjon et al. 2019, 2015), that occurs below 300°C, during the retrograde path of serpentinization.

In this study, we investigate the textures, mineralogy and chemistry of successive serpentine minerals and veins in serpentinized peridotites sampled from the remnants of an ancient Ocean Continent Transition (OCT) of the Alpine Tethys exposed in the Alps in SE Switzerland. We sampled in the Platta, Tasna and Totalp ophiolitic units, representing the OCT of the ancient Adriatic and European-Briançonnais conjugate rifted margins. These units preserve pre-Alpine, rift-related contacts Manatschal 2004 and were preserved from the low-grade prehnite-pumpellyite facies Alpine metamorphism (Froitzheim and Rubatto 1998; Chalot-Prat et al. 2003a; Picazo et al. 2013; Epin et al. 2019; Ribes et al. 2020). Thus, the study of serpentinized peridotites from these units can be used to unravel serpentinization sequences and chemical transfers occurring during continuous uplift and exposure on the Jurassic ocean floor. We also discuss the chemical composition of serpentinizing fluids and how successive fluid-rock interactions influence its composition during the formation of the OCT. Then we compare the mineralogical results of this study with data from modern analogs such as slow to ultra-slow mid-ocean ridges. Such characterization of serpentinization processes is necessary to better understand the tectonic and thermal evolution related to mantle exhumation.

4.2 Geological setting

Particularly well-preserved remnants of the Jurassic (OCT) of the Alpine Tethys are exposed as ophiolitic nappes in the Central Alps in southeastern Switzerland (Figure 4.1A,C ; Manatschal and Nievergelt 1997 ; Müntener et al. 2010, 2004). These ophiolite units represent OCTs of the ancient Adriatic-European-Briançonnais conjugate margins (Figure 4.1B ; Florineth and Froitzheim 1994 ; Manatschal 2004). In our study, we focused to three sites, the Platta and Totalp nappes, both derived from the SE margin of the Alpine Tethys (Adriatic margin), and the Tasna nappe, which was part of the conjugate European-Briançonnais margin Manatschal and Müntener 2009 (Figure 4.1B,C).

4.2.1 The Platta nappe

The Platta nappe belongs to the Austro-alpine/Upper Pennine nappes stack that was emplaced during Late Cretaceous top to the NW thrusting (Figure 4.1C). The Platta nappe is subdivided into two units separated by shear zones (Figure 4.1D ; Epin et al. 2019) : i) the Upper Platta unit in the hanging wall (originally located in a more proximal position, , consists of mantle rocks that originally formed the inherited subcontinental mantle of the Adriatic margin (i.e., the Err domain Schaltegger et al. 2002 ; Müntener et al. 2010, 2004 ; Picazo et al. 2016 ; Epin and Manatschal 2018) ; and ii) the Lower Platta unit, which was in a more distal position and consists of a large mantle domain locally intruded and covered by magmatic rocks (gabbros and lavas) of Jurassic age (~ 161 Ma ; Desmurs et al. 2002 ; Amann et al. 2020). Contrarily to mantle rocks from the Upper Platta unit that are free from any syn-rift melt imprint and equilibrated at \pm about 850°C , those from the Lower Platta unit have been largely percolated and refertilized by MORB-type melts (Müntener et al. 2010 ; Amann et al. 2020) during final rifting and breakup, and was equilibrated at higher temperature \pm at about 1000°C (Müntener et al., 2010, 2004). Slivers of continental origin also occur in the Platta nappe and have been interpreted as extensional allochthons (Froitzheim and Manatschal 1996). Some outcrops in the Platta nappe are overlain by ophicalcites (Dietrich 1970). The Platta nappe was relatively little affected by Alpine metamorphism (lower greenschist facies, $<350^{\circ}\text{C}$; Froitzheim and Rubatto 1998 ; Chalot-Prat et al. 2003b ; Epin et al. 2019 ; Coltat et al. 2021). However, an increase in Alpine metamorphism from north to south is characterized by the transition lizardite-chrysotile

in the northern Platta nappe to antigorite type in the southern Platta and Malenco unit, representing the southern continuation of the Upper Platta unit (Dietrich 1969; Trommsdorff and Evans 1977; Trommsdorff 1983; Burkhard and O'Neil 1988).

4.2.2 The Totalp nappe

The Totalp nappe is located to the north of the Platta nappe (Figure 4.1B), and belongs, like the Platta nappe, to the Late Cretaceous Austro Alpine/Upper Pennine nappe stack and was thrust later, during the late Eocene northward over the Middle and Lower Pennine units (Froitzheim and Manatschal 1996; Figure 4.1C). The slightly more complex polyphase Alpine overprint makes that its paleogeographic position is less well defined like that of the Platta nappe, but there is consensus in assuming that the Totalp nappe is derived from the SE margin of the Alpine Tethys. The Totalp nappe consists of foliated serpentized spinel lherzolites, occasionally crosscut by pyroxenites and covered by ophicalcites and pelagic sediments. Magmatic rocks are very rare and mainly consist of flaser gabbros and doleritic dykes (Peters and Mathews 1963). Comparatively to the Platta nappe, the Totalp nappe was affected by a weaker Alpine metamorphism peak of lower than prehnite facies (Peters and Mathews, 1963). Serpentized mantle is often crosscut by calcite veins (Weissert and Bernoulli 1985; Bernoulli and Weissert 1985; Picazo et al. 2013). Similarly to the Platta nappe, relics of the pre-Alpine contacts between exhumed mantle rocks, ophicalcites and sediments are locally well-preserved (Picazo et al. 2013), thus making a very good place to study fluid-rock interaction related to mantle exhumation to the seafloor. $^{40}\text{Ar}/^{39}\text{Ar}$ dating on phlogopite from pyroxenite suggest a cooling/exhumation ages of 160 ± 8 Ma of cooling/exhumation (Peters and Stettler 1987a,b; Manatschal et al. 2006).

4.2.3 The Tasna nappe

The Tasna nappe was derived from the Briançonnais/European margin (Figure 4.1B ; Florineth and Froitzheim 1994 ; Manatschal et al. 2006 ; Ribes et al. 2020). This nappe belongs to the Tertiary Alpine nappe stack made of Austro Alpine and Pennine nappes (Figure 4.1C) emplaced during Eocene to Oligocene period (Manatschal et al. 2006. Similarly to the Platta nappe, the Tasna nappe was only weakly affected by Alpine metamorphism (low grade <350°(greenschist facies) ; Florineth and Froitzheim 1994 ; Froitzheim and Manatschal 1996 ; Bousquet et al. 2008 ; Manatschal et al. 2006 ; Ribes et al. 2020), and preserves pre-Alpine, seafloor-related structures and contacts. The Tasna nappe is made of a wedge of continental crust that is separated from the underlying mantle by a detachment fault, the Lower Tasna Detachment (LTD), which separates continental rocks from mantle rocks. The Upper Tasna Detachment (UTD), that truncates the LTD, forms the exhumed top-basement (Froitzheim and Rubatto 1998, Manatschal et al. 2006) and is overlain, along a stratigraphic contact, by undeformed Upper Barremian post-rift sediments, characteristic of the Briançonnais/European domain Froitzheim and Rubatto 1998. Mantle rocks consist of serpentinized spinel lherzolites (serpentinization >90%) with abundant spinel websterite layers and preserving a high temperature spinel foliation Manatschal et al. 2006. The $^{40}\text{Ar}/^{39}\text{Ar}$ ages on phlogopites give an age of 170.5 ± 0.4 Ma Manatschal et al. 2006 which is similar to that obtained from Totalp Peters and Stettler 1987a. The clinopyroxene compositions and the calculated equilibrium temperatures on coexisting pyroxenes from mantle rocks provide temperatures similar to those from the Upper Platta unit Manatschal et al. 2006.

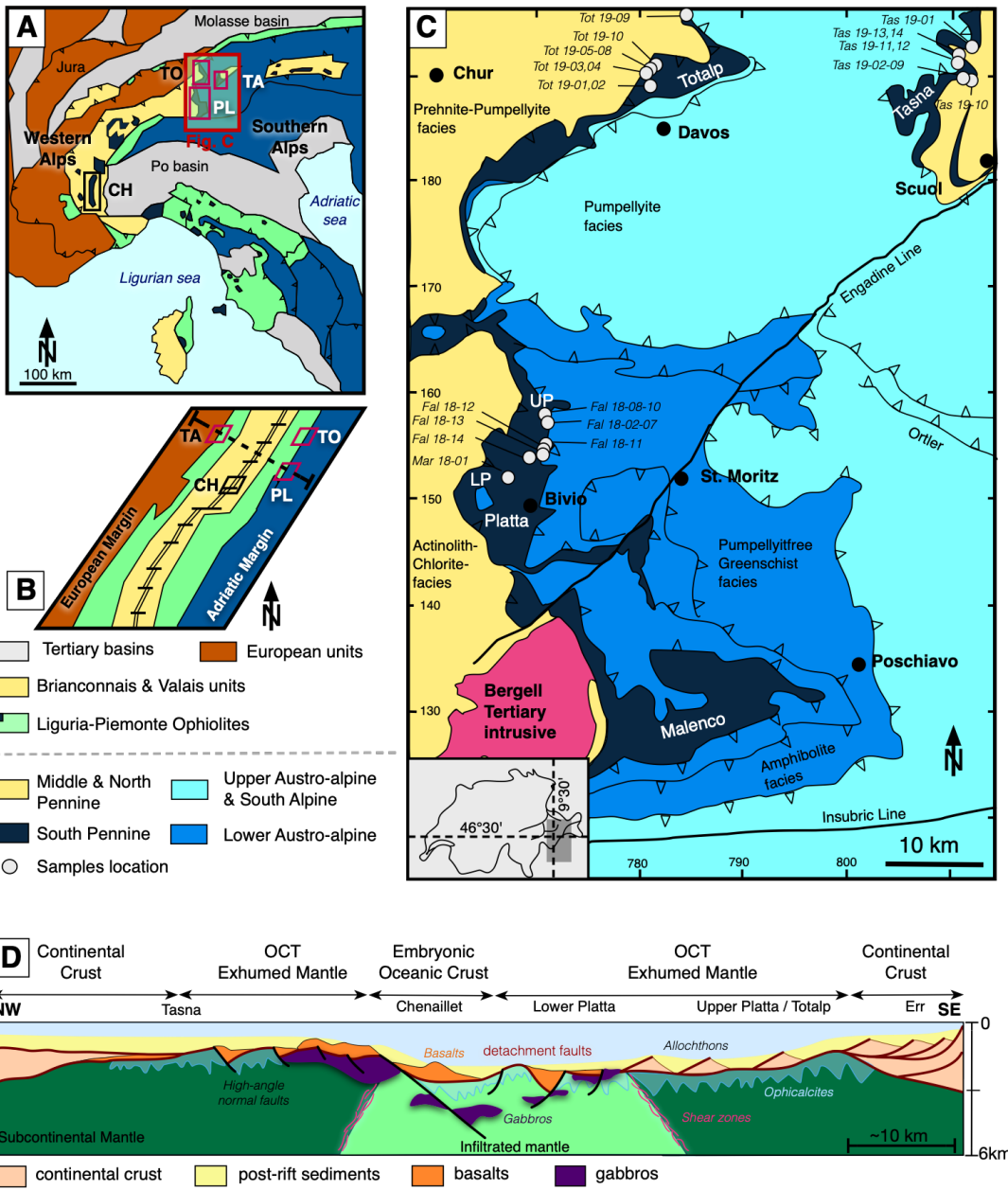


FIGURE 4.1 – A) Present-day location of ophiolitic massifs of the Central-Western Ligurian Alps, modified after Manatschal and Müntener 2009. B) Schematic paleo-reconstruction of the Piemonte-Ligurian oceanic basin at Late Jurassic time, with location of the major ophiolitic sequences, modified after Manatschal and Müntener 2009. C) Simplified geological map of the Penninic and Austro Alpine Nappes, modified after Froitzheim 1994, including samples location. D) Distribution of subcontinental and infiltrated mantle, along an ocean-continent-transition of the Alpine Tethys, modified after Müntener and Piccardo 2004. TO : Totalp ; TA : Tasna ; PL : Platta

4.3 Materials and methods

4.3.1 Sampling and analytical strategies

A total of 43 samples, including partially serpentinitized peridotites and serpentinites have been sampled, of which 13 are included in this study. The sampling was done with the aim to characterize fluid-rock interactions at different positions along the OCT, i.e., continentwards/proximal (Upper Platta, Tasna and Totalp) vs. oceanwards/distal (Lower Platta). All samples were characterized by i) X-ray diffraction, to identify minerals and their respective proportions in serpentinites; ii) Raman spectroscopy, to identify serpentine species, iii) major and trace element concentrations of each mineral species to assess chemical mobilities during serpentinitization and associated mass fluxes along the margin.

4.3.2 X-Ray Diffraction

XRD analyses were performed on sample powders using a Bruker D8 advance Eco diffractometer at the Institut Terre et Environnement de Strasbourg (ITES, University of Strasbourg). A large X-ray beam was emitted by a copper source with a 40 kV accelerating voltage and a 25 mA current. Intensities were recorded at $0.014^\circ 2\theta$ step intervals from 3 to $80^\circ 2\theta$, with a dwell time of 0.8 s. Size of the divergence slit was 0.4° . Table 4.3.4 provides the quantitative mineralogical compositions determined by Rietveld refinement using Profex-BGMN software (Doebelin and Kleeberg 2015), as well as the list of the reference structures used for refinement. The diffraction patterns and their respective fits are given in supplementary materials.

4.3.3 Raman spectroscopy

The raman spectra were acquired on $30 \mu\text{m}$ thick polished thin sections, using a HORIBA LabRAM ARAMIS spectrometer at the Laboratoire des sciences de l'ingénieur, de l'informatique et de l'imagerie (ICube, University of Strasbourg). We used an argon laser with a wavelength of 632 nm and an output laser power of 100 mW. Measurements were performed using an Olympus lens of 100X to focus the laser beam onto an area of $\sim 1 \mu\text{m}$ in diameter. All analyses were performed on $30 \mu\text{m}$ polished thin section using an integrating time of 30 s to optimize the signal/noise ratio. Raman spectra were recorded in two wavelength intervals : $100\text{-}1120 \text{ cm}^{-1}$ for structural bon-

ding characterization and 3500–3750 cm⁻¹ for the characterization of hydroxyl bonds. The serpentine species were identified by comparison with reference spectra taken from the literature, in particular on the stretching range of the OH groups (e.g., Auzende et al. 2004; Lemaire 2000).

4.3.4 Mineral chemistry

Typical major and trace element concentrations of serpentine minerals are presented in Table 4.3.4 (the complete dataset is available online in supplementary material). The major element concentrations were measured on 30 μ m thick polished thin sections using a micro X-Ray fluorescence Brucker M4 Tornado at ITES. The instrument is equipped with a Rh anode operating at 400 μ A with an acceleration voltage of 50 kV. Polycapillary lenses were used to focus the X-ray beam down to 20 μ m full-width-at-half-maximum at the sample surface. Two energy-dispersive silicon drift detectors of 125 eV resolution, and with an active area of 60 mm² each were used to measure fluorescence spectra (180 s counting time per point). Measurements were performed in a vacuum chamber at 2 mbar to minimize air absorption and ensure the best signal/noise ratio even for the lightest elements. Micro-XRF spectra were calibrated after repeated analyses of Smithsonian mineral standards Jarosewich 2002 of diopside (NMNH 117733) and San Carlos olivine (NMNH 111312-44), and in-house mineral standards of clinochlore, chrysotile and antigorite. Total Fe content was calculated on a divalent basis, as FeO.

TABLE 4.1 – Description of the 11 samples of serpentinized peridotite selected for detailed mineralogical and geochemical investigations. Mineral phases are detected by X-ray diffraction on powder, and their proportion (%) are estimated by the Rietveld refinement method of Doebelin and Kleeburg 2015 using Profex-BGMIN software. PM : pseudomorphic textures; b : banded ; f : fibrous ; g : granular ; l : lamellar ; s : spherical ; 1 : granular ; LA : laser ablation.

Site	Sample	Type	Srp	Mgt	Cc	And	Tr	Di	Fo	PM	textures	Serp. veins	Atg	Methodology
Totalp	Tot 19-02	Foliated	91.1	-	2.3	-	6.8	<1	X	b, s		XRD, Raman, μ XRF, LA		
	Tot 19-03a	Fibrous	92.7	-	3.2	-	3.7	-	X	b		XRD, Raman, μ XRF, LA		
LP	Fal 18-11	Massive	99.3	<1	-	-	-	-	X	b, f		XRD, Raman, μ XRF		
	Fal 18-13	Massive	99.5	<1	<1	-	-	-	X	b, f		XRD, Raman, μ XRF		
	Mar 18-01	Massive	98.8	1.2	<1	-	-	-	X	b, l, f	X	XRD, Raman, μ XRF		
UP	Fal 18-02	Massive + fib.	97.6	2.1	<1	-	-	-	X	b, g, s		XRD, Raman, μ XRF, LA		
	Fal 18-03	Massive	99.6	<1	<1	-	-	-	X	b, g, l, s		XRD, Raman, μ XRF, LA		
	Fal 18-06	Massive	95.0	5	<1	-	-	-	X	l, f	X	XRD, Raman, μ XRF, LA		
Tasna	Tas 19-02	Foliated	98.7	<1	<1	-	<1	-	X	b, g, f	X	XRD, Raman, μ XRF, LA		
	Tas 19-03	Massive	98.2	<1	<1	-	<1	-	X	b, g, f, s		XRD, Raman, μ XRF, LA		
	Tas 19-04	Fibrous	94.1	<1	<1	<1	1.2	3.3	-	b, g, l	X	XRD, Raman, μ XRF, LA		
	Tas 19-05	Massive	99.6	<1	-	-	-	-	X	1	X	XRD, Raman, μ XRF, LA		
	Tas 19-10	Massive + fib.	98.5	<1	-	-	1.1	-	X	b		XRD, Raman, μ XRF, LA		

Structural serpentine formulae for lizardite, chrysotile, polygonal and polyhedral serpentines were calculated based on 7 oxygens. Antigorite has a distinct formulae $Mg_{3m-3}Si_{2m}O_{5m}(OH)_{4m-6}$ that slightly differs from the idealized serpentine formulae ($Mg_3SiO_5(OH)_4$), where m is the number of tetrahedra along an entire wavelength of the crystalline structure. Here, structural formulae for antigorite was calculated based on $m = 17$ Mellini et al. 1987. The Fe^{2+} and Fe^{3+} contents of serpentine mineral were calculated following the approach of Ulrich et al. 2020 on the basis of the initial study of Beard and Frost 2017. The calculations assume a full dioctahedral substitution, i.e., ferric iron is accommodated in the serpentine by substitution for divalent cation plus the addition of a vacancy in the octahedral sheet.

Serpentine trace element compositions were acquired on a High-Resolution Laser Ablation Inductively Coupled Plasma Mass spectrometer (HR-LA-ICP-MS) Thermo-Finnigan Element 2 instrument coupled with a 193 nm Geolas laser at Géosciences Montpellier (France). Laser ablations were performed with an energy density of 12 Jcm² at a frequency of 6 Hz. At first time, a few laser pulses with a spot size of 130 μ m were used to clean up the sample surface. Then each acquisition was perform with a total of 240 pulses with a spot size of 110 μ m,sufficient to obtain a long and stable signal for integration. The ablated material is transported using a constant He flow and mixed with Ar in a cyclone coaxial mixer before entering the ICP torch and being ionized. The ions are then sampled, accelerated and focused before being separated and analyzed in the mass spectrometer. ^{29}Si content known from prior μ -XRF analyses were used as internal standard and concentrations were calibrated against the NIST 612 rhyolitic glass using reference values from Pearce et al. 1997. The reference basalt glass BIR-1G was analyzed repeatedly each 5 samples to ensure repeatability and accuracy of the measurements (available in supplementary files). Data reduction was operated with Matlab-based SILLS program Guillong et al. 2008, following the standard methods of Longerich et al. 1996. Detection limits were between 80 ppb and <1 ppm for most trace elements.

4.4 Results

4.4.1 Petrography and micro-textures of serpentinites

The samples analyzed in this study include mostly spinel-lherzolites (all localities) and plagioclase-lherzolites (Lower Platta unit). The degree of serpentinization based on macroscopic and microscopic observations and Rietveld refinements (Table 4.3.4) ranges between 60 and 100%. Most serpentinites from the Platta nappe are characterized by a dark green color (Massive serpentinite; Figure 4.2A); sometimes crosscut by a fibrous green pale serpentine (Figure 2B). At Tasna and Totalp, massive serpentinization is surrounded by a later foliated serpentinite characterized by a light blueish color and a fibrous aspect (Figure 4.2C, D, E). With exception of the Lower Platta serpentinites, the occurrence of fibrous serpentine veins are commonly observed crosscutting the massive serpentinization (Figure 4.2B). These veins display a typical light-green color and can reach up to 1 cm thickness. It should be noticed that some serpentinite samples integrate minor amount of calcite (< 1%, Table 4.3.4), consistently with the occurrence of carbonate veins observed in the field (Figure 4.2F). This carbonation is common in the uppermost few meters of the exhumed mantle and tightly linked to the detachment fault capping the exhumed mantle (e.g., Picazo et al. 2013).

Serpentine mesh and bastite textures S1

The first serpentinization event is recorded by the pseudomorphic replacement of olivine and pyroxenes by serpentine mesh and bastite textures, respectively (Figure 4.3A, B), although some relics of primary minerals, especially clinopyroxene and to a lesser extent olivine, can be occasionally preserved, especially in samples from Totalp. This first serpentinization event constitutes the bulk of serpentinization in most samples and corresponds to lizardite, as shown by the typical OH stretching bands at 3685 cm^{-1} and 3707 cm^{-1} on Raman spectra (Figure 4.3A, B). In all these samples, magnetite is ubiquitous, although the amount is highly variable (<1 to 2.1% Table 4.3.4). It mainly occurs as small grains disseminated along the mesh rims but is also observed in cleavages and around bastite grains (Figure 4.3B).

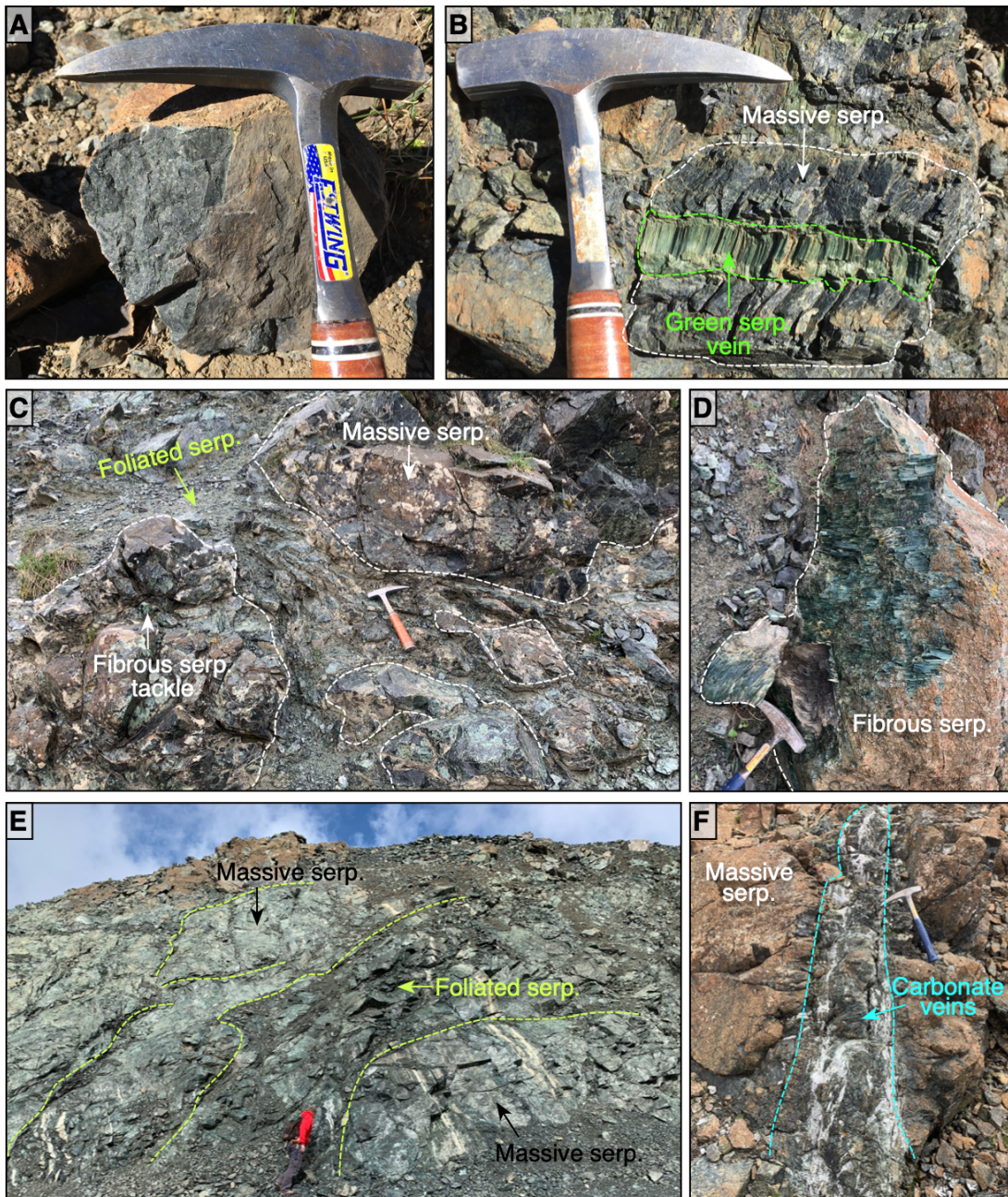


FIGURE 4.2 – A) Massive dark green serpentinite from UP (Fal18-03). B) Massive serpentinite with a dark green color, crosscut by a fibrous serpentine vein of pale green color from UP. C) Massive dark green serpentinite from Tasna (Tas19-03) surrounded by a foliated pale green fibrous serpentinite. D) Fibrous pale green serpentinite (Tas 19-07). E) Totalp outcrop near Weissfluhjoch, the massive serpentinite is surrounded by a later foliated serpentinite (Tot19-02), similar to Tasna. F) Massive serpentinite crosscut by later carbonates (Tot19-07, 08).

Serpentine veins

In most samples, several generations of serpentine veins crosscut the background mesh and bastite textures S1. We identified four main generations of veins based on the observation of serpentine micro-textures and Raman spectroscopy, and the following chronology was established :

Spherical serpentine S2

The second generation of serpentine forms a typical spherical texture that is characterized in microscopic view in crossed-polarized light by an extinction cross roughly parallel to polarizer (Figure 4.3C, D). Such spherical texture and the Raman signature (Figure 4.3C) are robust features in favor of a polyhedral serpentine. This serpentine species occurs in a few of our samples, either in pyroxenes cleavages (Figure 4.3C) or as veins crosscutting the previous serpentine mesh and bastite S1 (Figure 4.3D) and it is visible in few samples (Table 4.3.4). It is worth noting that the occurrence of small hydro-garnet grains ($\pm 10 \mu\text{m}$ diameter, identified as andradite in XRD patterns) has been systematically reported closely associated with the polyhedral serpentine (Figure 4.3C, D).

Banded veins S3

The third generation of serpentine (S3, Figure 4.3D), which has been reported in most of our samples consists of tens of μm to cm width veins made of finely spaced bands of a low birefringence that alternate between white and black color under the cross-polarized light (Figure 4.3D, E, F). All bands are parallel to each others and mimic the irregular shape of the vein margins, thus preserving the initial geometry of the fracture along the vein width. The Raman spectra show that the nature of serpentine minerals filling these banded veins are not homogeneous. Although recent studies have shown the distinction between lizardite and polygonal serpentine, is not obvious using Raman spectroscopy (Tarling et al. 2018, Compagnoni et al. 2021), we assume that most of the banded veins exhibiting the typical OH stretching bands at 3685 cm^{-1} and 3707 cm^{-1} are filled by lizardite. Other spectra showing two characteristic peaks at 3692 cm^{-1} and 3700 cm^{-1} (Figure 4.3E) may rather correspond to polygonal serpentine, while only rare occurrences of chrysotile are observed (i.e., main peaks at 3689 cm^{-1} and 3699 cm^{-1}).

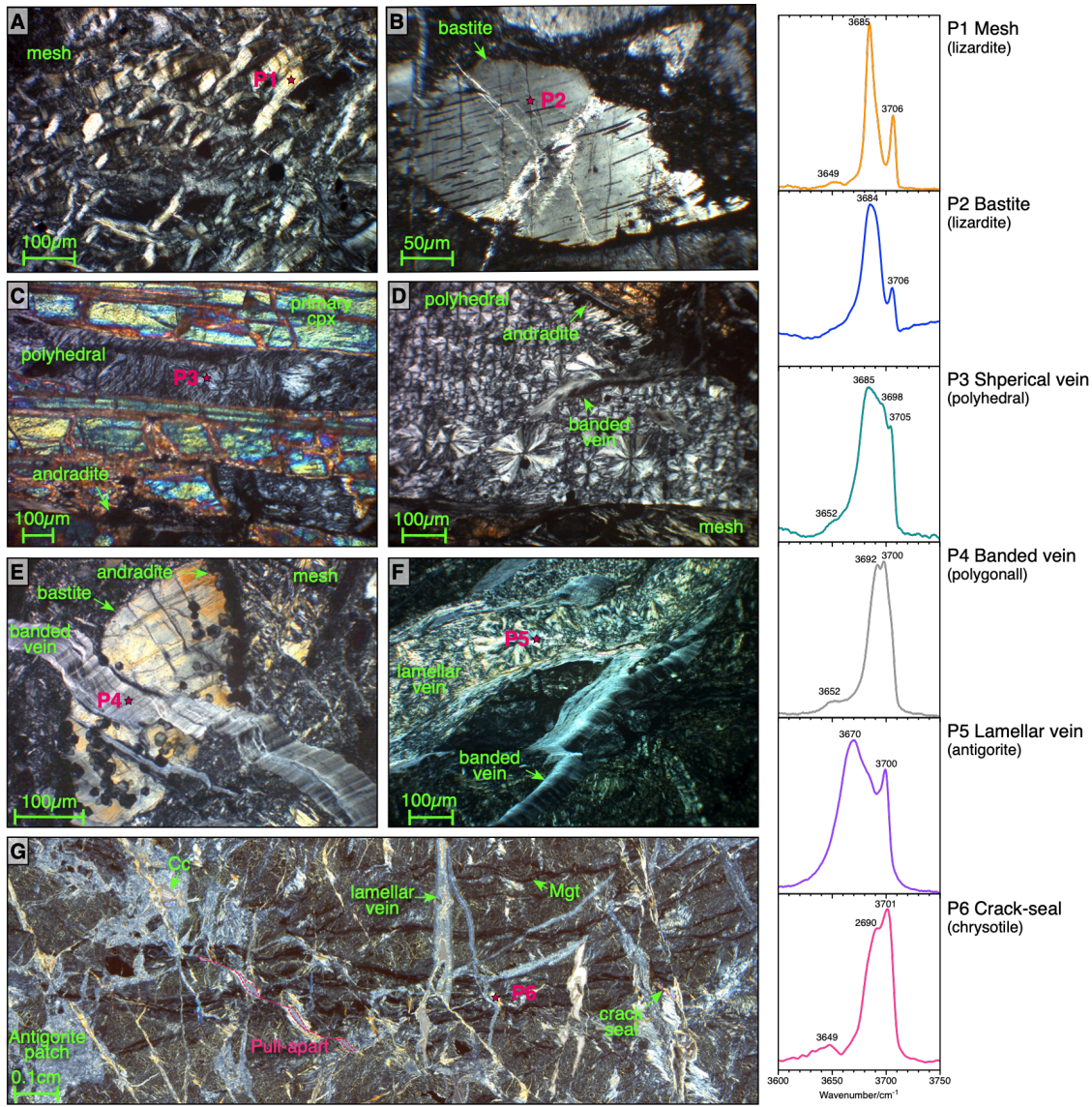


FIGURE 4.3 – Representative photography of serpentine textures at microscopic scale (cross-polarized light) and associated raman spectra. A) Mesh texture S1 made of lizardite. B) Bastite texture S1 made of lizardite. C) Polyhedral serpentine S2 in clinopyroxene cleavage. D) Polyhedral serpentine and andradite at rims of bastite, cut by a banded vein. E) Banded vein made of polygonal serpentine crosscut the previous bastite and mesh S1. F) Lamellar veins of antigorite S4 crosscut the previous mesh S1 and banded vein S3. G) Serpentine mesh S1 crosscut by lamellar veins S4, antigorite patches S4 and crack-seals of chrysotile S5.

Lamellar veins S4

The fourth generation of serpentine (S4) consist of disoriented serpentine lamellae displaying a first order grey to yellow birefringence under the cross-polarized light. These veins are typically in the range of 50-15 μm thick (Figure 4.3F, G). The Raman spectral signature indicates that these lamellar veins are made of antigorite, with typical peaks at 3670 cm^{-1} and 3700 cm^{-1} (Figure 4.3F). Occasionally, additional peaks at 3685 cm^{-1} suggest the local occurrence of small lizardite grains disseminated in these veins.

Fibrous veins S5

The last generation of serpentine (S5) are commonly observed in most of our samples. It forms crack-seal characterized by lens-shape extending along several mm-long and tens of μm width (Figure 4.3G, H). They have a typical fibrous aspect, and the serpentine fibers are preferentially oriented perpendicular to the vein edge and are characterized by a high birefringence under cross-polarized light. The characteristic shoulder at 3690 cm^{-1} preceding a peak at 3701 cm^{-1} matches the Raman spectral signature of chrysotile in high wavelength domain (Figure 4.3G).

4.4.2 Serpentine chemistry

In situ major and trace element concentrations were measured on a comprehensive set of serpentine species, including pseudomorphic textures (mesh and bastite) and serpentine-filling veins. Some representative compositions are presented in Table 4.4.2, and the bulk dataset is available in supplementary materials.

Major elements

In average, serpentine mesh contains 40.97 wt% SiO_2 ($\text{Si}=1.94 \text{ apfu}$), 38.92 wt% MgO ($\text{Mg} = 2.75 \text{ apfu}$), 5.06 wt% FeO ($\text{FeT} = 0.20 \text{ apfu}$), 1.40 wt% Al_2O_3 ($\text{Al} = 0.08 \text{ apfu}$). Comparatively, bastite texture are less enriched in SiO_2 39.40 wt% ($\text{Si} = 1.9 \text{ apfu}$), MgO 37.69 wt% ($\text{Mg} = 2.7 \text{ apfu}$) and FeO 4.33 wt% ($\text{FeT} = 0.17 \text{ apfu}$) but contains more Al_2O_3 4.53 wt% ($\text{Al} = 0.26 \text{ apfu}$) because they retain part of Al from pyroxene (Table 4.4.2). Consequently, serpentine mesh plot close to the Mg-pure lizardite/chrysotile end member in Si versus Mg+Fe diagram (Figure 4A), whereas serpentine bastite composition extends along the Tschermak's trend (Al replacing an

octahedral and tetrahedral cation ; Figure 4A, B). Serpentine bastite have in average slightly higher Mg# than mesh textures (Figure 4.4C).

The polyhedral serpentine S2 is generally characterized by lower FeO content (4.09 wt%, FeT = 0.16 apfu), while SiO₂ and MgO concentrations are similar relative to serpentine mesh (S1 ; Figure 4A). The polyhedral serpentine is also characterized by relatively high Al₂O₃ concentrations (2.89 wt%, Al = 0.16 apfu) and thus plot along the Tschermak's trend between mesh and bastite serpentines (Figure 4.4B) is worth noting. When occurring in clinopyroxene cleavages, polyhedral serpentine can integrate significant 0.56 wt% CaO (Ca = 0.03 apfu, Table 4.4.2). The polyhedral serpentine has Mg# values higher than 94 % in average (Figure 4.4C).

The banded veins S3 have similar SiO₂ and Al₂O₃ concentrations than previous serpentine S1 and S2 (Figure 4.4A, B). Similarly to that observed for S2 serpentine, the third generation of serpentine (i.e., banded veins S3), is characterized by a depletion in Fe relative to the mesh serpentine S1 (0.11 vs. 0.20 apfu, respectively, Table 4.4.2) and an higher Mg# (Figure 4.4C). More specifically, the banded veins can be subdivided into two groups based on their Mg and Fe contents (Figure 4.5) : a first group made of polygonal serpentine and characterized by a total iron content FeT = 0.15 apfu and Mg < 2.8 apfu in average and a second group made of lizardite serpentine characterized by FeT < 0.10 apfu and Mg > 2.7 apfu in average (Figure 4.5).

The serpentine S4 (i.e., lamellar veins) contains generally more SiO₂ (42.70 wt%, Si = 2.00 apfu), FeO (4.12 wt%, FeT = 0.16 apfu) and lower MgO (38.91 wt%, Mg = 2.72 apfu) and Al₂O₃ (0.94 wt%, Al = 0.05 apfu). Consequently, in the Si versus Mg + Fe diagram (Figure 4.4A) they plot close to the pure antigorite end member. Also, they are slightly staggered to the right of the Tschermak's substitution trend in the Si versus Al diagram (Figure 4.4B).

The chrysotile crack-seal S5 have higher MgO and Al₂O₃, and lower FeO concentrations than previous lamellar veins S4, with in average 42.43 wt% SiO₂ (Si = 1.99 apfu), 38.91 wt% MgO (Mg = 2.77), 1.17 wt% Al₂O₃ (Al = 0.06 apfu). Consequently in the Mg + Fe versus Si diagram (Figure 4.4A) and in the Al versus Si diagram (Figure 4.4B) they plot in the range of the previous serpentine. They have in average 0.96 Mg# (Figure 4.4C).

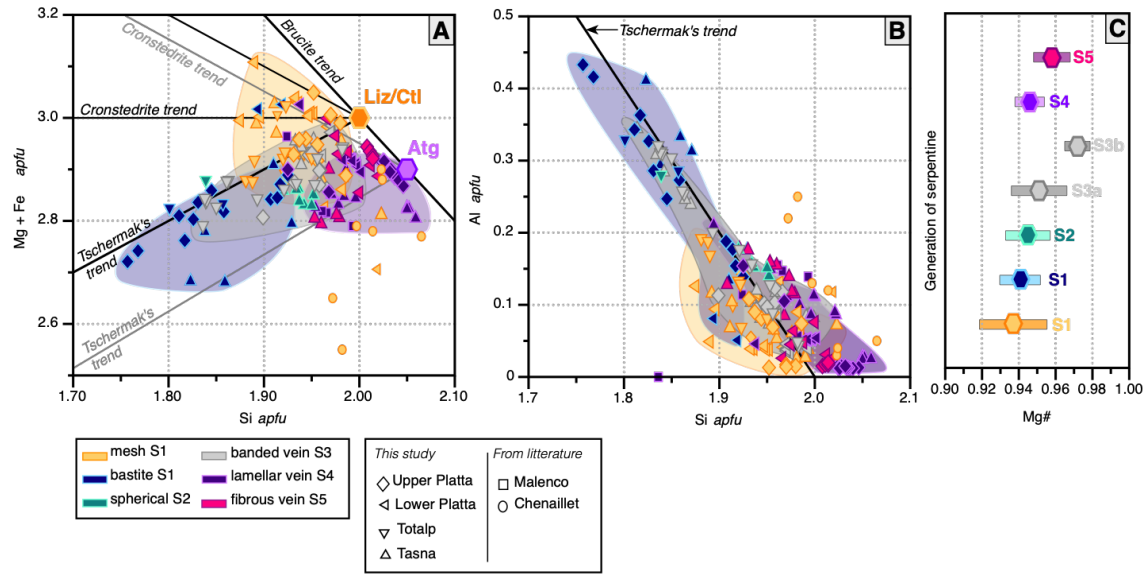


FIGURE 4.4 – A) Plot of $Mg + Fe$ versus Si diagram in cations per formula unit. B) Al versus Si . C) Serpentine generation versus Mg numbers. All cations are given in per formula units and are calculated on the basis of 7 oxygen atoms in the serpentine formula. Antigorite were calculated based on 6.823 oxygens and then converted to 7 oxygens for comparison with other serpentine species. In C), colored rectangles represent the variability of $Mg\#$ values. Lz/Ctl : pure Mg lizardite/chrysotile end-member. Atg : pure Mg antigorite end-member. Data of Chenaillet serpentinites are from Schwartz et al. 2013 and those of Malenco antigorite are from Liu et al. 2020.

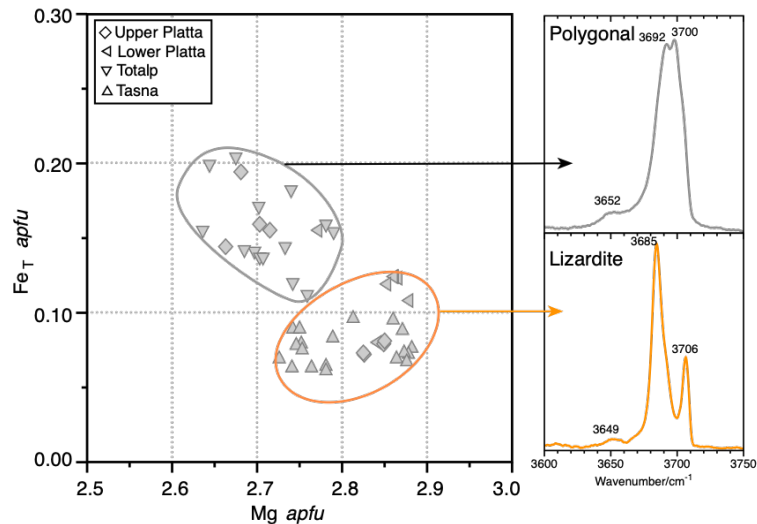


FIGURE 4.5 – Fe_T versus Mg apfu diagram of banded veins serpentine S3 and their respective Raman spectra. Two populations are distinguished, the banded veins made of polygonal serpentine in grey, and those made of lizardite in orange.

TABLE 4.2 – Representative major element concentrations of serpentine minerals measured by μ XRF.

Location	LP						UP			
Sample	MAR18-01 mesh (S1)	MAR18-01 lizardite	Mar18-01 banded vein (S3)	Mar18-01 lizardite	Mar18-01 antigorite	Fal18-11 lamellar vein (S4)	Fal18-11 chrysotile	Fal18-06 mesh (S1)	Fal18-02 lizardite	Fal18-03 banded vein (S3)
Type	ol	opx	-	-	-	-	ol	opx	-	
Primary minerals										
SiO ₂	40.5	40.1	42.1	42.3	43.4	41.5	39.4	41.24		
TiO ₂	0.035	0.035	0.035	0.028	0.015	0.028	0.088	0.66		
Al ₂ O ₃	1.34	1.18	0.665	0.965	0.496	0.265	4.70	2.12		
FeO	5.02	5.00	3.06	4.26	2.37	5.14	3.91	4.01		
MnO	0.155	0.135	0.120	0.272	0.099	0.125	0.090	0.200		
MgO	39.6	39.9	41.1	38.9	40.3	39.8	38.1	38.4		
CaO	0.063	0.055	0.065	0.064	0.465	0.088	0.175	0.607		
K ₂ O	-	-	-	-	b.d.l.	-	-	-		
Na ₂ O	-	-	-	-	b.d.l.	-	-	-		
Cr ₂ O ₃	0.483	0.905	0.073	0.049	0.042	0.090	0.786	0.143		
NiO	0.195	0.135	0.025	0.079	0.075	0.323	0.058	0.020		
H ₂ O	12.6	12.6	12.8	13.0	12.9	12.6	12.7	12.7		
Total	87.4	87.5	87.2	86.9	87.2	87.4	87.3	87.4		
Number of oxygen	7	7	7	6.82	7.00	7	7	7		
<i>a.p.f.u</i>										
Si	1.92	1.91	1.97	1.95	2.02	1.97	1.86	1.94		
Ti	0.001	0.001	0.001	0.001	0.001	0.001	0.003	0.024		
Al	0.075	0.066	0.037	0.051	0.027	0.015	0.261	0.118		
2+	0.189	0.162	0.120	0.174	0.071	0.180	0.154	0.105		
3+	0.009	0.034	0.000	0.000	0.020	0.022	0.000	0.048		
Mn	0.006	0.006	0.005	0.012	0.004	0.005	0.004	0.008		
Mg	2.80	2.83	2.87	2.66	2.80	2.81	2.68	2.69		
Ca	0.003	0.003	0.003	0.002	0.023	0.004	0.009	0.031		
K	-	-	-	-	-	-	-	-		
Na	-	-	-	-	-	-	-	-		
Cr	0.019	0.034	0.003	0.000	0.002	0.003	0.029	0.005		
Ni	0.008	0.006	0.001	0.001	0.003	0.012	0.002	0.001		
Mg#	0.937	0.946	0.960	0.939	0.975	0.940	0.946	0.963		
Fe ³⁺ /Fe _T	0.045	0.174	0.000	0.000	0.217	0.107	0.000	0.314		

Location		Totalp			Tasna			
Sample	Fal 18-06	Tot 19-02	Tot 19-02	Tot 19-02	Tas 19-02	Tas 19-03	Tas 19-02	
Texture	lamellar vein (S4)	mesh (S1)	bastite (S1)	spherical vein (S2)	mesh (S1)	bastite (S1)	lamellar vein (S4)	
Type	antigorite	lizardite	lizardite	polyhedral	lizardite	lizardite	antigorite	
Primary minerals	-	ol	cpx	-	ol	cpx	-	
SiO ₂	42.9	40.6	38.7	40.7	42.1	40.7	43.3	
TiO ₂	0.026	0.027	0.090	0.030	0.245	0.100	0.054	
Al ₂ O ₃	0.233	1.98	5.52	3.53	0.640	2.79	0.974	
FeO	4.57	4.90	4.64	2.79	4.02	4.14	3.46	
MnO	0.206	0.117	0.110	0.093	0.155	0.105	0.133	
MgO	38.9	39.2	37.5	39.6	39.4	38.2	38.4	
CaO	0.063	0.147	0.535	0.443	0.565	0.845	0.431	
K ₂ O	-	-	-	-	-	-	-	
Na ₂ O	-	-	-	-	-	-	-	
Cr ₂ O ₃	0.031	0.027	0.210	0.017	0.070	0.355	0.051	
NiO	0.083	0.427	0.090	-	0.150	0.060	0.097	
H ₂ O	13.0	12.6	12.6	12.8	12.7	12.7	13.1	
Total	87.0	87.4	87.3	87.2	87.3	87.3	86.9	
Number of oxygen a.p.f.u	6.82	7	7	7	7	7	6.82	
Si	1.98	1.92	1.83	1.90	1.98	1.92	1.98	
Ti	0.001	0.001	0.003	0.001	0.009	0.004	0.002	
Al	0.013	0.110	0.308	0.195	0.036	0.155	0.053	
Fe ²⁺	0.164	0.194	0.184	0.109	0.110	0.162	0.116	
Fe ³⁺	0.011	0.000	0.000	0.000	0.044	0.001	0.015	
Mn	0.008	0.005	0.005	0.003	0.006	0.004	0.005	
Mg	2.68	2.77	2.65	2.76	2.77	2.69	2.62	
Ca	0.003	0.007	0.027	0.022	0.029	0.043	0.021	
K	-	-	-	-	-	-	-	
Na	-	-	-	-	-	-	-	
Cr	0.001	0.001	0.008	0.001	0.003	0.014	0.002	
Ni	0.003	0.016	0.001	0.000	0.006	0.002	0.004	
Mg#	0.942	0.934	0.935	0.962	0.962	0.943	0.958	
Fe ³⁺ /Fer	0.053	0.000	0.000	0.000	0.286	0.006	0.117	

Trace elements

The Representative rare earth elements (REE) concentrations normalized to C1-Chondrite Anders and Grevesse 1989 of serpentine minerals and veins depending on their localities are illustrated in (Figure 4.6, 4.7). Normalized compositions for most type of serpentine generation are in the range of 0.001 and 10 times Chondrite values and mimic patterns of the bulk-rock (Table 4.3, Supplementary Figure 4.12). Most serpentine displays Depleted MORB Mantle (DMM) like patterns, characterized by a relatively flat Middle Rare Earth Elements (MREE) to Heavy Rare Earth Elements (HREE) with a depletion in Light Rare Earth Elements (LREE) characterized by low $(\text{La}/\text{Sm})_N$ ratios (0.27 in average, Table 4.3 ; Figure 4.6). Two samples from the Lower and Upper Platta units display U-shaped REE patterns characterized by enrichment of the LREE and HREE over the MREE, with $(\text{La}/\text{Sm})_N$ ratios of 0.86 and 4.99 in average, respectively (Table 4.3) and strong positive Eu anomalies ($\text{Eu}/\text{Eu}^* = 2.18$ and 2.83, respectively, Table 4.3; Figure 4.7). At Totalp, serpentine bastite S1 have REE patterns that mimic those of their pyroxene precursors, either clinopyroxene or orthopyroxene (Figure 4.7).

Primitive Mantle (PM-)normalized trace element spider-diagrams show that serpentine minerals and veins have similar patterns with depleted concentrations relative to PM McDonough and Sun 1995. More specifically, serpentine veins (S2-S5) are more depleted in trace elements relative to lizardite mesh S1 (Figure 4.6, 4.7). All serpentines are generally enriched in fluid-mobile elements (FME : Li, B, Cs, As) with concentrations ranging between 1 and > 100 time PM (Table 4.3 ; Figure 4.6, 4.7). In addition, a general positive U anomaly and strong negative Pb anomaly are observed ($(\text{Ce}/\text{Pb})_N = 11.66$ in average, Table 4.3). All serpentine types, whatever their generation or location, are strongly enriched in B in comparison with primary minerals (Figure 4.11A).

TABLE 4.3 – Representative trace element concentrations of serpentine minerals measured by HR-LA-ICP-MS.

Location	LP				UP			
Sample	MAR18-01 mesh (S1)	MAR18-01 bastite (S1)	Mar18-01 banded vein (S3)	Mar18-01 lizardite	Mar18-01 lamellar vein (S4) antigorite	Fal18-06 mesh (S1)	Fal18-06 bastite (S1)	Fal18-06 lizardite (S4) antigorite
Texture	lizardite	lizardite	banded vein (S3)	-	-	lizardite	lizardite	-
Type	ol	opx				ol	opx	
Primary minerals								
Li	3.98	2.71	4.96	2.54	2.85	13.8	11.2	
B	43.6	30.9	34.9	37.3	48.3	36.6	94.5	
V	17.2	85.5	17.3	29.3	5.89	76.8	10.2	
Cr	554	4809	358	38.2	136	3465	2.12	
Co	73.6	52.5	9.36	11.0	111	14.6	6.68	
Ni	1977	1053	188	224	2951	1019	210	
Zn	59.1	65.9	52.2	69.0	19.2	24.3	19.0	
As	1.67	1.06	0.103	0.219	2.85	0.147	1.33	
Rb	0.748	0.379	0.556	1.35	0.101	0.178	1.51	
Sr	4.10	3.09	2.88	2.05	1.99	5.39	1.25	
Y	0.281	0.176	0.200	0.110	0.374	2.00	0.136	
Zr	0.116	0.086	0.125	0.244	0.107	3.95	0.066	
Nb	0.101	0.094	0.069	0.038	0.018	0.033	0.010	
Cs	0.549	0.329	0.464	1.38	0.276	0.545	5.00	
Ba	1.22	0.863	0.738	0.545	0.812	3.47	0.589	
La	0.299	0.155	0.151	0.071	0.064	0.057	0.041	
Ce	0.397	0.308	0.293	0.153	0.197	0.252	0.144	
Pr	0.039	0.025	0.029	0.015	0.031	0.040	0.021	
Nd	0.136	0.087	0.110	0.045	0.149	0.233	0.116	
Sm	0.029	0.026	0.010	0.011	0.042	0.115	0.028	
Eu	0.088	0.050	0.054	0.033	0.062	0.054	0.039	
Gd	0.032	0.019	0.019	0.009	0.065	0.226	0.031	
Tb	0.004	0.003	0.004	0.002	0.008	0.049	0.004	
Dy	0.034	0.019	0.021	0.018	0.055	0.354	0.016	
Ho	0.007	0.005	0.005	0.003	0.010	0.080	0.004	
Er	0.021	0.009	0.013	0.006	0.029	0.251	0.014	
Tm	0.003	0.003	0.003	0.001	0.003	0.037	0.001	
Yb	0.037	0.022	0.018	0.013	0.022	0.298	0.008	
Lu	0.007	0.004	0.004	0.002	0.004	0.049	0.001	
Hf	0.00	<0.002	0.003	0.003	<0.003	0.145	<0.003	
Ta	0.002	0.001	0.002	0.002	<0.001	0.003	<0.001	
Pb	0.520	0.165	0.010	0.011	0.261	0.019	<0.002	
Th	0.000	0.001	0.002	0.001	0.000	0.007	0.000	
U	0.001	0.000	0.001	0.003	0.001	0.002	<0.001	
(La/Sm) _N	6.39	3.68	9.17	4.11	0.960	0.310	0.90	
(Ce/Pb) _N	0.762	1.86	29.9	13.4	0.754	13.6		
Eu/Eu*								
U/Pb	0.001	0.002	0.060	0.237	0.004	0.118		
	10.3	10.0	9.82	13.4	10.1	21.4	8.70	

Location	Totalp			Tasna		
	Tot 19-02 mesh (S1) lizardite ol	Tot 19-02 bastite (S1) lizardite cpx	Tot 19-02 spherical vein (S2) polyhedral -	Tas 19-02 mesh (S1) lizardite ol	Tas 19-03 bastite (S1) lizardite cpx	Tas 19-02 lamellar vein (S4) antigorite -
Li	0.213	1.51	0.287	7.33	26.9	6.13
B	19.4	24.4	13.3	25.1	52.7	23.7
V	6.56	72.0	3.34	112	129	18.2
Cr	8.76	2303	4.45	2665	4054	44.0
Co	162	39.6	1.00	57.0	53.0	35.9
Ni	2987	785	1.71	1663	909	1222
Zn	22.0	33.6	6.93	26.8	35.0	24.2
As	n.d	0.045	<0.06	0.093	0.063	<0.05
Rb	0.069	0.054	0.026	0.508	1.61	1.48
Sr	1.90	6.90	0.315	3.29	2.16	1.56
Y	0.433	1.06	0.007	1.36	1.28	0.851
Zr	0.531	1.32	<0.03	0.253	0.770	0.374
Nb	0.001	0.005	<0.0014	0.016	0.010	0.011
Cs	n.d	<0.004	<0.004	1.11	1.40	4.29
Ba	0.099	0.218	0.036	0.992	0.364	0.914
La	0.008	0.014	<0.001	0.031	0.002	0.019
Ce	0.056	0.108	0.004	0.078	0.018	0.066
Pr	0.013	0.027	0.001	0.012	0.010	0.010
Nd	0.065	0.169	0.004	0.097	0.074	0.062
Sm	0.028	0.058	<0.006	0.049	0.060	0.032
Eu	0.008	0.014	0.001	0.020	0.039	0.017
Gd	0.045	0.118	<0.007	0.111	0.119	0.100
Tb	0.010	0.019	0.001	0.031	0.028	0.016
Dy	0.059	0.150	<0.004	0.232	0.195	0.129
Ho	0.015	0.036	<0.0004	0.057	0.048	0.032
Er	0.045	0.118	0.001	0.186	0.135	0.104
Tm	0.009	0.022	0.000	0.025	0.028	0.018
Yb	0.062	0.208	0.002	0.194	0.213	0.103
Lu	0.012	0.038	<0.0008	0.029	0.035	0.020
Hf	0.023	0.053	0.003	0.033	0.052	0.033
Ta	n.d	<0.0003	<0.002	<0.001	<0.0006	<0.0008
Pb	0.142	0.005	0.014	0.071	0.051	0.006
Th	0.000	0.000	<0.0003	0.000	0.000	0.001
U	0.002	0.000	<0.0002	0.004	0.000	0.009
(La/Sm)N	0.170	0.150	-	0.390	0.020	0.370
(Ce/Pb)N	0.396	23.8	0.314	1.10	0.348	11.5
Eu/Eu*						
U/Pb	0.013	0.016		0.058	0.002	1.64
	33.6	64.2	72.1	42.0	122	23.5

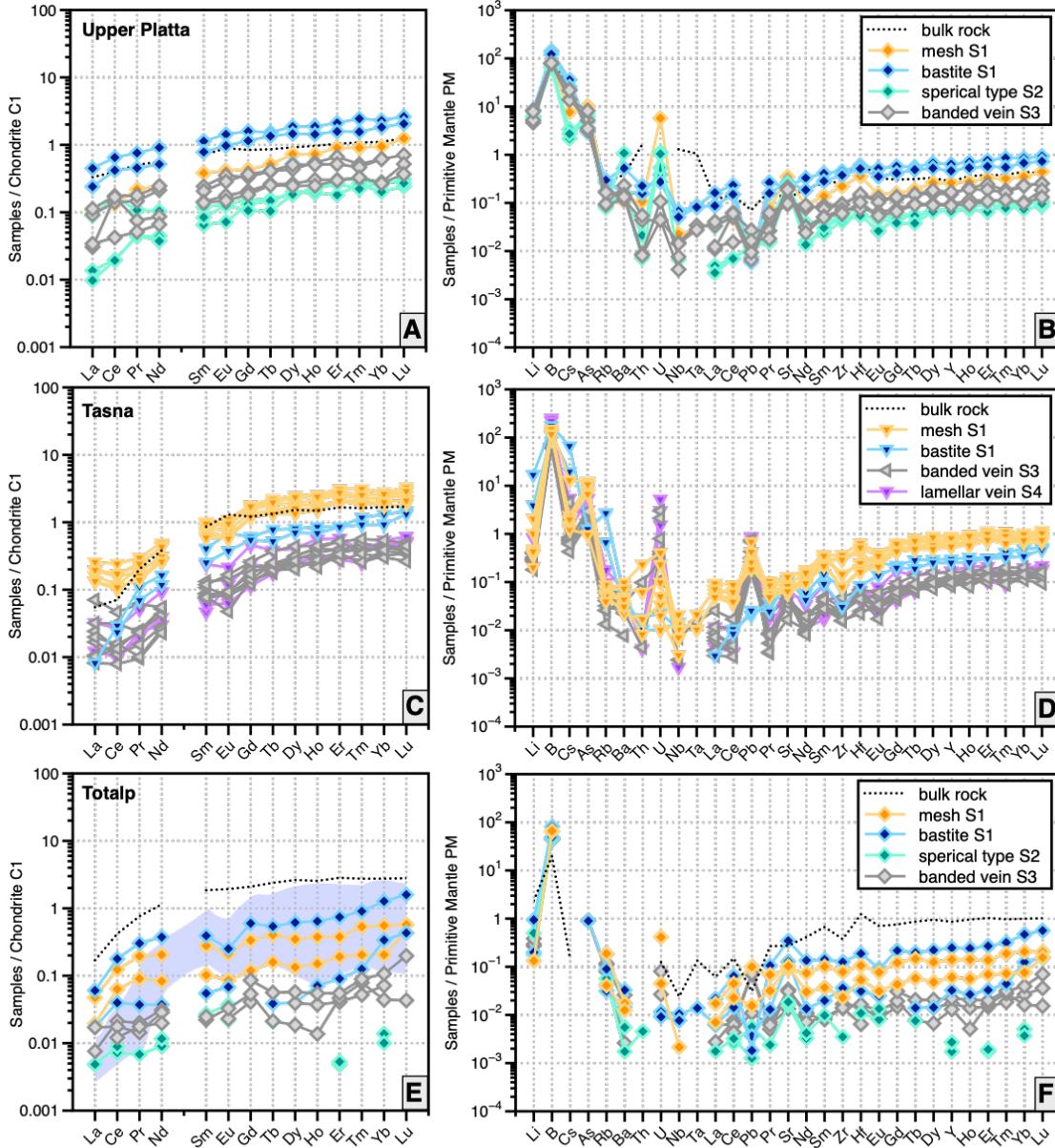


FIGURE 4.6 – Representative rare earth element (REE) patterns normalized to C1-Chondrite (left) and PM-normalized extended trace element patterns (right) of serpentine minerals and veins depending on their localities. Blue field correspond to serpentinites Grade 0 from the Chenaillet (data from Lafay et al. 2017)

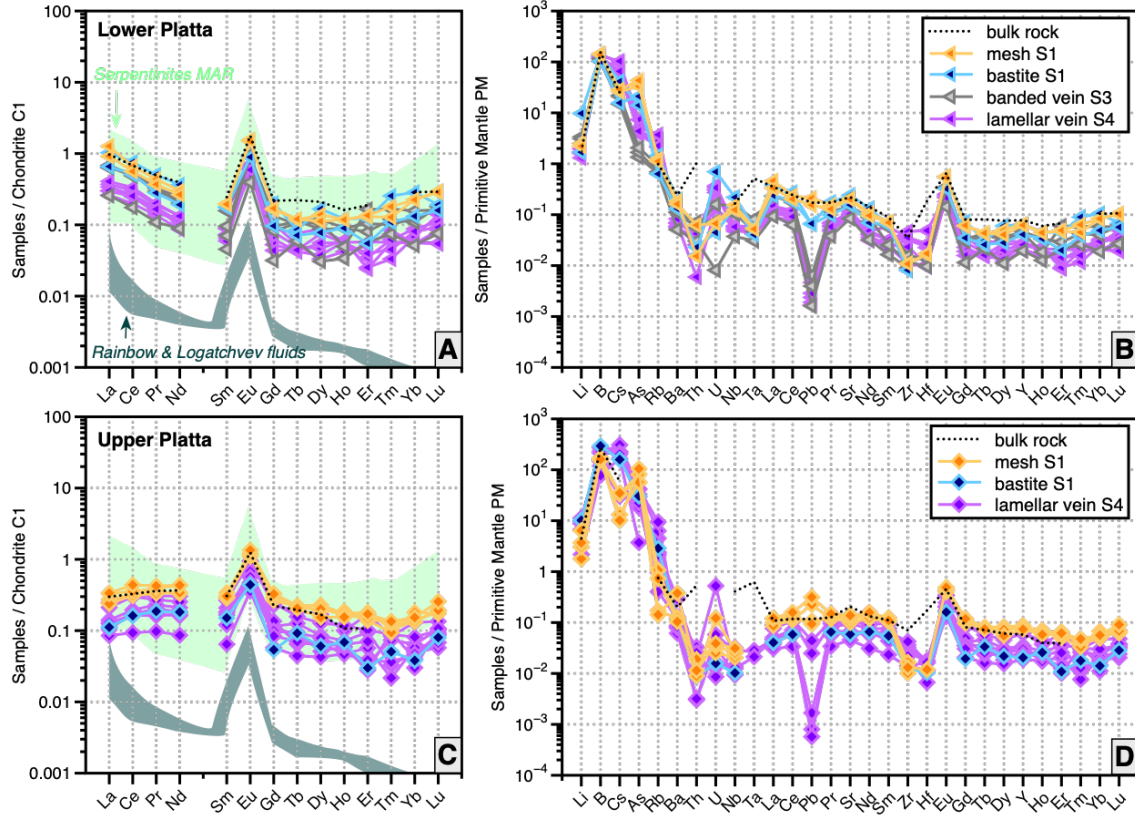


FIGURE 4.7 – Rare earth element (REE) patterns normalized to C1-Chondrite (left), Trace elements normalized to Primitive mantle (right) diagrams of the serpentine minerals and veins. Serpentine from the Lower Platta unit display U-shape patterns with strong positive Eu anomalies.

4.5 Discussion

Textural characteristics of serpentinites their respective chemical compositions indicate that serpentinization related to mantle exhumation at OCT of the Alpine Tethys was a complex and multiphase process that may be a consequence of local variations of temperature, pressure, fluid/rock ratio and/or fluid chemistry

Here below we compare and discuss (i) the serpentinization process in terms of depth of fluid/rock interactions (deepest pervasive serpentinization vs. shallower veining serpentinization) ; (ii) the serpentinization of subcontinental mantle along the OCT (i.e., proximal and distal parts). Finally, a comparative discussion about serpentinization at OCT relative to that at present-day oceanic domains is proposed.

4.5.1 Serpentinization as a marker of multi-stages mantle exhumation

Stage 1 : Static - formation of mesh and bastite (serpentine S1)

Along the cross-section of the OCT, pseudomorphic serpentine mesh texture and bastite are consistently observed as the earliest event of serpentinization replacing olivine and pyroxenes. Previous studies proposed that serpentinization at magma-poor rifted margins begins before mantle exhumation to the seafloor, when subcontinental lithospheric mantle was still capped by a thinned continental crust < 10 km thick (Manatschal 2004 ; Epin et al. 2019 ; Hochscheid et al. 2022). Serpentinization of primary olivine and pyroxenes begins by fluid circulation along detachment and high-angle normal faults (e.g., Escartin et al. 1997 ; Demartin et al. 2007 ; McCaig et al. 2010 ; Rouméjon and Cannat 2014). At depth, serpentinization is assumed to occur under static conditions and at very low fluid-rock ratios, as confirmed by the low mobility of major and REE in our samples of which patterns mimic those of the precursor minerals (e.g., Moody 1976 ; Wicks and Whittaker 1977 ; Viti and Mellini 1998 ; Rouméjon et al. 2015). In these conditions, the formation of lizardite mesh is favored by a narrow available space and confining pressure (e.g., Viti and Mellini 1998 ; Evans 2004). Complete serpentinization of olivine and pyroxenes is then achieved by increasing fluid/rock ratio and/or over a longer reaction time Viti and Mellini 1998.

In good agreement with the maximum depth of fluid circulation at the Trans-Atlantic Geotraverse (TAG) hydrothermal system along the MAR Demartin et al. 2007 and the model for the development of mesh texture in the context of tectonic

exhumation proposed by Rouméjon and Cannat 2014, we propose that the initiation of serpentinization, attested by the development of mesh and bastite textures, begins before mantle exhumation at relatively high depth (6-8 km, Figure 4.8 Stage1). A serpentinization temperature of $\sim 300^{\circ}\text{C}$ can be assumed since in partially serpentinized samples we systematically observed a preferential serpentinization of olivine, while pyroxenes remained preserved. This is consistent with an optimum temperature of 270-300 $^{\circ}\text{C}$ for olivine serpentinization and over 300 $^{\circ}\text{C}$ for orthopyroxene serpentinization as reported in the literature (e.g., Martin and Fyfe 1970; Janecky and Seyfried 1986; Allen and Seyfried Jr 2003). The mesh and bastite textures and the occurrence of relics of primary olivine and pyroxenes indicate that a limited amount of water reached the subcontinental mantle and initiate serpentinization under static conditions and near stoichiometry Viti and Mellini 1998.

Stage 2 : Extension - serpentine veining (serpentine S2 and S3)

Formation of serpentine S2

The first generation of veins are made of polyhedral serpentine (S2) that exhibit atypical spherical texture (Figure 3.3). They are mainly located in pyroxene and bastite cleavages, where a systematic association with andradite grains is reported. These veins mostly occurred in partially serpentinized samples from Totalp. According to Andreani et al. 2008, the formation of polyhedral serpentine vein requires three major conditions, including (i) an open space, (ii) a temperature $< 200\text{-}300^{\circ}\text{C}$, and (iii) an Al content > 0.1 apfu. Most trace element concentrations are significantly depleted in polyhedral serpentine relative to bastite and primary clinopyroxene precursors Figure 4.6. To deplete the concentrations in trace element, high quantity of fluid are required Andreani et al. 2008. This suggests that the formation of polyhedral serpentine S2 occurred at higher fluid fluxes than formation of serpentine bastite S1. Moreover, serpentinizing fluid forming polyhedral serpentine S2 has probably a low saturation degree. This is in accordance with the open-space required to form polyhedral serpentine as proposed by Andreani et al. 2008. Finally, consistently with the last requirement proposed by Andreani et al. 2008, polyhedral serpentine S2 contains enough Al ~ 0.16 apfu in average (Table 4.4.2) to promote the development of polyhedral serpentine. Such Al enrichment is consistent with alteration of Al-rich mineral phases like pyroxenes.

Comparatively to bastite, polyhedral serpentine is enriched in Si and Mg and depleted in Ca and Fe Figure (Figure 4.4; Table 4.4.2). This may be explained by the

preferential absorption of Ca and Fe by andradite Plümper et al. 2014. The absence of magnetite associated to polyhedral serpentine is thus a consequence of andradite formation, since andradite consumes Fe released either during pyroxene serpentinitization or after magnetite dissolution. Plümper et al. 2014 also showed that no addition of Ca is required if the protolith contains between 8 and 12% of clinopyroxene. The subcontinental mantle now exposed in Platta, Tasna and Totalp nappes was originally composed of fertile Spinel \pm Plagioclase lherzolites Müntener et al. 2010, so it is likely that serpentinitization of these peridotites released enough Ca to form andradite synchronously with polyhedral serpentine. According Frost and Beard 2007, the andradite serpentine assemblage is highly dependent on silica and calcium activities and pH rather than to temperature. However, they predicted a temperature interval of 200–230°C to be the most likely where andradite will become the Ca-phase in serpentinites. These temperatures are consistent with those reported by Plümper et al. 2014, who show that clinopyroxene is replaced by an assemblage of serpentine and andradite at $T < 280^\circ\text{C}$ and low pressure ($< 0.5 \text{ kbar}$). Considering that serpentine S1 formed at $\pm 300^\circ\text{C}$, serpentine S2 most likely formed shallower, under lower temperature and pressure conditions ($\pm 250^\circ\text{C}$, $< 0.5 \text{ kbar}$).

Based on textural evidences and serpentine chemistry, we propose that polyhedral serpentine S2 formed at different conditions than serpentine S1. However, formation of serpentine S2 is also involved in an early stage in the serpentinitization chronology during mantle exhumation, just after the beginning of pseudomorphic mesh and bastite S1 formation (Figure 4.8 Stage 2). The development of serpentine S2 took place probably at slightly shallower levels and at lower temperature and silica activity than serpentine S1 (Figure 4.8 Stage 2), since the presence of andradite closely associated to the polyhedral serpentine S2 is indicative for reducing conditions and temperature of serpentinitization below 280°C Plümper et al. 2014. The formation of serpentine S2 required also higher fluid/rock ratios (i.e., fluid dominated system), suggesting that the quantity of water available was higher than in the stage 1 (i.e., rock dominated system). This is in accordance with the serpentinitization at shallower depth and potentially the development of new faults, allowing to increase fluid/rock interactions.

Formation of banded veins S3

Contrarily to polyhedral veins (S2) which are limited in number in our samples, banded veins are observed frequently crosscutting the two latter generations (Figure

4.3, Table 1). Similar occurrences have been reported in oceanic serpentinites, and their formation largely documented (e.g., Andreani et al. 2004; Andreani et al. 2007; Rouméjon et al. 2015). A temporal successive paragenesis of proto-serpentine → chrysotile → polygonal serpentine → lizardite has been proposed based on experimental studies of Grauby et al. 1998 and Normand et al. 2002. Such temporal succession is assumed to occur isochemically subsequently to the decreasing supersaturation of the fluid. Alternatively, banded veins may result of crack-opening, either caused by incremental stress release due to progressive unroofing of serpentized peridotites, or by the accommodation of volume increase during serpentinization (e.g., Ramsay 1980 ; O'Hanley 1992 ; Dilek et al. 1997 ; Andreani et al. 2004). In our samples, banded veins S3 are mostly made of lizardite and polygonal serpentine, while chrysotile remains scarce. The banded veins made of polygonal serpentine contains more Fe_T and less Mg than banded veins made of lizardite (Figure 4.5). Thus, we can attribute this chemical evolution to the decreasing degree of supersaturation of the solution with respect to serpentine, and longer interaction time.

Our results suggest that the progressive mantle exhumation leads to strain relaxation and increase of fluid/rock ratio, the latter leading to the decrease of fluid supersaturation. The formation of these banded veins (S3) begins where the ultramafic rocks are fully serpentized, at shallower depth than serpentine S1 and S2, probably between 4 and 2 km along a detachment fault Andreani et al. 2007 (Figure 4.8 Stage 2b). Crack opened in response to volume expansion associated to serpentinization. The first banded veins S3 filled by chrysotile (rarely preserved in our samples) attested of crack opening at low strain and a middle to highly supersaturated fluid, thus moderate fluid/rock ratios (Figure 4.8 Stage 2b).

The transition from chrysotile to polygonal serpentine occurred spontaneously with additional time and the arrival of new fluid, allowing to decrease the fluid saturation degree (Viti and Mellini 1997 ; Figure 4.8 Stage 2). Development of the lizardite is kinetically favored by : i) increasing reaction times, ii) decreasing the degree of fluid supersaturation by new and less reacted fluid mixtures, and iii) decreasing temperature (Figure 4.8 Stage 2).

Stage 3 : Compression - formation of antigorite S4

Antigorite (S4) was identified in some fully serpentized samples from Upper Platta, Tasna and in one sample from Lower Platta. It mostly occurs in veins, sometimes

forming pull-apart, or in patches that seem to be propagated from micro-fractures up to several millimeters into the surrounding serpentinite (Figure 4.3F, G). The pull-apart are typical of extensional domains, and generally favored the development of chrysotile (e.g., Evans 2004). Thus, the occurrence of antigorite in veins which are usually attributed to the replacement of chrysotile thought a dissolution-recrystallization favored by intense shearing stress at mid-oceanic domains at relatively low temperature <300°C (e.g., Ribeiro Da Costa et al. 2008) and the peak at $\sim 3700 \text{ cm}^{-1}$ (typical of chrysotile) systematically observed in these antigorite may indicate that pull apart structures were initially filled by chrysotile. Then the transition into antigorite may result from local increase in pressure related to shear zones as demonstrated recently by numerical models proposed by Parnell-Turner et al. 2017 and Sandiford et al. 2021.

Antigorite patches resulted mostly from a replacement of the previous mesh textures and dissolution of magnetite, in a similar manner to that was proposed by Rouméjon et al. 2015 for the occurrence of antigorite observed at SWIR. Rouméjon et al. 2015 proposed that the intense alteration of pyroxene during the extensive serpentinization releases significant amount of silica promoting the development of antigorite. We can not exclude this explanation regarding the high degree of serpentinization of our samples.

In both case (i.e., formation of veins or patches) increase of temperature is not required to support antigorite growth. Furthermore, this episode of shortening is probably not sufficiently long and/or conditions not required to allow the complete replacement of previous serpentine generations by antigorite.

Stage 4 : relaxation - formation of crack-seal S5

Chrysotile crack-seals (S5) are the last generation of serpentine veins and very common in our samples, but exceptionally. Evans 2004 proposed that formation of cross-fiber chrysotile (i.e., crack-seal S5) is not really different from slip-fiber chrysotile (i.e., banded veins S3), although the latter is promoted by the presence of fluids rather than shear stress. We proposed that formation of serpentine S5 occurred mainly at shallower depths than banded veins S3, but probably in similar levels than serpentine S4 (Figure 4.8 Stage 4). They are formed by a late strain release at the end of mantle exhumation at seafloor, under high fluid/rock ratios and growth directly from fluid, that is consistent with previous studies (e.g., Evans 2004).

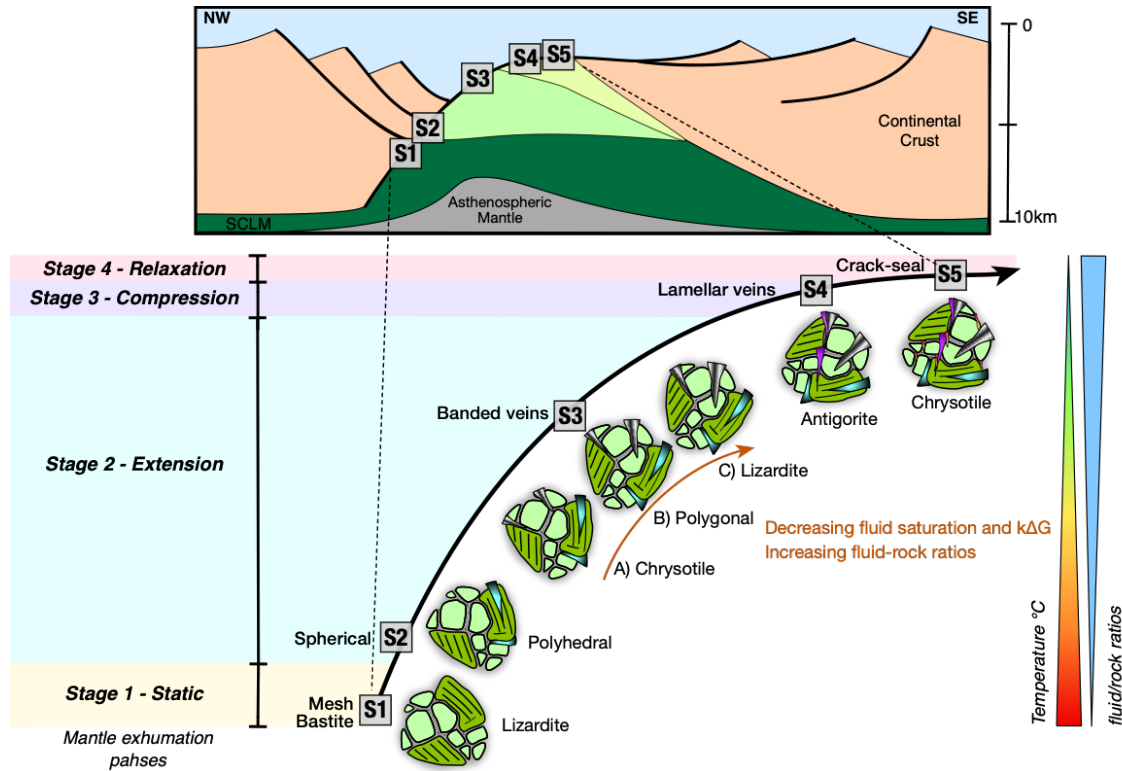


FIGURE 4.8 – Theoretical model proposed for the development of the sequence of serpentinization during continuous mantle exhumation at seafloor during Jurassic times. Pseudomorphic mesh and bastite form at very low w/r ratios and under static conditions at depth of ~6-8 km. Banded veins formation, resulting in three step : a) preferential growth of chrysotile from highly supersaturated fluid at low fluid/rock ratio, b) development of polygonal serpentine as a consequence of fluid saturation decreasing and fluid/rock ratio increasing, c) development of lizardite after longer time of fluid-rock interactions, at higher fluid/rock ratios, lower temperatures and with an undersaturated fluid. Antigorite forms at shallower levels than S3 and at local high pressure induced by the shortening. Finally, crack-seal forms at shallower depths and are associated to a decrease of local strain and high fluid/rock ratios.

4.5.2 Serpentinization along the Ocean-Continent Transition zone

An important observation is that at proximal domains of the OCT (Upper Platta and Tasna), the serpentinization chronology as reported above is fully developed, i.e., all generations of serpentine (S1 to S5) are observed. In contrast, at more distal domains of the OCT (Lower Platta), serpentine veins belonging to S2, S3 and S4 are not observed, and serpentinites are mainly made of S1 (i.e., mesh and bastite) and S5 (i.e., crack-seal), with exception of one sample from Marmorera, where only polyhedral serpentine veins (S2) are absent. In comparison, serpentinites from more oceanic domains, like those from the Chenaillet unit (e.g., Manatschal and Müntener 2009) display the same micro-textures as those from the Lower Platta unit (Schwartz et al. 2013; Lafay et al. 2013). Lafay et al. 2013 proposed that the serpentinization process at Chenaillet mostly occurred in static conditions, which is characteristic of abyssal serpentinites. At Totalp, serpentinization differs from other units from proximal domains : the peridotites are moderately serpentinized and are not affected by the intense veining as reported in other localities. The low degree of serpentinization is in favor of small amount of fluid that penetrated the mantle. Consequently, the complete serpentinization cannot be achieved and/or peridotites and fluid were not in contact during a long period. At the Lower Platta unit, the relics of primary olivine and pyroxenes are sparse compared to Totalp. the absence of intense serpentine veining suggests same processes. This is in agreement with the model of Rouméjon and Cannat 2014 suggesting that formation of the serpentine mesh texture is a quasi-instantaneous process at the plate tectonic timescales or that serpentine mesh texture results of a long time period controlled by small and intermittent supplied of fluids. Hence, we propose that subcontinental mantle exhumation proceeds rapidly at Totalp and Lower Platta.

Serpentinites from distal domains (i.e., Lower Platta unit) are almost completely devoid of serpentine veins, which is in favor of short period of fluid-rock interactions or low fluid inputs, could be also the consequence of : i) mantle inheritance (i.e., different mantle compositions Picazo et al. 2016 and/or equilibration temperatures Müntener et al. 2004, ii) the rheology of the serpentinized basement, or iii) temperature of serpentinization (and consequently slower kinetics of dissolution Knauss et al. 1993; Oelkers and Schott 2001; Oelkers et al. 2018; Rimstidt et al. 2012).

In contrast to serpentine from more proximal domains, serpentine from the Totalp unit display limited enrichment in fluid mobile elements (FME : Li : ~ 0.71 ppm in

average, Cs, As and U mostly below the detection limit) and the lowest enrichment in boron relative to the PM (in average 15 ppm ; Table 4.3, Figure 4.6, 4.7). Comparatively with other occurrences of serpentinites from distal domains, like in the Chenaillet, concentrations in FME are within the same range and correspond to those reported in abyssal environments where serpentinization is attributed to seawater interactions Lafay et al. 2013. This implies that the amount of seawater that penetrated the mantle was low, preventing the Totalp unit of being fully serpentinized.

The enrichment in uranium observed in most of our samples, whatever the location, is a common features in abyssal serpentinites (E;G ;, Niu 2004 ; Paulick et al. 2006 ; Kodolányi et al. 2012 ; Peters et al. 2017). Although such enrichment may be a consequence of mantle-melt interactions Niu 2004, this hypothesis is unlikely here since proximal parts of the OCT (Tasna, Upper Platta) were preserved from melt percolation Müntener et al. 2010. The occurrence of carbonate veins which can host significant amount of U may contribute to the U-enrichment observed in bulk-rock concentrations. However, high U concentrations are also found *in situ* in all serpentine species, even in samples devoid of carbonates. In addition, at the sample scale, serpentine species formed at shallow levels are in general more enriched in U than those formed deeper (Figure 4.6,4.7). U mobility during fluid-rock interactions is strongly dependent on its oxidation state. Uranium is highly soluble in oxidized environment which occurs as U^{6+} (e.g., Langmuir 1978). In contrast, in reduced environments uranium mostly occurs as U^{4+} and its mobility is severely reduced (e.g., Aumento 1979 ; Pettke et al. 2018. FROST 1985 have suggested that during serpentinization process uranium is relatively immobile. The progressive U-enrichment from S1 to S5 may be thus a proxy of the depth of fluid-rock interactions. The serpentine depleted in uranium were formed at depth under reducing conditions and low U-mobility, while serpentine veins enriched in uranium precipitated from fluids enriched in U at shallow depth.

Origin of LREE-enriched serpentines with Eu positive anomaly

As mentioned before, specific REE patterns have been identified in two samples from the Lower and Upper Platta units Figure 4.7. These samples are characterized by U-shaped REE patterns and exhibit a strong Eu positive anomaly. Two main processes have been proposed to account for such patterns in oceanic serpentinites : i) plagioclase crystallization after melt percolation (i.e., refertilization process ; Müntener et al. 2004 ; Müntener et al. 2010 ; Rampone et al. 1998 ; Rampone et al. 2020) ; or ii) large

fluid fluxes during serpentinization Paulick et al. 2006. Regarding the first assumption, the crystallization of melt-derived plagioclase may be consistent with the formation of LREE-enriched serpentinites in the Lower Platta unit since the latter was largely impregnated by melts during Jurassic times. However, this explanation cannot account for Upper Platta serpentinites, since this unit remained preserved from syn-rift melt imprint Müntener et al. 2010. In addition, Allen and Seyfried Jr 2005 have shown that LREE-rich serpentinite with positive Eu anomaly is not necessarily related to plagioclase recrystallization, as previously thought (e.g., Klinkhammer et al. 1994; Douville et al. 2002). This explanation was proposed to account for LREE enrichment and Eu positive anomaly observed in hydrothermal vent fluids from the MAR (Figure 4.7; Paulick et al. 2006). According to Paulick et al. 2006, such LREE-enrichment in serpentine is only possible under very high fluid-rock ratios so that the LREE content was entirely controlled by the fluid, and that the depleted character of the protolith was erased. At the opposite, the HREE are less affected since their concentrations in hydrothermal fluids are negligible relative to the initial peridotite. As a consequence, the specific REE pattern observed in two samples may therefore have been imposed by serpentinization, and may represent area where fluid-rock interactions were locally stronger, similar to some mature hydrothermal systems described along mid-ocean ridges (Paulick et al. 2006 ; Delacour et al. 2008 ; Andreani et al. 2014). This assumption is consistent with the recent discover of a well-preserved fossil ultramafic-hosted hydrothermal system, namely the Marmorera-Cotschen hydrothermal system in the Platta Nappe Coltat et al. 2019 ; Coltat et al. 2021 ; Hochscheid et al. 2022.

To synthesize, we propose that in proximal domains where mantle exhumation is a long-time and more continuous process (Upper Platta and Tasna units), serpentine veins can develop and record a succession of different serpentine types (S1 to S5) reflecting changes in the controlling parameters and resulting in the chronology observed at these sites Figure 4.8. However, in distal domains, where duration of exhumation is shorter, discontinuous and linked to magmatic activity (Lower Platta unit), the entirely serpentine chronology is not observed ; S2, S3 and S4 are missing. The observed differences in serpentinization are consistent with the recent study of Hochscheid et al. 2022 who showed that the Upper Platta recorded longer time of fluid/rock interactions than those from the Lower Platta. At Totalp, the low degree of serpentinization, the recurrent association of andradite with polyhedral serpentine (Figure 4.3C, D, E), the strong depletion of trace element concentrations and the limited enrichment in FME (Figure 4.6 ; Table 4.3) suggests that serpentinization took place at low temperatures

and at limited fluid/rock ratios.

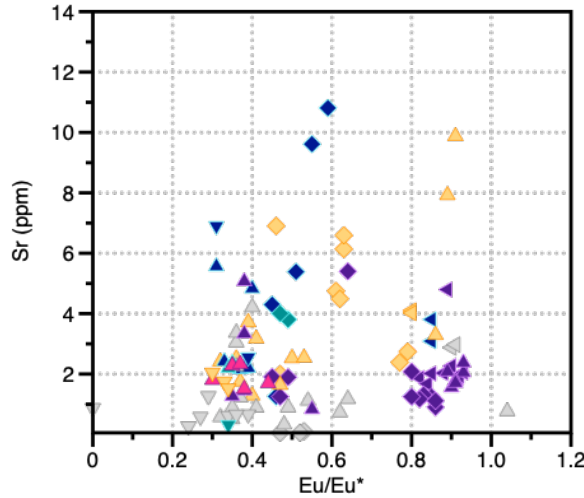


FIGURE 4.9 – Concentrations in Sr versus Eu/Eu* of the different serpentine type. No correlation is observed between Sr and Eu/Eu*

4.5.3 Is serpentinization in present-day MOR comparable to serpentinization in OCT ?

OCTs at passive rifted-margins are characterized by large domains of exhumed mantle. Mantle exhumation is also a common feature at slow and ultra-slow spreading centers (e.g., Cannat 1993; Blackman et al. 2002; Sauter et al. 2013). Thus, some similarities in hydrothermal processes may be expected between these two settings. Some evidences of this assumption can be found at 30°N (Atlantis massif; Rouméjon et al. 2018) and 23°N (the Kane fracture zone, MARK area; Andreani et al. 2007; Dilek et al. 1997) along the MAR, and at 62-65°E along the Southwest Indian Ridge (SWIR; Rouméjon and Cannat 2014; Rouméjon et al. 2015). In all places, very similar serpentine paragenesis to that reported in this present study was described, starting with the pseudomorphic replacement of primary minerals by lizardite mesh and bastite textures. A local recrystallization of the serpentine mesh into chrysotile may occur (e.g., Rouméjon et al. 2015; Rouméjon et al. 2018) but additional serpentinization events are dominated by abundant veining with a large variety of morphology and textures, testifying of variable mechanisms and conditions of formation.

The first generation of veins identified in our samples was the polyhedral serpentine, either in veins crosscutting the mesh texture or in alteration of pyroxenes. The

occurrence of polyhedral serpentine was not reported in SWIR serpentinites nor at Atlantis massif, but is described as the latest generation of veins in serpentinites from MARK Andreani et al. 2007; Andreani et al. 2008. According to Andreani et al. 2008, all Fe in polyhedral serpentine is ferrous, which in favor of a formation under reducing conditions. This is therefore more consistent with a formation at depth rather than at shallow depth where more oxidizing conditions are assumed. The close association with andradite, as reported above, is also in favor of reducing conditions Plümper et al. 2014. The reason why polyhedral serpentine formed earlier/deeper in OCT serpentinites relative to those at MOR is thus unclear. The availability of Al is an important parameter that seems to control the formation of polyhedral serpentine Andreani et al. 2008. The nature of the protolith may thus play a role in the early crystallization of polyhedral serpentine : OCT peridotites from the Alps are fertile lherzolites that are up to 3-4 times more enriched in Al than harzburgites that dominantly outcrop at MAR and SWIR. Lherzolite contains higher amounts of clinopyroxene than harzburgite ~ 8-12 % which host important quantity of Ca and Al. Additionally to clinopyroxene, lherzolite from specific mantle section along the OCT (refertilized mantle, Mantle type 2 from Picazo et al. 2016) can contain up to 12% of plagioclase that also stores significant amount of Al and Ca. Consequently, we assume that OCT lherzolites are more suitable to form polyhedral serpentine and associated andradite at early time of serpentinization relative to MOR harzburgites where Al and Ca are significantly less depleted. More fluid-rock interactions may thus be required to mobilize enough Al and subsequently form polyhedral serpentine.

Contrarily to polyhedral serpentine which was rarely observed, banded serpentine veins were often identified at MOR (Figure 4.10 ; e.g., Andreani et al. 2007 ; Dilek et al. 1997) and OCT (e.g., Agrinier et al. 1996). At both settings, banded veins are assumed to form at intermediate depth of 2-4 km. Here, serpentinization is controlled by fracturing (e.g., O'hanley 1991 ; Andreani et al. 2007 ; Dilek et al. 1997 ; Rouméjon et al. 2015 ; Rouméjon et al. 2018 ; Tarling et al. 2021), the latter being related to tectonics (i.e., stress relaxing during progressive mantle unroofing), and/or serpentinization-induced volume increase (e.g., Iyer et al. 2008 ; Jamtveit et al. 2009). Whatever their mode of formation, the systematic occurrence of serpentine in veins indicates that at depth <4 km, the extend of serpentinization is not only controlled by the replacement of primary minerals but rather by the filling of mantle cracks, where supersaturated fluids can infiltrate and precipitate.

Similarly to banded veins, antigorite veins or patches were also reported in serpentinites from MOR settings Figure 4.10. Although absent from the MARK area, it was described in other locations along the MAR (Atlantis Massif, Rouméjon et al. 2018; Rainbow and Menez Hom sites, Ribeiro Da Costa et al. 2008) and the SWIR Rouméjon et al. 2015. At each site, antigorite occurs as one of the latest generation of serpentine veins, usually post-dating the banded veins. Ribeiro Da Costa et al. 2008 attributes the antigorite formation to low temperature ($< 300^{\circ}\text{C}$) but high-deformation settings, characterized by intense tectonic activity and major shear zones. In contrast, Rouméjon et al. 2015 proposed that antigorite formation results to moderate Si-metasomatism, possibly consecutive to pyroxene serpentinization.

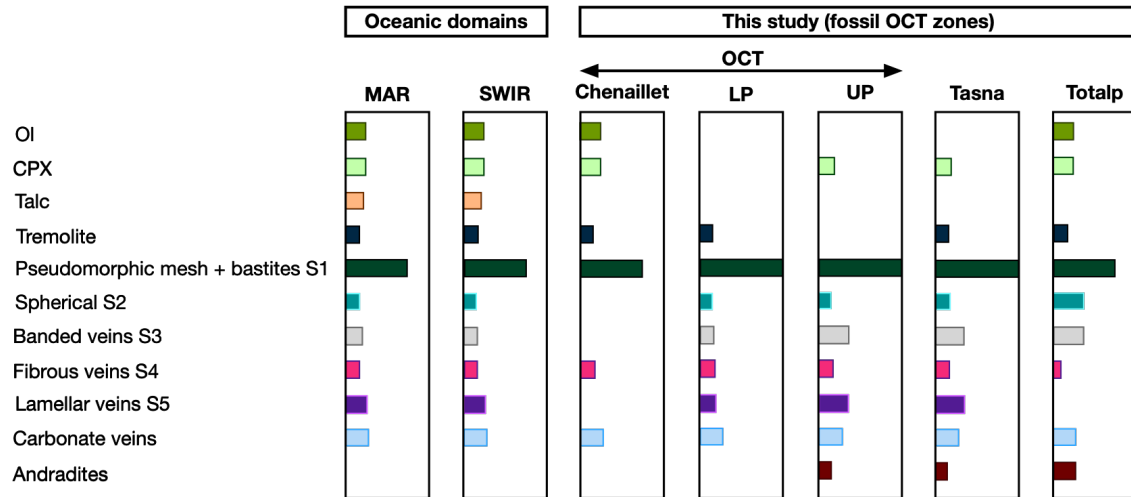


FIGURE 4.10 – Qualitative modal abundance of mineral assemblages observed in serpentinites from the Alpine Tethys OCT (this study), compared with those from the Chenaillet unit Lafay et al. 2013, and oceanic domains MAR Rouméjon et al. 2015 and SWIR Rouméjon et al. 2018.

Obviously, the discovery of antigorite veins at MOR settings rises the question about the origin of antigorite found in some Alpine ophiolites, where it was usually considered as a marker of the Alpine metamorphism related to the convergence (Dietrich 1969; Burkhard and O’Neil 1988; Scambelluri et al. 1995; Früh-Green et al. 2001; Debret et al. 2013; Lafay et al. 2013; Piccardo 2013; Liu et al. 2020). When it occurs, the transition from oceanic serpentine to antigorite in subduction zone is accompanied by a strong mobility of some trace elements. More specifically, the fluid mobile elements (FME) like B, Li, Cs and Sr are transferred to the mantle wedge during the lizardite to antigorite transition. Such element loss has been documented in several places in the

Alps, like in the Lanzo Massif Debret et al. 2013, in the Piedmont zone (Chenaillet - Queyras - Montviso Lafay et al. 2013) of the western Alps, and in the Central Alps, where the ophiolitic nappes recorded the prograde alpine metamorphism from north (Totalp) to south (Malenco ; Peters and Mathews 1963 ; Dietrich 1970, 1969 ; Vils et al. 2011). On the contrary, antigorite from Platta, Tasna and Totalp displays no depletion in FME, especially in B, Li, Cs and Sr relative to earlier serpentine type (Figure 4.11), thus ruling out a subduction origin for antigorite. In addition, the extended trace element patterns of antigorite are also very comparable to patterns of serpentine mesh, with nevertheless one order of depletion (Figure 4.6, 4.7), suggesting that antigorite formed subsequently to mesh recrystallization. During this recrystallization, magnetite may be dissolved, explaining why magnetite is so scarce at the rims of antigorite veins or patches in contrast to serpentine mesh. Based on the constant Mg# measured in serpentine mesh and antigorite in abyssal peridotites, Rouméjon et al. 2019 postulated that antigorite does not integrate additional iron even if magnetite is dissolved with mesh. However, a constant increase in Mg# is observed in our samples from S1 to S3 (Figure 4.4C), while Mg# decreases in antigorite (S4), suggesting that slight amount of iron may be integrated in antigorite veins and patches during serpentine mesh recrystallization.

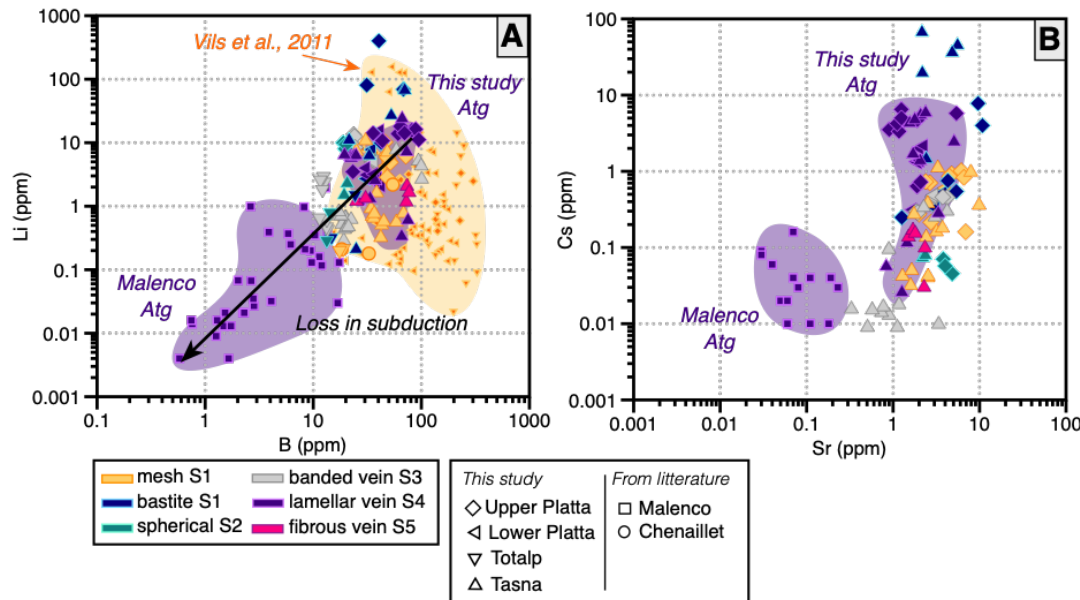


FIGURE 4.11 – A) Diagram showing the measured in situ concentrations of Li versus B of serpentine minerals and veins. B) In situ measured concentrations of Cs versus concentrations of Sr.

The final step of serpentinization in OCT serpentinites is marked by the filling of short cracks with pure chrysotile fibers. This serpentinization step is ubiquitous at MOR settings, and is commonly assumed to form from the precipitation of highly supersaturated fluids filling voids, with local dissolution of the surrounding serpentinite (Evans 2004; Andreani et al. 2004, 2007; Tarling et al. 2021).

4.6 Conclusions

We carried out petro-geochemical and mineralogical investigations of 11 serpentinites sampled in the ancient Ocean Continent Transition zone of the Alpine Te-thys ocean in the the Alpine ophiolites. Serpentinization recorded multiple stage (4) of mantle exhumation which is attested by five successive generations of serpentine.

The initiation of serpentinization attested by the pseudomorphic replacement of primary olivine and pyroxenes by serpentine lizardite mesh and bastite (S1), occurred before the mantle exhumation during the crustal thinning at $\sim 6\text{-}8$ km depth, relatively high temperature $\sim 300^\circ\text{C}$, very low fluid/rock ratios, and high reducing conditions. The development of these pseudomorphic textures take place under static conditions. This first serpentinization event recorded the first stage of the mantle exhumation history (Stage 1 : static).

The development of serpentine polyhedral (S2) occurs in an early stage in the serpentinization chronology, before the entirely expansion of the pseudomorphic mesh and bastite S1. The formation of banded veins (S3) occurs when the ultramafic rocks were fully serpentinized at shallower levels and higher water rock ratios than the serpentine S1 and S2. Crack develops in response to the volume expansion associated to serpentinization and decrease of the local strain. The transition \rightarrow chrysotile \rightarrow polygonal \rightarrow lizardite recorded by the banded veins S3 attests of the progressive increases of fluid/rock ratio with arrival of new fluids. The transition in lizardite is kinetically favored by the decrease of the fluid supersaturation and increasing reaction times. A decrease of temperatures occurs possibly with this transition. This kind of veins (S2 and S3) recorded the second stage of mantle exhumation (Stage 2 : extension).

Locally antigorite (S4) replaces the lizardite mesh S1 or some chrysotile banded veins S3 in response to a local increase of pressure induced by the shortening. This event took place at shallower levels the previous serpentinization events. (Stage 3 : compression). The end of the mantle exhumation (Stage 4 : relaxation) is evidenced by the develop-

ment of chrysotile crack-seal (S5) after a late strain release.

Serpentinization and related mantle exhumation differs along the OCT zone. In proximal domains (Upper Platta and Tasna), mantle exhumation is a long-time and continuous process, attested by the successive formation of serpentine (S1 to S5) in response to changes of conditions (depth, temperature, fluid/rock ratio). In contrast in distal domains, the duration of mantle exhumation is shorter, discontinuous and linked to the magmatic activity (Lower Platta unit), evidenced by the lack of serpentine S2, S3 and S4. The high degree of serpentinization and the REE patterns support serpentinization in fluid dominated system. At Totalp, the low degree of serpentinization and the association of andradite with polyhedral serpentine suggests that serpentinization took place at low temperatures and at limited fluid/rock ratios.

Serpentinization at OCT is relatively comparable to present day MOR although mantle rocks are initially different. In MOR settings, mantle rocks consists of harzburgite while at OCT spinel and plagioclase lherzolites are more abundant. In both settings, mantle rocks are extensively serpentinized (> 60%). The pseudomorphic mesh and bastite were crosscut by several generations of serpentine veins, including the banded veins, antigorite and crack seals. This suggests that exhumation processes are comparable in both settings. The presence of antigorite in MOR settings allow to reassess the formation of antigorite in ophiolites from the Alpine Tethys, which was systematically attributed to the Alpine subduction.

Acknowledgments

Amélie Aubert performed the XRD analyses at (ITES - University of Strasbourg). Jérémie Battringer helped for the Raman analyses (Icube - University of Strasbourg). Olivier Bruguier helped for the HR-LA-ICP-MS measurements (Géosciences Montpellier).

4.7 Supplementary materials

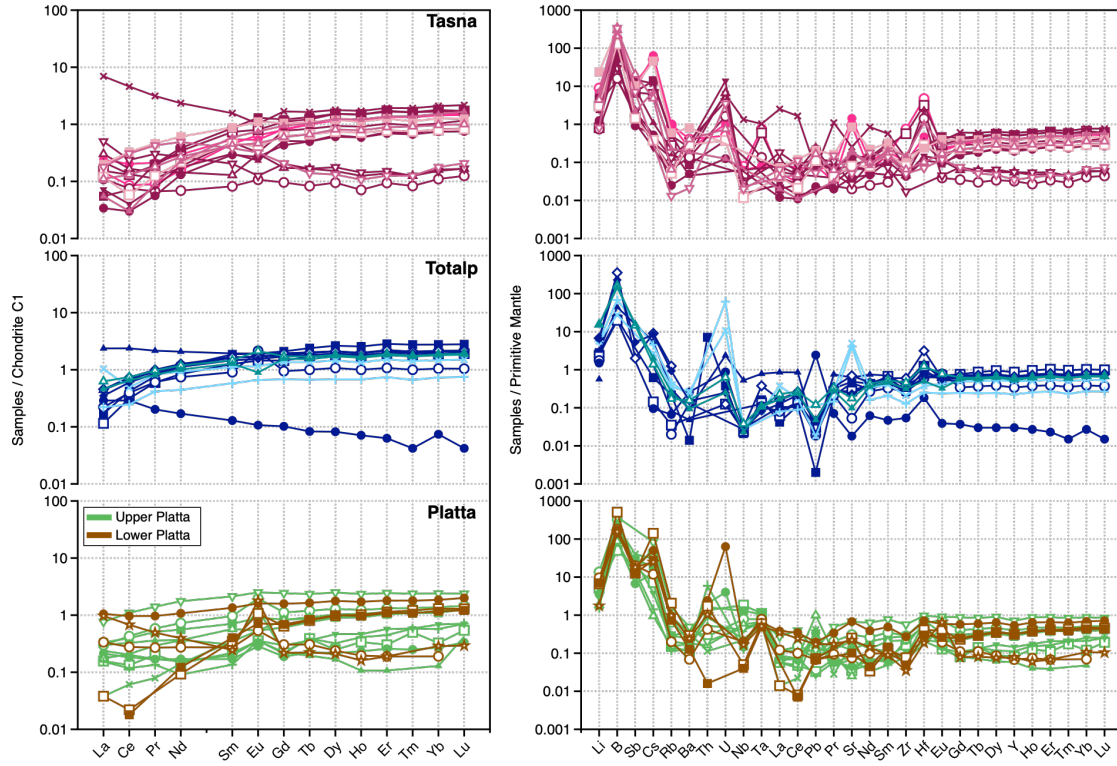


FIGURE 4.12 – Representative rare earth element (REE) patterns normalized to C1-Chondrite (left) and PM-normalized extended trace element patterns (right) of serpentinite from Tasna, Totalp and Platta.

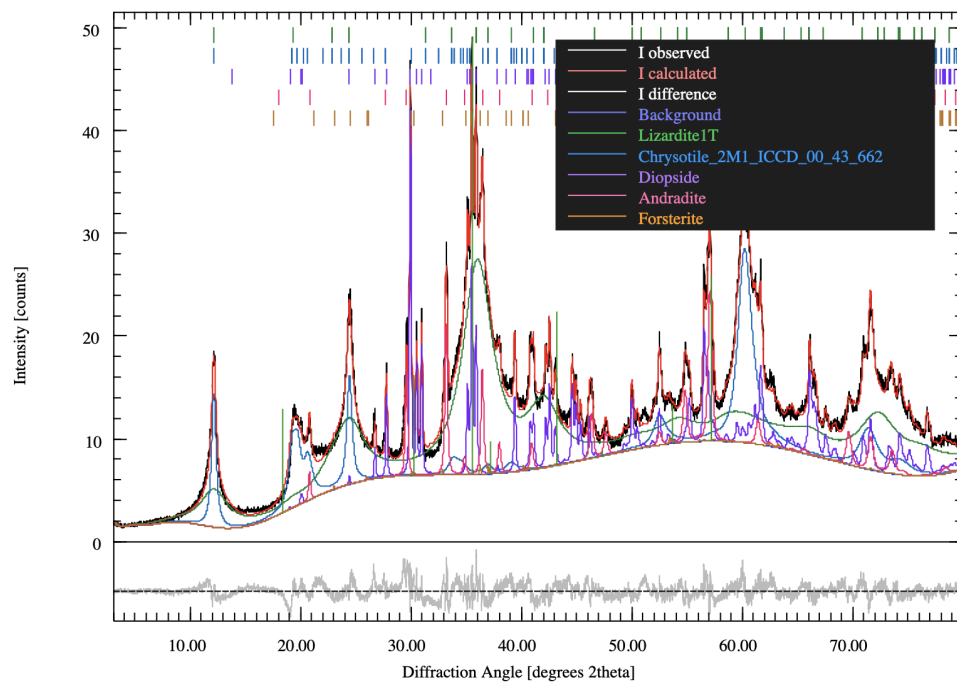


FIGURE 4.13 – XRD pattern for sample TOT-1902.

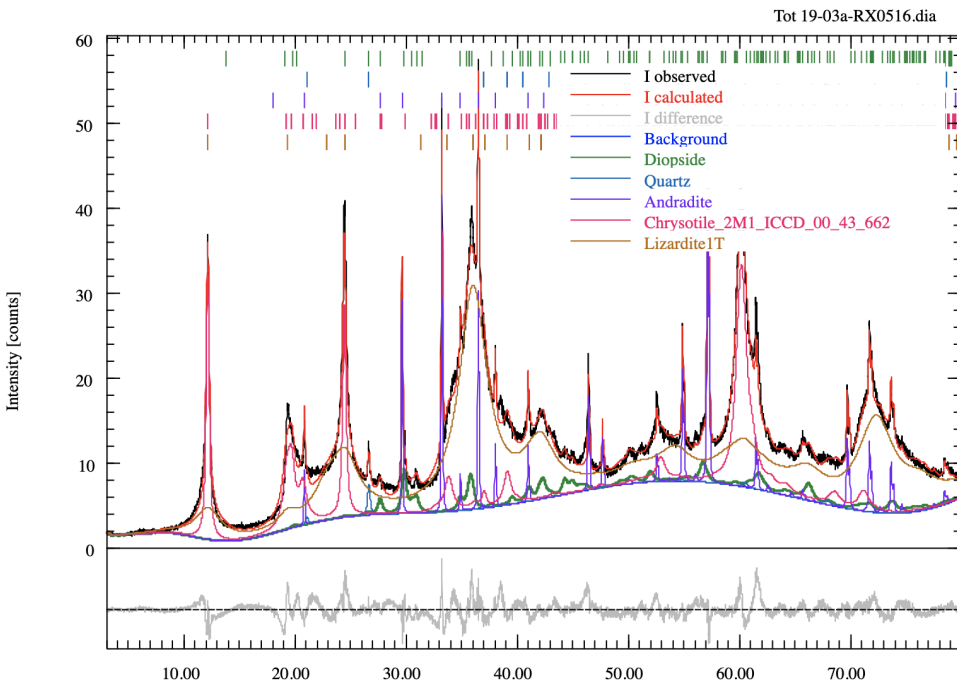


FIGURE 4.14 – XRD pattern for sample TOT-1903.

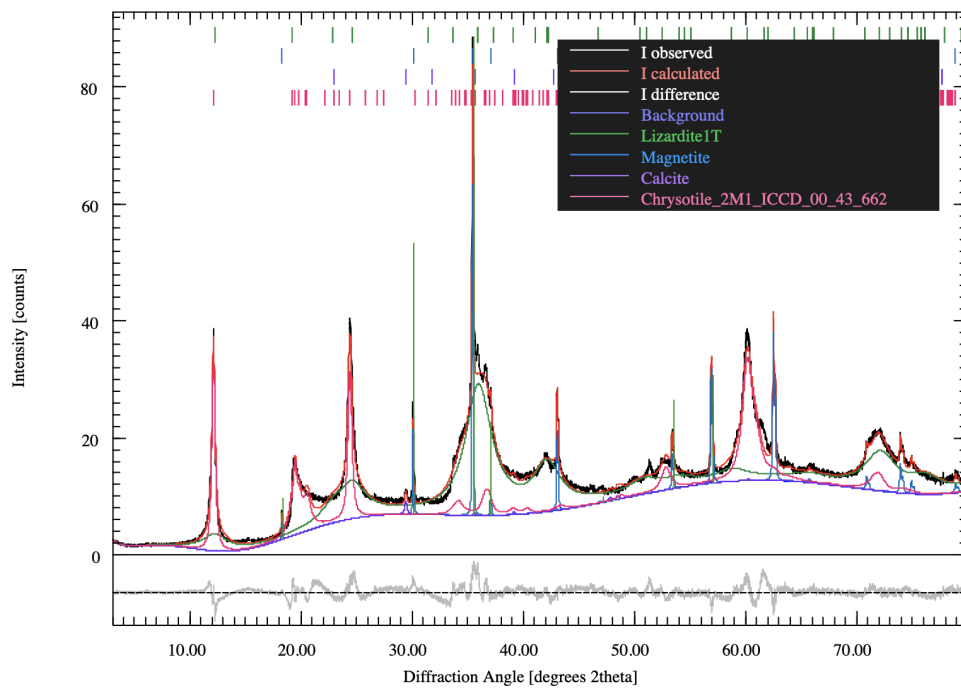


FIGURE 4.15 – XRD pattern for sample FAL-1802.

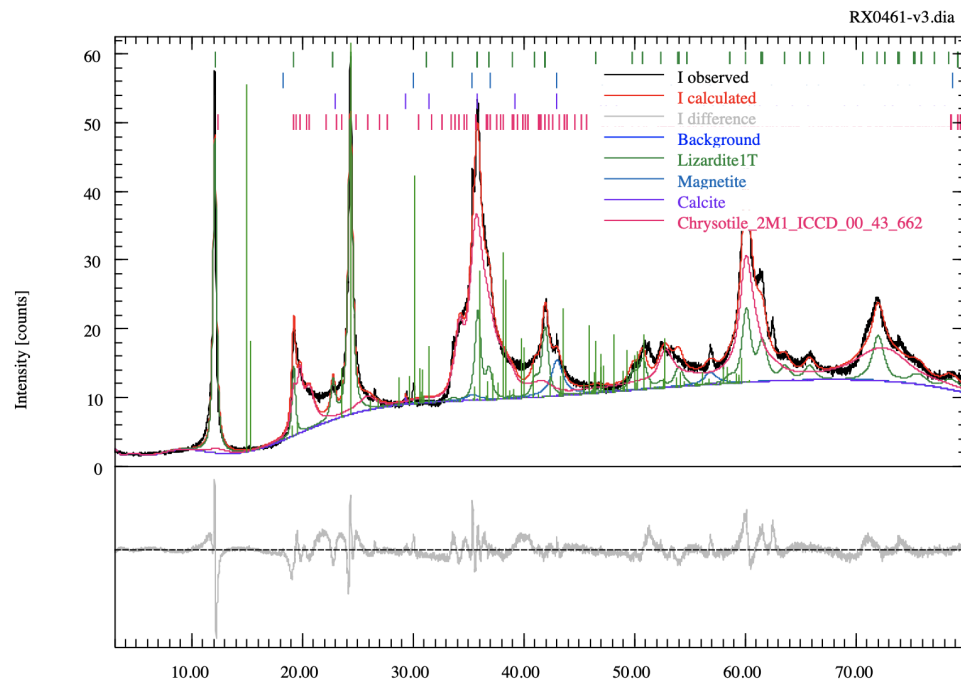


FIGURE 4.16 – XRD pattern for sample FAL-1803.

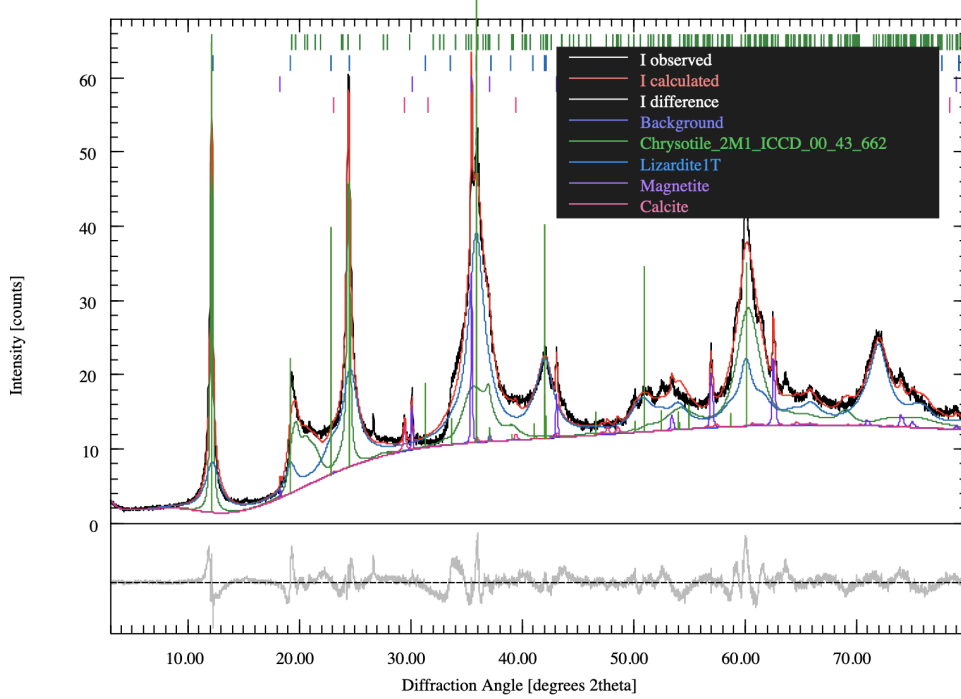


FIGURE 4.17 – XRD pattern for sample FAL-1806.

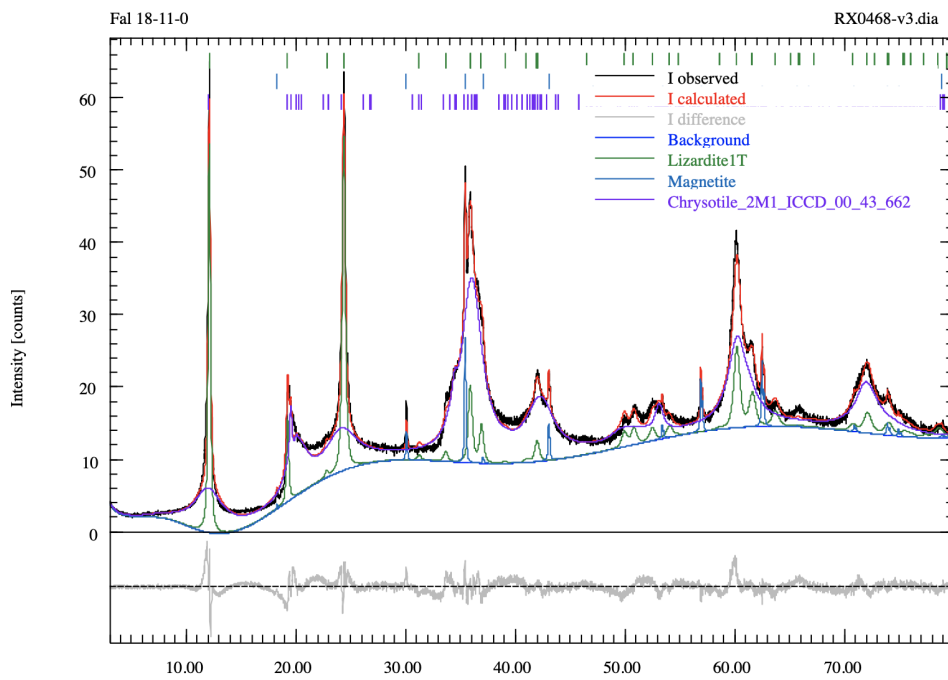


FIGURE 4.18 – XRD pattern for sample FAL-1811.

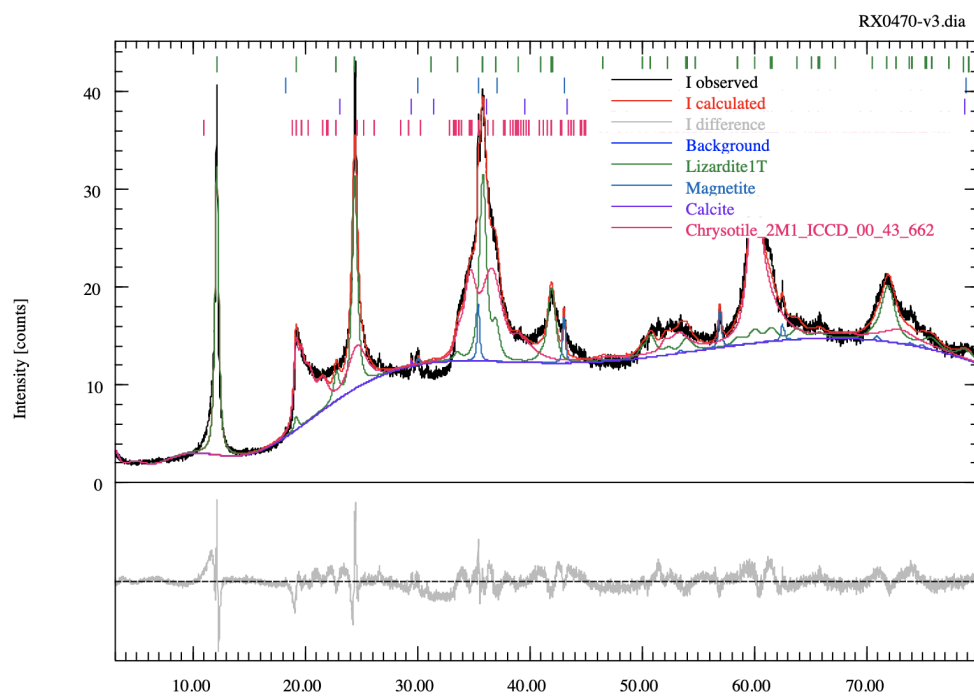


FIGURE 4.19 – XRD pattern for sample FAL-1813.

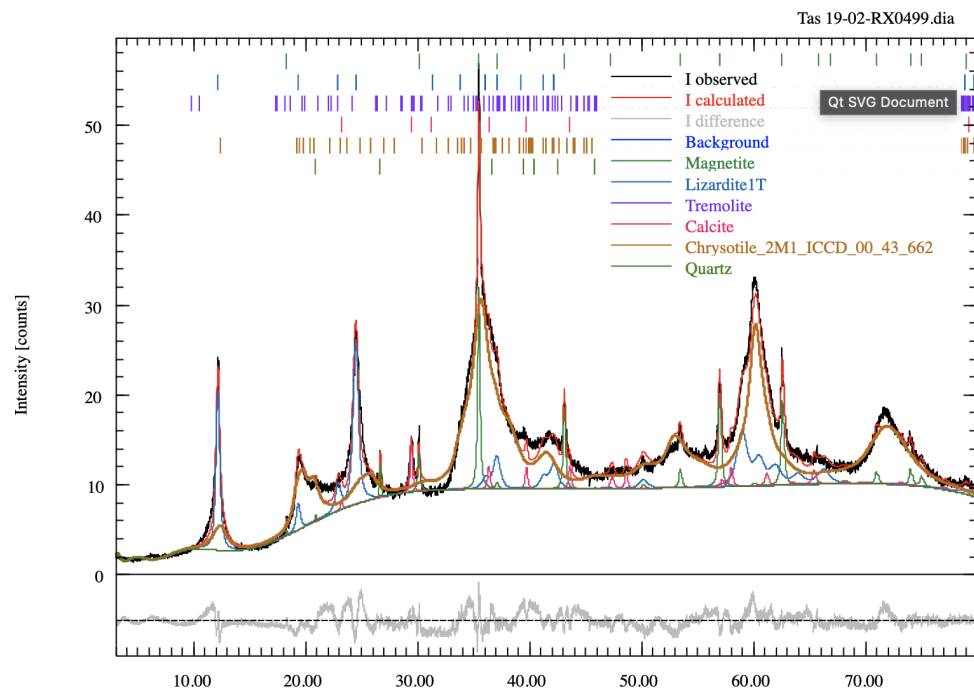


FIGURE 4.20 – XRD pattern for sample TAS-1902.

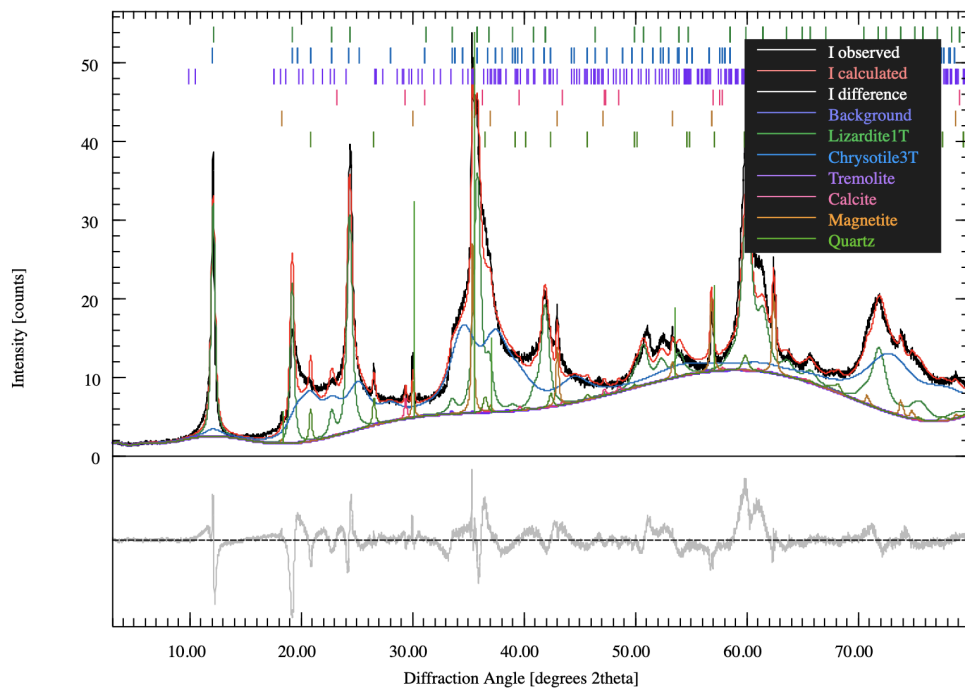


FIGURE 4.21 – XRD pattern for sample RAS-1903.

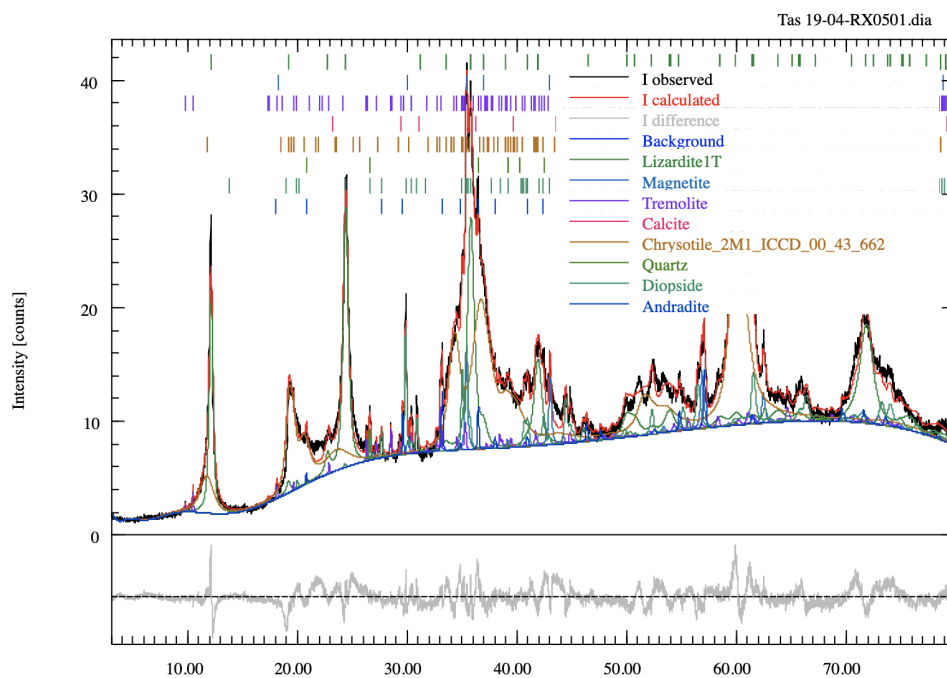


FIGURE 4.22 – XRD pattern for sample TAS-1904.

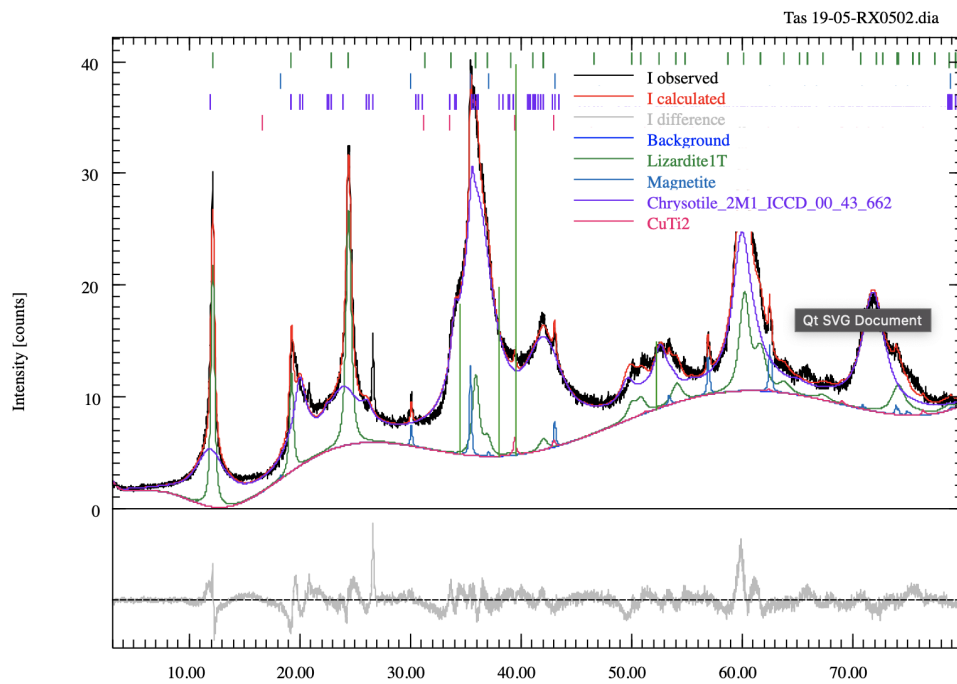


FIGURE 4.23 – XRD pattern for sample TAS-1905.

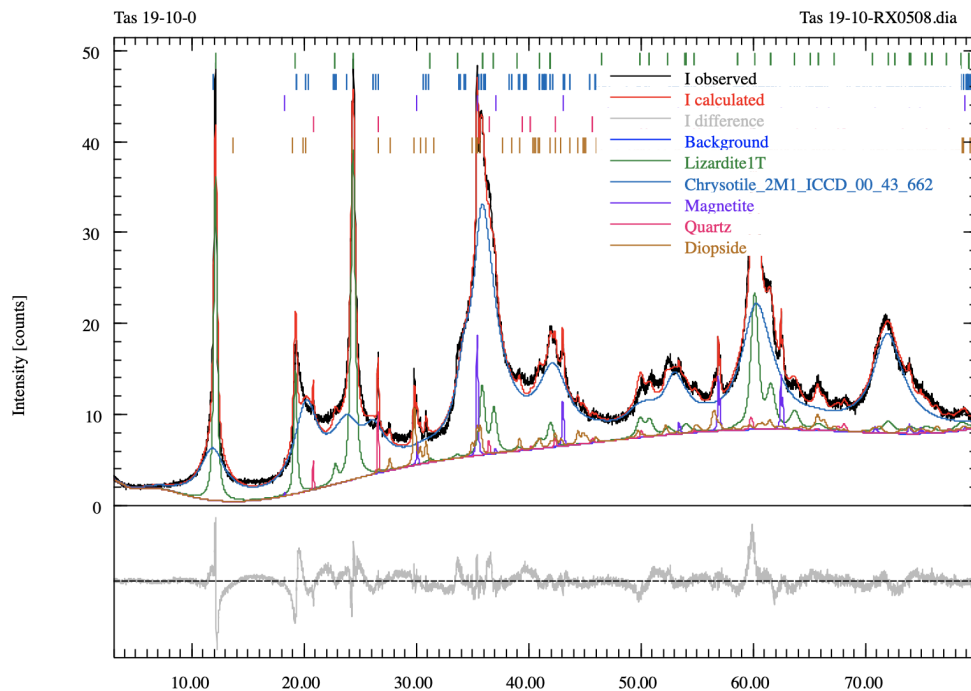


FIGURE 4.24 – XRD pattern for sample TAS-1910.

Bibliographie

- Agrinier, P., Cornen, G., and Beslier, M.-O. (1996). Mineralogical and oxygen isotopic features of serpentinites recovered from the ocean/continent transition in the iberia abyssal plain. In *Proceedings-Ocean Drilling Program Scientific Results*, pages 541–552. National science foundation.
- Allen, D. E. and Seyfried Jr, W. (2003). Compositional controls on vent fluids from ultramafic-hosted hydrothermal systems at mid-ocean ridges : An experimental study at 400 c, 500 bars. *Geochimica et Cosmochimica Acta*, 67(8):1531–1542.
- Allen, D. E. and Seyfried Jr, W. (2004). Serpentinization and heat generation : constraints from Lost City and Rainbow hydrothermal systems. *Geochimica et Cosmochimica Acta*, 68(6):1347–1354.
- Allen, D. E. and Seyfried Jr, W. (2005). Ree controls in ultramafic hosted mor hydrothermal systems : an experimental study at elevated temperature and pressure. *Geochimica et Cosmochimica Acta*, 69(3):675–683.
- Alt, J. C. (1995). Subseafloor processes in mid-ocean ridge hydrothermal systems. *Geophysical Monograph-American Geophysical Union*, 91:85–85.
- Alt, J. C. and Shanks III, W. C. (1998). Sulfur in serpentinized oceanic peridotites : Serpentinization processes and microbial sulfate reduction. *Journal of Geophysical Research : Solid Earth*, 103(B5):9917–9929.
- Amann, M., Ulrich, M., Manatschal, G., Pelt, E., Epin, M. E., Autin, J., and Sauter, D. (2020). Geochemical characteristics of basalts related to incipient oceanization : The example from the alpine-tethys ocs. *Terra Nova*, 32:75–88.
- Anders, E. and Grevesse, N. (1989). Abundances of the elements : Meteoritic and solar. *Geochimica et Cosmochimica acta*, 53(1):197–214.
- Andreani, M., Baronnet, A., Boullier, A.-M., and Gratier, J.-P. (2004). A microstructural study of a “crack-seal” type serpentine vein using sem and tem techniques. *European Journal of Mineralogy*, 16(4):585–595.
- Andreani, M., Escartin, J., Delacour, A., Ildefonse, B., Godard, M., Dymant, J., Fallick, A. E., and Fouquet, Y. (2014). Tectonic structure, lithology, and hydrothermal signature of the rainbow massif (mid-atlantic ridge 36° 14' n). *Geochemistry, Geophysics, Geosystems*, 15(9):3543–3571.
- Andreani, M., Grauby, O., Baronnet, A., and Muñoz, M. (2008). Occurrence, composition and growth of polyhedral serpentine. *European Journal of Mineralogy*, 20(2):159–171.

- Andreani, M., Mevel, C., Boullier, A. M., and Escartin, J. (2007). Dynamic control on serpentine crystallization in veins : Constraints on hydration processes in oceanic peridotites. *Geochemistry, Geophysics, Geosystems*, 8.
- Aumento, F. (1979). Distribution and evolution of uranium in the oceanic lithosphere. *Philosophical Transactions of the Royal Society of London. Series A, Mathematical and Physical Sciences*, 291(1381):423–431.
- Auzende, A.-L., Daniel, I., Reynard, B., Lemaire, C., and Guyot, F. (2004). High-pressure behaviour of serpentine minerals : a raman spectroscopic study. *Physics and Chemistry of Minerals*, 31(5):269–277.
- Auzende, A.-L., Guillot, S., Devouard, B., and Baronnet, A. (2006). Serpentinites in an alpine convergent setting : effects of metamorphic grade and deformation on microstructures. *European Journal of Mineralogy*, 18(1):21–33.
- Bach, W., Garrido, C. J., Paulick, H., Harvey, J., and Rosner, M. (2004). Seawater-peridotite interactions : First insights from ODP leg 209, MAR 15°N. *Geochemistry, Geophysics, Geosystems*, 5.
- Bach, W., Paulick, H., Garrido, C. J., Ildefonse, B., Meurer, W. P., and Humphris, S. E. (2006). Unraveling the sequence of serpentization reactions : petrography, mineral chemistry, and petrophysics of serpentinites from MAR 15 N (ODP leg 209, site 1274). *Geophysical research letters*, 33(13).
- Beard, J. S. and Frost, B. R. (2017). The stoichiometric effects of ferric iron substitutions in serpentine from microprobe data. *International Geology Review*, 59(5-6):541–547.
- Bernoulli, D. and Weissert, H. (1985). Sedimentary fabrics in alpine ophicalcites, south pennine arosa zone, switzerland. *Geology*, 13(11):755–758.
- Blackman, D. K., Karson, J. A., Kelley, D. S., Cann, J. R., Früh-Green, G. L., Gee, J. S., Hurst, S. D., John, B. E., Morgan, J., Noonan, S. L., et al. (2002). Geology of the atlantis massif (mid-atlantic ridge, 30 n) : Implications for the evolution of an ultramafic oceanic core complex. *Marine Geophysical Researches*, 23(5):443–469.
- Boschi, C., Bonatti, E., Ligi, M., Brunelli, D., Cipriani, A., Dallai, L., D’Orazio, M., Früh-Green, G. L., Tonarini, S., Barnes, J. D., et al. (2013). Serpentization of mantle peridotites along an uplifted lithospheric section, mid atlantic ridge at 11 n. *Lithos*, 178:3–23.
- Bousquet, R., Oberhänsli, R., Goffé, B., Wiederkehr, M., Koller, F., Schmid, S. M., Schuster, R., Engi, M., Berger, A., and Martinotti, G. (2008). Metamorphism of metasediments at the scale of an orogen : a key to the tertiary geodynamic evolution of the alps. *Geological Society, London, Special Publications*, 298(1):393–411.
- Burkhard, D. J. and O’Neil, J. R. (1988). Contrasting serpentization processes in the eastern central alps. *Contributions to Mineralogy and Petrology*, 99(4):498–506.
- Cann, J. R., Blackman, D., Smith, D., McAllister, E., Janssen, B., Mello, S., Avgerinos, E., Pascoe, A., and Escartin, J. (1997). Corrugated slip surfaces formed at ridge-transform intersections on the mid-atlantic ridge. *Nature*, 385(6614):329–332.
- Cannat, M. (1993). Emplacement of mantle rocks in the seafloor at mid-ocean ridges. *Journal of Geophysical Research : Solid Earth*, 98(B3):4163–4172.

- Carlson, R. L. and Miller, D. J. (1997). A new assessment of the abundance of serpentinite in the oceanic crust. *Geophysical Research Letters*, 24(4):457–460.
- Chalot-Prat, F., Ganne, J., and Lombard, A. (2003a). No significant element transfer from the oceanic plate to the mantle wedge during subduction and exhumation of the tethys lithosphere (western alps). *Lithos*, 69(3-4):69–103.
- Chalot-Prat, F., Ganne, J., and Lombard, A. (2003b). No significant element transfer from the oceanic plate to the mantle wedge during subduction and exhumation of the tethys lithosphere (western alps). *Lithos*, 69(3-4):69–103.
- Christensen, N. I. (1972). The abundance of serpentinites in the oceanic crust. *The Journal of Geology*, 80(6):709–719.
- Coleman, R. G. (1971). Petrologic and geophysical nature of serpentinites. *Geological Society of America Bulletin*, 82(4):897–918.
- Coltat, R., Boulvais, P., Riegler, T., Pelleter, E., and Branquet, Y. (2021). Element distribution in the root zone of ultramafic-hosted black smoker-like systems : Constraints from an Alpine analog. *Chemical Geology*, 559.
- Coltat, R., Branquet, Y., Gautier, P., Rodriguez, H. C., Poujol, M., Pelleter, E., McCleaghan, S., Manatschal, G., and Boulvais, P. (2019). Unravelling the root zone of ultramafic-hosted black smokers-like hydrothermalism from an Alpine analog. *Terra Nova*, 31:549–561.
- Compagnoni, R., Cossio, R., and Mellini, M. (2021). Raman anisotropy in serpentine minerals, with a caveat on identification. *Journal of Raman Spectroscopy*, 52(7):1334–1345.
- Debret, B., Nicollet, C., Andreani, M., Schwartz, S., and Godard, M. (2013). Three steps of serpentization in an eclogitized oceanic serpentinization front (lanzo massif–western alps). *Journal of Metamorphic Geology*, 31(2):165–186.
- Delacour, A., Früh-Green, G. L., Frank, M., Gutjahr, M., and Kelley, D. S. (2008). Sr-and Nd-isotope geochemistry of the atlantis massif (30 n, mar) : implications for fluid fluxes and lithospheric heterogeneity. *Chemical Geology*, 254(1-2):19–35.
- Demartin, B. J., Sohn, R. A., Pablo Canales, J., and Humphris, S. E. (2007). Kinematics and geometry of active detachment faulting beneath the trans-atlantic geotraverse (tag) hydrothermal field on the mid-atlantic ridge. *Geology*, 35(8):711–714.
- Desmurs, L., Müntener, O., and Manatschal, G. (2002). Onset of magmatic accretion within a magma-poor rifted margin : a case study from the Platta ocean-continent transition, eastern Switzerland. *Contributions to Mineralogy and Petrology*, 144(3):365–382.
- Dessimoulie, L., Delacour, A., Guillaume, D., Chevet, J., and Cottin, J.-Y. (2020). Major and trace elements exchanges during fluid-rock interaction at ultraslow-spreading oceanic lithosphere : Example of the south west indian ridge (swir). *Lithos*, 352:105233.
- Dietrich, V. (1970). *Die Stratigraphie der Platta-Decke : Faziente Zusammenhänge zwischen Oberpenninikum und Unterostalpin*. Geologisches Institut der Eidg. Technischen Hochschule und der Universität
- Dietrich, V. J. (1969). *Die Ophiolithe des Oberhalbsteins (Graubünden) und das Ophiolithmaterial der ostschweizerischen Molasseablagerungen : ein petrographischer Vergleich*. PhD thesis, ETH Zurich.

- Dilek, Y., Coulton, A., Hurst, S. D., et al. (1997). Serpentinization and hydrothermal veining in peridotites at site 920 in the mark area. In *Proceedings-Ocean Drilling Program Scientific Results*, pages 35–60. National Science Foundation.
- Doebelin, N. and Kleeberg, R. (2015). Profex : a graphical user interface for the rietveld refinement program bgmn. *Journal of applied crystallography*, 48(5):1573–1580.
- Douville, E., Charlou, J. L., Oelkers, E. H., Bienvenu, P., Colon, C. F. J., Donval, J. P., Fouquet, Y., Prieur, D., and Appriou, P. (2002). The rainbow vent fluids ($36^{\circ}14N$, MAR) : the influence of ultramafic rocks and phase separation on trace metal content in Mid-Atlantic Ridge hydrothermal fluids. *Chemical Geology*, 184:37–48.
- Epin, M.-E. and Manatschal, G. (2018). Three-dimensional architecture, structural evolution, and role of inheritance controlling detachment faulting at a hyperextended distal margin : The example of the err detachment system (SE Switzerland). *Tectonics*, 37(12):4494–4514.
- Epin, M. E., Manatschal, G., Amman, M., Ribes, C., Clausse, A., Guffon, T., and Lescanne, M. (2019). Polyphase tectono-magmatic evolution during mantle exhumation in an ultra-distal, magma-poor rift domain : example of the fossil platta ophiolite, se switzerland. *International Journal of Earth Sciences*, 108:2443–2467.
- Escartin, J., Hirth, G., and Evans, B. (1997). Effects of serpentization on the lithospheric strength and the style of normal faulting at slow-spreading ridges. *Earth and Planetary Science Letters*, 151(3-4):181–189.
- Escartin, J., Hirth, G., and Evans, B. (2001). Strength of slightly serpentinized peridotites : Implications for the tectonics of oceanic lithosphere. *Geology*, 29(11):1023–1026.
- Evans, B. W. (1977). Metamorphism of alpine peridotite and serpentinite. *Annual Review of Earth and Planetary Sciences*, 5(1):397–447.
- Evans, B. W. (2004). The serpentinite multisystem revisited : chrysotile is metastable. *International Geology Review*, 46(6):479–506.
- Florineth, D. and Froitzheim, N. (1994). Transition from continental to oceanic basement in the tasna nappe : evidence for early cretaceous opening of the valais ocean. *Schweizerische Mineralogische und Petrographische Mitteilungen*, 74(3):437 ?448.
- Foustoukos, D. I., Savov, I. P., and Janecky, D. R. (2008). Chemical and isotopic constraints on water/rock interactions at the lost city hydrothermal field, 30 n mid-atlantic ridge. *Geochimica et Cosmochimica Acta*, 72(22):5457–5474.
- Froitzheim, N. (1994). Repeated change from crustal shortening to orogenparallel extension in the austroalpine units of graubunden. *Eclogae Geol.*, 87:559–612.
- Froitzheim, N. and Manatschal, G. (1996). Kinematics of jurassic rifting, mantle exhumation, and passive-margin formation in the austroalpine and penninic nappes (eastern switzerland). *Geological society of America bulletin*, 108(9):1120–1133.
- Froitzheim, N. and Rubatto, D. (1998). Continental breakup by detachment faulting : field evidence and geochronological constraints (tasna nappe, switzerland). *Terra Nova*, 10(4):171–176.
- FROST, B. R. (1985). On the stability of sulfides, oxides, and native metals in serpentinite. *Journal of Petrology*, 26(1):31–63.

- Frost, B. R. and Beard, J. S. (2007). On silica activity and serpentinization. *Journal of petrology*, 48(7):1351–1368.
- Früh-Green, G. L., Connolly, J. A., Plas, A., Kelley, D. S., and Grobety, B. (2004). Serpentinization of oceanic peridotites : implications for geochemical cycles and biological activity. *The subseafloor biosphere at mid-ocean ridges*, 144:119–136.
- Früh-Green, G. L., Plas, A., and Lécuyer, C. (1996). 14. petrologic and stable isotope constraints on hydrothermal alteration and serpentinization of the epr shallow mantle at hess deep (site 895). In *Proceedings of the ocean drilling program, scientific results*, volume 147, pages 255–291.
- Früh-Green, G. L., Scambelluri, M., and Vallis, F. (2001). O–h isotope ratios of high pressure ultramafic rocks : implications for fluid sources and mobility in the subducted hydrous mantle. *Contributions to Mineralogy and Petrology*, 141(2):145–159.
- Früh-Green, G. L., Weissert, H., and Bernoulli, D. (1990). A multiple fluid history recorded in Alpine ophiolites. *Journal of the Geological Society*, 147(6):959–970.
- Grauby, O., Baronnet, A., Devouard, B., Schoumacker, K., and Demirdjian, L. (1998). The chrysotile-polygonal serpentine-lizardite suite synthesized from a 3mgo-2siO₂-excess h2O gel. In *The 7th International Symposium on Experimental Mineralogy, Petrology, and Geochemistry, Orléans, Abstracts. Terra Nova, supplement*, volume 1, page 24.
- Guillong, M., Meier, D. L., Allan, M. M., Heinrich, C. A., Yardley, B. W., et al. (2008). Appendix a6 : Sills : A matlab-based program for the reduction of laser ablation icp-ms data of homogeneous materials and inclusions. *Mineralogical Association of Canada Short Course*, 40:328–333.
- Hochscheid, F., Colttat, R., Ulrich, M., Munoz, M., Manatschal, G., and Boulvais, P. (2022). The sr isotope geochemistry of oceanic ultramafic-hosted mineralizations. *Ore Geology Reviews*, page 104824.
- Iyer, K., Jamtveit, B., Mathiesen, J., Malthe-Sørenssen, A., and Feder, J. (2008). Reaction-assisted hierarchical fracturing during serpentinization. *Earth and Planetary Science Letters*, 267(3-4):503–516.
- Jamtveit, B., Putnis, C. V., and Malthe-Sørenssen, A. (2009). Reaction induced fracturing during replacement processes. *Contributions to Mineralogy and Petrology*, 157(1):127–133.
- Janecky, D. and Seyfried, W. (1986). Hydrothermal serpentinization of peridotite within the oceanic crust : Experimental investigations of mineralogy and major element chemistry. *Geochimica et Cosmochimica Acta*, 50(7):1357–1378.
- Jarosewich, E. (2002). Smithsonian microbeam standards. *Journal of research of the National Institute of Standards and Technology*, 107(6):681.
- Karson, J. A. and Rona, P. A. (1990). Block-tilting, transfer faults, and structural control of magmatic and hydrothermal processes in the tag area, mid-atlantic ridge 26° n. *Geological Society of America Bulletin*, 102(12):1635–1645.
- Kelley, D. S., Karson, J. A., Blackman, D. K., Früh-Green, G. L., Butterfield, D. A., Lilley, M. D., Olson, E. J., Schrenk, M. O., Roe, K. K., Lebon, G. T., et al. (2001). An off-axis hydrothermal vent field near the mid-atlantic ridge at 30 n. *Nature*, 412(6843):145–149.

- Klein, F., Grozeva, N. G., Seewald, J. S., McCollom, T. M., Humphris, S. E., Moskowitz, B., Berquo, T. S., and Kahl, W.-A. (2015). Experimental constraints on fluid-rock reactions during incipient serpentinization of harzburgite. *American Mineralogist*, 100(4):991–1002.
- Klein, F. and Roux, V. L. (2020). Quantifying the volume increase and chemical exchange during serpentinization. *Geology*, 48:552–556.
- Klinkhammer, G., Elderfield, H., Edmond, J., and Mitra, A. (1994). Geochemical implications of rare earth element patterns in hydrothermal fluids from mid-ocean ridges. *Geochimica et Cosmochimica Acta*, 58(23):5105–5113.
- Knauss, K. G., Nguyen, S. N., and Weed, H. C. (1993). Diopside dissolution kinetics as a function of ph, co₂, temperature, and time. *Geochimica et Cosmochimica Acta*, 57(2):285–294.
- Kodolányi, J., Pettke, T., Spandler, C., Kamber, B. S., and Gméling, K. (2012). Geochemistry of ocean floor and fore-arc serpentinites : constraints on the ultramafic input to subduction zones. *Journal of Petrology*, 53(2):235–270.
- Lafay, R., Baumgartner, L. P., Stephane, S., Suzanne, P., German, M.-H., and Torsten, V. (2017). Petrologic and stable isotopic studies of a fossil hydrothermal system in ultramafic environment (chenaillet ophicalcites, western alps, france) : processes of carbonate cementation. *Lithos*, 294:319–338.
- Lafay, R., Deschamps, F., Schwartz, S., Guillot, S., Godard, M., Debret, B., and Nicollet, C. (2013). High-pressure serpentinites, a trap-and-release system controlled by metamorphic conditions : Example from the piedmont zone of the western alps. *Chemical Geology*, 343:38–54.
- Langmuir, D. (1978). Uranium solution-mineral equilibria at low temperatures with applications to sedimentary ore deposits. *Geochimica et Cosmochimica Acta*, 42(6):547–569.
- Lavier, L. L., Roger Buck, W., and Poliakov, A. N. (1999). Self-consistent rolling-hinge model for the evolution of large-offset low-angle normal faults. *Geology*, 27(12):1127–1130.
- Lemaire, C. (2000). *Application des spectroscopies vibrationnelles à la détection d'amiante dans les matériaux et à l'étude des serpentines*. PhD thesis, Paris 7.
- Liu, W., Cao, Y., Zhang, J., Zhang, Y., Zong, K., and Jin, Z. (2020). Thermo-structural evolution of the val malenco (italy) peridotite : A petrological, geochemical and microstructural study. *Minerals*, 10(11):962.
- Longerich, H. P., Jackson, S. E., and Günther, D. (1996). Inter-laboratory note. laser ablation inductively coupled plasma mass spectrometric transient signal data acquisition and analyte concentration calculation. *Journal of analytical atomic spectrometry*, 11(9):899–904.
- Malvoisin, B., Brunet, F., Carlut, J., Rouméjon, S., and Cannat, M. (2012). Serpentinization of oceanic peridotites : 2. kinetics and processes of san carlos olivine hydrothermal alteration. *Journal of Geophysical Research : Solid Earth*, 117(B4).
- Manatschal, G. (2004). New models for evolution of magma-poor rifted margins based on a review of data and concepts from west iberia and the alps. *International Journal of Earth Sciences*, 93:432–466.
- Manatschal, G., Engström, A., Desmurs, L., Schaltegger, U., Cosca, M., Müntener, O., and Bernoulli, D. (2006). What is the tectono-metamorphic evolution of continental break-up : the example of the tasna ocean–continent transition. *Journal of Structural Geology*, 28(10):1849–1869.

- Manatschal, G. and Müntener, O. (2009). A type sequence across an ancient magma-poor ocean-continent transition : the example of the western alpine tethys ophiolites. *Tectonophysics*, 473(1-2):4–19.
- Manatschal, G. and Nievergelt, P. (1997). A continent-ocean transition recorded in the err and platta nappes (eastern switzerland). *Eclogae Geologicae Helvetiae*, 90(1):3–28.
- Martin, B. and Fyfe, W. (1970). Some experimental and theoretical observations on the kinetics of hydration reactions with particular reference to serpentinization. *Chemical Geology*, 6:185–202.
- McCaig, A. M., Delacour, A., Fallick, A. E., Castelain, T., and Früh-Green, G. L. (2010). Detachment fault control on hydrothermal circulation systems : Interpreting the subsurface beneath the tag hydrothermal field using the isotopic and geological evolution of oceanic core complexes in the atlantic. *Diversity of Hydrothermal Systems on Slow Spreading Ocean Ridges, Geophys. Monogr. Ser.*, 188:207–240.
- McDonough, W. F. and Sun, S.-S. (1995). The composition of the earth. *Chemical geology*, 120(3-4):223–253.
- Mellini, M., Trommsdorff, V., and Compagnoni, R. (1987). Antigorite polysomatism : behaviour during progressive metamorphism. *Contributions to Mineralogy and Petrology*, 97(2):147–155.
- Mével, C. (2003). Serpentinization of abyssal peridotites at mid-ocean ridges. *Comptes Rendus Geoscience*, 335(10-11):825–852.
- Moody, J. B. (1976). Serpentinization : a review. *Lithos*, 9(2):125–138.
- Müntener, O., Manatschal, G., Desmurs, L., and Pettke, T. (2010). Plagioclase peridotites in ocean-continent transitions : refertilized mantle domains generated by melt stagnation in the shallow mantle lithosphere. *Journal of Petrology*, 51(1-2):255–294.
- Müntener, O., Pettke, T., Desmurs, L., Meier, M., and Schaltegger, U. (2004). Refertilization of mantle peridotite in embryonic ocean basins : trace element and nd isotopic evidence and implications for crust-mantle relationships. *Earth and Planetary Science Letters*, 221(1-4):293–308.
- Müntener, O. and Piccardo, G. B. (2004). Melt migration in ophiolitic peridotites : The message from alpine-apennine peridotites and implications for embryonic ocean basins. *Geological Society Special Publication*, 218:69–89.
- Niu, Y. (2004). Bulk-rock major and trace element compositions of abyssal peridotites : implications for mantle melting, melt extraction and post-melting processes beneath mid-ocean ridges. *Journal of Petrology*, 45(12):2423–2458.
- Normand, C., Williams-Jones, A. E., Martin, R. F., and Vali, H. (2002). Hydrothermal alteration of olivine in a flow-through autoclave : Nucleation and growth of serpentine phases. *American Mineralogist*, 87(11-12):1699–1709.
- Oelkers, E. H., Declercq, J., Saldi, G. D., Gislason, S. R., and Schott, J. (2018). Olivine dissolution rates : A critical review. *Chemical Geology*, 500:1–19.
- Oelkers, E. H. and Schott, J. (2001). An experimental study of enstatite dissolution rates as a function of ph, temperature, and aqueous mg and si concentration, and the mechanism of pyroxene/pyroxenoid dissolution. *Geochimica et Cosmochimica Acta*, 65(8):1219–1231.

- O'hanley, D. S. (1991). Fault-related phenomena associated with hydration and serpentine recrystallization during serpentinitization. *The Canadian Mineralogist*, 29(1):21–35.
- O'Hanley, D. S. (1992). Solution to the volume problem in serpentinitization. *Geology*, 20(8):705–708.
- Parnell-Turner, R., Sohn, R., Peirce, C., Reston, T., MacLeod, C., Searle, R., and Simão, N. (2017). Oceanic detachment faults generate compression in extension. *Geology*, 45(10):923–926.
- Paulick, H., Bach, W., Godard, M., De Hoog, J., Suhr, G., and Harvey, J. (2006). Geochemistry of abyssal peridotites (mid-atlantic ridge, 15°N, odp leg 209) : implications for fluid/rock interaction in slow spreading environments. *Chemical geology*, 234(3-4):179–210.
- Pearce, N. J., Perkins, W. T., Westgate, J. A., Gorton, M. P., Jackson, S. E., Neal, C. R., and Chereny, S. P. (1997). A compilation of new and published major and trace element data for nist srm 610 and nist srm 612 glass reference materials. *Geostandards newsletter*, 21(1):115–144.
- Peters, D., Bretscher, A., John, T., Scambelluri, M., and Pettke, T. (2017). Fluid-mobile elements in serpentinites : Constraints on serpentinitisation environments and element cycling in subduction zones. *Chemical geology*, 466:654–666.
- Peters, P. C. and Mathews, J. (1963). Gravitational radiation from point masses in a keplerian orbit. *Physical Review*, 131(1):435.
- Peters, T. and Stettler, A. (1987a). Radiometric age, thermobarometry and mode of emplacement of the totalp peridotite in the eastern swiss alps. *Schweizerische Mineralogische und Petrographische Mitteilungen*, 67(3):285–294.
- Peters, T. and Stettler, A. (1987b). Time, physico-chemical conditions, mode of emplacement and geologic setting of the totalp peridotite in the eastern swiss alps. *Schweiz. Mineral. Petrogr. Mitt*, 67:285–294.
- Pettke, T., Kodolányi, J., and Kamber, B. S. (2018). From ocean to mantle : new evidence for u-cycling with implications for the himu source and the secular pb isotope evolution of earth's mantle. *Lithos*, 316:66–76.
- Picazo, S., Manatschal, G., Cannat, M., and Andréani, M. (2013). Deformation associated to exhumation of serpentinitized mantle rocks in a fossil Ocean Continent Transition : The Totalp unit in SE Switzerland). *Lithos*, 175:255–271.
- Picazo, S., Müntener, O., Manatschal, G., Bauville, A., Karner, G., and Johnson, C. (2016). Mapping the nature of mantle domains in Western and OCentral Europe based on clinopyroxene and spinel chemistry : Evidence for mantle modification during an extensional cycle. *Lithos*, 266:233–263.
- Piccardo, G. B. (2013). Subduction of a fossil slow–ultraslow spreading ocean : a petrology-constrained geodynamic model based on the voltri massif, ligurian alps, northwest italy. *International Geology Review*, 55(7):787–803.
- Plümper, O., Beinlich, A., Bach, W., Janots, E., and Austrheim, H. (2014). Garnets within geode-like serpentinite veins : Implications for element transport, hydrogen production and life-supporting environment formation. *Geochimica et Cosmochimica Acta*, 141:454–471.

- Rampone, E., Borghini, G., and Basch, V. (2020). Melt migration and melt-rock reaction in the alpine-apennine peridotites : Insights on mantle dynamics in extending lithosphere. *Geoscience Frontiers*, 11(1):151–166.
- Rampone, E., Hofmann, A. W., and Raczek, I. (1998). Isotopic contrasts within the internal liguride ophiolite (n. italy) : the lack of a genetic mantle-crust link. *Earth and Planetary Science Letters*, 163:175–189.
- Ramsay, J. G. (1980). The crack-seal mechanism of rock deformation. *Nature*, 284(5752):135–139.
- Ribeiro Da Costa, I., Barriga, F. J., Viti, C., Mellini, M., and Wicks, F. J. (2008). Antigorite in deformed serpentinites from the mid-atlantic ridge. *European Journal of Mineralogy*, 20(4):563–572.
- Ribes, C., Petri, B., Ghienne, J.-F., Manatschal, G., Galster, F., Karner, G. D., Figueredo, P. H., Johnson, C. A., and Karpoff, A.-M. (2020). Tectono-sedimentary evolution of a fossil ocean-continent transition : Tasna nappe, central alps (se switzerland). *GSA Bulletin*, 132(7-8):1427–1446.
- Rimstidt, J. D., Brantley, S. L., and Olsen, A. A. (2012). Systematic review of forsterite dissolution rate data. *Geochimica et Cosmochimica Acta*, 99:159–178.
- Rouméjon, S., Andreani, M., and Früh-Green, G. L. (2019). Antigorite crystallization during oceanic retrograde serpentinization of abyssal peridotites. *Contributions to Mineralogy and Petrology*, 174(7):1–25.
- Rouméjon, S. and Cannat, M. (2014). Serpentinization of mantle-derived peridotites at mid-ocean ridges : Mesh texture development in the context of tectonic exhumation. *Geochemistry, Geophysics, Geosystems*, 15(6):2354–2379.
- Rouméjon, S., Cannat, M., Agrinier, P., Godard, M., and Andreani, M. (2015). Serpentinization and fluid pathways in tectonically exhumed peridotites from the southwest indian ridge (62–65 e). *Journal of Petrology*, 56(4):703–734.
- Rouméjon, S., Williams, M. J., and Früh-Green, G. L. (2018). In-situ oxygen isotope analyses in serpentine minerals : Constraints on serpentinization during tectonic exhumation at slow-and ultraslow-spreading ridges. *Lithos*, 323:156–173.
- Sandiford, D., Brune, S., Glerum, A., Naliboff, J., and Whittaker, J. M. (2021). Kinematics of footwall exhumation at oceanic detachment faults : solid-block rotation and apparent unbending. *Geochemistry, Geophysics, Geosystems*, 22(4):e2021GC009681.
- Sauter, D., Cannat, M., Rouméjon, S., Andreani, M., Birot, D., Bronner, A., Brunelli, D., Carlut, J., Delacour, A., Guyader, V., et al. (2013). Continuous exhumation of mantle-derived rocks at the southwest indian ridge for 11 million years. *Nature Geoscience*, 6(4):314–320.
- Scambelluri, M., Müntener, O., Hermann, J., Piccardo, G. B., and Trommsdorff, V. (1995). Subduction of water into the mantle : history of an alpine peridotite. *Geology*, 23(5):459–462.
- Schaltegger, U., Desmurs, L., Manatschal, G., Müntener, O., Meier, M., Frank, M., and Bernoulli, D. (2002). The transition from rifting to sea-floor spreading within a magma-poor rifted margin : Field and isotopic constraints. *Terra Nova*, 14(3):156–162.

- Schwartz, S., Guillot, S., Reynard, B., Lafay, R., Debret, B., Nicollet, C., Lanari, P., and Auzende, A. L. (2013). Pressure–temperature estimates of the lizardite/antigorite transition in high pressure serpentinites. *Lithos*, 178:197–210.
- Schwarzenbach, E. M., Vogel, M., Früh-Green, G. L., and Boschi, C. (2021). Serpentinization, Carbonation, and Metasomatism of Ultramafic Sequences in the northern Apennine Ophiolite (NW Italy). *Journal of Geophysical Research : Solid Earth*, 126.
- Seyfried Jr, W. and Dibble Jr, W. (1980). Seawater-peridotite interaction at 300 °C and 500 bars : implications for the origin of oceanic serpentinites. *Geochimica et Cosmochimica Acta*, 44(2):309–321.
- Smith, D. K., Cann, J. R., and Escartín, J. (2006). Widespread active detachment faulting and core complex formation near 13°N on the mid-atlantic ridge. *Nature*, 442(7101):440–443.
- Snow, J. E. and Dick, H. J. (1995). Pervasive magnesium loss by marine weathering of peridotite. *Geochimica et Cosmochimica Acta*, 59(20):4219–4235.
- Tao, C., Seyfried, W., Lowell, R., Liu, Y., Liang, J., Guo, Z., Ding, K., Zhang, H., Liu, J., Qiu, L., et al. (2020). Deep high-temperature hydrothermal circulation in a detachment faulting system on the ultra-slow spreading ridge. *Nature communications*, 11(1):1–9.
- Tarling, M. S., Rooney, J. S., Viti, C., Smith, S. A., and Gordon, K. C. (2018). Distinguishing the raman spectrum of polygonal serpentine. *Journal of Raman Spectroscopy*, 49(12):1978–1984.
- Tarling, M. S., Smith, S. A., Rooney, J. S., Viti, C., and Gordon, K. C. (2021). A common type of mineralogical banding in serpentine crack-seal veins. *Earth and Planetary Science Letters*, 564:116930.
- Thompson, G. and Melson, W. G. (1970). Boron contents of serpentinites and metabasalts in the oceanic crust : implications for the boron cycle in the oceans. *Earth and Planetary Science Letters*, 8(1):61–65.
- Trommsdorff, V. (1983). Metamorphose magnesiumreicher gesteine : kristallischer vergleich von natur, experiment und thermodynamischer datenbasis. *Fortschritte der Mineralogie*, 61(2):283–308.
- Trommsdorff, V. and Evans, B. W. (1977). Antigorite-ophicarbonates : contact metamorphism in valmalenco, italy. *Contributions to Mineralogy and Petrology*, 62(3):301–312.
- Ulrich, M., Muñoz, M., Boulvais, P., Cathelineau, M., Cluzel, D., Guillot, S., and Picard, C. (2020). Serpentinization of new caledonia peridotites : from depth to (sub-) surface. *Contributions to Mineralogy and Petrology*, 175(9):1–25.
- Vils, F., Müntener, O., Kalt, A., and Ludwig, T. (2011). Implications of the serpentine phase transition on the behaviour of beryllium and lithium–boron of subducted ultramafic rocks. *Geochimica et Cosmochimica Acta*, 75(5):1249–1271.
- Viti, C. and Mellini, M. (1997). Contrasting chemical compositions in associated lizardite and chrysotile in veins from elba, italy. *European Journal of Mineralogy*, 9(3):585–596.
- Viti, C. and Mellini, M. (1998). Mesh textures and bastites in the elba retrograde serpentinites. *Eur. J. Mineral.*, 10:1341–1359.
- Weissert, B. J. H. and Bernoulli, D. (1985). A transform margin in the Mesozoic Tethys : evidence from the Swiss Alps. *Geologische Rundschau*, 74:665–679.

Wicks, F. J. and Whittaker, E. (1977). Serpentine textures and serpentinization. *The Canadian Mineralogist*, 15(4):459–488.

Wunder, B. and Schreyer, W. (1997). Antigorite : High-pressure stability in the system MgO-SiO₂-H₂O (msh). *Lithos*, 41(1-3):213–227.

Chapitre 5

**Fluid and mineral geochemistry
during experimental seawater-based
serpentinization**

Abstract

At (ultra-)slow spreading settings (mid-ocean ridges and rifted margins) mantle exhumation leads to the serpentinization of ultramafic rocks exposed at the seafloor. The hydrothermal alteration of primary iron bearing minerals such as olivine and pyroxene leads to the oxidation of the ferrous iron, coupled to the reduction of molecular water. Such a redox reaction leads to the release of molecular H₂, an energetic gas, also considered as a fuel-for-life in anaerobic environments. Additionally, serpentinization reactions may also be involved in the formation of (ultramafic-)volcanic massive sulfide (U-VMS) deposits in which numerous transition metals concentrate. The latter process implies important mass fluxes, widely documented in the field, but still poorly investigated experimentally. Indeed, most of hydrothermal experiments in the literature focused on basalt-hosted hydrothermal systems. In order to characterize the mass fluxes that occur during serpentinization, a series of batch reaction between fresh peridotites powder and natural seawater were conducted at 450 bar, from 225 to 325°C, and during 500 to 3290 h. The resulting serpentinite was characterized by SEM and XRD, and H₂ degassing was measured using gas chromatography. Major and trace element mobility were investigated by : i) monitoring the chemical composition of fluid through time, and ii) analyzing reactant solid products at the end of experiments. Our results show that primary minerals were almost completely replaced by a mineral assemblage dominated by serpentine and magnetite, with minor amounts of calcite precipitate at 225, 280 and 325°C. H₂ maximum production is observed at 280-300°C, reaching 80-100 mmol/kg. Mass balance calculations show that transition metals such as Cr, Co, Ni and Zn are significantly transferred to the fluid, suggesting that serpentinite-derived fluids may play a key-role in the formation of U-VMS. Hence, ophiolites bearing serpentinized mantle rocks may represent a potential resource of transition metals that may be targeted for exploration in the forthcoming years.

Keywords : Serpentinization, Hydrothermal experiments, Chemical mobilities, Reaction pathways, U-VMS

5.1 Introduction

Seafloor expeditions have shown that Mid-ocean ridge (MOR) systems are affected by important hydrothermal circulations, highlighted by hydrothermal vents on the seafloor. About 65% of hydrothermal sites recorded on the seafloor, are located at MOR (Hannington et al., 2005). The sampling of these hydrothermal vents, reveals that fluids are discharged under a wide range of temperature, pH and chemical compositions (e.g., Von Damm 1990; Hannington et al. 2005; Humphris and Klein 2018). These hydrothermal circulations induce important mass transfer between the lithosphere and the hydrosphere, and the formation of a variety of mineral deposits such as polymetallic nodules, cobalt rich crusts and polymetallic volcanic massive sulfides. These deposits are composed by elements of economic interest such as Cu, Zn, Pb, Au and Ag (e.g., Jamieson and Gartman 2020).

The seafloor expeditions provided access to the hydrothermal vents and associated metals deposits, allowing to measure their chemical compositions. However, today their process of formation, as well the source of metals remains poorly constrained, because fluids can interact with a variety of rocks (i.e. mafic, ultramafic and sediments). Moreover, several type of fluids can interact with these rocks (i.e., seawater, serpentinizing fluids, magmatic fluids, e.g., Von Damm 1990) that make the understanding of this process more difficult. Similarly, temperatures of the hydrothermal vents can be directly measured before fluid sampling and/or estimated by stable isotopes (e.g., Shanks III 2001), but temperatures of fluid/rock interactions leading to these hydrothermal vents and associated metal deposits remain still poorly constrained.

At slow and ultra-slow spreading settings (MOR), large-offset normal (detachment) fault allowed to expose ultramafic rocks on the seafloor (e.g., Cann et al. 1997). Numerous hydrothermal sites are hosted by these faults, such as Rainbow, Lost City or Logatchev which are preferentially pathways for fluids circulations (e.g., Escartín et al. 2008). Interactions of seawater with ultramafic rocks results in serpentinization reactions which can occurred over a wide range of temperature, from $\pm 450^{\circ}\text{C}$ to lower than 50°C (e.g., Agrinier et al. 1995 ; Früh-Green et al. 1996 ; Früh-Green et al. 2004). During this process, important mineral changes and mass transfer occurred and reducing conditions can be generated (e.g., Allen and Seyfried Jr 2003). Mineral changes associated to serpentinization are relatively well know, but the related mass transfers, and particularly how trace elements metals are mobilized are less clear.

Numerous hydrothermal experiments have been carried out with the aim of understanding the chemistry of fluids observed in basalt and gabbro-hosted MOR hydrothermal systems (Seyfried and Bischoff 1977; Seyfried Jr and Mottl 1982; Mottl and Holland 1978; Mottl et al. 1979; Seewald and Seyfried Jr 1990), however fluids issuing from ultramafic-hosted hydrothermal systems have been less studied, and only a few of hydrothermal experiments were focus on the chemical composition of resulting fluids (Seyfried Jr and Dibble Jr 1980; Janecky and Seyfried Jr 1986; Allen and Seyfried Jr 2003; Seyfried Jr et al. 2007). Although numerous ultramafic hydrothermal experiments were done in the past decades, most of them was focus solely on solid products (e.g., Malvoisin et al. 2012; Lafay et al. 2012). With exception of the study of Seyfried Jr and Dibble Jr 1980 who conducted serpentinization experiments using natural seawater and Seyfried Jr et al. 2007 who reproduced the real composition of seawater by adjusting concentrations of chloride, sulfate and bicarbonate and were focused more on resulting fluids composition, most of the serpentinization experiments were conducted using deionized water or with \pm Na/Cl (e.g., Martin and Fyfe 1970; Wegner et al. 1983; Marcaillou et al. 2011; Lafay et al. 2012; Malvoisin and Brunet 2014; McCollom et al. 2016; McCollom et al. 2020a,b). The use of Na/Cl or deionized water displays numerous advantages. Firstly, deionized water is available in most of laboratory of geochemistry, and Na/Cl is easy to prepare and is a option of lower cost. Indeed, certified standards of seawater are expensive, and not everyone have the possibility to go sampling seawater in the ocean. Secondly, for the problematic of most previous study, the use of Na/Cl solution was enough because they only focused on solid products. However, the used of this kind of solutions are not optimum for understand the resulting fluid chemistry during serpentinization. Indeed, some studies have shown that serpentinites integrated seawater sulfates (e.g., Delacour et al. 2008a,b; Alt et al. 2013; Schwarzenbach et al. 2021). More recently Huang et al. 2018) have shown that serpentine minerals can integrate significant amounts of chlorine.

In this study, we propose to characterize fluids and mineralogical changes associated to serpentinization experiments with natural seawater, at temperature ranging from 225°C to 325°C, with the aim to better understanding the composition of hydrothermal vent fluids and metals mobilization related to ultramafic rock serpentinization.

5.2 Methods

In order to characterize and quantify the effect of temperature and seawater on chemical mobility occurring during serpentinization, a series of six experiments were conducted in this study, as summarized in (Table 5.1). Four lherzolite-seawater experiments were conducted at nominal temperatures of 225°C, 260°C, 300°C and 325°, with reaction times ranging between 1728 and 3288 hours. Additionally, two harzburgite-seawater experiments were done at 280°C and duration time of 504 hours and 1996 hours. For all these hydrothermal experiments, water/rock mass ratios (W/R) were comprised between 1.6 and 2.2.

TABLE 5.1 – Summary of experimental parameters. W/R : water/rock ratios.

exp	T	time	mass	mass	W/R	Peridotite
	(°C)	(h)	of fluid	of rock		type
ISTO1	300	1992	60.15	97.91	1.6	Lhz Cpt1806
ISTO2	225	3288	99.05	60.72	1.6	Lhz Cpt1806
ISTO3	260	1944	45.47	100.3	2.2	Lhz Cpt1806
ISTO4	325	1728	61.5	118.83	1.9	Lhz Cpt1806
ISTO5	280	504	60.48	116.43	1.9	Hzb Cpt1801
ISTO6	280	1296	61.79	132.16	2.1	Hzb Cpt1801

5.2.1 Starting materials

Fresh peridotites were sampled at Mont-Coupet (French Massif-Central), where they occurred as xenoliths in a basaltic flow. Two distinct protoliths were used for hydrothermal experiments. The first one is a spinel-lherzolite (Cpt1806) and the second one is a spinel-harzburgite (Cpt1801). The lherzolite contains 13.2 vol.% of clinopyroxene and 61.2 vol.% of olivine, while the harzburgite contains a significantly lower proportion of clinopyroxene (4.50 vol.%) but an higher proportions of olivine (72.4 vol.%). Both peridotites have relatively similar proportions of orthopyroxene (23.6 and 22.4 vol.%, respectively, Table 5.3). The chemical compositions in major and trace elements for both peridotites are given in Table 5.2.

The initial composition in major and minor elements of primary minerals for both harzburgite (Cpt18-01) and lherzolite (Cpt18-06) used (Table 5.2), and are in the range

of peridotites from the same locality (Downes and Dupuy 1987; Xu et al. 1998). Bulk compositions in major, minor and trace elements of both protolith is show in Table 5.4.

Before hydrothermal experiments, peridotites were disaggregated and grounded in an agate ball miller to fine particles with an average grain size $<20\ \mu\text{m}$. Natural seawater was sampled in the Atlantic ocean near the French coast. Seawater was filtered with 45 μm cellulose filters, and its chemical major and trace element composition (mmol/kg) is presented in Table 5.

5.2.2 Experimental setup

Hydrothermal experiments were performed at the Institut des Sciences de la Terre d'Orléans (ISTO). Peridotite powders and natural seawater were loaded into a flexible titanium reaction cell with titanium exit tube and sampling valve, placed in a steel-alloy autoclave filled with water, as described by Seyfried Jr et al. 1987. All titanium surfaces in contact with the fluid were cleaned with nitric acid and oxidized in a furnace at 400°C for a minimum of 12 hours prior to each experiments. The flexible titanium bag permits external control of pressure. The pressure was regulated at the beginning of each experiments and controlled during the entirely course of experiments using a piston-pump (PMHP100-500, Top Industries) which can inject and pump water into the autoclave in order to maintain the requested pressure. The titanium sample valve allows for the periodic sampling of fluids during experiments for chemical characterization. Fluid sampled periodically using gas-tight glass syringes, which prevent the loss of volatile species, like hydrogen. The temperature was controlled by thermocouple ($\pm 1^\circ\text{C}$) measuring the temperature of the confining water as close as possible to the Titanium bag. All hydrothermal experiments were performed at 45 MPa total pressure and various temperature and time mentioned before (Table 5.1). Each experiments were terminated by shutting off the power supply of the furnace, allowing the vessel to cool down to room conditions in about 12 hours. Due to the large volume of the autoclave, no quenching was possible.

5.2.3 Solid samples analyses

A small fraction of each experiments was taken for X-Ray Diffraction (XRD) and Scanning Electron Microscope (SEM) analyses. X-Ray Diffraction analyses were performed at the Institut Terre et Environnement de Strasbourg laboratory (ITES, University of Strasbourg) using a Bruker D8 advance eco diffractometer. A large X-ray beam was emitted by a copper source with a 40 kV accelerating voltage and a 25 mA current. Intensities were recorded at $0.014^\circ 2\theta$ step intervals from 3 to 80° , with a dwell time of 0.8s. Size of the divergence slit was 0.4° . Semi quantitative mineralogical compositions in Table 5.3 were determined by Rietveld refinement using Profex-BGMM programs (Doebelin and Kleeberg 2015). The mineral phases were identified based on JCPDS/ICDD and AMCD references. X-Ray Diffraction patterns and summary of the rietveld refinement are available in Supplementary Material at the end of this chapter. SEM analyses were performed on powders by a Merlin compact Zeiss instrument at the Institut des Sciences de la Terre d'Orléans laboratory (ISTO), using both secondary (SE) and back scattered electron (BSE) detectors (resolution 15 kV, 0.8 nm). One solid product (ISTO 300) was analyzed by Raman spectrometry using a HORIBA LabRAM ARAMIS spectrometer at the Laboratoire des sciences de l'ingénieur, de l'informatique et de l'imagerie (ICube, University of Strasbourg).

The in situ chemical composition of peridotite-bearing minerals before hydrothermal experiments were measured on $30 \mu\text{m}$ thick polished thin sections using a (μ -XRF) fluorescence Brucker M4 Tornado instrument at ITES laboratory (University of Strasbourg). The spot size was $20 \mu\text{m}$, under a 50 kV acceleration voltage and intensity of 400 μA , for 180s counting time.

The bulk rock composition in major and minor elements of peridotites before and after hydrothermal experiments were also measured by (μ -XRF) at ITES laboratory (University of Strasbourg). For each samples, 10 measurements were performed in order to check the reproducibility. The spot size was 1 mm, under a 50 kV acceleration voltage and intensity of 700 μA , for 300s counting time.

Trace elements compositions were measured by Inductively Coupled Plasma Mass Spectrometry (ICP-MS) using a Thermo Scientific iCAP RQ instrument at ITES laboratory (University of Strasbourg). Following the analytical procedure of Chauvel et al. 2011, about 100 mg of rock powder was precisely weighed and dissolved in Savillex beakers in a HF-HNO₃-HClO₄ (5:1:1) mixture, during a minimum of 7 days at 140°C on a hot plate. The solution was then evaporated and the residue dissolved in concentrated

HNO_3 and evaporated before dilution in about 40 ml of 7 M HNO_3 .

TABLE 5.2 – In situ composition in major and minor elements of primary minerals from harzburgite (Cpt18-01) and lherzolite (Cpt18-06) used in hydrothermal experiments measured by μ -XRF. Mg# = $100 * \text{Mg} / (\text{Mg} + \text{Fe})$

	Cpt1801 ol (n=4)	Cpt1801 cpx (n=7)	Cpt1801 opx (n=10)	Cpt1801 spl (n=4)	Cpt1806 ol (n=7)	Cpt1806 cpx (n=3)	Cpt1806 opx (n=13)	Cpt1806 sp (n=6)
<i>Major (wt.%)</i>								
SiO ₂	39.7	53.6	55.8	0.000	39.7	52.2	54.4	0.000
TiO ₂	0.006	0.260	0.120	0.254	0.030	0.660	0.150	0.065
Al ₂ O ₃	0.053	3.25	1.73	26.7	0.070	6.37	3.66	58.5
Fe ₂ O ₃	6.13	2.08	4.05	19.8	7.31	2.54	4.91	10.4
MgO	53.2	16.8	37.1	14.5	52.1	14.9	35.6	21.7
CaO	0.264	21.8	0.696	0.115	0.280	21.4	0.860	0.056
MnO	0.135	0.091	0.097	0.149	0.100	0.060	0.120	0.124
Na ₂ O	0.202	0.622	0.000	-	0.100	0.940	0.000	-
K ₂ O	0.006	0.000	0.006	0.003	0.000	0.000	0.060	-
Cr ₂ O ₃	0.002	1.44	0.362	38.1	0.020	0.770	0.240	8.68
Total	99.7	99.9	99.9	99.5	99.7	99.9	99.9	99.6
Mg#	88.2	87.5	88.8	38.6	86.0	83.5	86.2	64.2
Cr#	0.039	0.364	0.213	0.648	0.270	0.135	0.078	0.161
<i>Minor (ppm)</i>								
Ni	1929	394	476	1634	1831	586	353	2852
Cu	19.8	11.5	83.8	194	9.37	22.1	14.5	0.000
Zn	17.1	50.9	31.9	1358	26.8	84.2	24.9	899
<i>Atoms</i>								
	4 (O)	6 (O)	6 (O)		4 (O)	6 (O)	6 (O)	
Si	0.96	1.94	1.92		0.97	1.89	1.88	
Ti	0.00	0.01	0.00		0.00	0.02	0.00	
Al	0.00	0.14	0.07		0.00	0.27	0.15	
Fe ²⁺	0.12	0.06	0.23		0.15	0.08	0.28	
Mg	1.93	0.91	1.90		1.90	0.80	1.83	
Ca	0.01	0.84	0.03		0.01	0.83	0.03	
Mn	0.00	0.00	0.00		0.00	0.00	0.00	
Na	0.01	0.04	0.00		0.00	0.07	0.00	
K	0.00	0.00	0.00		0.00	0.00	0.00	
Cr	0.00	0.04	0.01		0.00	0.02	0.01	

5.2.4 Aqueous solution samples analyses

Dissolved hydrogen was determined with a Perkin-Elmer Clarus 580 gas chromatograph (GC), using a 30 m, 0.53 mm (ID) fused silica capillary column (Carboxen 1010 PLOT) (Superclo) and a thermal conductivity captor (TCD), at ISTO. Hydrogen quantification was made following the procedure described by Fauguerolles 2016. For each sampling, three analyses were performed to check the reproducibility.

The major element analyses, fluids were diluted 100 times in 2M HNO₃ and then analyzed by inductively coupled plasma atomic emission spectroscopy (ICP-AES) using a Thermo Scientific ICAP 6500 instrument (cations) and ion chromatography (IC) using a ICS-5000+ Thermo Fischer instrument for anions.

Trace element concentrations were analyzed by diluting sampled fluids 100 times in 0.5M HNO₃, before measurements with inductively coupled plasma mass spectrometry (ICP-MS ; Thermo Scientific iCAP-RQ instrument). Both analyses were performed at ITES laboratory (University of Strasbourg).

5.3 Results

5.3.1 Characterization of solid phase reactants and products

Following the experiments, solid products from both lherzolite-seawater and harzburgite-seawater experiments were carefully characterized in term of mineralogy and geochemistry. Representative minerals of solid products observed by SEM at the end of hydrothermal experiments are show in (Figure 5.1). The proportion of each minerals at the end of hydrothermal experiment was estimated by Rietveld refinement are summarized in (Table 5.3). This method is relatively efficient for anhydrous samples and well crystallized minerals, typically the primary olivine, pyroxenes and spinel contained in fresh peridotites, which are characterized by "beautiful" spikes in XRD patterns. In contrast, hydrated samples and particularly phyllosilicates minerals like serpentine, brucite or talc (the potential minerals formed during serpentization) have extended spikes on the XRD patterns. Figure 5.2 mineral proportions are graphically represented versus temperature and time.

TABLE 5.3 – Summary of minerals identified in protoliths and solid products at the end of seawater-peridotite experiments. Mineral phases are detected by X-ray diffraction on powder, and their proportion (%) are estimated by the Rietveld refinement method of Doebelin and Kleeberg 2015 using Profex software. Aragonite, anhydrite and halite are always below the detection limits and thus not represented in this table.

Sample	Phases XRD	Phases SEM	Fo	Di	En	Srp	Spl	Mag	Cal	Talc	Brc	sum
Cpt1806	Fo-Di-En-Spl	Fo-Di-En-Spl	61.2	13.2	23.6	2.10	-	-	-	-	-	100.1
IST03	Srp-Mag-Di-Spl-Fo-Cal	Srp-Mag-Di-Spl-Cal	3.78	8.29	-	1.37	85.7	0.350	0.547	-	-	bdl
IST02	Srp-Mag-Di-Spl-Fo-Cal	Srp-Mag-Di-Spl-Fo	1.51	8.75	-	1.21	85.0	2.72	0.779	-	-	bdl
IST01	Srp-Mag-Di-Spl-Fo-Cal-Tlc	Srp-Mag-Di-Spl	4.61	9.09	-	0.629	79.6	4.69	0.400	0.940	bdl	100.0
IST04	Srp-Mag-Di-Fo-Cal-Hal	Srp-Mag-Di-Spl-Fo-Anh-Hal	6.83	10.4	-	0.391	77.7	3.93	0.748	-	-	bdl
Cpt1801	Fo-Di-En-Spl	Fo-Di-En-Spl	72.4	4.50	22.4	0.730	-	-	-	-	-	100.0
IST05	Srp-Di-Spl-Fo-Cal	Srp-Mag-Di-Spl-Fo-Brc-Cal-Arg	11.5	4.22	-	0.952	78.8	1.91	1.15	-	1.45	100.0
IST06	Srp-Mag-Di-Spl-Fo-Cal	Srp-Mag-Di-Spl-Fo-Brc-Cal	6.62	3.29	-	1.14	84.9	1.65	0.580	-	1.84	100.0

SEM observations

In all solids products from both lherzolite-seawater and harzburgite-seawater experiments, residual clinopyroxene and olivine are observed by SEM and consist of crystals of $\sim 20 \mu\text{m}$ which are characterized by dissolution features such as denticles and etch pits (Figure 5.1A, B, D). Residual orthopyroxene was never observed by SEM. Residual spinel are characterized by multi-faceted crystals of variable size ranging between $5\text{--}20 \mu\text{m}$ (Figure 5.1E). Serpentine is the main secondary mineral formed during the hydrothermal experiment. Serpentine forms dense aggregates constituted by stubby and short fibers of $\sim 2 \mu\text{m}$ long and formed elongated fibers $>10\mu\text{m}$ in experiment ISTO 4 at 325°C (Figure 5.1F). Chrysotile is the dominant serpentine polymorph identified by the Raman spectrometry (see Supplementary material). Magnetite crystals are observed in all solid products and display rather well-shaped and their mean size are $\sim 2 \mu\text{m}$ and never exceeding $10\mu\text{m}$ (Figure 5.1B, E). Brucite occurred as platy euhedral crystals of size mostly $>20 \mu\text{m}$ (Figure 5.1C, D), and were only observed in harzburgite-seawater experiments (i.e., ISTO 5, 6). Calcite crystals forms typical cubic shape of $\sim 10\text{--}15 \mu\text{m}$ (Figure 5.1C), and was not observed in experiment ISTO 1 and 2 (i.e., lherzolite-seawater experiement at 300 and 260°C , respectively, Table 5.3). Aragonite crystals that are $>20 \mu\text{m}$ long are only observed in experiment ISTO 5 (i.e., harzburgite-seawater at 280°C and 21 days of reaction, 5.1G). Halite and anhydrite crystals were observed in experiment ISTO 4 (i.e., lherzolite-seawater at 325°C , Figure 5.1H).

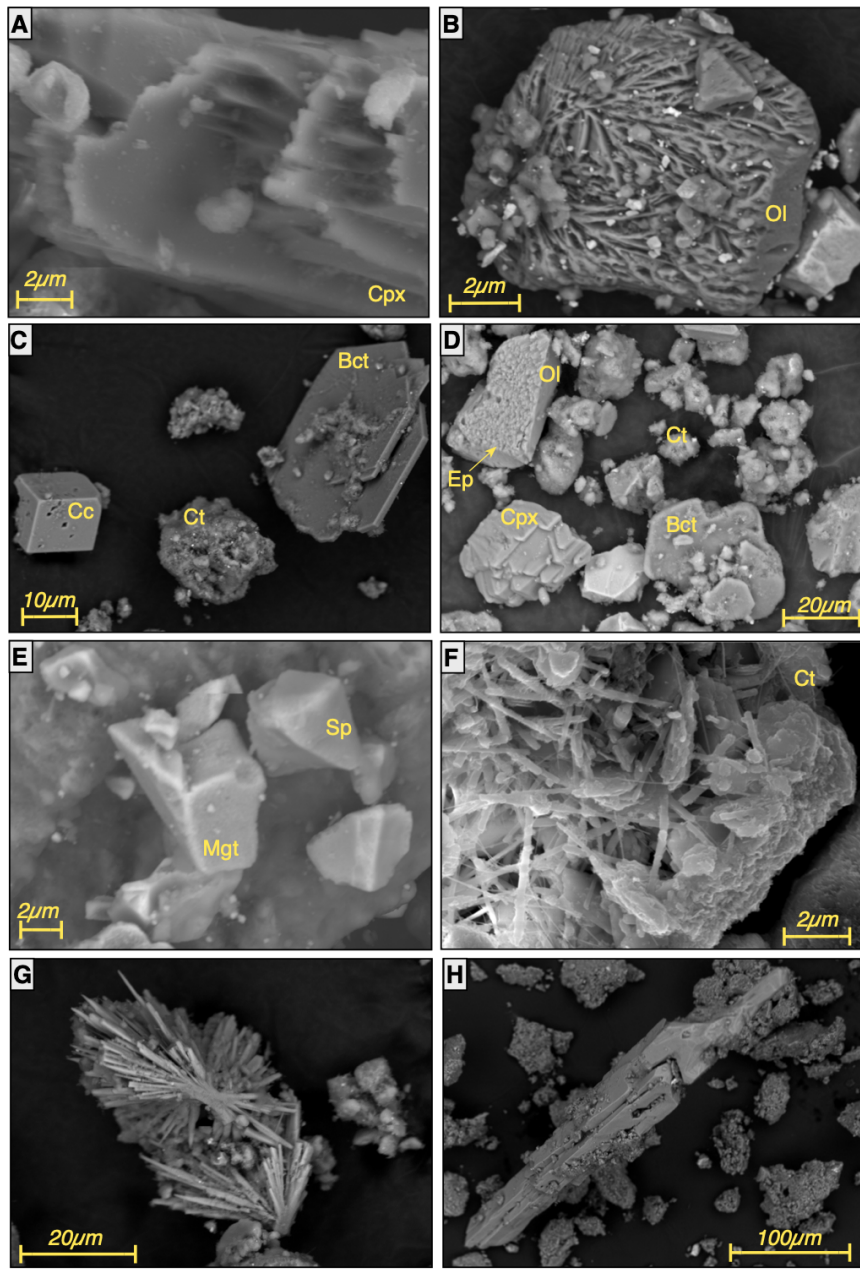


FIGURE 5.1 – SEM characterization of solid reaction products from the lherzolite-seawater and harzburgite-seawater experiments. A) Etch pitch on residual clinopyroxene (Cpx) from experiment ISTO2. B) Olivine (Ol) dissolution features from experiment ISTO3. C) Cubic calcite (Cc), euhedral hexagonal shaped brucite (Bct) crystal and chrysotile (Ct) serpentine observed in at the end of experiment ISTO5. D) Etch pits (Ep) in olivine, dissolution features associated to clinopyroxene and euhedral hexagonal brucite observed in experiment ISTO6. E) Euhedral and octahedral crystals of magnetite (Mgt) and spinel (Sp) from experiment ISTO1. F) Chrysotile fibers in experiment ISTO4. G) Aragonite crystal observed in experiment ISTO5. H) Anhydrite crystal from experiment ISTO4.

Mineral proportions

Lherzolite-seawater experiments

At the end of lherzolite-seawater experiments, in all solid products, primary clinopyroxene, olivine and spinel are still present and constitute approximately 15 to 20 vol.% of the solid products (Table 5.3; Figure 5.2A). Estimated proportions of clinopyroxene ranged from ~ 8.29 to ~ 10.4 vol.%, olivine are comprising between ~ 1.95 vol.% to ~ 6.83 vol.% and estimated proportions of spinel are < 1.37 vol.% (Table 5.3; Figure 5.2A). Residuals orthopyroxene was not observed by SEM nor XRD, and estimated proportions are below the detection limits. Serpentine, magnetite and calcite were the principal secondary phases formed, with calculated proportions of serpentine ranging between 77.7 vol.% at 325°C and 85.7 vol.% at 225°C after 3288 hours of reaction. Magnetite concentrations range from ~ 0.35 vol.% at 225°C and 4.69 at 300°C. Concentration of calcite minerals are systematically below 1 vol.% (Table 5.3; Figure 5.2A). In the experiment ISTO 3 at 300°C, talc was identified by XRD although it was not observed by SEM, its estimated proportion was ~ 0.940 vol.% (Table 5.3). In solid products from experiment ISTO 4 at 325°C, anhydrite and halite crystals were occasionally identified by SEM and XRD, but estimated proportions were below the detection limits (Table 5.3).

Harzburgite-seawater experiments

In solid products of the harzburgite-seawater experiments, in contrast to the lherzolite-seawater experiments, estimated proportions of clinopyroxene are in the range of the initial protolith ~ 4.22 vol.% after 504 hours of interaction and 3.29 vol.% after 1296 hours of experiment (Table 5.3; Figure 5.2B). Proportions of olivine minerals are comprise between ~ 6.62 vol.% to ~ 11.5 vol.%, and spinel are comprise between ~ 0.952 and 1.14 vol.% (Table 5.3; Figure 5.2B). Similar to the lherzolite-seawater experiments, the proportions of serpentine minerals ranged from ~ 78.8 vol.% to ~ 84.9 vol.% after 21 days and 55 days of reaction, respectively, (Table 2; Figure 5.2B). Magnetite proportions range between ~ 1.65 and 1.91 vol.% (Table 5.3). Small proportions of calcite occur, in similar proportions to those observed in lherzolite-seawater experiments, mostly < 1.15 vol.% (Table 5.3; Figure 5.2B). Small amounts of brucite were detected in the both harzburgite-experiments and range between ~ 1.45 and ~ 1.84 vol.% (Table 5.3). In the shorter experiment ISTO 5, aragonite was observed by SEM, but in proportions below

detection limits of XRD (Table 5.3).

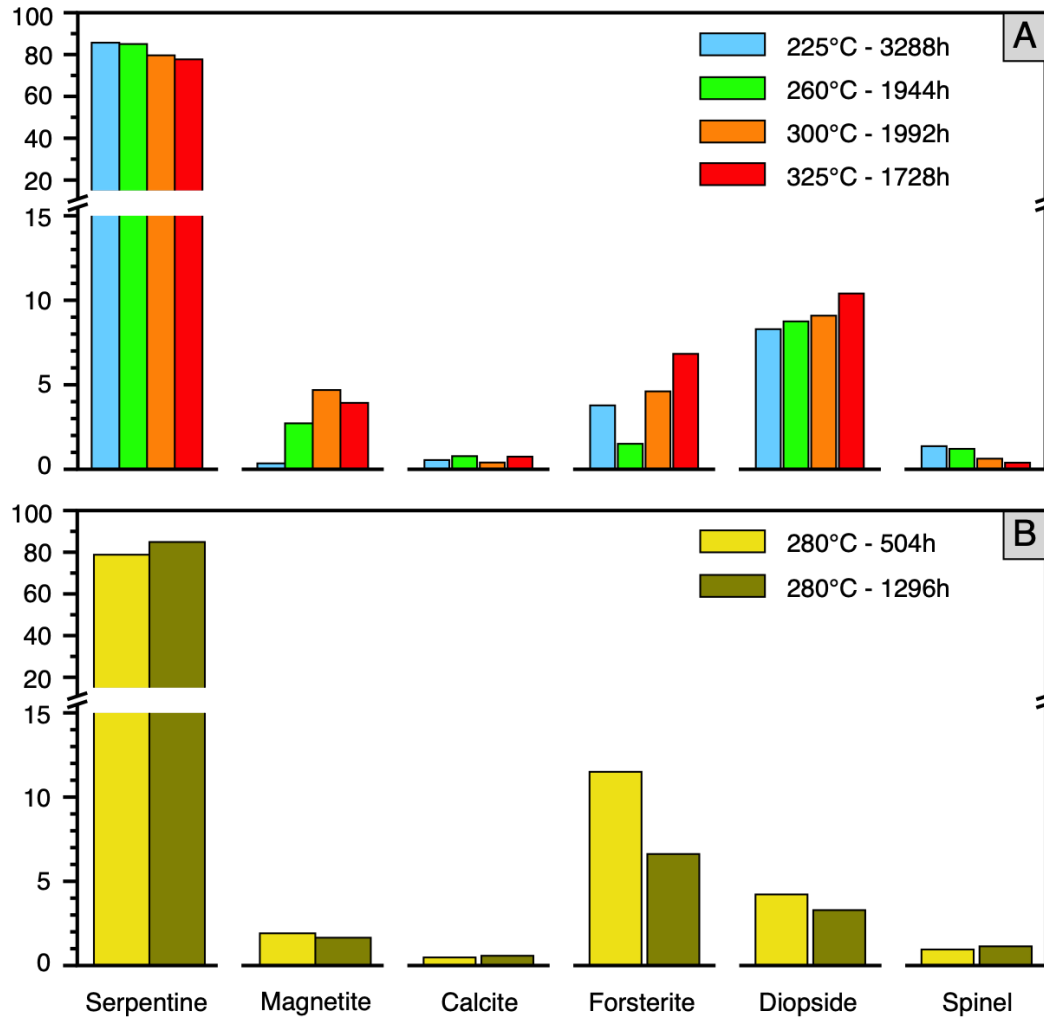
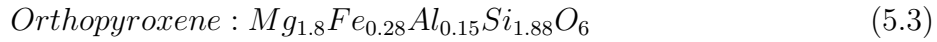


FIGURE 5.2 – Schematic representation of the mineral proportions estimated at the end of lherzolite seawater experiments ISTO 1-4 (A) and the harzburgite-seawater experiments ISTO 5 and 6 (B).

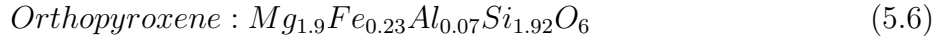
Geochemical composition of reactant and product minerals

The chemical composition of primary minerals was measured in both protoliths before hydrothermal experiments (Table 5.2). Olivine structural formula was calculated on the basis of 4 oxygens, while those for clinopyroxene and orthopyroxene were calculated on the basis of 6 oxygens (Table 5.2).

Primary olivine, clinopyroxene and orthopyroxene from lherzolite protolith gives the following structural formulae :



Primary minerals from harzburgite protolith have relatively similar compositions than those from the lherzolite protolith, with the respective structural formulae :



The composition of solid reaction products was not yet determined, but will be carried out subsequently by electron microprobe analysis.

5.3.2 Bulk rock geochemistry

Lherzolite-seawater experiments

Solid products (i.e., serpentinites) contain significantly higher H₂O compared to the initial protolith (i.e., fresh peridotites) with loss on ignition (LOI) ranging from 10.9 to 14.3 (Table 5.4). The concentrations in SiO₂ and Fe₂O₃ are systematically lower than those in the initial protolith, with SiO₂ contents comprised between 42.1 and 43.9 wt.%, and Fe₂O₃ contents comprised between 8.60 and 9.55 wt.%. In contrast Mg and Ca contents are mostly higher in solids products with MgO concentrations ranging between 39.1 and 42.0 wt.%, CaO from 2.34 to 4.14 wt.%. Concentration in Al₂O₃ range from 1.96 to 3.25 wt.% in solid products (Table 5.4).

Solid products have concentrations in transition metals lower than the initial protolith, with the respective concentration ranges : Cr 2225-2412 ppm, Ni 1551-1737 ppm, Cu 16.4-25.6 ppm, Zn 26.4-44.2 ppm, V 51.2-86.5 ppm and Co 95.7-117 ppm (Table 5.4). At the opposite, the lherzolite contains \sim 1943 ppm of Ni, \sim 2827 ppm of Cr, \sim 48.2 ppm of Zn, \sim 19.9 ppm of Cu and \sim 101 ppm of V (Table 5.4).

Harzburgite-seawater experiments

Similarly to the lherzolite-seawater experiments, solid products from harzburgite-seawater experiments contain significantly H₂O with LOI ranging from 14.2 to 15.8 (Table 5.4). Solids products have relatively similar concentration in SiO₂ and Fe₂O₃ (\sim 42.7 wt.% and \sim 8.40 wt.%, in average respectively). Concentration of MgO is comprised between 46.6 and 47.37 wt.% which is significantly higher than in solid products from the lherzolite-seawater experiments, in contrast solid products from harzburgite-seawater experiments have lower concentrations in Al₂O₃ and CaO, with \sim 0.37wt.% and 0.67 wt.% (in average respectively, Table 5.4).

Concentrations of transition metals are relatively in the same proportions in the two harzburgite experiments ISTO 5 and ISTO 6, however compared to solid products from the lherzolite experiments, concentration of Cr and Ni are higher with \sim 3550 and \sim 1839 ppm (in average, respectively Table 5.4). Compared to the lherzolite experiments, solid products from the harzburgite-seawater experiments have lower concentrations in Cu and Zn with \sim 14.1 ppm and \sim 35.2 ppm (in average, Table 5.4), but relatively similar concentrations in Co with an average concentration of 118 ppm (Table 5.4), concentration in V range from 29.0 to 71.1 ppm (Table 5.4). The initial harzburgite contains \sim 2315 ppm of Ni, \sim 4467 ppm of Cr, \sim 35.4 ppm of Zn, \sim 15.1 ppm of Cu and \sim 71 ppm of V (Table 5.4).

TABLE 5.4 – Bulk rock composition (anhydrous) in major and minor elements measured by μ -XRF before and after hydrothermal experiments. Mg# = 100*Mg/Mg+Fe

	Cpt1806	225	260	300	325	325 dup	Cpt1801	280	280 Bis
<i>Major (wt.%)</i>									
SiO ₂	44.2	42.4	43.9	42.9	42.3	42.1	44.1	42.7	42.7
TiO ₂	0.104	0.215	0.152	0.137	0.103	0.110	0.028	0.031	0.032
Al ₂ O ₃	2.86	2.25	1.96	3.25	2.41	2.46	0.552	0.371	0.367
Fe ₂ O ₃	9.75	9.41	9.41	9.55	8.66	8.60	8.63	8.42	8.37
MgO	39.6	41.4	41.6	39.1	42.0	41.9	44.8	46.6	47.4
CaO	2.76	3.77	2.34	4.14	3.35	3.32	0.805	1.06	0.312
MnO	0.140	0.129	0.126	0.139	0.120	0.118	0.128	0.115	0.122
Na ₂ O	0.135	0.003	0.106	0.342	0.700	1.07	0.282	0.078	0.157
K ₂ O	0.000	0.000	0.000	0.002	0.000	0.000	0.000	0.000	0.000
Cr ₂ O ₃	0.418	0.409	0.397	0.478	0.371	0.366	0.659	0.623	0.598
LOI	0.550	13.5	14.3	10.9	12.1	12.1	0.040	15.8	14.2
Total	98.5	99.6	99.9	99.9	99.8	99.7	98.7	100	99.9
Mg#	77.8	79.1	79.2	77.9	80.7	80.8	81.7	82.7	83.0
<i>Minor (ppm)</i>									
Cr	2827	2412	2323	2912	2225	2195	4467	3590	3511
Ni	1943	1679	1599	1737	1551	1535	2315	1834	1845
Cu	19.9	25.6	16.4	18.6	23.4	24.2	15.1	13.9	14.2
Zn	48.2	44.2	26.4	41.5	34.3	33.3	47.0	35.4	35.0
Sr	8.96	37.2	7.48	7.49	15.3	14.6	3.48	7.32	1.74
<i>Trace (ppm)</i>									
Li	-	-	5.10	6.80	5.60	-	-	5.60	6.00
V	101	-	51.2	86.5	69.2	-	59.3	71.1	29.0
Co	124	-	117	95.7	110	-	148	110	125
Cu	13.2	-	15.8	15.7	9.40	-	6.60	10.8	6.00
Zn	51.0	-	22.0	29.8	28.0	-	49.6	30.0	29.0
As	-	-	0.180	0.140	0.250	-	-	0.130	0.080
Rb	0.130	-	0.040	-	0.120	-	0.130	0.030	-
Sr	10.6	-	3.68	8.97	23.8	-	3.60	10.1	2.26
Y	2.32	-	1.28	2.20	2.13	-	0.300	2.16	0.264
Zr	4.16	-	2.44	3.62	3.45	-	1.63	3.65	1.47
Nb	0.380	-	0.217	0.210	0.215	-	0.220	0.196	0.110
Cd	0.018	-	0.256	-	0.103	-	0.017	0.035	0.057
Sn	0.300	-	8.20	0.680	0.500	-	0.700	0.600	0.700
Sb	-	-	0.930	-	0.060	-	-	-	-
Cs	-	-	0.004	-	0.008	-	-	0.002	-
Ba	3.98	-	1.89	1.18	1.79	-	1.50	0.770	0.290
La	0.447	-	0.248	0.412	0.377	-	0.287	0.379	0.246
Ce	0.873	-	0.500	0.848	0.700	-	0.367	0.740	0.320
Pr	0.100	-	0.053	0.099	0.086	-	0.036	0.089	0.028
Pm	-	-	0.256	0.490	0.442	-	-	0.465	0.128
Nd	0.525	-	0.263	0.525	0.450	-	0.161	0.466	0.129
Sm	0.210	-	0.095	0.195	0.181	-	0.059	0.175	0.049
Eu	0.081	-	0.042	0.074	0.073	-	0.023	0.071	0.019
Gd	0.304	-	0.128	0.284	0.255	-	0.069	0.266	0.055
Tb	0.058	-	0.031	0.057	0.053	-	0.014	0.053	0.008
Dy	0.402	-	0.214	0.396	0.359	-	0.059	0.374	0.048
Ho	0.090	-	0.047	0.091	0.086	-	-	0.081	0.010
Er	0.290	-	0.155	0.268	0.255	-	0.030	0.268	0.032
Tm	0.042	-	0.022	0.040	0.039	-	0.008	0.037	0.005
Yb	0.297	-	0.162	0.289	0.263	-	0.039	0.254	0.036
Lu	0.045	-	0.026	0.045	0.041	-	0.009	0.040	0.007
Hf	0.173	-	0.066	0.120	0.102	-	0.181	0.114	0.031
Ta	0.028	-	0.004	0.002	0.004	-	0.049	0.003	0.006
W	38.0	-	18.4	20.7	18.8	-	55.0	18.8	39.6
Pb	0.190	-	1.50	1.20	1.15	-	0.080	1.09	0.120
Th	0.070	-	0.025	0.024	0.025	-	0.200	0.024	0.021
U	0.018	-	0.033	0.021	0.015	-	0.013	0.019	0.010

5.3.3 Fluid chemistry

Fluid compositions of lherzolite-seawater experiments conducted at temperatures ranging from 225°C to 325°C are summarized in Table 5.5 and presented in Figure 5.3. The initial seawater chemistry was significantly modified during seawater-peridotite experiments (Table 5.5, Figure 5.3). Dissolved major elements display a complex evolution in fluid with reaction progress, depending to the temperature and the duration of the experiments.

Dissolved major elements

Concentrations of dissolved Na, Cl, K, SO₄²⁻

Dissolved concentrations of Na, Cl, K and SO₄²⁻ are represented in Figure 5.3. Initial seawater contains about 448 mmol/L of Na, 551 mmol/L of Cl, 10.5 mmol/L of K and 59.9 mmol/L of SO₄²⁻ (Table 5.5). Concentrations of these elements changed greatly during the course of experiments, which is probably a consequence of the low water/rock ratios used in our experiments (1.6-2.2, Table 4.3.4). Indeed, if water/rock ratios used is low, little variations in concentrations of elements release or uptake during the serpentinization reaction will be directly recorded by fluid concentrations. In contrast, at high water/rock ratios are high (>10), little variations will be not visible in fluid composition.

The concentrations of Na, Cl, K, SO₄²⁻ in fluids from all experiments, are strongly modified (Figure 5.3) and three distinct stages can be observed. Although the experiment at 280°C (ISTO 6) is based on a different protolith (i.e., harzburgite), the dissolved species Na, Cl, K and SO₄²⁻ display similar patterns with time, to those in the lherzolite experiments and have concentrations in the same range (Table 5.5, Figure 5.3). Consequently, in this section the data from both experiments will be observed together. Between 0-750 hours of reaction (stage 1), concentrations in Na and K in fluids at 225°C, 300°C and 325°C, decrease of about half compared to the initial seawater. In contrast, in fluid from the experiment at 260°C, concentrations of Na and K increase at 539 and 11.7 mmol/L, respectively. At 280°C concentrations in Na and Cl in the fluid increase between 0 and 500 hours.

Between ~750-1500 hours of reaction (stage 2), concentrations of Na and K increase in all fluids, but are still lower than the initial seawater value (Figure 5.3). Concentrations of Na and K measured in fluids at 225°C, 260°C and 280°C are in average ~400

mmol/L and \sim 8 mmol/L, respectively (Table 5.5). In fluids from experiments at 300°C and 325°C, concentrations in Na and K are lower than in fluids from lower temperatures of experiment with in Na <300 mmol/L and K \sim 6 mmol/L.

Finally, after 1500 hours and until the end of experiment, concentrations of Na and K increase in fluids from all experiments, and reach concentrations higher than the initial seawater with Na >448 mmol/L and K >10.5 mmol/L (Table 5.5, Figure 5.3), suggesting that Na and K was released by solid phases during serpentinization experiments. In contrast, in fluid from 225°C, concentrations of Na and K decrease reaching 181 and 4.12 mmol/L, respectively (Table 5.5, Figure 5.3), suggesting that Na and K was integrated in a solid phase that precipitate in the last step of reaction.

The measured concentration in Cl in fluids are systematically lower than the initial seawater (Table 5.5, Figure 5.3) highlighting that Cl is consumed during the serpentinization. In fluid from the experiment at 225°C, concentration of Cl decrease slightly during the whole reaction from about ± 200 to ± 150 mmol/L at the end of the experiment (Table 5.5, Figure 5.3). Similar to the experiment at 225°C, concentrations in Cl in fluids from the experiment at 260°C, 280°C and 325°C remains relatively constant until 1500h of reaction at about ± 290 mmol/L, ± 310 mmol/L and ± 260 mmol/L respectively (Table 5.5). The concentration of Cl in fluid from the experiment at 300°C display a more complex evolution, with concentration relatively stable at ~ 414 mmol/L between 0 and 264h of reaction and then decrease at about 281 mmol/L at 1500h of reaction.

At stage 3, after 1500h of reaction, concentrations in Cl increase strongly in fluids from experiments at 260°C, 300°C and 325°C and reach concentrations >400 mmol/L, but remain still lower than the initial seawater value (Table 5.5, Figure 5.3), suggesting that a part of the Cl was still integrated in solid phases.

The concentrations of SO_4^{2-} display similar patterns in most experiments, and are relatively constant before 1500h in fluid from the experiment at 225°C and during the entirely time of reaction at about 2000h for the other experiments (Figure 5.3). The concentrations of SO_4^{2-} are constant during the entirely experiment and only slightly below the seawater value at about ± 55 mmol/L and ± 58 mmol/L, respectively (Table 5.5, Figure 5.3). However, after 1500h of reaction, concentration of SO_4^{2-} in fluid from the experiment at 225°C decrease and reach a concentration of ± 5 mmol/L after 2500h of reaction (Table 5.5, Figure 5.3).

In fluid from experiment at 300°C, the concentration of SO_4^{2-} is about ± 31 mmol/L which is half as in fluids from experiments at 225°C and 260°C and the initial seawater

(Table 5.5, Figure 5.3). The concentrations of SO_4^{2-} measured in fluids at 280°C and 325°C are very low during the entirely experiment, with about 3 mmol/L and ± 3.5 mmol/L, respectively (Table 5.5, Figure 5.3).

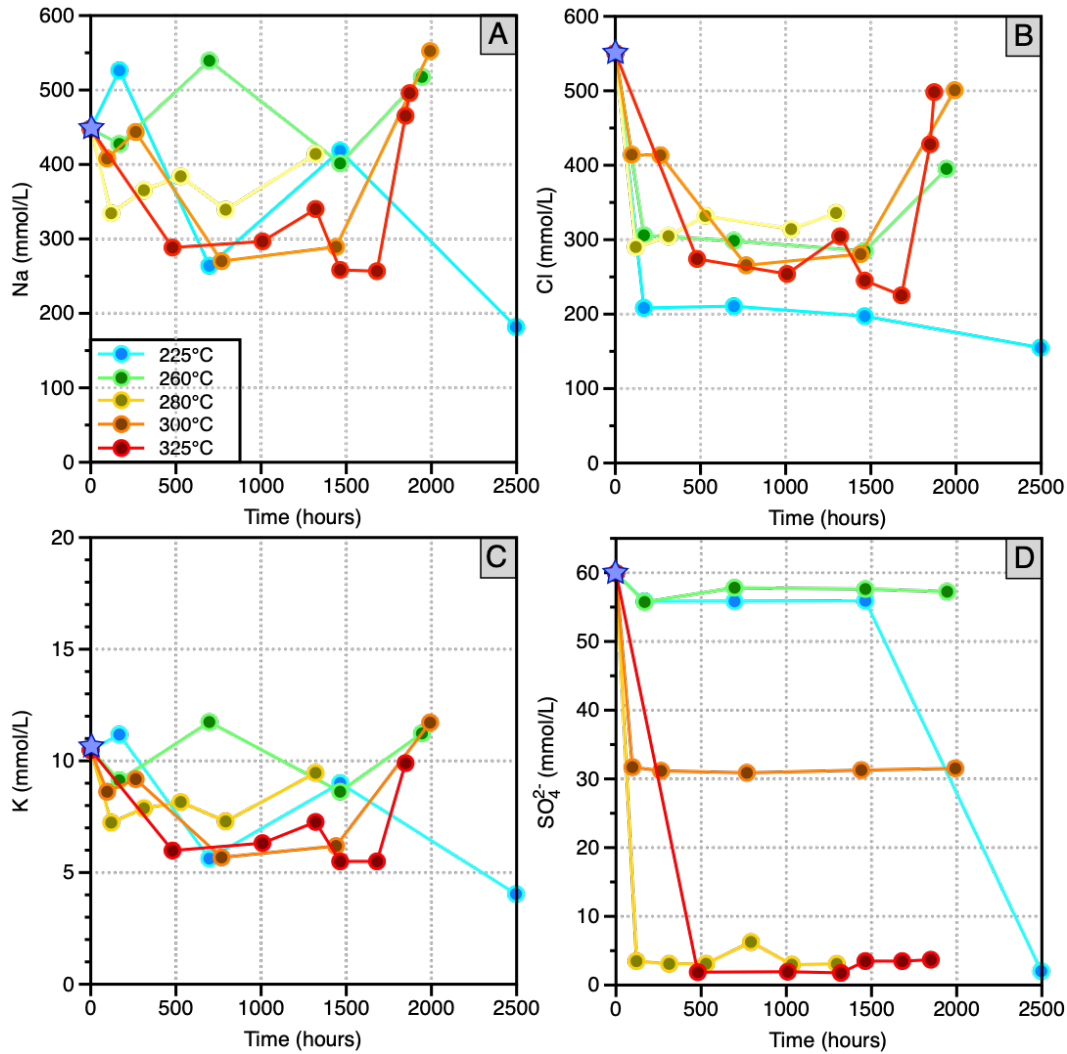


FIGURE 5.3 – Changes in concentrations of selected trace elements A) Na, B) Cl, C) K and D) SO_4^{2-} in fluid during lherzolite-seawater experiment (ISTO 1-4) at 225°C (blue), 260°C (green), 300°C (orange) and 325 °C (red) and harzburgite seawater experiment (ISTO 6) at 280°C (yellow). Blue star represent concentration in initial seawater.

TABLE 5.5 – Concentration of dissolved $\text{Cl}, \text{SO}_4^{2-}$ and H_2 (mmol/L) measured by chromatography ionic and gas chromatography in the fluids during interaction the serpen-tinization experiments. (-) not analyzed

Experiments	time (hour)	mmol/kg (IS-GS)			mmol/kg (ICP-AES)								
		Cl	SO_4^{2-}	H_2		Si	Al	Mg	Ca	Fe	Mn	Ti	Na
ISTO SW in	0	551	59.9	-	0.178	0.000	52.7	12.1	0.038	0.000	0.000	448	10.5
ISTO 300 T0	24	489	55.9	-	0.360	0.022	49.4	9.66	0.000	0.000	0.000	448	9.74
ISTO 300 T1 (+4)	96	414	31.7	0.146	0.609	0.022	3.31	21.3	0.003	0.027	0.000	408	8.62
ISTO 300 T2 (+11)	264	413	31.2	1.78	0.919	0.037	1.34	30.9	0.004	0.038	0.000	444	9.18
ISTO 300 T3 (+32)	768	266	30.9	38.8	0.096	0.015	0.008	9.06	0.000	0.000	0.000	270	5.68
ISTO 300 T4 (+60)	1440	281	31.3	45.00	0.025	0.000	0.000	5.26	0.000	0.001	0.000	289	6.19
ISTO 300 T5 (+83)	1992	501	31.5	96.8	0.021	0.000	0.029	7.96	0.000	0.000	0.000	552	11.7
ISTO 300 Tf AC (+84)	2016	561	42.5	-	0.000	0.222	0.165	20.8	0.000	0.000	0.000	570	14.8
ISTO 260 T1 (+7)	168	306	55.7	0.278	0.684	0.000	2.20	24.7	0.000	0.014	0.000	428	9.13
ISTO 260 T2 (+29)	696	298	57.8	27.6	0.694	0.022	0.008	14.7	0.000	0.000	0.000	539	11.7
ISTO 260 T3 (+61)	1464	285	57.6	15.4	0.623	0.000	0.000	7.16	0.000	0.000	0.000	401	8.62
ISTO 260 T4 (+81)	1944	395	57.2	28.4	0.260	0.000	0.000	8.78	0.000	0.000	0.000	518	11.2
ISTO 260 Tf AC (+83)	1992				0.000	0.148	0.165	26.7	0.029	0.000	0.000	618	14.3
ISTO 225 T1 (+7)	168	208	55.9	0.068	0.595	0.000	12.3	21.3	0.003	0.014	0.000	526	11.2
ISTO 225 T2 (+29)	696	211	55.9	0.068	0.164	0.000	0.786	13.3	0.000	0.001	0.000	264	5.63
ISTO 225 T3 (+61)	1464	197	55.9	11.7	0.046	0.019	0.033	12.8	0.000	0.000	0.000	418	9.00
ISTO 225 T4 (+104)	2496	155	2.03	15.1	0.032	0.022	0.012	3.97	0.000	0.000	0.000	182	4.04
ISTO 225 T5 (+126)	3024	46.8	2.02	23.20	0.018	0.030	0.012	3.67	0.000	0.000	0.000	181	4.12
ISTO 225 T6 (+137)	3288	268	2.54	46.20	0.025	0.022	0.000	6.56	0.000	0.000	0.000	296	6.34
ISTO 225 Tf AC (+138)	3312	284	6.94	39.50	0.285	0.259	0.206	17.5	0.000	0.000	0.000	360	7.93
ISTO 325 T0	24	-	-	-	0.320	0.011	23.9	4.44	0.000	0.001	0.000	211	4.86
ISTO 325 T1 (+20)	480	274	1.88	3.47	0.541	0.000	0.555	22.0	0.000	0.036	0.000	288	5.98
ISTO 325 T2 (+42)	1008	254	1.94	37.8	0.075	0.000	0.008	12.4	0.000	0.001	0.000	297	6.32
ISTO 325 T3 (+50)	1320	305	1.78	-	0.071	0.015	0.169	11.4	0.000	0.000	0.000	340	7.26
ISTO 325 T4 (+66)	1464	245	3.49	36.7	0.057	0.011	0.021	8.21	0.000	0.001	0.000	258	5.50
ISTO 325 T5 (+72)	1680	225	3.48	32.9	0.057	0.019	0.016	7.86	0.000	0.000	0.000	257	5.50
ISTO 325 T6 (+73)	1848	428	3.68	-	0.121	0.015	0.025	12.9	0.000	0.000	0.000	465	9.90
ISTO 325 Tf AC	1872	498	14.8	-	0.214	0.000	0.123	29.2	0.020	0.000	0.000	496	11.0
ISTO 280 T0	24	209	3.69	-	0.207	0.019	28.7	5.29	0.004	0.000	0.000	256	5.58
ISTO 280 T1 (+6)	168	189	3.50	3.92	0.142	0.000	2.90	7.66	0.000	0.006	0.000	234	5.06
ISTO 280 T2 (+13)	336	126	3.43	22.6	0.036	0.000	0.243	6.21	0.000	0.000	0.000	225	4.83
ISTO 280 T3 (+)	384	260	3.80	-	0.032	0.019	0.169	4.94	0.000	0.000	0.000	156	3.61
ISTO 280 T4 (+21)	504	255	10.8	43.2	0.117	0.015	0.037	6.44	0.000	0.000	0.000	260	5.70
ISTO 280 Tf AC (+22)	528	-	-	-	0.000	0.185	0.206	20.0	0.000	0.000	0.000	322	9.72
ISTO 280 bis T0	24	186	12.4	-	0.199	0.000	22.3	3.94	0.000	0.000	0.000	200	4.50
ISTO 280 bis T1 (+5)	120	290	3.48	4.29	0.235	0.019	10.4	7.39	0.000	0.056	0.000	334	7.24
ISTO 280 bis T2 (+13)	312	305	3.08	43.4	0.050	0.015	2.77	8.58	0.000	0.021	0.000	365	7.88
ISTO 280 bis T3 (+22)	528	332	3.09	46.4	0.018	0.011	0.272	8.26	0.000	0.000	0.000	384	8.16
ISTO 280 bis T4 (+33)	792	645	6.27	-	0.028	0.000	0.099	8.21	0.000	0.000	0.000	339	7.29
ISTO 280 bis T5 (+43)	1032	314	2.96	87.6	0.000	0.004	0.082	8.11	0.000	0.000	0.000	324	7.29
ISTO 280 bis T6 (+54)	1296	336	3.08	-	0.000	0.000	0.041	11.2	0.000	0.000	0.000	392	8.82
ISTO 280 bis Tf AC (+55)	1320	-	-	-	0.000	0.148	0.288	25.2	0.030	0.000	0.000	414	9.46

Experiments	time (hour)	mmol/kg	(ICP-MS)												
			Li	B	V	Cr	Mn	Co	Ni	Cu	Zn	Ga	Ge	Rb	Sr
ISTO SW in	0	0.032	0.460	0.000	0.000	0.001	0.000	0.000	0.004	0.000	0.000	0.000	0.000	0.001	0.089
ISTO 300 T0	24	0.029	0.314	0.000	0.000	0.001	0.000	0.001	0.006	0.000	0.000	0.000	0.000	0.000	0.068
ISTO 300 T1 (+4)	96	0.055	0.173	0.000	0.000	0.027	0.000	0.002	0.011	0.023	0.000	0.000	0.000	0.039	
ISTO 300 T2 (+11)	264	0.076	0.228	0.000	0.000	0.037	0.000	0.001	0.018	0.012	0.000	0.000	0.000	0.042	
ISTO 300 T3 (+32)	768	0.032	0.107	0.000	0.000	0.001	0.000	0.000	0.003	0.000	0.000	0.000	0.000	0.023	
ISTO 300 T4 (+60)	1440	0.020	0.033	0.001	0.000	0.001	0.000	0.000	0.003	0.000	0.000	0.000	0.000	0.023	
ISTO 300 T5 (+83)	1992	0.035	0.060	0.006	0.000	0.001	0.000	0.000	0.005	0.000	0.000	0.000	0.000	0.042	
ISTO 300 Tf AC (+84)	2016	0.035	0.052	0.000	0.000	0.001	0.000	0.001	0.006	0.003	0.000	0.000	0.000	0.065	
ISTO 260 T1 (+7)	168	0.056	0.153	0.000	0.000	0.013	0.000	0.001	0.007	0.005	0.000	0.000	0.000	0.000	0.022
ISTO 260 T2 (+29)	696	0.073	0.062	0.000	0.000	0.000	0.000	0.000	0.005	0.000	0.007	0.000	0.000	0.000	0.030
ISTO 260 T3 (+61)	1464	0.039	0.039	0.000	0.000	0.000	0.000	0.000	0.005	0.000	0.022	0.000	0.000	0.000	0.025
ISTO 260 T4 (+81)	1944	0.049	0.052	0.000	0.000	0.000	0.000	0.000	0.005	0.000	0.017	0.000	0.000	0.000	0.033
ISTO 260 Tf AC (+83)	1992	0.052	0.047	0.000	0.000	0.001	0.000	0.000	0.005	0.000	0.000	0.000	0.000	0.000	0.067
ISTO 225 T1 (+7)	168	0.062	0.243	0.001	0.000	0.014	0.000	0.001	0.012	0.012	0.000	0.000	0.000	0.000	0.031
ISTO 225 T2 (+29)	696	0.043	0.045	0.000	0.000	0.001	0.000	0.000	0.003	0.002	0.000	0.000	0.000	0.000	0.016
ISTO 225 T3 (+61)	1464	0.073	0.045	0.001	0.000	0.001	0.000	0.000	0.006	0.002	0.000	0.000	0.000	0.000	0.031
ISTO 225 T4 (+104)	2496	0.024	0.017	0.000	0.000	0.000	0.000	0.000	0.002	0.000	0.000	0.000	0.000	0.000	0.015
ISTO 225 T5 (+126)	3024	0.026	0.018	0.001	0.000	0.001	0.000	0.000	0.002	0.000	0.000	0.000	0.000	0.000	0.015
ISTO 225 T6 (+137)	3288	0.043	0.032	0.001	0.000	0.000	0.000	0.000	0.003	0.000	0.000	0.000	0.000	0.000	0.024
ISTO 225 Tf AC (+138)	3312	0.045	0.031	0.000	0.000	0.000	0.000	0.000	0.004	0.000	0.000	0.000	0.000	0.000	0.040
ISTO 325 T0	24	0.014	0.154	0.000	0.000	0.002	0.000	0.004	0.004	0.000	0.000	0.000	0.000	0.000	0.032
ISTO 325 T1 (+20)	480	0.039	0.103	0.000	0.000	0.034	0.000	0.000	0.008	0.005	0.000	0.000	0.000	0.000	0.021
ISTO 325 T2 (+42)	1008	0.027	0.077	0.000	0.000	0.001	0.000	0.000	0.003	0.000	0.007	0.000	0.000	0.000	0.022
ISTO 325 T3 (+50)	1320	0.029	0.081	0.000	0.000	0.001	0.000	0.000	0.004	0.000	0.004	0.000	0.000	0.000	0.027
ISTO 325 T4 (+66)	1464	0.022	0.062	0.000	0.000	0.001	0.000	0.000	0.003	0.000	0.003	0.000	0.000	0.000	0.021
ISTO 325 T5 (+72)	1680	0.020	0.048	0.000	0.000	0.001	0.000	0.000	0.003	0.000	0.001	0.000	0.000	0.000	0.024
ISTO 325 T6 (+73)	1848	0.037	0.101	0.000	0.000	0.001	0.000	0.000	0.004	0.000	0.000	0.000	0.000	0.000	0.045
ISTO 325 Tf AC	1872	0.042	0.062	0.000	0.000	0.001	0.000	0.000	0.005	0.000	0.000	0.000	0.000	0.000	0.079
ISTO 280 T0	24	0.016	0.219	0.000	0.000	0.001	0.000	0.000	0.004	0.003	0.000	0.000	0.000	0.000	0.040
ISTO 280 T1 (+6)	168	0.039	0.069	0.000	0.000	0.006	0.000	0.000	0.004	0.005	0.000	0.000	0.000	0.000	0.010
ISTO 280 T2 (+13)	336	0.043	0.048	0.000	0.000	0.001	0.000	0.000	0.003	0.002	0.000	0.000	0.000	0.000	0.010
ISTO 280 T3 (+)	384	0.032	0.033	0.000	0.000	0.001	0.000	0.000	0.002	0.003	0.000	0.000	0.000	0.000	0.015
ISTO 280 T4 (+21)	504	0.062	0.049	0.001	0.000	0.001	0.000	0.000	0.003	0.000	0.000	0.000	0.000	0.000	0.025
ISTO 280 Tf AC (+22)	528	0.073	0.040	0.000	0.000	0.001	0.000	0.000	0.003	0.000	0.000	0.000	0.000	0.000	0.049
ISTO 280 bis T0	24	0.014	0.133	0.001	0.001	0.001	0.000	0.000	0.003	0.000	0.000	0.000	0.000	0.000	0.026
ISTO 280 bis T1 (+5)	120	0.042	0.117	0.000	0.000	0.047	0.000	0.000	0.004	0.015	0.000	0.000	0.000	0.000	0.009
ISTO 280 bis T2 (+13)	312	0.063	0.099	0.000	0.000	0.020	0.000	0.000	0.006	0.006	0.000	0.000	0.000	0.000	0.012
ISTO 280 bis T3 (+22)	528	0.076	0.063	0.000	0.000	0.001	0.000	0.000	0.004	0.002	0.000	0.000	0.000	0.000	0.016
ISTO 280 bis T4 (+33)	792	0.076	0.054	0.000	0.000	0.001	0.000	0.000	0.004	0.000	0.000	0.000	0.000	0.000	0.017
ISTO 280 bis T5 (+43)	1032	0.078	0.051	0.000	0.000	0.000	0.000	0.001	0.005	0.008	0.000	0.000	0.000	0.000	0.017
ISTO 280 bis T6 (+54)	1296	0.095	0.065	0.001	0.000	0.000	0.000	0.001	0.004	0.003	0.000	0.000	0.000	0.000	0.022
ISTO 280 bis Tf AC (+55)	1320	0.104	0.058	0.000	0.000	0.001	0.000	0.000	0.004	0.000	0.000	0.000	0.000	0.000	0.062

Concentrations of dissolved Si, Mg, Ca, Mn

Concentrations of dissolved Si, Mg, Ca and Mn in the fluid phases show a wide evolution during the course of experiments in response to mineral dissolution and precipitation occurred during the experiments (Figure 5.4).

During stage 1, the concentrations of Si, Ca and Mn in fluids from all experiments with lherzolite (i.e., ISTO 1, 2, 3 and 4) increase strongly to reach concentrations that are significantly higher than those of the initial seawater (Table 5.5, Figure 5.4). This increase is correlated to the temperature of experiments. For example, the concentrations of Si, Ca and Mn released at 225°C are about 0.6 mmol/L, 21 mmol/L and 0.015 mmol/L respectively, Table 5.5. These values are systematically lower than those measured in experiments at 260°C and 300°C (Table 5.5, Figure 5.4). In fluid from the experiment at 260°C a maximum of 0.7 mmol/L of Si, 25 mmol/L of Ca and 0.15 mmol/L of Mn was measured, and 0.9 mmol/L of Si, 31 mmol/L of Ca and 0.4 mmol/L of Mn, and in fluid from the experiment at 300°C (Table 5.5, Figure 5.4). Surprisingly, lower concentrations of Si, Ca and Mn were measured in the fluid from experiment at 325°C compared to those at 300°C (Table 5.5, Figure 5.4). These results suggest that in this first stage, these elements are released by the alteration of primary minerals, and are dependent of the temperature of experiment. The silica are released from the primary olivine and pyroxenes and calcium is mostly released from the primary clinopyroxene.

The concentration of Si measured in fluid from the harzburgite experiment increases significantly less than that in the lherzolite experiments, with average concentrations of \sim 0.24 mmol/L (Table 5.5, Figure 5.4). Surprisingly, the quantity of Mn measured in fluid from the experiment at 280°C is higher than fluids from all lherzolite experiments and is \sim 0.055 mmol/L (Table 5.5, Figure 5.4). That is probably a consequence of the protolith used. The harzburgite contains 72.4 vol.% of olivine vs 61.2 vol.% of olivine in the lherzolite (Table 5.3) which is the main contributor of Mn (Table 5.2). In contrast to fluids from the lherzolite experiments concentrations of Ca decrease below the initial seawater value at about 8 mmol/L, which is also a direct consequence of the composition of the protolith. Indeed, the harzburgite contains an higher proportion of clinopyroxene (\sim 4.50 vol.%) compared to the lherzolite (\sim 13.2 vol.%, Table 5.3). Furthermore, this observation suggest that Ca from seawater is consumed by the formation of secondary minerals associated to the serpentinization.

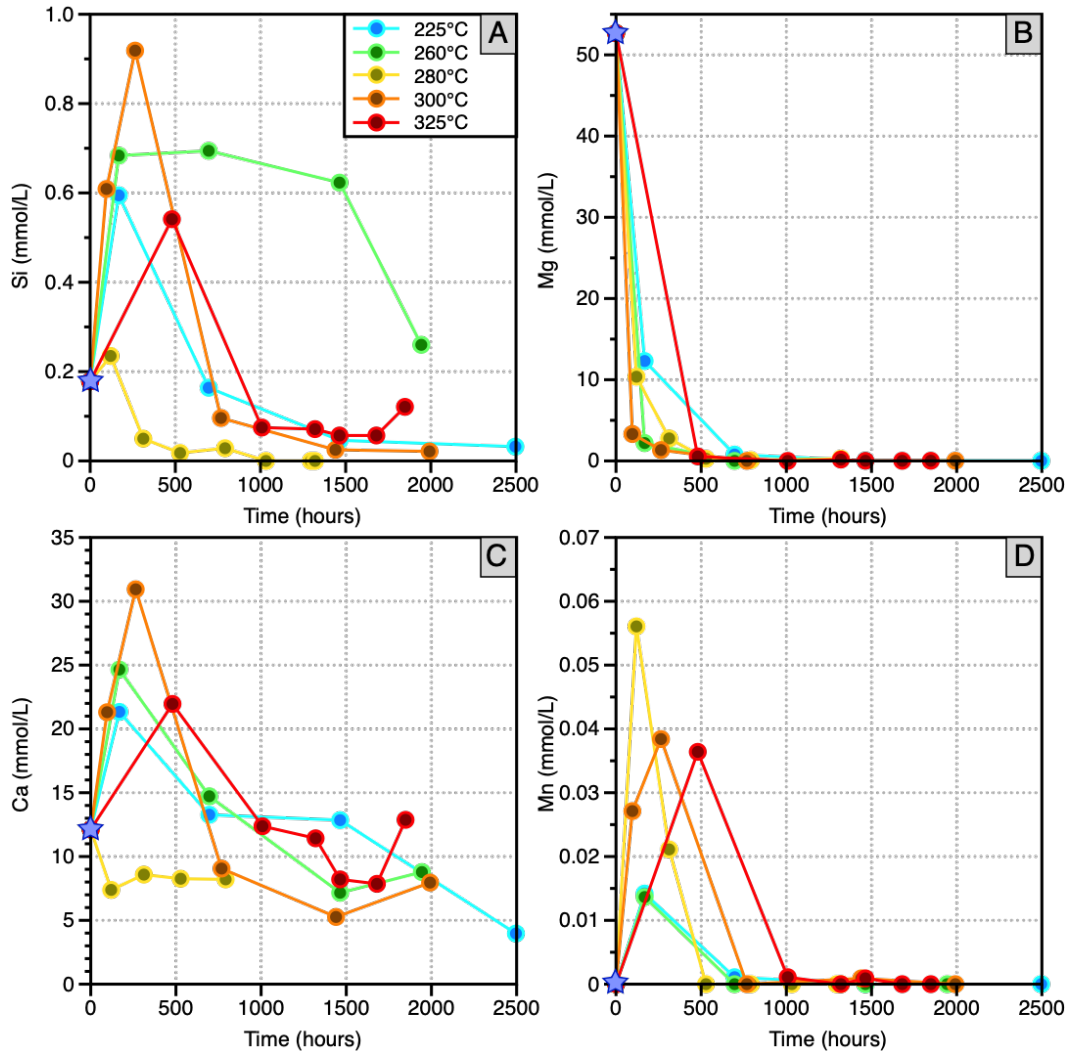


FIGURE 5.4 – Changes in concentrations of selected trace elements A) Si, B) Mg, C) Ca and D) Mn in fluid during lherzolite-seawater experiment (ISTO 1-4) at 225°C (blue), 260°C (green), 300°C (orange) and 325 °C (red) and harzburgite seawater experiment (ISTO 6) at 280°C (yellow). Blue star represent concentration in initial seawater.

In stage 2, the concentrations of Si, Ca and Mn decrease significantly in fluids from all experiments, and reach concentrations below those in the initial seawater value (Table 5.5, Figure 5.4). The concentration of Si in fluid from the experiment at 260°C where Si decrease very slowly from ~0.7 mmol/L to ~0.6 mmol/L between 500 to 1500h (Table 5.5, Figure 5.4).

After ~1500h of reaction, concentration of Ca increase slightly in fluids from the experiments at 260°C, 300°C and 325°C (Table 5.5, Figure 5.4), suggesting than very low quantity of Ca are released by minerals probably newly formed or residual clinopyroxene in this last step of reaction.

In both lherzolite and harzburgite experiments, concentrations in dissolved Mg rapidly decrease and was below the detection limits before the end of experiment (Figure 5.4). However, concentrations of Mg measured in fluids in the stage 1 vary in function of the temperature of experiment and depend also of the protolith used. Indeed, we can see that measured concentrations of Mg is significantly higher in fluids from experiment at 225°C and 280°C with 12.3 and 10.4 mmol/L, respectively Table 5.5, compared to those at 260°C and 280°C (Figure 5.4). For the lherzolite experiments, this is a consequence of the kinetics of reaction, which is higher at 260°C and 300°C than experiment at 225°C and 280°C, while it is rather a consequence of the protolith used for the harzburgite experiment. Indeed, the quantity of olivine is higher in the harzburgite compared to the lherzolite, thus higher amounts of Mg can be released during its alteration. The fact that concentrations of Mg only decrease during the experiments suggests that it is directly consumed by the formation of secondary mineral products like serpentine or brucite which can integrate significant amounts of Mg.

Hydrogen production

Di-hydrogen was produced in all hydrothermal experiments of this study similarly to that was reported in the literature (e.g., Klein et al. 2009; Klein et al. 2013; McCollom et al. 2020a). Moreover, the production of hydrogen can also be an indicator of the progress of the serpentinization reaction. Indeed, Marcaillou et al. 2011 characterize three steps of hydrogen production, i) firstly H₂ production is controlled by the crystallization of magnetite, ii) the increase of H₂ production is related to the incorporation of ferric iron in serpentine, and iii) in the last step of reaction production of H₂ decrease in response to an increase of magnetite production and also an increase of the Fe³⁺/Fe_{total} ratio.

Our present results show that in most experiments, the quantity of hydrogen increases with time (Table 5.5, Figure 5.5). In the lherzolite-seawater experiments at 225°C and 260°C, between ~12 mmol/kg and 46 mmol/kg of dissolved hydrogen was released. In the experiment at 225°C the production of hydrogen increases more slowly compared to experiment at 260°C. In experiment at 325°C, the maximum of hydrogen is after 1000h with ~40 mmol/kg. Then, the production of hydrogen decreases slowly, reaching ~30 mmol/kg at about 2000h, which is relatively similar to the quantity of hydrogen produced in experiment at 260°C (Table 5.5, Figure 5.5). Significantly higher amounts of hydrogen were released during the lherzolite-seawater experiments at 300°C, reaching ~100 mmol/kg at the end of the experiment at about 2000 hours (Table 5.5, Figure 5.5). In the harzburgite-seawater experiments at 280°C bis at the end of reactions (1030 hours) the amount of dissolved hydrogen is ~90 mmol/kg, which is in the same range than the amount of hydrogen produced at 300°C after about 2000 hours of reaction (Table 5, Figure 5.5).

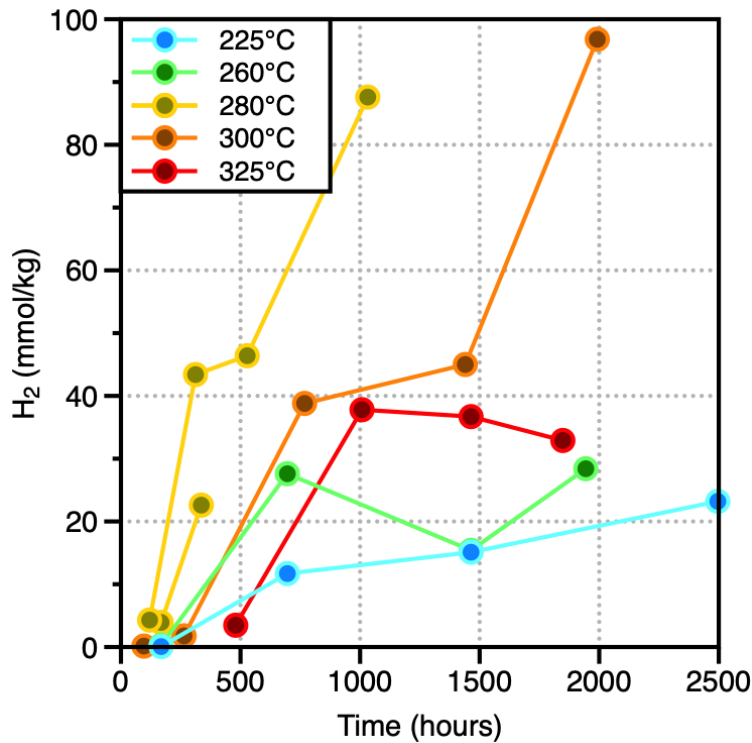


FIGURE 5.5 – Measured $\text{H}_2(\text{aq})$ concentrations (mmol/kg) as a function of time (in hours) for lherzolite-seawater experiments at 225°C (blue), 260°C (green), 300°C (orange) and 325°C (red), and harzburgite-seawater experiments at 280°C (yellow).

Trace element concentrations in fluid phases

The concentrations of rare earth elements (REE) in the reacting fluids are mostly below the detection limits in fluids. Our discussion about the concentrations of trace elements in fluids is thus restricted to Li, B, Ba, Sr, Zn and Cu.

In the case of experiments based on lherzolite starting material, the concentrations of Sr and B measured in the reacting fluids as a function of temperature, decrease during the entire reaction, suggesting that they are consumed by the formation of secondary minerals during the serpentinization reaction (Table 5.5, Figure 5.6). That is in accordance with the fact that B is mainly hosted by the seawater (4.5 ppm) while, in the primary lherzolite, B concentrations is mostly below the detection limits and about 0.06 ppm (Salters and Stracke 2004). In contrast, in the first step of reaction between 0 and 250 hours, the concentrations of Ba, Li, Zn and Cu, increase slightly in the reacting fluids. The primary clinopyroxene contains higher Li content than the primary olivine and orthopyroxene (e.g., Vils et al. 2008), we can therefore assume that the dissolution of primary clinopyroxene have started. Then, after 250 hours of reactions, the concentrations of Ba, Li, Zn and Cu in the reacting fluids decrease (Table 5.5, Figure 5.6), that suggest that they are consumed by the formation of secondary minerals during serpentinization reaction. In the last step of reaction after ± 1500 hours at 260°C, 300°C and 325°C (Figure 5.6), concentrations in trace elements increased very slightly, supporting that these elements are released partially in the reacting fluids by the solids.

Finally, at the end of the experiments, except Li which is mostly enriched in the reacting fluids at the end of the reaction, the concentrations of all these trace elements in the resulting fluids are systematically lower than in the initial seawater (Table 5.5, Figure 5.6), supporting that the formation of secondary minerals during serpentinization integrated these elements.

In the reacting fluid from the harzburgite experiment (ISTO 6) at 280°C, the concentration of Sr and B decrease during the entire experiment, similarly to the fluids from the lherzolite experiments (Figure 5.6), supporting that they are consumed by the formation of secondary minerals associate to the serpentinization reaction. However, in contrast to the lherzolite experiments, the concentrations of Ba, Li and Cu, only increase in the reacting fluids during the reaction (Figure 5.6). This is probably the consequence of the protolith. Indeed, clinopyroxene are the main host of Li and the quantity of clinopyroxene in the harzburgite is significantly lower than in the lherzolite.

Consequently, less clinopyroxene and thus less Li are available. Furthermore, our

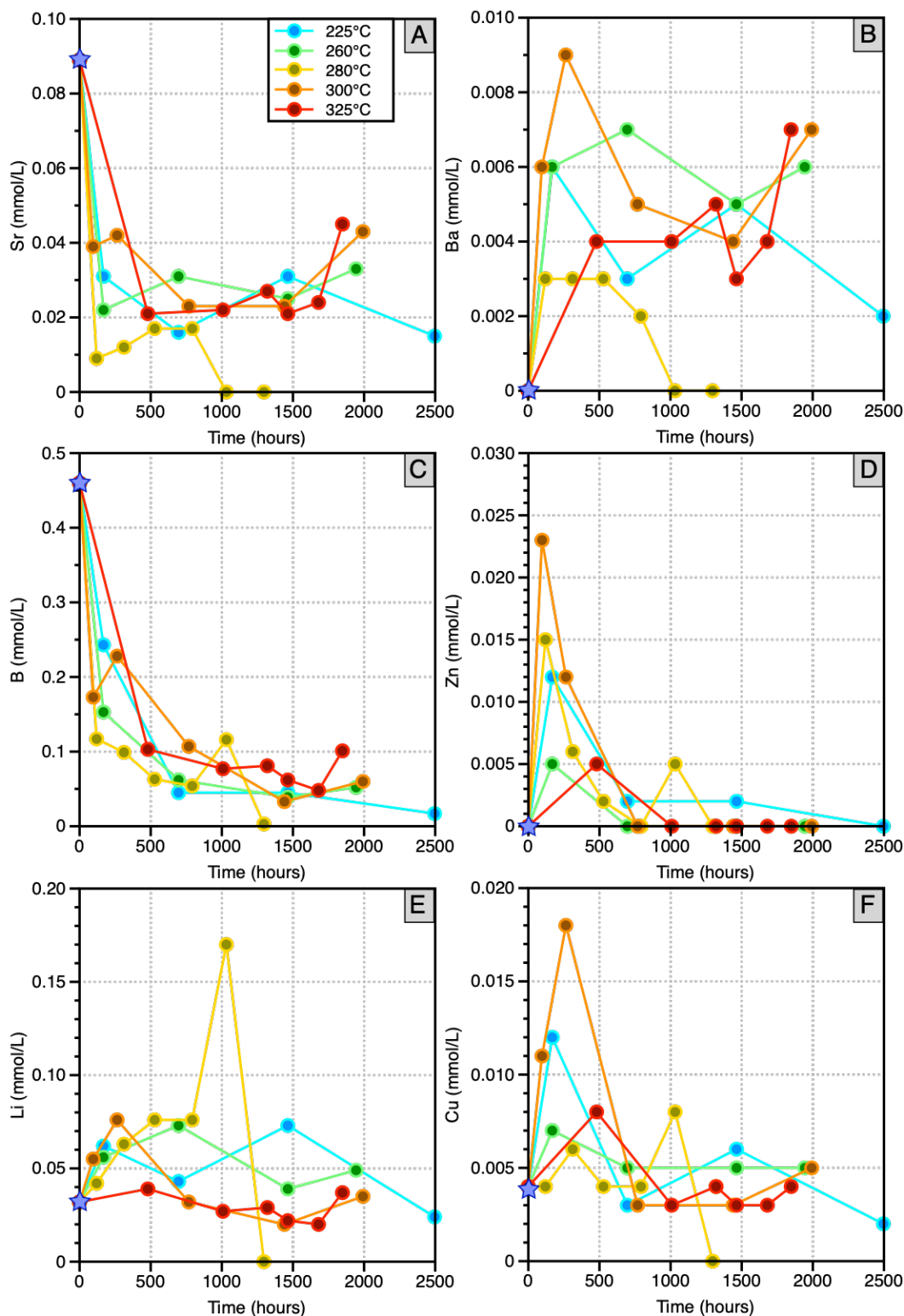


FIGURE 5.6 – Measured concentrations in mmol/L versus time (hours) of selected trace elements (Sr, Ba, B, Zn, Li and Cu) in fluids.

SEM observations, highlighted that the primary clinopyroxene are still present at the end of the harzburgite experiment, which is confirmed by the XRD patterns and the calculated proportions by the Rietveld method suggests that the proportions of primary clinopyroxene at the end of the experiment is the same that before the experiment.

5.3.4 Mass balance calculations

In order to quantify mass fluxes (i.e., the gain and loss of elements) during the serpentinization process in our hydrothermal experiments, mass balance calculations have been conducted. For that, the Gresens equation (Gresens 1967) revisited by Grant 1986 ; Grant 2005 was used. In the absence of particularly immobile components during serpentinization, and the important volume increase associated to serpentinization about $\sim 30\%$ (e.g., O'Hanley 1992 Klein and Le Roux 2020), we assume mass constant (i.e., mass of protolith (M^0) is equivalent to mass of altered rock (M^A)), and thus that both volume and composition changes during serpentinization experiments.

The isocon analysis method of (Grant 1986 ; Grant 2005) allow to illustrate graphically the mass transfer. The isocon corresponds to a line through the origine, in the plot of the concentration of an element (i), in solid products (i.e., serpentinite, C_i^A) against its concentration in the initial protolith (i.e., lherzolite or harzburgite, C_i^0), following the equation :

$$C_i^A = \frac{M^0}{M^A} (C_i^0 + \Delta C_i) \quad (5.7)$$

Where ΔC_i is the change in concentration of an element i, and M^0 and M^A are the masses before and after alteration. All elements plotting above the line through the origin, are gained in the altered rocks and inversely, all elements under the line are lost. For expand the visibility, all elements were plot in a semi-circle which have the same distance from the origin (Figure 5.7, 5.9) following the procedure described in Jöns et al. 2010. In their procedure, all elements are normalized so that the sum of squares equals 1.

Lherzolite-seawater experiments

The major elements SiO_2 and Fe_2O_3 do not show any significant deviation from the constant mass isocon (Figure 5.7), suggesting that they are mostly "immobile" during the serpentinization reaction. This is also evidenced by $\Delta C_i^0/C_i^0 = 0$ (Figure 5.8). The results from this mass balance calculation are in accordance with the concentrations of Si and Fe which are below the detection limits at the end of the experiments Table 5.5.

In contrast, MgO is mostly enriched with $\Delta C_i^0/C_i^0$ about +0.1 (Figure 5.8). Which is supported by the lost of 100% of Mg in fluids at the end of experiments Table 5.5 and the addition of $\sim 2\text{-}3$ mmol of Mg in solids.

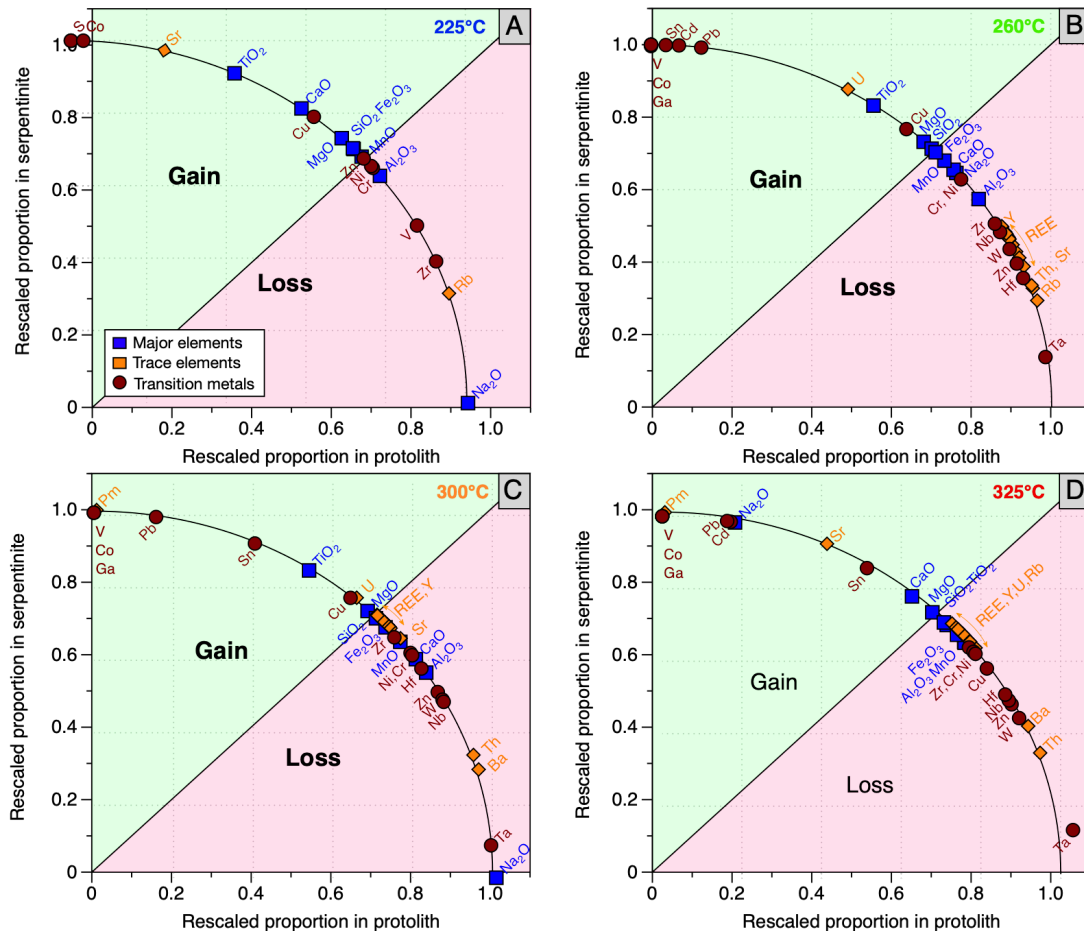


FIGURE 5.7 – Isocon diagrams for the lherzolite-seawater experiments. Concentrations in solid product are plotted against compositions of the protolith. A) 225°C, B) 260°C, C) 300°C, D) 325°C.

However, Al_2O_3 and MnO are systematically below the constant mass isocon (Figure 5.7), and are characterized by $\Delta C_i^0/C_i^0 < -0.2$ and ~ -0.1 , respectively (Figure 5.8). This suggests that Al_2O_3 and MnO are lost from the solids and enriched in the reacting fluids. In accordance with the concentrations of fluids, which are systematically higher than those to the initial seawater Table 5.5.

The CaO is above the constant mass isocon in the solid products from the experiments at 225°C and 325°C, and have $\Delta C_i^0/C_i^0$ of +0.4 and +0.3, respectively (Figure 5.8), highlighting an enrichment in Ca of the solid products. This result is supported by the observation of carbonates by SEM and XRD (Table 5.3). This is also supported by the decrease in concentrations of Ca in fluids during the experiments (Figure 5.3), and the loss of 40 and 30 % of Ca in fluids (~ 0.5 and 0.2 mmol of Ca). In contrast, in the solid products from the experiments at 260°C and 300°C, CaO plot below the constant mass isocon and have negative $\Delta C_i^0/C_i^0 (< -0.1)$, Figure 5.8), supporting that CaO is lost from the solids and enriched in the reacting fluids. This is confirmed by the gain of about 52 and 15% of Ca in the final fluids (+0.3 and +0.1 mmol of Ca) compared to the initial seawater.

In all solid products from the lherzolite experiments, the concentrations of Cr, Ni, Zn, Hf, Nb and Ta plot below the constant mass isocon (Figure 5.7) with negative $\Delta C_i^0/C_i^0$ comprising between -0.1 and -0.9 (Figure 5.8). This suggests that during serpentinization these elements are not integrated in the solid products and thus are expected to be enriched in the reacting fluids. However, the concentrations of these elements are almost below the detection limits in the diluted reacting fluids. Consequently we can not affirm with certainty that these elements are enriched in fluids.

The Cu is plot above the constant mass isocon in the solid products from the experiments at 225°C, 260°C and 300°C (Figure 5.7) with $+0.2 < \Delta C_i^0/C_i^0 < +0.3$, suggesting an enrichment in Cu in solids. The Cu is hosted by all the primary minerals (Table 5.2), and the primary seawater contains a few proportions of Cu ($\sim 0.031 \text{ mmol/L}$). Our data suggest that the Cu from the initial seawater is integrated in the secondary minerals.

Rare earth elements, Y, Rb, Ba, and Th plot largely below the constant mass isocon, suggesting that they are mobilized during serpentinization experiments (Figure 5.7) with $\Delta C_i^0/C_i^0 < 0$. Here again, the concentrations of Y and Th are below the detection limits in the diluted reacting fluids (Table 5.5). The concentration of Ba in the reacting fluids at the end of the serpentinization experiment is always higher than the initial seawater Table 5.5.

In the solids products at 225°C and 325°C Sr is above the constant mass isocon and

have $\Delta C_i^0/C_i^0$ of +3 and +0.7, respectively. Thus Sr is enriched in the solids at 225°C and 325°C, in accordance with the observation of systematic lower Sr proportions in the reacting fluid at the end of the experiment compared to the initial seawater value Table 5.5.

In contrast, at 325°C U plot below the isocon (Figure 5.7) with $\Delta C_i^0/C_i^0$ of -0.2 (Figure 5.8), suggesting that it is removed from the primary lherzolite.

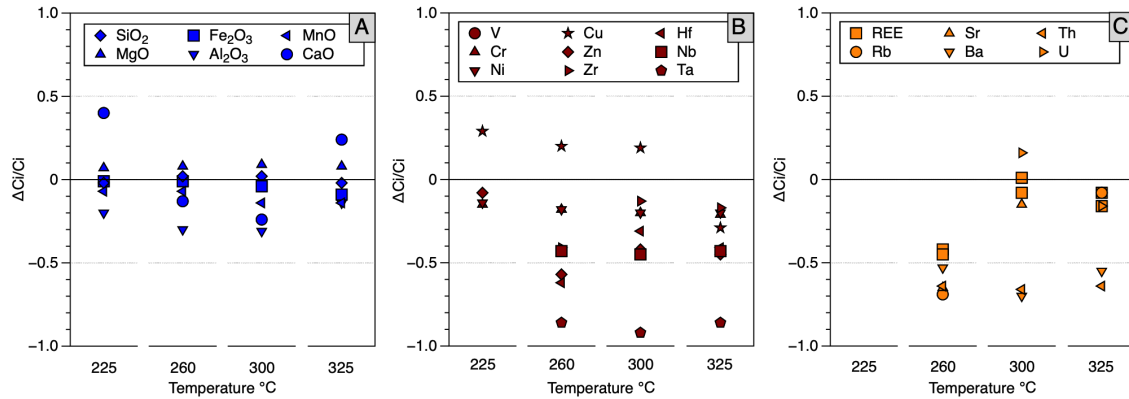


FIGURE 5.8 – $\Delta C_i^0/C_i^0$ versus temperature (°C) for each lherzolite-seawater experiments. A) major elements, B) transition metals elements, C) trace elements.

Harzburgite-seawater experiments

Only few differences are observed in the isocon plots for the major elements from the two harzburgite experiments after different time of interaction (i.e., 504 hours and 1296 hours), compared to the those in the lherzolite experiments. Indeed, SiO_2 and Fe_2O_3 do not show a significant deviation from the constant mass isocon (Figure 5.9) and have $\Delta C_i^0/C_i^0 = 0$ (Figure 5.10) suggesting that they are mostly immobile during the serpentinization.

Similar to solids from the lherzolite experiments, MgO plot above the isocon and have systematically $\Delta C_i^0/C_i^0 > 0$ (Figure 5.10) supporting that Mg is mostly enriched in solids evidenced by the addition of +3 mmol of Mg in the solids and the lost of 100% of Mg in the fluids.

Similar to the lherzolite experiments, Al_2O_3 and MnO plot below the isocon (Figure 5.9) and have $-0.3 < \Delta C_i^0/C_i^0 < -0.1$ (Figure 5.10).

The CaO plot above the constant mass isocon and have $\Delta C_i^0/C_i^0$ of +0.4 in the shorter experiment (Figure 5.9, 5.10), which is correlated to the precipitation of calcite observed

by SEM and XRD. In contrast, in the longer experiment CaO plot below the isocon (Figure 5.9) and have negative $\Delta C_i^0/C_i^0$ (-0.6, Figure 5.10). Although the concentration of Ca in fluid is below the seawater and relatively constant during the whole reaction (Figure 5.4), mass balance calculations highlighted a gain of 10 and 2% of Ca in fluids, corresponding to the lost of ± 0.28 mmol of Ca in solids.

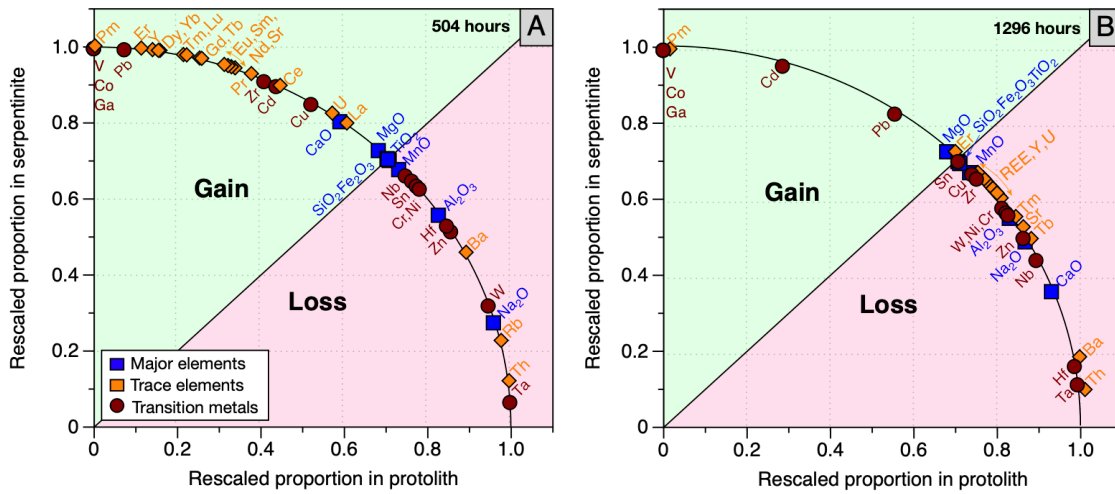


FIGURE 5.9 – Isocon diagrams for the harzburgite-seawater experiments at 280°C. Concentrations in solid product are plotted against compositions of the protolith. A) 504 hours, B) 1296 hours

Rare earth elements, Y, Rb, Ba, and Th are always enriched in solids products after 504h of experiment at 280°C, while after 1296h they are depleted and plotted below the constant mass isocon (Figure 5.9). This highlighted that in the shorter experiments, not enough primary minerals are dissolved to removes completely these elements from the solids. The Sr and U plot above the constant mass isocon in the shorter experiment (Figure 5.9) and have positive $\Delta C_i^0/C_i^0$ ($>+0.5$, Figure 5.10), suggesting that these elements are not depleted in solids from the shorter experiment. The $\Delta C_i^0/C_i^0$ of Cu is ± 0 , supporting that Cu is mostly immobile.

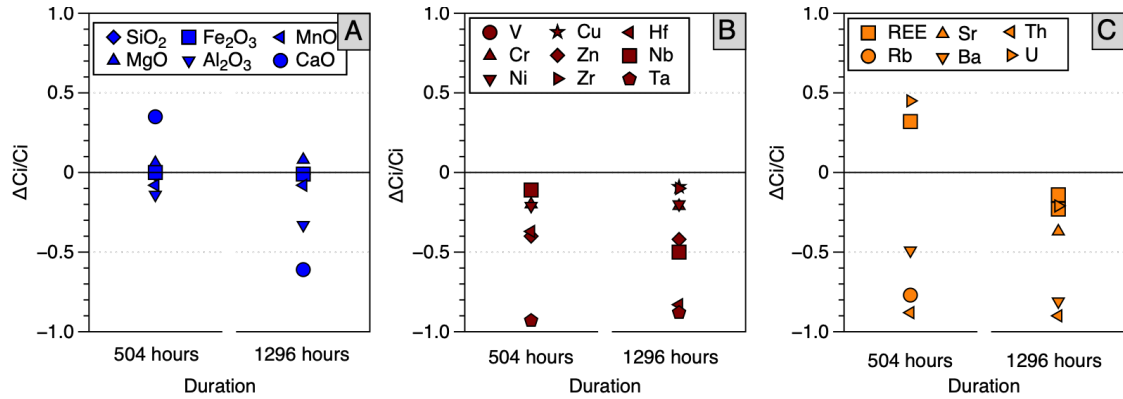


FIGURE 5.10 – $\Delta C_i^0/C_i^0$ versus duration of harzburgite-seawater experiments (hours). A) major elements, B) transition metals elements, C) trace elements. A) 504 hours, B) 1296 hours

5.4 Discussion

5.4.1 Mineralogical evolution

The examination of the solid products by XRD and SEM highlighted that mineral assemblages in our experiments are similar to those expected and from previous serpentinization experiments in the literature (e.g., Klein et al. 2013). At the end of all experiments presented in this study, the observed minerals assemblage are relatively the same, with nevertheless some differences are observed in the amount of mineral proportions (Table 5.3). The solid products from both lherzolite experiments and harzburgite experiments are characterized by abundant serpentine (mostly chrysotile), magnetite, and minor calcite which crystallized as reaction products, and relics of primary olivine and clinopyroxene (Table 5.3). Low amounts of brucite and aragonite were detected in the solid products from the harzburgite experiments, in response to the higher proportions of olivine in the initial harzburgite compared to the lherzolite (Table 5.3). Several parameters need to be considered to explain such differences of minerals proportions calculated at the end of hydrothermal experiments, such as the nature of protoliths used and thus their respective proportions of primary minerals including olivine, pyroxenes and spinel, the temperatures and the duration of each experiments (see Table 5.1).

Mineral proportions

Lherzolite-seawater experiments

In the solid products from the lherzolite experiments, the estimated proportions of serpentine and spinel decrease with the temperature of experiments while proportions of magnetite, olivine and clinopyroxene increase (Figure 5.2).

The lowest proportions of serpentine ($\text{Mg}_3\text{Si}_2\text{O}_5(\text{OH})_4$) is observed at 325°C and is related to the highest proportions of olivine and clinopyroxene relics. This is due to the proximity of the temperature stability of olivine near 350°C (e.g., Klein et al. 2009; McCollom and Bach 2009) which decrease its kinetics of dissolution. In addition, these relics of minerals correspond to the coarser grain ($>20\mu\text{m}$) which have consequently a higher reactive surface and thus higher time is required for convert the entirely crystal. Indeed, the experiment at 325°C is the shorter (1728 hours), maybe additional time would allow to decrease the proportion of olivine relics. In contrast, the highest proportion of serpentine was observed at 225°C. However, at 225°C kinetics of dissolution of primary minerals are lower than at 260°C and 300°C. But this experiment is also the longer (~ 3288 hours), suggesting here that the duration of experiment allows to convert higher proportions of olivine and clinopyroxene in serpentine than in the other experiments.

At 225°C, spinel ($>20\mu\text{m}$) is still present, while very low quantity of magnetite was produced (± 1.4 vol.% and ± 0.35 vol.%, respectively Table 5.3, Figure 5.2). This is in accordance with previous numerical models, which predict than magnetite may not form at temperature below 150°C and $w/r < 1$ Klein et al. 2009, and that the amount of Fe released from primary Fe-Mg minerals and subsequent incorporation into magnetite decrease with temperature decreasing because Fe is more integrated in serpentine McCollom and Bach 2009. Moreover, recently McCollom et al. 2020b showed that during serpentization at 200-230°C, significant amount of Fe is partitioned into brucite and chrysotile and thus less magnetite is formed. and thus less amounts of H₂ are generated. It would be interesting to compare the concentrations of Fe in serpentine and brucite. If the serpentine formed at lower temperature of reaction contains higher Fe than in the serpentine formed at higher temperature of experiment, this would allow to confirm the observation of McCollom et al. 2020b. At 225°C, the lower proportions of hydrogen released are calculated (Table 5.5, Figure 5.5), which is in accordance with the lower production of magnetite. The low proportions of magnetite formed at 225°C can reflects also an effect of the mineral reaction kinetics and/or an higher proportion

of iron integrated in secondary serpentine and/or brucite Seyfried Jr et al. 2007. At this temperature spinel is almost stable and is few altered (1.37 vol.% Table 5.3).

The highest proportions of magnetite calculated was in experiments at 300 and 325°C (4.69 and 3.93 vol.%, respectively Table 5.3, Figure 5.2), which is here again in accordance with predictions from numerical models (Klein et al. 2013 ; Marcaillou et al. 2011 ; McCollom et al. 2016), and correspond to high proportions of hydrogen release, reaching ± 100 mmol/kg for experiment at 300°C (Table 5.5, Figure 5.5). At higher temperatures, spinel is also more altered, and only a minor proportion is still present (0.629 and 0.391 vol.%, respectively, Table 5.3), suggesting that at these temperatures spinel becomes unstable.

Harzburgite-seawater experiments

Two harzburgite-seawater experiments were conducted during different time (504 and 1296 hours). These experiments highlight that after only 504h, 78.8 vol.% of serpentine was already formed, only 11.5 vol.% of olivine was not converted, and orthopyroxene is already totally converted into serpentine (Table 5.3, Figure 5.2). This in accordance with the lower proportions of orthopyroxene and confirms that orthopyroxene reacted faster than olivine in these conditions, according to the previous study of Klein et al. 2015a, Grozeva et al. 2017 and McCollom et al. 2020a. In contrast to experiments on lherzolite, primary clinopyroxene was relatively preserved, with proportions similar to those in the protolith (4.22 vol.% at 504 hours and 3.29 vol.% after 1296 hours, Table 5.3). This observation is in accordance with previous experiments involving harzburgite (Klein et al. 2015a) and numerical models (Klein et al. 2013) which predicting that clinopyroxene is mostly unaltered during serpentization of harzburgite due to the low silica activity imposed by serpentine and brucite.

Minor amounts of magnetite (Fe_3O_4) was formed (1.91 vol.% and 1.65 vol.% , respectively Table 5.3), which is lower than in the lherzolite experiments at 260°C and 300°C (Figure 5.2). However, high proportion of hydrogen was measured, reaching 90 mmol/kg after 1296h of reaction (Table 5.5, Figure 5.5). The different mineralogical proportions between the harzburgite and the lherzolite can affects the amount of hydrogen released. Indeed, in experiments on harzburgite, the reaction is dominated by olivine which leads to the precipitation of brucite and magnetite in addition to serpentine. This can contribute to the generation of hydrogen in higher proportion compared to the experiments on lherzolite (Klein et al. 2009 ; McCollom et al. 2020b).

We suggest that in our experiments, the preservation of reactant phases (i.e., olivine and clinopyroxene) depend to i) the duration of the experiments, ii) the temperature of reaction and thus the kinetic of mineral dissolution and iii) the initial grain size.

In all experiments, orthopyroxene is absent in solids at the end of experiments, according to the experimental results of Klein et al. 2015a, Fauguerolles 2016, Grozeva et al. 2017 and McCollom et al. 2020b. This suggests that orthopyroxene are more rapidly convert into serpentine, than olivine and clinopyroxene. Furthermore, because orthopyroxene are present in significant lower proportions than olivine, orthopyroxene is exhausted from the equilibrium mineral assemblage before the olivine. Consequently, in this early step of reaction between 0-500h, talc and brucite can not be formed as stable phases because orthopyroxene and olivine reacted probably simultaneously, favoring the growth of serpentine. In this first step, low quantity of hydrogen are released in all experiments (Figure 5.5) supporting that serpentinization has already started and that serpentine and/or magnetite are already formed.

When all primary orthopyroxene have reacted (probably after 500h), especially in the harzburgite experiments, olivine continues to react with fluid, and thus Mg is released in higher proportions than Si, favoring the formation of brucite, consistently with the predicted model of McCollom et al. 2020a. In the lherzolite experiments, the serpentinization of olivine and clinopyroxene occurred simultaneously after 500h, preventing probably the formation of brucite under low silica activity. At this time the quantity of hydrogen released increases in all experiments, supporting that serpentinization play a key role in the hydrogen production and/or that amount of magnetite formed increases as proposed by Marcaillou et al. 2011.

Brucite formation

As mentioned above, minor amounts of brucite ($Mg(OH)_2$) was observed by SEM only in the harzburgite-seawater experiments (ISTO 5 and 6, Table 5.3). The formation of brucite in the harzburgite experiments can be explained by the higher proportions of olivine than in the lherzolite (72.4 vol.% vs 61.2 vol.%, Table 5.3), inducing an excess in magnesium (in average ~ 1363 mmol) relative to silica (in average ~ 901 mmol) in solution. That is in accordance with the lower proportion of silica release (0.142 mmol/L, Table 5.5) and the higher proportions of magnesium (10.4 mmol/L, Table 5.5) measured in the fluids during the first step of harzburgite experiments (Figure 5.4).,The molar ratios MgO/SiO_2 in harzburgite is higher than 1, favoring the formation of brucite. In

contrast, in the initial lherzolite, MgO/SiO_2 is less than 1, thus brucite can not develop (Li et al. 2004). This results are in accordance with previous models, which predict the formation of brucite in alteration of harzburgite of relatively similar rock composition (Ol:Opx:Cpx = 80:15:5 vol.%, Klein et al. 2009).

Thus, occurrence of brucite in the harzburgite experiments in this study, results in the higher proportions of olivine in the harzburgite compared to the lherzolite, which lead to the release of higher proportion of Mg in the reacting fluids allowing the formation of brucite. The occurrence of brucite only in the shorter experiments suggests also that it is a metastable phase in contrast to serpentine (e.g., Klein et al. 2009). Probably, at longer duration of experiments, brucite will not be observed anymore as observed by McCollom et al. 2020b.

Carbonate formation

In all experiments, carbonates (CaCO_3) were detected by SEM and XRD analyses (Table 5.3). Most carbonates observed by SEM consist of calcite, but aragonite was identified by SEM in the shorter harzburgite-seawater experiment (Figure 5.1).

In the reacting fluids from the lherzolite experiments, the concentration of Ca increases during the stage 1 (0-500h), which is coupled to an increase in concentrations of Si and Mn (Figure 5.4). Such concomitant increase of Ca and Si concentrations in the fluid suggests that these elements are released from the primary minerals, most likely the clinopyroxene which contains ~21 wt.% of CaO and ~53 wt.% of SiO_2 (Table 5.2). Taking into account the proportions of clinopyroxene in lherzolite (13.2 vol.%, Table 5.3), it is an important source of calcium. In contrast, no increase in the concentration of Ca is observed in the reacting fluids from the harzburgite experiments (Figure 5.4). The harzburgite contains significantly less clinopyroxene compared to the lherzolite, hence, the quantity of Ca available is lower in the harzburgite experiments than in the lherzolite experiments (with an average ~18 mmol and 45 mmol of Ca in initial solids). In the reacting fluids from harzburgite experiment, the concentration of dissolved Ca decrease between T0 and T1, and the concentration of Ca is always below the concentrations in the initial seawater (<12.1 mmol/L, Table 5.5, Figure 5.4). This highlights that Ca is only consumed by formation of secondary minerals : calcite and aragonite.

We propose that during the stage 1 in experiments on lherzolite, only a part of clinopyroxene is serpentinized, releasing Ca in the fluid, as evidenced by dissolution textures observed in SEM images (Figure 5.1). In contrast, in the harzburgite experi-

ments, the proportion of clinopyroxene is lower and consequently lower quantity of Ca are available, thus no excess in Ca is observed in the reacting fluids.

In the stage 2 (after 500h), the concentration of Ca in the fluid decreases (Figure 5.4), suggesting that Ca is integrated in secondary minerals. However, Ca is not integrated in the structure of serpentine ($(\text{Mg}, \text{Fe})_3\text{Si}_2\text{O}_5(\text{OH})_4$), and thus it was necessary integrated in carbonates.

In the last stage (after 1500h), the concentration of Ca increases in the reacting fluids (Figure 5.4) suggesting that a part of the calcite and/or aragonite previously formed were dissolved.

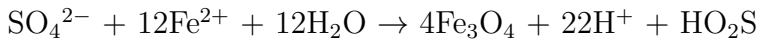
Anhydrite formation

At 225°C and 260°C concentrations of SO_4^{2-} are slightly lower than initial seawater (Figure 5.3), however at 225°C after about 1500h of reaction, concentration of SO_4^{2-} decrease strongly, suggesting that SO_4^{2-} is integrated in secondary minerals (possibly in anhydrite which is detected by SEM) during the course of experiment in contrast to the other experiments.

The SO_4^{2-} can form secondary minerals by complexion with Ca such as anhydrite (CaSO_4) or Magnesium Hydroxide Sulfate Hydrate (MHSH), which precipitates in natural environment with seawater at temperature $>250^\circ\text{C}$ (e.g., Seyfried Jr and Dibble Jr 1980). Janecky and Seyfried Jr 1986 have shown that anhydrite is a stable component of alteration assemblage of peridotite-seawater experiment at 300°C. Thus, it is not surprising to detect anhydrite in solids from lherzolite experiment at 325°C. In this experiment, anhydrite is observed simultaneously with relics of olivine, highlighting the lack of equilibrium between sulfate and sulfide as proposed by Seyfried Jr et al. 2007. MHSH minerals was not detected in any solid products (similarly to experiments of Janecky and Seyfried Jr 1986), but we cannot exclude their precipitation during our hydrothermal experiments. The absence of MHSH minerals and crystal of anhydrite in the solid products can be explained by their retrograde solubility Bischoff and Seyfried 1978. Consequently, these minerals, in particular anhydrite are probably formed during the hydrothermal experiments at 225°C, 280°C, 325°C and to a lesser extent at 300°C, but dissolved during the cooling time.

The formation of such minerals is a direct consequence of seawater, which contains $\sim 60 \text{ mmol/L}$ of SO_4^{2-} . Furthermore, reduction of SO_4^{2-} from seawater can affect the pH of resulting fluids, and thus the mobility of some elements. Seyfried Jr and Dibble Jr

1980 proposed that the reduction of SO_4^{2-} from seawater and oxidation of iron from primary ferro-magnesian minerals, can alone produce magnetite as the following reaction :



In our experiments, all of the Ca from seawater and clinopyroxene is integrated in the formation of carbonates (CaCO_3) and anhydrite (CaSO_4). We suggest that the precipitation of carbonates follow the precipitation of anhydrite and/or MSH (although this last one are not observed in our experiments), in response to the lack of Mg and SO_4^{2-} in fluids and possibly with alkaline pH like proposed Janecky and Seyfried Jr 1986.

Halite formation

Some halite crystals were observed by SEM and detected by XRD in the experiment at 325°C (ISTO 4), however it possibly occurs in all experiments. Because the solids products were successive rinse before their analysis, halite which have precipitated during the reaction can be dissolved and thus not detected by XRD and SEM. Indeed, concentrations of Na and Cl in reacting fluids have the same behavior as in all experiments and the evolution of Na (mmol/L) is positively correlated to those of Cl (mmol/L, Figure 5.11), although their evolution is not linear with time of reaction, as shown previously (Figure 5.3). In first steps of reaction, the concentrations of Na and Cl decrease and then are relatively stable with time (Figure 5.3), suggesting than they are incorporated in secondary minerals. However, at the end of hydrothermal experiments, their concentrations increased in the reacting fluids (Figure 5.3), suggesting that these elements are released from solids phases.

The integration of Cl and Na in secondary solid products is consistent with Sharp and Barnes 2004 who proposed that chlorine is integrated in serpentine as $\text{MgCl}_2 \cdot 6\text{H}_2\text{O}$ and NaCl salts such as halite. More recently, Huang et al. 2018, 2017 demonstrated that chlorine can be hosted in a weak bound or in structural position in serpentine minerals.

We agree that Na and Cl are integrated in secondary minerals during the first steps of reaction. However, at the present time the chemical composition of the secondary minerals were not analyzed, and it is consequently difficult to constrain their formation. An another possibility it is that halite precipitation occurs during the hydrothermal experiments, but it maybe dissolved during the successive rinsing carried out before analysis of solids products.

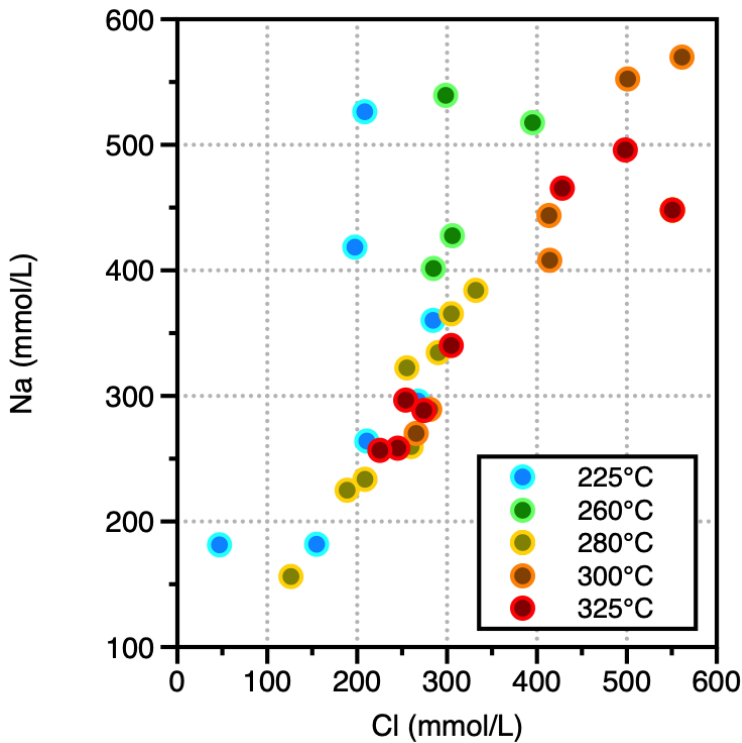


FIGURE 5.11 – Measured concentrations of Na in mmol/L versus measured concentrations of Cl in mmol/L.

Source of aluminium

Mass balance calculations highlight a loss in aluminium in solid products from all experiments (Figure 5.8, 5.10) and enrichment in the reacting fluids. Spinel is the primary mineral containing the higher proportion of aluminium (26.7wt.% in the lherzolite and 58.5 wt.% in the harzburgite, Table 5.2), but both lherzolite and harzburgite contain low amounts of spinel (<2 vol.%, Table 2). However, clinopyroxene and to a lesser extent orthopyroxene which constitutes $\pm 27\text{vol.}\%$ of the lherzolite and $\pm 37\text{vol.}\%$ of the harzburgite (Table 5.3) are also contributor of aluminium (Table 5.2).

The dissolution of primary spinel and pyroxenes can explain the depletion in aluminium of solids products at end of all hydrothermal experiments (Figure 5.8, 5.10). The alteration of primary spinel can also contribute, to a lesser extent to the formation of magnetite and ferritchromite, although the main source of iron remain the primary Fe-Mg minerals. The analysis of spinel achieve by SEM-EDS show that it have heterogeneous concentration of Al, Cr and Fe at the sample scale. Thus, in order to characterize the contribution of spinel to the formation of magnetite and/or ferritchromite and also

to quantify the release in solution of these elements in situ analyses are required.

To resume, the iron and magnesium content are mostly transfers in the secondary minerals serpentine and magnetite. Serpentine integrates the Mg released from primary olivine and pyroxenes. In the Harzburgite experiments, the excess of magnesium generated by the high proportion of olivine, leads to the formation of brucite. Although iron is mainly integrate in magnetite, serpentine and brucite can integrate a part of iron, especially at low temperatures of experiments. Furthermore, spinel can also release a part of their Fe. The formation of carbonates and anhydrite integrate a part of the calcium from seawater and released from clinopyroxene dissolution. The dissolution of clinopyroxene contributes to increase Li in the reacting fluids. The aluminium, and transition metals are mostly released in the reacting fluids which is attested by the systematic depletion of solid products compared to the initial lherzolite and harzburgite. However, the dilution inhibit their detection in the reacting fluids, consequently we can not quantify exactly the proportion release in the reacting fluids.

5.4.2 Serpentinization, mass-fluxes and (U-)VMS, what can we learn ?

Seawater is composed by many ligands in addition to Cl^- , such as OHCl^- , HS^- , H_2S , SO_2 , which may complex metals and thus strongly affect their solubility (e.g., Brugger et al. 2016). Susak and Crerar 1985 have already suggested that during hydrothermal interactions, under increasing temperature and chloride concentrations, some elements like Ni, Co can change their coordination geometry, such as from octahedral to tetrahedral. This change in coordination impacts the mobility, and thus the transport and deposit of elements. Especially, Fouquet et al. 1998 showed that hydrothermal vent fluids from Rainbow and related metal deposits are strongly enriched in Cu, Zn, Co and Ni relative to the initial seawater. More recently, Patten et al. 2022 proposed that massive sulfide deposits observed at ultramafic hosted hydrothermal systems contain secondary Ni-Co-bearing minerals including pentlandite, Co-pentlandite, Ni-Co sulfarsenides and arsenides. Douville et al. 2002 and Charlou et al. 2002 showed that the abundance of some metals such as Fe, Mn, Ni, Cu, Zn, Co and Ni in the hydrothermal fluids from MOR ultramafic-hosted hydrothermal systems such as Rainbow and Logatchev, is strongly favoured by Cl-complexion at low pH and high temperature. In particular, Douville et al. 2002 postulated that 80% of the Mn, Fe Zn, Ag, Pb, and REE in the Rainbow fluids at 300°C would form complexes with Cl^- .

In hydrothermal fluids, most elements occurred in divalent form as Fe(II), Mn(II), Ni(II), Co(II), Zn(II), Cu(II), except chromium and vanadium which occurred preferentially in trivalent form Cr(III) and V(III) in reducing conditions at 300°C, and can complex with Cl⁻ (e.g., Tian et al. 2014). Fe(II) can complex as octahedral or tetrahedral coordination Scholten et al. 2019, the first one which predominate at low temperature and salinity, while the second predominate at temperature of >300°C and high salinity as FeCl²⁻₄ Testemale et al. 2009. The dissolved Ni and Co complexes with Cl⁻ as NiCl₂ and CoCl₂ Brugger et al. 2016. Cu(I) is the most common oxidation state of Cu in hydrothermal fluids, but it is not stable in water and rapidly transformed in Cu(II) or native copper Brugger et al. 2016. Tetrahedral ZnCl₄²⁻ is stable in saline solution Brugger et al. 2016. Although, chromium has three oxidation state Cr²⁺, Cr³⁺ and Cr⁶⁺, Cr³⁺ is predominant in the hydrothermal fluids and thus complex as tetrahedral coordination as CrCl²⁻₄ or Cr(OH)Cl₃(aq) or as CrCl_x(H₂O)_y(OH)_z^{3-x-z} Brugger et al. 2016.

Our hydrothermal experiments, highlight that the serpentinization of olivine and pyroxenes and to a lesser extend, spinel alteration lead to the mobilization of Fe, Mg, Ca, Al, Mn, Zn, Ni, Cr, Co, Cu and Li. The measured concentrations of iron in the diluted reacting fluids are almost below the detection limits (Table 5.5). But, important amounts of magnetite are formed, suggesting that iron release from primary ferromagnesian minerals is mostly integrated into secondary magnetite in our experiments. This is in accordance with our mass balance calculations, highlighting that iron is poorly soluble during all experiments (Figure 5.8, 5.10) and therefore weakly transported in natural systems.

In contrast to iron, the concentration of dissolved Mn was measured in the diluted reacting fluids and have mostly the same behavior than Si and Ca, which is firstly enriched in the fluids between 0-500h of reaction and then Mn is consumed by the formation of secondary minerals (Figure 5.4). This observation fit with the mass balance calculations for major elements, where Mn is enriched in the solid products compared to the initial lherzolite and harzburgite (Table 5.4, Figure 5.8, 5.10). This highlights that Mn is poorly soluble in our batch experiments, and similarly to iron, probably weakly transported. It is important to note that in open and natural systems, that Ca and Mn released in fluids are available to form secondary minerals calcite, aragonite or manganese nodules. Klein et al. 2015b observe that chimneys of the Lost City hydrothermal fluids are composed by calcium carbonate (calcite and aragonite) and brucite. The release of Ca, is also available for rodingitization reaction (e.g., Palandri and Reed

2004).

Concerning the transition metals elements : Ni, Cr, Co, V, Cu and Zn are systematically depleted in solids products compared to the initial lherzolite and harzburgite (Table 5.4), suggesting that these elements are mobilized during serpentinization and would be enriched in the reacting fluids, and thus probably transported in natural systems. The concentration of Zn measured in the reacting fluids are systematically higher than those measured in the initial seawater (Table 5.5). However, the concentration of Cu in fluids at end of experiments is similar to those in the initial seawater (Table 5.5), suggesting that Cu is mostly insoluble. The concentrations of Ni, Cr, Co, and V are mostly below the detection limits of the diluted reacting fluids (Table 5.5). Because the reacting fluids were diluted before the analysis by ICP-AES and ICP-MS, if only minor quantity of these elements were released in the reacting fluids, the dilution inhibit their detection by ICP-AES/MS.

Similar to the hydrothermal fluids at Rainbow, Logatchev or Lost City, the reacting fluids from our experiments are systematically enriched in Ba and Li (Table 5.5) and the solid products depleted in Li compared to the initial lherzolite and harzburgite (Table 5.4). This supports that Ba and Li are transported during the serpentinization experiments and can be potentially deposited. This observation is very interesting because, Li is an element with an important economic interest, with numerous applications. Especially, the growing demand of batteries, at the time when environmental issues increase. In contrast to the results of our study, high amounts of Si, Ca, Fe, Mn, Co, Ni, Cu were measured in hydrothermal fluids at Rainbow and Logatchev Douville et al. 2002. Nevertheless, the hydrothermal fluids at Rainbow have very low pH 2.8, high chloride concentration >750 mM and high temperature 365°C (Douville et al. 2002). Furthermore, Hannington et al. 2005 have suggested that the high concentrations of Fe measured in the hydrothermal fluids from submarine hydrothermal systems results of leaching of magnetite formed during serpentinization, previously release from primary Fe-Mg minerals of peridotites. In contrast, in hydrothermal fluids from Lost City, Fe, Mn, Cu and Zn were not detected (e.g., Humphris and Klein 2018), similar to the reacting fluids of our study.

Here, the highest temperature of experiment is 325°C and the concentrations of Cl at the end of most hydrothermal experiments are significantly lower than those measured in the initial seawater and than those measured in the hydrothermal fluids at Rainbow (Table 5.5), which probably affect the metal complexation with Cl^- and thus their mobility has suggested earlier. We can also suppose that the pH values of the reacting

fluids in our experiments are not the same (although pH was not measured) than those measured at Rainbow or Logatchev. In particular, at lower temperature of experiments 225°C and 260°C, lower amounts of magnetite was formed and alkaline conditions can be generated in response to higher partitioning of Fe into serpentine and brucite and less into the magnetite as suggested recently by McCollom et al. 2020a. Furthermore, Seyfried Jr et al. 2007 have suggested that the dissolution of clinopyroxene released Na₂O inducing an increase of the pH. In the lherzolite experiments at temperature <280°C, higher quantity of clinopyroxene were dissolved compared to the experiments at higher temperature (Figure 5.2). In addition, previous study have already shown that (hyper)-alkaline pH can be generated at low temperature (e.g., Seyfried Jr et al. 2007 ; Hansen et al. 2017 ; McCollom et al. 2020b ; McCollom et al. 2020a). High pH values are also measured in vent fluids from the Lost City hydrothermal systems (pH 9-9.8, Kelley et al. 2001) and recalculated (8.1 at 200°C, Allen and Seyfried Jr 2004) and in fluids related in serpentization of peridotites from the Oman, Ligurian and Ronda ophiolites with pH >10.5 (e.g., Chavagnac et al. 2013 ; Giampouras et al. 2019).

As a consequence, we suggest that the reacting fluids in our study are generated in conditions which are not systematically favorable to transport Fe, Mn, Co, Ni and Cu. Especially at low temperatures of experiments <280°C, the reacting fluids have probably higher pH values in response to low amounts of Fe²⁺ oxidized to Fe³⁺ attested by low quantity of magnetites, coupled to an increase of pH associated to a greater proportion of altered clinopyroxene. At high temperatures of experiments >280°C, higher reducing conditions are generated because more Fe²⁺ are oxidized to Fe³⁺ in magnetites, in accordance with the high amounts of magnetites observed (Table 5.3). The reducing conditions allowed the stabilization of some native metals such as awaruite (Ni,Fe-alloys) Frost 1975. Although, in our experiments awaruite was not observed, numerical models suggests that awaruite may forms at temperatures above 315°C at very low fluid/rock ratios and also at lower temperatures between 315°C and 250°C (e.g., McCollom and Bach 2009).

5.5 Conclusions

The analysis of the reacting fluids during the experiments allow to highlight that the composition of the initial seawater is strongly modified during our serpentinization experiments. In particular, Cl, Na, K and SO_4^{2-} vary during the course of experiments. The concentration of SO_4^{2-} is strongly affected by the temperature of experiments, with very low concentrations at 280°C and 325°C, while at 225°C and 260°C concentrations are similar to the initial seawater.

The analysis of the reacting fluids during the experiments allow also to constrain the mineralogical evolution. Numerical models are currently in progress by using the numerical code KIRMAT (Kinetic Reaction and Mass Transport). These numerical models aims to understand and characterize the reactions leading to the measured reacting fluids. In addition, these models aims to constrain the apparition and the dissolution of intermediate phases, not always visible in the solids products at the end of the experiments.

The concentrations of Fe, Mn, Ni, Cr, Co, V, Cu are not detected in the reacting fluids, probably due to the dilution for the ICP-AES/MS analyses. However, the examination of the concentrations of these elements in the solids products and the mass balance calculation reveal that Si, Mg, Fe and Mn are mostly immobile during serpentinization, (i.e., transferred from the peridotite to the bulk serpentinite). However, the resulting bulk serpentinite are systematically depleted Ni, Cr, Co, V, Cu and Zn compared to the initial lherzolite and harzburgite, suggesting that these elements are released in the reacting fluids, but this is not observed. We can not exclude that these elements were stuck in the alloy of the titanium bag, although it is normally inert. This can also suggests an high mobility of this elements in open environment.

The concentrations of Si, Ca, Mn, Ba, Li and Cu measured in the reacting fluids, increase in the first steps of reaction between 0-500 hours. In a second step of reaction the concentrations of these elements decrease, suggesting that they are incorporate in the formation of secondary minerals. In natural and open systems, these elements would be available for precipitation of carbonates and/or rodingitization reaction for example.

The examination of the solids products of the lherzolite and harzburgite seawater experiments, reveal that the resulting mineral assemblage are relatively similar, but variability in minerals proportions are observed. In the solids products from both lherzolite and harzburgite experiments, orthopyroxene is absent. Because, orthopyroxene is less abundant than olivine, orthopyroxene is more rapidly consumed during serpenti-

nization. Furthermore, the kinetics of orthopyroxene dissolution is faster than olivine at the conditions of our experiments. Some relics of primary olivine is observed in all the solids products, in increasing proportions with temperature of experiments. Relics of primary clinopyroxene is also observed in all solid products, and the proportion of clinopyroxene altered is inversely correlate to the increase of temperature in the lherzolite experiments. In the harzburgite experiments, clinopyroxene is unaffected by the serpentinization. In all solids products minor amounts of carbonates was observed in proportions apparently not correlated to the temperature of the experiments, but rather to the protolith. Indeed, higher proportions of carbonates are generated in the lherzolite experiments in comparison to the harzburgite experiments. Magnetite is formed in all solids products, however, lower amounts are generated in the harzburgite experiments. Proportions of secondary minerals from our experiments are dependent of the time of reaction and the temperature of reaction and thus the kinetic of mineral dissolution.

In the lherzolite-seawater experiments, olivine, orthopyroxene and clinopyroxene reacted simultaneously to formed the typical assemblage of serpentine-magnetite-calcite, as observed in natural systems. At low temperatures of experiments 225°C and 260°C the higher quantity of clinopyroxene dissolved release Na₂O in the reacting fluids. This coupled to the low amounts of magnetite formed in response to higher iron partitioning in serpentine than into magnetite, lead to increase the pH values, less favorable to the mobilization of elements. At higher temperatures of experiments (300°C and 325°C) more reducing conditions are generated, supported by high quantity of magnetite formed, high quantity of hydrogen released and a strong decrease of sulfur in the reacting fluids, generate conditions more favorable to the transport of elements in the natural systems.

In the harzburgite-seawater experiments, because orthopyroxene is rapidly consumed and clinopyroxene unaffected, the serpentinization is dominated by the dissolution of olivine. Consequently, an excess of magnesium is released in the reacting fluids coupled to low silica activity favors the formation of brucite. The lower quantity of magnetite formed in comparison to the lherzolite experiments at temperatures > 225°C is probably due to an higher partitioning of Fe in serpentine and brucite and less into magnetite. However, the partitioning of Fe into serpentine and brucite allow to generate similar proportion of hydrogen than the lherzolite experiment at 300°C.

Acknowledgments

Colin Fourtet (ITES - University of Strasbourg) performed the Ion chromatography analyses of the reacting fluids. René Boutin (ITES - University of Strasbourg) performed the ICP-AES and ICP-MS analyses of the reacting fluids. Amélie Aubert (ITES - University of Strasbourg) performed the X-RD analyses of the solid products. Ida di Carlo (ISTO) help for the SEM analysis. Thanks a lot Rémi Champallier and Frédéric Savoy (ISTO) for their assistance with the experimental setup.

5.6 Supplementary materials

Cpt 18 - 01_RX0453

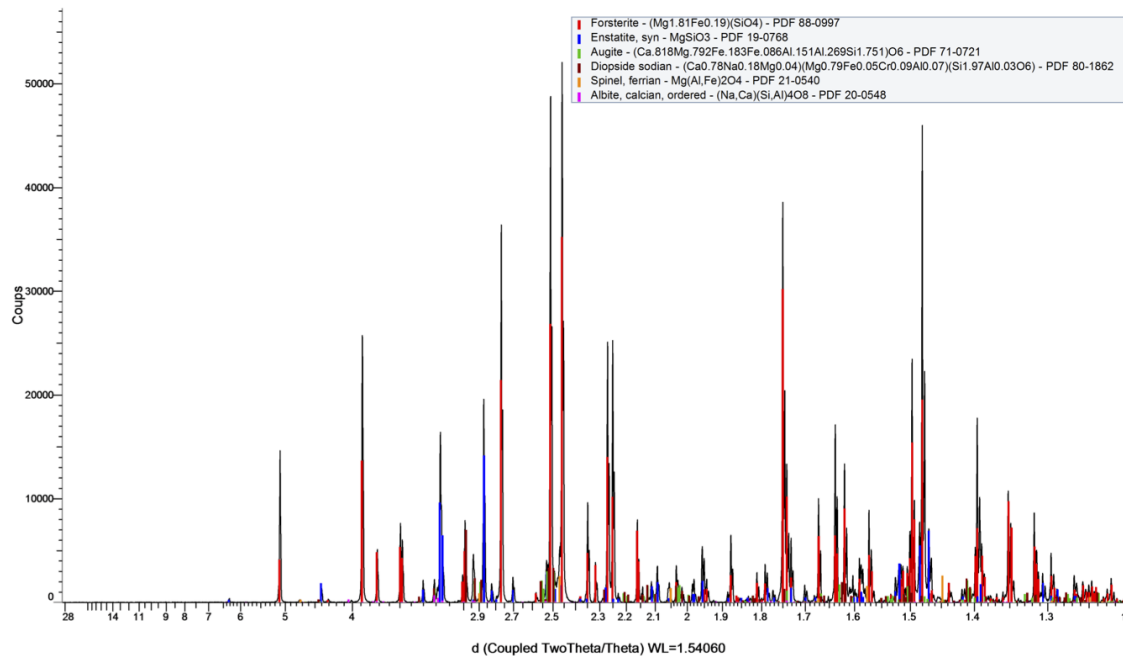


FIGURE 5.12 – XRD pattern of the primary harzburgite Cpt1801

Cpt 18 - 06_RX0457

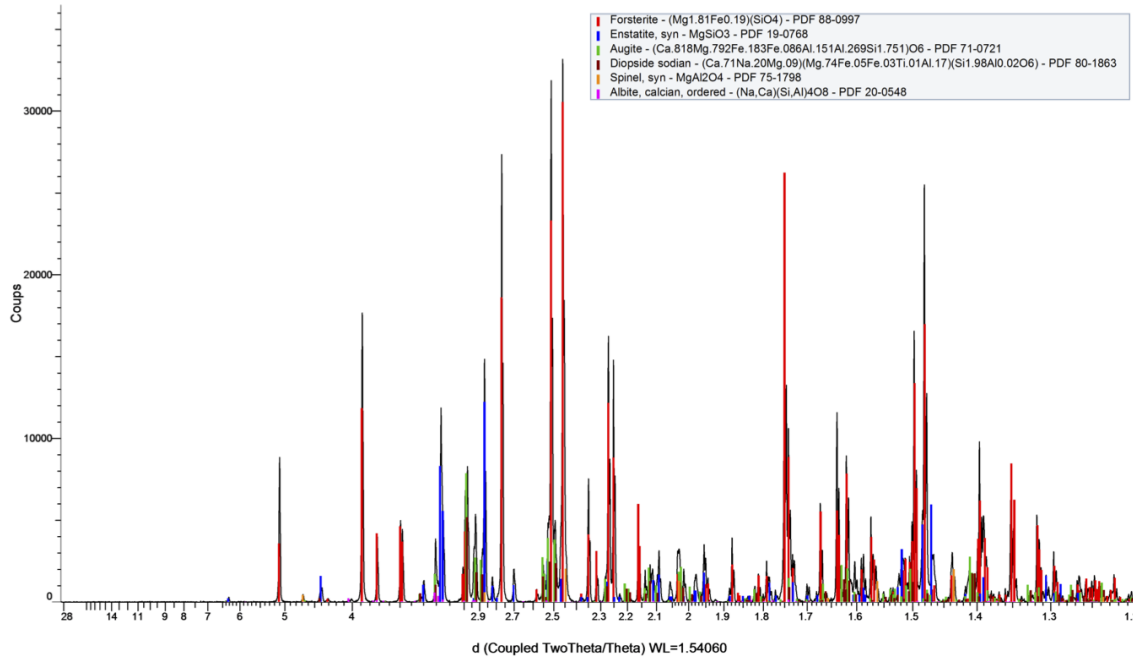


FIGURE 5.13 – XRD pattern of the primary lherzolite Cpt1806.

225 bulk - RX0727

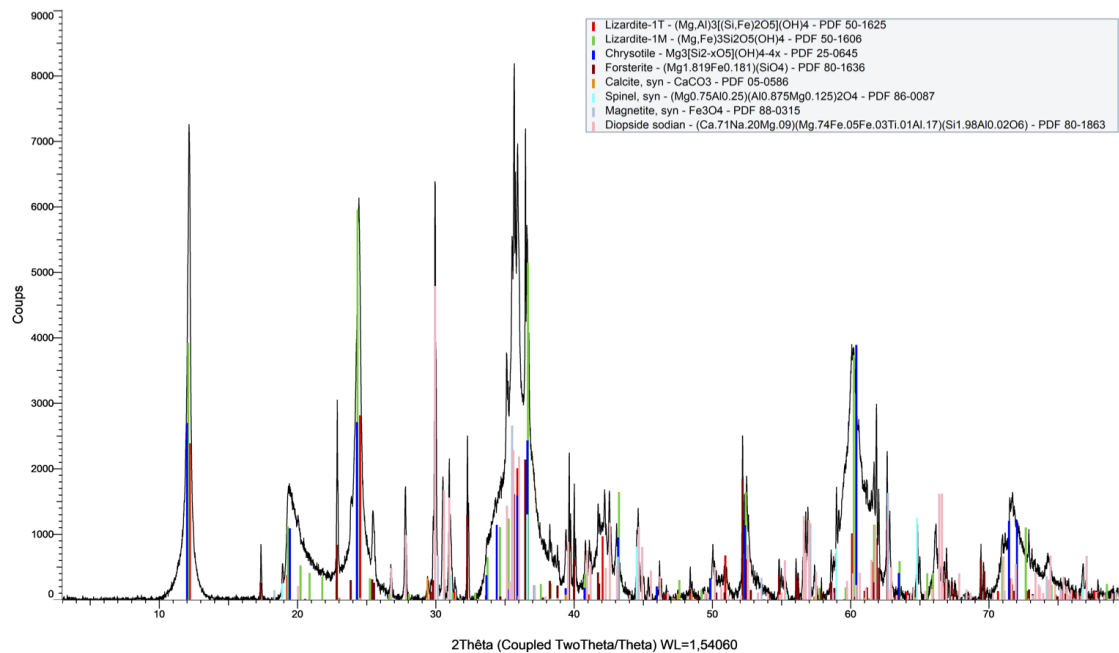


FIGURE 5.14 – XRD pattern of serpentinite at 225°C.

260 bulk - RX0730

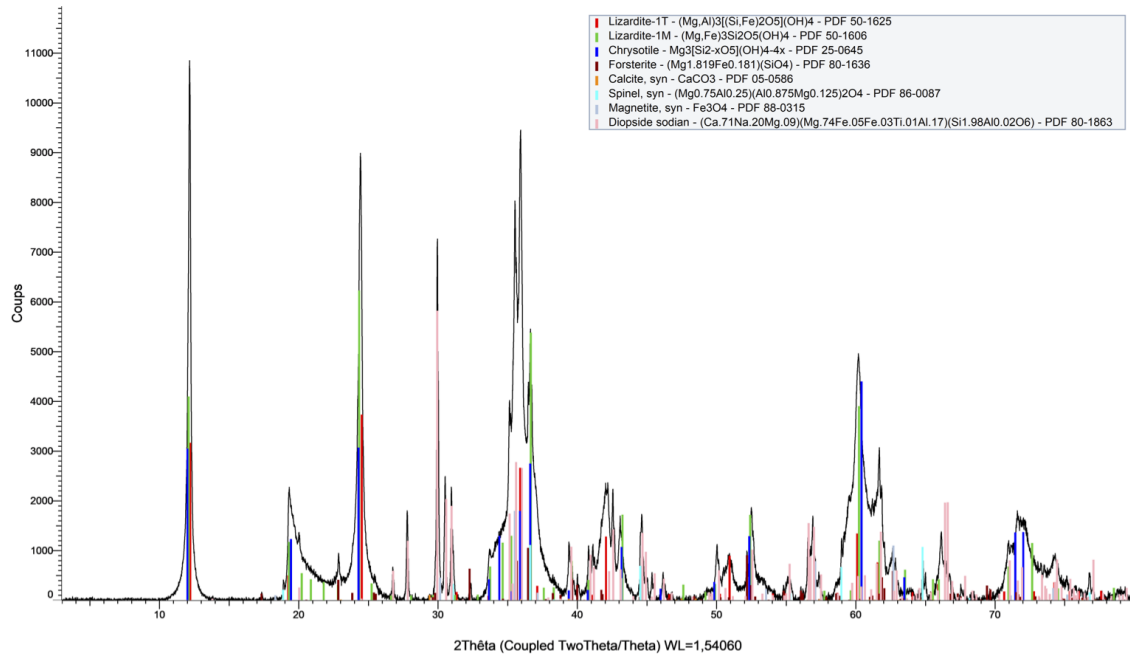


FIGURE 5.15 – XRD pattern of serpentinite at 260°C.

280 bulk - RX0733

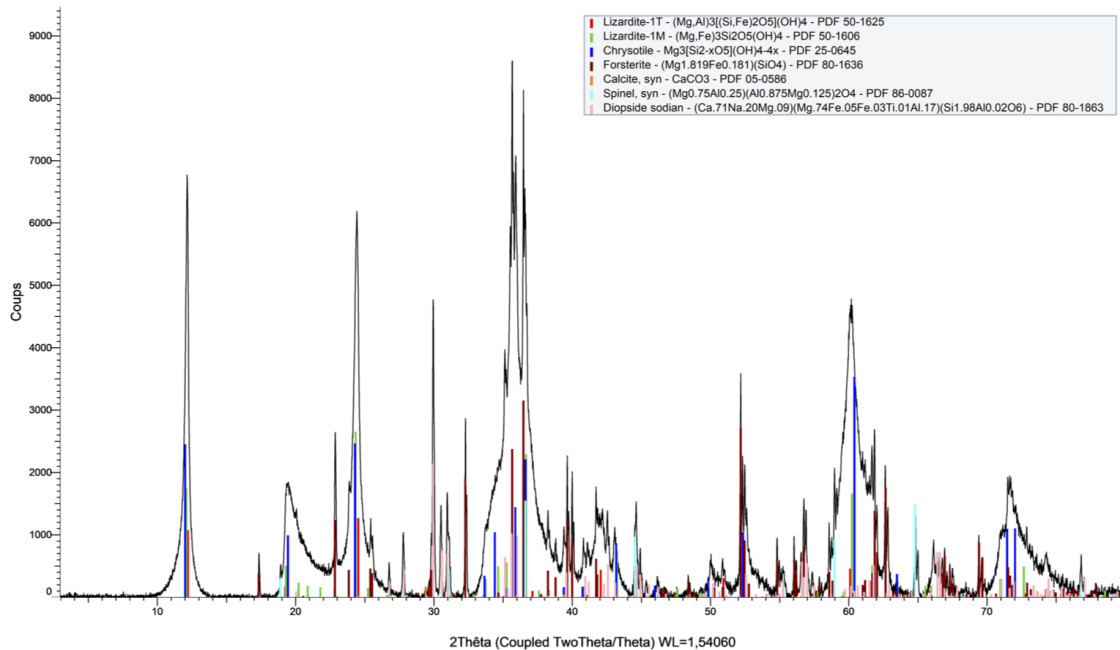


FIGURE 5.16 – XRD pattern of serpentinite at 280°C.

280 bis bulk - RX0736

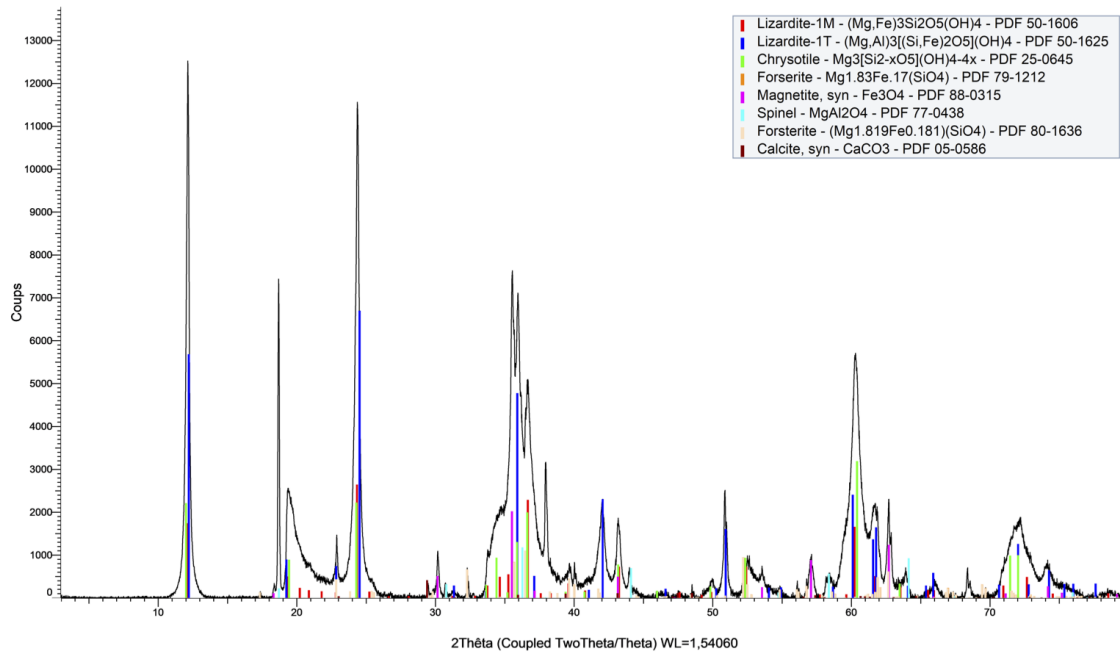


FIGURE 5.17 – XRD pattern of serpentinite at 280°C bis.

300 bulk - RX0739

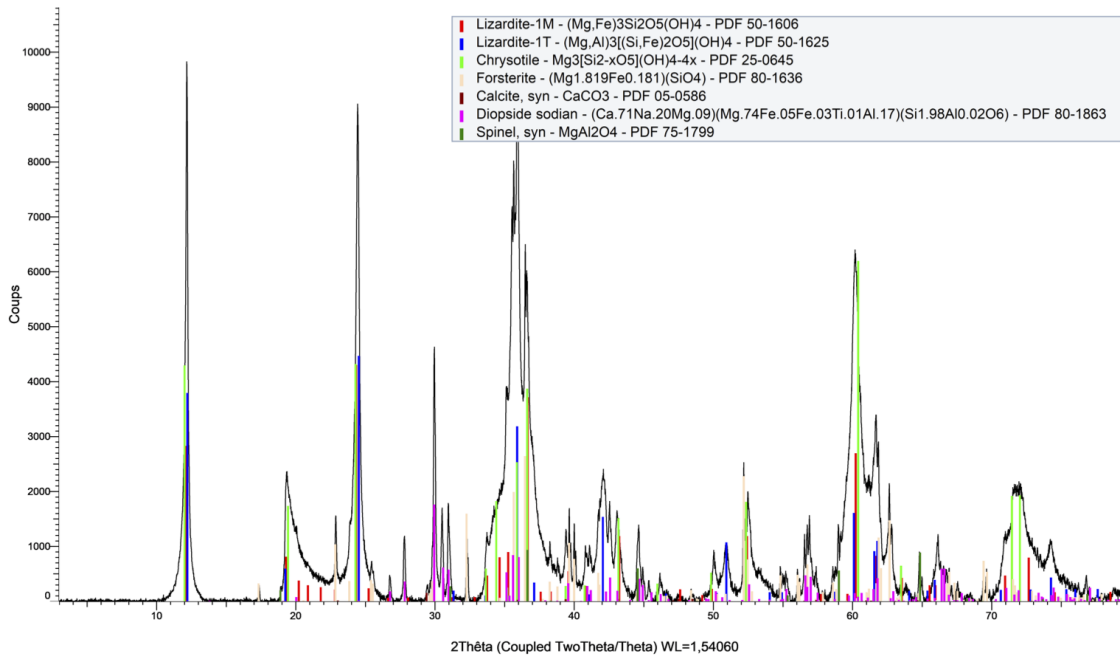


FIGURE 5.18 – XRD pattern of serpentinite at 300°C.

325 bulk - RX0742

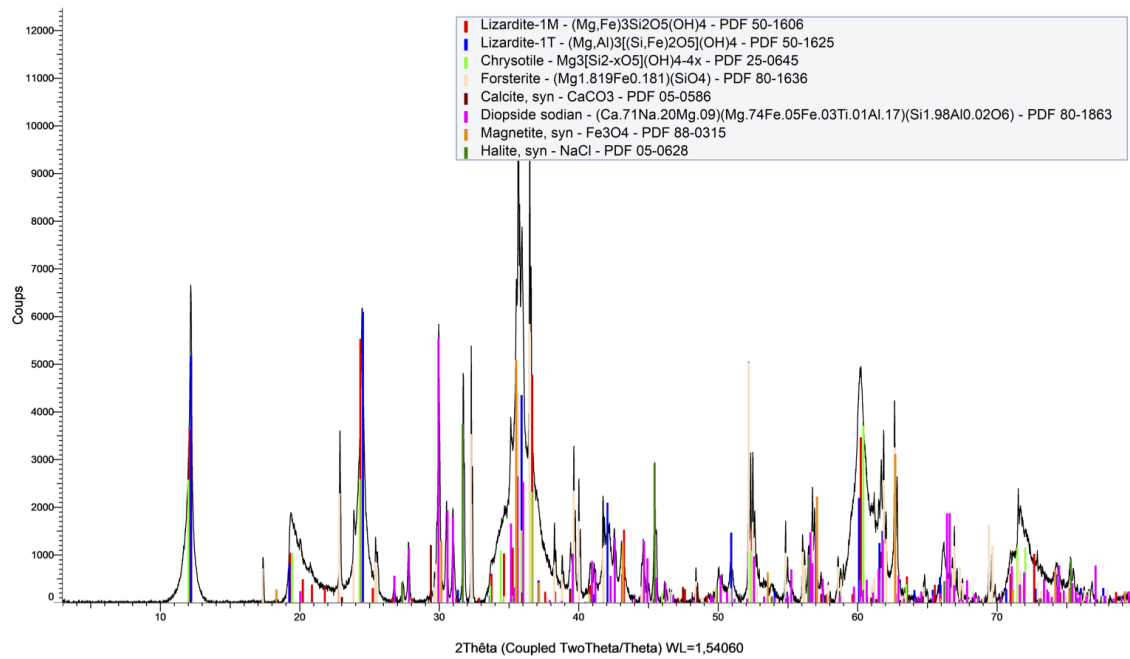


FIGURE 5.19 – XRD pattern of serpentinite at 325°C.

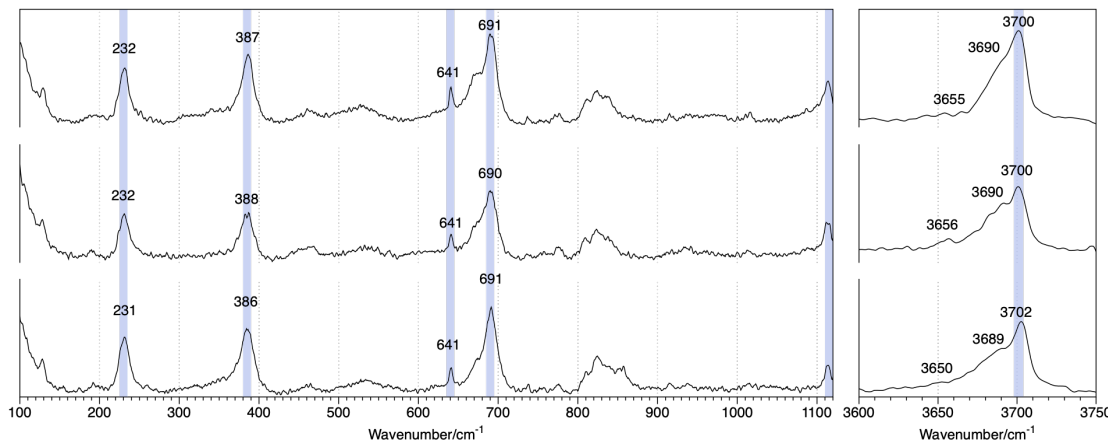


FIGURE 5.20 – Raman spectra of the solid product from experiment at 300 °C.

Bibliographie

- Agrinier, P., Hékinian, R., Bideau, D., and Javoy, M. (1995). O and h stable isotope compositions of oceanic crust and upper mantle rocks exposed in the hess deep near the galapagos triple junction. *Earth and Planetary Science Letters*, 136(3-4):183–196.
- Allen, D. E. and Seyfried Jr, W. (2003). Compositional controls on vent fluids from ultramafic-hosted hydrothermal systems at mid-ocean ridges : An experimental study at 400 c, 500 bars. *Geochimica et Cosmochimica Acta*, 67(8):1531–1542.
- Allen, D. E. and Seyfried Jr, W. (2004). Serpentinization and heat generation : constraints from Lost City and Rainbow hydrothermal systems. *Geochimica et Cosmochimica Acta*, 68(6):1347–1354.
- Alt, J. C., Schwarzenbach, E. M., Früh-Green, G. L., Shanks III, W. C., Bernasconi, S. M., Garrido, C. J., Crispini, L., Gaggero, L., Padrón-Navarta, J. A., and Marchesi, C. (2013). The role of serpentinites in cycling of carbon and sulfur : Seafloor serpentinization and subduction metamorphism. *Lithos*, 178:40–54.
- Bischoff, J. L. and Seyfried, W. E. (1978). Hydrothermal chemistry of seawater from 25 degrees to 350 degrees c. *American Journal of Science*, 278(6):838–860.
- Brugger, J., Liu, W., Etschmann, B., Mei, Y., Sherman, D. M., and Testemale, D. (2016). A review of the coordination chemistry of hydrothermal systems, or do coordination changes make ore deposits ? *Chemical Geology*, 447:219–253.
- Cann, J. R., Blackman, D., Smith, D., McAllister, E., Janssen, B., Mello, S., Avgerinos, E., Pascoe, A., and Escartin, J. (1997). Corrugated slip surfaces formed at ridge-transform intersections on the mid-atlantic ridge. *Nature*, 385(6614):329–332.
- Charlou, J., Donval, J., Fouquet, Y., Jean-Baptiste, P., and Holm, N. (2002). Geochemistry of high h2 and ch4 vent fluids issuing from ultramafic rocks at the rainbow hydrothermal field (36°14N, MAR). *Chemical geology*, 191(4):345–359.
- Chauvel, C., Bureau, S., and Poggi, C. (2011). Comprehensive chemical and isotopic analyses of basalt and sediment reference materials. *Geostandards and Geoanalytical Research*, 35(1):125–143.
- Chavagnac, V., Monnin, C., Ceuleneer, G., Boulart, C., and Hoareau, G. (2013). Characterization of hyperalkaline fluids produced by low-temperature serpentization of mantle peridotites in the oman and ligurian ophiolites. *Geochemistry, Geophysics, Geosystems*, 14(7):2496–2522.
- Delacour, A., Früh-Green, G. L., and Bernasconi, S. M. (2008a). Sulfur mineralogy and geochemistry of serpentinites and gabbros of the atlantis massif (iodp site u1309). *Geochimica et Cosmochimica Acta*, 72(20):5111–5127.

- Delacour, A., Früh-Green, G. L., Bernasconi, S. M., and Kelley, D. S. (2008b). Sulfur in peridotites and gabbros at lost city (30°N, MAR) : Implications for hydrothermal alteration and microbial activity during serpentinization. *Geochimica et Cosmochimica Acta*, 72(20):5090–5110.
- Doebelin, N. and Kleeberg, R. (2015). Profex : a graphical user interface for the Rietveld refinement program bgmn. *Journal of applied crystallography*, 48(5):1573–1580.
- Douville, E., Charlou, J. L., Oelkers, E. H., Bienvenu, P., Colon, C. F. J., Donval, J. P., Fouquet, Y., Prieur, D., and Appriou, P. (2002). The rainbow vent fluids (36°14'N, MAR) : the influence of ultramafic rocks and phase separation on trace metal content in Mid-Atlantic Ridge hydrothermal fluids. *Chemical Geology*, 184:37–48.
- Downes, H. and Dupuy, C. (1987). Textural, isotopic and ree variations in spinel peridotite xenoliths, massif central, france. *Earth and Planetary Science Letters*, 82(1-2):121–135.
- Escartín, J., Smith, D. K., Cann, J., Schouten, H., Langmuir, C. H., and Escrig, S. (2008). Central role of detachment faults in accretion of slow-spreading oceanic lithosphere. *Nature*, 455(7214):790–794.
- Fauguerolles, C. (2016). *Experimental study of H₂ generation associated with peridotite serpentinization at slow spreading ridges*. PhD thesis, Université d'Orléans.
- Fouquet, Y., Barriga, F., Charlou, J.-L., Elderfield, H., German, C., Ondreas, H., Parson, L., Radford-Knoery, J., Relvas, J., Ribeiro, A., et al. (1998). Flores diving cruise with nautile near the azores-first dives on the rainbow field : hydrothermal seawater/mantle interaction. *InterRidge News*, 7(1):24–28.
- Frost, R. (1975). Contact metamorphism of serpentinite, chloritic blackwall and rodingite at paddy-go-easy pass, central cascades, washington. *Journal of Petrology*, 16(2):272–313.
- Früh-Green, G. L., Connolly, J. A., Plas, A., Kelley, D. S., and Grobety, B. (2004). Serpentinization of oceanic peridotites : implications for geochemical cycles and biological activity. *The subseafloor biosphere at mid-ocean ridges*, 144:119–136.
- Früh-Green, G. L., Plas, A., and Lécuyer, C. (1996). 14. petrologic and stable isotope constraints on hydrothermal alteration and serpentinization of the epr shallow mantle at hess deep (site 895). In *Proceedings of the ocean drilling program, scientific results*, volume 147, pages 255–291.
- Giampouras, M., Garrido, C. J., Zwicker, J., Vadillo, I., Smrzka, D., Bach, W., Peckmann, J., Jiménez, P., Benavente, J., and García-Ruiz, J. M. (2019). Geochemistry and mineralogy of serpentinization-driven hyperalkaline springs in the ronda peridotites. *Lithos*, 350:105215.
- Grant, J. A. (1986). The isocon diagram ; a simple solution to gresens' equation for metasomatic alteration. *Economic geology*, 81(8):1976–1982.
- Grant, J. A. (2005). Isocon analysis : A brief review of the method and applications. *Physics and Chemistry of the Earth, Parts A/B/C*, 30(17-18):997–1004.
- Gresens, R. L. (1967). Composition-volume relationships of metasomatism. *Chemical geology*, 2:47–65.
- Grozeva, N. G., Klein, F., Seewald, J. S., and Sylva, S. P. (2017). Experimental study of carbonate formation in oceanic peridotite. *Geochimica et Cosmochimica Acta*, 199:264–286.

- Hannington, M. D., De Ronde, C. E., and Petersen, S. (2005). Sea-floor tectonics and submarine hydrothermal systems. *Society of Economic Geologists*, pages 111–141.
- Hansen, C. T., Meixner, A., Kasemann, S. A., and Bach, W. (2017). New insight on li and b isotope fractionation during serpentinization derived from batch reaction investigations. *Geochimica et Cosmochimica Acta*, 217:51–79.
- Huang, R., Ding, X., Lin, C.-T., Zhan, W., and Ling, M. (2018). Effect of saline fluids on chlorine incorporation in serpentine. *Solid Earth Sciences*, 3(3):61–66.
- Huang, R., Sun, W., Zhan, W., Ding, X., Zhu, J., and Liu, J. (2017). Influence of temperature, pressure, and fluid salinity on the distribution of chlorine into serpentine minerals. *Journal of Asian Earth Sciences*, 145:101–110.
- Humphris, S. E. and Klein, F. (2018). Progress in deciphering the controls on the geochemistry of fluids in seafloor hydrothermal systems. *Annual review of marine science*, 10:315–343.
- Jamieson, J. W. and Gartman, A. (2020). Defining active, inactive, and extinct seafloor massive sulfide deposits. *Marine Policy*, 117:103926.
- Janecky, D. and Seyfried Jr, W. (1986). Hydrothermal serpentinization of peridotite within the oceanic crust : Experimental investigations of mineralogy and major element chemistry. *Geochimica et Cosmochimica Acta*, 50(7):1357–1378.
- Jöns, N., Bach, W., and Klein, F. (2010). Magmatic influence on reaction paths and element transport during serpentinization. *Chemical Geology*, 274(3-4):196–211.
- Kelley, D. S., Karson, J. A., Blackman, D. K., FruÈh-Green, G. L., Butterfield, D. A., Lilley, M. D., Olson, E. J., Schrenk, M. O., Roe, K. K., Lebon, G. T., et al. (2001). An off-axis hydrothermal vent field near the mid-atlantic ridge at 30 n. *Nature*, 412(6843):145–149.
- Klein, F., Bach, W., Jöns, N., McCollom, T., Moskowitz, B., and Berquó, T. (2009). Iron partitioning and hydrogen generation during serpentinization of abyssal peridotites from 15 n on the mid-atlantic ridge. *Geochimica et Cosmochimica Acta*, 73(22):6868–6893.
- Klein, F., Bach, W., and McCollom, T. M. (2013). Compositional controls on hydrogen generation during serpentinization of ultramafic rocks. *Lithos*, 178:55–69.
- Klein, F., Grozeva, N. G., Seewald, J. S., McCollom, T. M., Humphris, S. E., Moskowitz, B., Berquó, T. S., and Kahl, W.-A. (2015a). Experimental constraints on fluid-rock reactions during incipient serpentinization of harzburgite. *American Mineralogist*, 100(4):991–1002.
- Klein, F., Humphris, S. E., Guo, W., Schubotz, F., Schwarzenbach, E. M., and Orsi, W. D. (2015b). Fluid mixing and the deep biosphere of a fossil lost city-type hydrothermal system at the iberia margin. *Proceedings of the National Academy of Sciences*, 112(39):12036–12041.
- Klein, F. and Le Roux, V. (2020). Quantifying the volume increase and chemical exchange during serpentinization. *Geology*, 48(6):552–556.
- Lafay, R., Montes-Hernandez, G., Janots, E., Chiriac, R., Findling, N., and Toche, F. (2012). Mineral replacement rate of olivine by chrysotile and brucite under high alkaline conditions. *Journal of Crystal Growth*, 347(1):62–72.
- Li, X.-P., Rahn, M., and Bucher, K. (2004). Serpentinites of the zermatt-saas ophiolite complex and their texture evolution. *Journal of metamorphic Geology*, 22(3):159–177.

- Malvoisin, B. and Brunet, F. (2014). Water diffusion-transport in a synthetic dunite : Consequences for oceanic peridotite serpentinization. *Earth and Planetary Science Letters*, 403:263–272.
- Malvoisin, B., Brunet, F., Carlut, J., Rouméjon, S., and Cannat, M. (2012). Serpentinization of oceanic peridotites : 2. kinetics and processes of san carlos olivine hydrothermal alteration. *Journal of Geophysical Research : Solid Earth*, 117(B4).
- Marcaillou, C., Munoz, M., Vidal, O., Parra, T., and Harfouche, M. (2011). Mineralogical evidence for h2 degassing during serpentinization at 300 c/300 bar. *Earth and Planetary Science Letters*, 303(3-4):281–290.
- Martin, B. and Fyfe, W. (1970). Some experimental and theoretical observations on the kinetics of hydration reactions with particular reference to serpentinization. *Chemical Geology*, 6:185–202.
- McCollom, T. M. and Bach, W. (2009). Thermodynamic constraints on hydrogen generation during serpentinization of ultramafic rocks. *Geochimica et Cosmochimica Acta*, 73(3):856–875.
- McCollom, T. M., Klein, F., Moskowitz, B., Berquó, T. S., Bach, W., and Templeton, A. S. (2020a). Hydrogen generation and iron partitioning during experimental serpentinization of an olivine–pyroxene mixture. *Geochimica et Cosmochimica Acta*, 282:55–75.
- McCollom, T. M., Klein, F., Robbins, M., Moskowitz, B., Berquó, T. S., Jöns, N., Bach, W., and Templeton, A. (2016). Temperature trends for reaction rates, hydrogen generation, and partitioning of iron during experimental serpentinization of olivine. *Geochimica et Cosmochimica Acta*, 181:175–200.
- McCollom, T. M., Klein, F., Solheid, P., and Moskowitz, B. (2020b). The effect of ph on rates of reaction and hydrogen generation during serpentinization. *Philosophical Transactions of the Royal Society A*, 378(2165):20180428.
- Mottl, M. J. and Holland, H. D. (1978). Chemical exchange during hydrothermal alteration of basalt by seawater—i. experimental results for major and minor components of seawater. *Geochimica et Cosmochimica Acta*, 42(8):1103–1115.
- Mottl, M. J., Holland, H. D., and Corr, R. F. (1979). Chemical exchange during hydrothermal alteration of basalt by seawater—ii. experimental results for fe, mn, and sulfur species. *Geochimica et Cosmochimica Acta*, 43(6):869–884.
- O'Hanley, D. S. (1992). Solution to the volume problem in serpentinization. *Geology*, 20(8):705–708.
- Palandri, J. L. and Reed, M. H. (2004). Geochemical models of metasomatism in ultramafic systems : serpentinization, rodingitization, and sea floor carbonate chimney precipitation. *Geochimica et Cosmochimica Acta*, 68(5):1115–1133.
- Patten, C. G., Coltat, R., Junge, M., Peillod, A., Ulrich, M., Manatschal, G., and Kolb, J. (2022). Ultramafic-hosted volcanogenic massive sulfide deposits : an overlooked sub-class of vms deposit forming in complex tectonic environments. *Earth-Science Reviews*, page 103891.
- Salters, V. J. and Stracke, A. (2004). Composition of the depleted mantle. *Geochemistry, Geophysics, Geosystems*, 5(5).

- Scholten, L., Schmidt, C., Lecumberri-Sanchez, P., Newville, M., Lanzirotti, A., Sirbescu, M.-L. C., and Steele-MacInnis, M. (2019). Solubility and speciation of iron in hydrothermal fluids. *Geochimica et Cosmochimica Acta*, 252:126–143.
- Schwarzenbach, E. M., Vogel, M., Früh-Green, G. L., and Boschi, C. (2021). Serpentinitization, Carbonation, and Metasomatism of Ultramafic Sequences in the northern Apennine Ophiolite (NW Italy). *Journal of Geophysical Research : Solid Earth*, 126.
- Seewald, J. S. and Seyfried Jr, W. E. (1990). The effect of temperature on metal mobility in subseafloor hydrothermal systems : constraints from basalt alteration experiments. *Earth and Planetary Science Letters*, 101(2-4):388–403.
- Seyfried, W. and Bischoff, J. L. (1977). Hydrothermal transport of heavy metals by seawater : The role of seawater/basalt ratio. *Earth and Planetary Science Letters*, 34(1):71–77.
- Seyfried Jr, W. and Dibble Jr, W. (1980). Seawater-peridotite interaction at 300 c and 500 bars : implications for the origin of oceanic serpentinites. *Geochimica et Cosmochimica Acta*, 44(2):309–321.
- Seyfried Jr, W., Foustoukos, D., and Fu, Q. (2007). Redox evolution and mass transfer during serpentinitization : An experimental and theoretical study at 200 c, 500 bar with implications for ultramafic-hosted hydrothermal systems at mid-ocean ridges. *Geochimica et Cosmochimica Acta*, 71(15):3872–3886.
- Seyfried Jr, W., Janecky, D. R., and Berndt, M. (1987). Rocking autoclaves for hydrothermal experiments ii. the flexible reaction-cell system. *Hydrothermal Experimental Techniques* (ed GC Ulmer, pages 216–239.
- Seyfried Jr, W. E. and Mottl, M. J. (1982). Hydrothermal alteration of basalt by seawater under seawater-dominated conditions. *Geochimica et Cosmochimica Acta*, 46(6):985–1002.
- Shanks III, W. C. (2001). Stable isotopes in seafloor hydrothermal systems : vent fluids, hydrothermal deposits, hydrothermal alteration, and microbial processes. *Reviews in Mineralogy and Geochemistry*, 43(1):469–525.
- Sharp, Z. and Barnes, J. (2004). Water-soluble chlorides in massive seafloor serpentinites : a source of chloride in subduction zones. *Earth and Planetary Science Letters*, 226(1-2):243–254.
- Susak, N. J. and Crerar, D. A. (1985). Spectra and coordination changes of transition metals in hydrothermal solutions : Implications for ore genesis. *Geochimica et Cosmochimica Acta*, 49(2):555–564.
- Testemale, D., Brugger, J., Liu, W., Etschmann, B., and Hazemann, J.-L. (2009). In-situ x-ray absorption study of iron (ii) speciation in brines up to supercritical conditions. *Chemical Geology*, 264(1-4):295–310.
- Tian, Y., Etschmann, B., Mei, Y., Grundler, P. V., Testemale, D., Hazemann, J.-L., Elliott, P., Ngothai, Y., and Brugger, J. (2014). Speciation and thermodynamic properties of manganese (ii) chloride complexes in hydrothermal fluids : in situ xas study. *Geochimica et Cosmochimica Acta*, 129:77–95.
- Vils, F., Pelletier, L., Kalt, A., Müntener, O., and Ludwig, T. (2008). The lithium, boron and beryllium content of serpentinized peridotites from odp leg 209 (sites 1272a and 1274a) : implications for lithium and boron budgets of oceanic lithosphere. *Geochimica et Cosmochimica Acta*, 72(22):5475–5504.

- Von Damm, K. (1990). Seafloor hydrothermal activity : black smoker chemistry and chimneys. *Annual Review of Earth and Planetary Sciences*, 18:173.
- Wegner, W. W., Ernst, W., et al. (1983). Experimentally determined hydration and de-hydration reaction rates in the system mgo-sio₂-h₂o. *American Journal of Science*, 283:151–180.
- Xu, Y.-G., Menzies, M., Bodinier, J.-L., Bedini, R., Vroon, P., and Mercier, J.-C. (1998). Melt percolation and reaction atop a plume : evidence from the poikiloblastic peridotite xenoliths from borée (massif central, france). *Contributions to Mineralogy and Petrology*, 132(1):65–84.

Chapitre 6

**Experimental study of boron
isotope fractionation during
peridotite serpentinization by
seawater from 225 to 325°C and 450
bars**

Abstract

Boron concentrations and isotope in the seawater-peridotite system have been measured during laboratory experiments of peridotite serpentinization in contact with seawater from 225°C to 325°C at 450 bars. The boron concentrations in reacting fluids strongly decrease in the first 500 hours, leading to a transfer of $\sim 90\%$ of the total B into the solid phase. Treatment of the residual solids with mannitol indicates that most of the boron remains water soluble. After semi-quantitative mineral separation, it is observed that the boron concentration in serpentine minerals is positively correlated to the temperature, while being negatively correlated in magnetite. Starting at +39.6‰ at the beginning of each experiment, the boron isotopic composition of reacting fluids ($\delta^{11}\text{B}_{fluid}$) end between +32.2‰ and +44.2‰ indicating a preferential incorporated into the solids of either the light (^{10}B) isotope at 225°C and 260°C or the heavy (^{11}B) one at higher temperatures (280-325°C). Based on the pH strong dependence of the boron isotopic fractionation, this opposite behavior of boron isotopes is interpreted as reflecting different pH values of the reacting fluid. The higher temperature the higher pH, thus making the temperature an indirect parameter of the boron isotope fractionation during serpentinization. After removal of the water-soluble boron, bulk solids are characterized by $\delta^{11}\text{B}_{solid}$ ranging between +25.5‰ and +32.6‰. $\delta^{11}\text{B}_{mgt}$ in magnetite varies between +25.1‰ and +34.5‰ and increases with temperature. Serpentine minerals show larger isotopic fractionation with $\delta^{11}\text{B}_{srp}$ comprised between +8.1‰ and +32.8‰ and are negatively correlated to the temperature. These results suggest that the boron may be used as a proxy of temperature and pH of the fluid during peridotite serpentinization.

Keywords : Serpentinization, Hydrothermal experiments, serpentinization, boron isotopes, geothermometer

6.1 Introduction

Serpentinization is the alteration of primary ferro-magnesian minerals of mantle peridotite, mainly composed of olivine and the two pyroxenes. In contact with fluids under a large range of temperature (<50-350°C ; e.g., Wenner and Taylor 1971 ; Agrinier et al. 1995 ; Früh-Green et al. 2004, 1996 ; Skelton and Valley 2000 ; Mével 2003 ; Alt and Shanks III 2003), these minerals are transformed into serpentine with minor secondary by-products such as brucite, talc and iron oxides such as magnetite and hematite. The serpentine minerals can integrate up to ~13 wt.% of H₂O in their structure, depending on the serpentine type. Serpentinization can also release H₂ enabling the formation of abiotic methane CH₄ by reduction of carbon via a Fischer-Tropsch type and Sabatier type reactions (e.g., Proskurowski et al. 2006, 2008 ; Russell et al. 2010 ; Holm et al. 2015) supporting development of life in anaerobic environments. These reactions have major consequences on the physical properties of the lithosphere, such as the rheology and the density (Christensen 1972 ; Carlson and Miller 1997 ; Escartin et al. 1997) as well as on the chemical properties of the lithosphere and the geochemical budget of the oceans (Thompson and Melson 1970 ; Snow and Dick 1995). For example, Snow and Dick 1995 have estimated that serpentinization releases about 10¹² moles of magnesium per year in the ocean. Additionally, the upper part of the lithospheric mantle is strongly enriched in some fluid-mobile elements like boron (e.g., Thompson and Melson 1970 ; Moody 1976 ; Spivack and Edmond 1987 ; Vils et al. 2008 ; Boschi et al. 2008 ; Marschall 2018 ; McCaig et al. 2018). Such B enrichment, which is concentrated in the seawater (~4.5 ppm, Spivack and Edmond 1987) but depleted in the mantle (0.05 ppm, Salters and Stracke 2004), highlights the chemical exchanges that occur during interactions between the mantle and the hydrosphere (e.g., Moody 1976 ; Spivack and Edmond 1987). The Serpentinization process takes place wherever water can interact with mantle rocks and thus occurs in most geological settings, although largely documented in subduction zones and at mid-ocean ridges (e.g., Hyndman and Peacock 2003 ; Mével 2003 ; Ranero et al. 2003 ; Andreani et al. 2007 ; Deschamps et al. 2011, 2010 ; Rouméjon and Cannat 2014 ; Guillot et al. 2015). Serpentinization is particularly active along (ultra-) slow spreading centers and passive margins, where peridotites are exposed on the seafloor by large-offset normal and detachment faults Cann et al. 1997. These faults are preferential pathways for fluids Jackson 1987 ; O'hanley 1991 ; Escartín et al. 2008. These faults are preferential pathways for fluids leading to the intense hydration observed in the surrounding mantle rocks. Previous studies have shown that

serpentization occurred also under a wide range of pH and redox conditions, leading to the formation of hydrothermal fluids with variable chemical compositions depending of the temperature. Indeed, at low temperatures of serpentization <150 °C the fluids produced are hyperalkaline ($8.5 < \text{pH} < 12$) Mg poor and Na, K, Cl⁻ and Ca rich (e.g., Barnes and O'Neil 1969 ; Kelley et al. 2001 ; Allen and Seyfried Jr 2004 ; Chavagnac et al. 2013 ; Etiope et al. 2013 ; Schrenk et al. 2013 ; D'Alessandro et al. 2018 ; Giampouras et al. 2019). In contrast at higher temperature (>300 °C) of serpentization more reducing fluids characterized by low pH < 5.5 and relatively high chlorinity, SiO₂ or Fe content are produced (e.g., Charlou et al. 2002 ; Douville et al. 2002 ; Allen and Seyfried Jr 2003).

The determination of temperature at which serpentization occurred is thus fundamental for the understanding of rheology, the seafloor spreading rate and the thermal regime at magma-poor rifted margins. So far, the determination of serpentization temperature is based on two geothermometers : the first one was developed on the oxygen isotopes (¹⁸O/¹⁶O) fractionation between coexisting Fe-Ti oxides and chlorite from low-grade pelitic schists, with temperature that was previously constrained by applying the quartz-muscovite geothermometer (Wenner and Taylor 1971). It was then repetitively extrapolated to the serpentine-magnetite mineral pair in serpentinites, while it is essentially based on the assumption that the fractionation of oxygen isotopes between serpentine and magnetite is similar to that of chlorite-magnetite mineral pairs (Bonatti et al. 1984 ; Burkhard and O'Neil 1988 ; Agrinier and Cannat 1997 ; Agrinier et al. 1996, 1995 ; Skelton and Valley 2000 ; Alt and Shanks III 2006 ; Alt et al. 2007 ; Rouméjon et al. 2018). The second geothermometer was proposed more recently by Saccoccia et al. 2009. It relies on oxygen and hydrogen isotopes fractionation between serpentine and water, but it focuses on ¹⁸O and D partitioning during the recrystallization of lizardite to chrysotile. Moreover, the calibration of this geothermometer was limited to temperatures between 250°C and 450°C, which may problematic for its application in some geological settings where lower temperatures of serpentization are assumed. For example, serpentization temperature at passive margins is estimated to be (<200°C ; Agrinier et al. 1995 ; Skelton et al. 2000). Thus the development of a new geothermometer is needed for a more accurate determination of temperature during mantle-fluid interactions.

This study aims at determining the boron isotopes fractionation in seawater - serpentinite systems, and in serpentine-magnetite mineral pairs. To do so, our approach is based on laboratory experiments using fresh peridotites and natural seawater. These

new results are intended to be used for a new geothermometer to constrain serpentinization temperatures on natural samples from various geological settings.

6.1.1 The distribution of boron and boron isotopes between the earth envelopes

Boron has received an increasing interest in the past two decades to characterize of fluid-rock interactions in surface and deep geological settings (e.g., Spivack et al. 1987; Vils et al. 2009 ; Boschi et al. 2013; Martin et al. 2016; Yamada et al. 2019). Boron is an element with a low atomic mass and two stable isotopes, ^{10}B and ^{11}B , with relative abundance of about 20% and 80%, respectively. It is a highly incompatible and soluble element Spivack et al. 1987 leading to a strong partitioning in Earth reservoirs. It is mainly concentrated in the continental crust (11 ppm ; Rudnick et al. 2003) and in the oceans (seawater : 4.5 ppm ; Spivack and Edmond 1987) but depleted in the mantle and in MORBs (0.06 ppm and between 0.28 and 3 ppm, respectively ; Spivack and Edmond 1987; Ryan and Langmuir 1993; Salters and Stracke 2004). The continental crust varies from -20 to $+10\text{\textperthousand}$, depending on the B-isotope composition of the protoliths and on fractionation effects caused by phase transitions (Chaussidon and Jambon 1994; Trumbull and Slack 2018). The Mantle shows a narrower range, with an average $\delta^{11}\text{B}$ of $-7.1 \pm 0.9\text{\textperthousand}$ for the uppermost mantle (i.e., the DMM ; Marschall et al. 2017), while the deeper mantle (primitive-like) $\delta^{11}\text{B}$ is slightly lower at $-10 \pm 2\text{\textperthousand}$, based on the analyses of ocean island basalts worldwide Chaussidon and Marty 1995. Finally, modern seawater has remarkably uniform boron isotopic composition of $+39.6\text{\textperthousand}$ Spivack and Edmond 1987 with a very long residence time of about 15 Ma Lemarchand et al. 2000. Considering the large variations in boron concentrations and isotopic composition between mantle and seawater, boron is commonly used as a tracer of fluid-rock interactions such as serpentinization.

6.1.2 B isotope speciation and isotopic fractionation

In aqueous fluids, boron forms a weak acid / weak base couple with a $\text{pK}_\text{a}=9.23$ in diluted water, which value drops down to $\text{pK}_\text{a} = 8.83$ at 25°C in seawater Figure 6.1 under the influence of the salinity (Hershey et al. 1986 ; Kakihana et al. 1977 ; Hershey et al. 1986 ; Dickson 1990 ; Liu and Tossell 2005 ; Boschi et al. 2008). It is trigonally coordinated $\text{B}(\text{OH})_3$ in the boric acid form whereas being tetrahedrally coordinated

$\text{B}(\text{OH})_4^-$ in the borate form.

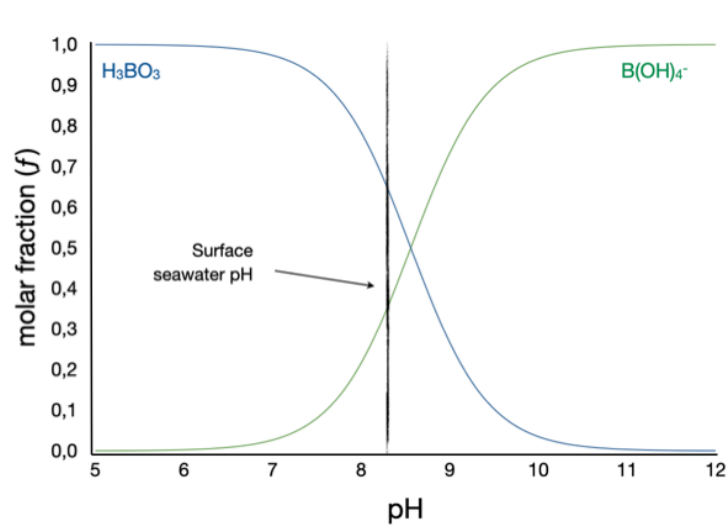
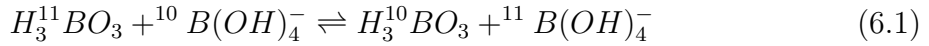


FIGURE 6.1 – Fraction of the boron species dissolved in seawater. blue $\text{H}_3\text{B}(\text{OH})_3$; green : $\text{B}(\text{OH})_4^-$

The marked difference of structure between the two species affects the relative distribution of isotopes and can be described by the following equilibrium :



The constant of this reaction gives the value of the isotopic fractionation (classically noted α) between the two species.

$$\alpha_{III-IV} = \frac{(^{11}B/^{10}B)_{trigonal}}{(^{11}B/^{10}B)_{tetrahedral}} \quad (6.2)$$

The boric acid form is slightly enriched in ^{11}B compared to the borate one with an isotopic fractionation $\alpha = 0.981$ at 25 °C (Kakihana and Kotaka 1977), a value that converges to 1 with increasing temperature (Boschi et al. 2008). An important feature of the boron chemical properties is that the relative proportion of each species and, in turn, the distribution of boron isotopes is dependent of the pH Figure 6.2.

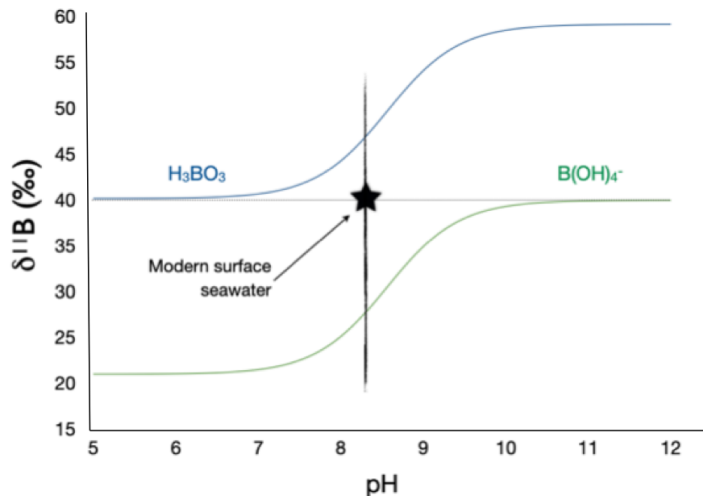


FIGURE 6.2 – Distribution of boric acid and borate in seawater in function of pH.

It is commonly observed that the boron isotopic composition of precipitated minerals is similar to the one of the aqueous borate form, making boron a recognized proxy for the pH of the reacting fluid as long as the $\delta^{11}\text{B}$ of the fluid is known (e.g. Palmer et al. 1987 ; Hemming and Hanson 1992 ; Pagani et al. 2005 ; Lemarchand et al. 2015).

In solids, boron can also be present in both trigonal and tetrahedral coordination, which has a direct influence on the mineral isotopic composition. A recent work proposed a simplified theoretical model that link the boron isotopic composition of silicate minerals, the relative proportion of trigonal and tetrahedral boron and the B/Si ordering Li et al. 2021. It is concluded that "the temperature dependency of boron isotope fractionation is greater for acidic fluids than for basic fluids, reinforcing the conclusion that the difference in the coordination of boron in trigonal/tetrahedral structures in the two phases dominates boron isotope fractionation". The main implication is that temperature affects boron coordination as well as the magnitude of the boron isotopic fractionation factor between the aqueous fluid and a given mineral, and that this fractionation also depends on B-Si ordering, i.e., the crystallographic structure. The comparison of boron isotopes between two co-genetic minerals therefore allows to record the temperature of their formation as illustrated in the Figure 6.3.

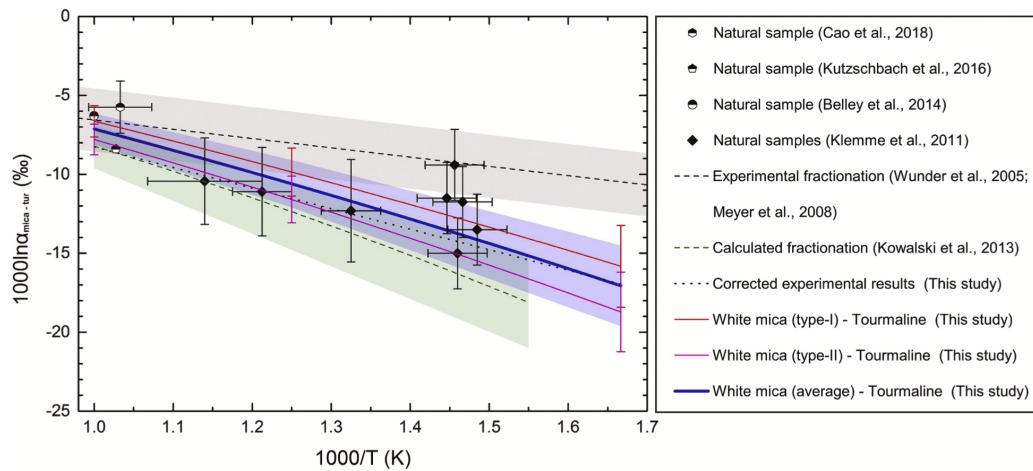


FIGURE 6.3 – Comparison of theoretically and experimentally determined boron isotope fractionation factors ($1000 \ln \alpha$ mica-tur) between mica and tourmaline. Figure from Li et al. 2021.

6.1.3 The boron behavior during serpentinization

During serpentinization processes, mantle peridotites react with seawater to form serpentinites that are strongly enriched in B compared to the initial peridotite (from 10 to > 100 ppm, see review by Marschall 2018, and display a large range of $\delta^{11}\text{B}$ compositions (+8 ‰ to +41 ‰; e.g., Spivack and Edmond 1987; Boschi et al. 2008 ; Vils et al. 2009). Pabst et al. 2011 have demonstrated that boron is integrated in the serpentine crystal structure during serpentinization. Three serpentine minerals including lizardite, chrysotile and antigorite can form depending of the temperature and pressure (e.g., Mével 2003 ; Evans et al. 2013). Today, it is commonly accepted that formation of serpentine chrysotile/lizardite in Mid Oceanic Ridge settings integrate variable amount of boron (e.g., Pelletier et al. 2008 ; Boschi et al. 2008 ; Vils et al. 2009). Moreover, Boschi et al. 2008 have shown that serpentinites from at low temperature and high pH integrate higher amount of boron than at higher temperature and lower pH. In contrast, during the transition from chrysotile/lizardite to antigorite which occurs during subduction, about 65-90% of boron is release to the fluid (Moran et al. 1992 ; Scambelluri et al. 2004 ; Scambelluri and Tonarini 2012 ; Savov et al. 2007 ; Deschamps et al. 2013, 2010 ; Kodolányi and Pettke 2011 ; Vils et al. 2011 ; Debret et al. 2013 ; Harvey et al. 2014 ; Martin et al. 2016 ; Hoog et al. 2018 ; Cannaò 2020).

6.2 Methods

In order to characterized i) the boron isotopes evolution in seawater reacting with peridotite during serpentinization and ii) the boron isotopes fractionation between coexisting serpentine and magnetite mineral phases, a series of six experiments were conducted in laboratory. Four lherzolite-seawater experiments were conducted at the nominal temperatures of 225°C, 260°C, 300°C and 325°C, with reaction times varying from 1728 and 3288 hours (i.e., 72 - 137 days). In complement, two harzburgite seawater experiments at 280°C and duration time of 504 hours and 1996 hours (i.e., 21 and 83 days). These hydrothermal experiments were conducted at 450 bars under a low water/rock ratios (W/R), ranging between 1.6 and 2.2. A w/r >1 was chosen to promote the formation of magnetite which is indispensable for the development of a geothermometer based on the serpentine-magnetite mineral pairs. A summary of experimental parameters is given in Table 5.1 of chapter 5. In this chapter we focus only to the boron geochemistry during serpentinization, but it is not exclude that the solid

products impact the fractionation of B isotopes.

6.2.1 Starting materials

Fresh mantle xenoliths were sampled at Mont Coupet (Massif-Central, France). These peridotites were powdered in an agate miller to fine particles with an average grain size $<20\mu\text{m}$. Two distinct lithologies were used during experiments, the first one consisting of a spinel-lherzolite (Cpt-1806) and the second to a spinel-harzburgite (Cpt-1801), which contains a significantly lower proportion of clinopyroxene (13.2 vs. 4.50 vol.%, respectively) and a higher proportion of olivine (61.2 vs. 72.4 vol.%, respectively), both containing relatively similar proportions of orthopyroxene (22.4 vs. 23.6 vol.%, respectively). The detailed concentrations of major elements in bulk-rock and in minerals can be found in Table 5.2 and 5.4 respectively in the previous chapter.

Natural seawater was sampled at rising tide at the mouth of Gironde estuary, between La Palmyre and the Cordouan lighthouse (west coast of France). Each sample was immediately filtered with $45\ \mu\text{m}$ cellulose filters to remove the potential organic matter. Seawater have an initial boron concentration of 4.40 ppm and an isotopic signature $\delta^{11}\text{B}$ of +39.9‰ (Table 6.1), which is in accordance with certified seawater standards (e.g., IAPSO) and previous seawater measurements (Foster et al., 2010).

6.2.2 Experimental setup

The hydrothermal experiments were conducted at the Institut des Sciences de la Terre d'Orléans laboratory (ISTO), using an experimental configuration similar to that of Seyfried Jr et al. 1987. Peridotite powders and natural seawater were loaded into a flexible titanium reaction cell with titanium exit tube and sampling valve, the overall being placed into a steel-alloy autoclave filled with water, as described by Seyfried Jr et al. 1987. All titanium surfaces in contact with the fluid were oxidized in a furnace at 400°C for a minimum of 12 hours prior to each experiments. The flexible titanium bag allow external control of the pressure which was regulated at the beginning of each experiments by pumping or injected water into the autoclave. The titanium sample valve was used for periodic sampling of the fluid during experiments for chemical characterization. Gas-tight glass syringes were used to sample volatile species inclunding H₂ during the reactions. The temperature was controlled by a thermocouple ($\pm 1^\circ\text{C}$) located at the top of the autoclave. Each experiments were terminated by shutting off

TABLE 6.1 – Measured boron concentration in ppm and isotopic composition $\delta^{11}\text{B}$ of in ‰ in seawater and standard UB-N. Measured B of UB-N range between 135-181.2 ppm and $\delta^{11}\text{B}$ UB-N vary between 9.4 and 13.1 ‰ (source GeoRem website).

date	Seawater		UB-N	
	B (ppm)	$\delta^{11}\text{B}$ (‰)	B (ppm)	$\delta^{11}\text{B}$ (‰)
2019-03-06	4.3	39.7		
2019-03-06	4.2	39.8		
2019-03-06	4.4	40.0		
2019-03-06	4.4	40.0		
2019-03-06	4.4	40.0		
2019-03-06	4.5	39.9		
2019-07-15		39.8	120.3	11.1
2019-07-22	4.4	39.4	135.8	10.6
2019-09-27	4.6	38.9	116.0	10.2
2019-10-18	4.1	39.7	139.9	10.9
2019-10-22	4.5	38.5	110.3	10.8
2019-10-23	4.2	39.4	140.4	11.2
2019-10-30	4.4	39.4	152.9	10.3
2019-11-06	4.6	39.8	103.5	11.3
2019-11-07	4.5	39.3	117.8	10.1
2020-07-10	4.6	39.6		
2020-11-24	4.7	39.6	141.4	11.2
Mean	4.4	39.9	127.8	10.8
(Standard Error)*2	3.6	0.6	25.4	0.9

the power supply of the furnace, leaving the vessel to cool down to room conditions. All hydrothermal experiments were performed at 450 MPa total pressure at 5 distinct temperatures : 225°C, 260°C, 280°C, 300°C and 325°C. Duration of experiments is comprising between 504 hours and 3288 hours, for more information, see Table 1 in the previous Chapter.

6.2.3 Mineral separation

Solids products formed during our experiments were mainly serpentine and magnetite, even if few relics of primary minerals were still present at the end of reaction (<20 vol.%). In addition, some accessories minerals were also formed like calcite or brucite in very low quantities (<2.5 vol.%). A complete overview of the mineral proportions for each experiment are given in Table 5.3, Chapter 5. Serpentine and magnetite were

separated to determine their respective boron concentrations and isotopic composition. Serpentinite powder was loaded in a beaker with about 200 mL of ultrapure ethanol. The beaker was then placed in an ultrasonic bath during which the magnetite was separated from the serpentine using a hand-magnet. Although the procedure was repeated several times, the complete separation was never achieved, mainly due to the hanging of magnetite grains by serpentine fibers. X-ray diffraction patterns of separates magnetite and serpentine phases are available in supplementary materials.

6.2.4 Analyses of solids products

X-Ray Diffraction analyses were performed on sample powders using a Bruker D8 advance eco diffractometer at the Institut Terre et Environnement de Strasbourg laboratory (ITES, University of Strasbourg). A large X-ray beam was emitted by a copper source with a 40 kV accelerating voltage and a 25 mA current. Intensities were recorded at $0.014^{\circ}2\theta$ step intervals from 3 to 80° , with a 0.8 s counting time per step.

6.2.5 Mannitol procedure

According to Spivack and Edmond 1987, up to 10-20% of the total boron in clay minerals can be sorbed at their surface. In natural systems, this boron is susceptible to exchange with the last fluids in contact with the minerals and thus needs to be removed. All solid products were washed using mannitol, a polyhydric alcohol that complexes B, following the procedure described by Williams and Hervig 2002. About 50 mL of a 1.82% mannitol solution was added to 200 mg of rock powder. This mixture was then ultrasonified and suspended during two hours to remove the boron potentially adsorbed. The samples were then rinsed three times with a suspension of the Amberlite IRA 743-B specific resin in ultra-pure water.

6.2.6 Boron isotopes geochemistry

The sample digestion, boron separation and purification of the solid phases including bulk powders and separated serpentine powders were made following the procedure described by Lemarchand et al. 2012 and Roux et al. 2015. For more details about the procedure, see Chapter 2 of this thesis. A sample aliquot of 50 mg was mixed with 250 mg of powdered K_2CO_3 , fused in Pt-Au crucibles, in a furnace at 975°C during 45

minutes. The fusion residue is then dissolved with 400 μL of bi-distilled HCl and completed and with 35 mL of ultrapure water (18.2 M Ω -cm H₂O). Repeated centrifugation and decantation assured quantitative extraction of boron. For magnetite separated, ± 50 mg of powder was diluted in 600 μL of 3N HCl at 80°C during 3 hours. This mixture was then centrifuged and diluted with HCl 0.01N to have 5 mL for introduction in the column for ion exchange chromatography.

Boron purification of fluid samples was only proceeded by using the Amberlite resin. Indeed, fluids previously filtered and with a pH of ~ 8 were directly loaded onto the Amberlite IRA743 B-specific column. In order to increase the signal in the MC-ICP-MS, only 100 μL of Amberlite resin was used, which increases the boron concentration in the elution by limiting the volume of acid used.

The boron isotope compositions of the purified solids and fluids were determined by MC-ICP-MS using a Neptune Thermo Scientific instrument at the Institut Terre et Environnement de Strasbourg laboratory (ITES, University of Strasbourg). Procedure accuracy was evaluated by repeated analyses of certified rock and fluids standards (UB-N and Seawater, respectively Table 6.1).

6.3 Results

6.3.1 Boron isotope geochemistry of fluid phases

Boron concentrations

Boron concentrations in fluids ($[B]_{fluid}$) after all experiments are given in Table 6.2. Whatever the nature of the rock protolith, reacting fluids after all experiments have boron concentrations that decrease drastically and rapidly during the first 500 hours. To the first order, the rate of decrease is correlated is positively correlated to the temperature Figure 6.4.

In more details, after 168h at 225°C $[B]_{fluid}$ decreases of about half (2630 ppb, Table 6.2). After 266h, 90% of B in fluid was loss (~ 490 ppb, Table 6.2 ; Figure : 6.4). At 260°C after 168h $[B]_{fluid}$ is lower than at 225°C (1650 ppb, Table 6.2), and then continues to decrease until the end of reaction. At 300°C after 96h $[B]_{fluid}$ is relatively similar to those at 260°C (1870 ppb, Table 6.2). Surprisingly, after 264h $[B]_{fluid}$ increases (2460 ppb, Table 6.2) and then decreases slightly until the end of reaction, at about 1500h $[B]_{fluid}$ is relatively similar than at 225°C and 260°C (670 ppb, Table 6.2; Figure :

6.4). At 325°C, $[B]_{fluid}$ decreases more rapidly than in the other experiments, and reach a value of 830 ppb at 500h (Table 6.2 ; Figure 6.4). Then $[B]_{fluid}$ is relatively higher than the other experiments (Figure 6.4). Surprisingly, between 1680 and 1848 hours of reaction, $[B]_{fluid}$ increases from 520 ppb to 1090 ppb (Figure 6.4).

Boron isotopes

Boron isotopic compositions of fluids ($\delta^{11}\text{B}_{fluid}$) strongly depend on the temperature but show two contrasted behaviors : at low temperatures (< 260°C), $\delta^{11}\text{B}_{fluid}$ gradually decreases with time, indicating a preferential uptake of the light isotope (^{10}B). $\delta^{11}\text{B}_{fluid}$ becomes lower than the $\delta^{11}\text{B}$ of initial seawater ($\delta^{11}\text{B}_{sw}$) with values around +35‰ after ~2000h (Table 6.2, Figure 6.5). In contrast, at temperature >260°C, $\delta^{11}\text{B}_{fluid}$ increases with time, becoming greater than $\delta^{11}\text{B}_{sw}$ (up to +39.9‰ ; Figure 6.5). $\delta^{11}\text{B}_{fluid}$ at 280°C and 325°C display very similar evolution until 750 hours of experimental run time (+42.9‰ ; Table 6.2, Figure 6.5). The evolution of $\delta^{11}\text{B}_{fluid}$ at 300°C displays a particular behavior compared to the other experiments (Figure 6.5). Between 0 and 96h, $\delta^{11}\text{B}_{fluid}$ strongly increases above the value of initial seawater (up to +43.4‰, Figure 6.5).

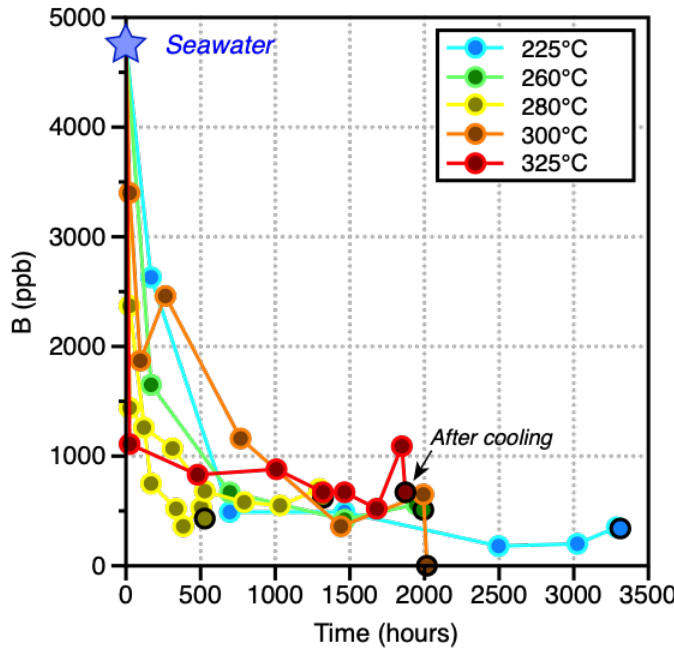


FIGURE 6.4 – B concentrations in fluids (ppb) versus experimental run-time (hours) for the reaction of serpentinization. Effect of cooling at the end of experiment is evidenced by black circles.

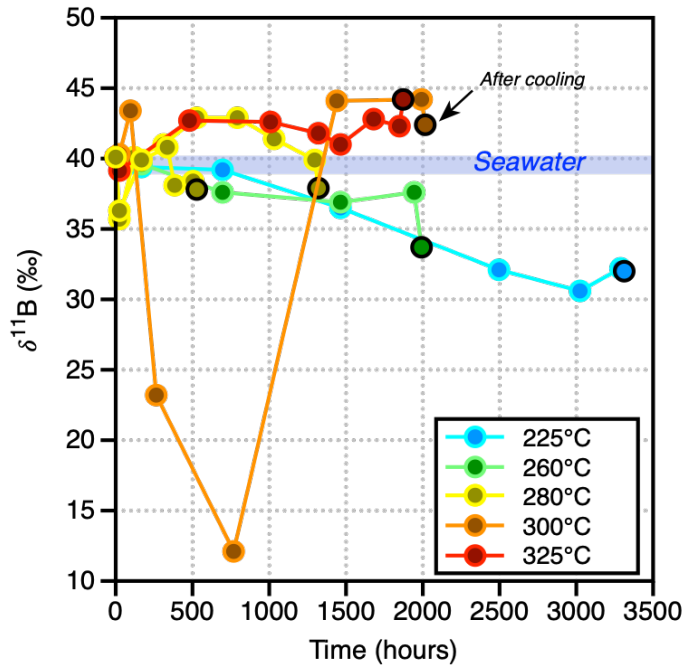


FIGURE 6.5 – Evolution of isotopic composition of the fluids $\delta^{11}\text{B}$ (‰) vs. experimental run-time (hours) for the reaction of serpentinization. Effect of cooling at the end of experiment is evidenced by black circles.

At least for 264h, the isotopic excursion is associated with the significant increase in concentration. After 1440 hours, $\delta^{11}\text{B}_{\text{fluid}}$ increases again to values close to those observed at 325 °C (+44.1‰, Table 6.2).

Boron behavior during cooling

B concentrations and isotopic compositions in fluids at the end of experiments at both high and room temperature were measured to allow mass balance calculation and reconstruct the solid composition before cooling. The results show that $[\text{B}]_{\text{fluid}}$ decreases slightly during cooling (Table 6.2, Figure 6.4), consistently with the study of Seyfried Jr and Dibble Jr 1980 indicating a B removal from the fluid, most likely through adsorption onto the mineral surfaces. Similarly, $\delta^{11}\text{B}_{\text{fluid}}$ is affected by cooling (Table 6.2, Figure 6.5). In almost all experiments, except at 325°C, $\delta^{11}\text{B}_{\text{fluid}}$ is systematically lower after cooling than just before the end of experiments (6.2; Figure 6.5). These results reflect a preferential removal of the heavy ^{11}B isotope, in line with the results of Hansen et al. 2017 at 200°C. At 325°C a preferential removal of the light ^{11}B isotope. We can explain that by a strong changes in conditions during cooling, in particular, fluids became more alkaline and B speciation will shift fully to the tetrahedral species. Furthermore, the two experiments at 280°C highlighted that the decrease of $\delta^{11}\text{B}_{\text{fluid}}$ during cooling during the serpentinization experiment is an irreversible process.

Reproducibility of the serpentinization experiments

Two experiments at 280°C were performed during 504 hours and 1296 hours, respectively. The first experiment suffered a power cut of several hours, causing the experimental device to cool down and was then stopped. This failure was the occasion to test the reproducibility of the experimental results as well as the reversibility of the water/rock interactions. To the opposite of boron concentrations, the isotopic ratios were strongly affected (Figure 6.4). $\delta^{11}\text{B}_{\text{fluid}}$ of the two experiments were strictly identical before the power cut at ~ 300 hours, and then $\delta^{11}\text{B}_{\text{fluid}}$ is affected by an irreversible process characterized by a strong decrease of the isotopic composition at +38.1‰ (Figure 6.5).

These results highlight that i) a excellent reproducibility of B concentrations and isotopic ratios during the serpentinization reactions before the power cut, ii) cooling does not affect significantly affect the boron concentrations of fluids but has a strong and irreversible impact on isotopes.

TABLE 6.2 – Evolution of the boron concentrations $[B]_{fluid}$ and isotopic compositions $\delta^{11}B_{fluid}$ during seawater-peridotite experiments.

Experiments	time (hour)	$[B]_{fluid}$ (ppb)	$\delta^{11}B_{fluid}$ (‰)
ISTO SW in	0	4750	40.1
ISTO 300 T0	24	3400	40.3
ISTO 300 T1 (+4)	96	1870	43.4
ISTO 300 T2 (+11)	264	2460	23.2
ISTO 300 T3 (+32)	768	1160	12.1
ISTO 300 T4 (+60)	1440	360	44.1
ISTO 300 T5 (+83)	1992	650	44.2
ISTO 300 Tf AC (+84)	2016	0	42.4
ISTO 260 T1 (+7)	168	1650	39.6
ISTO 260 T2 (+29)	696	670	37.6
ISTO 260 T3 (+61)	1464	420	36.9
ISTO 260 T4 (+81)	1944	560	37.6
ISTO 260 Tf AC (+83)	1992	510	33.7
ISTO 225 T1 (+7)	168	2630	39.4
ISTO 225 T2 (+29)	696	490.00	39.2
ISTO 225 T3 (+61)	1464	490.00	36.5
ISTO 225 T4 (+104)	2496	180.00	32.1
ISTO 225 T5 (+126)	3024	200	30.6
ISTO 225 T6 (+137)	3288	350	32.2
ISTO 225 Tf AC (+138)	3312	340	32.0
ISTO 325 T0	24	1110	39.2
ISTO 325 T1 (+20)	480	830	42.7
ISTO 325 T2 (+42)	1008	880	42.6
ISTO 325 T3 (+50)	1320	670	41.8
ISTO 325 T4 (+66)	1464	670	41.0
ISTO 325 T5 (+72)	1680	520	42.8
ISTO 325 T6 (+73)	1848	1090	42.3
ISTO 325 Tf AC	1872	670	44.2
ISTO 280 T0	24	2370	36.3
ISTO 280 T1 (+6)	168	750	39.9
ISTO 280 T2 (+13)	336	520	40.8
ISTO 280 T3 (+)	384	360	38.1
ISTO 280 T4 (+21)	504	530	38.4
ISTO 280 Tf AC (+22)	528	430	37.8
ISTO 280 bis T0	24	1440	35.7
ISTO 280 bis T1 (+5)	120	1260	40.1
ISTO 280 bis T2 (+13)	312	1070	41.0
ISTO 280 bis T3 (+22)	528	680	42.9
ISTO 280 bis T4 (+33)	792	580	42.9
ISTO 280 bis T5 (+43)	1032	550	41.4
ISTO 280 bis T6 (+54)	1296	700	39.9
ISTO 280 bis Tf AC (+55)	1320	620	37.9

6.3.2 Boron isotope geochemistry of solid phases

Boron concentrations

After the mannitol treatment, boron concentrations of serpentinite bulk (B_{bulk}) range between 2.7 ppm and 5.7 ppm (Table 6.3.2) and display no significant variation with temperature of experiments (Figure 6.6). Boron concentrations of magnetite separates (B_{mgt}) is comprising between 4.2 ppm and 8.6 ppm (Table 6.3.2) and is inversely correlated to temperature of experiment (Figure 6.6). In contrast, boron concentrations measured in serpentine separates (B_{srp}) is positively correlated with temperature (Figure 6.6) and vary from 4.44 ppm and 6.59 ppm (Table 6.3.2). These opposite trends highlight that boron incorporation in magnetite decreases with increasing temperature and that its incorporation in serpentine is positively correlated to an increase of temperature. However, this trend can be also explained by a poor mineral separation, a point that will be discussed in more details in the coming section.

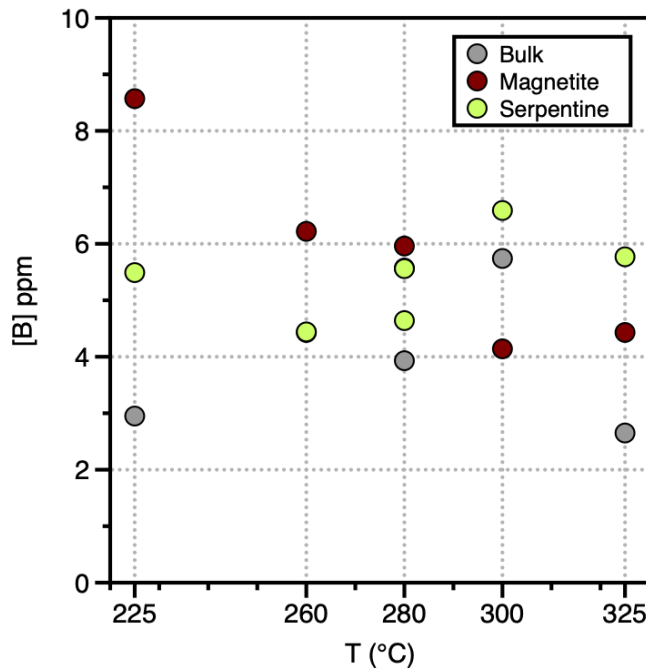


FIGURE 6.6 – B concentrations (ppm) versus temperature (°C) in bulk-rock, serpentine, and magnetite separates at the end of serpentinization experiments. The purple circles correspond to the shorter experiment at 280°C.

Boron isotopes

The $\delta^{11}\text{B}$ measured in solids products display a more complex evolution as a function of temperature compared to B concentrations (Figure 6.7). The $\delta^{11}\text{B}$ in serpentinite $\delta^{11}\text{B}_{bulk}$ at the end of serpentinization experiments range between +25.5‰ and 32.6‰ (Table 6.3.2), which is strongly higher than in the primary peridotite (-7.1‰). The $\delta^{11}\text{B}$ in magnetite $\delta^{11}\text{B}_{mgt}$ tends to increase with temperature of experiments, from +25.2‰ at 225°C to +34.8‰ at 325°C and are systematically higher than $\delta^{11}\text{B}_{bulk}$ (Table 6.3.2; Figure 6.7). At 280°C the lower $\delta^{11}\text{B}$ values (+29.2‰) correspond to the shorter experiment. The $\delta^{11}\text{B}$ measured in separated serpentine $\delta^{11}\text{B}_{srp}$ are comprising between +8.1‰ and +32.8‰ (Table 6.3.2) and are always lower than $\delta^{11}\text{B}$ measured in magnetite and serpentinite bulk. The $\delta^{11}\text{B}$ of separated serpentine decrease with temperature (Figure 6.7), but $\delta^{11}\text{B}$ in serpentine from experiment at 300°C is much lower than those from experiment at 325°C (Figure 6.7).

In all solids products, including serpentinite, magnetite and serpentine separates, the isotopic composition $\delta^{11}\text{B}$ are inversely correlated to the boron concentrations, in contrast, for reacting fluids, $\delta^{11}\text{B}_{fluid}$ are positively correlated to the boron concentrations (Figure 6.8).

TABLE 6.3 – Measured boron concentration in ppm and $\delta^{11}\text{B}$ (‰) in solids products including bulk serpentinite, separated serpentine and separated magnetite at the end of serpentinization experiments and also in final fluid before cooling.

Sample	T°C	w/r	Time (hours)	B_{bulk} (ppm)	B_{srp} (ppm)	B_{mgt} (ppm)	B_{swf} (ppm)	$\delta^{11}\text{B}_{bulk}$ (‰)	$\delta^{11}\text{B}_{mgt}$ (‰)	$\delta^{11}\text{B}_{srp}$ (‰)	$\delta^{11}\text{B}_{fluid}$ (‰)
ISTO 3	225	1.6	3288	2.95	5.49	8.57	0.350	30.8	25.0	24.5	32.2
ISTO 2	260	2.2	1944	4.43	4.44	6.22	0.560	31.0	32.2	24.7	37.6
ISTO 5	280	1.9	504	3.93	4.64	5.57	0.530	32.6	29.2	19.9	38.4
ISTO 6	280	1.9	1296	n.d.	5.56	5.96	0.700	29.8	33.7	32.8	39.9
ISTO 1	300	1.6	1992	5.74	6.59	4.15	0.650	25.5	32.3	8.1	44.2
ISTO 4	325	1.9	1752	2.65	5.77	4.43	1.09	31.1	34.4	16.3	42.3

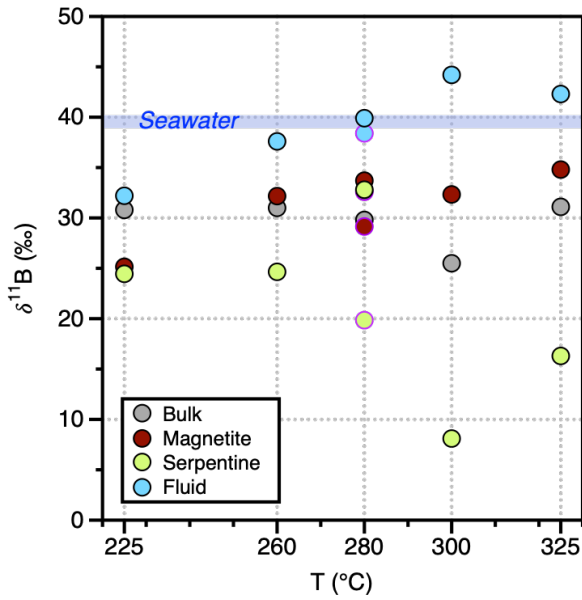


FIGURE 6.7 – Evolution of the isotopic composition $\delta^{11}\text{B}$ (‰) depending on temperature of reaction (°C) in bulk products, serpentine and magnetite separates and fluid sampled immediately at the end of reaction. The purple circles correspond to the shorter experiment at 280°C. Error bars are below the point size.

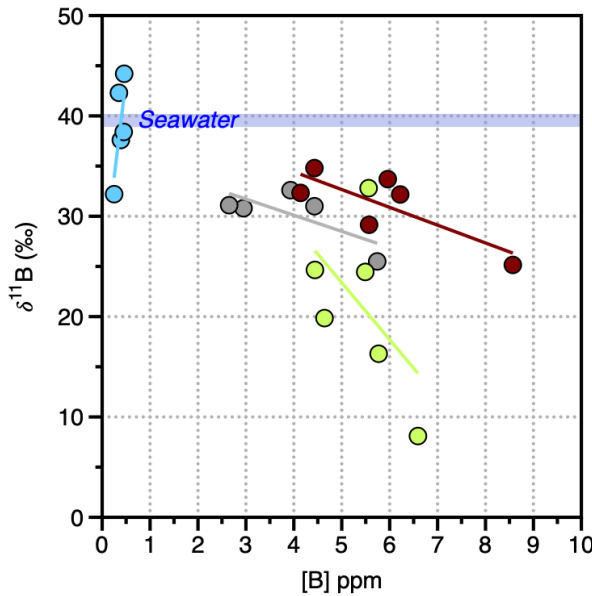


FIGURE 6.8 – $\delta^{11}\text{B}$ (‰) versus B (ppm) for the serpentinites, serpentine and magnetite separates and fluid at the end of experiments. Error bars are below the point size.

Boron adsorption during serpentinization

Previous study have shown that adsorption of boron can occurred simultaneously than boron incorporation, especially during the formation of phyllosilicate minerals (e.g., Palmer et al. 1987 ; Pabst et al. 2011 ; Xiao et al. 2011). In addition, Hansen et al. 2017 noticed from mass balance calculations in their serpentinization experiments that approximately 49% of boron was lost at 200°C and 39% at 100°C.

To estimate whether boron was adsorbed and lost in the rinse fluid during our analytical procedure, a rapid calculation can be done. Since, we know the initial quantity of boron introduced in the system, and assuming that the boron bring by the initial solid is negligible, all boron comes from seawater (see the schematic representation in Figure 6.9). We know also the boron content in the resulting fluid at the end of experiments and those in the serpentinite. Thus, the quantification of boron adsorbed $B_{adsorbed}$ at the mineral surfaces correspond to the boron bring by the initial seawater $B_{initial}^{fluid}$ minus the boron measured in the final fluid B_{final}^{fluid} plus the boron in the final solid $B_{integrated}$ which correspond to the quantity of boron integrated in the crystal structure (i.e., not removed by the procedure with mannitol).

$$B_{adsorbed} = B_{initial}^{fluid} - (B_{final}^{fluid} + B_{integrated}) \quad (6.3)$$

This calculation reveals a boron loss in solids after separation and mannitol procedures, varying between 20% to 63%. One way to explain this loss of boron measured in bulk, is that a mineral phase was probably removed during our analytical procedure and/or that our mineral separations are not "pure". We will discuss this in detail in the next section.

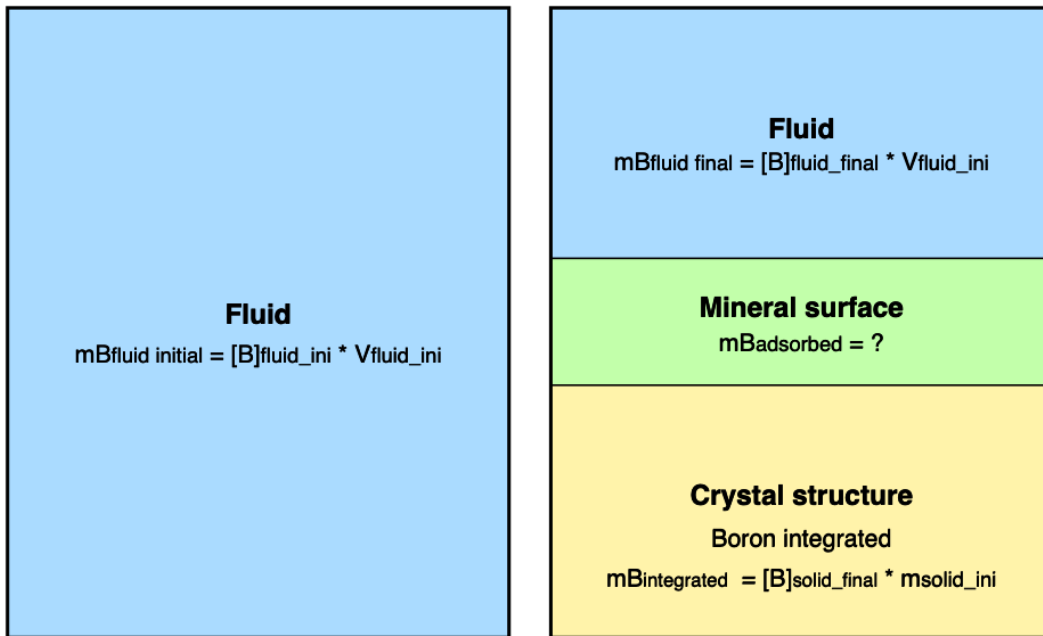


FIGURE 6.9 – Schematic representation of the integration of boron in solid products during serpentinization experiments. We assume that seawater contains all the boron available before the serpentinization experiments. At the end of serpentinization experiments, 90% of B in seawater was released and partitioned into the mineral surface (green : B adsorbed) and the crystal structure (yellow : B integrated).

6.4 Discussion

6.4.1 How to explain the different boron isotopes fractionation recorded by fluids ?

A major observation is that boron isotopes fractionation in fluids at the end of serpentinization experiments display distinct behavior at low temperatures (225 and 260°C) with $\delta^{11}\text{B}_{\text{fluid}} < \delta^{11}\text{B}_{\text{sw}}$, and at temperatures $\geq 280^\circ\text{C}$ with $\delta^{11}\text{B}_{\text{fluid}} > \delta^{11}\text{B}_{\text{sw}}$. These results highlight different B isotopic fractionation depending of the temperature of serpentinization. The apparent B isotopic fractionation factor (α_{apparent}) does not really make sense because it considers the $\delta^{11}\text{B}_{\text{fluid}}$ measured in fluid and $\delta^{11}\text{B}_{\text{bulk}}$ which has recorded all the isotopic evolution during serpentinization and the cooling phase. However, we have previously shown that the final cooling phase and the analytical procedure affect strongly the B budgets and isotopic compositions.

$$\alpha_{\text{apparent}} = \frac{\delta_{\text{fluid}} + 1000}{\delta_{\text{bulk}} + 1000} \quad (6.4)$$

In order to avoid the impact of cooling on B isotopic fractionation, we calculated the B isotopic fractionation factor (α) of the reaction from fluid sampled before cooling. For this we used the Rayleigh distillation, which considers i) a single B reservoir (i.e., the seawater) ii) fluid and solid evolution results of multiple fluid increments and iii) it is the same reaction that takes place at each new increment of fluid. We found this approach more relevant than the "batch equilibrium" which considers equilibrium between fluid and solid at any point in the reaction, which is only true for exchangeable boron (i.e., the boron adsorbed). The fractionation factor (α) of the reaction was calculated from :

$$\begin{aligned} R_f &= R_0 f^{\alpha-1} \\ R_0 &= \frac{m_f}{m_i}^{\alpha-1} \\ \ln \frac{R_f}{R_0} &= (\alpha - 1) * \ln \frac{m_f}{m_i} \\ \alpha &= \frac{\ln \frac{R_f}{R_0}}{\ln \frac{m_f}{m_i}} + 1 \end{aligned} \quad (6.5)$$

With R_0 and R_f the initial and final boron isotopic ratios ($^{11}\text{B}/^{10}\text{B}$) respectively, m_i and m_f the initial and final mass of boron (μg). The B isotopic fractionation factor

of the reaction vary between 1.002 at 225°C and 0.998 at 325°C, and decrease with temperature increasing Figure 6.10. Surprisingly, the α evolution with temperature crosses the value of 1 at the lower temperatures of serpentinization. This is inconsistent from a thermodynamic point of view, considering ΔG the free energy, R the universal gas constant and T the temperature in Kelvin. Thus, this suggest a more complex process, not only affected by temperature.

$$\ln \alpha = \frac{-\Delta G}{RT} \quad (6.6)$$

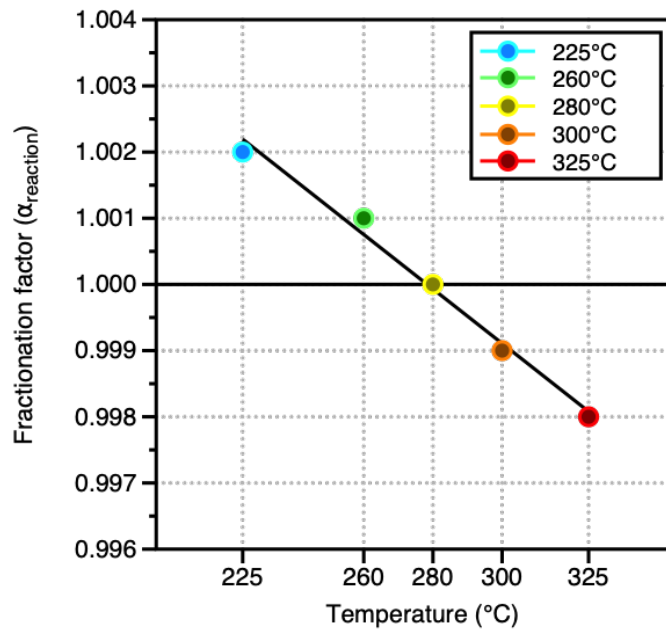


FIGURE 6.10 – Fractionation factor versus temperature (°C).

From mass balance calculation, we calculate the B partition coefficient (K_d) of the reacting fluid, considering m_{total} the total mass of boron of the system, m_s the initial mass of boron in solid (μg), and m_f the initial mass of boron in fluid (μg), K_d the

partition coefficient, WR the water/rock ratios :

$$\begin{aligned}
 m_{total} &= m_s + m_f \\
 m_s &= \frac{K_d}{WR} * m_f \\
 m_{total} &= \left(\frac{K_d}{WR} + 1 \right) * m_f \\
 m_f &= \frac{m_{total}}{\frac{K_d}{WR}} + 1 \\
 K_d &= \left(\frac{m_{total}}{m_f - 1} \right) * WR
 \end{aligned} \tag{6.7}$$

The partition coefficient (K_d) is ranges from 20 to 60 and display a bell shaped curve in function of the temperature, with K_d value that increase from 225°C to 260°C and decreases at $T > 260^\circ\text{C}$ (Figure 6.11).

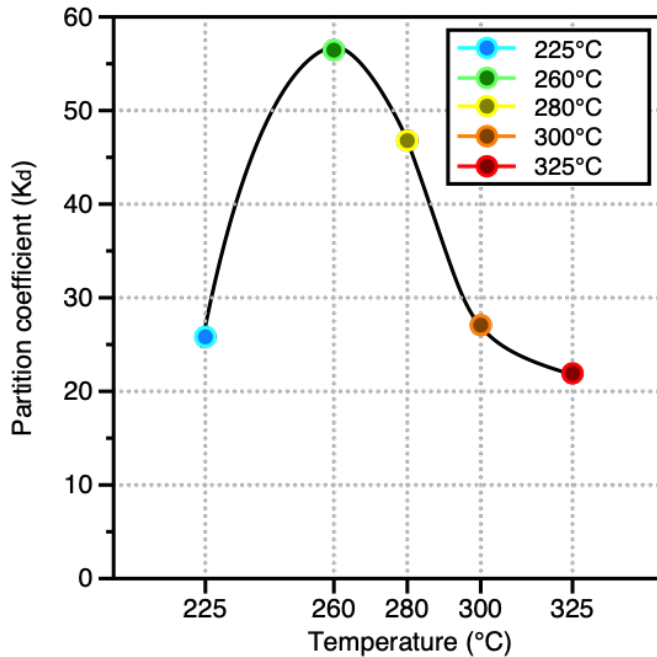


FIGURE 6.11 – Partition coefficient versus temperature (°C).

If the temperature was the only parameter affecting the B isotopic fractionation factor and the partition coefficient, then α would converge to 1 and K_d would only increase or decrease, which is not our observation.

To date, it is recognized that the pH influences boron speciation in the fluid (e.g., Kakihana et al. 1977; Palmer et al. 1987; Klochko et al. 2006; Noireaux et al. 2015), and consequently in secondary minerals such as serpentine (e.g., Boschi et al. 2008), brucite (e.g., Xiao et al. 2011) or calcite (e.g., Sanyal et al. 2000; Mavromatis et al. 2015 ; Saldi et al. 2018). In particular, as mentioned above in seawater at $\text{pH} < 8$ B(OH)_3^- is more abundant and at $\text{pH} > 8$ B(OH)_4^- dominates (Figure 6.2).

In addition, Lemarchand et al. 2015 presented a review of the K_d and α dependence with pH for different minerals (Figure 6.12). In particular, they show that birnessite ($\text{MnO}_2 \cdot n\text{H}_2\text{O}$) which is a hydrous manganese dioxide, exhibits α that also cross the value of 1, which is very similarly to what our data tend to show, and K_d with bell shaped curve with a maximum at pH between 8 and 10 (Figure 6.12).

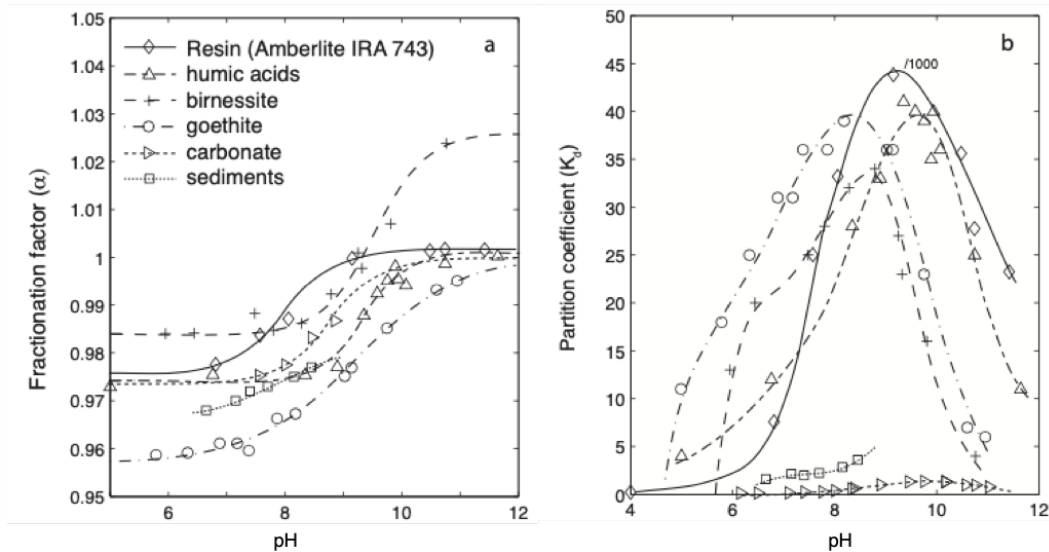


FIGURE 6.12 – a) B isotopic fractionation factor and b) Partition coefficient dependence with pH. Figure from Lemarchand et al. 2015.

Consequently, we propose that the α and K_d of fluid recorded by fluid during our serpentinization experiments attested to a change in pH. We propose that at $T \geq 260^\circ\text{C}$ fluid attests of acidic pH at favoring the preferential incorporation of the heavier isotope (^{11}B) in solid. At $T \leq 260^\circ\text{C}$ more alkaline pH are generated leading to the preferential incorporation of the light isotope in solid (^{10}B). In the previous Chapter, we proposed that at $T \leq 260^\circ\text{C}$ high pH values are generated in response to higher iron partitioning in serpentine than into magnetite. While at $T \geq 260^\circ\text{C}$, more acidic pH are generated, supported by higher amount of Fe^{2+} are oxidized to Fe^{3+} in magnetites. That is also in accordance with pH measured in previous serpentinization experiments. Indeed, fluids

formed during serpentinization at low temperatures are generally (hyper)-alkaline (e.g., Seyfried Jr et al. 2007; Hansen et al. 2017; McCollom et al. 2020). High pH are also measured in fluids from hydrothermal vents such as Lost City (pH 9-9.8, Kelley et al. 2001) and recalculated (8.1 at 200°C Allen and Seyfried Jr 2004) and in fluids related to serpentinization of peridotites in Oman, Ligurian and Ronda or New Caledonia ophiolites with pH >10.5 (e.g., Chavagnac et al. 2013 ; Giampouras et al. 2019). In contrast, low pH were measured in serpentinization experiments at higher temperatures, mostly comprised between 2.8 and 5.24 at 300°C Seyfried Jr and Dibble Jr 1980 and about 4.90-5.50 at 400°C (Allen and Seyfried Jr 2003 ; Allen and Seyfried Jr 2005). Similarly, low pH (\pm 2.8 at 365°C) are reported in hydrothermal vent fluids from Rainbow (MAR ; Charlou et al. 2002).

More precisely, based on the pH change recorded by the birnessite at about pH 9 Lemarchand et al. 2015, which correspond also to the pKa of B, we hypothesize that serpentinite can behave in a similar way. In accordance with our experimental results and the measured pH in fluids from serpentinization experiments, we proposed that a pH change occurs at 280°C, with pH > 9 at 225 and 260°C, and more acidic pH at 300 and 325°, at about 5 (Figure 6.13. However, the pH values should be confirmed.

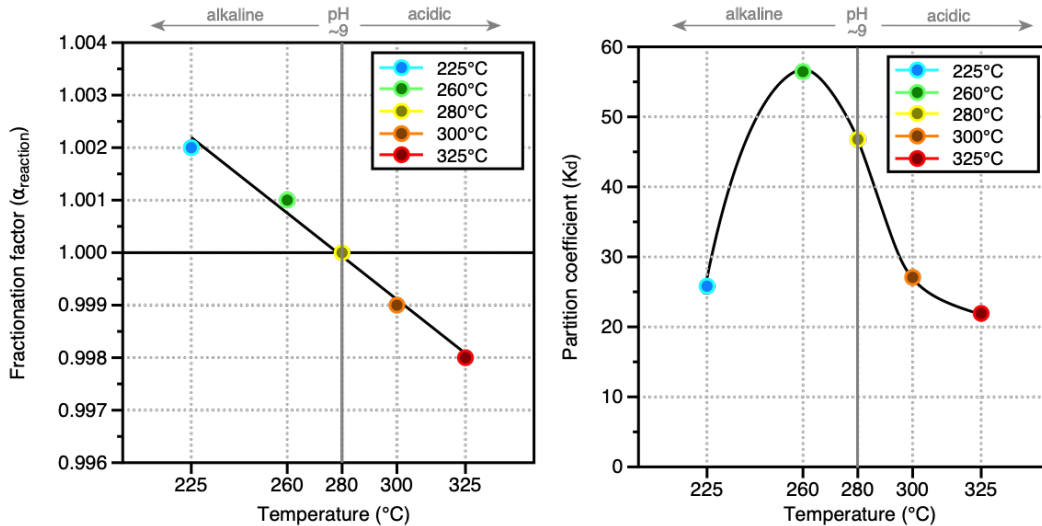


FIGURE 6.13 – a) B isotopic fractionation factor versus temperature (°C) and b) Partition coefficient versus temperature (°C) with a proposed pH change at about 280 °degrees which correspond to the change of α .

The $\delta^{11}\text{B}_{fluid}$ measured during the serpentinization experiments display variation in function of time (Figure 6.5). Especially, the $\delta^{11}\text{B}_{fluid}$ measured during the serpentinization at 300°C, decrease strongly in the first step of reaction reaching +12‰ at about 750h, and then increase at about +44‰ (Figure 6.5). Several assumptions can be considered i) a technical problem during the experiment, ii) the precipitation of an intermediate phase, iii) a strong variation of the pH. The first assumption can be quickly eliminated because no leakage was detected by the pressure control during the experiment.

The second assumption can be tested by mass balance calculation. If we consider that an intermediate phase like brucite precipitates from brucite between T0 and T1, we can calculate the boron mass (m_{bct}) and the boron isotopic ratios (R_{bct}) that brucite should have :

$$\begin{aligned}
 m_{olivine} + m_{f_{ini}} &= m_{f_f} + m_{bct} \\
 m_{olivine} &= 0 \\
 m_{bct} &= m_{f_{ini}} - m_{f_f} \\
 [B]_{bct} * m_{bct} &= [B]_{f_{ini}} * V_{f_{ini}} - [B]_{f_f} * V_{f_f} \\
 m_{f_{ini}} * R_{f_{ini}} &= m_{f_f} * R_{f_f} + m_{bct} * R_{bct} \\
 R_{bct} &= \frac{m_{f_{ini}} * R_{f_{ini}} - m_{f_f} * R_{f_f}}{m_{bct}}
 \end{aligned} \tag{6.8}$$

Considering the mass of boron in olivine ($m_{olivine} = 0$), in the initial and final fluid ($m_{f_{ini}}$) and (m_{f_f}), respectively, and $R_{f_{ini}}$, R_{f_f} the initial and final boron isotopic ratios in fluid.

The decrease of B concentrations in fluid, suggested that this intermediate phase incorporates B from fluid. Moreover, this intermediate phase should preferably incorporates the lightest isotope (10) to explain the increase of $\delta^{11}\text{B}_{fluid}$ between T0 and T1. The results of the mass balance calculation suggests that at T1 the intermediate phase would have m_{bct} 87.440 µg and an isotopic ratio R_{bct} of +36.8‰.

Between T1 and T2 $[B]_{fluid}$ increases, attesting of a potential dissolution of this intermediate phase. This increase of $[B]_{fluid}$ is correlated to a decrease of the $\delta^{11}\text{B}_{fluid}$. If we consider that between T1 and T2 this intermediate phase releases only a part of B, the mass balance calculation suggests $m_{bct-dissolved} = 31.949$ µg. The theoretical isotopic ratio of fluid at T2 considering $m_{bct-dissolved}$ would be $R_{bct} = 41.8$ ‰. However, this result is very different to the measured isotopic compositions ($\delta^{11}\text{B}_{fluid} = +23.2$ ‰).

Now, if we consider that between T1 and T2 this intermediate phase releases all the B it has previously incorporated, $[B]_{fluid}$ and $\delta^{11}B_{fluid}$ at T2 should be the same than at T0, and consequently [B] of the secondary mineral ($[B]_{secondary-mineral}$) = 940 μg and $R_{secondary-mineral} = +85\%$ which is very huge.

To resume, the mass balance calculation cannot explain the evolution of the isotopic composition of fluid at 300°C.

The third assumption is therefore the most probable. The strong decrease of $\delta^{11}B_{fluid}$ between T0 and T1, could be explained by a strong and temporary increase of pH (≥ 9) favoring the incorporation of the lightest isotope (^{10}B).

6.4.2 B geochemistry of separated minerals : what do we really read ?

In the previous chapter (Table 5.3) we have shown that bulk formed during our experiments contained >78 vol.% of serpentine, small amounts of magnetite (<5 vol.%) and calcite (<1 vol.%) and also relics of olivine and diopside. However, XRD patterns suggested that these separated phases contain not exclusively magnetite and serpentine crystals (see XRD patterns in supplementary materials). In addition, slight or no differences are observed between the XRD patterns of the two separated phases and bulk. The investigations by SEM confirms the poor separation of the serpentine and magnetite separates. In particular we observed that small magnetite grains remain in trapped in serpentine fibers (Figure 6.14).

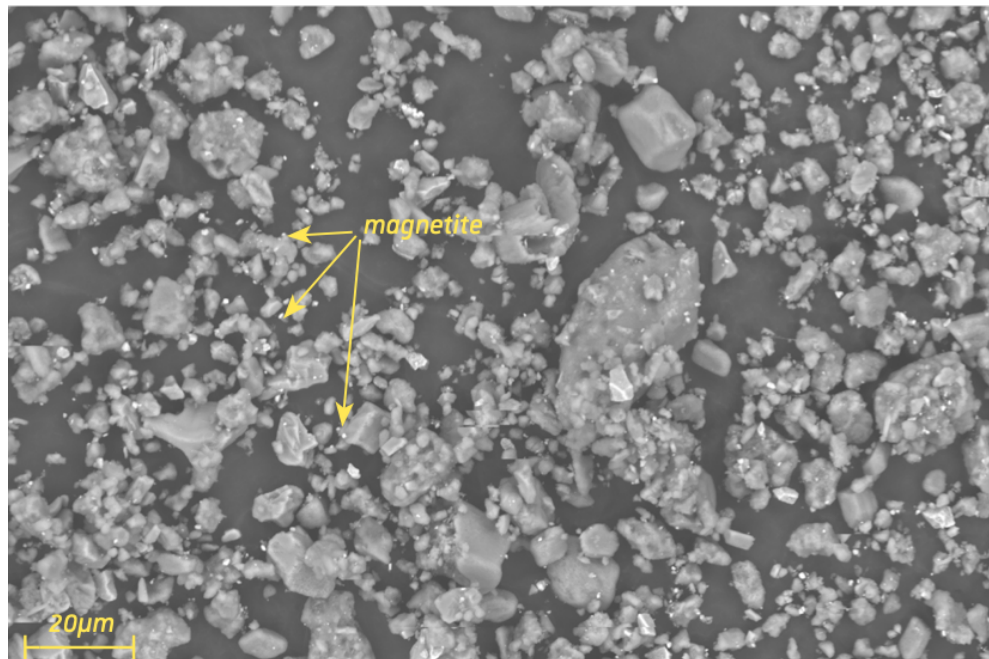


FIGURE 6.14 – SEM characterization of serpentine separated phases from experiment at 260°C. It can be observed that very small grains of magnetite are still present after the separation procedure.

The poor separation can also be observed by plotting B and $\delta^{11}\text{B}$ as a function of major element concentrations in (wt.%) in bulk, serpentine and magnetite separates (Figure 6.15 and 6.16, respectively). Here again, no correlation is visible between B and $\delta^{11}\text{B}$ and major elements concentrations. This supports that a serpentine and magnetite are not the only species that constitute the bulk.

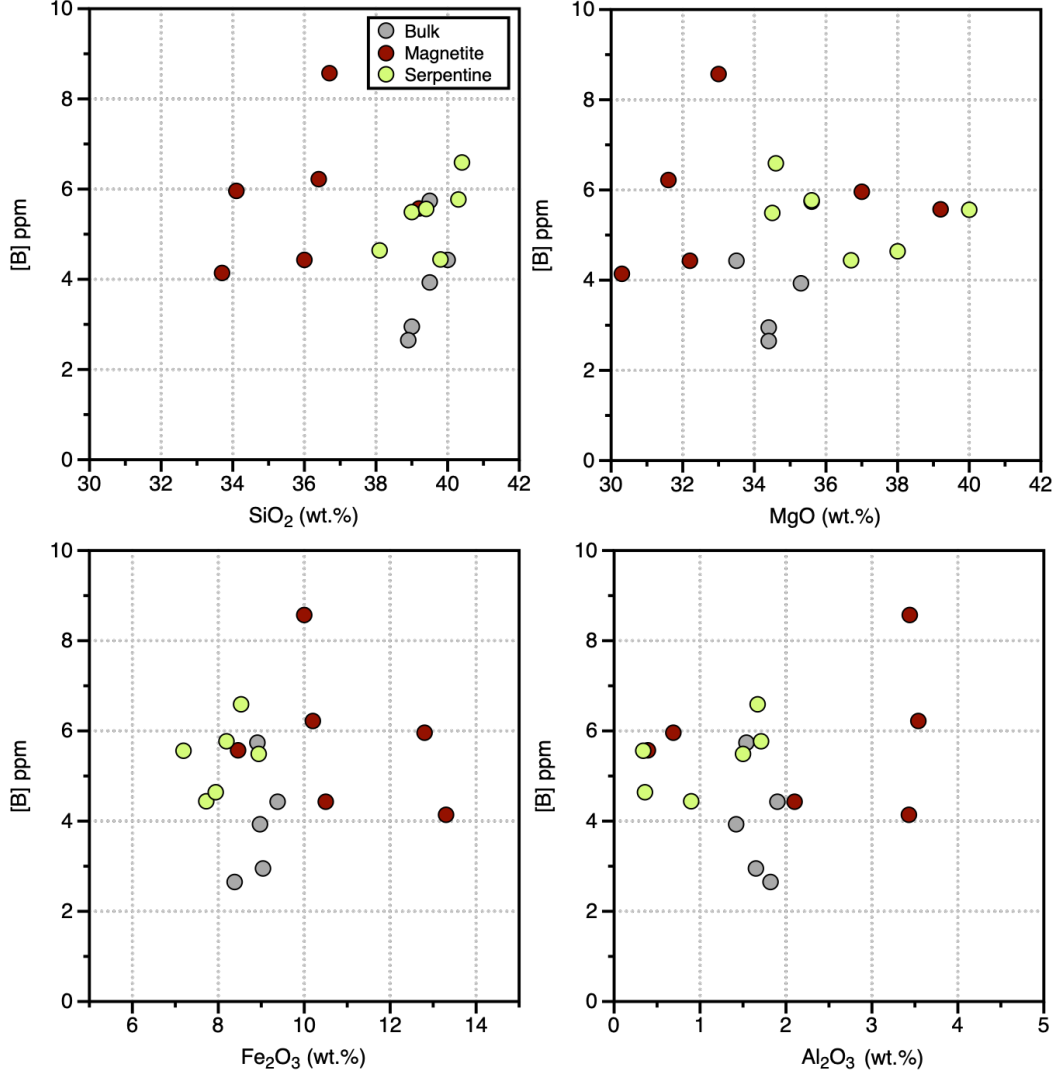


FIGURE 6.15 – Boron concentration in ppm versus concentrations of major elements in (wt.%) measured in serpentinite bulk, serpentine separated and magnetite separated.

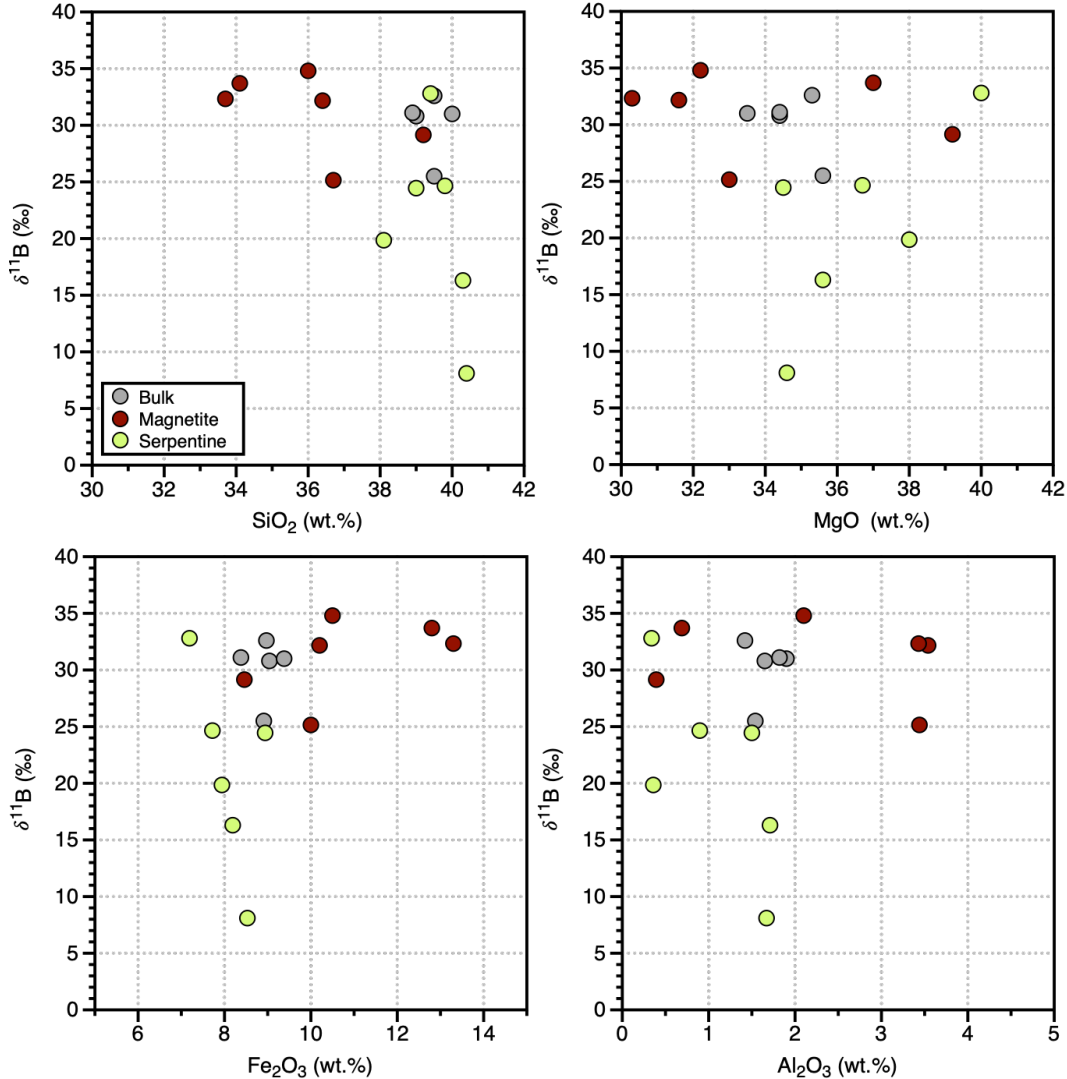


FIGURE 6.16 – B isotopic composition $\delta^{11}\text{B}$ in ‰ versus the concentrations of major elements in (wt.%) measured in serpentinite bulk, serpentine separated and magnetite separated.

If i) the bulk was only composed by serpentine and magnetite, ii) the separate serpentine and magnetite fractions were pure, and iii) serpentine and magnetite are the only phases that contain B, then $\delta^{11}\text{B}_{bulk}$ should be located between those measured in serpentine $\delta^{11}\text{B}_{srp}$ and magnetite $\delta^{11}\text{B}_{mgt}$ as a function of $1/[\text{B}]$ in this Figure 6.17. However, this is not what we observe, indeed, in this Figure 6.17, $1/[\text{B}]_{mgt} < 1/[\text{B}]_{srp} < 1/[\text{B}]_{bulk}$, suggesting that magnetite and serpentine contained higher amount of B than bulk. This observation supports that during the separation procedure i) B was added in serpentine and magnetite separates, ii) a part of solids containing B were removed from the bulk, iii) some of the boron was lost during the mannitol procedure. The first assumption can be quickly rejected, since all separations were made with milli-q water and ethanol. However, the second assumption is more probable, because as mentioned above, we have separated magnetite and serpentine crystals by successive decantation. This successive separations by decantation could have led to an accidental elimination of very fine phases containing B, which is potentially the case for serpentine. Moreover, during the successive rinse, some phases like halite (only observed in serpentinite at 325 °C), brucite, aragonite and anhydrite which may contain significant amount of boron (e.g., Xiao et al. 2011 ; Mavromatis et al. 2015) can be also removed. This accidental remove can produce a slight isotopic fractionation between serpentinite and fluid.

The third hypothesis has already been confirmed previously by mass balance calculation indicating that during the mannitol procedure, between 20 and 60% of B was removed from the bulk. As a reminder, we have cleaned all solids with mannitol in order to removes the adsorbed boron and focus on the structural boron. It is possible to calculate $[\text{B}]_{bulk-theoretical}$ and $R_{bulk-theoretical}$ by subtracting the mass of boron in fluid at the end of experiment (before cooling ; m_{f-f}) to the initial fluid (m_{ini}) :

$$\begin{aligned} m_{bulk-theoretical} &= m_{ini} - m_{f-f} \\ [\text{B}]_{bulk-theoretical} &= \frac{[B]_{f-ini} * V_{f-ini} - [B]_{f-f} * V_{f-f}}{m_{bulk}} \\ R_{bulk-theoretical} &= \frac{m_{ini} * R_{ini} - \sum m_{f-f} * R_{f-f}}{m_{bulk}} \end{aligned} \quad (6.9)$$

We calculate also $[B]_{bulk-theoretical}$ by subtracting the mass of B in all fluid sampled during the experiment (m_{f-prel}) :

$$\begin{aligned} m_{bulk-theoretical} &= m_{ini} - \sum m_{prel} \\ [B]_{bulk-theoretical} &= \frac{[B]_{f-ini} * V_{f-ini} - \sum [B]_{f-prel} * V_{f-prel}}{m_{bulk}} \\ R_{bulk-theoretical} &= \frac{m_{ini} * R_{ini} - \sum m_{prel} * R_{prel}}{m_{bulk}} \end{aligned} \quad (6.10)$$

The theoretical $[B]_{bulk-theoretical}$ and $R_{bulk-theoretical}$ calculated from mass balance calculation are compared with the $[B]_{bulk-mes}$ and $\delta^{11}\text{B}_{bulk-mes}$ measured in bulk in Table 6.4.2. We observe that $[B]_{bulk-mes}$ and $\delta^{11}\text{B}_{bulk-mes}$ are systematically lower than the $[B]_{bulk-theoretical}$ and $R_{bulk-theoretical}$. This support that $[B]_{bulk-mes}$ and $\delta^{11}\text{B}_{bulk-mes}$ are not comparable to $[B]_{bulk-theoretical}$ and $R_{bulk-theoretical}$, because the first one reflects the structural B while the second considers the exchangeable B (i.e. B adsorbed).

TABLE 6.4 – Comparison between B concentration and isotopic compositions measured (mes) in bulk and the theoretical values.

	[B] bulk (mes)	[B] bulk (ini - final)	[B] bulk (ini - prel)	$\delta^{11}\text{B}$ bulk (mes)	$\delta^{11}\text{B}$ bulk (ini - final)	$\delta^{11}\text{B}$ bulk (ini - prel)
ISTO 3	2.95	7.21	7.5	30.8	39.9	39.6
ISTO 2	4.43	9.95	10.1	31	39.6	39.5
ISTO 5	3.93	8.67	8.8	32.6	39.6	39.9
ISTO 6	n.d	9.61	10.0	29.8	39.5	39.5
ISTO 1	5.74	7.22	7.2	25.5	39.2	39.5
ISTO 4	2.65	8.35	8.8	31.1	39.3	39.9

Nevertheless, we have reason to believe that $[B]_{mgt}$ and $\delta^{11}\text{B}_{mgt}$ in magnetite separated phases are not so bad. As reminder, our analytical procedure by acid attack for boron analyses in magnetite is different than for serpentine and bulk. Indeed, the magnetite separates did not undergo alkali fusion, but are only dissolved with 3 M HCl. This procedure is not efficient to digest silicates minerals. Hence, we think that the boron concentrations and isotopes of magnetite are not affected by the silicates minerals including serpentine, olivine and clinopyroxene. However, if calcite and brucite are present in the separated magnetite phases, the measured boron concentrations and isotopes can be impacted and thus not usable. Unfortunately, the XRD patterns combined to the SEM observations reveals that some calcite crystals are present in the separated magnetite phases. Although only few crystals of calcite were observed, it is

not clear how that affects the boron concentrations and isotopes of separated magnetite phases.

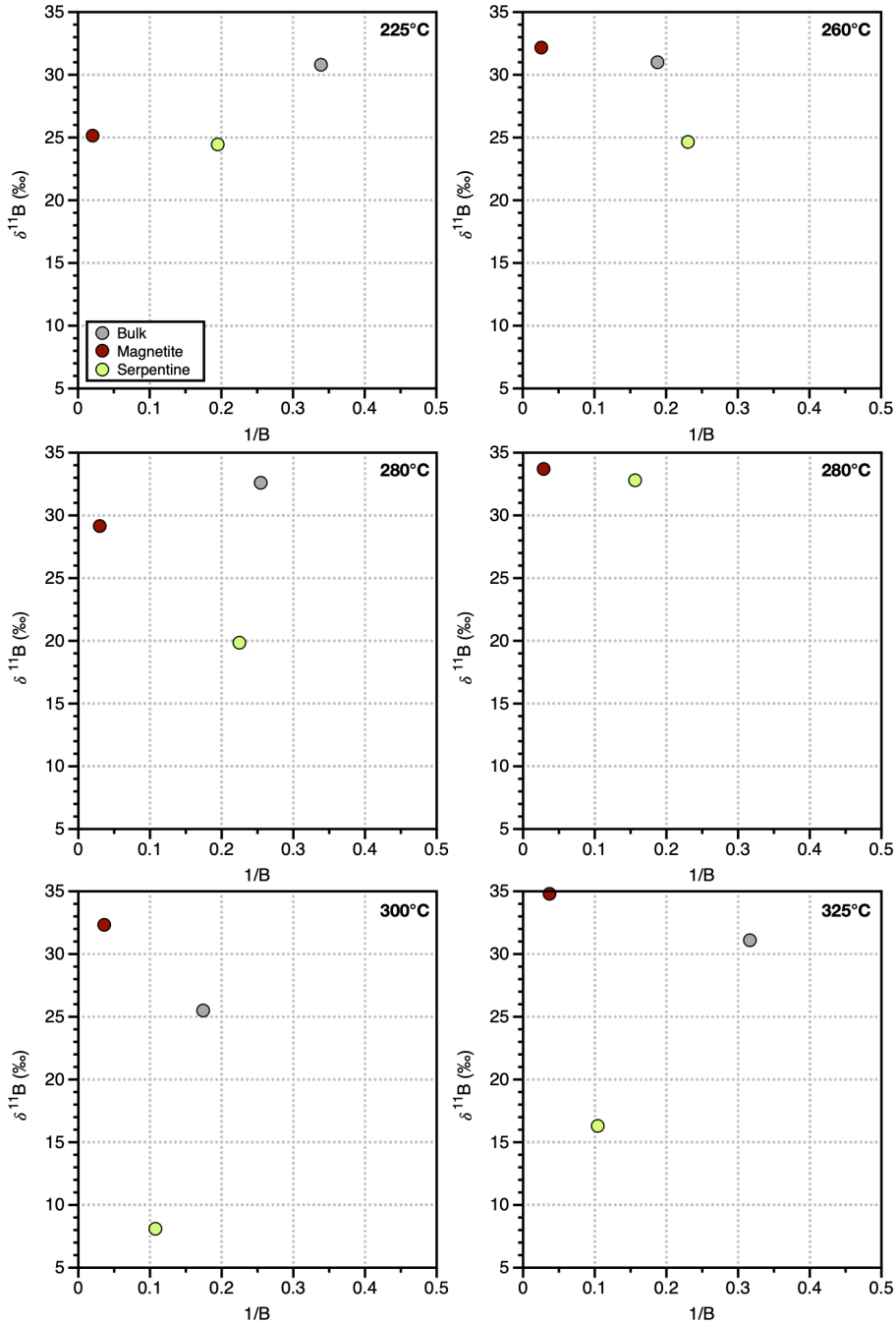


FIGURE 6.17 – SEM characterization of serpentine separated phases from experiment at 260°C. It can be observed that very small grains of magnetite are still present after the separation procedure.

6.4.3 Effect of the temperature on B geochemistry

Bonatti et al. 1984 observed that boron content of oceanic serpentinites is inversely related to the temperature at $T < 200^\circ\text{C}$, which is supported by the experimental results of Hansen et al. 2017. In contrast, other studies have documented boron incorporation in serpentine at moderate temperatures $T \geq 200^\circ\text{C}$ (e.g., Palmer and Helvaci 1997; Boschi et al. 2008). It is important to note that most of these studies are focused on boron concentrations in bulk-rocks and not in serpentine minerals, and that the samples were not cleaned with mannitol to removes the $\text{B}_{\text{adsorbed}}$. Our results show that $[\text{B}]_{\text{srp}}$ is positively correlated to the temperature (Figure 6.6) and thus that B uptake in serpentine increases with temperature. In contrast, no boron correlation with temperature is observed in $[\text{B}]_{\text{bulk}}$, but previously we have show that a mineral phase was probably removes during the successive rinse. However, $[\text{B}]_{\text{mgt}}$ (which is the cleanest separate phase) is inversely correlated (Figure 6.6). $\delta^{11}\text{B}_{\text{bulk}}$ is closer to the $\delta^{11}\text{B}_{\text{mgt}}$ than $\delta^{11}\text{B}_{\text{srp}}$ (Figure 6.7). In addition, $\delta^{11}\text{B}_{\text{bulk}}$ and $\delta^{11}\text{B}_{\text{mgt}}$ are positively correlated to the increasing temperature (Figure 6.7), highlighting that magnetite influences $\delta^{11}\text{B}_{\text{bulk}}$. Furthermore, there is no correlation between the B_{bulk} content and isotopes $\delta^{11}\text{B}_{\text{bulk}}$ with the proportions of serpentine (vol.%) Figure 6.18, probably because of the problems caused by the separation and cleaning with mannitol that were mentioned above.

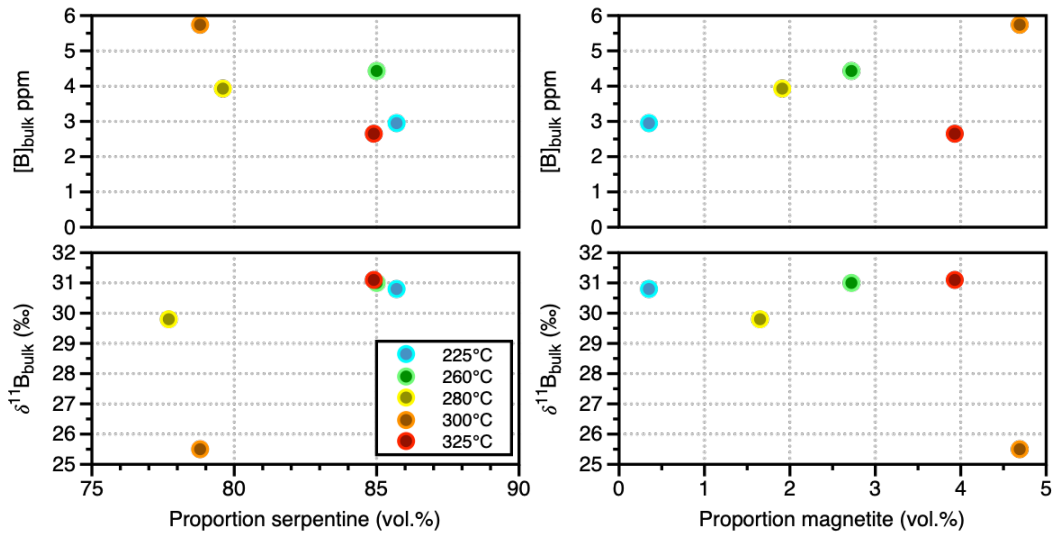


FIGURE 6.18 – Boron content (ppm) and isotopes ($\delta^{11}\text{B}$) of serpentinite bulk versus the estimated proportion of serpentine (vol.%) and magnetite (vol.%) in the different experiments.

An another explanation could be that different boron behavior occurred at low temperature of serpentinization ($T < 200^\circ\text{C}$) in response to pH variation in the fluid. This is in accordance with the previous results of Janecky and Seyfried Jr 1986 which showed that at moderate temperature, pH of fluid increase, while at 300°C pH of fluid is about 5. This is also consistent with the different behavior of $\delta^{11}\text{B}_{\text{fluid}}$ (Figure 6.5), suggesting high pH values in experiment at $T < 280^\circ\text{C}$, and low pH values in experiments at higher temperature.

Our results also highlight that both magnetite and serpentine separates, have lower $\delta^{11}\text{B}$ than seawater and the resulting fluids after serpentinization, demonstrating that both minerals preferentially integrate the heaviest isotope (^{11}B), consistently with that was previously shown by earlier investigations on natural samples Vils et al. 2009. However, different fractionation are recorded during their crystallization, with a $\delta^{11}\text{B}_{\text{serpentine}} < \delta^{11}\text{B}_{\text{magnetite}}$ (Figure 6.7). These results suggested that magnetite uptake less heavier isotope (^{11}B) than serpentine.

The serpentine and magnetite have different apparent B isotopic fractionation factor (α_{apparent}). Indeed, magnetite display low isotopic fractionation in contrast to serpentine Figure 6.19. This suggests that serpentine is potentially more impacted by variation in pH than magnetite during serpentinization. In addition, $\Delta_{\text{srp}-\text{mgt}} = \delta^{11}\text{B}_{\text{srp}} - \delta^{11}\text{B}_{\text{mgt}}$ increases with the temperature (Figure 6.20). Our results revealed the potential of these two minerals to be used as indicator of pH and temperature of serpentinization.

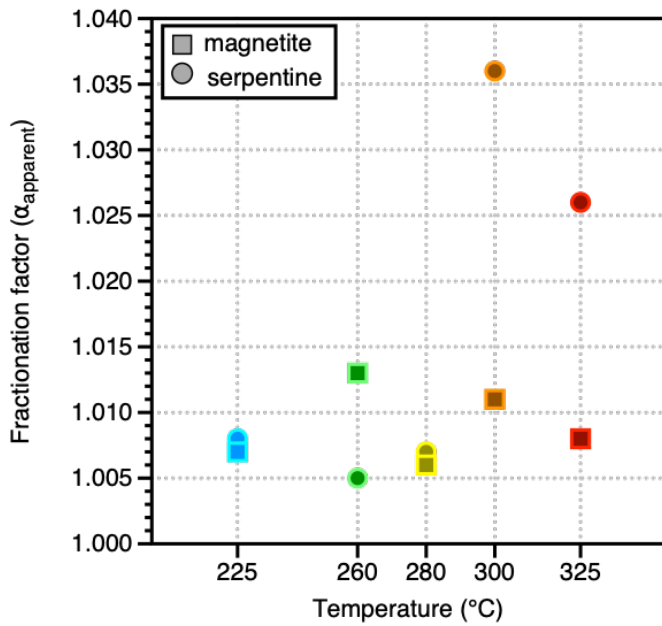


FIGURE 6.19 – Apparent B isotopic fractionation factor of magnetite and serpentine versus temperature (°C).

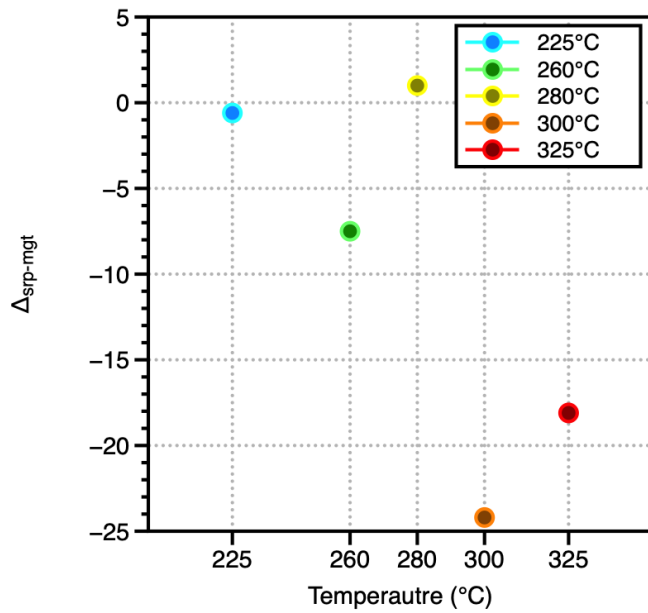


FIGURE 6.20 – $\Delta_{\text{srp-mgt}}$ versus temperature (°C).

6.5 Conclusions and perspectives

To summarize, the boron isotopes recorded by fluids attested of changes in pH mainly related to the temperature of the serpentinization. At experiments temperatures $\leq 260^{\circ}\text{C}$, $\delta^{11}\text{B}_{\text{fluid}}$ attests of high pH values due to the low oxidation of Fe^{2+} to Fe^{3+} in magnetite, and higher proportion of iron partitioning in serpentine. At $T \geq 260^{\circ}\text{C}$, $\delta^{11}\text{B}_{\text{fluid}}$ attests to more acidic pH, generated by higher amount of Fe^{2+} are oxidized to Fe^{3+} in magnetite.

The boron isotopes recorded by fluids during the serpentinization experiments also revealed temporary strong increase of pH at the begining of serpentinization experiments at 300°C , probably to low conversion of Fe^{2+} in Fe^{3+} .

However, in natural environment we do not have access to the fluid leading to the serpentinization reaction. Moreover, this fluid evolved progressively during serpentinization and is therefore a significant approximation to consider a single value of fluid, which is generally those of the seawater like for oxygen isotopes geothermometer. For this reason, we have focused on solid products which formed simultaneously during the serpentinization (i.e., serpentine and magnetite).

Analysis of solids, in particular bulk reveals that during serpentinization between 20 and 60% of Boron is adsorbed and not integrate in the mineral strucutre. All solids were cleaned with mannitol to focus only on the B structural, which is dependant of the temperature. However, a fine phase containing B was accidentally removed during the analytical procedure and the serpentine and magnetite separates are not totally pure. Consequently the results of solids must be interpreted with care. Nevertheless, B integration increases in serpentine and decrease in magnetite with temperature increasing, highlighting a contrasted behavior. In addition, different B isotopic fractionation occurred, with low fractionation factor in magnetite and higher fractionation factor serpentine Figure 6.19. This suggests that serpentine is potentially more impacted by variation in pH than magnetite during serpentinization. Hence, it is reasonable to assume that these two minerals can be used for the calibration of the new geothermometer of the serpentinization.

So, in order to overcome the problem of poor separation, it would be better to analyse the boron concentrations and isotopes by an in-situ method analysis, by Electron Probe Micro analysis (EPMA) and secondary ion mass spectrometry (SIMS). These analytical methods would allow to gain some time and to have the "real" values of each mineral phases. They are also more applicable for the study natural serpentinites

samples. In the previous part of this manuscript, we have highlighted that natural serpentinites are often constituted by several generations of serpentine veins, each one being potentially associated to the formation of magnetite. We have also noticed that these different generations of serpentine are characterized by various boron concentrations and formed in different conditions (see Chapter 4). Thus, the analysis of boron in bulk-rock for this kind of samples is not really appropriate, because it reflects an average of all generations. However, the *in situ* analysis of each generations of the sample, enable to constrain more precisely the conditions including temperature and pH for a better understanding of their environment of formation.

Acknowledgments

Mathieu Granet (ITES - University of Strasbourg) helped a lot for the boron measurements by MC-ICP-MS. René Boutin (ITES - University of Strasbourg) performed the ICP-AES and ICP-MS analyses of fluid phases. Amélie Aubert (ITES - University of Strasbourg) performed the X-RD analyses. Ida di Carlo (ISTO) help for the MEB analysis. Jérôme Specht (Master 2 student at the University of Strasbourg) helped for the serpentine and magnetite separation.

6.6 Supplementary materials

TABLE 6.5 – Serpentine separated, magnetite separated and Bulk rock composition in major and minor elements measured by μ -XRF

	225 Serp	225 Mgt	225 Bulk	260 Serp	260 Mgt	260 bulk	280 Serp	280 Mgt	280 Bulk
<i>Major (wt.%)</i>									
SiO ₂	39.0	36.7	39.0	39.8	36.4	40.0	38.1	39.2	39.5
TiO ₂	0.195	0.240	0.213	0.076	0.275	0.305	0.062	0.063	0.195
Al ₂ O ₃	1.50	3.44	1.65	0.897	3.54	1.90	0.359	0.393	1.42
Fe ₂ O ₃	8.94	10.0	9.04	7.72	10.2	9.38	7.94	8.46	8.97
MgO	34.5	33.0	34.4	36.7	31.6	33.5	38.0	39.2	35.3
CaO	2.03	2.43	2.74	0.143	2.99	3.31	0.581	0.575	1.92
MnO	0.125	0.131	0.129	0.125	0.135	0.128	0.109	0.115	0.128
Na ₂ O	0.381	0.066	0.044	1.15	0.137	0.254	0.422	0.617	0.235
K ₂ O	0.000	0.000	0.000	0.000	0.000	0.001	0.000	0.000	0.000
<i>Minor (ppm)</i>									
Cr	1406	5376	1848	548	3950	2086	2163	3210	1746
Ni	1479	1527	1473	1455	1522	1348	1655	1753	1451
Cu	18.3	18.3	13.7	18.8	15.3	15.0	11.5	11.0	14.4
Zn	36.3	96.8	37.7	19.6	64.0	32.3	28.9	36.4	33.9
Sr	10.5	10.7	18.1	1.97	8.34	7.83	5.74	5.30	7.01

	280bis Serp	280bis mgt	300 Serp	300 Mgt	300 Bulk	325 Serp	325 Mgt	325 Bulk
<i>Major (wt.%)</i>								
SiO ₂	39.4	34.1	40.4	33.7	39.5	40.3	36.0	38.9
TiO ₂	0.065	0.093	0.171	0.378	0.245	0.169	0.220	0.166
Al ₂ O ₃	0.339	0.689	1.67	3.43	1.54	1.72	2.10	1.82
Fe ₂ O ₃	7.19	12.8	8.53	13.3	8.91	8.19	10.5	8.38
MgO	40.0	37.0	34.6	30.3	35.6	35.6	32.2	34.4
CaO	0.223	0.459	1.83	2.13	2.25	2.37	2.87	2.56
MnO	0.109	0.140	0.125	0.158	0.124	0.116	0.135	0.123
Na ₂ O	0.719	0.889	0.302	0.072	0.242	0.286	0.184	0.883
K ₂ O	0.000	0.000	0.000	0.000	0.000	0.000	0.000	0.015
<i>Minor (ppm)</i>								
Cr	1602	6337	1152	6539	1824	1178	3522	1642
Ni	1665	1898	1539	1605	1438	1436	1463	1365
Cu	10.3	15.8	17.2	22.2	22.3	10.9	10.5	13.3
Zn	27.1	55.0	29.2	100	31.7	23.9	51.3	31.2
Sr	2.17	2.76	5.26	7.53	8.63	10.1	15.9	16.5

225 serp. fine - RX0729

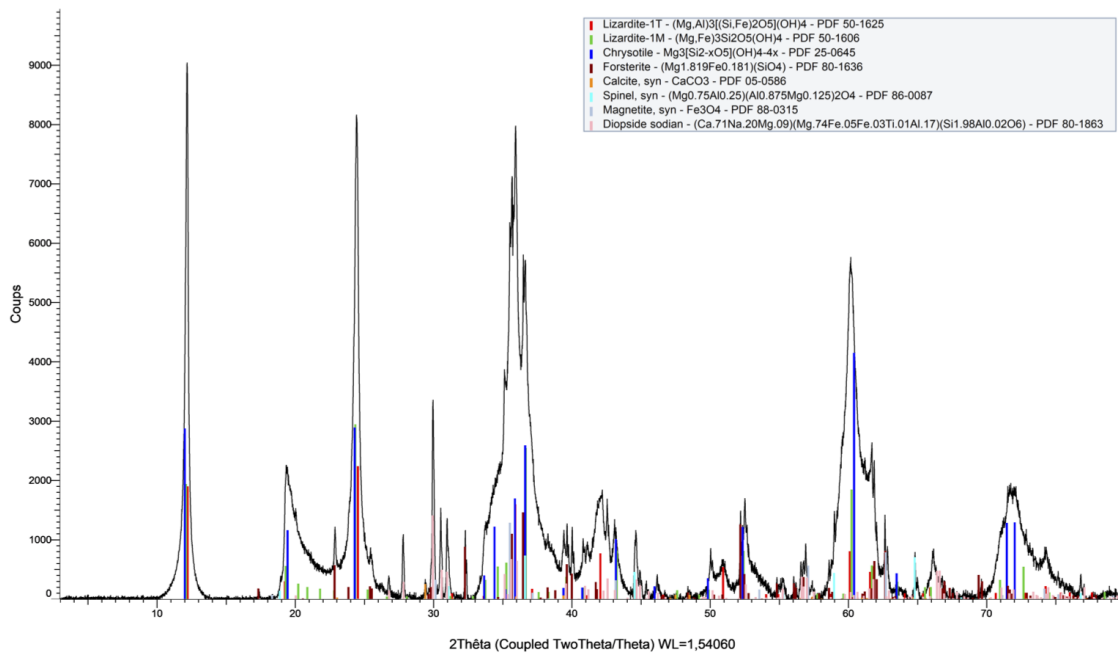


FIGURE 6.21 – XRD pattern of serpentine separates at 225°C.

225 Mgt - RX0728

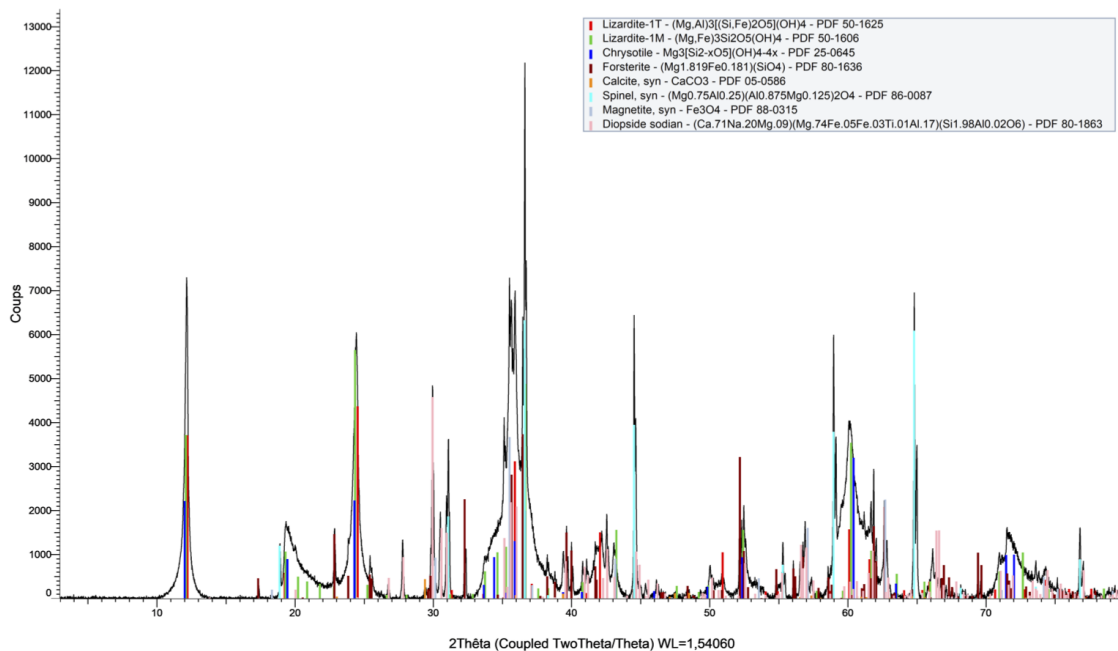


FIGURE 6.22 – XRD pattern of magnetite separates at 225°C.

260 serp - RX0732

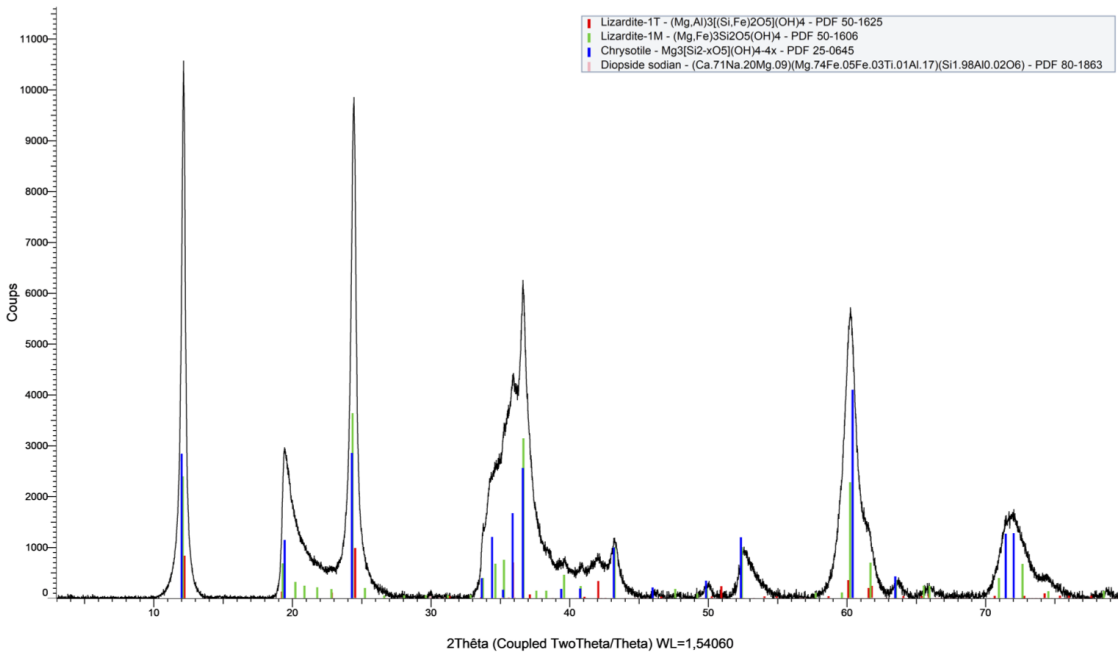


FIGURE 6.23 – XRD pattern of serpentine separates at 260°C.

260 Mgt - RX0731

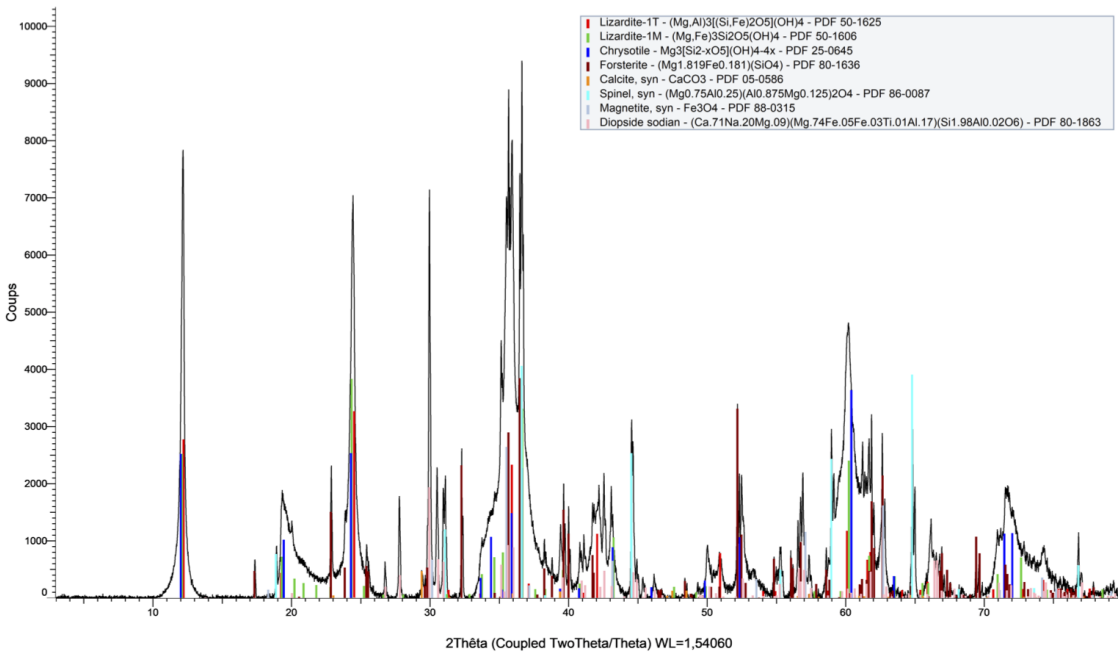


FIGURE 6.24 – XRD pattern of magnetite separates at 260°C.

280 serp - RX0735

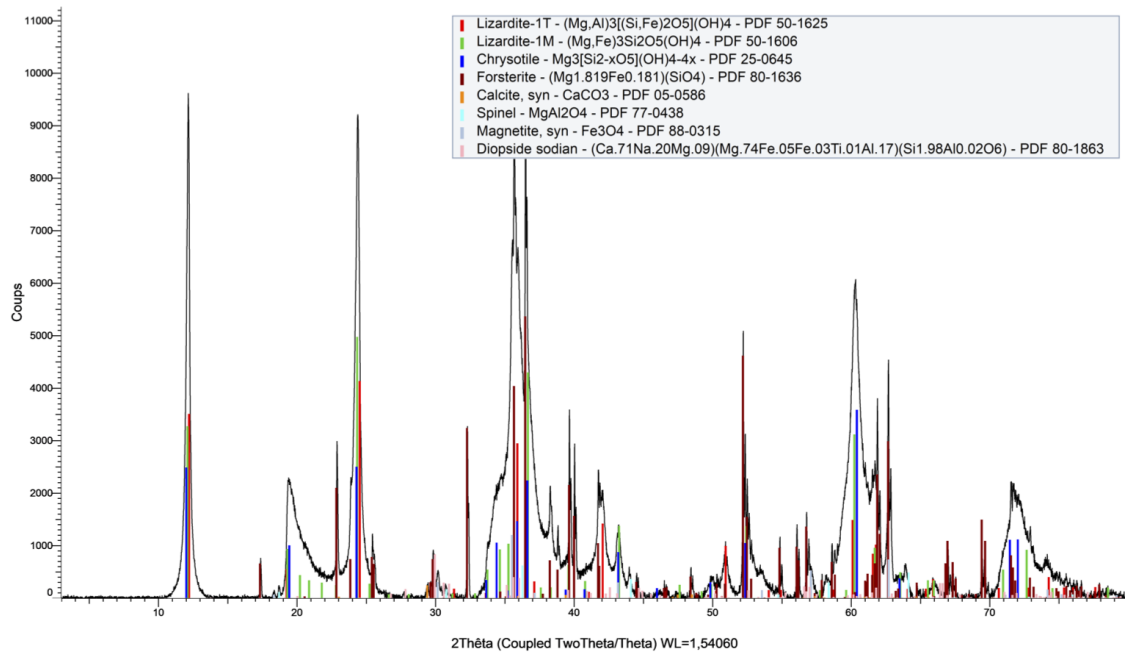


FIGURE 6.25 – XRD pattern of serpentine separates at 280°C.

280 mgt - RX0734

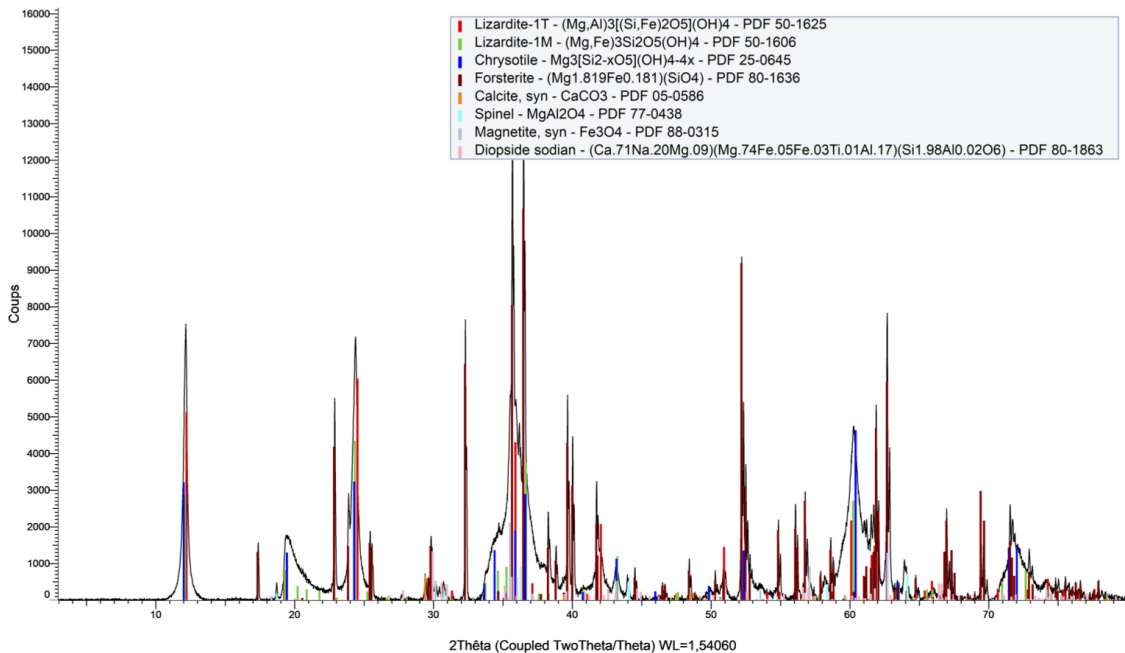


FIGURE 6.26 – XRD pattern of magnetite separates at 280°C.

280 bis serp-RX0738

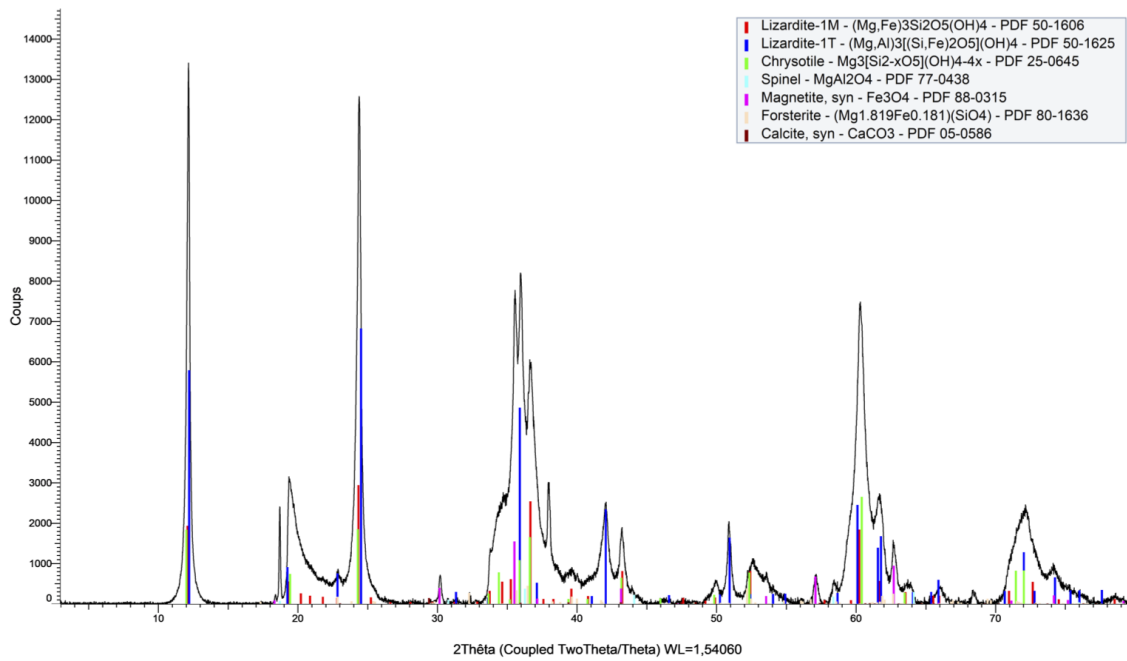


FIGURE 6.27 – XRD pattern of serpentine separates at 280°C bis.

280 bis mgt - RX0737

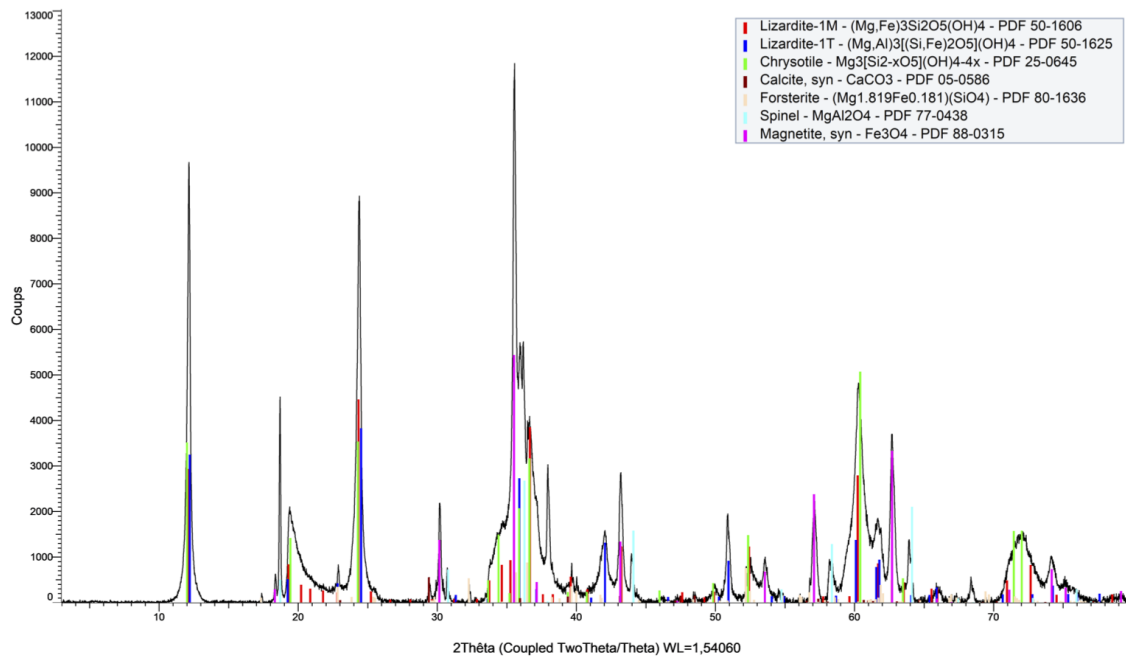


FIGURE 6.28 – XRD pattern of magnetite separates at 280°C bis.

300 serp - RX0741

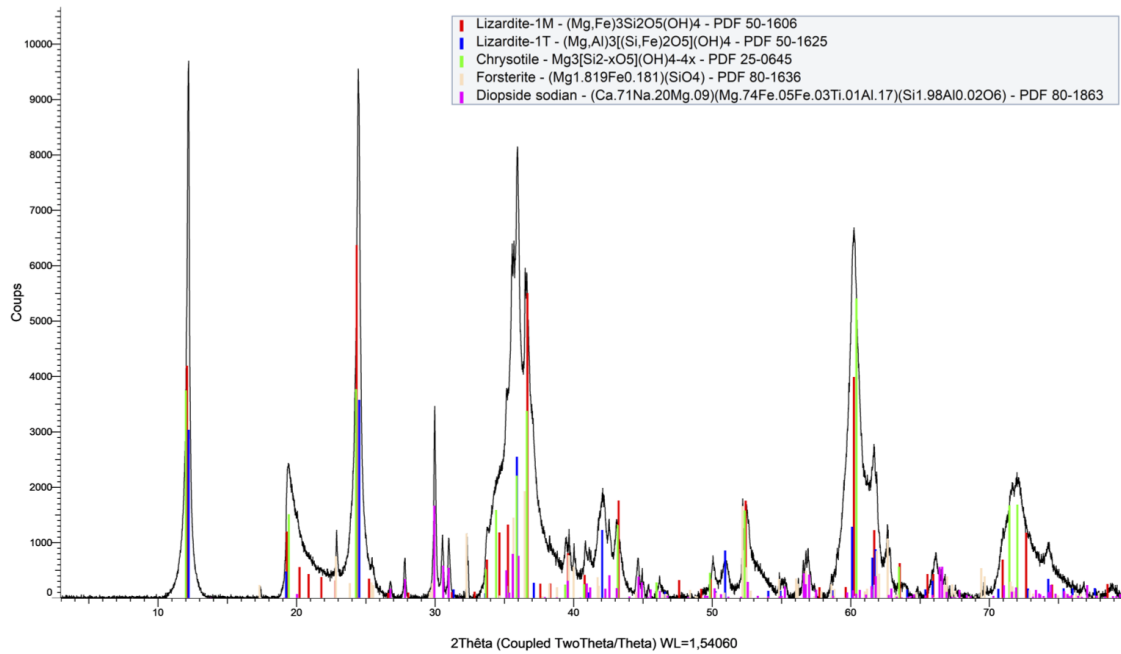


FIGURE 6.29 – XRD pattern of serpentine separates at 300°C.

300 mgt - RX0740

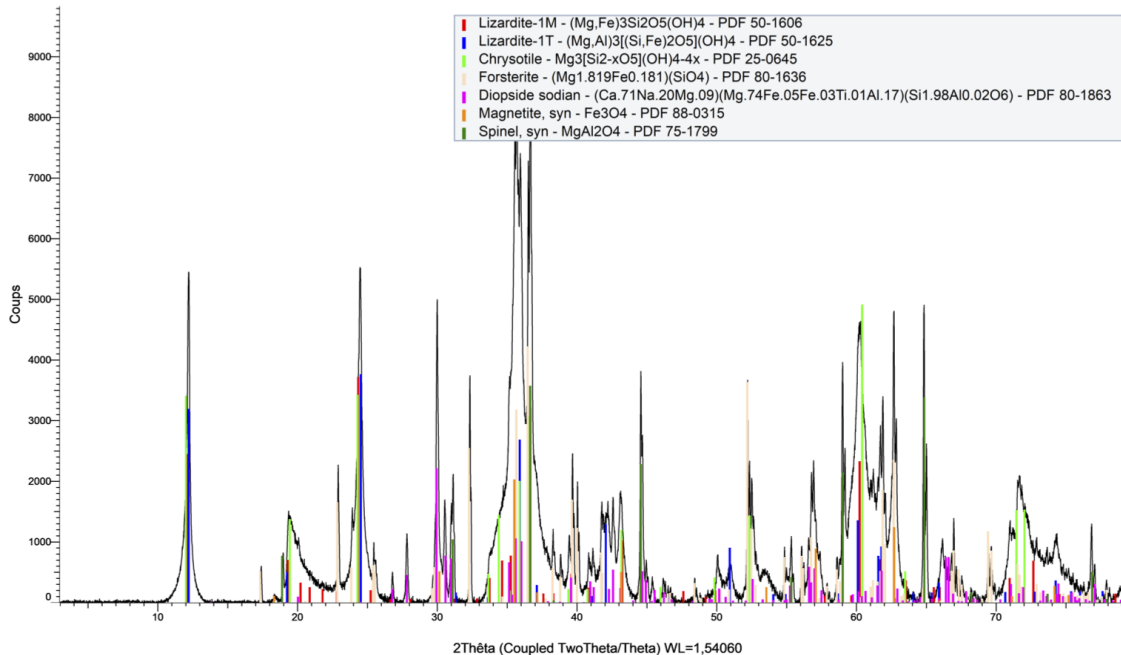


FIGURE 6.30 – XRD pattern of magnetite separates at 300°C.

325 serp - RX0744

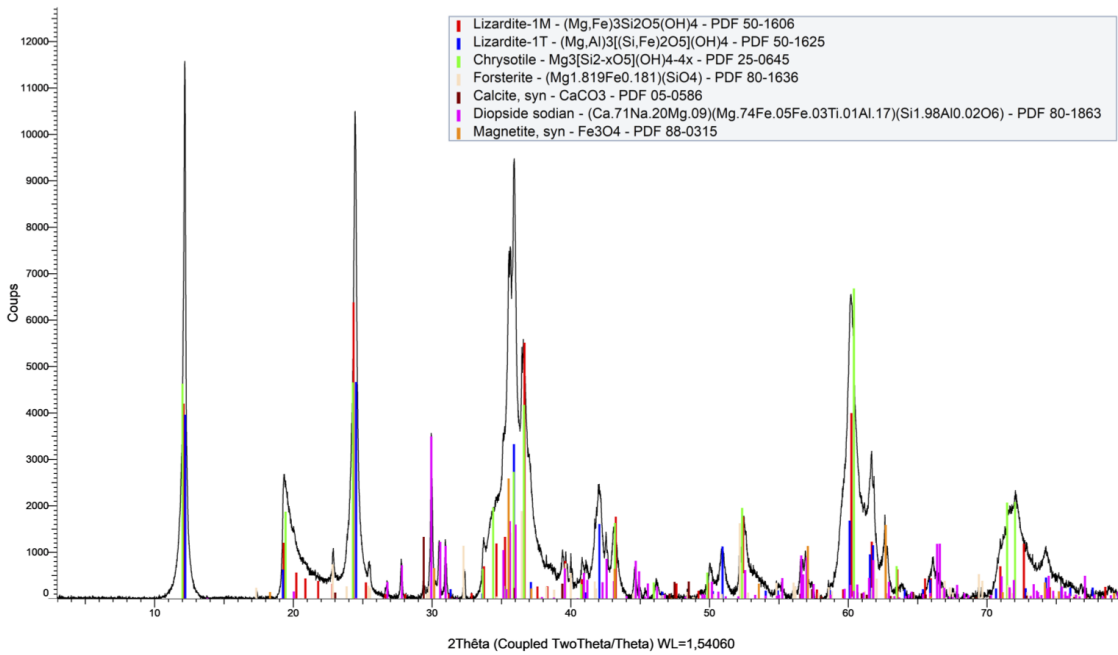


FIGURE 6.31 – XRD pattern of serpentine separates at 325°C.

325 mgt - RX0743

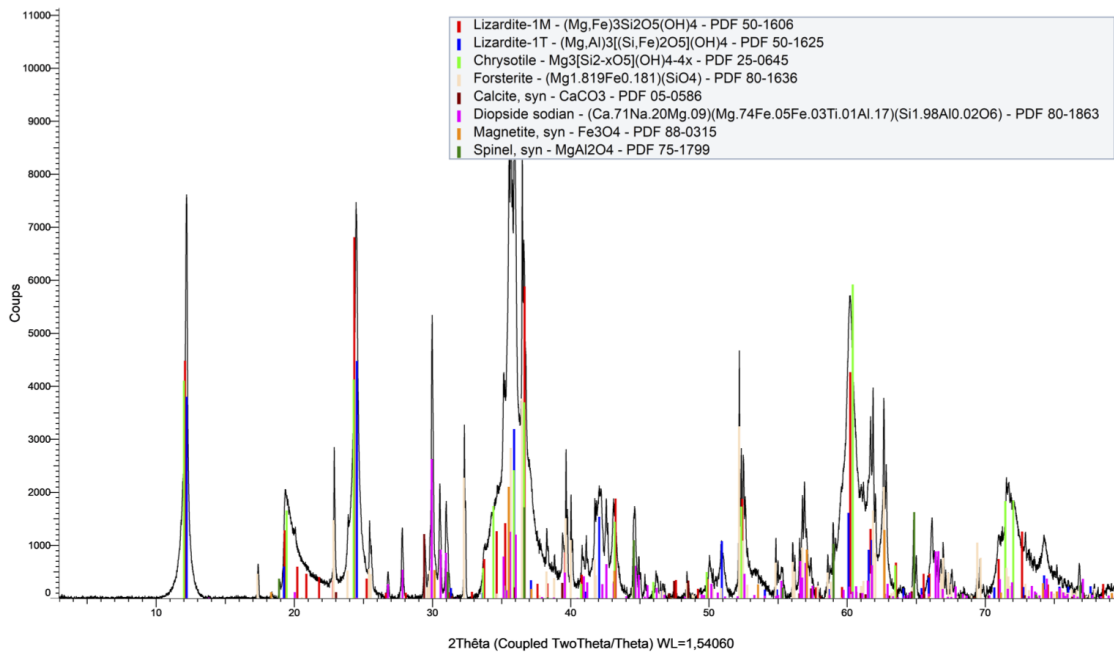


FIGURE 6.32 – XRD pattern of magnetite separates at 325°C.

Bibliographie

- Agrinier, P. and Cannat, M. (1997). Oxygen-isotope constraints on serpentinization processes in ultramafic rocks from the mid-atlantic ridge (23 n). *Notes*, 47:95–1.
- Agrinier, P., Cornen, G., and Beslier, M.-O. (1996). Mineralogical and oxygen isotopic features of serpentinites recovered from the ocean/continent transition in the iberia abyssal plain. In *Proceedings-Ocean Drilling Program Scientific Results*, pages 541–552. National science foundation.
- Agrinier, P., Hékinian, R., Bideau, D., and Javoy, M. (1995). O and h stable isotope compositions of oceanic crust and upper mantle rocks exposed in the hess deep near the galapagos triple junction. *Earth and Planetary Science Letters*, 136(3-4):183–196.
- Allen, D. E. and Seyfried Jr, W. (2003). Compositional controls on vent fluids from ultramafic-hosted hydrothermal systems at mid-ocean ridges : An experimental study at 400 c, 500 bars. *Geochimica et Cosmochimica Acta*, 67(8):1531–1542.
- Allen, D. E. and Seyfried Jr, W. (2004). Serpentinization and heat generation : constraints from Lost City and Rainbow hydrothermal systems. *Geochimica et Cosmochimica Acta*, 68(6):1347–1354.
- Allen, D. E. and Seyfried Jr, W. (2005). Ree controls in ultramafic hosted mor hydrothermal systems : an experimental study at elevated temperature and pressure. *Geochimica et Cosmochimica Acta*, 69(3):675–683.
- Alt, J. C. and Shanks III, W. C. (2003). Serpentinization of abyssal peridotites from the mark area, mid-atlantic ridge : sulfur geochemistry and reaction modeling. *Geochimica et cosmochimica Acta*, 67(4):641–653.
- Alt, J. C. and Shanks III, W. C. (2006). Stable isotope compositions of serpentinite seamounts in the mariana forearc : Serpentinization processes, fluid sources and sulfur metasomatism. *Earth and Planetary Science Letters*, 242(3-4):272–285.
- Alt, J. C., Shanks III, W. C., Bach, W., Paulick, H., Garrido, C. J., and Beaudoin, G. (2007). Hydrothermal alteration and microbial sulfate reduction in peridotite and gabbro exposed by detachment faulting at the mid-atlantic ridge, 15 20 n (odp leg 209) : A sulfur and oxygen isotope study. *Geochemistry, Geophysics, Geosystems*, 8(8).
- Andreani, M., Mevel, C., Boullier, A. M., and Escartin, J. (2007). Dynamic control on serpentine crystallization in veins : Constraints on hydration processes in oceanic peridotites. *Geochemistry, Geophysics, Geosystems*, 8.
- Barnes, I. and O'Neil, J. R. (1969). The relationship between fluids in some fresh alpine-type ultramafics and possible modern serpentinization, western united states. *Geological Society of America Bulletin*, 80(10):1947–1960.

- Bonatti, E., Lawrence, J. R., and Morandi, N. (1984). Serpentinization of oceanic peridotites : temperature dependence of mineralogy and boron content. *Earth and Planetary Science Letters*, 70(1):88–94.
- Boschi, C., Bonatti, E., Ligi, M., Brunelli, D., Cipriani, A., Dallai, L., D’Orazio, M., Früh-Green, G. L., Tonarini, S., Barnes, J. D., et al. (2013). Serpentinization of mantle peridotites along an uplifted lithospheric section, mid atlantic ridge at 11 n. *Lithos*, 178:3–23.
- Boschi, C., Dini, A., Früh-Green, G. L., and Kelley, D. S. (2008). Isotopic and element exchange during serpentinization and metasomatism at the atlantis massif (mar 30 n) : insights from b and sr isotope data. *Geochimica et Cosmochimica Acta*, 72(7):1801–1823.
- Burkhard, D. J. and O’Neil, J. R. (1988). Contrasting serpentinization processes in the eastern central alps. *Contributions to Mineralogy and Petrology*, 99(4):498–506.
- Cann, J. R., Blackman, D., Smith, D., McAllister, E., Janssen, B., Mello, S., Avgerinos, E., Pascoe, A., and Escartin, J. (1997). Corrugated slip surfaces formed at ridge-transform intersections on the mid-atlantic ridge. *Nature*, 385(6614):329–332.
- Cannaò, E. (2020). Boron isotope fractionation in subducted serpentinites : a modelling attempt. *Lithos*, 376:105768.
- Carlson, R. L. and Miller, D. J. (1997). A new assessment of the abundance of serpentinite in the oceanic crust. *Geophysical Research Letters*, 24(4):457–460.
- Charlou, J., Donval, J., Fouquet, Y., Jean-Baptiste, P., and Holm, N. (2002). Geochemistry of high h2 and ch4 vent fluids issuing from ultramafic rocks at the rainbow hydrothermal field (36°14N, MAR). *Chemical geology*, 191(4):345–359.
- Chaussidon, M. and Jambon, A. (1994). Boron content and isotopic composition of oceanic basalts : geochemical and cosmochemical implications. *Earth and Planetary Science Letters*, 121(3-4):277–291.
- Chaussidon, M. and Marty, B. (1995). Primitive boron isotope composition of the mantle. *Science*, 269(5222):383–386.
- Chavagnac, V., Monnin, C., Ceuleneer, G., Boulart, C., and Hoareau, G. (2013). Characterization of hyperalkaline fluids produced by low-temperature serpentinization of mantle peridotites in the oman and ligurian ophiolites. *Geochemistry, Geophysics, Geosystems*, 14(7):2496–2522.
- Christensen, N. I. (1972). The abundance of serpentinites in the oceanic crust. *The Journal of Geology*, 80(6):709–719.
- D’Alessandro, W., Daskalopoulou, K., Calabrese, S., and Bellomo, S. (2018). Water chemistry and abiogenic methane content of a hyperalkaline spring related to serpentinization in the argolida ophiolite (ermioni, greece). *Marine and petroleum geology*, 89:185–193.
- Debret, B., Andreani, M., Godard, M., Nicollet, C., Schwartz, S., and Lafay, R. (2013). Trace element behavior during serpentinization/de-serpentinization of an eclogitized oceanic lithosphere : A la-icpms study of the lanzo ultramafic massif (western alps). *Chemical Geology*, 357:117–133.
- Deschamps, F., Godard, M., Guillot, S., and Hattori, K. (2013). Geochemistry of subduction zone serpentinites : A review. *Lithos*, 178:96–127.

- Deschamps, F., Guillot, S., Godard, M., Andreani, M., and Hattori, K. (2011). Serpentinites act as sponges for fluid-mobile elements in abyssal and subduction zone environments. *Terra Nova*, 23(3):171–178.
- Deschamps, F., Guillot, S., Godard, M., Chauvel, C., Andreani, M., and Hattori, K. (2010). In situ characterization of serpentinites from forearc mantle wedges : timing of serpentinitization and behavior of fluid-mobile elements in subduction zones. *Chemical Geology*, 269(3-4):262–277.
- Dickson, A. G. (1990). Thermodynamics of the dissociation of boric acid in synthetic seawater from 273.15 to 318.15 k. *Deep Sea Research Part A. Oceanographic Research Papers*, 37(5):755–766.
- Douville, E., Charlou, J. L., Oelkers, E. H., Bienvenu, P., Colon, C. F. J., Donval, J. P., Fouquet, Y., Prieur, D., and Appriou, P. (2002). The rainbow vent fluids (36°14N, MAR) : the influence of ultramafic rocks and phase separation on trace metal content in Mid-Atlantic Ridge hydrothermal fluids. *Chemical Geology*, 184:37–48.
- Escartin, J., Hirth, G., and Evans, B. (1997). Effects of serpentinization on the lithospheric strength and the style of normal faulting at slow-spreading ridges. *Earth and Planetary Science Letters*, 151(3-4):181–189.
- Escartín, J., Smith, D. K., Cann, J., Schouten, H., Langmuir, C. H., and Escrig, S. (2008). Central role of detachment faults in accretion of slow-spreading oceanic lithosphere. *Nature*, 455(7214):790–794.
- Etiope, G., Tsikouras, B., Kordella, S., Ifandi, E., Christodoulou, D., and Papatheodorou, G. (2013). Methane flux and origin in the othrys ophiolite hyperalkaline springs, greece. *Chemical Geology*, 347:161–174.
- Evans, B. W., Hattori, K., and Baronnet, A. (2013). Serpentinite : what, why, where ? *Elements*, 9(2):99–106.
- Foster, G., Pogge von Strandmann, P. A., and Rae, J. (2010). Boron and magnesium isotopic composition of seawater. *Geochemistry, Geophysics, Geosystems*, 11(8).
- Früh-Green, G. L., Connolly, J. A., Plas, A., Kelley, D. S., and Grobety, B. (2004). Serpentinization of oceanic peridotites : implications for geochemical cycles and biological activity. *The subseafloor biosphere at mid-ocean ridges*, 144:119–136.
- Früh-Green, G. L., Plas, A., and Lécuyer, C. (1996). 14. petrologic and stable isotope constraints on hydrothermal alteration and serpentinization of the epr shallow mantle at hess deep (site 895). In *Proceedings of the ocean drilling program, scientific results*, volume 147, pages 255–291.
- Giampouras, M., Garrido, C. J., Zwicker, J., Vadillo, I., Smrzka, D., Bach, W., Peckmann, J., Jiménez, P., Benavente, J., and García-Ruiz, J. M. (2019). Geochemistry and mineralogy of serpentinization-driven hyperalkaline springs in the ronda peridotites. *Lithos*, 350:105215.
- Guillot, S., Schwartz, S., Reynard, B., Agard, P., and Prigent, C. (2015). Tectonic significance of serpentinites. *Tectonophysics*, 646:1–19.
- Hansen, C. T., Meixner, A., Kasemann, S. A., and Bach, W. (2017). New insight on li and b isotope fractionation during serpentinization derived from batch reaction investigations. *Geochimica et Cosmochimica Acta*, 217:51–79.

- Harvey, J., Garrido, C. J., Savov, I., Agostini, S., Padrón-Navarta, J. A., Marchesi, C., Sánchez-Vizcaíno, V. L., and Gómez-Pugnaire, M. T. (2014). 11b-rich fluids in subduction zones : The role of antigorite dehydration in subducting slabs and boron isotope heterogeneity in the mantle. *Chemical Geology*, 376:20–30.
- Hemming, N. G. and Hanson, G. N. (1992). Boron isotopic composition and concentration in modern marine carbonates. *Geochimica et Cosmochimica Acta*, 56(1):537–543.
- Hershey, J. P., Fernandez, M., Milne, P. J., and Millero, F. J. (1986). The ionization of boric acid in nacl, na ca cl and na mg cl solutions at 25°C. *Geochimica et cosmochimica acta*, 50(1):143–148.
- Holm, N. G., Oze, C., Mousis, O., Waite, J., and Guilbert-Lepoutre, A. (2015). Serpentization and the formation of h2 and ch4 on celestial bodies (planets, moons, comets). *Astrobiology*, 15(7):587–600.
- Hoog, J., De, C., and Savov, I. P. (2018). Boron isotopes as a tracer of subduction zone processes. *Boron Isotopes*, pages 217–247.
- Hyndman, R. D. and Peacock, S. M. (2003). Serpentization of the forearc mantle. *Earth and Planetary Science Letters*, 212(3-4):417–432.
- Jackson, J. A. (1987). Active normal faulting and crustal extension. *Geological Society, London, Special Publications*, 28:3–17.
- Janecky, D. and Seyfried Jr, W. (1986). Hydrothermal serpentinization of peridotite within the oceanic crust : Experimental investigations of mineralogy and major element chemistry. *Geochimica et Cosmochimica Acta*, 50(7):1357–1378.
- Kakihana, H. and Kotaka, M. (1977). Equilibrium constants for boron isotope-exchange reactions. *Bulletin of the Research Laboratory for Nuclear Reactors (Tokyo Institute of Technology)*, 2.
- Kakihana, H., Kotaka, M., Satoh, S., Nomura, M., and Okamoto, M. (1977). Fundamental studies on the ion-exchange separation of boron isotopes. *Bulletin of the chemical society of Japan*, 50(1):158–163.
- Kelley, D. S., Karson, J. A., Blackman, D. K., FruÈh-Green, G. L., Butterfield, D. A., Lilley, M. D., Olson, E. J., Schrenk, M. O., Roe, K. K., Lebon, G. T., et al. (2001). An off-axis hydrothermal vent field near the mid-atlantic ridge at 30 n. *Nature*, 412(6843):145–149.
- Klochko, K., Kaufman, A. J., Yao, W., Byrne, R. H., and Tossell, J. A. (2006). Experimental measurement of boron isotope fractionation in seawater. *Earth and Planetary Science Letters*, 248(1-2):276–285.
- Kodolányi, J. and Pettke, T. (2011). Loss of trace elements from serpentinites during fluid-assisted transformation of chrysotile to antigorite—an example from guatemala. *Chemical Geology*, 284(3-4):351–362.
- Lemarchand, D., Cividini, D., Turpault, M.-P., and Chabaux, F. (2012). Boron isotopes in different grain size fractions : Exploring past and present water–rock interactions from two soil profiles (strengbach, vosges mountains). *Geochimica et Cosmochimica Acta*, 98:78–93.
- Lemarchand, D., Gaillardet, J., Lewin, E., and Allegre, C. (2000). The influence of rivers on marine boron isotopes and implications for reconstructing past ocean ph. *Nature*, 408(6815):951–954.

- Lemarchand, D., Jacobson, A. D., Cividini, D., and Chabaux, F. (2015). The major ion, $^{87}\text{Sr}/^{86}\text{Sr}$, and $\delta^{11}\text{B}$ geochemistry of groundwater in the wyodak-anderson coal bed aquifer (powder river basin, wyoming, usa). *Comptes Rendus Geoscience*, 347(7-8):348–357.
- Li, Y.-C., Wei, H.-Z., Palmer, M. R., Jiang, S.-Y., Liu, X., Williams-Jones, A. E., Ma, J., Lu, J.-J., Lin, Y.-B., and Dong, G. (2021). Boron coordination and b/si ordering controls over equilibrium boron isotope fractionation among minerals, melts, and fluids. *Chemical Geology*, 561:120030.
- Liu, Y. and Tossell, J. A. (2005). Ab initio molecular orbital calculations for boron isotope fractionations on boric acids and borates. *Geochimica et Cosmochimica Acta*, 69(16):3995–4006.
- Marschall, H. R. (2018). Boron isotopes in the ocean floor realm and the mantle. *Boron isotopes*, pages 189–215.
- Marschall, H. R., Wanless, V. D., Shimizu, N., Von Strandmann, P. A. P., Elliott, T., and Monteleone, B. D. (2017). The boron and lithium isotopic composition of mid-ocean ridge basalts and the mantle. *Geochimica et Cosmochimica Acta*, 207:102–138.
- Martin, C., Flores, K. E., and Harlow, G. E. (2016). Boron isotopic discrimination for subduction-related serpentinites. *Geology*, 44(11):899–902.
- Mavromatis, V., Montouillout, V., Noireaux, J., Gaillardet, J., and Schott, J. (2015). Characterization of boron incorporation and speciation in calcite and aragonite from co-precipitation experiments under controlled ph, temperature and precipitation rate. *Geochimica et Cosmochimica Acta*, 150:299–313.
- McCaig, A. M., Titarenko, S. S., Savov, I. P., Cliff, R. A., Banks, D., Boyce, A., and Agostini, S. (2018). No significant boron in the hydrated mantle of most subducting slabs. *Nature communications*, 9(1):1–10.
- McCollom, T. M., Klein, F., Solheid, P., and Moskowitz, B. (2020). The effect of ph on rates of reaction and hydrogen generation during serpentinization. *Philosophical Transactions of the Royal Society A*, 378(2165):20180428.
- Mével, C. (2003). Serpentinization of abyssal peridotites at mid-ocean ridges. *Comptes Rendus Geoscience*, 335(10-11):825–852.
- Moody, J. B. (1976). Serpentinization : a review. *Lithos*, 9(2):125–138.
- Moran, A. E., Sisson, V. B., and Leeman, W. P. (1992). Boron depletion during progressive metamorphism : implications for subduction processes. *Earth and Planetary Science Letters*, 111(2-4):331–349.
- Noireaux, J., Mavromatis, V., Gaillardet, J., Schott, J., Montouillout, V., Louvat, P., Rollion-Bard, C., and Neuville, D. (2015). Crystallographic control on the boron isotope paleo-ph proxy. *Earth and Planetary Science Letters*, 430:398–407.
- O’hanley, D. S. (1991). Fault-related phenomena associated with hydration and serpentine recrystallization during serpentinization. *The Canadian Mineralogist*, 29(1):21–35.
- Pabst, S., Zack, T., Savov, I. P., Ludwig, T., Rost, D., and Vicenzi, E. P. (2011). Evidence for boron incorporation into the serpentine crystal structure. *American Mineralogist*, 96(7):1112–1119.

- Pagani, M., Lemarchand, D., Spivack, A., and Gaillardet, J. (2005). A critical evaluation of the boron isotope-ph proxy : The accuracy of ancient ocean ph estimates. *Geochimica et Cosmochimica Acta*, 69(4):953–961.
- Palmer, M. and Helvaci, C. (1997). The boron isotope geochemistry of the neogene borate deposits of western turkey. *Geochimica et Cosmochimica Acta*, 61(15):3161–3169.
- Palmer, M., Spivack, A., and Edmond, J. (1987). Temperature and ph controls over isotopic fractionation during adsorption of boron on marine clay. *Geochimica et Cosmochimica Acta*, 51(9):2319–2323.
- Pelletier, L., Vils, F., Kalt, A., and Gmeling, K. (2008). Li, b and be contents of harzburgites from the dramala complex (pindos ophiolite, greece) : Evidence for a mor-type mantle in a supra-subduction zone environment. *Journal of Petrology*, 49(11):2043–2080.
- Proskurowski, G., Lilley, M. D., Kelley, D. S., and Olson, E. J. (2006). Low temperature volatile production at the lost city hydrothermal field, evidence from a hydrogen stable isotope geothermometer. *Chemical Geology*, 229(4):331–343.
- Proskurowski, G., Lilley, M. D., Seewald, J. S., Früh-Green, G. L., Olson, E. J., Lupton, J. E., Sylva, S. P., and Kelley, D. S. (2008). Abiogenic hydrocarbon production at lost city hydrothermal field. *Science*, 319(5863):604–607.
- Ranero, C. R., Phipps Morgan, J., McIntosh, K., and Reichert, C. (2003). Bending-related faulting and mantle serpentinization at the middle america trench. *Nature*, 425(6956):367–373.
- Rouméjon, S. and Cannat, M. (2014). Serpentinization of mantle-derived peridotites at mid-ocean ridges : Mesh texture development in the context of tectonic exhumation. *Geochemistry, Geophysics, Geosystems*, 15(6):2354–2379.
- Rouméjon, S., Williams, M. J., and Früh-Green, G. L. (2018). In-situ oxygen isotope analyses in serpentine minerals : Constraints on serpentinization during tectonic exhumation at slow-and ultraslow-spreading ridges. *Lithos*, 323:156–173.
- Roux, P., Lemarchand, D., Hughes, H. J., and Turpault, M.-P. (2015). A rapid method for determining boron concentration (id-icp-ms) and $\delta^{11}\text{B}$ (mc-icp-ms) in vegetation samples after microwave digestion and cation exchange chemical purification. *Geostandards and Geoanalytical Research*, 39(4):453–466.
- Rudnick, R., Gao, S., Holland, H., Turekian, K., et al. (2003). Composition of the continental crust. *The crust*, 3:1–64.
- Russell, M., Hall, A., and Martin, W. (2010). Serpentinization as a source of energy at the origin of life. *Geobiology*, 8(5):355–371.
- Ryan, J. G. and Langmuir, C. H. (1993). The systematics of boron abundances in young volcanic rocks. *Geochimica et Cosmochimica Acta*, 57(7):1489–1498.
- Saccoccia, P. J., Seewald, J. S., and Shanks III, W. C. (2009). Oxygen and hydrogen isotope fractionation in serpentine–water and talc–water systems from 250 to 450 °C, 50 mpa. *Geochimica et Cosmochimica Acta*, 73(22):6789–6804.
- Saldi, G. D., Noireaux, J., Louvat, P., Faure, L., Balan, E., Schott, J., and Gaillardet, J. (2018). Boron isotopic fractionation during adsorption by calcite–implication for the seawater ph proxy. *Geochimica et Cosmochimica Acta*, 240:255–273.

- Salter, V. J. and Stracke, A. (2004). Composition of the depleted mantle. *Geochemistry, Geophysics, Geosystems*, 5(5).
- Sanyal, A., Nugent, M., Reeder, R., and Bijma, J. (2000). Seawater ph control on the boron isotopic composition of calcite : evidence from inorganic calcite precipitation experiments. *Geochimica et Cosmochimica Acta*, 64(9):1551–1555.
- Savov, I. P., Ryan, J. G., D'Antonio, M., and Fryer, P. (2007). Shallow slab fluid release across and along the mariana arc-basin system : Insights from geochemistry of serpentized peridotites from the mariana fore arc. *Journal of Geophysical Research : Solid Earth*, 112(B9).
- Scambelluri, M., Fiebig, J., Malaspina, N., Müntener, O., and Pettke, T. (2004). Serpentinite subduction : implications for fluid processes and trace-element recycling. *International Geology Review*, 46(7):595–613.
- Scambelluri, M. and Tonarini, S. (2012). Boron isotope evidence for shallow fluid transfer across subduction zones by serpentized mantle. *Geology*, 40(10):907–910.
- Schrenk, M. O., Brazelton, W. J., and Lang, S. Q. (2013). Serpentization, carbon, and deep life. *Reviews in Mineralogy and Geochemistry*, 75(1):575–606.
- Seyfried Jr, W. and Dibble Jr, W. (1980). Seawater-peridotite interaction at 300 c and 500 bars : implications for the origin of oceanic serpentinites. *Geochimica et Cosmochimica Acta*, 44(2):309–321.
- Seyfried Jr, W., Foustaoukos, D., and Fu, Q. (2007). Redox evolution and mass transfer during serpentization : An experimental and theoretical study at 200 c, 500 bar with implications for ultramafic-hosted hydrothermal systems at mid-ocean ridges. *Geochimica et Cosmochimica Acta*, 71(15):3872–3886.
- Seyfried Jr, W., Janecky, D. R., and Berndt, M. (1987). Rocking autoclaves for hydrothermal experiments ii. the flexible reaction-cell system. *Hydrothermal Experimental Techniques* (ed GC Ulmer, pages 216–239.
- Skelton, A., Valley, J., Graham, C., Bickle, M., and Fallick, A. (2000). The correlation of reaction and isotope fronts and the mechanism of metamorphic fluid flow. *Contributions to Mineralogy and Petrology*, 138(4):364–375.
- Skelton, A. D. and Valley, J. W. (2000). The relative timing of serpentisation and mantle exhumation at the ocean-continent transition, iberia : constraints from oxygen isotopes. *Earth and Planetary Science Letters*, 178(3-4):327–338.
- Snow, J. E. and Dick, H. J. (1995). Pervasive magnesium loss by marine weathering of peridotite. *Geochimica et Cosmochimica Acta*, 59(20):4219–4235.
- Spivack, A. and Edmond, J. (1987). Boron isotope exchange between seawater and the oceanic crust. *Geochimica et Cosmochimica Acta*, 51(5):1033–1043.
- Spivack, A., Palmer, M., and Edmond, J. (1987). The sedimentary cycle of the boron isotopes. *Geochimica et Cosmochimica Acta*, 51(7):1939–1949.
- Thompson, G. and Melson, W. G. (1970). Boron contents of serpentinites and metabasalts in the oceanic crust : implications for the boron cycle in the oceans. *Earth and Planetary Science Letters*, 8(1):61–65.

- Trumbull, R. B. and Slack, J. F. (2018). Boron isotopes in the continental crust : granites, pegmatites, felsic volcanic rocks, and related ore deposits. In *Boron Isotopes*, pages 249–272. Springer.
- Vils, F., Müntener, O., Kalt, A., and Ludwig, T. (2011). Implications of the serpentine phase transition on the behaviour of beryllium and lithium–boron of subducted ultramafic rocks. *Geochimica et Cosmochimica Acta*, 75(5):1249–1271.
- Vils, F., Pelletier, L., Kalt, A., Müntener, O., and Ludwig, T. (2008). The lithium, boron and beryllium content of serpentized peridotites from odp leg 209 (sites 1272a and 1274a) : implications for lithium and boron budgets of oceanic lithosphere. *Geochimica et Cosmochimica Acta*, 72(22):5475–5504.
- Vils, F., Tonarini, S., Kalt, A., and Seitz, H.-M. (2009). Boron, lithium and strontium isotopes as tracers of seawater–serpentinite interaction at mid-atlantic ridge, odp leg 209. *Earth and Planetary Science Letters*, 286(3-4):414–425.
- Wenner, D. B. and Taylor, H. P. (1971). Temperatures of serpentization of ultramafic rocks based on $\delta^{18}\text{O}$ / $\delta^{16}\text{O}$ fractionation between coexisting serpentine and magnetite. *Contributions to mineralogy and petrology*, 32(3):165–185.
- Williams, L. B. and Hervig, R. L. (2002). Exploring intra-crystalline b-isotope variations in mixed-layer illite-smectite. *American Mineralogist*, 87(11-12):1564–1570.
- Xiao, J., Xiao, Y., Liu, C., and Jin, Z. (2011). Boron isotope fractionation during brucite deposition from artificial seawater. *Climate of the Past*, 7(3):693–706.
- Yamada, C., Tsujimori, T., Chang, Q., and Kimura, J.-I. (2019). Boron isotope variations of franciscan serpentinites, northern California. *Lithos*, 334:180–189.

Chapitre 7

Conclusions and perspectives

7.1 General conclusions

This thesis focused on the serpentinization process occurring during mantle exhumation at magma-poor rifted passive margins, with the aims to :

- characterizing the different steps of fluid-rock interaction during mantle exhumation
- estimating the conditions of serpentinization (temperature, depth and fluid/rock ratios)
- determining the sources of serpentizing fluids
- understanding how these fluids interacted with mantle rocks and characterizing their evolution
- characterizing the mobilization of transition metals and formation of metal deposits in hydrothermal system

These questions have been addressed applying two complementary approaches. The first one consists in the study of serpentinized peridotites sampled in Alpine ophiolites. In the second, serpentinization reaction was reproducing experimentally.

7.1.1 Geological study

Primarily, the chapter 3 presented in this thesis (which was published in Ore Geology Reviews in March 2022), focused to the identification of the sources of fluids involved in the formation of Fe-Ca silicates formed in metals deposits of a Jurassic mineralized system hosted in serpentinites described in the Platta nappe by (Coltat et al., 2019). The application of the Sr isotope geochemistry to Fe-Ca silicates and secondary alteration products including serpentinites, altered mafic and carbonated rocks reveals that several reservoirs, including seawater, subcontinental mantle and mafic rocks contributed to the formation of polymetallic deposits. In addition, these results allowed to reconstruct the timing of the hydrothermal alteration and that the hydrothermal activity started early in the process of mantle exhumation. In particular, the Sr isotope composition of serpentinites suggests multiple and long-time fluid/rock interactions. Serpentinization is initiated when seawater percolated along normal faults through the hyper-thinned crust, attested by $^{87}\text{Sr}/^{86}\text{Sr}$ higher to the Jurassic seawater. The involvement of seawater became dominant during serpentinization and carbonation near the paleo-seafloor. Fe-Ca silicates and the ophicalcites mostly recorded latest stages of fluid/rock interactions dominated by seawater under high fluid/rock ratios.

The petro-geochemical and mineralogical investigations applied to the serpentinites presented in the chapter 4, highlighted also that serpentinization results of a multiple and long-time fluid/rock interactions. These results highlighted that serpentinization recorded the multiple steps of mantle exhumation, and that serpentinization from distal and proximal domains of the OCT displays differences. In particular, in proximal domains (Upper Platta and Tasna), serpentinization is characterized by multiple serpentine generations that we have assigned to different stages of mantle exhumation.

The first stage is marked by initiation of serpentinization which is attested by the pseudomorphic replacement of primary olivine and pyroxenes by serpentine lizardite mesh and bastite (S1). Serpentinization begin before the mantle exhumation during the crustal thinning at $\sim 6\text{-}8$ km depth, relatively high temperature $\sim 300^\circ\text{C}$, very low fluid/rock ratios, and high reducing conditions.

In stage 2, mantle exhumation is recorded by the development of polyhedral serpentine (S2) and banded veins (S3) attesting of a the progressive increases of fluid/rock ratios. Crack develops in response to the volume expansion associated to serpentinization and decrease of the local strain.

In stage 3 antigorite (S4) replaces locally the lizardite mesh S1 or some chrysotile banded veins S3 in response to a local increase of pressure induced by the shortening. This event took place at shallower levels the previous serpentinization events. (Stage 3 : compression).

The end of the mantle exhumation (Stage 4 : relaxation) is evidenced by the development of chrysotile crack-seal (S5) after a late strain release. This study highlights also that mantle exhumation is a long process in proximal domains (Upper Platta and Tasna) marked by the all generations of serpentine (S1 to S5). In contrast, serpentinization in distal domains (Lower Platta) results of a shorter process, marked by the absence of some serpentine generation. Similar to the Lower Platta, at Totalp some serpentine generations are missing. Moreover, the low degree of serpentinization attests of very low fluid/rock ratios. These results evidences that serpentinization at passive margins is comparable to MOR settings, and that antigorite is not only restricted to convergent domains, and that it may be more common in rifted margins and (ultra-)slow spreading centers than previously thought.

7.1.2 Experimental study

The experimental results presented in the Chapter 5 showed that the mineralogy

of the protolith (lherzolite versus harzburgite) influences the nature and proportions of secondary minerals. In harzburgite-seawater experiments, brucite formed while it is not observed during experiments with lherzolite. The second minerals phases is also influenced by seawater. In all experiments, calcite (CaCO_3), and anhydrite (CaSO_4) were formed, the latter being exclusively formed at high temperatures (325°C), attesting of the reaction of sulfates from seawater with calcium from clinopyroxene and seawater. Furthermore, composition of seawater changes drastically during serpentinization. This change is marked by an enrichment in some metals such as Cu, Zn, Ni, Cr and a depletion in major elements Cl, SO_4^{2-} , Si, Mg, and trace elements Sr, B, Li. Temperature of serpentinization influence the partitioning of iron and the sulfate reduction. At low temperatures ($225\text{-}260^\circ\text{C}$) minor reduction of seawater sulfates occurred. In addition, minor amounts of magnetite are formed due to the poor conversion of Fe^{2+} to Fe^{3+} and the uptake of Fe^{3+} by serpentine. In contrast, at $T \leq 260^\circ\text{C}$, higher quantity of magnetite are produced due to important oxidation of Fe^{2+} to Fe^{3+} . Moreover, sulfate from seawater are strongly reduced.

The chapter 6, focused to the boron isotopes fractionation during serpentinization. The measurement of boron concentrations in fluid and solid products have shown that 90% of the boron from seawater was consumed during serpentinization. Boron is preferentially integrated into magnetite in comparison to serpentine. The boron uptake in serpentine is positively correlated to temperature, while it is inversely correlated in magnetite. However, mass balance calculations suggested that more than 50% of Boron is removed during the cleaning procedure with mannitol, suggesting that 50% of boron is adsorbed and not integrate in the mineral structures of secondary minerals. Analysis of boron isotopes in fluids sampled during experiments highlighted different isotopic fractionation between experiments at low temperatures ($225\text{-}260^\circ\text{C}$) and those at high temperatures ($280\text{-}325^\circ\text{C}$). Fluids from experiments at $T \leq 260^\circ\text{C}$ have $\delta^{11}\text{B}_{fluid} < \delta^{11}\text{B}_{sw}$ evidencing a preferential uptake of the heavier isotope (^{11}B) by solids. In contrast, at $T \geq 280^\circ\text{C}$ solids uptake preferentially the lighter isotope (^{10}B), resulting in $\delta^{11}\text{B}_{fluid} > \delta^{11}\text{B}_{sw}$. We propose that at $T \leq 260^\circ\text{C}$, fluids have high pH values (> 8), according to minor conversion of Fe^{2+} to Fe^{3+} and uptake of Fe^{3+} in serpentine. At $T \geq 260^\circ\text{C}$, fluids with low pH (< 5) formed due to the important oxidation of Fe^{2+} to Fe^{3+} in magnetite and important reduction of sulfate from seawater.

Although, the serpentine were poorly separated, the results suggest that it has a different isotope fractionation than those magnetite as a function of temperature. The B isotope ratios of magnetite are systematically higher to serpentine ($\delta^{11}\text{B}_{magnetite} >$

$\delta^{11}\text{B}_{\text{serpentine}}$). In addition, $\delta^{11}\text{B}_{\text{magnetite}}$ increase with increasing temperature , while $\delta^{11}\text{B}_{\text{serpentine}}$ decreases. As is, the geothermometer is not applicable to natural serpentinites. However, in situ determination of the isotopic composition in serpentine and magnetite will allow a better determination of the isotopic fractionation, with the aims of applying it on natural serpentinites.

7.2 Perspectives

7.2.1 Publication strategies

After I submitted my thesis manuscript, I will focus to the submission of the Chapter 4 of this thesis (The Alpine Tethys passive margins : Serpentinization as a tape recorder of mantle exhumation). I would like to submit this paper as soon as possible in the Journal of Petrology, which seems the most suitable journal, with respect to the issue and the methods used.

Then, I would like promote the data acquired during the experimental study. I think, our experimental results may be published in two articles, in a similar way to what was proposed in this thesis. The first article will be focused on the chemical mobility associated to serpentinization with seawater, and the potential mobilization of transitions metals during hydrothermal alteration of mantle and the formation of U-VMS. The second will be focused to the boron isotopes fractionation observed in fluids during serpentinization experiments, discussing the potential of boron isotopes as a marker of pH and temperature.

I would like also promote the Sr and B isotopic compositions that were measured in natural serpentinites during my thesis. So far, only Sr isotopic compositions measured in serpentinites from Platta have been published. However, the Sr isotopic compositions were measured in all samples presented in this study. Moreover, serpentinites from Tasna display similar behavior than Upper Platta, with $^{87}\text{Sr}/^{86}\text{Sr}$ higher to the Jurassic seawater value (Figure 7.1). In contrast at Totalp and Lower Platta lower Sr isotopic compositions were measured with $^{87}\text{Sr}/^{86}\text{Sr}$ ranging between the seawater and DMM. These results appear to be consistent with our conclusion in the Chapter 4. The boron isotopic composition of these serpentinites vary over a wide range of values, from +2 to +39 ‰ (Figure 7.1). Boron and strontium signatures would better constrain the conditions (water/rock ratios, temperature and pH of fluids) in which serpentinization and mantle exhumation occurred.

In particular, these isotopic data may be coupled with reactive transport modeling using a porous flow reference model as described by (DePaolo, 2006) with the aims to i) determine the depth of fluids and ii) constrain the duration of fluid-rock interactions in proximal versus distal domains. The porous flow reference model allow to modelling the concentration and isotopic ratios evolution with time.

During my field excursion in the Alps with the co-workers from the University of Rennes, with Pierre Gauthier and Hector Campos, we have sampling serpentinites at Cotschen. These serpentinites were study from a petrological, mineralogical and structural approaches during the Master stage of Hector, with the aim to characterize the Alpine deformation imprints on the pre Alpine structures (related to the oceanic opening). I have collected some samples with the aim to determine the temperature of the Alpine deformation. Finally, I have only determined the major and trace elements as well the Sr isotopes ratios of these samples. I think that these data could be used (together) in a paper supervised by Pierre Gauthier, who was strongly involved in the characterization of the Alpine deformation.

7.2.2 Perspectives

The results of the two studies based on natural samples presented in this thesis, allowed to determine the sources of serpentinizing fluids and to better understand the conditions, in particular the fluid/rocks ratios occurring during the mantle exhumation at rifted passive margins. However, despite our results suggest that the temperature progressively decreases with mantle exhumation and the conditions become more reducing, an isotopic study based on oxygen and sulphur isotopes, could provide more precise answers. The determination of sulfur isotopes will quantify and the chemical fluxes and constrain the redox conditions of the hydrothermal circulations during the mantle exhumation. In complement to the Sr isotopes results from the Platta hydrothermal system, sulfur isotopes determination of Fe-Ca silicates, serpentinites, and altered mafic rocks, will allow to determine the source of sulfur of the Fe-Ca silicates.

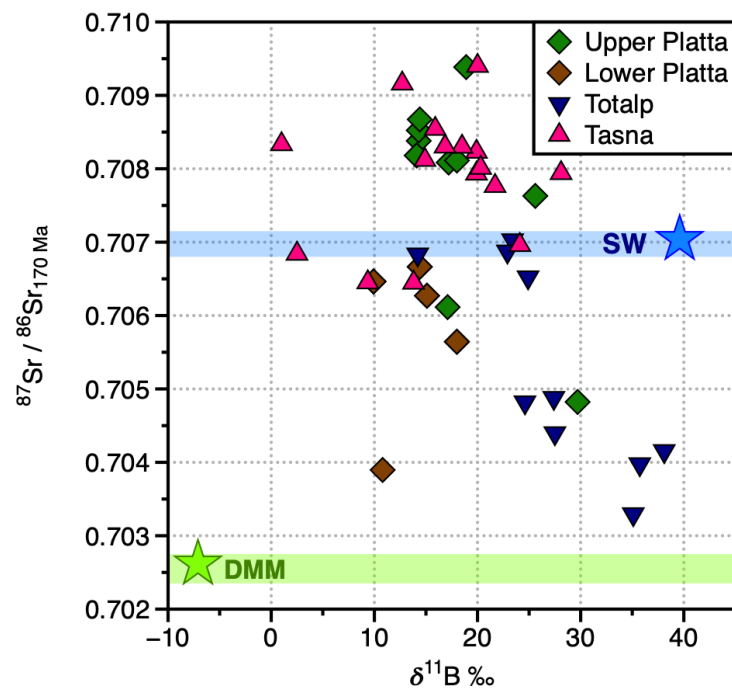


FIGURE 7.1 – $^{87}\text{Sr}/^{86}\text{Sr}$ versus $\delta^{11}\text{B}$ of serpentinites sampled in this thesis.

Bibliographie

- Amann, M., Ulrich, M., Manatschal, G., Pelt, E., Epin, M. E., Autin, J., and Sauter, D. (2020). Geochemical characteristics of basalts related to incipient oceanization : The example from the alpine-tethys ocs. *Terra Nova*, 32:75–88.
- Andreani, M., Grauby, O., Baronnet, A., and Muñoz, M. (2008). Occurrence, composition and growth of polyhedral serpentine. *European Journal of Mineralogy*, 20(2):159–171.
- Coltat, R., Boulvais, P., Branquet, Y., Collot, J., Epin, M. E., and Manatschal, G. (2019). Syntectonic carbonation during synmagmatic mantle exhumation at an ocean-continent transition. *Geology*, 47:183–186.
- Coltat, R., Boulvais, P., Branquet, Y., Richard, A., Tarantola, A., and Manatschal, G. (2022). Moho carbonation at an ocean-continent transition. *Geology*, 50(3):278–283.
- DePaolo, D. J. (2006). Isotopic effects in fracture-dominated reactive fluid–rock systems. *Geochimica et Cosmochimica Acta*, 70(5):1077–1096.
- Deschamps, F., Godard, M., Guillot, S., and Hattori, K. (2013). Geochemistry of subduction zone serpentinites : A review. *Lithos*, 178:96–127.
- Epin, M. E., Manatschal, G., Amman, M., Ribes, C., Clausse, A., Guffon, T., and Lescanne, M. (2019). Polyphase tectono-magmatic evolution during mantle exhumation in an ultra-distal, magma-poor rift domain : example of the fossil platta ophiolite, se switzerland. *International Journal of Earth Sciences*, 108:2443–2467.
- Fauguerolles, C. (2016). *Experimental study of H_2 generation associated with peridotite serpentinization at slow spreading ridges*. PhD thesis, Université d’Orléans.
- Florineth, D. and Froitzheim, N. (1994). Transition from continental to oceanic basement in the tasna nappe : evidence for early cretaceous opening of the valais ocean. *Schweizerische Mineralogische und Petrographische Mitteilungen*, 74(3):437 ?448.
- Froitzheim, N. (1994). Repeated change from crustal shortening to orogenparallel extension in the austroalpine units of graubunden. *Eclogae Geol.*, 87:559–612.
- Hochscheid, F., Coltat, R., Ulrich, M., Munoz, M., Manatschal, G., and Boulvais, P. (2022). The sr isotope geochemistry of oceanic ultramafic-hosted mineralizations. *Ore Geology Reviews*, page 104824.
- Huang, R., Sun, W., Ding, X., Zhao, Y., and Song, M. (2020). Effect of pressure on the kinetics of peridotite serpentinization. *Physics and Chemistry of Minerals*, 47(7):1–14.
- Johnson, D. E. (2019). Protecting the lost city hydrothermal vent system : All is not lost, or is it ? *Marine Policy*, 107:103593.

- Jones, C. E., Jenkyns, H. C., Coe, A. L., and Hesselbo, S. P. (1994). Quantification and restoration of extensional deformation along the Western Iberia and Newfoundland rifted margins. *Geochimica et Cosmochimica Acta*, 58(14):3061–3074.
- Kerrick, D. (2002). Serpentinite seduction. *Science*, 298(5597):1344–1345.
- Klein, F., Bach, W., and McCollom, T. M. (2013). Compositional controls on hydrogen generation during serpentinization of ultramafic rocks. *Lithos*, 178:55–69.
- Lafay, R., Baumgartner, L. P., Stephane, S., Suzanne, P., German, M.-H., and Torsten, V. (2017). Petrologic and stable isotopic studies of a fossil hydrothermal system in ultramafic environment (chenaillet ophicalcites, western alps, france) : processes of carbonate cementation. *Lithos*, 294:319–338.
- Lafay, R., Deschamps, F., Schwartz, S., Guillot, S., Godard, M., Debret, B., and Nicollet, C. (2013). High-pressure serpentinites, a trap-and-release system controlled by metamorphic conditions : Example from the piedmont zone of the western alps. *Chemical Geology*, 343:38–54.
- Lamadrid, H., Zajacz, Z., Klein, F., and Bodnar, R. (2021). Synthetic fluid inclusions xxiii. effect of temperature and fluid composition on rates of serpentinization of olivine. *Geochimica et Cosmochimica Acta*, 292:285–308.
- Malvoisin, B., Brunet, F., Carlut, J., Rouméjon, S., and Cannat, M. (2012). Serpentinization of oceanic peridotites : 2. kinetics and processes of san carlos olivine hydrothermal alteration. *Journal of Geophysical Research : Solid Earth*, 117(B4).
- Manatschal, G., Chenin, P., Ghienne, J.-F., Ribes, C., and Masini, E. (2022). The syn-rift tectono-stratigraphic record of rifted margins (part i) : Insights from the alpine tethys. *Basin Research*, 34(1):457–488.
- Manatschal, G. and Müntener, O. (2009). A type sequence across an ancient magma-poor ocean–continent transition : the example of the western alpine tethys ophiolites. *Tectonophysics*, 473(1-2):4–19.
- McDonough, W., McCulloch, M., and Sun, S. (1985). Isotopic and geochemical systematics in tertiary-recent basalts from southeastern australia and implications for the evolution of the sub-continental lithosphere. *Geochimica et Cosmochimica Acta*, 49(10):2051–2067.
- Mével, C. (2003). Serpentinization of abyssal peridotites at mid-ocean ridges. *Comptes Rendus Geoscience*, 335(10-11):825–852.
- Müntener, O. and Piccardo, G. B. (2004). Melt migration in ophiolitic peridotites : The message from alpine-apennine peridotites and implications for embryonic ocean basins. *Geological Society Special Publication*, 218:69–89.
- Picazo, S., Manatschal, G., Cannat, M., and Andréani, M. (2013). Deformation associated to exhumation of serpentinized mantle rocks in a fossil Ocean Continent Transition : The Totalp unit in SE Switzerland). *Lithos*, 175:255–271.
- Pokrovsky, O. S. and Schott, J. (2000). Kinetics and mechanism of forsterite dissolution at 25 °C and pH from 1 to 12. *Geochimica et Cosmochimica Acta*, 64(19):3313–3325.
- Ribes, C., Petri, B., Ghienne, J.-F., Manatschal, G., Galster, F., Karner, G. D., Figueredo, P. H., Johnson, C. A., and Karpoff, A.-M. (2020). Tectono-sedimentary evolution of a fossil ocean-continent transition : Tasna nappe, central alps (se switzerland). *Bulletin*, 132(7-8):1427–1446.

- Schaltegger, U., Desmurs, L., Manatschal, G., Müntener, O., Meier, M., Frank, M., and Bernoulli, D. (2002). The transition from rifting to sea-floor spreading within a magma-poor rifted margin : Field and isotopic constraints. *Terra Nova*, 14(3):156–162.
- Schwartz, S., Guillot, S., Reynard, B., Lafay, R., Debret, B., Nicollet, C., Lanari, P., and Auzende, A. L. (2013). Pressure–temperature estimates of the lizardite/antigorite transition in high pressure serpentinites. *Lithos*, 178:197–210.
- Schwarzenbach, E. M., Vogel, M., Früh-Green, G. L., and Boschi, C. (2021). Serpentinization, Carbonation, and Metasomatism of Ultramafic Sequences in the northern Apennine Ophiolite (NW Italy). *Journal of Geophysical Research : Solid Earth*, 126.
- Shanks, W., Boehlke, J. K., Seal, R., et al. (1995). Stable isotopes in mid-ocean ridge hydrothermal systems : Interactions between fluids, minerals, and organisms. *Geophysical Monograph-American Geophysical Union*, 91:194–194.
- Stille, P., Clauer, N., and Abrech, J. (1989). Nd isotopic composition of jurassic tethys seawater and the genesis of alpine mn-deposits : Evidence from sr-nd isotope data. *Geochemica et Cosmochimica*, 53:1095–1099.
- Tarling, M. S., Rooney, J. S., Viti, C., Smith, S. A., and Gordon, K. C. (2018). Distinguishing the raman spectrum of polygonal serpentine. *Journal of Raman Spectroscopy*, 49(12):1978–1984.
- Tutolo, B. M., Luhmann, A. J., Tosca, N. J., and Seyfried Jr, W. E. (2018). Serpentinization as a reactive transport process : The brucite silicification reaction. *Earth and Planetary Science Letters*, 484:385–395.
- Willbold, M. and Andreas, S. (2010). Formation of enriched mantle components by recycling of upper and lower continental crust. *Chemical Geology*, 276(3-4):188–197.

Table des figures

1.1 Schematic representation of serpentine minerals crystal structure. A) planar lizardite, B) cylindrical chrysotile, C) modulated antigorite, D) tubular polygonal serpentine. Triangles represent 4-coordinated Si and more or less deformed squares represent 6-coordinated Mg (Figure from Mével 2003).	11
1.2 A possible phase diagram for the $\text{MgO}-\text{SiO}_2-\text{H}_2\text{O}$ (MSH) system, in function of pressure (kbar) and temperature ($^{\circ}\text{C}$). Continuous lines represent stable reaction curves, dashed lines, metastable reaction curves. Atg : antigorite, Bct : brucite, Ctl : chrysotile, Fo : forsterite, Lz : lizardite, Tc : talc (Figure from Mével 2003).	12
1.3 Representative texture of serpentine observed under cross-polarized light. A) lizardite in pseudomorphing olivine, B) lizardite pseudomorphing bastite, C) chrysotile in banded veins, D) chrysotile in crack-seals, E) polyhedral serpentine, F) interlocking texture of antigorite (personal micro-photographs).	14
1.4 Photography from scanning electron microscopy (SEM) and transmission electron microscopy (TEM) of the various type of serpentine. A) cylindrical chrysotile (SEM Figure), B) polygonal serpentine (TEM image), C) conical chrysotile (SEM image), D) planar lizardite (TEM image), E) modulated structure of antigorite (TEM), F) spherical polyhedral serpentine (Figure from Andreani et al. 2008).	15
1.5 Representative Raman spectra of the different species of serpentine, including antigorite, chrysotile, lizardite, polygonal and polyhedral serpentine (Figure from Tarling et al. 2018).	17
1.6 Schematic representations of the major location of the serpentization process on the Earth's surface (Figure from Kerrick 2002).	18
1.7 Schematic representations of the geochemical transfer associate to serpentization from oceanic domains to subduction zone. (Figure from Deschamps et al. 2013).	19

1.8 Schematic model of the composition of major hydrothermal deposits along the Mid Atlantic Ridge. Vent locations related to detachment faults (heavy green line) Figure from Johnson 2019.	20
1.9 Main phases of the Alpine Tethys rift evolution, from Manatschal et al. 2022 A) mantle exhumation phase (formation of proto-oceanic crust) during the Middle Jurassic ; B) hyperextension phase at late Early Jurassic (Pliensbachian–Toarcian) ; C) necking phase at Early Jurassic (Sinemurian–Pliensbachian) ; D) stretching phase from latest Triassic to Early Jurassic and E) pre-rift situation in Late Triassic.	24
1.10 A) Present-day location of the ophiolites massifs in the Central-Western-Ligurian Alps (modified after Manatschal and Müntener 2009. B) Schematic paleo-reconstruction of the Piemonte-Ligurian oceanic basin at Late Jurassic time, with location of the major ophiolite sequences (modified after Manatschal and Müntener 2009). C) Simplified geological map of the Penninic and Austro Alpine Nappes (modified after Florineth and Froitzheim 1994), including samples location. D) Distribution of subcontinental and infiltrated mantle along an ocean-continent-transition of the Alpine Tethys (modified after Müntener and Piccardo 2004).	26
1.11 Panoramic view of the Platta nappe (personal photography).	27
1.12 Geological map of the Platta nappe with samples location, Figure from Hochscheid et al. (2022)	28
1.13 Serpentinites outcrop from the Totalp nappe (personal photography).	29
1.14 Geological map of the Totalp nappe with samples location, modified after Picazo et al. 2013.	30
1.15 Panoramic view of the Tasna nappe (personal photography).	31
1.16 A) Simplified geological map of the Alpine system in Western Europe, from Schaltegger et al. 2002. B) Geological map of the Engadine window in the southeastern Alps, Switzerland. C) North-south-striking cross section along the Tasna nappe and schematic representation of the nappe stacking architecture from Coltat et al. 2022 modified after Ribes et al. 2020 ; OCT : ocean continent transition ; P : Piz. D,E) Southwest-northeast-oriented field view of the Tasna section from Ribes et al. 2020.	32
1.17 Photography of the large volume autoclave, personal photography.	34
1.18 Photography of the gold capsule from the ISTO laboratory.	34

1.19 Schematic representation of one type of experimental apparatus utilized for reactive transport experiments, illustrating the injection, collection, and confining pumps, hydrothermal pressure vessel, pressure transducers used for permeability measurements, and valve for monitoring fluid chemistry Figure from Tutolo et al. 2018	34
1.20 Figure summarizing the serpentinization rates from the literature in log J (quantity of energy) versus the temperature (°C), figure from Lamadrid et al. 2021.	36
1.21 Serpentinization reaction rate (%) as function of initial grain size versus time of reaction in days, for pressure of 3kbar (a) and 20 kbar (b)figure from Huang et al. 2020.	37
1.22 Mineral assemblages predicted for serpentinization of olivine and clinopyroxene-free harzburgite as function of temperature and water-rock ratios from Klein et al. 2013.	39
1.23 Summary of serpentinization rates from literature and the study of Malvoisin et al. 2012a depending to initial grain size and temperature. Figure from Malvoisin et al. 2012a.	40
1.24 Mineral assemblage for serpentinization of peridotite and pyroxenite, from Klein et al. 2013.	43
1.25 Dependence of serpentinization rates on fluid chemistry, figure from Lamadrid et al. 2021.	44
1.26 Schematic representation of the isotopic signatures in D, C, O and S of the different reservoirs at the mid oceanic ridge hydrothermal system. Figure from Shanks et al. 1995.	46
 2.1 Photography of the Brucker D8 Advance Eco instrument used for the XRD analyses (photography from ITES website).	68
2.2 Photography of the HORIBA LabRAM ARAMIS spectrometer used for the Raman analyses (photography from ICube website).	68
2.3 Photography of the M4 tornado used for μ XRF measurements (photography from ICube website).	70
2.4 Photography of the (MC-ICP-MS) Neptune Thermo Scientific instrument (photography from ITES website).	72
2.5 Photography of the Triton TIMS Thermo Scientific instrument (photography from ITES website).	73
2.6 Schematic representation of the procedure for boron separation and calculation of the boron concentrations.	75

2.7	Schematic representation of the principle of the experimental apparatus for mixed flow reactor experiments described by Pokrovsky and Schott 2000	80
2.8	Photography of the open flow experimental setup used at the beginning of this thesis. (personal photography)	80
2.9	Photography of the close experimental setup used at the beginning of this thesis. (personal photography)	81
2.10	Photography of the experimental setup used in this thesis. In this picture is represented the temperature and pressure command (in the left) and the two autoclaves used (i.e., Robert and Raymonde) are in the center (personal photography).	82
2.11	Schematic illustration of the experimental setup used in this thesis, figure modified from Fauguerolles 2016	82
3.1	A) Simplified map of the major paleogeographic units of the Western and Central Alps and the Apennines, with location of the study area (white frame) modified after Manatschal and Müntener 2009. B) Geological map of the Platta nappe with samples location (modified after Schaltegger et al. 2002). C) Distribution of subcontinental and infiltrated mantle domains along an ocean-continent-transition of the former Alpine Tethys (modified after Müntener and Piccardo 2004).	93
3.2	Representative macroscopic and microscopic pictures illustrating the different lithologies reported in the Platta nappe (Cotschen and Falotta sites). A) Fe-Ca silicates (ilvaite and andradite) associated with sulfides (sphalerite, chalcopyrite) and oxides (magnetite (Mt) pervasively replacing serpentinite. B) Fe-Ca silicate (ilvaite) in veins (stockwork structure) cutting through serpentinite. C) Discrete calcite veins crosscutting an epidotized basalt. D) Calcite shear band cutting through serpentinite. E) Green serpentine vein crosscutting a massive dark serpentine. F) Basalt altered to an assemblage made of chlorite, actinolite and pumpellyite. Chl=chlorite ; Act=actinolite ; Pump=pumpellyite ; Ilv=ilvaite ; Adr=(hydro)andradite ; Srp=serpentine ; Mt=magnetite ; Sph=sphalerite ; Cp=chalcopyrite ; Cc=calcite	97
3.3	Histograms of $^{87}\text{Sr}/^{86}\text{Sr}$ recalculated at 160 Ma for the different lithologies. SCLM : Sub Continental Lithospheric Mantle from McDonough et al. 1985, SW : Seawater from Jones et al. 1994 and CC : Continental Crust values from Willbold and Andreas 2010. N. Apennine serpentinites from Schwarzenbach et al. 2021.	100

3.4 Schematic model showing the evolution of the OCT and associated fluid circulations leading to the formation of Fe-Ca silicates, modified from Epin et al. 2019. A) Stage 1 : serpentization initiated from fluids with radiogenic Sr (CC-derived fluids) leading to formation of serpentinites with Sr isotope compositions higher than SW. B) Stage 2 : first exhumation of subcontinental lithospheric mantle previously serpentized and onset of magmatism, serpentization continues to occur by seawater with a lesser continental influence. C) Stage 3 : increase of magmatic rocks and alteration (rodingitization, epidotization-chloritization of mafic extrusives) by serpentization derived fluids mixing with seawater infiltrated along faults. Serpentization continues to occur with pristine seawater. D) Schematic model showing fluids pathways, the different alteration products and their associated Sr isotope compositions. Fluids resulting from the alteration of mafic rocks and serpentization migrated upwards and mixed with seawater to form Fe-Ca silicates. Carbonation was the last hydrothermal event recording in ultramafic and mafic rocks.	106
4.1 A) Present-day location of ophiolitic massifs of the Central-Western-Ligurian Alps, modified after Manatschal and Müntener 2009. B) Schematic paleo-reconstruction of the Piemonte-Ligurian oceanic basin at Late Jurassic time, with location of the major ophiolitic sequences, modified after Manatschal and Müntener 2009. C) Simplified geological map of the Penninic and Austro Alpine Nappes, modified after Froitzheim 1994, including samples location. D) Distribution of subcontinental and infiltrated mantle, along an ocean-continent-transition of the Alpine Tethys, modified after Müntener and Piccardo 2004. TO : Totalp ; TA : Tasna ; PL : Platta	128
4.2 A) Massive dark green serpentinite from UP (Fal18-03). B) Massive serpentinite with a dark green color, crosscut by a fibrous serpentine vein of pale green color from UP. C) Massive dark green serpentinite from Tasna (Tas19-03) surrounded by a foliated pale green fibrous serpentinite. D) Fibrous pale green serpentinite (Tas 19-07). E) Totalp outcrop near Weissfluhjoch, the massive serpentinite is surrounded by a later foliated serpentinite (Tot19-02), similar to Tasna. F) Massive serpentinite crosscut by later carbonates (Tot19-07, 08).	134

4.3 Representative photography of serpentine textures at microscopic scale (cross-polarized light) and associated raman spectra. A) Mesh texture S1 made of lizardite. B) Bastite texture S1 made of lizardite. C) Polyhedral serpentine S2 in clinopyroxene cleavage. D) Polyhedral serpentine and andradite at rims of bastite, cut by a banded vein. E) Banded vein made of polygonal serpentine crosscut the previous bastite and mesh S1. F) Lamellar veins of antigorite S4 crosscut the previous mesh S1 and banded vein S3. G) Serpentine mesh S1 crosscut by lamellar veins S4, antigorite patches S4 and crack-seals of chrysotile S5.	136
4.4 A) Plot of Mg + Fe versus Si diagram in cations per formula unit. B) Al versus Si. C) Serpentine generation versus Mg numbers. All cations are given in per formula units and are calculated on the basis of 7 oxygen atoms in the serpentine formula. Antigorite were calculated based on 6.823 oxygens and then converted to 7 oxygens for comparison with other serpentine species. In C), colored rectangles represent the variability of Mg# values. Lz/Ctl : pure Mg lizardite/chrysotile end-member. Atg : pure Mg antigorite end-member. Data of Chenaillet serpentinites are from Schwartz et al. 2013 and those of Malenco antigorite are from Liu et al. 2020.	139
4.5 Fe _T versus Mg apfu diagram of banded veins serpentine S3 and their respective Raman spectra. Two populations are distinguished, the banded veins made of polygonal serpentine in grey, and those made of lizardite in orange.	139
4.6 Representative rare earth element (REE) patterns normalized to C1-Chondrite (left) and PM-normalized extended trace element patterns (right) of serpentine minerals and veins depending on their localities. Blue field correspond to serpentinites Grade 0 from the Chenaillet (data from Lafay et al. 2017)	145
4.7 Rare earth element (REE) patterns normalized to C1-Chondrite (left), Trace elements normalized to Primitive mantle (right) diagrams of the serpentine minerals and veins. Serpentine from the Lower Platta unit display U-shape patterns with strong positive Eu anomalies.	146

4.8 Theoretical model proposed for the development of the sequence of serpentini- zation during continuous mantle exhumation at seafloor during Jurassic times. Pseudomorphic mesh and bastite form at very low w/r ratios and under static conditions at depth of ~6-8 km. Banded veins formation, resulting in three step : a) preferential growth of chrysotile from highly supersaturated fluid at low fluid/rock ratio, b) development of polygonal serpentine as a consequence of fluid saturation decreasing and fluid/rock ratio increasing, c) development of lizardite after longer time of fluid-rock interactions, at higher fluid/rock ra- tios, lower temperatures and with an undersaturated fluid. Antigorite forms at shallower levels than S3 and at local high pressure induced by the shortening. Finally, crack-seal forms at shallower depths and are associated to a decrease of local strain and high fluid/rock ratios.	152
4.9 Concentrations in Sr versus Eu/Eu* of the different serpentine type. No corre- lation is observed between Sr and Eu/Eu*	156
4.10 Qualitative modal abundance of mineral assemblages observed in serpentinites from the Alpine Tethys OCT (this study), compared with those from the Che- naillet unit Lafay et al. 2013, and oceanic domains MAR Rouméjon et al. 2015 and SWIR Rouméjon et al. 2018.	158
4.11 A) Diagram showing the measured in situ concentrations of Li versus B of serpentine minerals and veins. B) In situ measured concentrations of Cs versus concentrations of Sr.	159
4.12 Representative rare earth element (REE) patterns normalized to C1-Chondrite (left) and PM-normalized extended trace element patterns (right) of serpen- tinite from Tasna, Totalp and Platta.	162
4.13 XRD pattern for sample TOT-1902.	163
4.14 XRD pattern for sample TOT-1903.	163
4.15 XRD pattern for sample FAL-1802.	164
4.16 XRD pattern for sample FAL-1803.	164
4.17 XRD pattern for sample FAL-1806.	165
4.18 XRD pattern for sample FAL-1811.	165
4.19 XRD pattern for sample FAL-1813.	166
4.20 XRD pattern for sample TAS-1902.	166
4.21 XRD pattern for sample RAS-1903.	167
4.22 XRD pattern for sample TAS-1904.	167
4.23 XRD pattern for sample TAS-1905.	168
4.24 XRD pattern for sample TAS-1910.	168

5.1 SEM characterization of solid reaction products from the lherzolite-seawater and harzburgite-seawater experiments. A) Etch pitch on residual clinopyroxene (Cpx) from experiment ISTO2. B) Olivine (Ol) dissolution features from experiment ISTO3. C) Cubic calcite (Cc), euhedral hexagonal shaped brucite (Bct) crystal and chrysotile (Ct) serpentine observed in at the end of experiment ISTO5. D) Etch pits (Ep) in olivine, dissolution features associated to clinopyroxene and euhedral hexagonal brucite observed in experiment ISTO6. E) Euhedral and octahedral crystals of magnetite (Mgt) and spinel (Sp) from experiment ISTO1. F) Chrysotile fibers in experiment ISTO4. G) Aragonite crystal observed in experiment ISTO5. H) Anhydrite crystal from experiment ISTO4.	191
5.2 Schematic representation of the mineral proportions estimated at the end of lherzolite seawater experiments ISTO 1-4 (A) and the harzburgite-seawater experiments ISTO 5 and 6 (B).	193
5.3 Changes in concentrations of selected trace elements A) Na, B) Cl, C) K and D) SO_4^{2-} in fluid during lherzolite-seawater experiment (ISTO 1-4) at 225°C (blue), 260°C (green), 300°C (orange) and 325 °C (red) and harzburgite seawater experiment (ISTO 6) at 280°C (yellow). Blue star represent concentration in initial seawater.	199
5.4 Changes in concentrations of selected trace elements A) Si, B) Mg, C) Ca and D) Mn in fluid during lherzolite-seawater experiment (ISTO 1-4) at 225°C (blue), 260°C (green), 300°C (orange) and 325 °C (red) and harzburgite seawater experiment (ISTO 6) at 280°C (yellow). Blue star represent concentration in initial seawater.	203
5.5 Measured $\text{H}_{2(aq)}$ concentrations (mmol/kg) as a function of time (in hours) for lherzolite-seawater experiments at 225°C (blue), 260°C (green), 300°C (orange) and 325°C (red), and harzburgite-seawater experiments at 280°C (yellow).	205
5.6 Measured concentrations in mmol/L versus time (hours) of selected trace elements (Sr, Ba, Li, B, Zn and Cu) in fluids.	207
5.7 Isocon diagrams for the lherzolite-seawater experiments. Concentrations in solid product are plotted against compositions of the protolith. A) 225°C, B) 260°C, C) 300°C, D) 325°C.	209
5.8 $\Delta\text{C}_i^0/\text{C}_i^0$ versus temperature (°C) for each lherzolite-seawater experiments. A) major elements, B) transition metals elements, C) trace elements.	211
5.9 Isocon diagrams for the harzburgite-seawater experiments at 280°C. Concentrations in solid product are plotted against compositions of the protolith. A) 504 hours, B) 1296 hours	212

5.10 $\Delta C_i^0/C_i^0$ versus duration of harzburgite-seawater experiments (hours). A) major elements, B) transition metals elements, C) trace elements.A) 504 hours, B) 1296 hours	213
5.11 Measured concentrations of Na in mmol/L versus measured concentrations of Cl in mmol/L.	220
5.12 XRD pattern of the primary harzburgite Cpt1801	227
5.13 XRD pattern of the primary lherzolite Cpt1806.	228
5.14 XRD pattern of serpentinite at 225°C.	228
5.15 XRD pattern of serpentinite at 260°C.	229
5.16 XRD pattern of serpentinite at 280°C.	229
5.17 XRD pattern of serpentinite at 280°C bis.	230
5.18 XRD pattern of serpentinite at 300°C.	230
5.19 XRD pattern of serpentinite at 325°C.	231
5.20 Raman spectra of the solid product from experiment at 300 °C.	231
 6.1 Fraction of the boron species dissolved in seawater. blue $H_3B(OH)_3$; green : $B(OH)_4^-$	243
6.2 Distribution of boric acid and borate in seawater in function of pH.	244
6.3 Comparison of theoretically and experimentally determined boron isotope fractionation factors (1000 $\ln \alpha$ mica-tur) between mica and tourmaline. Figure from Li et al. 2021.	245
6.4 B concentrations in fluids (ppb) versus experimental run-time (hours) for the reaction of serpentinization. Effect of cooling at the end of experiment is evidenced by black circles.	252
6.5 Evolution of isotopic composition of the fluids $\delta^{11}B$ (‰) vs. experimental run-time (hours) for the reaction of serpentinization. Effect of cooling at the end of experiment is evidenced by black circles.	252
6.6 B concentrations (ppm) versus temperature (°C) in in bulk-rock, serpentine, and magnetite separates at the end of serpentinization experiments. The purple circles correspond to the shorter experiment at 280°C.	255
6.7 Evolution of the isotopic composition $\delta^{11}B$ (‰) depending on temperature of reaction (°C) in bulk products,serpentine and magnetite separates and fluid sampled immediately at the end of reaction. The purple circles correspond to the shorter experiment at 280°C. Error bars are below the point size.	257
6.8 $\delta^{11}B$ (‰) versus B (ppm) for the serpentinites, serpentine and magnetite separates and fluid at the end of experiments. Error bars are below the point size.	257

6.9 Schematic representation of the integration of boron in solid products during serpentinization experiments. We assume that seawater contains all the boron available before the serpentinization experiments. At the end of serpentinization experiments, 90% of B in seawater was released and partitioned into the mineral surface (green : B adsorbed) and the crystal structure (yellow : B integrated).	259
6.10 Fractionation factor versus temperature (°C).	261
6.11 Partition coefficient versus temperature (°C).	262
6.12 a) B isotopic fractionation factor and b) Partition coefficient dependence with pH. Figure from Lemarchand et al. 2015.	263
6.13 a) B isotopic fractionation factor versus temperature (°C) and b) Partition coefficient versus temperature (°C) with a proposed pH change at about 280 degrees which correspond to the change of α	264
6.14 SEM characterization of serpentine separated phases from experiment at 260°C. It can be observed that very small grains of magnetite are still present after the separation procedure.	267
6.15 Boron concentration in ppm versus concentrations of major elements in (wt.%) measured in serpentinite bulk, serpentine separated and magnetite separated.	268
6.16 B isotopic composition $\delta^{11}\text{B}$ in (‰) versus the concentrations of major elements in (wt.%) measured in serpentinite bulk, serpentine separated and magnetite separated.	269
6.17 SEM characterization of serpentine separated phases from experiment at 260°C. It can be observed that very small grains of magnetite are still present after the separation procedure.	272
6.18 Boron content (ppm) and isotopes ($\delta^{11}\text{B}$) of serpentinite bulk versus the estimated proportion of serpentine (vol.%) and magnetite (vol.%) in the different experiments.	273
6.19 Apparent B isotopic fractionation factor of magnetite and serpentine versus temperature (°C).	275
6.20 $\Delta_{\text{srp}-\text{mgt}}$ versus temperature (°C).	275
6.21 XRD pattern of serpentine separates at 225°C.	279
6.22 XRD pattern of magnetite separates at 225°C.	279
6.23 XRD pattern of serpentine separates at 260°C.	280
6.24 XRD pattern of magnetite separates at 260°C.	280
6.25 XRD pattern of serpentine separates at 280°C.	281
6.26 XRD pattern of magnetite separates at 280°C.	281
6.27 XRD pattern of serpentine separates at 280°C bis.	282
6.28 XRD pattern of magnetite separates at 280°C bis.	282

6.29 XRD pattern of serpentine separates at 300°C.	283
6.30 XRD pattern of magnetite separates at 300°C.	283
6.31 XRD pattern of serpentine separates at 325°C.	284
6.32 XRD pattern of magnetite separates at 325°C.	284
 7.1 $^{87}\text{Sr}/^{86}\text{Sr}$ versus $\delta^{11}\text{B}$ of serpentinites sampled in this thesis.	299
 8.1 Représentation schématique de la structure cristalline des minéraux de serpentine. A) lizardite plane, B) chrysotile cylindrique, C) antigorite modulée, D) serpentine polygonale tubulaire. Les triangles représentent le Si à 4 coordinations et les carrés plus ou moins déformés représentent le Mg à 6 coordinations. (Mével 2003).	321
8.2 Diagramme de phase possible pour le système MgO-SiO ₂ -H ₂ O (MSH), en fonction de la pression (kbar) et de la température (°C). Les lignes continues représentent les courbes de réaction stables, les lignes pointillées, les courbes de réaction métastables. Atg : antigorite, Bct : brucite, Ctl : chrysotile, Fo : forstérite, Lz : lizardite, Tc : talc (Figure issue de Mével 2003).	323
8.3 Texture représentative de la serpentine observée en lumière polarisée croisée. A) lizardite en olivine pseudomorphe, B) lizardite en bastite pseudomorphe, C) chrysotile en veines rubanées, D) chrysotile , E) serpentine polyhedrale, F) texture enchevêtrée de l'antigorite (microphotographies personnelles).	325
8.4 Photographies en microscopie électronique à balayage (MEB) et en microscopie électronique à transmission (MET) des différents types de serpentine. A) chrysotile cylindrique (figure MEB), B) serpentine polygonale (image MEB), C) chrysotile conique (image MEB), D) lizardite planaire (image MEB), E) structure modulée de l'antigorite (MEB), F) serpentine polyhedrale sphérique (figure de Andreani et al. 2008).	326
8.5 Spectres Raman représentatifs des différentes espèces de serpentine, y compris l'antigorite, le chrysotile, la lizardite, la serpentine polygonale et la serpentine polyhedrale (figure issue de Tarling et al. 2018).	328
8.6 Représentations schématiques de la localisation principale du processus de serpentinitisation à la surface de la Terre (Figure de Kerrick 2002).	329
8.7 Représentations schématiques du transfert géochimique associé à la serpentinitisation depuis les domaines océaniques jusqu'à la zone de subduction. (Figure tirée de Deschamps et al. 2013).	330
8.8 Modèle schématique de la composition des principaux dépôts hydrothermaux le long de la dorsale médio-atlantique. Emplacements des événements liés aux failles de détachement (Figure issue de Johnson 2019).	331

8.9 Principales phases de l'évolution du rift alpin de la Téthys, d'après Manatschal et al. 2022 A) phase d'exhumation du manteau (formation de la croûte proto-océanique) au Jurassique moyen ; B) phase d'hyperextension à la fin du Jurassique inférieur (Pliensbachien-Toarcien) ; C) phase d'amincissement au Jurassique inférieur (Sinémurien-Pliensbachien) ; D) phase d'étirement à partir du Trias supérieur (Pliensbachien-Toarcien). (Sinémurien-Pliensbachien) ; D) phase d'étirement du dernier Trias au Jurassique précoce et E) situation de pré-rift au Trias tardif.	335
8.10 A) Localisation actuelle des massifs d'ophiolites dans les Alpes centrales-occidentales-ligures (modifié d'après Manatschal and Müntener 2009). B) Paléo-reconstruction schématique du bassin océanique piémontais-ligure au Jurassique supérieur, avec localisation des principales séquences ophiolitiques (modifié d'après Manatschal and Müntener 2009). C) Carte géologique simplifiée des nappes penninique et austro-alpine (modifiée d'après Florineth and Froitzheim 1994), y compris l'emplacement des échantillons. D) Distribution du manteau sous-continentale et infiltré le long d'une transition océan-continent de la Téthys alpine (modifié d'après Müntener and Piccardo 2004).	337
8.11 Vue panoramique de la nappe de Platta (photographie personnelle).	338
8.12 Carte géologique de la nappe de Platta avec localisation des échantillons, Figure issue de Hochscheid et al. (2022)	339
8.13 Affleurement de serpentinites de la nappe de Totalp (photographie personnelle)	340
8.14 Geological map of the Totalp nappe with samples location, modified after Carte géologique de la nappe de Totalp avec localisation des échantillons, modifiée d'après Picazo et al. 2013.	341
8.15 Vue panoramique de la nappe de Tasna (photographie personnelle)	342
8.16 A) Carte géologique simplifiée du système alpin en Europe occidentale, d'après Schaltegger et al. 2002. B) Carte géologique de la fenêtre de l'Engadine dans les Alpes du sud-est, Suisse. C) Coupe transversale nord-sud le long de la nappe de Tasna et représentation schématique de l'architecture d'empilement de la nappe d'après Coltat et al. 2022 modifié d'après Ribes et al. 2020 ; OCT : transition océan-continent ; P : Piz. D,E) Vue de champ orientée sud-ouest-nord-est de la coupe de Tasna à partir de Ribes et al. 2020.	343
8.17 Photographie d'une autoclave à grand volume, photographie personnelle.	345
8.18 Photographie d'une capsule en or du laboratoire ISTO.	345

8.19 Représentation schématique d'un type d'appareil expérimental utilisé pour les expériences de transport réactif, illustrant les pompes d'injection, de collecte et de confinement, la cuve à pression hydrothermale, les transducteurs de pression utilisés pour les mesures de perméabilité et la vanne de contrôle de la chimie des fluides Figure from Tutolo et al. 2018	346
8.20 Figure résumant les taux de serpentinisation de la littérature en log J (quantité d'énergie) en fonction de la température (°C), figure issue de Lamadrid et al. 2021.	348
8.21 Vitesse de réaction de la serpentinisation (%) en fonction de la taille de grain initiale et de l'avancement de la réaction en jours, pression de 3kbar (a) et 20 kbar (b) Figure issue de Huang et al. 2020.	350
8.22 Assemblages minéraux prédis pour la serpentinisation de l'olivine et de l'harzburgite sans clinopyroxène en fonction de la température et des rapports eau-roche à partir de Klein et al. 2013.	352
8.23 Résumé des taux de serpentinisation tirés de la littérature et de l'étude du Malvoisin et al. 2012a en fonction de la taille initiale des grains et de la température. Figure de Malvoisin et al. 2012a.	353
8.24 Assemblage minéral pour la serpentinisation de périclase et de pyroxénite, Figure de Klein et al. 2013.	356
8.25 Dépendance des taux de serpentinisation par rapport à la chimie des fluides, figure tirée de Lamadrid et al. 2021.	358
8.26 Représentation schématique des signatures isotopiques en D, C, O et S des différents réservoirs du système hydrothermal de la dorsale océanique moyenne. Figure issue de Shanks et al. 1995.	361

Liste des tableaux

2.1	Different steps for the major elements separation using the 2 mL Biorad AG 50Wx8 200-400 mesh cationic resin.	71
2.2	Different steps for the Sr recovery using the Eichrom Sr-spec resin.	71
2.3	First step column procedure using the Biorade AG50W-X12 (200-400 mesh) cationic resin.	74
2.4	Second step columns procedure using the Amberlite specific resin.	78
3.1	Sr isotope compositions of Fe-Ca silicates and carbonates, serpentinites, carbonates and mafic rocks sampled in the Platta nappe, $^{87}\text{Sr}/^{86}\text{Sr}$ in italic refers as $^{87}\text{Sr}/^{86}\text{Sr}$ without Rb correction. ep : epidotized, ch : chloritized, PR : pervasive replacement, MI : mafic intrusion.	111
3.2	Sr isotope compositions of mafic rocks, rodingite and blackwall collected in the Platta nappe from previous studies. Metabasalt from Stille et al. 1989, basalt and gabbros from Schaltegger et al. 2002 and rodingite and blackwall from Amann et al. 2020.	112
4.1	Description of the 11 samples of serpentinized peridotite selected for detailed mineralogical and geochemical investigations. Mineral phases are detected by X-ray diffraction on powder, and their proportion (%) are estimated by the Rietveld refinement method of Doebelin and Kleeberg 2015 using Profex-BGMIN software. PM : pseudomorphic textures ; b : banded ; f : fibrous ; g : granular ; l : lamellar ; s : spherical ; LA : laser ablation.	131
4.2	Representative major element concentrations of serpentine minerals measured by μXRF	140
4.3	Representative trace element concentrations of serpentine minerals measured by HR-LA-ICP-MS.	143
5.1	Summary of experimental parameters. W/R : water/rock ratios.	184

5.2	In situ composition in major and minor elements of primary minerals from harzburgite (Cpt18-01) and lherzolite (Cpt18-06) used in hydrothermal experiments measured by μ -XRF. Mg# = 100*Mg/Mg+Fe	187
5.3	Summary of minerals identified in protoliths and solid products at the end of seawater-peridotite experiments. Mineral phases are detected by X-ray diffraction on powder, and their proportion (%) are estimated by the Rietveld refinement method of Doebelin and Kleeberg 2015 using Profex software. Aragonite, anhydrite and halite are always below the detection limits and thus not represented in this table.	189
5.4	Bulk rock composition (anhydrous) in major and minor elements measured by μ -XRF before and after hydrothermal experiments. Mg# = 100*Mg/Mg+Fe . .	196
5.5	Concentration of dissolved $\text{Cl}, \text{SO}_4^{2-}$ and H_2 (mmol/L) measured by chromatography ionic and gas chromatography in the fluids during interaction the serpentinization experiments. (-) not analyzed	200
6.1	Measured boron concentration in ppm and isotopic composition $\delta^{11}\text{B}$ of in ‰ in seawater and standard UB-N. Measured B of UB-N range between 135-181.2 ppm and $\delta^{11}\text{B}$ UB-N vary between 9.4 and 13.1 ‰ (source GeoRem website). . .	248
6.2	Evolution of the boron concentrations $[\text{B}]_{fluid}$ and isotopic compositions $\delta^{11}\text{B}_{fluid}$ during seawater-peridotite experiments.	254
6.3	Measured boron concentration in ppm and $\delta^{11}\text{B}$ (‰) in solids products including bulk serpentinite, separated serpentine and separated magnetite at the end of serpentinization experiments and also in final fluid before cooling. . . .	256
6.4	Comparison between B concentration and isotopic compositions measured (mes) in bulk and the theoretical values.	271
6.5	Serpentine separated, magnetite separated and Bulk rock composition in major and minor elements measured by μ -XRF	278

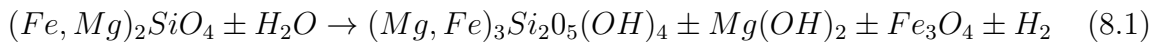
Chapitre 8

Introduction

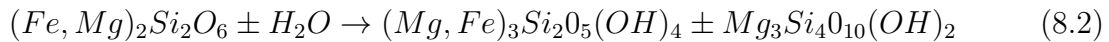
8.1 Contexte général

8.1.1 La serpentinisation

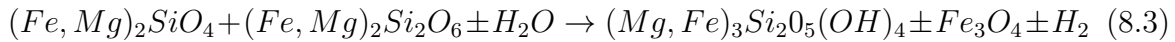
La serpentinisation consiste en l'hydratation de roches ultramafiques (c'est-à-dire des périclites) qui constituent le manteau supérieur. Ces périclites sont composées de minéraux primaires ferro-magnésiens, typiquement de l'olivine, de l'orthopyroxène et du clinopyroxène. Au cours de la serpentinisation, au contact des fluides, ces minéraux ferro-magnésiens sont remplacés par des minéraux hydratés secondaires et des (hydr)-oxydes comme la serpentine \pm le talc \pm la brucite \pm la magnétite. Le di-hydrogène peut également être libéré si les conditions sont favorables (par exemple, Mével 2003), les réactions peuvent être résumées comme suit :



olivine \pm eau \rightarrow serpentine \pm brucite \pm magnétite \pm hydrogène



orthopyroxene \pm eau \rightarrow serpentine \pm talc



olivine \pm orthopyroxene \pm eau \rightarrow serpentine \pm magnétite \pm hydrogène

Les minéraux de serpentine peuvent intégrer une quantité significative d'eau dans leur structure, jusqu'à 13% en poids, selon l'espèce de serpentine. Le processus de serpentinisation s'effectue dans la plupart des contextes géodynamiques, qu'il s'agisse des contextes divergents, comme les dorsales océaniques et les marges passives, ou dans les contextes convergents, comme les zones de subduction. Par conséquent, la serpentinisation a lieu dès que l'eau peut interagir avec les roches ultramafiques et donc dans des conditions variées, allant des basses températures <50°C et pressions près du plancher océanique à des températures et pressions plus élevées pm450°C dans les zones de subduction (par exemple, Mével 2003).

8.1.2 Les minéraux de serpentine

Les minéraux de serpentine sont des phyllosilicates hydratés dont la formule idéalisée est $Mg_3Si_2O_5(OH)_4$. Les minéraux de serpentine sont constitués d'une alternance de couches tétraédriques (Si à 4 coordinations) et de couches octaédriques (Mg à 6 coordinations ; Wicks and Whittaker 1975 ; Figure 8.1). Comme indiqué précédemment, le processus de serpentinitisation est omniprésent à la surface de la Terre, ce qui explique que les minéraux de serpentine se forment dans une large gamme de température, de pression et de chimie des fluides, et que différentes variétés de serpentine (c'est-à-dire de polymorphes) peuvent être générées (par exemple, Mével 2003). Les polymorphes de serpentine les plus courants sont la lizardite, le chrysotile, la polygonale et l'antigorite. La lizardite, le chrysotile et la serpentine polygonale sont principalement observés dans les domaines divergents. Cependant, la présence d'antigorite dans les domaines océaniques est moins fréquente, bien que certaines études aient signalé leur présence (par exemple, Roumejon et al. 2015 ; Ribeiro Da Costa et al. 2008). L'antigorite est plutôt observée dans les serpentinites provenant de domaines convergents comme les zones de subduction Trommsdorff and Evans 1977.

Ces polymorphes de serpentine résultent de différentes configurations structuralles Wicks and O'Hanley 2018. La lizardite est caractérisée par une structure plane (Figure 8.1A), le chrysotile a une structure cylindrique (Figure 8.1B), et la serpentine polygonale présente une structure tubulaire (Figure 8.1D). L'antigorite se caractérise par une structure ondulée (Figure 8.1C), avec une perte de sites octaédriques due à une inversion périodique de l'inter-couche Mellini et al. 1987. Le feuillet tétraédrique inverse sa polarité à travers 6 et 8 anneaux tétraédriques Capitani and Mellini 2004. Cette inversion périodique de l'inter-couche permet de renforcer les liaisons covalentes Si-O Capitani and Mellini 2004. L'antigorite a une formule distincte des autres espèces de serpentine, caractérisée par : $Mg_{3m-3}Si_{2m}O_{5m}(OH)_{4m-6}$, m étant le nombre de tétraèdres sur une longueur d'onde entière Mellini et al. 1987.

Le chrysotile, la lizardite et l'antigorite sont caractérisés par des rapports Fe^{3+}/Fe_{tot} et Si/Mg différents, les rapports Fe^{3+}/Fe_{tot} diminuant et les rapports Si/Mg augmentant de la lizardite au chrysotile et à l'antigorite O'Hanley and Dyar 1993. L'antigorite est systématiquement enrichie en silice en raison de la perte de Mg et de $(OH)_4$ par rapport au Si Wicks and Zussman 1975. En outre, dans la plupart des minéraux de serpentine, des substitutions de Si par Al et Fe^{3+} peuvent se produire dans les sites tétraédriques, et Fe^{2+} , Fe^{3+} , Cr, Al^{3+} , Ni et Mn peuvent se substituer à Mg dans les sites octaédriques

(par exemple, Page 1968 ; Mével 2003).

Caruso and Chernosky 1979 soutiennent que les substitutions d' Al^{3+} et de Fe^{3+} pour Mg et Si permettent de stabiliser la lizardite. La structure cylindrique du chrysotile affecte fortement sa stabilité (Evans 2004). Il semblerait que les structures cristallines et les substitutions puissent toutes deux affecter la stabilité des minéraux de serpentine.

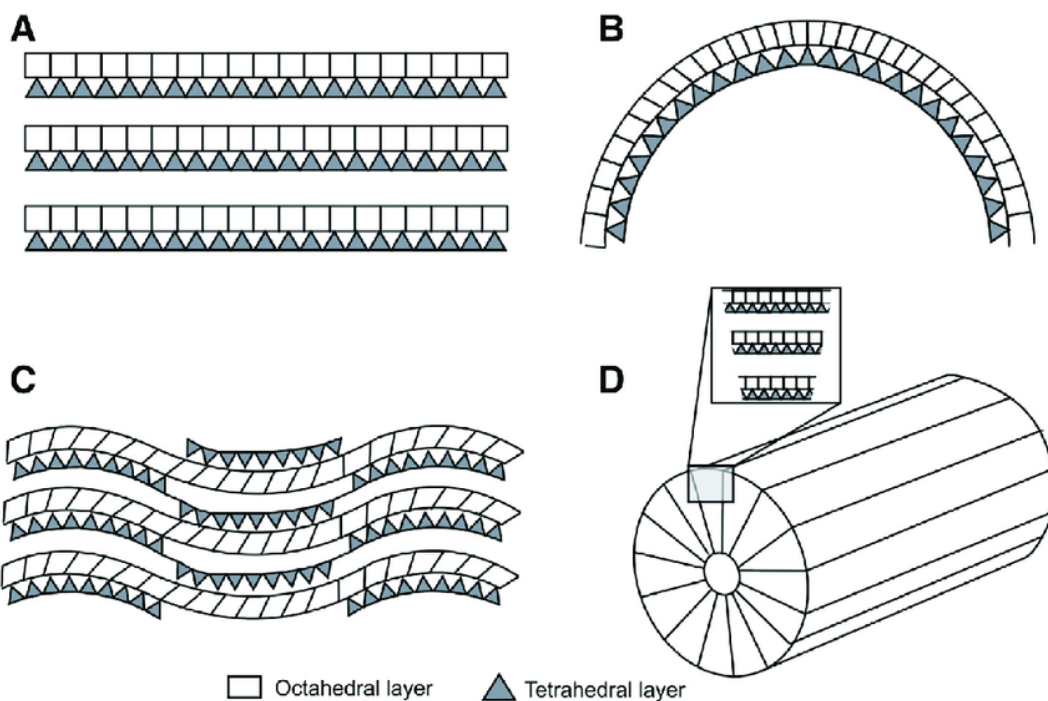


FIGURE 8.1 – Représentation schématique de la structure cristalline des minéraux de serpentine. A) lizardite plane, B) chrysotile cylindrique, C) antigorite modulée, D) serpentinite polygonale tubulaire. Les triangles représentent le Si à 4 coordinations et les carrés plus ou moins déformés représentent le Mg à 6 coordinations. (Mével 2003).

8.1.3 Stabilité des espèces serpentineuse

Sur la base d'une étude expérimentale couplée à des données thermodynamiques et isotopiques, l'analyse de l'eau de mer a été réalisée. En effet, il est généralement reconnu que dans le système $\text{MgO-SiO}_2\text{-H}_2\text{O}$ (MSH), la lizardite et le chrysotile sont stables à des températures plus basses que l'antigorite Figure 8.2 (par exemple, Moody 1976 ; Mével 2003 ; Evans 2004). A partir d'analyses isotopiques de serpentinites naturelles, Wenner and Taylor 1971 estime la température de formation de la lizardite à 125°C, celle du chrysotile à 180°C et celle de l'antigorite à 235°C (Figure 8.2). Evans

et al. 1976 propose que la transition du chrysotile à l'antigorite se produise à des températures comprises entre 270 et 300°C et à une pression inférieure à 0,7 GPa. Plus récemment, les résultats expérimentaux de Grauby et al. 1998, suggèrent que la lizardite est plus stable que le chrysotile à 200°C et 300°C. Viti and Mellini 1998 propose que le chrysotile évolue spontanément vers la serpentine polygonale et ensuite vers la serpentine lizardite par l'arrivée de nouveaux fluides et du temps additionnel. Le chrysotile est-il une phase métastable ? Il semblerait que la structure courbée du chrysotile affecte sa stabilité.

Les observations sur le terrain combinées aux études isotopiques et expérimentales suggèrent que la formation de l'antigorite est principalement attribuée à une augmentation de la température de $\sim 250^{\circ}\text{C}$ à $>500^{\circ}\text{C}$ et/ou de la pression (par exemple, Coleman 1971 ; Wenner and Taylor 1971 ; Moody 1976 ; Wunder et al. 2001). Capitani and Mellini 2004 propose que les inversions périodiques de l'intercouche dans l'antigorite permettent de stabiliser l'antigorite à des températures et des pressions plus élevées que la lizardite. Ceci est en accord avec le diagramme de phase proposé par Evans 2004 (Figure 8.2), attestant que l'antigorite est stable à une température supérieure à 350°C . Cependant, certaines études ont signalées la présence d'antigorite dans des domaines océaniques (par exemple : Roumejon et al. 2015 ; Ribeiro Da Costa et al. 2008), ce qui soulève des questions sur leurs champs de stabilité et leurs conditions de formation. En particulier, pouvons-nous encore attribuer la formation de l'antigorite exclusivement aux zones de subduction ou leur présence dans les domaines divergents a-t-elle été sous-estimée ?

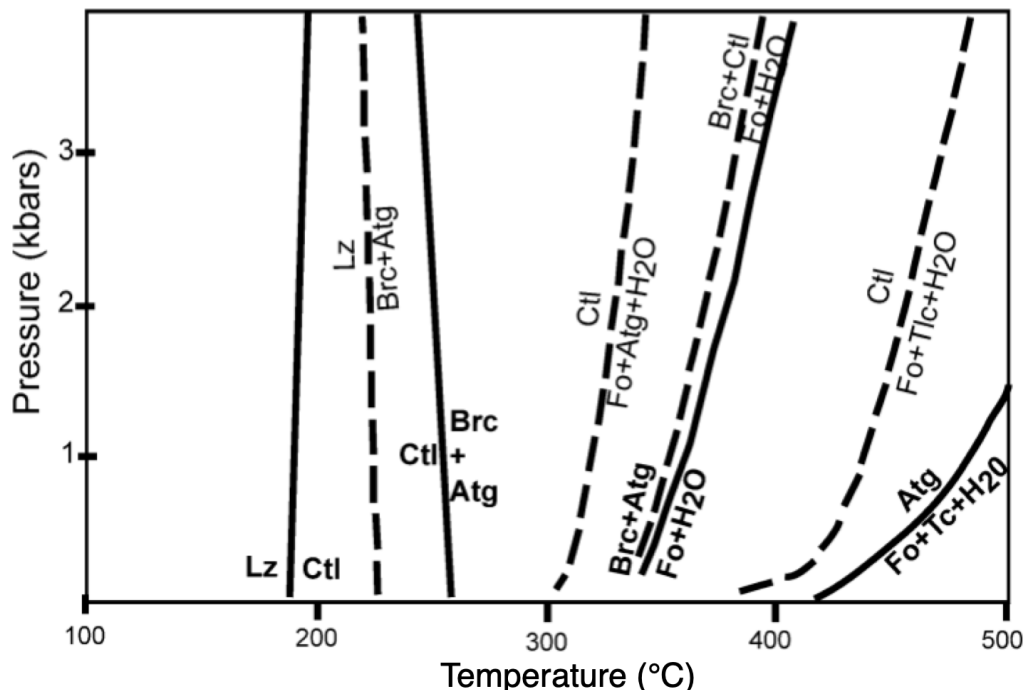


FIGURE 8.2 – Diagramme de phase possible pour le système MgO-SiO₂-H₂O (MSH), en fonction de la pression (kbar) et de la température (°C). Les lignes continues représentent les courbes de réaction stables, les lignes pointillées, les courbes de réaction métastables. Atg : antigorite, Bct : brucite, Ctl : chrysotile, Fo : forstérite, Lz : lizardite, Tc : talc (Figure issue de Mével 2003).

8.1.4 Les (micro)-textures de serpentine

Comme la serpentinitisation s'est produite dans des conditions variées (à basse température près du plancher océanique et à haute température/pression à des profondeurs plus importantes), une grande variété de (micro)-textures de serpentine a été observée.

Le premier stade de la serpentinitisation s'est généralement produit dans des conditions statiques, conduisant au remplacement pseudomorphique de l'olivine par de la lizardite sous forme de maille, et les pyroxènes sont remplacés par de la lizardite sous forme de bastite (Wicks et al. 1977; Figure 8.3A, B respectivement). Ces textures sont typiquement développées dans les serpentinites abyssales des domaines océaniques Mével 2003.

Cependant, les serpentinites contiennent généralement plusieurs générations de veines de serpentine qui recoupent les textures de mesh et de bastites précédentes, comme cela a été observé dans les domaines océaniques (par exemple, Früh-Green et al. 1996, 1990; Dilek et al. 1997).

En général, le chrysotile se trouve surtout dans les veines des serpentinites qui présentent déjà un degré considérable de serpentinitisation. Le chrysotile forme des veines rubanées composées de bandes finement espacées perpendiculaires à la paroi de la fissure avec une faible biréfringence qui alterne entre le blanc et le noir sous la lumière polarisée croisée (Figure 8.3C), ou des scellements de fissures caractérisés par une forme de lentille et une biréfringence plus élevée (Figure 8.3D). Ce type de veines se forment typiquement par extension ou par cisaillement en extension où la formation d'une fracture étroite est suivie par le remplissage de l'espace ouvert (par exemple, Ramsay 1980; Andreani et al. 2004). Cependant, au microscope, il n'est pas facile de distinguer la serpentine polygonale du chrysotile car ils peuvent avoir la même apparence.

La serpentine polygonale est caractérisée par une croix d'extinction typique sous la lumière polarisée Figure 8.3E. La serpentine polyhedrale se forme principalement comme produit d'altération des pyroxènes ou dans des veines tardives Andreani et al. 2008.

L'antigorite se présente sous forme de veines ou de patches remplaçant les textures de serpentine précédentes, comme les mailles ou les veines de lizardite serpentine. Sous la lumière polarisée, l'antigorite se caractérise par une texture typique de lamelles en chevêtée (Figure 8.3F).

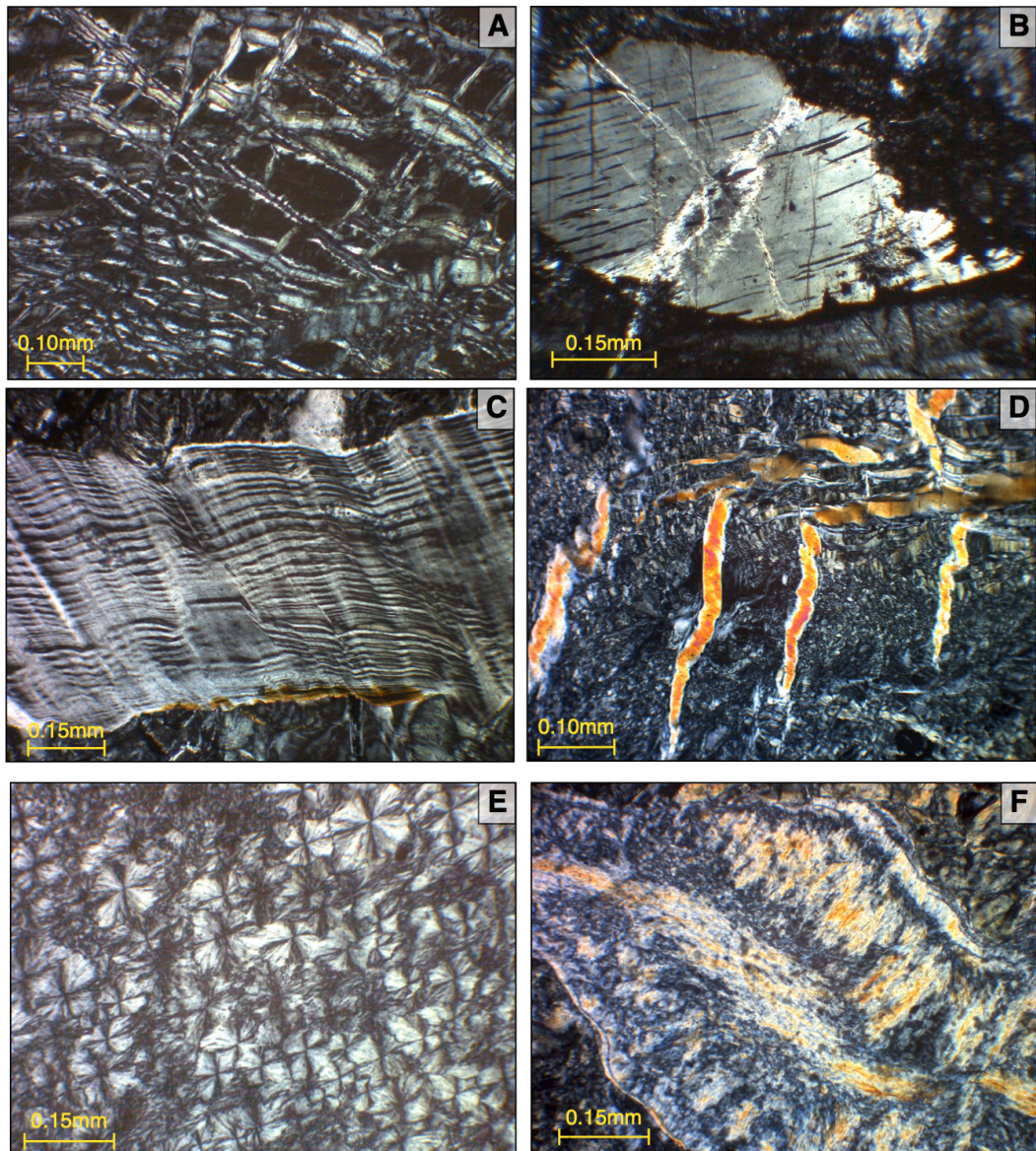


FIGURE 8.3 – Texture représentative de la serpentine observée en lumière polarisée croisée. A) lizardite en olivine pseudomorphe, B) lizardite en bastite pseudomorphe, C) chrysotile en veines rubanées, D) chrysotile , E) serpentinite polyhedrale, F) texture enchevêtrée de l'antigorite (microphotographies personnelles).

8.1.5 Méthodes pour identifier les polymorphes de serpentine

Comme mentionné ci-dessus, il n'est pas toujours facile d'identifier les polymorphes de serpentine uniquement sur la base des micro-textures de la serpentine. Il est particulièrement difficile de distinguer la serpentine polygonale et polyhedrale du chrysotile. Par conséquent, plusieurs méthodes ont été développées pour déterminer les polymorphes de la serpentine.

La première méthode utilisée pour distinguer les différentes espèces de serpentine a été la diffraction des rayons X (XRD) Whittaker and Zussman 1956, Wicks and Zussman 1975. Cependant, cette méthode nécessite de broyer l'échantillon, ce qui détruit la relation structurelle entre les phases coexistantes. Bien que l'antigorite se distingue facilement de la lizardite et du chrysotile, la lizardite, le chrysotile, la serpentine polygonale et la serpentine polyhedrale se distinguent mal par leurs diagrammes XRD.

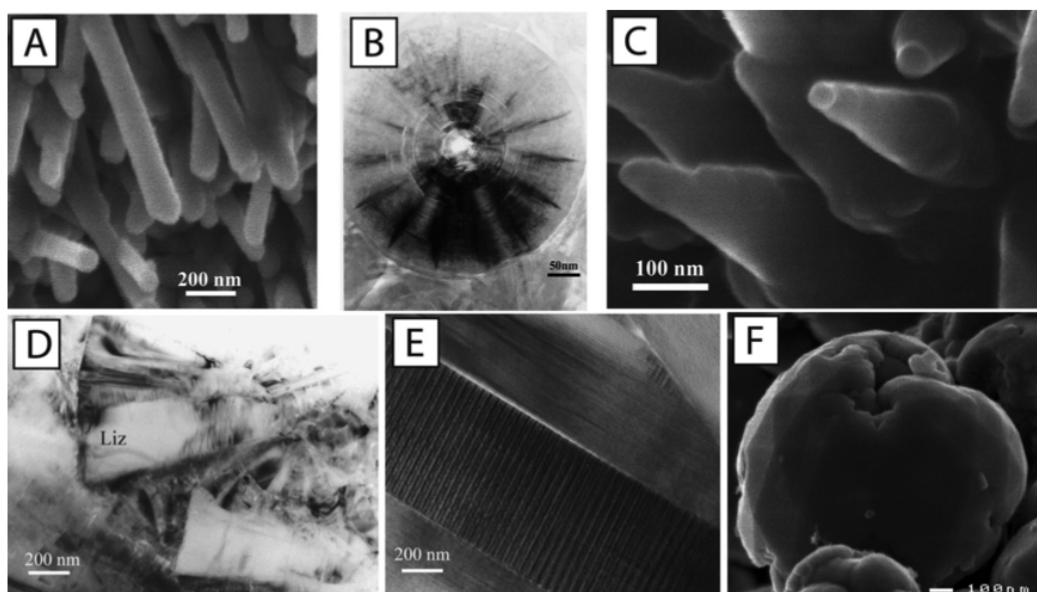


FIGURE 8.4 – Photographies en microscopie électronique à balayage (MEB) et en microscopie électronique à transmission (MET) des différents types de serpentine. A) chrysotile cylindrique (figure MEB), B) serpentine polygonale (image MEB), C) chrysotile conique (image MEB), D) lizardite planaire (image MEB), E) structure modulée de l'antigorite (MEB), F) serpentine polyhedrale sphérique (figure de Andreani et al. 2008).

La microscopie électronique à balayage (MEB) et la microscopie électronique à transmission (MET) permettent de mieux distinguer les différentes espèces de serpentine ; par exemple, Andreani et al. 2004, 2008 ; Figure 8.4). La méthode TEM permet d'observer la structure cristalline de la serpentine. En particulier, cette méthode permet de distinguer la serpentine polygonale du chrysotile, le premier se caractérisant par un diamètre de fibres plus important Baronnet and Devouard 1996. Aujourd'hui, le TEM est probablement le meilleur outil pour déterminer les polymorphes de la serpentine. Néanmoins, l'interprétation des diagrammes de diffraction électronique n'est pas toujours aisée et la préparation des échantillons est complexe.

La spectroscopie Raman est également une méthode puissante pour distinguer les différentes espèces de serpentine et présente plusieurs avantages. En effet, la spectroscopie Raman est une méthode rapide, non destructive et relativement peu coûteuse. Cette méthode permet de distinguer rapidement les minéraux de serpentine les plus courants, notamment la lizardite, le chrysotile et l'antigorite. Aujourd'hui, cette méthode est probablement la plus utilisée pour différencier la chrysotile, la lizardite et l'antigorite. En effet, la lizardite, le chrysotile et l'antigorite sont caractérisés par des spectres raman différents dans la région des 100-1200 et aussi dans la région des nombres d'ondes élevés (entre 3600 et 3750 nombres d'ondes/cm) (par exemple, Auzende et al. 2004 ; Groppo et al. 2006 ; Figure 8.5). Cependant, certaines études récentes (Tarling et al. 2018 ; Compagnoni et al. 2021) ont montré que la serpentine polygonale et la lizardite peuvent être difficilement distinguables.

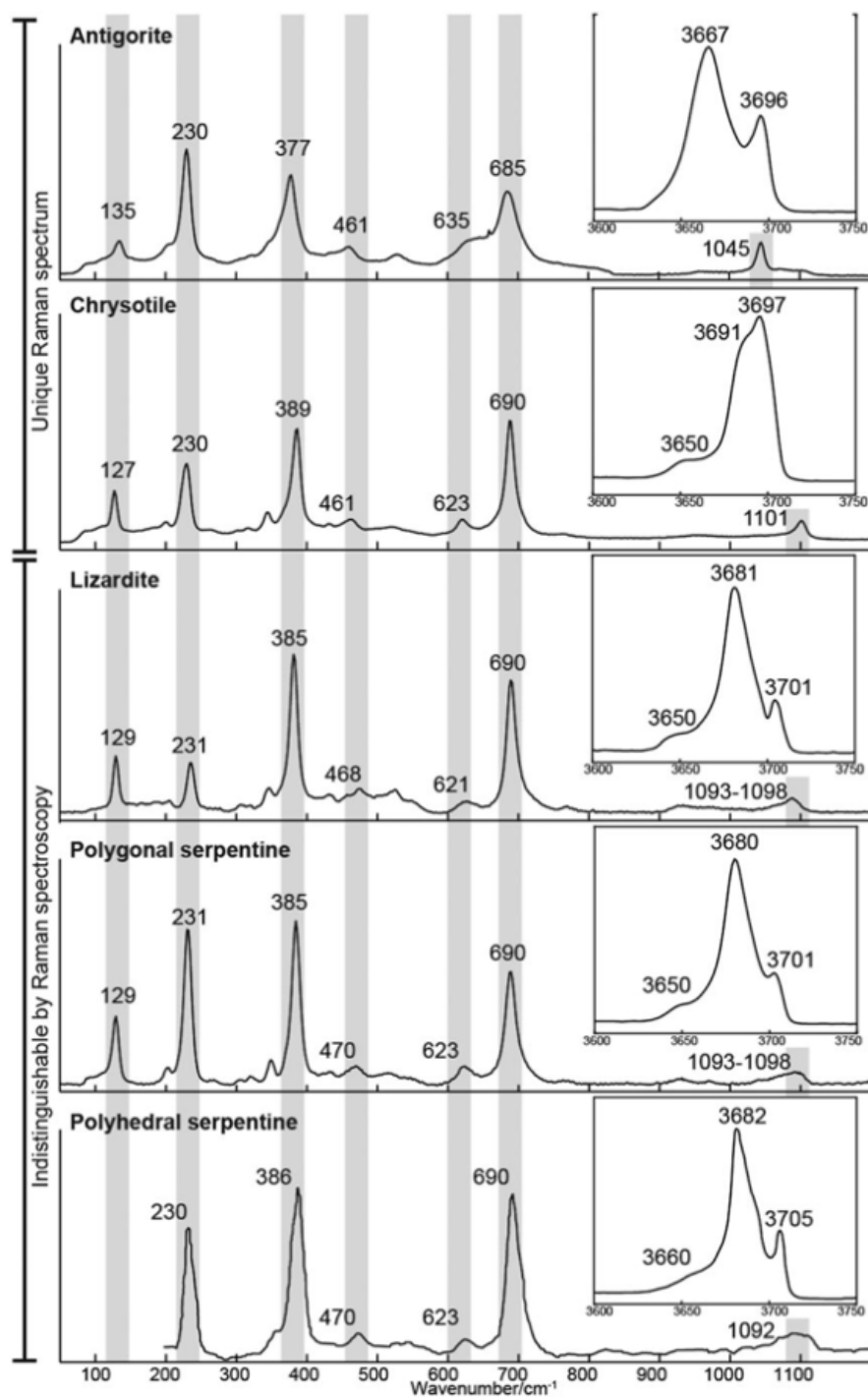


FIGURE 8.5 – Spectres Raman représentatifs des différentes espèces de serpentine, y compris l’antigorite, le chrysotile, la lizardite, la serpentine polygonale et la serpentine polyédrale (figure issue de Tarling et al. 2018).

8.1.6 Serpentinisation dans les environnements naturels

Le processus de serpentinisation étant omniprésent à la surface de la Terre, il se produit dans la plupart des contextes tectoniques, qu'il s'agisse de domaines convergents comme les zones de subduction ou des domaines divergents comme les dorsales océaniques et les marges passives (Figure 8.6). La serpentinisation joue un rôle clé dans de nombreux processus, notamment géodynamiques, dans le recyclage des éléments et dans l'origine de la vie.

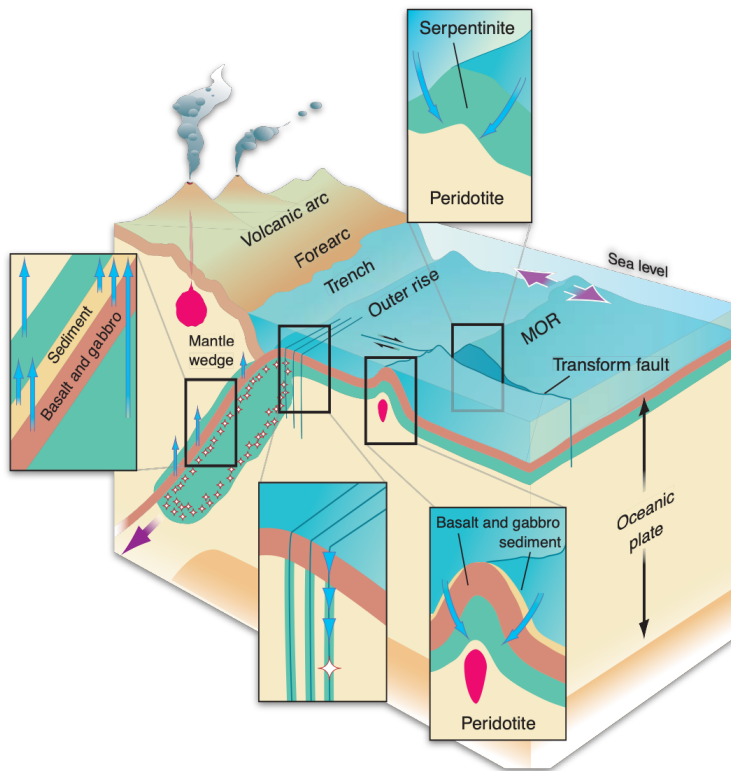


FIGURE 8.6 – Représentations schématiques de la localisation principale du processus de serpentinisation à la surface de la Terre (Figure de Kerrick 2002).

L'intégration de l'eau par les minéraux de serpentinite entraîne une augmentation du volume de la roche altérée d'environ 30 %, ce qui se traduit par une roche plus faible avec une densité nettement inférieure $\sim 2,60 \text{ g/cm}^3$ (par exemple, O'Hanley 1992 ; Klein and Roux 2020). Ces effets induits par le processus de serpentinisation ont eu un impact considérable sur la résistance de la lithosphère océanique (par exemple, Escartin et al. 1997, 2001). En particulier dans les domaines de la dorsale océanique moyenne (MOR), la serpentinisation permet de localiser la déformation (par exemple, Pérez-Gussinyé

and Reston 2001) et de faciliter l'exhumation du manteau (par exemple, Bayrakci et al. 2016). Au cours du rifting final et de la rupture, la tectonique extensionnelle conduit à la formation de failles normales et d'exhumation à angle élevé, qui créent des chemins préférentiels pour la circulation des fluides Jackson 1987. Certaines études ont montré que la phase finale de l'écartement et de la rupture lithosphérique dans les marges passives est contrôlée par la serpentinitisation (par exemple, Manatschal 2004 ; Manatschal et al. 2007). Le processus de serpentinitisation est donc clairement lié à l'exhumation du manteau. Cependant, les conditions dans lesquelles l'exhumation du manteau s'est produite dans les marges passives, notamment la température, la pression et les rapports fluide/roche, sont encore mal connues aujourd'hui. Dans les zones de subduction, les serpentinites agissent comme un lubrifiant pour l'exhumation des roches de haute pression à ultra haute pression (Guillot et al. 2000).

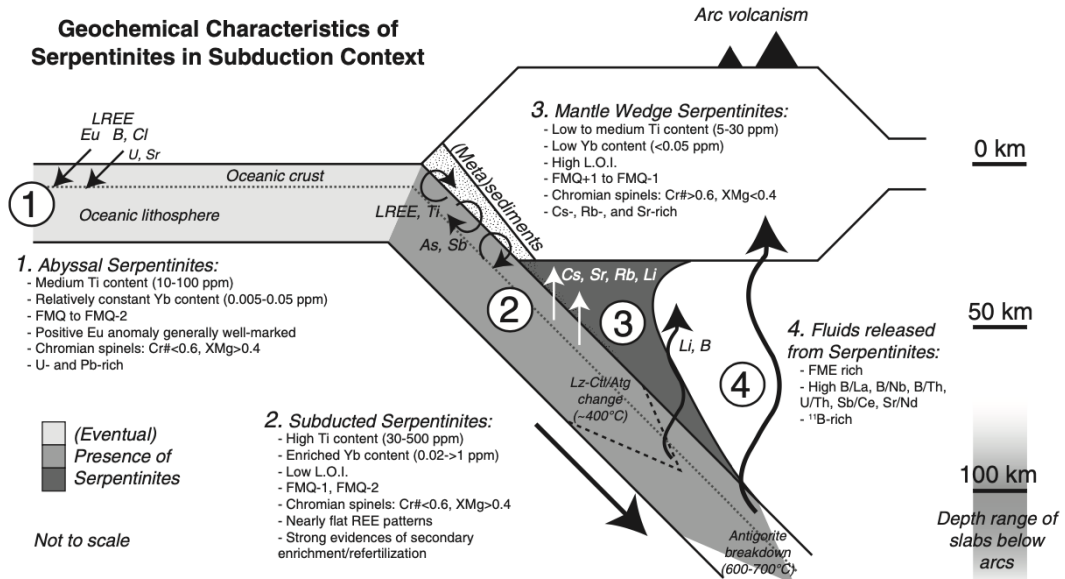


FIGURE 8.7 – Représentations schématiques du transfert géochimique associé à la serpentinitisation depuis les domaines océaniques jusqu'à la zone de subduction. (Figure tirée de Deschamps et al. 2013).

La réaction de serpentinitisation affecte fortement les bilans géochimiques de la lithosphère et des océans par l'absorption et/ou la libération de nombreux composants majeurs et mineurs (par exemple, Thompson and Melson 1970 ; Snow and Dick 1995 ; Bach et al. 2001 ; Früh-Green et al. 2004). Par exemple, Snow and Dick 1995 a estimé que la serpentinitisation libère environ 10^{12} moles de magnésium par an dans l'océan, le principal composant des minéraux du manteau. Certaines études ont montré que pen-

dant la serpentinitisation, la partie supérieure de la lithosphère était fortement enrichie en certains éléments mobiles dans les fluides (par exemple, Vils et al. 2008 ; Alt et al. 2013). Le bore, qui est concentré dans l'eau de mer et appauvri dans le manteau, est considérablement enrichi dans les serpentinites (p. ex, Thompson and Melson 1970 ; Moody 1976 ; Spivack and Edmond 1987 ; Vils et al. 2008 ; Boschi et al. 2008 ; Marschall 2018 ; McCaig et al. 2018), ce qui met en évidence les échanges chimiques entre le manteau et l'hydrosphère. Dans leur étude, Deschamps et al. 2011 proposent que les serpentinites puissent intégrer de grandes quantités d'éléments mobiles fluides (FME : B, Li, As, Sb, Pb, U, Cs, Sr, Ba) à proximité du plancher océanique et transporter ces éléments à faible profondeur (entre 100 et 170 km) dans les zones de subduction. L'incorporation et la libération d'éléments traces des domaines océaniques vers les zones de subduction sont représentées dans la Figure 8.7.

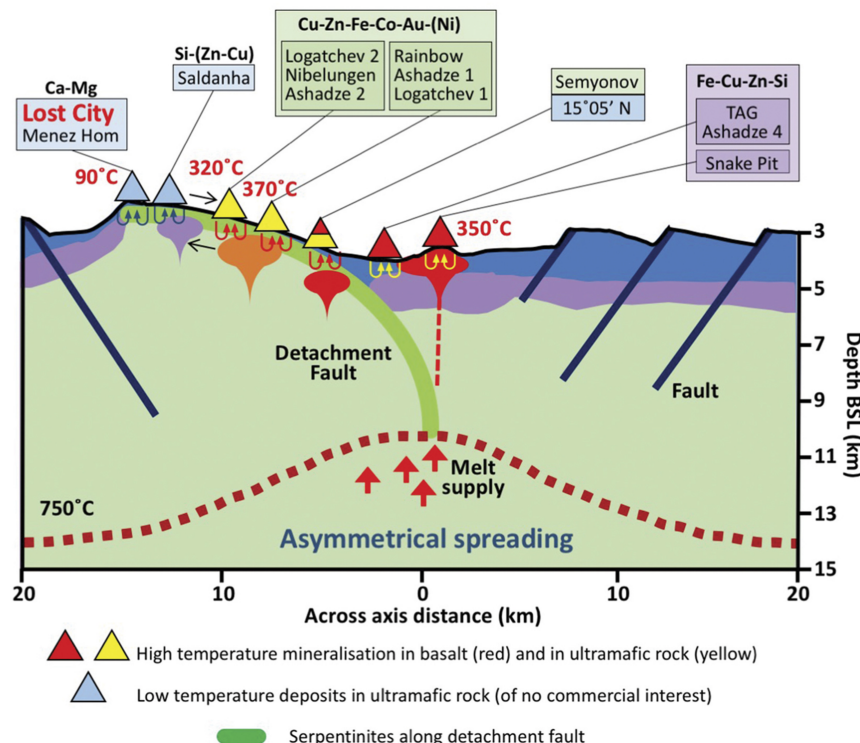


FIGURE 8.8 – Modèle schématique de la composition des principaux dépôts hydrothermaux le long de la dorsale médio-atlantique. Emplacements des événements liés aux failles de détachement (Figure issue de Johnson 2019).

Les explorations des fonds marins ont révélé la présence d'événements hydrothermaux en eaux profondes et de divers gisements de métaux tels que des nodules polymétalliques, des encroûtements riches en cobalt et des sulfures massifs polymétalliques sur

les fonds marins ou à proximité (par exemple, Hannington et al. 2005). Ces gisements sont composés d'éléments d'intérêt économique tels que Cu, Zn, Pb, Au et Ag (Figure 8.8 ; e.g., Fouquet et al. 2013 ; Jamieson and Gartman 2020). Près de 65% des sites hydrothermaux se trouvent dans les contextes de dorsales océaniques moyennes Hannington et al. 2005. Ces systèmes hydrothermaux et les gisements de métaux associés résultent de circulations de fluides le long de failles normales (par exemple, Rona 1984 ; Rona et al. 1993 ; Hannington et al. 2001). Les nombreuses études sur des échantillons naturels, les expériences hydrothermales ou la modélisation numérique, ont suggérées que les roches ultramafiques jouent potentiellement un rôle clé dans la formation de dépôts minéraux sur le plancher océanique (par exemple, Allen and Seyfried Jr 2003 ; Klein et al. 2015 ; Klein and McCollom 2013). Cependant, à l'heure actuelle, les impacts de la serpentisation sur le transfert d'éléments traces, y compris les métaux de transition dans la formation des dépôts minéraux, sont mal connus.

La réaction de serpentisation peut générer de l'hydrogène moléculaire H₂ en raison de l'oxydation du fer ferreux (par exemple, Marcaillou et al. 2011 ; Klein and McCollom 2013 ; McCollom et al. 2020a, 2016), conduisant à la formation de fluides avec différentes valeurs de pH, en fonction de la température. Aux basses températures <200°C, la serpentisation conduit à la formation de conditions fortement réductrices et de fluides alcalins au pH ~9-10 (par exemple, Barnes and O'NEIL 1969 ; Kelley et al. 2001 ; Seyfried Jr et al. 2007 ; Hansen et al. 2017 ; McCollom et al. 2020b). À des températures élevées >300°C, la serpentisation génère des fluides plus acides avec des valeurs de pH comprises entre 2,8 et 5,4, comme le suggèrent les expériences de serpentisation (par exemple, Seyfried Jr and Dibble Jr 1980 ; Allen and Seyfried Jr 2003, 2005). Dans les domaines océaniques, les rejets de H₂ peuvent être utilisés comme source d'énergie par les bactéries lithotrophes Holm and Charlou 2001. De plus, la libération continue d'hydrogène permet la formation de méthane abiotique (CH₄) par la réduction du carbone (HCO₃⁻, CO, CO₂) via des réactions de type Fischer-Tropsch et de type Sabatier (ex, Proskurowski et al. 2006 ; Proskurowski et al. 2008 ; Holm et al. 2015 ; Etiope 2017). Cela favorise les activités microbiennes sur le fond marin ou à proximité (par exemple, Holm and Charlou 2001 ; Kelley et al. 2001 ; Früh-Green et al. 2004 ; McCollom and Seewald 2007 ; Delacour et al. 2008a ; Russell et al. 2010 ; Miller et al. 2016).



8.2 Principaux enjeux

Comme indiqué précédemment, la serpentinitisation se produit dans la plupart des contextes géodynamiques et dans diverses conditions, qu'il s'agisse de température et de pression relativement basses près du plancher océanique au niveau des dorsales médo-océaniques (MOR ; par ex, Alt and Shanks III 2003 ; Mével 2003 ; Ranero et al. 2003 ; Andreani et al. 2007 ; Rouméjon and Cannat 2014) à des températures et des pressions élevées dans les zones de subduction (par exemple, Deschamps et al. 2013, 2011, 2010). Au cours des deux dernières décennies, le processus de serpentinitisation a été largement documenté dans ces deux contextes géologiques majeurs (par exemple, Guillot et al. 2015), contrairement à celui des marges riftées pauvres en magma. Cependant, sur les marges de rift, la serpentinitisation intervient largement dans le transfert d'éléments entre le manteau et l'eau de mer (par exemple, Pinto et al. 2017) et les processus tectoniques conduisant à l'exhumation du manteau Manatschal 2004. En outre, sur les marges riftées et pauvres en magma, les réactions de serpentinitisation peuvent également participer à la formation de gisements de sulfures massifs (ultramafiques) volcaniques (U-VMS) dans lesquels se concentrent de nombreux métaux de transition Patten et al. 2021. Albers et al. 2021 suggèrent que dans les marges passives, la serpentinitisation peut produire des quantités particulièrement élevées de H₂. A l'heure actuelle, la serpentinitisation dans les marges passives soulève encore de grandes questions :

- Quel est l'impact des interactions fluide-roche sur l'exhumation du manteau ?
- Quelle est la source des fluides de serpentinitisation dans les marges passives ?
- Dans quelles conditions, et en particulier à quelle température, les interactions fluide-roche se sont-elles produites ?
- Comment les éléments chimiques sont-ils mobilisés pendant la serpentinitisation et existe-t-il un lien entre la serpentinitisation et la formation de gisements métalliques ?

En particulier, la détermination de la température à laquelle la serpentinitisation s'est produite est fondamentale pour la compréhension de la rhéologie, de la vitesse d'étalement et également du régime thermique associé aux marges riftées pauvres en magma. La température influence également la mobilité chimique et la formation des minéraux secondaires.

8.3 Etude géologique

8.3.1 Évolution temporelle des marges riftées pauvres en magma de la Téthys Alpine

Le bassin alpin de la Téthys, qui sépare les plaques eurasienne et ibérique des plaques adriatique et africaine, s'est ouvert au Trias supérieur à environ 200 Ma (figure 8.9E). Avant le début de l'écartement des plaques au Trias, la croûte était large d'environ 30 km.

Pendant la phase d'étirement entre 200 ± 5 et 185 ± 5 Ma (Figure 8.9D), de nombreuses failles normales se sont développées dans la croûte supérieure, ce qui a permis de répartir l'extension sur une large zone Manatschal et al. 2022.

Ensuite, pendant la phase d'amincissement initiée à 185 ± 5 Ma (Figure 8.9C), la déformation a commencé à se concentrer sur la future marge distale et les sédiments post-tectoniques ont commencé à se remplir dans les graben. À cette époque, des failles de détachement extensionnelles ont permis d'exhumer les niveaux de croûte moyenne jusqu'au plancher océanique Mohn et al. 2012.

Le début de la phase d'hyper-extension (Figure 8.9B) est marqué par la formation de nouvelles failles (c'est-à-dire des failles de détachement extensionnel successives en séquence et hors séquence) qui sont capables de pénétrer dans le manteau sous continental sous-jacent (Mohn et al. 2012 ; Gillard et al. 2016a). Pendant la phase d'hyper extensions, la déformation est clairement asymétrique Gillard et al. 2016b. Les circulations de fluides hydrothermaux ont été mis en évidence par la présence d'éléments dérivés du manteau (Ni, Cr et V) dans des minéraux secondaires le long des failles de détachement en extension dans la croûte continentale (par exemple, Pinto et al. 2015). Les failles de détachement en extension permettent d'exhumer sur le plancher océanique le manteau lithosphérique sous-continentale à environ 170 Ma.

L'exhumation du manteau s'accompagne du début de l'activité magmatique dans les domaines distaux qui caractérisent la phase proto-océanique (figure 8.9A). L'activité magmatique est attestée par la présence de laves en coussins et d'intrusions gabbroïques datées de 161 ± 1 Ma (Desmurs et al. 2001 ; Desmurs et al. 2002 ; Schaltegger et al. 2002 ; Epin et al. 2019 ; Amann et al. 2020a).

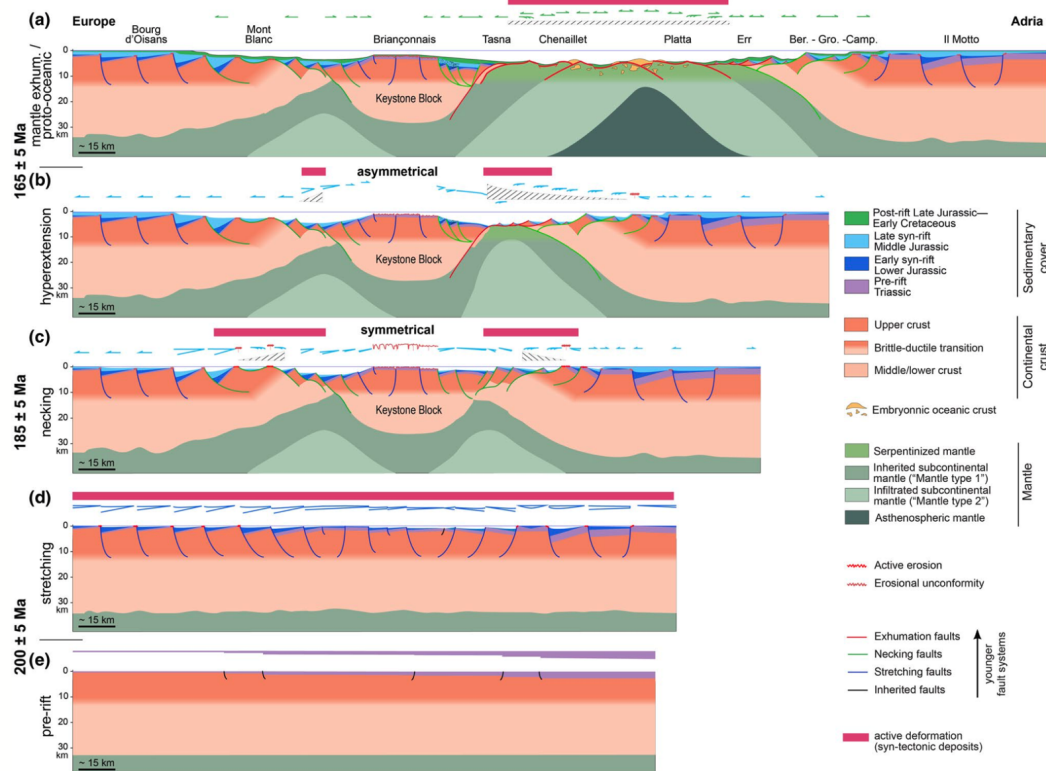


FIGURE 8.9 – Principales phases de l'évolution du rift alpin de la Téthys, d'après Manatschal et al. 2022 A) phase d'exhumation du manteau (formation de la croûte proto-océanique) au Jurassique moyen ; B) phase d'hyperextension à la fin du Jurassique inférieur (Pliensbachien-Toarcien) ; C) phase d'amincissement au Jurassique inférieur (Sinémurien-Pliensbachien) ; D) phase d'étirement à partir du Trias supérieur (Pliensbachien-Toarcien) ; E) phase d'étirement du dernier Trias au Jurassique précoce et F) situation de pré-rift au Jurassique tardif.

8.3.2 Contexte Géologique

La transition océan-continent (OCT) de Téthys Alpine est particulièrement bien préservée dans la partie sud-est des Alpes Suisse. En particulier, dans les nappes de Platta, Tasna et Totalp qui ont été échantillonnées dans cette étude. Dans ces nappes, les contacts liés au rift pré-alpin entre le manteau sous-continental et les sédiments syn-rift ont particulièrement bien préservé les Manatschal 2004. Par conséquent, les résultats pétrologiques et minéralogiques des serpentinites de ces unités ne sont pas (ou peu) affectés par la subduction alpine. La serpentinitisation associée à l'exhumation du manteau dans ces unités est donc comparable à celle des zones OCT actuelles, y compris la marge passive ibéro-terre-neuvienne (par exemple, Manatschal et al. 2007).

Ces vestiges sont aujourd’hui exposés sous forme de nappes ophiolitiques dans les Alpes centrales, dans la partie sud-est de la Suisse (Figure 8.10 ; Manatschal and Nievergelt 1997 ; Müntener et al. 2004 ; Müntener and Piccardo 2004). Comme indiqué plus haut, ces ophiolites représentent des OCT des anciennes marges conjuguées Adriatique-Europe-Briançonnais (Figure 8.10B ; Florineth and Froitzheim 1994). Ces nappes ophiolitiques sont situées au nord de la ligne de l’Engadine, qui correspond à une antiforme orientée nord-est - sud-ouest (NE-SW) dans le sud-est de la Suisse (Figure 8.10C).

Les trois localités échantillonnées dans cette thèse (nappes de Platta, Totalp et Tasna) proviennent des marges sud-est de la Téthys alpine. Les nappes de Platta et de Totalp proviennent de la marge adriatique (Figure 8.10B, C), et la nappe de Tasna fait partie de la marge conjuguée Europe-Briançonnais (Figure 8.10B ; Manatschal and Müntener 2009).

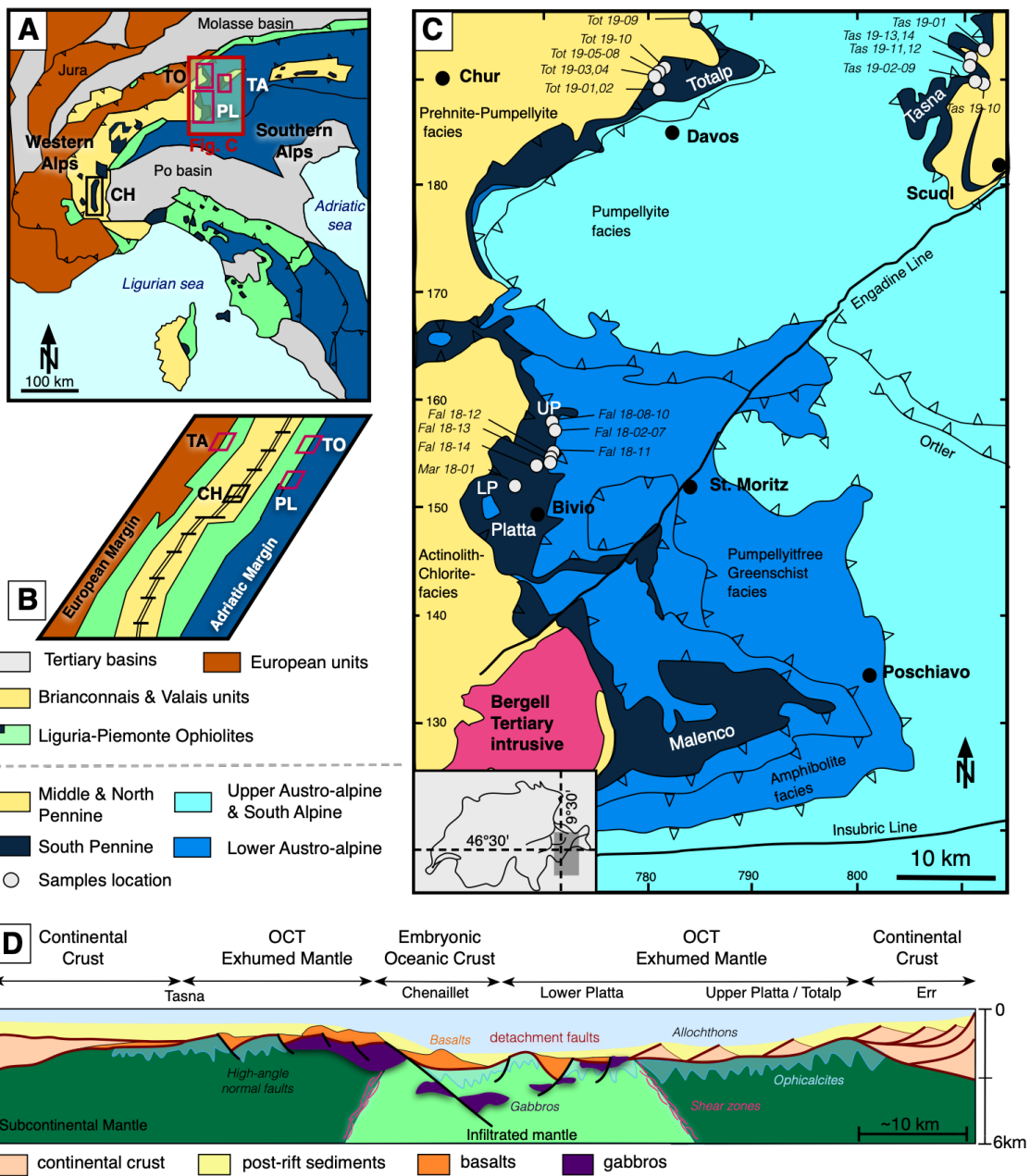


FIGURE 8.10 – A) Localisation actuelle des massifs d'ophiolites dans les Alpes centrales-occidentales-ligures (modifié d'après Manatschal and Müntener 2009). B) Paléo-reconstruction schématique du bassin océanique piémontais-ligure au Jurassique supérieur, avec localisation des principales séquences ophiolitiques (modifié d'après Manatschal and Müntener 2009). C) Carte géologique simplifiée des nappes penninique et austro-alpine (modifiée d'après Florineth and Froitzheim 1994), y compris l'emplacement des échantillons. D) Distribution du manteau sous-continental et infiltré le long d'une transition océan-continent de la Téthys alpine (modifié d'après Müntener and Piccardo 2004).

La nappe de Platta



FIGURE 8.11 – Vue panoramique de la nappe de Platta (photographie personnelle).

La nappe de Platta provient de la marge SE de la Téthys alpine et fait partie des nappes austro-alpine et pennine (Figure 1D). La nappe de Platta se subdivise en deux unités séparées par des zones de cisaillement (figure 1D) : i) l'unité de Platta supérieure, qui se compose principalement de roches mantelliennes ayant formé à l'origine le manteau sous-continental hérité de la marge adriatique (c.à.d. le domaine d'Err), ii) la nappe de Platta supérieure, qui se subdivise en deux unités séparées par des zones de cisaillement (figure 1D), le domaine Err Schallegger et al. 2002 ; Müntener et al. 2010, 2004 ; Picazo et al. 2016 ; Epin and Manatschal 2018) ; et ii) l'unité Lower Platta, qui était à l'origine située vers l'océan et se compose d'un vaste domaine mantellique localement pénétré et recouvert par des roches dérivées de la fusion (gabbros et laves) d'âge jurassique (Desmurs et al. 2002 ; Amann et al. 2020b). Contrairement aux roches du manteau de la partie supérieure de la plaine, qui sont exemptes de toute empreinte de fusion syn-rift et équilibrées à basse température ($\sim 850^\circ\text{C}$), celles de la partie inférieure de la plaine ont été largement refertilisées par percolation de la fonte au cours du rifting final et ont enregistré une température plus élevée ($\sim 1000^\circ\text{C}$; Müntener et al. 2010, 2004). Des lames d'origine continentale sont également présentes dans la nappe de Platta et ont été interprétées comme des allochtones d'extension (Froitzheim and Manatschal 1996). Certains affleurements de la nappe de Platta sont recouverts par des ophicalcites (Dietrich 1970).

La nappe de Platta a été relativement préservée du métamorphisme alpin (métamorphisme à basse température à prehnite-pumpellyite, $< 350^\circ\text{C}$; Froitzheim and Rubatto 1998 ; Chalot-Prat et al. 2003 ; Epin et al. 2019). Cependant, une augmentation du métamorphisme alpin du nord au sud est caractérisée par la transition entre le type de serpentine lizardite/chrysotile dans la nappe de Platta et le type d'antigorite à Malenco, représentant la continuation méridionale de l'unité de Platta supérieure (Dietrich

1969 ; Trommsdorff 1983 ; Trommsdorff and Evans 1977 ; Burkhard and O'Neil 1988).

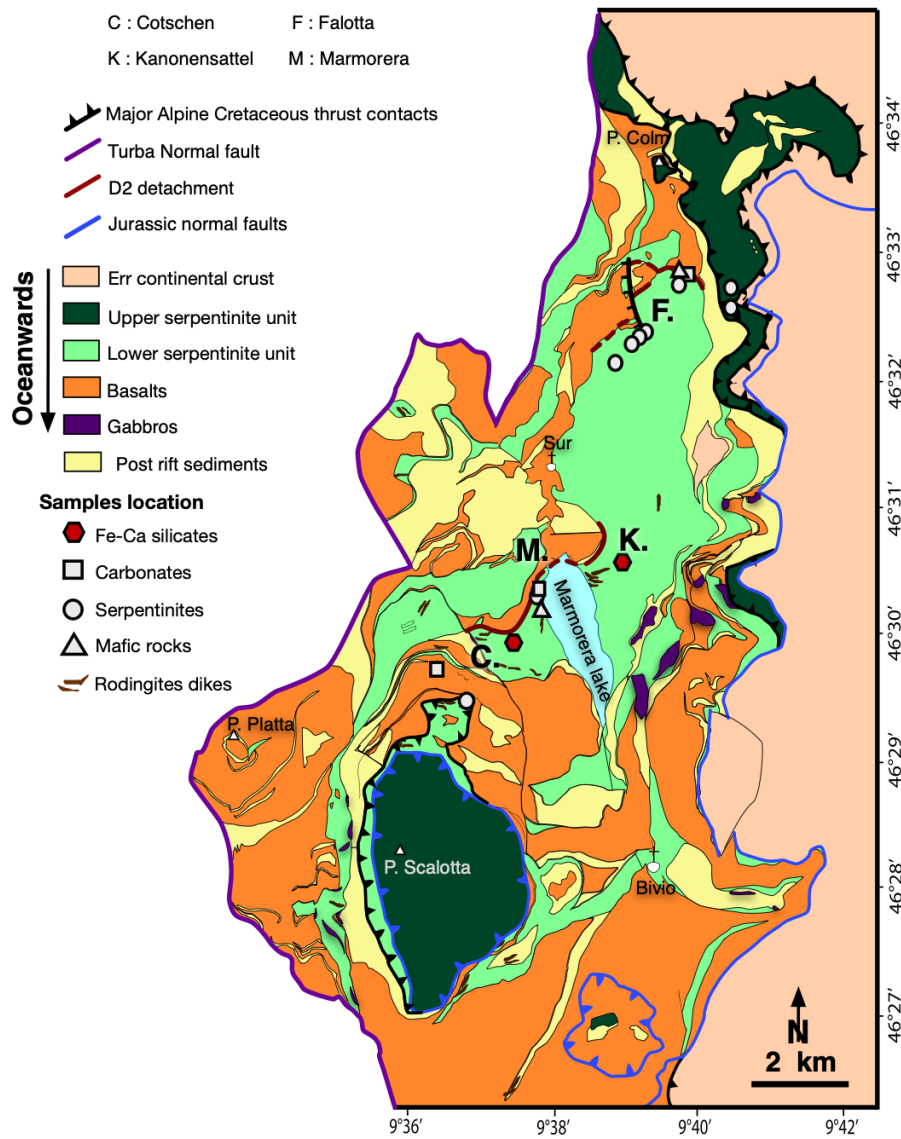


FIGURE 8.12 – Carte géologique de la nappe de Platta avec localisation des échantillons, Figure issue de Hochscheid et al. (2022)

La nappe de Totalp



FIGURE 8.13 – Affleurement de serpentinites de la nappe de Totalp (photographie personnelle).

La nappe de Totalp, actuellement située au nord de la nappe de Platta (Figure 8.10B), fait également partie des nappes de Pennine du Sud et Austro Alpine, dérivées de la marge SE de la Téthys alpine et poussées sur les unités de Penninique moyen et nord pendant l'Éocène tardif (Froitzheim and Manatschal 1996 ; Figure 8.10C). La nappe de Totalp est constituée de lherzolites à spinelles serpentiniisées et foliées, parfois recoupées par des pyroxénites et recouvertes par des ophicalcites et des sédiments pélagiques. Les roches magmatiques sont rares et consistent principalement en des flaser gabbros et en dykes doléritiques (Peters and Mathews 1963).

Par rapport à la nappe de Platta, la nappe de Totalp a subi un métamorphisme alpin légèrement plus important, avec un assemblage de préhnite près de la zone de contact avec les gneiss environnants Peters and Mathews 1963, ce qui permet une meilleure reconstruction paléogéographique que la nappe septentrionale de Platta (Manatschal, 2004 ; Manatschal and Müntener, 2009). Le manteau serpentiniisé est souvent recoupé par des veines de calcite en raison de son emplacement près du plancher océanique (Weissert and Bernoulli 1985 ; Bernoulli and Weissert 1985 ; Picazo et al. 2013). Comme dans la nappe de Platta, les vestiges des contacts préalpins entre les roches mantelliques exhumées, les ophicalcites et les sédiments sont localement bien préservés Picazo et al. 2013, ce qui en fait un très bon endroit pour étudier l'interaction fluide-roche liée à l'exhumation du manteau au niveau du plancher océanique. Le $^{40}\text{Ar}/^{39}\text{Ar}$ sur la phlogopite de la pyroxénite suggère un âge jurassique de 160 ± 8 Ma de refroidissement/exhumation (Peters and Stettler 1987a ; Peters and Stettler 1987b ; Manatschal et al. 2006).

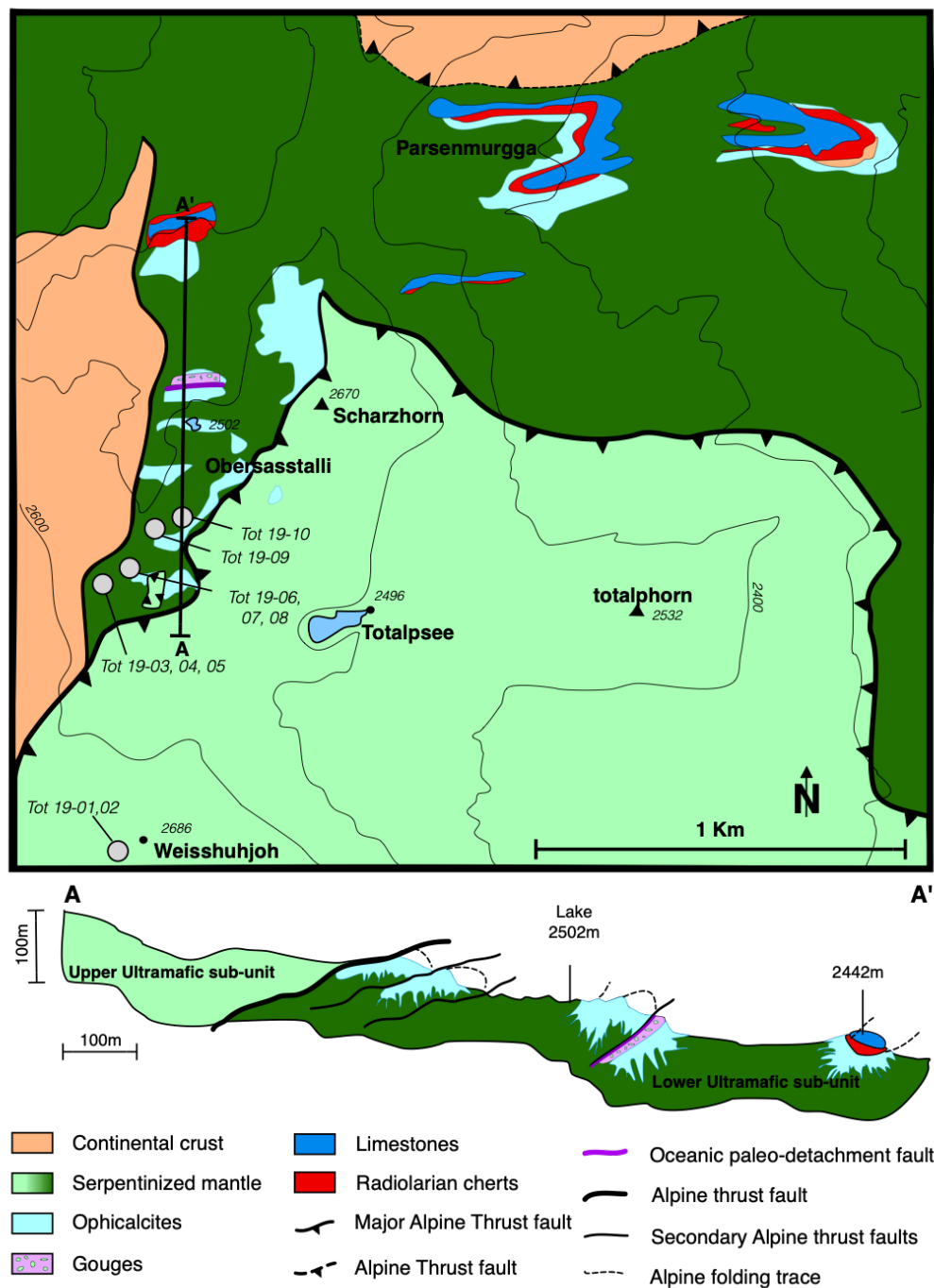


FIGURE 8.14 – Geological map of the Totalp nappe with samples location, modified after Carte géologique de la nappe de Totalp avec localisation des échantillons, modifiée d'après Picazo et al. 2013.

La nappe de Tasna

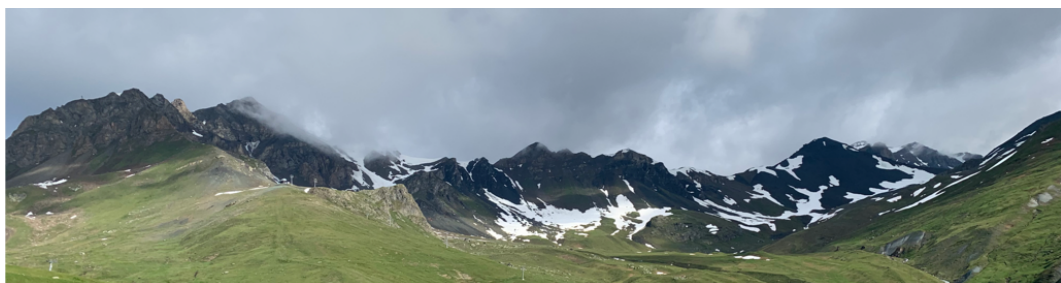


FIGURE 8.15 – Vue panoramique de la nappe de Tasna (photographie personnelle).

La nappe de Tasna était initialement située le long de la marge Briançonnais/Europe (Figure 1B ; Florineth and Froitzheim 1994 ; Manatschal et al. 2006). Cette nappe est constituée d'un empilement de nappes austro-alpines et de nappes pennines établies entre l'Éocène et l'Oligocène (Figure 1B ; Florineth and Froitzheim 1994 ; Manatschal et al. 2006). Comme la nappe de Platta, la nappe de Tasna n'a été que faiblement affectée par le métamorphisme alpin à faible degré <350° correspondant au faciès greenschiste (Florineth and Froitzheim 1994 ; Froitzheim and Manatschal 1996 ; Bousquet et al. 2008 ; Manatschal et al. 2006 ; Ribes et al. 2020). Par conséquent, les contacts pré-alpin de la nappe de Tasna ne sont pas affectés par le métamorphisme alpin.

La nappe de Tasna est constituée d'un coin de croûte continentale séparé du manteau sous-jacent par deux failles de détachement, le détachement de Tasna inférieur (DTI), qui sépare les roches continentales des roches du manteau, et le détachement de Tasna supérieur (DTU), qui tronque le DTI et représente une faille de détachement du soubassement supérieur exhumée (Figure 8.16 ; Froitzheim and Rubatto 1998 ; Manatschal et al. 2006 ; Ribes et al. 2020). Les roches mantelliques et continentales ont été recouvertes par des sédiments post-rift non déformés du Barrémien tardif, caractéristiques du domaine Briançonnais/Européen (*cite alt Froitzheim 1998*). Les roches du manteau sont constituées de lherzolites à spinelle fortement serpentinisées avec d'abondantes couches de websérite à spinelle et une foliation de spinelle à haute température (Manatschal et al. 2006). Les âges $^{40}\text{Ar}/^{39}\text{Ar}$ mesurés sur les phlogopites, ainsi que la composition du clinopyroxène et la température d'équilibre calculée sur les pyroxènes coexistants des lherzolites à spinelle et des pyroxénites (Manatschal et al., 2006) sont similaires à ceux de l'unité Totalp à $\sim 900^\circ\text{C} \pm 50^\circ\text{C}$ (Peters and Stettler, 1987a).

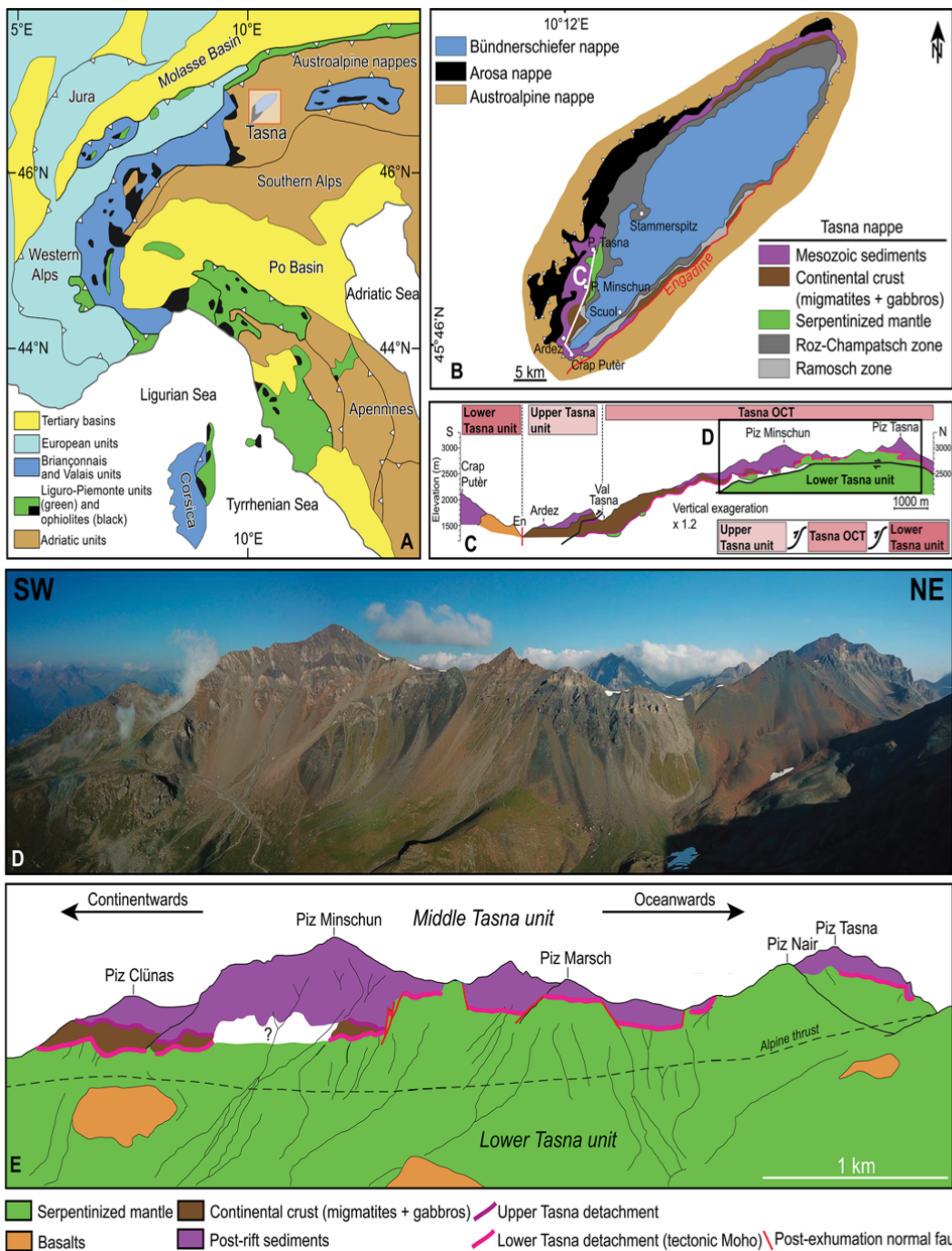


FIGURE 8.16 – A) Carte géologique simplifiée du système alpin en Europe occidentale, d'après Schaltegger et al. 2002. B) Carte géologique de la fenêtre de l'Engadine dans les Alpes du sud-est, Suisse. C) Coupe transversale nord-sud le long de la nappe de Tasna et représentation schématique de l'architecture d'empilement de la nappe d'après Coltat et al. 2022 modifié d'après Ribes et al. 2020 ; OCT : transition océan-continent ; P : Piz. D,E) Vue de champ orientée sud-ouest-nord-est de la coupe de Tasna à partir de Ribes et al. 2020.

8.4 Etude expérimentale

8.4.1 Etudes expérimentales de serpentisation antérieures

Au cours des quatre dernières décennies, afin de comprendre les systèmes hydrothermaux observés sur les fonds marins, la réaction de serpentisation a été largement étudiée dans des conditions de laboratoire, avec les premières expériences de (Martin and Fyfe 1970 ; Seyfried Jr and Dibble Jr 1980 ; Seyfried Jr 1987 ; Janecky and Seyfried 1986), puis (e.g., Marcaillou et al. 2011 ; Malvoisin et al. 2012a,b ; Klein et al. 2015 ; McCollom et al. 2016) ; et plus récemment (par exemple, McCollom et al. 2020a,b ; Tichadou 2021). Lors des expériences de serpentisation, de nombreux paramètres ont été testés : température, pression, composition du fluide et pH, composition du protolith et taille initiale des grains... Ces expériences ont montré que ces différents paramètres affectent la cinétique de la réaction et la production d'hydrogène. Martin and Fyfe 1970 et Wegner et al. 1983 ont été les premiers à montrer expérimentalement que la température, la pression et la taille initiale des grains affectaient la conversion de l'olivine en serpentine au contact de l'eau. Depuis, de nombreuses expériences ont été réalisées. Ci-dessous, nous avons résumé les impacts des différents paramètres sur la serpentisation.

Il existe différents dispositifs expérimentaux fermés, mais les plus couramment utilisés sont les cellules de réaction flexibles en or-titane conçues par Seyfried Jr 1987 Figurefig:autoclave et les capsules d'or Figurefig:trempe, chacune présentant des avantages et des inconvénients.

Le premier permet de réaliser des expériences sur de grands volumes avec un contrôle précis de la pression. Cet appareil permet d'utiliser un grand volume de fluide et/ou de roche et donc de tester différents rapports eau/roche. En outre, cet appareil permet de prélever des échantillons de fluides pendant les expériences et de caractériser les changements de fluides pendant les expériences hydrothermales telles que la serpentisation. Le principal inconvénient est la longue durée des expériences, le chauffage et le refroidissement durant plusieurs heures et le risque non négligeable de fuite pendant les expériences.

Le deuxième type de réglage permet des expériences plus rapides à une pression plus élevée, mais avec un volume restreint de réactifs (quelques grammes seulement), ni d'échantillonnage de fluide pendant les expériences. Cependant, avec cet appareil, il est possible de mesurer la susceptibilité magnétique sans ouvrir la cellule d'expéri-

mentation (Malvoisin et al. 2012b), ce qui peut être utile pour surveiller la cinétique de serpentinitisation et la production d'hydrogène, liée à la production de magnétite au cours de la serpentinitisation.



FIGURE 8.17 – Photographie d'une autoclave à grand volume, photographie personnelle.

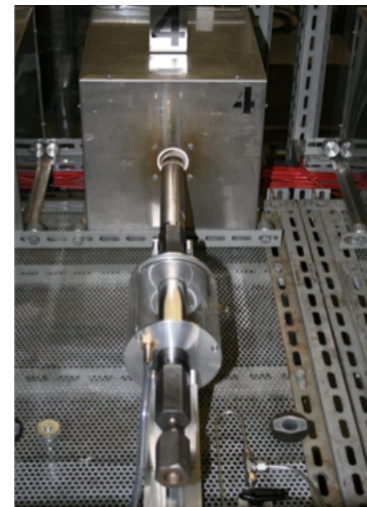


FIGURE 8.18 – Photographie d'une capsule en or du laboratoire ISTO.

Ces dernières années, de nouveaux appareils ont été développés afin de mener des expériences dans des systèmes ouverts (c'est-à-dire le transport réactif), les plus représentatifs des systèmes naturels. Ces appareils visent à quantifier le transport des éléments au cours des interactions fluide-roche ou l'évolution des caractéristiques pétrophysiques de l'échantillon (par exemple, Escario et al. 2018; Tutolo et al. 2018; Osselin et al. 2022).

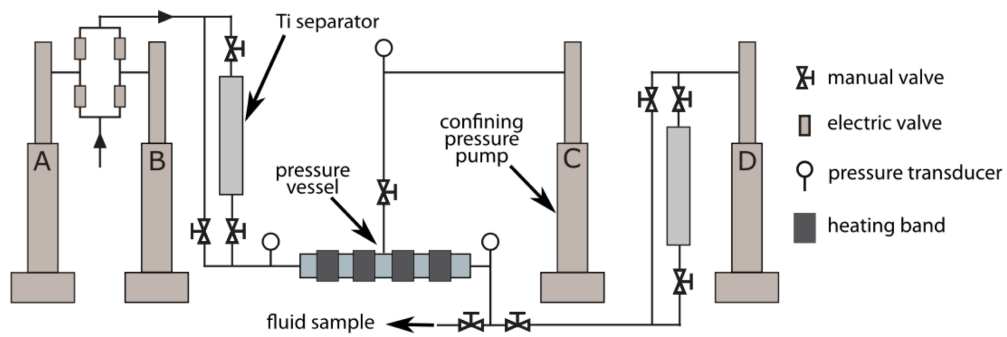


FIGURE 8.19 – Représentation schématique d'un type d'appareil expérimental utilisé pour les expériences de transport réactif, illustrant les pompes d'injection, de collecte et de confinement, la cuve à pression hydrothermale, les transducteurs de pression utilisés pour les mesures de perméabilité et la vanne de contrôle de la chimie des fluides Figure from Tutolo et al. 2018

Température

Martin and Fyfe 1970 ont été les premiers à démontrer que le taux de réaction de serpentinitisation est lié à la température en menant des expériences de serpentinitisation dans des capsules d'or. En faisant réagir de la forstérite synthétique avec de l'eau, ils ont déterminé que le taux de réaction de serpentinitisation forme une courbe en forme de cloche en fonction de la température, avec un pic (c'est-à-dire la conversion maximale de l'olivine en serpentine) entre 250°C et 300°C, pour une taille de grain initiale de 58 à 79 µm. Wegner et al. 1983 a réalisé les mêmes expériences dans des capsules d'or et a déterminé un pourcentage maximum de conversion à environ 305°C en accord avec les résultats précédents de Martin and Fyfe 1970. Cependant, la dépendance des taux de serpentinitisation avec la température a formé une courbe en cloche asymétrique. Les résultats de Wegner et al. 1983 ont été confirmés par l'étude de Malvoisin et al. 2012a, qui diffèrent fortement de ceux de Martin and Fyfe 1970, avec un taux de réaction de serpentinitisation environ 60 fois plus lent. Malvoisin et al. 2012a propose que ces différences de taux de réaction de serpentinitisation soient une conséquence de la nature de la forstérite qui diffère entre les trois études (synthétique dans Martin and Fyfe 1970 et olivine naturelle de san Carlos dans les deux autres). Les résultats de l'étude de McCollom et al. 2016 étaient également cohérents avec ceux de Malvoisin et al. 2012a, ce qui suggère que le taux de réaction de serpentinitisation de l'olivine dans les systèmes naturels peut être significativement plus lent que les études antérieures de Martin and Fyfe 1970 et Wegner et al. 1983.

Contrairement à ces expériences précédentes, Lamadrid et al. 2021 a montré que la serpentinitisation de l'olivine est plus rapide à 250°C, et que les taux de serpentinitisation affichent une courbe concave presque symétrique de forme descendante. Néanmoins, contrairement aux expériences précédentes, Lamadrid et al. 2021 a utilisé une composition différente de fluides, qui affecte les taux de serpentinitisation en augmentant le taux de serpentinitisation en présence d'une solution aqueuse d'eau de mer. Les auteurs ont comparé leurs résultats avec les taux de serpentinitisation de la littérature (Figure 8.20). Il est maintenant clairement établi que les taux de réaction de serpentinitisation dépendent de la température.

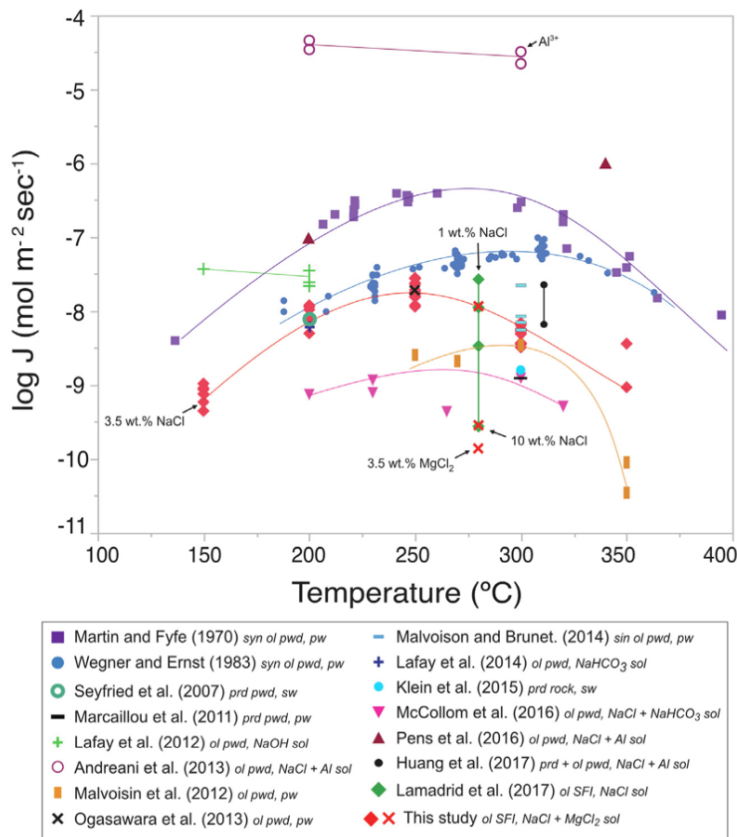


FIGURE 8.20 – Figure résumant les taux de serpentinisation de la littérature en $\log J$ (quantité d'énergie) en fonction de la température ($^{\circ}\text{C}$), figure issue de Lamadrid et al. 2021.

Pression

Contrairement à d'autres paramètres, l'influence de la pression sur le processus de serpentinisation a été moins étudiée jusqu'à présent et reste mal définie. Cependant, des études antérieures suggèrent que la pression est une caractéristique non négligeable qui contrôle la serpentinisation.

Wegner et al. 1983 ont étudié les effets de la pression sur les taux de serpentinisation par le biais d'expériences à 270°C pendant 20 jours. Leurs principaux résultats ont montré une augmentation du degré de serpentinisation de 21

Nakatani and Nakamura 2016 a réalisé une série d'expériences d'hydratation à des températures de 400-580 °C et à des pressions de 13 et 18 kabr avec trois compositions en vrac différentes : olivine, mélange orthopyroxène-clinopyroxène et mélange olivine-orthopyroxène, afin de déterminer le taux de serpentinisation dans des condi-

tions d'avant-arc. Dans toutes les expériences, de la lizardite et de la lizardite albumineuse ont été formées, sauf à 18 kbar et 580°C dans le système olivine-orthopyroxène, où de l'antigorite a été formée parce que les réactions obéissaient généralement à une loi de vitesse contrôlée par l'interface. A 400°C, où la lizardite se développe, les réactions sont contrôlées par le transport.

Récemment, Huang et al. 2017 a mis en évidence que la diminution de la teneur en chlore dans les minéraux de serpentine avec l'augmentation des pressions peut être liée à une augmentation de la teneur en SiO_2 et à une diminution de la teneur en FeO. Ensuite, Huang et al. 2020 a montré que les taux de serpentisation augmentent fortement avec la pression, avec 19% de l'étendue de la réaction atteinte en 20 jours pour des expériences à 500°C et 3,0 kbar pour des tailles de grains d'olivine inférieures à $30\mu\text{m}$, ce qui a augmenté à 96% à 20 kbar sur la même période et la même température (Figure 8.21). Grâce à des calculs thermodynamiques, ils montrent également que l'énergie de Gibbs pendant la serpentisation de l'olivine diminue avec l'augmentation de la pression. Les travaux futurs pourraient être développés pour mieux comprendre les systèmes naturels, en particulier la stabilité et la croissance des différentes espèces de serpentine.

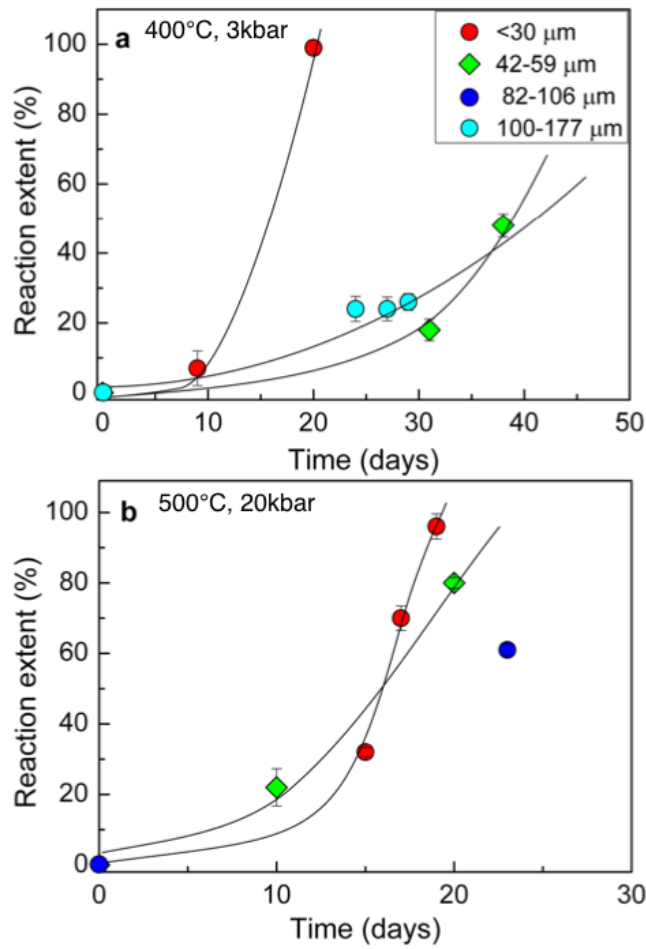


FIGURE 8.21 – Vitesse de réaction de la serpentinitisation (%) en fonction de la taille de grain initiale et de l'avancement de la réaction en jours, pression de 3kbar (a) et 20 kbar (b) Figure issue de Huang et al. 2020.

Rapports fluide/roche

L'influence du rapport eau/roche sur la serpentinisation a été peu étudiée expérimentalement et numériquement, alors qu'il s'agit d'un paramètre clé des circulations hydrothermales ayant un impact sur la formation des dépôts minéraux (par exemple, Nast and Williams-Jones 1991).

Janecky and Seyfried 1986 a mené des expériences de serpentinisation en faisant interagir de la péridotite naturelle avec de l'eau de mer standard IAPSO dans une cellule de réaction flexible Au/Ti à 200 °C et 300 °C et des rapports eau-roche de 10 et 30. Dans ces expériences, ils observent des assemblages similaires à des rapports eau/roche de 10 et 30 mais dans des proportions différentes. En particulier, dans l'expérience à un rapport eau/roche de 10, la solution approche la saturation avec l'enstatite et l'olivine, tandis que des quantités plus faibles d'enstatite sont observées dans l'expérience à un rapport eau/roche de 30.

Dans l'étude numérique de Klein et al. 2013, la réaction de serpentinisation a été modélisée en fonction de trois rapports eau-roche : 0,5, 1 et 10 (Figure 8.22). Leurs résultats ne suggèrent aucune variation dans les assemblages minéraux pour la serpentinisation de l'olivine mais de légères variations dans les proportions de minéraux secondaires en accord avec les résultats expérimentaux de Janecky and Seyfried 1986. Leurs résultats suggèrent également que la production d'hydrogène est fortement influencée par la quantité d'eau. Lorsque les rapports w/r sont faibles, la quantité d'hydrogène est concentrée dans un petit volume de fluide en interaction. En revanche, lorsque le rapport w/r est élevé, l'hydrogène est dilué dans un plus grand volume de fluide, les conditions sont donc moins réductrices et la production d'hydrogène est moindre.

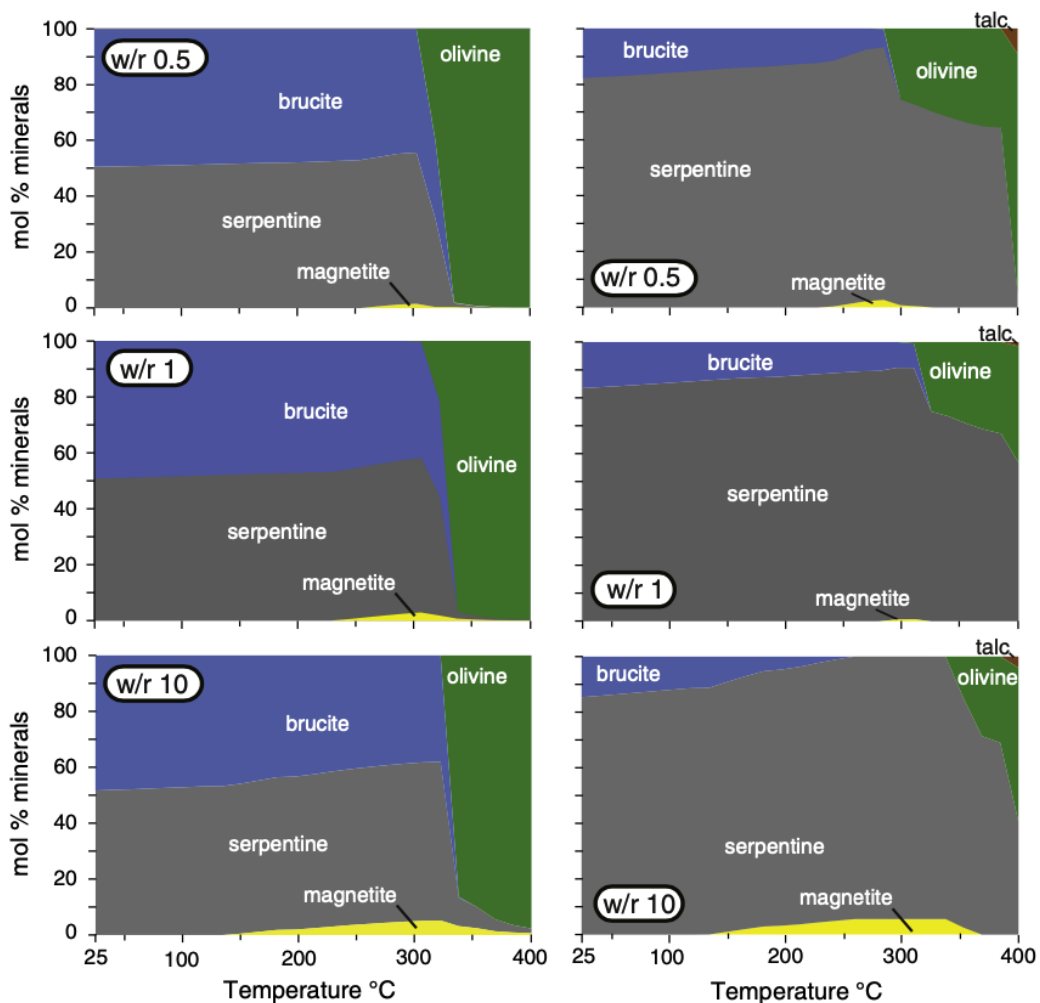


FIGURE 8.22 – Assemblages minéraux prédicts pour la serpentinisation de l’olivine et de l’harzburgite sans clinopyroxène en fonction de la température et des rapports eau-roche à partir de Klein et al. 2013.

Taille de grains initiale

Plusieurs études ont porté sur les effets de la taille initiale des grains sur les taux de serpentinitisation. Les premières expériences de serpentinitisation réalisées par Martin and Fyfe 1970, dans lesquelles les auteurs ont montré que pour des expériences de serpentinitisation à 250°C pendant 3 semaines, la quantité de serpentine produite pour une augmentation de la taille initiale des grains de 50µm à 150µm diminue de 25% à 0%. Plus récemment, Lafay et al. 2012 a fait la même observation et a déterminé des taux de serpentinitisation à 200°C variant de $3,6 \times 10^{-6} s^{-1}$ pour les grains d'olivine inférieurs à 30µm à $1,4 \times 10^{-7} s^{-1}$ pour les grains d'olivine de 56-150µm. Malvoisin et al. 2012a a montré que 80

Ces études ont permis de mettre en évidence l'importance de la porosité et de la surface réactive sur la cinétique de serpentinitisation et le développement d'espèces et de textures secondaires de serpentine. Ces résultats ont permis de mieux estimer le moment de la réaction de serpentinitisation et la durée de vie des systèmes hydrothermaux naturels.

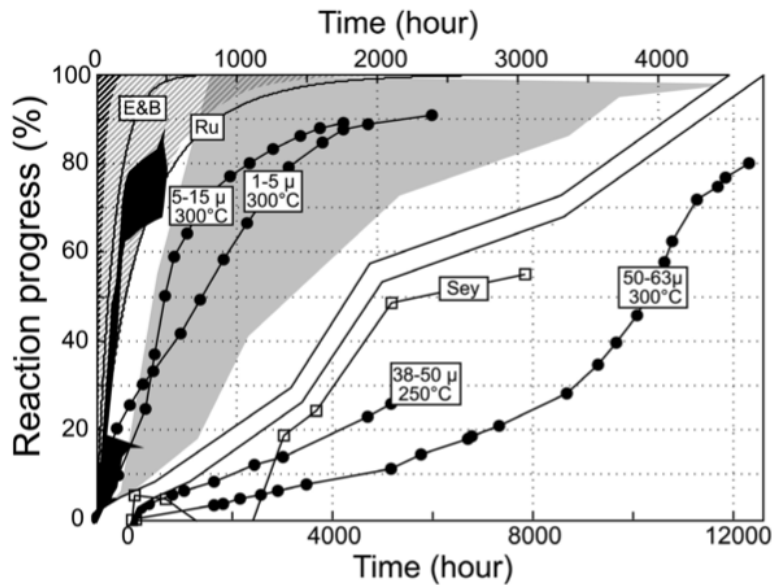


FIGURE 8.23 – Résumé des taux de serpentinitisation tirés de la littérature et de l'étude du Malvoisin et al. 2012a en fonction de la taille initiale des grains et de la température. Figure de Malvoisin et al. 2012a.

Composition du protolithé

Allen and Seyfried Jr 2003 a étudié expérimentalement différents protolithes afin de mieux évaluer l'altération et le transfert de masse dans les systèmes hydrothermaux ultramafiques des dorsales médio-océaniques. Quatre expériences ont été menées en faisant interagir de l'olivine, de l'orthopyroxène et du clinopyroxène individuellement et en combinaisons (y compris orthopyroxène/clinopyroxène 60). Dans ces conditions, les pyroxènes sont plus réactifs que l'olivine et produisent des concentrations dissoutes élevées de SiO₂, Ca et H₂, ce qui entraîne la production de fluides à faible pH (~4.90-5.30). Les fluides résultant du mélange olivine/pyroxènes sont similaires à ceux produits par la seule réaction des pyroxènes.

L'étude expérimentale de Huang et al. 2017 s'est concentrée sur la production d'oxyde de fer pendant la serpentinitisation de la péridotite et en particulier sur l'influence du pyroxène. Ils ont mené des expériences de serpentinitisation à 311 °C et 3 kbar dans des capsules d'or sur de l'orthopyroxène naturel, de l'olivine et de la péridotite. Ils ont observé que l'oxyde de fer se formait de préférence après la serpentinitisation de l'olivine et que le pyroxène de la péridotite gagnait du Fe de l'olivine pendant le processus de serpentinitisation, ce qui pourrait diminuer la production d'oxyde de fer comme la magnétite process, which may decrease the production of iron oxide like magnetite.

Klein et al. 2009 élevée que dans les expériences sur l'olivine pure. Ces modèles numériques ont également mis en évidence que les produits minéraux secondaires changent en fonction du protolithé utilisé, conformément aux résultats expérimentaux de Allen and Seyfried Jr 2003. La serpentinitisation d'un protolithé d'olivine pure produit principalement de la serpentine avec une quantité mineure de brucite et de magnétite, conformément à ce qui est observé pour la serpentinitisation de la dunite. En revanche, la serpentinitisation d'un protolithé qui intègre une quantité significative de pyroxène (typiquement harzburgite), libère de la silice qui peut conduire à la production de phases minérales supplémentaires comme le talc, la trémolite en fonction de la température.

Par la suite, Klein et al. 2013 a réalisé une modélisation thermodynamique pour examiner les assemblages minéraux, la composition minérale des produits secondaires et la composition du fluide résultant de 21 compositions différentes de roches ultramafiques et de 10 compositions distinctes d'olivine entre 25 °C et 400 °C à 50 MPa. Leur modélisation thermodynamique montre des différences systématiques entre la serpentinitisation de la péridotite et de la pyroxénite, telles que la serpentinitisation de la

péridotite produit de la serpentine pauvre en Fe, de la brucite riche en Fe à une température inférieure à 320 °C et de la magnétite à des températures supérieures à 200 °C. Alors qu'aucune magnétite n'a été générée et que de la serpentine riche en Fe et du talc se sont formés lors de la serpentinisation de la pyroxénite (Figure 8.24). L'absence de magnétite résulte principalement de la partition du fer dans la serpentine. La proportion d'hydrogène libéré est systématiquement plus élevée lors de la serpentinisation de la péridotite et du protolith riche en olivine, car la production de fer ferrique dans les minéraux secondaires est plus importante.

Aujourd'hui, il est clair que la nature du protolith utilisé dans les expériences de serpentinisation affecte fortement la composition des produits solides et des fluides qui en résultent. D'autres travaux sont nécessaires pour mieux comprendre la composition des fluides observés dans les systèmes hydrothermaux des fonds marins et la composition des produits minéraux secondaires.

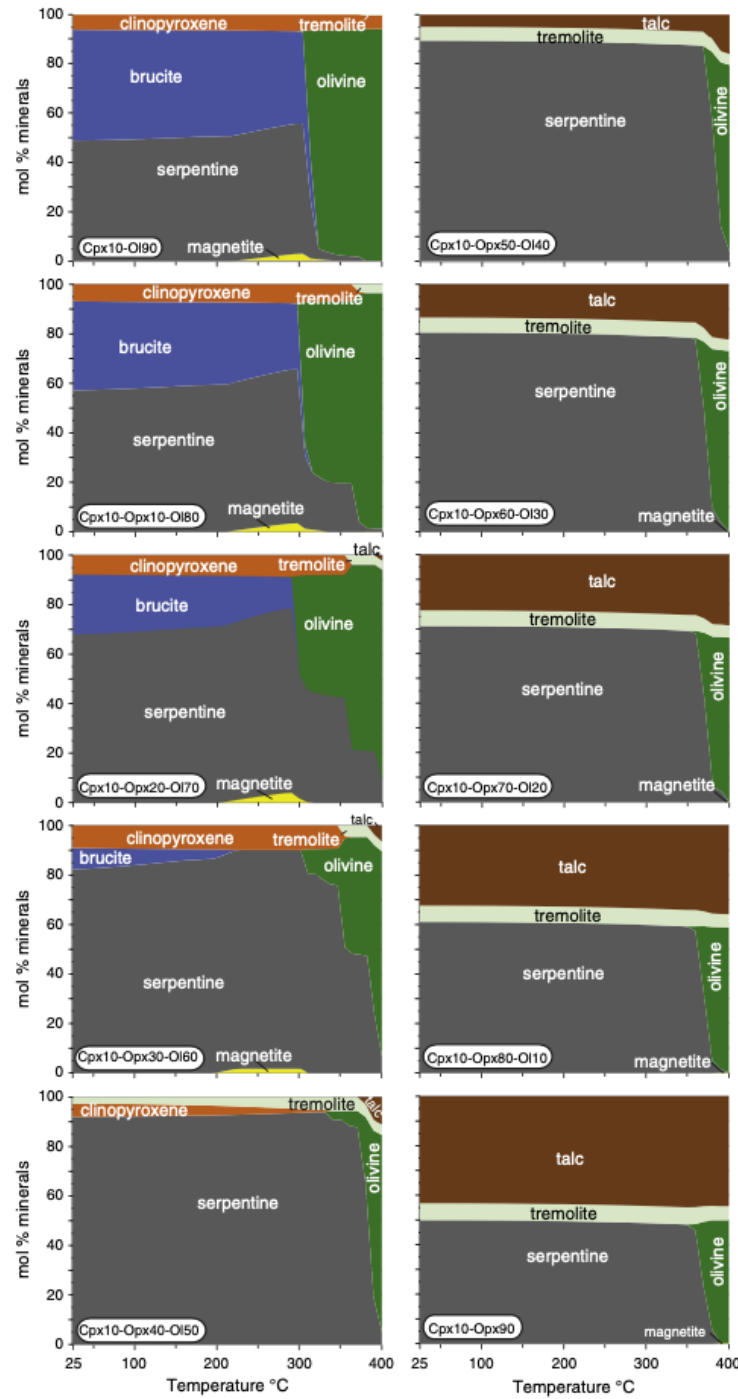


FIGURE 8.24 – Assemblage minéral pour la serpentinitisation de péridotite et de pyroxénite, Figure deKlein et al. 2013.

Composition du fluide initial

Sur la base d'expériences de serpentinitisation, Lafay et al. 2012 a proposé que les solutions alcalines augmentent les taux de serpentinitisation. Par la suite, Pens et al. 2016 a suggéré que la présence d'aluminium dans le fluide affecte la vitesse de serpentinitisation de l'olivine et de l'orthopyroxène, avec des vitesses de serpentinitisation plus rapides de l'olivine en présence d'aluminium.

Récemment, une importance particulière a été accordée à l'influence de la salinité du fluide pendant la serpentinitisation. Lamadrid et al. 2017 a montré que les taux de serpentinitisation de l'olivine sont fortement contrôlés par la salinité du fluide, qui diminue de 1 à 2 ordres de grandeur avec l'augmentation de la salinité du fluide de 1 wt% à 10 wt% NaCl. Huang et al. 2018, 2017 a suggéré que le chlore est hébergé dans un site structurellement lié à la serpentine. La proportion de chlore intégrée dans les minéraux de serpentine dépend fortement de la mobilité du fer, de l'aluminium et de la silice. Ils ont proposé que le chlore soit nécessaire à la redistribution des cations pendant la serpentinitisation. Lamadrid et al. 2021 a démontré que l'augmentation de la salinité du fluide et la diminution associée de l'activité de l'eau ralentissent la réaction de serpentinitisation (Figure 1.25). Ils ont également démontré que la présence de cations Mg^{2+} dans le fluide peut favoriser la dissolution congruente de l'olivine. Ces auteurs ont proposé que les différences dans les taux de serpentinitisation déterminés expérimentalement résultent de l'utilisation de différentes compositions de fluides de départ.

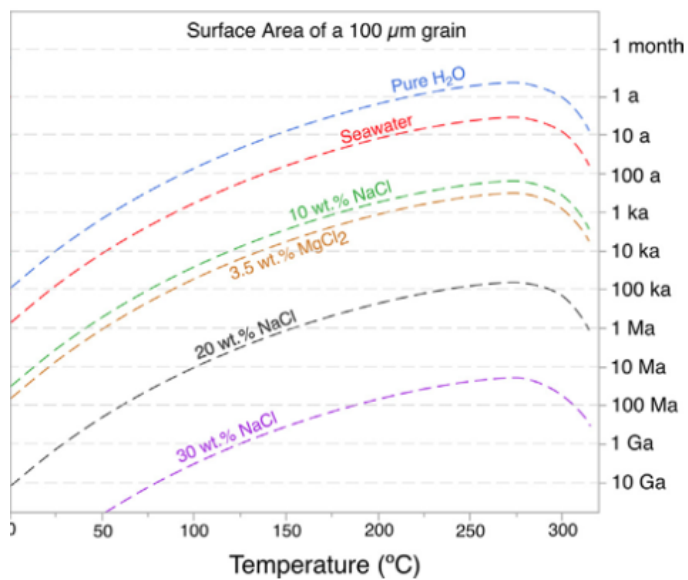


FIGURE 8.25 – Dépendance des taux de serpentinitisation par rapport à la chimie des fluides, figure tirée de Lamadrid et al. 2021.

8.5 Les outils géochimiques

Depuis la découverte de systèmes hydrothermaux sur les fonds marins (par exemple, Rona 1984), de nombreuses études ont été réalisées dans le but de i) caractériser la source des fluides conduisant à la formation de ces systèmes hydrothermaux et des gisements de métaux associés, et ii) déterminer à quelles températures les interactions fluides-roches se sont produites. Les isotopes radiogéniques (par exemple Sr, Nd, Hf) et stables (par exemple C, O, S, B, Li) sont des traceurs puissants et complets des interactions fluides-roches dans les domaines océaniques (par exemple Mcculloch et al. 1980 ; Albarede et al. 1981 ; Shanks et al. 1995 ; Vils et al. 2008). Les isotopes stables ont également permis de déterminer la température des interactions fluide-roche (par exemple, Wenner and Taylor 1971).

8.5.1 Les traceurs géochimiques

Les isotopes radiogéniques

Les principaux réservoirs hydrothermaux, notamment l'eau de mer, le manteau, la croûte océanique et la croûte continentale, ont des teneurs en Sr et des signatures isotopiques différentes. Par exemple, l'eau de mer contient 8 ppm de Sr avec $^{87}\text{Sr}/^{86}\text{Sr} = 0,70917$ tandis que le manteau (DMM) contient 6 ppm de Sr et a $^{87}\text{Sr}/^{86}\text{Sr} = 0,7022$ (Veizer and Compston 1974 ; Salters and Stracke 2004). Par conséquent, les isotopes du Sr ont été largement appliqués aux systèmes hydrothermaux et aux systèmes ophiolitiques afin de déterminer les sources de fluides, de quantifier les interactions fluide-roche ou d'estimer la profondeur de pénétration des fluides dans les ophiolites (par exemple, Spooner and Fyfe 1973), *Spooner et al. 1977; Albarede et al. 1981; Staudige et al. 1995; Bachet et al. 2004; Delacour et al. 2004*, car le Nd est essentiellement immobile et n'est pas affecté par les faibles rapports fluides/roches (par exemple, Snow et al. 1994 ; Delacour et al. 2008b). Cependant, les isotopes du Nd sont principalement utilisés pour déterminer les sources magmatiques des basaltes ou des gabbros (par exemple, Schaltegger et al. 2002).

Les isotopes stables

Les isotopes stables peuvent également être utilisés comme traceurs des interactions fluide-roche dans la plupart des contextes tectoniques. En effet, à l'instar des isotopes radiogéniques du Sr, les isotopes stables ont des signatures isotopiques très différentes dans la plupart des réservoirs de la Terre, y compris l'eau de mer, les croûtes continentale et océanique ou le manteau (Figure 8.26 ; Shanks et al. 1995). Par conséquent, les isotopes stables comme l'oxygène ont été particulièrement utilisés dans les domaines océaniques (par exemple, Agrinier et al. 1995 ; Shanks et al. 1995 ; Früh-Green et al. 1996) et dans les contextes ophiolitiques des serpentinites (par exemple, ? ; Shanks et al. 1995), Wenner and Taylor Jr 1973 ; Früh-Green et al. 1990 ; Ulrich et al. 2020), des roches carbonatées (Weissert and Bernoulli 1984) pour déterminer les rapports fluide/roche et la source des fluides. Cependant, l'importance des isotopes de l'oxygène dans l'ophicalcite des Alpes est débattue. Bernoulli and Weissert 2021 a suggéré que les compositions isotopiques de l'oxygène des ophicalcites océaniques du Jurassique ont été entièrement rééquilibrées pendant l'orogenèse alpine. En revanche, Coltat et al. 2021 a soutenu que la signature isotopique de l'oxygène d'une exposition spécifique dans la nappe de Platta (Falotta) n'a pas été affectée par la surimpression alpine et a enregistré la signature isotopique acquise pendant l'hydrothermalisme océanique au cours de l'orogenèse jurassique.

Les isotopes du soufre ont été utilisés pour déterminer les conditions redox et les variations des flux de fluides, dans les domaines océaniques (par exemple, Delacour et al. 2008a) et les ophiolites (par exemple, Schwarzenbach et al. 2012). Les isotopes du soufre permettent également de déterminer la source des minéraux sulfurés dans les gisements de sulfures massifs (par exemple, Garuti et al. 2008). Des valeurs élevées de $\delta^{34}\text{S} \sim 8,9\text{\textperthousand}$ ont été mesurées dans les basaltes où le soufre provient de la lixiviation des sources de sulfures magmatiques et de la réduction inorganique de l'eau de mer. En revanche, les serpentinites formées près du plancher océanique présentent un faible ^{34}S (2,5-5,8 ‰), ce qui suggère des conditions plus oxydantes en réponse à un processus bactérien de réduction des sulfates. Plus récemment, les isotopes stables du fer, du zinc et du cuivre ont montré leur potentiel pour la détermination de la source des métaux et le suivi de la mobilité des métaux dans les systèmes hydrothermaux (par exemple, Rouxel et al. 2004a,b ; Debret et al. 2018). Les isotopes du bore sont également des traceurs intéressants des interactions fluides-roches, en particulier entre l'hydrosphère et les réservoirs lithosphériques. Le bore a des concentrations et une signature isotopique suffisamment

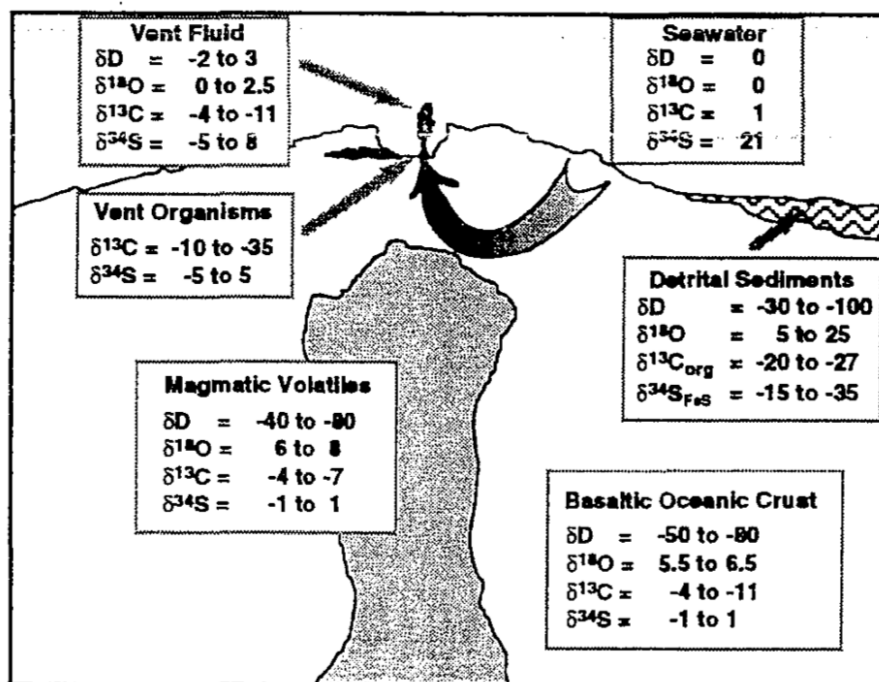


FIGURE 8.26 – Représentation schématique des signatures isotopiques en D, C, O et S des différents réservoirs du système hydrothermal de la dorsale océanique moyenne. Figure issue de Shanks et al. 1995.

différentes dans ces réservoirs pour être utilisé comme traceur efficace des sources. Le bore dans le réservoir d'eau de mer est d'environ $\sim 4,5$ ppm Spivack et al. 1987 avec un rapport isotopique $\delta^{11}\text{B} = +39,6\text{\textperthousand}$ Foster et al. 2010. Dans le réservoir mantellique, y compris le manteau MORB appauvri (DMM), la concentration en bore est faible, avec une moyenne de 0,06 ppm Salters and Stracke 2004 et un rapport isotopique $\delta^{11}\text{B} = -7,1\text{\textperthousand}$ Marshall et al. 2017. Au cours des deux dernières décennies, plusieurs études ont utilisé les isotopes du Li comme traceurs efficaces des interactions fluide-roche, car, à l'instar d'autres isotopes stables, les concentrations de Li et la signature isotopique des réservoirs terrestres sont différentes. Dans le DMM, les concentrations de Li sont élevées ($\pm 1,20$ ppm Marschall et al. 2017), par rapport à l'eau de mer ($\pm 0,18$ ppm Li 1982). L'eau de mer a un $\delta^7\text{Li} = +30,8\text{\textperthousand}$ plus élevé que le DMM $\delta^7\text{Li} = +3,4\text{\textperthousand}$ Tomascak et al. 2008. Cependant, des travaux récents ont montré que les isotopes du Li ne permettaient pas de retracer les interactions fluide-roche, car un fort fractionnement diffusif se produisait dans les systèmes magmatiques et métamorphiques. Cependant, le fractionnement lié à la diffusivité peut être utilisé comme géochronomètre potentiel des échelles de temps des processus géologiques. Liu et al. 2020 ont suggéré que les variations élémentaires et isotopiques enregistrées par l'olivine, le clinopyroxène et l'orthopyroxène des péridotites abyssales mettaient en évidence un processus en deux étapes, avec i) une diffusion de Li à haute température entre le minéral et la matière fondue pendant l'imprégnation de la matière fondu, et ii) une diffusion de Li à basse température entre le minéral et le fluide pendant la dissolution et la serpentisation.

Les isotopes stables ne peuvent être utilisés comme traceurs que si aucun fractionnement ne s'est produit. Le fractionnement correspond au partage des isotopes entre les phases (par exemple, aqueuse ou solide). Les circulations hydrothermales dépendent de nombreux facteurs, notamment la température, l'oxydo-réduction et le pH, qui peuvent influer sur le fractionnement des isotopes. Cela peut avoir une incidence sur l'interprétation des isotopes stables en tant que traceurs des sources. Dans ce cas, il peut être plus pertinent d'utiliser les isotopes radiogéniques, comme le Sr, qui ne sont pas affectés par le fractionnement isotopique. Cependant, le fractionnement isotopique conduit à utiliser les isotopes stables pour déterminer les conditions, notamment la température ou le pH, de ces interactions fluide-roche. Par conséquent, plusieurs géothermomètres ont été développés sur la base du fractionnement de ces isotopes.

8.5.2 Géothermomètres

Actuellement, la température de serpentinitisation est estimée sur la base de deux géothermomètres qui n'ont pas été calibrés sur la serpentinite. Le premier a été développé par Wenner and Taylor 1971 et est basé sur le fractionnement des isotopes de l'oxygène ($^{18}\text{O}/^{16}\text{O}$) entre les oxydes de Fe-Ti et la chlorite coexistants dans les schistes pélitiques de faible qualité. Les résultats ont ensuite été extrapolés sur le couple serpentine-magnétite de la serpentinite, bien que son application à un tel système n'ait jamais été clairement démontrée jusqu'à présent. Le second géothermomètre a été proposé plus récemment par Saccoccia et al. 2009. Cette étude a porté sur le fractionnement des isotopes de l'oxygène et de l'hydrogène entre la serpentine et l'eau au cours de la recristallisation de la lizardite en chrysotile dans la plage de 250-450°C. Cependant, des températures plus basses de serpentinitisation sont attendues dans les marges passives (<200°C ; Agrinier et al. 1995 ; Skelton and Valley 2000). Le développement d'un nouveau géothermomètre est nécessaire pour une détermination plus précise de la température de serpentinitisation. Bien que jusqu'à présent ce géothermomètre ait été largement utilisé pour déterminer la température des interactions fluide-roche, de la serpentinitisation et de la carbonatation dans les systèmes hydrothermaux (par ex, Hess Deep Früh-Green et al. 1996 ; Iberia Abyssal plain Skelton and Valley 2000) et les domaines ophiolitiques (par exemple, Western Alps Lafay et al. 2017; Eastern Central Alps Burkhard and O'Neil 1988 ; Incerpi et al. 2020).

La modélisation a indiqué que la teneur en bore et les isotopes dans les serpentinites dépendent de la température et du pH. Récemment, la géothermométrie du bore basée sur le fractionnement des isotopes entre la muscovite et la tourmaline a été calibrée expérimentalement par Codeço et al. 2019 dans le but d'étudier les conditions de minéralisation et l'évolution des fluides associés aux systèmes hydrothermaux magmatiques. La muscovite et la tourmaline coexistent dans de nombreux gisements de minéraux hydrothermaux et dans les granites ou pegmatites associés. La différence entre les rapports $\delta^{11}\text{B}/\delta^{10}\text{B}$ entre ces minéraux coexistants, exprimée par $\Delta^{11}\text{B}_{mica-tourmaline} = \delta^{11}\text{B}_{mica}-\delta^{11}\text{B}_{tourmaline}$, est thermo-dépendante. Millot et al. 2010 a mené des expériences sur l'eau de mer et le basalte et a montré que l'échange isotopique du lithium dépendait fortement de la température et qu'un fractionnement important se produisait pendant la formation des minéraux secondaires. Leurs résultats soulignent également que les isotopes du lithium ont permis de caractériser l'origine des eaux géothermiques et la nature de leurs roches réservoirs.

8.6 Approche de la thèse

Dans cette thèse, nous avons étudié le processus de serpentinitisation pendant l'exhumation du manteau sur les marges passives riftées pauvres en magma. En particulier, nous avons cherché à :

- caractériser les différentes étapes de l'interaction fluide-roche pendant l'exhumation du manteau
- estimer les conditions de la serpentinitisation (température, profondeur et rapports fluide/roche)
- déterminer les sources des fluides de serpentinitisation
- comprendre comment ces fluides interagissent avec les roches du manteau et caractériser leur évolution
- Caractériser la mobilisation des métaux de transition et la formation de dépôts métalliques dans le système hydrothermal.

Toutes ces questions ont été abordées en appliquant deux approches complémentaires :

La première consiste en l'étude de péridotites serpentinitisées échantillonnées dans des ophiolites alpines, qui sont des vestiges d'une ancienne transition océan-continent (OCT) de l'océan Téthys alpin qui a séparé les marges européenne et adriatique au Jurassique. Les trois nappes de Platta, Tasna et Totalp, toutes situées dans le sud-est de la Suisse, ont été échantillonnées dans le cadre de cette thèse. Ces nappes ont été principalement préservées de la surimpression métamorphique alpine (par exemple, Froitzheim and Rubatto 1998), conservant ainsi les contacts liés au rift pré-alpin entre le manteau sous-continentale et les sédiments syn-rift particulièrement bien préservés Manatschal 2004. Dans cette partie, nous avons combiné des études pétrologiques, minéralogiques et géochimiques sur les serpentinites dans le but de déterminer les différentes étapes de l'exhumation du manteau et leurs conditions (température, rapports fluide/roche, pression) enregistrées par les différents événements de serpentinitisation. En parallèle, une étude complémentaire a été menée dans le but d'identifier les sources de fluides impliqués dans la formation des silicates Fe-Ca formés dans les gisements de métaux d'un système minéralisé jurassique encaissé dans les serpentinites décrites dans la nappe de Platta Coltat et al. 2019. Ici, nous avons combiné des approches pétrologiques et isotopiques. Nous avons mesuré les compositions isotopiques en Sr des silicates Fe-Ca et des contributeurs potentiels (c'est-à-dire les roches métasomatiques : serpentinites, gabbros et basaltes altérés).

La deuxième approche de cette thèse consiste à reproduire expérimentalement la réaction de serpentinisation, afin i) d'identifier et de quantifier les flux de masse lors de la serpentinisation dans le but d'estimer la mobilisation potentielle des métaux de transition lors de l'altération hydrothermale du manteau et de la formation des U-VMS ; ii) déterminer le fractionnement isotopique du bore entre la serpentine et le fluide et entre la serpentine et la magnétite, afin de développer un nouveau géothermomètre de serpentinisation, dans le but d'être appliqué sur des échantillons naturels, et de déterminer la température de serpentinisation. En effet, le bore étant un élément mobile dans les fluides, appauvri dans le manteau mais enrichi dans l'eau de mer, il est donc un traceur sensible des interactions fluides-roches entre ces deux réservoirs. Certaines études ont démontré que les serpentinites océaniques sont fortement enrichies en bore, contrairement aux péridotites du manteau appauvri (par exemple, Vils et al. 2009). Nous avons mené des expériences de serpentinisation en faisant interagir des péridotites fraîches, dont la lherzolite et la harzburgite, avec de l'eau de mer naturelle dans un sac en titane lui-même placé dans un autoclave. Ce dispositif expérimental permet de contrôler précisément la température et la pression des expériences et d'échantillonner le fluide pendant les expériences. Ces expériences ont été menées à 5 températures : 225°C, 260°C, 280°C, 300°C and 325°C bars et à de faibles rapports fluide/roche compris entre 1,6 et 2,1, favorisant la formation de magnétite nécessaire au développement d'un nouveau géothermomètre.

Bibliographie

- Agrinier, P., Hékinian, R., Bideau, D., and Javoy, M. (1995). O and h stable isotope compositions of oceanic crust and upper mantle rocks exposed in the hess deep near the galapagos triple junction. *Earth and Planetary Science Letters*, 136(3-4):183–196.
- Albarede, F., Michard, A., Minster, J. F., and Michard, G. (1981). 87sr/86sr ratios in hydrothermal waters and deposits from the east pacific rise at 21°N. *Earth and Planetary Science Letters*, 55:229–236.
- Albers, E., Bach, W., Pérez-Gussinyé, M., McCammon, C., and Frederichs, T. (2021). Serpentinization-driven h₂ production from continental break-up to mid-ocean ridge spreading : unexpected high rates at the west iberia margin. *Frontiers in Earth Science*, 9.
- Allen, D. E. and Seyfried Jr, W. (2003). Compositional controls on vent fluids from ultramafic-hosted hydrothermal systems at mid-ocean ridges : An experimental study at 400 c, 500 bars. *Geochimica et Cosmochimica Acta*, 67(8):1531–1542.
- Allen, D. E. and Seyfried Jr, W. (2005). Ree controls in ultramafic hosted mor hydrothermal systems : an experimental study at elevated temperature and pressure. *Geochimica et Cosmochimica Acta*, 69(3):675–683.
- Alt, J. C., Schwarzenbach, E. M., Früh-Green, G. L., Shanks III, W. C., Bernasconi, S. M., Garrido, C. J., Crispini, L., Gaggero, L., Padrón-Navarta, J. A., and Marchesi, C. (2013). The role of serpentinites in cycling of carbon and sulfur : Seafloor serpentinization and subduction metamorphism. *Lithos*, 178:40–54.
- Alt, J. C. and Shanks III, W. C. (2003). Serpentinization of abyssal peridotites from the mark area, mid-atlantic ridge : sulfur geochemistry and reaction modeling. *Geochimica et cosmochimica Acta*, 67(4):641–653.
- Amann, M., Ulrich, M., Manatschal, G., Pelt, E., Epin, M.-e., Autin, J., and Sauter, D. (2020a). Geochemical characteristics of basalts related to incipient oceanization : The example from the alpine-tethys ocs. *Terra Nova*, 32(1):75–88.
- Amann, M., Ulrich, M., Manatschal, G., Pelt, E., Epin, M. E., Autin, J., and Sauter, D. (2020b). Geochemical characteristics of basalts related to incipient oceanization : The example from the alpine-tethys ocs. *Terra Nova*, 32:75–88.
- Andreani, M., Baronnet, A., Boullier, A.-M., and Gratier, J.-P. (2004). A microstructural study of a “crack-seal” type serpentine vein using sem and tem techniques. *European Journal of Mineralogy*, 16(4):585–595.
- Andreani, M., Grauby, O., Baronnet, A., and Muñoz, M. (2008). Occurrence, composition and growth of polyhedral serpentine. *European Journal of Mineralogy*, 20(2):159–171.

- Andreani, M., Mevel, C., Boullier, A. M., and Escartin, J. (2007). Dynamic control on serpentine crystallization in veins : Constraints on hydration processes in oceanic peridotites. *Geochemistry, Geophysics, Geosystems*, 8.
- Auzende, A.-L., Daniel, I., Reynard, B., Lemaire, C., and Guyot, F. (2004). High-pressure behaviour of serpentine minerals : a raman spectroscopic study. *Physics and Chemistry of Minerals*, 31(5):269–277.
- Bach, W., Alt, J. C., Niu, Y., Humphris, S. E., Erzinger, J., and Dick, H. J. (2001). The geochemical consequences of late-stage low-grade alteration of lower ocean crust at the sw indian ridge : Results from odp hole 735b (leg 176). *Geochimica et Cosmochimica Acta*, 65(19):3267–3287.
- Bach, W., Garrido, C. J., Paulick, H., Harvey, J., and Rosner, M. (2004). Seawater-peridotite interactions : First insights from ODP leg 209, MAR 15°N. *Geochemistry, Geophysics, Geosystems*, 5.
- Barnes, I. and O’NEIL, J. R. (1969). The relationship between fluids in some fresh alpine-type ultramafics and possible modern serpentization, western united states. *Geological Society of America Bulletin*, 80(10):1947–1960.
- Baronnet, A. and Devouard, B. (1996). Topology and crystal growth of natural chrysotile and polygonal serpentine. *Journal of Crystal Growth*, 166(1-4):952–960.
- Bayrakci, G., Minshull, T., Sawyer, D. S., Reston, T. J., Klaeschen, D., Papenberg, C., Ranero, C., Bull, J., Davy, R., Shillington, D., et al. (2016). Fault-controlled hydration of the upper mantle during continental rifting. *Nature Geoscience*, 9(5):384–388.
- Bernoulli, D. and Weissert, H. (1985). Sedimentary fabrics in alpine ophicalcites, south pennine arosa zone, switzerland. *Geology*, 13(11):755–758.
- Bernoulli, D. and Weissert, H. (2021). Oxygen isotopes in ophicalcites : an ever-lasting controversy ? *International Journal of Earth Sciences*, 110(1):1–8.
- Boschi, C., Dini, A., Früh-Green, G. L., and Kelley, D. S. (2008). Isotopic and element exchange during serpentization and metasomatism at the atlantis massif (mar 30 n) : insights from b and sr isotope data. *Geochimica et Cosmochimica Acta*, 72(7):1801–1823.
- Bousquet, R., Oberhänsli, R., Goffé, B., Wiederkehr, M., Koller, F., Schmid, S. M., Schuster, R., Engi, M., Berger, A., and Martinotti, G. (2008). Metamorphism of metasediments at the scale of an orogen : a key to the tertiary geodynamic evolution of the alps. *Geological Society, London, Special Publications*, 298(1):393–411.
- Burkhard, D. J. and O’Neil, J. R. (1988). Contrasting serpentization processes in the eastern central alps. *Contributions to Mineralogy and Petrology*, 99(4):498–506.
- Capitani, G. and Mellini, M. (2004). The modulated crystal structure of antigorite : The m= 17 polysome. *American Mineralogist*, 89(1):147–158.
- Caruso, L. J. and Chernosky, J. (1979). The stability of lizardite. *Can. Mineral*, 17(4):757–769.
- Chalot-Prat, F., Ganne, J., and Lombard, A. (2003). No significant element transfer from the oceanic plate to the mantle wedge during subduction and exhumation of the tethys lithosphere (western alps). *Lithos*, 69(3-4):69–103.
- Codeço, M. S., Weis, P., Trumbull, R. B., Glodny, J., Wiedenbeck, M., and Romer, R. L. (2019). Boron isotope muscovite-tourmaline geothermometry indicates fluid cooling during magmatic-hydrothermal w-sn ore formation. *Economic Geology*, 114(1):153–163.

- Coleman, R. G. (1971). Petrologic and geophysical nature of serpentinites. *Geological Society of America Bulletin*, 82(4):897–918.
- Coltat, R., Boulvais, P., Branquet, Y., Collot, J., Epin, M. E., and Manatschal, G. (2019). Syntectonic carbonation during synmagmatic mantle exhumation at an ocean-continent transition. *Geology*, 47:183–186.
- Coltat, R., Boulvais, P., Branquet, Y., Poujol, M., Gautier, P., and Manatschal, G. (2021). Discussion to “oxygen isotope in ophicalcites : an ever-lasting controversy ?”. *International Journal of Earth Sciences*, 110(3):1117–1121.
- Coltat, R., Boulvais, P., Branquet, Y., Richard, A., Tarantola, A., and Manatschal, G. (2022). Moho carbonation at an ocean-continent transition. *Geology*, 50(3):278–283.
- Compagnoni, R., Cossio, R., and Mellini, M. (2021). Raman anisotropy in serpentine minerals, with a caveat on identification. *Journal of Raman Spectroscopy*, 52(7):1334–1345.
- Debret, B., Beunon, H., Mattielli, N., Andreani, M., da Costa, I. R., and Escartin, J. (2018). Ore component mobility, transport and mineralization at mid-oceanic ridges : A stable isotopes (zn, cu and fe) study of the rainbow massif (mid-atlantic ridge 36°14N). *Earth and Planetary Science Letters*, 503:170–180.
- Delacour, A., Früh-Green, G. L., Bernasconi, S. M., and Kelley, D. S. (2008a). Sulfur in peridotites and gabbros at lost city (30 n, mar) : Implications for hydrothermal alteration and microbial activity during serpentinization. *Geochimica et Cosmochimica Acta*, 72(20):5090–5110.
- Delacour, A., Früh-Green, G. L., Frank, M., Gutjahr, M., and Kelley, D. S. (2008b). Sr-and Nd-isotope geochemistry of the atlantis massif (30 n, mar) : implications for fluid fluxes and lithospheric heterogeneity. *Chemical Geology*, 254(1-2):19–35.
- Deschamps, F., Godard, M., Guillot, S., and Hattori, K. (2013). Geochemistry of subduction zone serpentinites : A review. *Lithos*, 178:96–127.
- Deschamps, F., Guillot, S., Godard, M., Andreani, M., and Hattori, K. (2011). Serpentinites act as sponges for fluid-mobile elements in abyssal and subduction zone environments. *Terra Nova*, 23(3):171–178.
- Deschamps, F., Guillot, S., Godard, M., Chauvel, C., Andreani, M., and Hattori, K. (2010). In situ characterization of serpentinites from forearc mantle wedges : timing of serpentinization and behavior of fluid-mobile elements in subduction zones. *Chemical Geology*, 269(3-4):262–277.
- Desmurs, L., Manatschal, G., and Bernoulli, D. (2001). The Steinmann Trinity revisited : mantle exhumation and magmatism along an ocean-continent transition : the Platta nappe, eastern Switzerland. *Contributions to Mineralogy and Petrology*, 144:365–382.
- Desmurs, L., Müntener, O., and Manatschal, G. (2002). Onset of magmatic accretion within a magma-poor rifted margin : a case study from the Platta ocean-continent transition, eastern Switzerland. *Contributions to Mineralogy and Petrology*, 144(3):365–382.
- Dietrich, V. (1970). *Die Stratigraphie der Platta-Decke : Fazielle Zusammenhänge zwischen Oberpenninikum und Unterostalpin*. Geologisches Institut der Eidg. Technischen Hochschule und der Universität.

- Dietrich, V. J. (1969). *Die Ophiolithe des Oberhalbsteins (Graubünden) und das Ophiolithmaterial der ostschweizerischen Molasseablagerungen : ein petrographischer Vergleich.* PhD thesis, ETH Zurich.
- Dilek, Y., Coulton, A., Hurst, S. D., et al. (1997). Serpentinization and hydrothermal veining in peridotites at site 920 in the mark area. In *Proceedings-Ocean Drilling Program Scientific Results*, pages 35–60. National Science Foundation.
- Epin, M.-E. and Manatschal, G. (2018). Three-dimensional architecture, structural evolution, and role of inheritance controlling detachment faulting at a hyperextended distal margin : The example of the err detachment system (SE Switzerland). *Tectonics*, 37(12):4494–4514.
- Epin, M. E., Manatschal, G., Amman, M., Ribes, C., Clausse, A., Guffon, T., and Lescanne, M. (2019). Polyphase tectono-magmatic evolution during mantle exhumation in an ultra-distal, magma-poor rift domain : example of the fossil platta ophiolite, se switzerland. *International Journal of Earth Sciences*, 108:2443–2467.
- Escario, S., Godard, M., Gouze, P., and Leprovost, R. (2018). Experimental study of the effects of solute transport on reaction paths during incipient serpentinization. *Lithos*, 323:191–207.
- Escartin, J., Hirth, G., and Evans, B. (1997). Effects of serpentinization on the lithospheric strength and the style of normal faulting at slow-spreading ridges. *Earth and Planetary Science Letters*, 151(3-4):181–189.
- Escartin, J., Hirth, G., and Evans, B. (2001). Strength of slightly serpentinized peridotites : Implications for the tectonics of oceanic lithosphere. *Geology*, 29(11):1023–1026.
- Etiope, G. (2017). Abiotic methane in continental serpentinization sites : an overview. *Procedia Earth and Planetary Science*, 17:9–12.
- Evans, B. W. (2004). The serpentinite multisystem revisited : chrysotile is metastable. *International Geology Review*, 46(6):479–506.
- Evans, B. W. et al. (1976). Stability of chrysotile and antigorite in the serpentinite multisystem. *Schweiz. Mineral. Petrol. Mitt.*, 56(1):79–93.
- Florineth, D. and Froitzheim, N. (1994). Transition from continental to oceanic basement in the tasna nappe : evidence for early cretaceous opening of the valais ocean. *Schweizerische Mineralogische und Petrographische Mitteilungen*, 74(3):437 ?448.
- Foster, G., Pogge von Strandmann, P. A., and Rae, J. (2010). Boron and magnesium isotopic composition of seawater. *Geochemistry, Geophysics, Geosystems*, 11(8).
- Fouquet, Y., Cambon, P., Etoubleau, J., Charlou, J. L., Ondreas, H., Barriga, F. J., Cherkašov, G., Semkova, T., Poroshina, I., Bohn, M., Donval, J. P., Henry, K., Murphy, P., and Rouxel, O. (2013). Geodiversity of hydrothermal processes along the Mid-Atlantic Ridge and ultramafic-hosted mineralization : A new type of oceanic cu-zn-co-au volcanogenic massive sulfide deposit. *Geophysical Monograph Series*, 188:321–367.
- Froitzheim, N. and Manatschal, G. (1996). Kinematics of jurassic rifting, mantle exhumation, and passive-margin formation in the austroalpine and penninic nappes (eastern switzerland). *Geological society of America bulletin*, 108(9):1120–1133.

- Froitzheim, N. and Rubatto, D. (1998). Continental breakup by detachment faulting : field evidence and geochronological constraints (tasna nappe, switzerland). *Terra Nova*, 10(4):171–176.
- Früh-Green, G. L., Connolly, J. A., Plas, A., Kelley, D. S., and Grobety, B. (2004). Serpentinization of oceanic peridotites : implications for geochemical cycles and biological activity. *The subseafloor biosphere at mid-ocean ridges*, 144:119–136.
- Früh-Green, G. L., Plas, A., and Lécuyer, C. (1996). 14. petrologic and stable isotope constraints on hydrothermal alteration and serpentinization of the epr shallow mantle at hess deep (site 895). In *Proceedings of the ocean drilling program, scientific results*, volume 147, pages 255–291.
- Früh-Green, G. L., Weissert, H., and Bernoulli, D. (1990). A multiple fluid history recorded in Alpine ophiolites. *Journal of the Geological Society*, 147(6):959–970.
- Garuti, G., Bartoli, O., Scacchetti, M., and Zaccarini, F. (2008). Volcanic massive sulfide deposits in the northern apennines, italy geological setting and structural styles of volcanic massive sulfi de deposits in the northern apennines (italy) : evidence for seafloor and sub-seafloor hydrothermal activity in unconventional ophiolites of the mesozoic tethys. *Boleten dela Sociedad Geologica Mexicana*, 60:121–145.
- Gillard, M., Autin, J., and Manatschal, G. (2016a). Fault systems at hyper-extended rifted margins and embryonic oceanic crust : Structural style, evolution and relation to magma. *Marine and Petroleum Geology*, 76:51–67.
- Gillard, M., Manatschal, G., and Autin, J. (2016b). How can asymmetric detachment faults generate symmetric ocean continent transitions ? *Terra Nova*, 28(1):27–34.
- Grauby, O., Baronnet, A., Devouard, B., Schoumacker, K., and Demirdjian, L. (1998). The chrysotile-polygonal serpentine-lizardite suite synthesized from a 3mgo-2sio₂-excess h₂o gel. In *The 7th International Symposium on Experimental Mineralogy, Petrology, and Geochemistry, Orléans, Abstracts. Terra Nova, supplement*, volume 1, page 24.
- Groppi, C., Rinaudo, C., Cairo, S., Gastaldi, D., and Compagnoni, R. (2006). Micro-raman spectroscopy for a quick and reliable identification of serpentine minerals from ultramafics. *European Journal of Mineralogy*, 18(3):319–329.
- Guillot, S., Hattori, K. H., and de Sigoyer, J. (2000). Mantle wedge serpentinization and exhumation of eclogites : insights from eastern ladakh, northwest himalaya. *Geology*, 28(3):199–202.
- Guillot, S., Schwartz, S., Reynard, B., Agard, P., and Prigent, C. (2015). Tectonic significance of serpentinites. *Tectonophysics*, 646:1–19.
- Hannington, M., Herzig, P., Stoffers, P., Scholten, J., Botz, R., Garbe-Schönberg, D., Jonasson, I., and Roest, W. (2001). First observations of high-temperature submarine hydrothermal vents and massive anhydrite deposits off the north coast of iceland. *Marine Geology*, 177(3-4):199–220.
- Hannington, M. D., De Ronde, C. E., and Petersen, S. (2005). Sea-floor tectonics and submarine hydrothermal systems. *Society of Economic Geologists*, pages 111–141.
- Hansen, C. T., Meixner, A., Kasemann, S. A., and Bach, W. (2017). New insight on li and b isotope fractionation during serpentinization derived from batch reaction investigations. *Geochimica et Cosmochimica Acta*, 217:51–79.

- Hochscheid, F., Coltat, R., Ulrich, M., Munoz, M., Manatschal, G., and Boulvais, P. (2022). The sr isotope geochemistry of oceanic ultramafic-hosted mineralizations. *Ore Geology Reviews*, page 104824.
- Holm, N. G. and Charlou, J. L. (2001). Initial indications of abiotic formation of hydrocarbons in the rainbow ultramafic hydrothermal system, mid-atlantic ridge. *Earth and Planetary Science Letters*, 191(1-2):1–8.
- Holm, N. G., Oze, C., Mousis, O., Waite, J., and Guillet-Lepoutre, A. (2015). Serpentization and the formation of h₂ and ch₄ on celestial bodies (planets, moons, comets). *Astrobiology*, 15(7):587–600.
- Huang, R., Ding, X., Lin, C.-T., Zhan, W., and Ling, M. (2018). Effect of saline fluids on chlorine incorporation in serpentine. *Solid Earth Sciences*, 3(3):61–66.
- Huang, R., Song, M., Ding, X., Zhu, S., Zhan, W., and Sun, W. (2017). Influence of pyroxene and spinel on the kinetics of peridotite serpentinization. *Journal of Geophysical Research : Solid Earth*, 122(9):7111–7126.
- Huang, R., Sun, W., Ding, X., Zhao, Y., and Song, M. (2020). Effect of pressure on the kinetics of peridotite serpentinization. *Physics and Chemistry of Minerals*, 47(7):1–14.
- Incerpi, N., Martire, L., Manatschal, G., Bernasconi, S. M., Gerdes, A., Czuppon, G., Palcsu, L., Karner, G. D., Johnson, C. A., and Figueredo, P. H. (2020). Hydrothermal fluid flow associated to the extensional evolution of the adriatic rifted margin : Insights from the pre-to post-rift sedimentary sequence (se switzerland, n italy). *Basin Research*, 32(1):91–115.
- Jackson, J. A. (1987). Active normal faulting and crustal extension. *Geological Society, London, Special Publications*, 28:3–17.
- Jamieson, J. W. and Gartman, A. (2020). Defining active, inactive, and extinct seafloor massive sulfide deposits. *Marine Policy*, 117:103926.
- Janecky, D. and Seyfried, W. (1986). Hydrothermal serpentinization of peridotite within the oceanic crust : Experimental investigations of mineralogy and major element chemistry. *Geochimica et Cosmochimica Acta*, 50(7):1357–1378.
- Johnson, D. E. (2019). Protecting the lost city hydrothermal vent system : All is not lost, or is it ? *Marine Policy*, 107:103593.
- Kelley, D. S., Karson, J. A., Blackman, D. K., Früh-Green, G. L., Butterfield, D. A., Lilley, M. D., Olson, E. J., Schrenk, M. O., Roe, K. K., Lebon, G. T., et al. (2001). An off-axis hydrothermal vent field near the mid-atlantic ridge at 30° n. *Nature*, 412(6843):145–149.
- Kerrick, D. (2002). Serpentinite seduction. *Science*, 298(5597):1344–1345.
- Klein, F., Bach, W., Jöns, N., McCollom, T., Moskowitz, B., and Berquo, T. (2009). Iron partitioning and hydrogen generation during serpentinization of abyssal peridotites from 15° n on the mid-atlantic ridge. *Geochimica et Cosmochimica Acta*, 73(22):6868–6893.
- Klein, F., Bach, W., and McCollom, T. M. (2013). Compositional controls on hydrogen generation during serpentinization of ultramafic rocks. *Lithos*, 178:55–69.
- Klein, F., Grozeva, N. G., Seewald, J. S., McCollom, T. M., Humphris, S. E., Moskowitz, B., Berquo, T. S., and Kahl, W.-A. (2015). Experimental constraints on fluid-rock reactions during incipient serpentinization of harzburgite. *American Mineralogist*, 100(4):991–1002.

- Klein, F. and McCollom, T. M. (2013). From serpentinization to carbonation : new insights from a co₂ injection experiment. *Earth and Planetary Science Letters*, 379:137–145.
- Klein, F. and Roux, V. L. (2020). Quantifying the volume increase and chemical exchange during serpentinization. *Geology*, 48:552–556.
- Lafay, R., Baumgartner, L. P., Stephane, S., Suzanne, P., German, M.-H., and Torsten, V. (2017). Petrologic and stable isotopic studies of a fossil hydrothermal system in ultramafic environment (chenaillet ophicalcites, western alps, france) : processes of carbonate cementation. *Lithos*, 294:319–338.
- Lafay, R., Montes-Hernandez, G., Janots, E., Chiriac, R., Findling, N., and Toche, F. (2012). Mineral replacement rate of olivine by chrysotile and brucite under high alkaline conditions. *Journal of Crystal Growth*, 347(1):62–72.
- Lamadrid, H., Zajacz, Z., Klein, F., and Bodnar, R. (2021). Synthetic fluid inclusions xxiii. effect of temperature and fluid composition on rates of serpentinization of olivine. *Geochimica et Cosmochimica Acta*, 292:285–308.
- Lamadrid, H. M., Rimstidt, J. D., Schwarzenbach, E. M., Klein, F., Ulrich, S., Dolocan, A., and Bodnar, R. J. (2017). Effect of water activity on rates of serpentinization of olivine. *Nature Communications*, 8(1):1–9.
- Li, Y.-H. (1982). A brief discussion on the mean oceanic residence time of elements. *Geochimica et Cosmochimica Acta*, 46(12):2671–2675.
- Liu, P.-P., Liang, J., Dick, H. J., Li, X.-H., Chen, Q., Zuo, H.-Y., and Wu, J.-C. (2020). Enormous lithium isotopic variations of abyssal peridotites reveal fast cooling and melt/fluid-rock interactions. *Journal of Geophysical Research : Solid Earth*, 125(9):e2020JB020393.
- Malvoisin, B., Brunet, F., Carlut, J., Rouméjon, S., and Cannat, M. (2012a). Serpentinization of oceanic peridotites : 2. kinetics and processes of san carlos olivine hydrothermal alteration. *Journal of Geophysical Research : Solid Earth*, 117(B4).
- Malvoisin, B., Carlut, J., and Brunet, F. (2012b). Serpentinization of oceanic peridotites : 1. a high-sensitivity method to monitor magnetite production in hydrothermal experiments. *Journal of Geophysical Research : Solid Earth*, 117(B1).
- Manatschal, G. (2004). New models for evolution of magma-poor rifted margins based on a review of data and concepts from west iberia and the alps. *International Journal of Earth Sciences*, 93:432–466.
- Manatschal, G., Chenin, P., Ghienne, J.-F., Ribes, C., and Masini, E. (2022). The syn-rift tectono-stratigraphic record of rifted margins (part i) : Insights from the alpine tethys. *Basin Research*, 34(1):457–488.
- Manatschal, G., Engström, A., Desmurs, L., Schaltegger, U., Cosca, M., Müntener, O., and Bernoulli, D. (2006). What is the tectono-metamorphic evolution of continental break-up : the example of the tasna ocean–continent transition. *Journal of Structural Geology*, 28(10):1849–1869.
- Manatschal, G. and Müntener, O. (2009). A type sequence across an ancient magma-poor ocean–continent transition : the example of the western alpine tethys ophiolites. *Tectonophysics*, 473(1-2):4–19.

- Manatschal, G., Müntener, O., Lavier, L., Minshull, T., and Péron-Pinvidic, G. (2007). Observations from the alpine tethys and iberia–newfoundland margins pertinent to the interpretation of continental breakup. *Geological Society, London, Special Publications*, 282(1):291–324.
- Manatschal, G. and Nievergelt, P. (1997). A continent-ocean transition recorded in the err and platta nappes (eastern switzerland). *Eclogae Geologicae Helvetiae*, 90(1):3–28.
- Marcaillou, C., Munoz, M., Vidal, O., Parra, T., and Harfouche, M. (2011). Mineralogical evidence for h2 degassing during serpentization at 300 c/300 bar. *Earth and Planetary Science Letters*, 303(3-4):281–290.
- Marschall, H. R. (2018). Boron isotopes in the ocean floor realm and the mantle. *Boron isotopes*, pages 189–215.
- Marschall, H. R., Wanless, V. D., Shimizu, N., Von Strandmann, P. A. P., Elliott, T., and Monteleone, B. D. (2017). The boron and lithium isotopic composition of mid-ocean ridge basalts and the mantle. *Geochimica et Cosmochimica Acta*, 207:102–138.
- Marshall, E. W., Barnes, J. D., and Lassiter, J. C. (2017). The role of serpentinite-derived fluids in metasomatism of the colorado plateau (usa) lithospheric mantle. *Geology*, 45(12):1103–1106.
- Martin, B. and Fyfe, W. (1970). Some experimental and theoretical observations on the kinetics of hydration reactions with particular reference to serpentization. *Chemical Geology*, 6:185–202.
- McCaig, A. M., Titarenko, S. S., Savov, I. P., Cliff, R. A., Banks, D., Boyce, A., and Agostini, S. (2018). No significant boron in the hydrated mantle of most subducting slabs. *Nature communications*, 9(1):1–10.
- McCollom, T. M., Klein, F., Moskowitz, B., Berquó, T. S., Bach, W., and Templeton, A. S. (2020a). Hydrogen generation and iron partitioning during experimental serpentization of an olivine–pyroxene mixture. *Geochimica et Cosmochimica Acta*, 282:55–75.
- McCollom, T. M., Klein, F., Robbins, M., Moskowitz, B., Berquó, T. S., Jöns, N., Bach, W., and Templeton, A. (2016). Temperature trends for reaction rates, hydrogen generation, and partitioning of iron during experimental serpentization of olivine. *Geochimica et Cosmochimica Acta*, 181:175–200.
- McCollom, T. M., Klein, F., Solheid, P., and Moskowitz, B. (2020b). The effect of ph on rates of reaction and hydrogen generation during serpentization. *Philosophical Transactions of the Royal Society A*, 378(2165):20180428.
- McCollom, T. M. and Seewald, J. S. (2007). Abiotic synthesis of organic compounds in deep-sea hydrothermal environments. *Chemical reviews*, 107(2):382–401.
- Mcculloch, M. T., Gregory, R. T., Wasserburg, G. J., and Taylor, H. P. (1980). A neodymium, strontium, and oxygen isotopic study of the cretaceous samail ophiolite and implications for the petrogenesis and seawater-hydrothermal alteration of oceanic crust. *Earth and Planetary Science Letters*, 46:201.
- Mellini, M., Trommsdorff, V., and Compagnoni, R. (1987). Antigorite polysomatism : behaviour during progressive metamorphism. *Contributions to Mineralogy and Petrology*, 97(2):147–155.

- Mével, C. (2003). Serpentization of abyssal peridotites at mid-ocean ridges. *Comptes Rendus Geoscience*, 335(10-11):825–852.
- Miller, H. M., Matter, J. M., Kelemen, P., Ellison, E. T., Conrad, M. E., Fierer, N., Ruchala, T., Tominaga, M., and Templeton, A. S. (2016). Modern water/rock reactions in oman hyperalkaline peridotite aquifers and implications for microbial habitability. *Geochimica et Cosmochimica Acta*, 179:217–241.
- Millot, R., Scaillet, B., and Sanjuan, B. (2010). Lithium isotopes in island arc geothermal systems : Guadeloupe, martinique (french west indies) and experimental approach. *Geochimica et Cosmochimica Acta*, 74(6):1852–1871.
- Mohn, G., Manatschal, G., Beltrando, M., Masini, E., and Kusznir, N. (2012). Necking of continental crust in magma-poor rifted margins : Evidence from the fossil alpine tethys margins. *Tectonics*, 31(1).
- Moody, J. B. (1976). Serpentization : a review. *Lithos*, 9(2):125–138.
- Müntener, O., Manatschal, G., Desmurs, L., and Pettke, T. (2010). Plagioclase peridotites in ocean-continent transitions : refertilized mantle domains generated by melt stagnation in the shallow mantle lithosphere. *Journal of Petrology*, 51(1-2):255–294.
- Müntener, O., Pettke, T., Desmurs, L., Meier, M., and Schaltegger, U. (2004). Refertilization of mantle peridotite in embryonic ocean basins : trace element and nd isotopic evidence and implications for crust–mantle relationships. *Earth and Planetary Science Letters*, 221(1-4):293–308.
- Müntener, O. and Piccardo, G. B. (2004). Melt migration in ophiolitic peridotites : The message from alpine-apennine peridotites and implications for embryonic ocean basins. *Geological Society Special Publication*, 218:69–89.
- Nakatani, T. and Nakamura, M. (2016). Experimental constraints on the serpentization rate of fore-arc peridotites : Implications for the upwelling condition of the slab-derived fluid. *Geochemistry, Geophysics, Geosystems*, 17(8):3393–3419.
- Nast, H. J. and Williams-Jones, A. E. (1991). The role of water-rock interaction and fluid evolution in forming the porphyry-related sisson brook w-cu-mo deposit, new brunswick. *Economic Geology*, 86(2):302–317.
- O'Hanley, D. S. (1992). Solution to the volume problem in serpentization. *Geology*, 20(8):705–708.
- O'Hanley, D. S. and Dyar, M. D. (1993). The composition of lizardite 1t and the formation of magnetite in serpentinites. *American Mineralogist*, 78(3-4):391–404.
- Osselin, F., Pichavant, M., Champallier, R., Ulrich, M., and Raimbourg, H. (2022). Reactive transport experiments of coupled carbonation and serpentization in a natural serpentinite. implication for hydrogen production and carbon geological storage. *Geochimica et Cosmochimica Acta*, 318:165–189.
- Page, N. J. (1968). Chemical differences among the serpentine “polymorphs”. *American Mineralogist : Journal of Earth and Planetary Materials*, 53(1-2):201–215.
- Patten, C. G., Coltat, R., Junge, M., Peillod, A., Ulrich, M., Manatschal, G., and Kolb, J. (2021). Ultramafic-hosted volcanogenic massive sulfide deposits : an overlooked sub-class of vms deposit forming in complex tectonic environments. *Earth-Science Reviews*, page 103891.

- Pens, M., Andreani, M., Daniel, I., Perrillat, J.-P., and Cardon, H. (2016). Contrasted effect of aluminum on the serpentinization rate of olivine and orthopyroxene under hydrothermal conditions. *Chemical Geology*, 441:256–264.
- Pérez-Gussinyé, M. and Reston, T. J. (2001). Rheological evolution during extension at nonvolcanic rifted margins : Onset of serpentinization and development of detachments leading to continental breakup. *Journal of Geophysical Research : Solid Earth*, 106(B3):3961–3975.
- Peters, P. C. and Mathews, J. (1963). Gravitational radiation from point masses in a keplerian orbit. *Physical Review*, 131(1):435.
- Peters, T. and Stettler, A. (1987a). Radiometric age, thermobarometry and mode of emplacement of the totalp peridotite in the eastern swiss alps. *Schweizerische Mineralogische und Petrographische Mitteilungen*, 67(3):285–294.
- Peters, T. and Stettler, A. (1987b). Time, physico-chemical conditions, mode of emplacement and geologic setting of the totalp peridotite in the eastern swiss alps. *Schweiz. Mineral. Petrogr. Mitt*, 67:285–294.
- Picazo, S., Manatschal, G., Cannat, M., and Andréani, M. (2013). Deformation associated to exhumation of serpentized mantle rocks in a fossil Ocean Continent Transition : The Totalp unit in SE Switzerland). *Lithos*, 175:255–271.
- Picazo, S., Müntener, O., Manatschal, G., Bauville, A., Karner, G., and Johnson, C. (2016). Mapping the nature of mantle domains in Western and OCentral Europe based on clinopyroxene and spinel chemistry : Evidence for mantle modification during an extensional cycle. *Lithos*, 266:233–263.
- Pinto, V. H. G., Manatschal, G., Karpoff, A. M., Ulrich, M., and Viana, A. R. (2017). Seawater storage and element transfer associated with mantle serpentinization in magma-poor rifted margins : A quantitative approach. *Earth and Planetary Science Letters*, 459:227–237.
- Pinto, V. H. G., Manatschal, G., Karpoff, A. M., and Viana, A. (2015). Tracing mantle-reacted fluids in magma-poor rifted margins : The example of a lpine t ethyan rifted margins. *Geochemistry, Geophysics, Geosystems*, 16(9):3271–3308.
- Proskurowski, G., Lilley, M. D., Kelley, D. S., and Olson, E. J. (2006). Low temperature volatile production at the lost city hydrothermal field, evidence from a hydrogen stable isotope geothermometer. *Chemical Geology*, 229(4):331–343.
- Proskurowski, G., Lilley, M. D., Seewald, J. S., Fruh-Green, G. L., Olson, E. J., Lupton, J. E., Sylva, S. P., and Kelley, D. S. (2008). Abiogenic hydrocarbon production at lost city hydrothermal field. *Science*, 319(5863):604–607.
- Ramsay, J. G. (1980). The crack–seal mechanism of rock deformation. *Nature*, 284(5752):135–139.
- Ranero, C. R., Phipps Morgan, J., McIntosh, K., and Reichert, C. (2003). Bending-related faulting and mantle serpentinization at the middle america trench. *Nature*, 425(6956):367–373.
- Ribeiro Da Costa, I., Barriga, F. J., Viti, C., Mellini, M., and Wicks, F. J. (2008). Antigorite in deformed serpentinites from the mid-atlantic ridge. *European Journal of Mineralogy*, 20(4):563–572.

- Ribes, C., Petri, B., Ghienne, J.-F., Manatschal, G., Galster, F., Karner, G. D., Figueredo, P. H., Johnson, C. A., and Karpoff, A.-M. (2020). Tectono-sedimentary evolution of a fossil ocean-continent transition : Tasna nappe, central alps (se switzerland). *Bulletin*, 132(7-8):1427–1446.
- Rona, P. A. (1984). Hydrothermal activity at the trans-atlantic geotraverse hydrothermal field, mid-atlantic ridge crest at 26°N. *Journal of Geophysical Research*, 89:11365–11377.
- Rona, P. A., Hannington, M. D., Raman, C., Thompson, G., Tivey, M. K., Humphris, S. E., Lalou, C., and Petersen, S. (1993). Active and relict sea-floor hydrothermal mineralization at the TAG hydrothermal field, Mid-Atlantic Ridge. *Economic Geology*, 88(8):1989–2017.
- Rouméjon, S. and Cannat, M. (2014). Serpentinitization of mantle-derived peridotites at mid-ocean ridges : Mesh texture development in the context of tectonic exhumation. *Geochemistry, Geophysics, Geosystems*, 15(6):2354–2379.
- Roumejon, S., Cannat, M., Agrinier, P., Godard, M., and Andreani, M. (2015). Serpentinitization and fluid pathways in tectonically exhumed peridotites from the southwest indian ridge (62–65 e). *Journal of Petrology*, 56(4):703–734.
- Rouxel, O., Fouquet, Y., and Ludden, J. N. (2004a). Copper isotope systematics of the lucky strike, rainbow, and logatchev sea-floor hydrothermal fields on the Mid-Atlantic Ridge. *Economic Geology*, 99:585–600.
- Rouxel, O., Fouquet, Y., and Ludden, J. N. (2004b). Subsurface processes at the lucky strike hydrothermal field, Mid-Atlantic Ridge : Evidence from sulfur, selenium, and iron isotopes. *Geochimica et Cosmochimica Acta*, 68:2295–2311.
- Russell, M., Hall, A., and Martin, W. (2010). Serpentinitization as a source of energy at the origin of life. *Geobiology*, 8(5):355–371.
- Saccoccia, P. J., Seewald, J. S., and Shanks III, W. C. (2009). Oxygen and hydrogen isotope fractionation in serpentine–water and talc–water systems from 250 to 450 c, 50 mpa. *Geochimica et Cosmochimica Acta*, 73(22):6789–6804.
- Salters, V. J. and Stracke, A. (2004). Composition of the depleted mantle. *Geochemistry, Geophysics, Geosystems*, 5(5).
- Schaltegger, U., Desmurs, L., Manatschal, G., Müntener, O., Meier, M., Frank, M., and Bernoulli, D. (2002). The transition from rifting to sea-floor spreading within a magma-poor rifted margin : Field and isotopic constraints. *Terra Nova*, 14(3):156–162.
- Schwarzenbach, E. M., Früh-Green, G. L., Bernasconi, S. M., Alt, J. C., Shanks III, W. C., Gaggero, L., and Crispini, L. (2012). Sulfur geochemistry of peridotite-hosted hydrothermal systems : comparing the ligurian ophiolites with oceanic serpentinites. *Geochimica et Cosmochimica Acta*, 91:283–305.
- Schwarzenbach, E. M., Vogel, M., Früh-Green, G. L., and Boschi, C. (2021). Serpentinitization, Carbonation, and Metasomatism of Ultramafic Sequences in the northern Apennine Ophiolite (NW Italy). *Journal of Geophysical Research : Solid Earth*, 126.
- Seyfried Jr, W. (1987). Experimental and theoretical constraints on hydrothermal alteration processes at mid-ocean ridges. *Annual Review of Earth and Planetary Sciences*, 15(1):317–335.

- Seyfried Jr, W. and Dibble Jr, W. (1980). Seawater-peridotite interaction at 300 °C and 500 bars : implications for the origin of oceanic serpentinites. *Geochimica et Cosmochimica Acta*, 44(2):309–321.
- Seyfried Jr, W., Foustaoukos, D., and Fu, Q. (2007). Redox evolution and mass transfer during serpentinization : An experimental and theoretical study at 200 °C, 500 bar with implications for ultramafic-hosted hydrothermal systems at mid-ocean ridges. *Geochimica et Cosmochimica Acta*, 71(15):3872–3886.
- Shanks, W., Boehlke, J. K., Seal, R., et al. (1995). Stable isotopes in mid-ocean ridge hydrothermal systems : Interactions between fluids, minerals, and organisms. *Geophysical Monograph-American Geophysical Union*, 91:194–194.
- Skelton, A. D. and Valley, J. W. (2000). The relative timing of serpentinisation and mantle exhumation at the ocean-continent transition, Iberia : constraints from oxygen isotopes. *Earth and Planetary Science Letters*, 178(3-4):327–338.
- Snow, J. E. and Dick, H. J. (1995). Pervasive magnesium loss by marine weathering of peridotite. *Geochimica et Cosmochimica Acta*, 59(20):4219–4235.
- Snow, J. E., Hart, S. R., and Dick, H. J. (1994). Nd and Sr isotope evidence linking mid-ocean-ridge basalts and abyssal peridotites. *Nature*, 371(6492):57–60.
- Spivack, A. and Edmond, J. (1987). Boron isotope exchange between seawater and the oceanic crust. *Geochimica et Cosmochimica Acta*, 51(5):1033–1043.
- Spivack, A., Palmer, M., and Edmond, J. (1987). The sedimentary cycle of the boron isotopes. *Geochimica et Cosmochimica Acta*, 51(7):1939–1949.
- Spooner, E., Chapman, H., and Smewing, J. (1977). Strontium isotopic contamination and oxidation during ocean floor hydrothermal metamorphism of the ophiolitic rocks of the Troodos Massif, Cyprus. *Geochimica et Cosmochimica Acta*, 41(7):873–890.
- Spooner, E. T. C. and Fyfe, W. S. (1973). Sub-sea-floor metamorphism, heat and mass transfer. *Contr. Mineral. and Petrol.*, 42:287–304.
- Staudigel, H., Davies, G., Hart, S. R., Marchant, K., and Smith, B. M. (1995). Large scale isotopic Sr, Nd and O isotopic anatomy of altered oceanic crust : DSDP/ODP sites 417/418. *Earth and Planetary Science Letters*, 130(1-4):169–185.
- Tarling, M. S., Rooney, J. S., Viti, C., Smith, S. A., and Gordon, K. C. (2018). Distinguishing the Raman spectrum of polygonal serpentine. *Journal of Raman Spectroscopy*, 49(12):1978–1984.
- Thompson, G. and Melson, W. G. (1970). Boron contents of serpentinites and metabasalts in the oceanic crust : implications for the boron cycle in the oceans. *Earth and Planetary Science Letters*, 8(1):61–65.
- Tichadou, C. (2021). *Etude des processus de serpentinisation et de production d'hydrogène dans la zone Nord-Pyrénéenne occidentale : du terrain à la caractérisation expérimentale*. PhD thesis, Université Montpellier.
- Tomascak, P. B., Langmuir, C. H., le Roux, P. J., and Shirey, S. B. (2008). Lithium isotopes in global mid-ocean ridge basalts. *Geochimica et Cosmochimica Acta*, 72(6):1626–1637.
- Trommsdorff, V. (1983). Metamorphose magnesiumreicher gesteine : kristallitischer Vergleich von Natur, Experiment und thermodynamischer Datenbasis. *Fortschritte der Mineralogie*, 61(2):283–308.

- Trommsdorff, V. and Evans, B. W. (1977). Antigorite-ophicarbonates : contact metamorphism in valmalenco, italy. *Contributions to Mineralogy and Petrology*, 62(3):301–312.
- Tutolo, B. M., Luhmann, A. J., Tosca, N. J., and Seyfried Jr, W. E. (2018). Serpentinization as a reactive transport process : The brucite silicification reaction. *Earth and Planetary Science Letters*, 484:385–395.
- Ulrich, M., Muñoz, M., Boulvais, P., Cathelineau, M., Cluzel, D., Guillot, S., and Picard, C. (2020). Serpentinization of new caledonia peridotites : from depth to (sub-) surface. *Contributions to Mineralogy and Petrology*, 175(9):1–25.
- Veizer, J. and Compston, W. (1974). $^{87}\text{Sr}/^{86}\text{Sr}$ composition of seawater during the phanerozoic. *Geochimica et Cosmochimica Acta*, 38.
- Vils, F., Pelletier, L., Kalt, A., Müntener, O., and Ludwig, T. (2008). The lithium, boron and beryllium content of serpentinized peridotites from odp leg 209 (sites 1272a and 1274a) : implications for lithium and boron budgets of oceanic lithosphere. *Geochimica et Cosmochimica Acta*, 72(22):5475–5504.
- Vils, F., Tonarini, S., Kalt, A., and Seitz, H.-M. (2009). Boron, lithium and strontium isotopes as tracers of seawater–serpentinite interaction at mid-atlantic ridge, odp leg 209. *Earth and Planetary Science Letters*, 286(3-4):414–425.
- Viti, C. and Mellini, M. (1998). Mesh textures and bastites in the elba retrograde serpentinites. *Eur. J. Mineral*, 10:1341–1359.
- Wegner, W. W., Ernst, W., et al. (1983). Experimentally determined hydration and de-hydration reaction rates in the system mgo-sio₂-h₂o. *American Journal of Science*, 283:151–180.
- Weissert, B. J. H. and Bernoulli, D. (1985). A transform margin in the Mesozoic Tethys : evidence from the Swiss Alps. *Geologische Rundschau*, 74:665–679.
- Weissert, H. and Bernoulli, D. (1984). Oxygen isotope composition of calcite in alpine ophicarbonates : a hydrothermal or alpine metamorphic signal ? *Eclogae Geologicae Helvetiae*, 77(1):29–43.
- Wenner, D. B. and Taylor, H. P. (1971). Temperatures of serpentinization of ultramafic rocks based on o₁₈/o₁₆ fractionation between coexisting serpentine and magnetite. *Contributions to mineralogy and petrology*, 32(3):165–185.
- Wenner, D. B. and Taylor Jr, H. P. (1973). Oxygen and hydrogen isotope studies of the serpentinization of ultramafic rocks in oceanic environments and continental ophiolite complexes. *American Journal of Science*, 273(3):207–239.
- Whittaker, E. and Zussman, J. (1956). The characterization of serpentine minerals by x-ray diffraction. *Mineralogical magazine and journal of the Mineralogical Society*, 31(233):107–126.
- Wicks, F., Whittaker, E., and Zussman, J. (1977). An idealized model for serpentine textures after olivine. *The Canadian Mineralogist*, 15(4):446–458.
- Wicks, F. and Zussman, J. (1975). Microbeam x-ray diffraction patterns of the serpentine minerals. *The Canadian Mineralogist*, 13(3):244–258.
- Wicks, F. J. and O'Hanley, D. S. (2018). Serpentine minerals : structures and petrology. In *Hydrous phyllosilicates*, pages 91–168. De Gruyter.

Wicks, F. J. and Whittaker, E. (1975). A reappraisal of the structures of the serpentine minerals. *The Canadian Mineralogist*, 13(3):227–243.

Wunder, B., Wirth, R., and Gottschalk, M. (2001). Antigorite : Pressure and temperature dependence of polysomatism and water content. *European Journal of Mineralogy*, 13(3):485–496.